



**UNIVERSITÉ
DE GENÈVE**

UNIVERSITÉ DE GENÈVE

Département d'Informatique

FACULTÉ DES SCIENCES

Pr S. Voloshynovskiy

Département de Radiologie et
Informatique Médicale

FACULTÉ DE MÉDECINE

PD H. Zaidi

Development of image reconstruction and correction techniques in PET/CT and PET/MR imaging

THÈSE

présentée à la Faculté des sciences de l'Université de Genève
pour obtenir le grade de Docteur ès sciences, mention interdisciplinaire

par

Abolfazl Mehranian

de

Kashan, Iran

Thèse N° 4780

GENÈVE

Service de reprographie de l'Uni Mail

2015



**UNIVERSITÉ
DE GENÈVE**

FACULTÉ DES SCIENCES

**Doctorat ès sciences
Mention interdisciplinaire**

Thèse de **Monsieur Abolfazl MEHRANIAN**

intitulée :

**"Development of Image Reconstruction and Correction
Techniques in PET-CT and PET-MR Imaging"**

La Faculté des sciences, sur le préavis de Monsieur S. VOLOSHYNOVSKYY, professeur associé et directeur de thèse (Département d'informatique), Monsieur H. ZAIDI, docteur et codirecteur de thèse (Faculté de Médecine, Département de radiologie et informatique médicale), Madame M. BECKER, professeure associée (Faculté de Médecine, Département de radiologie et informatique médicale), Monsieur O. RATIB, professeur ordinaire (Faculté de Médecine, Département de radiologie et informatique médicale), Monsieur J.-P. THIRAN, professeur associé (Ecole Polytechnique Fédérale de Lausanne, Signal Processing Laboratory 5, Lausanne), Monsieur F. BEEKMAN, professeur (Delft University of Technology, Section Radiation, Detection & Medical Imaging, Delft, Netherlands) et Monsieur J. NUYS, professeur (University of Leuven, Nuclear Medicine and Medical Imaging Research Center, Leuven, Belgium), autorise l'impression de la présente thèse, sans exprimer d'opinion sur les propositions qui y sont énoncées.

Genève, le 13 mai 2015

Thèse - 4780 -

Le Doyen

Summary

Positron emission tomography (PET) is one of the leading molecular imaging techniques for the non-invasive detection and quantitative assessment of a variety of biochemical processes associated with neoplasms and physiopathological conditions. Following injection of a positron-emitting radiotracer to the patient, the PET scanner measures the biodistribution and kinetics of the administered radiopharmaceutical. However, this modality does not provide the anatomical information necessary for localization of metabolically active lesions. This has motivated the combination of PET with anatomical imaging modalities such as x-ray computed tomography (CT) and magnetic resonance imaging (MRI). The advent of hybrid PET/CT and PET/MRI systems and their introduction in clinical practice has tremendously improved the diagnostic confidence of PET findings. Specifically, the additional information provided by CT and MRI can be exploited for PET image reconstruction and data correction. In PET/CT, CT images can be directly converted to 511-keV attenuation maps for attenuation correction of PET data, eliminating the lengthy transmission scans required on stand-alone PET scanners. In PET/MRI, MR images provide a superior soft tissue contrast than CT which not only improves lesion localization but can also be employed for anatomically-guided partial volume correction and PET image reconstruction. Moreover, in simultaneous PET/MRI, MRI can provide the motion information required for motion correction of the PET data and also improve in-plane PET image resolution by restricting positron range in the magnetic field. Despite the fact that CT and MRI maximize the potential of PET imaging, the integration of these imaging modalities into hybrid imaging systems present some limitations and technical challenges that can adversely affect PET quantification or restrict their applications. CT images of patients having metallic implants usually suffer from dark and bright streaking artifacts that not only impair the diagnostic quality of CT images but also induce pseudo uptakes in PET images through CT-based attenuation correction of PET data and thus can lead to missed or equivocal findings. Attenuation correction in PET/MRI is more challenging, since MRI does not provide sufficient information about the attenuation characteristics of different biological tissues and in contrary to CT, MR images cannot be directly converted to PET attenuation maps. Moreover, MRI data acquisition is time-consuming, limiting the acquisition of complementary MR sequences.

The work presented in this dissertation focuses on addressing some of the prevalent challenges encountered in PET/CT and PET/MRI image reconstruction and correction through further development of current state-of-the-art techniques and the investigation and validation of new algorithms. In particular, robust algorithms were developed for CT metal artifact reduction, anatomically guided PET image reconstruction, compressed sensing MR image reconstruction and MRI-guided emission-based estimation of PET attenuation map for time-of-flight (TOF) PET/MRI.

Two efficient metal artifact reduction (MAR) algorithms were developed for recovery of the projection data (sinograms) corrupted by metallic implants using sparsity regularization techniques and the prior information obtained from tissue classification of the original uncorrected CT images. In the first algorithm, the recovery of missing projections was formulated as a regularized inverse problem in the wavelet domain, with the objective of reconstructing the wavelet coefficients of the target sinogram using an L_0 sparsity-promoting prior and the detail wavelet coefficients obtained from a prior CT sinogram. In the second algorithm, the concept of subtraction sparsification was used to best exploit the information obtained from a tissue-classified prior CT image with the aim of recovering the missing projection data in 3D multi-slice or cone-beam CT. In this algorithm, a prior function was designed to exploit and promote the sparsity of a residual sinogram obtained from the subtraction of the unknown target sinogram from the projection dataset of a prior CT image. The performance of both proposed algorithms was evaluated against the standard linear interpolation and the state-of-the-art normalized metal artifact reduction (NMAR) algorithms using simulation and clinical studies with different metallic implants. In a comprehensive simulation and clinical study, the performance of the proposed 3D MAR algorithm along with four different MAR algorithms was evaluated for the reduction of the artifacts induced by uni- or bilateral hip prostheses. The results showed that the proposed algorithms effectively reduce metal artifacts without introducing new artifacts owing to more accurate utilization of prior information in comparison with its state-of-the-art counterparts.

The incorporation of edge-preserving and anatomical prior into iterative PET image reconstruction algorithms can promote the preservation of organ boundaries while reducing noise, which has a great potential in PET/MRI. However, the resulting image reconstruction problem either is not amenable to optimization or suffers

from slow convergence using the existing optimization algorithms. In this thesis, we proposed an accelerated optimization algorithm for the penalized weighted least-squares reconstruction of PET data. The proposed splitting-based preconditioned gradient algorithm was accelerated by ordered-subsets and step size optimization and benchmarked against the separable paraboloidal surrogates accelerated with ordered-subsets algorithm. It was demonstrated that the proposed algorithm achieves a considerable improved convergence rate over its counterpart and therefore allows for the incorporation of CT or MRI anatomical boundary information into the reconstruction process without compromising the convergence rate.

MRI often suffers from long data acquisition time, which impedes the acquisition of supplementary functional, motion-tracking or ultra-short echo time scans in simultaneous PET/MRI. Emerging trends for scan time reduction focus on partial Fourier and parallel MRI, which are based on the undersampling of k -space. Along this line, compressed sensing (CS) provides a promising framework for MR image reconstruction from highly undersampled data, thereby improving signal-to-noise ratio in the reconstructed images. In this dissertation, a new sparsity-promoting prior was applied for CS-MR image reconstruction through iterative linearization of the non-convex smoothly clipped absolute deviation (SCAD) norm with the aim of reducing the k -space sampling rate lower than what is required by the conventional L_1 norm. The optimization problem was solved using a variable splitting and augmented Lagrangian methods for discrete gradients and wavelet sparsifying transforms. The results showed that the linearization of SCAD results in an iteratively reweighted L_1 norm, which reduces aliasing artifacts and therefore improves image quality.

In TOF PET/MRI systems, TOF technology offers great capabilities for improving image quality and lesion detectability or reducing the scan time or the administered dose of radiopharmaceuticals. It has been demonstrated that TOF-PET image reconstruction is less sensitive to inconsistencies between emission and correction data compared to non-TOF reconstruction. In this thesis, we conducted, for the first time, a clinical study for the evaluation of TOF image reconstruction on PET quantification errors induced by the standard MRI segmentation-based attenuation correction (MRAC). In the derived MRAC maps, the bone tissue class and inter/intra-patient variability of tissue attenuation maps are ignored, which along with metal susceptibility and respiratory-phase mismatch artifacts can lead to PET quantification errors. The results of this study were also supported with TOF PET simulations using different TOF timing resolutions. The results showed that TOF-PET substantially reduces artifacts and improves the quantitative accuracy of standard MRAC methods. Therefore, MRAC should be less of a concern on future TOF PET/MR scanners with improved timing resolution.

Accurate PET attenuation correction in quantitative PET/MRI examinations is of paramount importance. It has recently been shown that the attenuation map can be estimated from TOF PET emission data using maximum likelihood reconstruction of attenuation and activity (MLAA). However, theoretical and experimental studies have shown that attenuation information can be derived from emission data up to an unknown scale factor. Moreover, the performance of MLAA depends on TOF timing resolution, count level and activity distribution. In this thesis, the performance of the MLAA algorithm was improved by exploiting prior MR spatial and CT statistical information using a constrained Gaussian mixture model. The performance of the proposed algorithm was evaluated against current state-of-the-art MLAA algorithms using simulation, experimental and clinical studies for two different radiotracers. The results showed that our proposed algorithm can effectively exploit MR information, thereby outperforming its counterparts in suppressing the cross-talk and scaling problems of activity and attenuation and producing PET images of improved quantitative accuracy.

In standard 4- or 3-class MRAC methods on PET/MRI systems, the inter/intra-patient variability of linear attenuation coefficients (LACs) of tissue classes is ignored. This can lead to PET quantification errors, especially in the lung regions. In this thesis, we aimed to derive continuous and patient-specific lung LACs from TOF PET emission data using a simplified version of our proposed MLAA algorithm using clinical studies. In this algorithm, the lung LACs in the standard 4-class MR attenuation maps were estimated from emission data and using Gaussian lung tissue preference and Markov random field smoothness priors. The results show that our MLAA algorithm is capable of retrieving lung density gradients and compensate fairly for respiratory-phase mismatch between PET and corresponding attenuation maps and can therefore outperform the MRAC method for accurate PET quantification.

This dissertation engages an interdisciplinary approach involving biomedical instrumentation, medical physics and computational models and algorithms for molecular multi-modal imaging, justifying its categorization as an interdisciplinary dissertation.

Résumé

La tomographie par émission de positons (TEP) est l'une des techniques d'imagerie moléculaire de pointe permettant la détection non-invasive et l'évaluation quantitative d'une variété de procédés biochimiques associés à des tumeurs et à des conditions physiopathologiques. Après l'injection de produits radiopharmaceutiques au patient, la technique d'imagerie TEP mesure la biodistribution et la cinétique du radiopharmaceutique administré. Cependant, cette modalité ne fournit pas, à elle seule, l'information nécessaire pour la localisation anatomique de lésions métaboliquement actives. Ceci a motivé la combinaison du TEP avec des modalités d'imagerie anatomiques telles que la tomodensitométrie (TDM) et l'imagerie par résonance magnétique (IRM). L'avènement de l'imagerie hybride TEP/TDM et TEP/IRM dans la pratique clinique a énormément amélioré la fiabilité du diagnostic via l'imagerie TEP. Plus précisément, les informations supplémentaires fournies par la TDM et l'IRM peut être exploitée pour la reconstruction des images TEP ainsi que la correction des données d'émission. En imagerie TEP/TDM, les images TDM peuvent être directement converties en cartes d'atténuation à 511 keV pour la correction d'atténuation des images TEP, éliminant ainsi les longs scans de transmission requis en TEP conventionnelle. En TEP/IRM, les images IRM offrent un contraste des tissus mous supérieur à la TDM qui non seulement améliore la localisation de lésions mais peut aussi être utilisé pour la correction de l'effet de volume partiel et guider la reconstruction des images TEP. En outre, en imagerie TEP/IRM simultanée, l'IRM peut fournir les informations nécessaires sur le mouvement du patient pour la correction de mouvement et TEP améliorer la résolution des images TEP en limitant le parcours des positons dans le champ magnétique. Malgré le fait que la TDM et l'IRM permettant de maximiser le potentiel de l'imagerie TEP, ces modalités d'imagerie ont des limites et présentent des défis techniques qui peuvent desservir la quantification des données TEP ou restreindre son application en imagerie hybride. Les images TDM de patients ayant des implants métalliques présentent habituellement des artefacts visibles sombres et claires qui non seulement nuisent à la qualité diagnostique des images TDM mais aussi induisent des 'pseudos' hyperfixations sur les images TEP suite à la correction d'atténuation des données TEP basée sur la TDM, et peuvent ainsi induire des faux positifs ou conduire à des résultats équivoques. La correction d'atténuation au TEP/IRM est plus difficile, car l'IRM ne fournit pas suffisamment d'informations sur les caractéristiques des différents tissus biologiques en termes d'interaction rayonnement matière (atténuation), et contrairement au CT, les images IRM ne peuvent être directement converties en cartes d'atténuation. En outre, l'acquisition de données IRM est un processus fastidieux et coûteux, ce qui limite l'acquisition de différentes séquences IRM complémentaires.

Le travail présenté dans cette thèse vise à aborder certains des défis prévalents rencontrés en reconstruction et correction d'images en TEP/TDM et TEP/IRM grâce au développement et la validation de nouveaux algorithmes permettant un progrès au delà de l'état de l'art actuel. En particulier, des algorithmes robustes ont été développés pour la réduction d'artefacts métalliques des images TDM, la reconstruction d'images TEP guidée par l'imagerie anatomique, la reconstruction des images IRM utilisant le concept de 'Compressed Sensing' et l'estimation de cartes d'atténuation au TEP/IRM basée sur l'imagerie d'émission seule avec l'acquisition TEP en temps de vol (TOF) combinée avec l'imagerie IRM.

En l'occurrence, deux algorithmes efficaces pour la réduction d'artefacts métalliques (MAR) ont été développés pour compléter les projections (sinogramme) corrompues par les implants métalliques moyennant des techniques de régularisation exploitant l'information a priori provenant de la classification des tissus des images TDM avant correction. Dans le premier algorithme, le recouvrement des projections manquantes a été formulé comme un problème inverse régularisé dans le domaine des ondelettes, avec l'objectif de la reconstruction des coefficients d'ondelettes du sinogramme cible en utilisant les coefficients d'ondelettes L0 et le 'sparsity-promoting prior' obtenu à partir d'un 'prior' sinogramme CT. Dans le second algorithme, le concept de la soustraction sparsification a été utilisé pour exploiter au mieux les informations obtenues à partir d'une 'prior' image TDM classifiée dans le but de compléter les données de projection manquantes en imagerie TDM multi-coupes ou à faisceau conique. Dans cet algorithme (MAR 3D), une fonction préalable a été conçue pour exploiter et promouvoir la sparsité d'un sinogramme résiduel obtenu à partir de la soustraction du sinogramme cible inconnu des projections d'une 'prior' image TDM. Les performances des deux algorithmes proposés ont été évaluées en les confrontant aux algorithmes d'interpolation linéaire standard et la réduction d'artefact métallique normalisée (NMAR) en utilisant des simulations et des études cliniques avec différents implants métalliques. Dans une étude impliquant des simulations et études cliniques, la performance de l'algorithme MAR 3D proposé

a été comparée à quatre autres algorithmes différents en terme de réduction d'artefacts induits par des prothèses de hanche uni- ou bi-latéraux. Les résultats ont montré que les algorithmes proposés dans le cadre de cette thèse réduisent efficacement les artefacts produits par les objets métalliques sans introduire de nouveaux artefacts du à une utilisation plus précise de l'information à priori par rapport autres techniques proposés par d'autres groupes.

L'incorporation d'information à priori de préservation de bord et d'images anatomiques dans les algorithmes de itératives reconstruction d'images TEP peut promouvoir la préservation des limites d'organes tout en réduisant le bruit, ce qui présente un grand potentiel en imagerie hybride TEP/IRM. Cependant, le problème de reconstruction d'images soit ne se prête pas à l'optimisation ou souffre de convergence lente lorsque les algorithmes d'optimisation existants sont utilisées. Dans cette thèse, nous avons proposé un algorithme d'optimisation accéléré pour la reconstruction TEP utilisant une pénalisation des moindres carrés pondérés. L'algorithme de gradient préconditionné proposé, basé sur le fractionnement, a été accéléré par sous-ensembles ordonnés et optimisation de la taille de l'étape et leur comparabilité avec les substituts paraboloidales séparables accéléré avec sous-ensembles commandés algorithme. Il a été démontré que l'algorithme proposé permet une amélioration considérable du taux de convergence par rapport à son homologue et permet l'incorporation des informations TDM ou IRM anatomique dans le processus de reconstruction sans compromettre la vitesse de convergence.

L'IRM présente l'inconvénient de durée d'acquisition longue, ce qui entrave l'acquisition de séquences supplémentaires en imagerie simultanée TEP/IRM pour tracer le mouvement du patient, ou des séquences spécifique telles que 'ultra-short echo time' qui permet d'identifier les os. Les tendances actuelles visant à réduire le temps d'acquisition mettent l'accent sur le concept de Fourier partiel et l'IRM parallèle, qui sont basées sur le sous-échantillonnage de l'espace k . Parmi ces techniques, le concept de 'compressed sensing' (CS) fournit un cadre prometteur pour la reconstruction d'image IRM provenant de données hautement sous-échantillonnées, ce qui améliore le rapport signal-sur-bruit dans les images reconstruites. Dans cette thèse, un nouveau 'sparsity-promoting prior' a été appliqué pour la reconstruction CS-MR d'images grâce à la linéarisation itérative de la norme 'non-convex smoothly clipped absolute deviation (SCAD)' dans le but de réduire le taux d'échantillonnage dans l'espace k , qui est inférieur à ce qui est requis par la norme L1 classique. Le problème d'optimisation a été résolu en utilisant des méthodes de fractionnement variable et Lagrange augmentées pour des gradients discrets et transformées en ondelettes 'sparsifiantes'. Les résultats montrent que la linéarisation des résultats SCAD à une norme L1 itérativement repondérée réduit les 'aliasing' artefacts, et donc améliore la qualité de l'image.

Dans les systèmes TOF TEP/IRM, la technologie TOF offre une grande capacité pour améliorer la qualité des images et la détectabilité de lésions ou de réduire le temps d'acquisition ou la dose de produits radiopharmaceutiques administrée. Il a été démontré que la reconstruction TOF-TEP est moins sensible aux incohérences entre les données d'émission et de correction par rapport à la reconstruction non-TOF. Dans cette thèse, nous avons mené une première étude clinique pour l'évaluation des reconstructions TOF TEP sur les erreurs de quantification induites par la correction d'atténuation standard basée sur la segmentation des images IRM (MRAC). Dans les cartes MRAC, la classe de tissu osseux ainsi que la variabilité inter/intra-patient de coefficients d'atténuation des tissus sont ignorés, qui la avec les artefacts de susceptibilité et de respiration peuvent conduire à des erreurs de quantification TEP considérables. Les résultats de cette étude ont également été effectués moyennant des simulations TOF TEP de différentes résolutions temporelles TOF. Les résultats ont montré que le TOF-TEP permet de réduire sensiblement les artefacts et améliore la précision quantitative des méthodes MRAC standard. Par conséquent, la technique MRAC devrait poser moins de problèmes pour les futurs scanners TOF TEP/IRM ayant une meilleure résolution temporelle.

La correction d'atténuation en imagerie quantitative TEP/IRM est d'une importance primordiale. Il a été montré récemment que la carte d'atténuation peut être estimée à partir de données d'émission à l'aide de la reconstruction TEP TOF du maximum de vraisemblance de l'atténuation et de l'activité ('maximum likelihood reconstruction of attenuation and activity (MLAA)'). Cependant, des études théoriques et expérimentales ont montré que l'information sur l'atténuation peut être dérivée de données d'émission seules mais avec un facteur de calibration qui reste inconnu. De plus, la performance de MLAA dépend de la résolution temporelle TOF, les statistiques de comptage et de la distribution d'activité. Dans cette thèse, la performance de l'algorithme MLAA a été améliorée en exploitant l'information spatiale IRM et les informations statistiques TDM à priori en utilisant un modèle de mélange gaussien limité 'Gaussian mixture model (GMM)'. La performance de l'algorithme proposé a été évaluée en comparaison à des algorithmes MLAA proposées par d'autres groupes en utilisant des

simulations, études expérimentales et cliniques pour deux radiotraceurs différents. Les résultats ont montré que notre algorithme peut effectivement exploiter les informations MR, surpassant ainsi ses homologues dans la suppression de le ‘cross-talk’ entre l'activité et de l'atténuation et les problèmes du facteur d'échelle et produit ainsi des images TEP de meilleure précision quantitative.

Dans les méthodes MRAC standards 3- ou 4-classes implémentés sur les systèmes TEP/IRM, la variabilité inter/intra-patient des coefficients d'atténuation linéaires (CLA) de classes de tissus est ignorée. Cela peut conduire à des erreurs de quantification en TEP, en particulier dans les régions pulmonaires. Dans cette thèse, nous avons cherché à produire des CLA continues et spécifiques à chaque patient moyennant le TOF TEP en utilisant une version simplifiée de notre algorithme MLAA en utilisant 19 études de patients. Dans cet algorithme, les CLA pulmonaires dans les cartes standards d'atténuation 4-classe IRM ont été estimés à partir des données d'émission en utilisant ‘Gaussian lung tissue preference and Markov random field smoothness priors’. Les résultats montrent que notre algorithme MLAA est capable de recouvrer les gradients de densité pulmonaires et de compenser équitablement les décalages de phase respiratoires entre les images TEP et les cartes d'atténuation correspondantes, et peut donc présenter une meilleure performance comparé à la méthode MRAC.

Cette thèse engage une approche interdisciplinaire impliquant l'instrumentation biomédicale, physique médicale, des modèles mathématiques et des algorithmes d'imagerie multi-modale moléculaire, justifiant sa catégorisation comme une thèse interdisciplinaire.

To My Parents

Papers included in this dissertation

This dissertation is based on a number of studies reported in the following peer-reviewed original journal articles. Published articles are reprinted by the kind permission of the referred publisher.

1. **Mehranian A**, Ay MR, Rahmim A and Zaidi H "X-ray CT metal artifact reduction using wavelet domain L0 sparse regularization" *IEEE Trans Med Imaging* Vol. 32, No. 9, pp 1707-1722 (2013).
2. **Mehranian A**, Ay MR, Rahmim A and Zaidi H "3D prior image constrained projection completion for X-ray CT metal artifact reduction" *IEEE Trans Nucl Sci* Vol. 60, No. 5, pp 1-15 (2013).
3. Abdoli M, **Mehranian A**, Ailianou A, Becker M, and Zaidi H, "Comparative methods for hip prosthesis metal artifact reduction in pelvic CT" *Phys Med Biol* (2015) *under revision*
4. **Mehranian A**, Rahmim A, Ay MR, Kotasidis F and Zaidi H "An ordered-subsets proximal preconditioned gradient algorithm for edge-preserving PET image reconstruction" *Med Phys* Vol. 40, No. 5, pp 52503-14 (2013).
5. **Mehranian A**, Salighe Rad H, Ay MR, Rahmim A and Zaidi H "Smoothly clipped absolute deviation (SCAD) regularization for compressed sensing MRI using an augmented Lagrangian scheme" *Magn Reson Imaging*, Vol. 31, No. 8, pp 1399-1411 (2013).
6. **Mehranian A**, Arabi H, Zaidi H, "Magnetic resonance imaging-guided attenuation correction in PET/MRI: challenges, solutions and opportunities" *Med Phys* (2015) *submitted*
7. **Mehranian A** and Zaidi H "Impact of time-of-flight PET on quantification errors in MRI-based attenuation correction", *J Nucl Med* Vol. 56, No. 4, pp 635-641 (2015).
8. **Mehranian A** and Zaidi H "Joint estimation of activity and attenuation in whole-body TOF PET/MRI using constrained Gaussian mixture models" *IEEE Trans Med Imaging* (2015), *in press*
9. **Mehranian A** and Zaidi H "Emission-based estimation of lung attenuation coefficients for PET/MR attenuation correction", *Phys Med Biol* (2015) *in press*
10. **Mehranian A** and Zaidi H "Clinical assessment of emission- and segmentation-based MRI-guided attenuation correction in whole-body time-of-flight PET/MRI" *J Nucl Med*, Vol. 56, No.6, pp 877-883 (2015).

Contents

	<i>Summary</i>	iii
	<i>Résumé</i>	vi
	<i>Papers included in this thesis</i>	ix
Chapter 1	Introduction	2
	Aim and outline of thesis	5
Chapter 2	X-ray CT metal artifact reduction using wavelet domain L_0 sparse regularization <i>IEEE Trans Med Imaging 32(9), 1707-1722 (2013)</i>	9
Chapter 3	3D prior image constrained projection completion for x-ray CT metal artifact reduction <i>IEEE Trans Nucl Sci 60(5), 1-15 (2013)</i>	32
Chapter 4	Comparative methods for hip prosthesis metal artifact reduction in pelvic CT <i>Phys Med Biol (2015) under revision</i>	53
Chapter 5	An ordered-subsets proximal preconditioned gradient algorithm for edge-preserving PET image reconstruction <i>Med Phys, 40(5) 52503-14 (2013).</i>	67
Chapter 6	Smoothly clipped absolute deviation (SCAD) regularization for compressed sensing MRI using an augmented Lagrangian scheme <i>Magn Reson Imaging 31(8), 1399-1411 (2013)</i>	88
Chapter 7	Magnetic resonance imaging-guided attenuation correction in PET/MRI: challenges, solutions and opportunities <i>Med Phys (2015) submitted</i>	107
Chapter 8	Impact of time-of-flight PET on quantification errors in MR Imaging-based attenuation correction <i>J Nucl Med 56(4), 635-641 (2015)</i>	148
Chapter 9	Joint estimation of activity and attenuation in whole-body TOF PET/MRI using constrained Gaussian mixture models <i>IEEE Trans Med Imaging (2015) in press</i>	163
Chapter 10	Emission-based estimation of lung attenuation coefficients for attenuation correction in time-of-flight PET/MR <i>Phys Med Biol (2015) in press</i>	186
Chapter 11	Clinical assessment of emission- and segmentation-based MRI-guided attenuation correction in whole-body time-of-flight PET/MRI <i>J Nucl Med 56(6), 877-883 (2015)</i>	206
Chapter 12	Conclusions and future perspectives	222
	<i>Acknowledgements.</i>	227
	<i>Publication list.</i>	228

Chapter 1

Introduction

I. Introduction

The continuous technical advancements in biomedical research have led to the advent of molecular imaging techniques for the quantitative evaluation and monitoring of biological processes associated with various pathophysiological conditions and the development of new drugs and biomarkers for the early detection and treatment of life threatening diseases [1]. Radiotracers usually consist a direct radiolabeled version of a naturally occurring compound or an analog of a natural compound specifically designed to enter certain biochemical processes. Owing to its high sensitivity and good spatial resolution, PET imaging allows for the measurement of the picomolar concentrations of a wide range of tracers and molecules labeled with positron-emitting radionuclides. This imaging technique has therefore gained a widespread acceptance in clinical oncology for the staging and follow-up of metabolically active lesions, in neuroimaging for assessing neurodegenerative diseases and in cardiology for viability and myocardial perfusion studies, among others [2]. PET imaging provides information about the physiological distribution of the tracers in different organs and tissues. Depending on the characteristics of the tracer and targeted organs, this information might be spatially localized and therefore should be combined with high-resolution anatomical information provided by other imaging modalities, such as x-ray computed tomography (CT) and magnetic resonance imaging (MRI), to improve the diagnostic interpretation of PET images.

Currently, combined PET/CT imaging is the method of choice in clinical practice. In fact, combining the two modalities is a practical solution to overcome the shortcomings of each modality alone and therefore to increase the diagnostic confidence of PET and CT findings [3]. X-ray CT is a fast imaging technique which uses transmission x-ray beams to produce tomographic images of underlying tissues and structures based on their attenuation properties. The additional anatomical information of CT in hybrid PET/CT scans not only allows for accurate localization of PET findings but also improves the quantitative accuracy through CT-based attenuation correction (CTAC) of PET data [4]. Since CT image intensities are related to the attenuation properties of tissue, the images can be easily converted into attenuation maps at the photon energy of 511 keV to correct the PET data for attenuation, thereby replacing lengthy and noisy transmission scans commonly acquired on stand-alone PET scanners. Despite the fact that CTAC substantially facilitates the task of lesion localization and PET attenuation correction, CT images usually suffer from artifacts and data inconsistencies that not only impair the diagnostic quality of these images but also can propagate into PET images through the CTAC process. Metal induced streaking artifacts [5], respiratory-phase mismatch between CT and PET images [6], truncation artifacts [7] due to the limited transaxial field-of-view (FOV) are frequently observed artifacts in CT-based attenuation correction of PET data. As shown in Fig.1, the artifacts caused by metallic implants with high-atomic number such as hip prostheses can especially result in over and underestimation of PET tracer uptake in the vicinity of implant [5]. The increased patient radiation dose during CT scanning is a major concern in PET/CT scanning, especially in follow-up and serial studies and pediatric patients. Moreover, CT images hardly provide complementary functional information to PET data or motion information with a reasonable dose for motion correction of PET data.

MRI can also be used as an anatomical imaging technique in combination with the molecular informed provided by PET. MRI has a high spatial resolution and its soft-tissue contrast is superior to CT. Therefore, combined PET/MRI is expected to be the method-of-choice in clinical oncology with neoplasms associated with soft-tissue regions, e.g. lesions in the pelvis, head-and-neck region, or brain. The image contrast factor in MRI is based on the proton density and relaxation time properties of tissues in an external magnetic field. Contrary to CT, MRI therefore does not impose additional radiation dose to patients, which is a matter of great concern in pediatric patients [8]. Moreover, MRI can provide complementary functional information using techniques such as diffusion weighted imaging, dynamic contrast-enhanced MRI, fMRI and MR spectroscopy [10]. Therefore, simultaneous PET/MRI data acquisition brings an opportunity for the spatial and temporal correlation of measured signals and the concurrent assessment of functional and molecular processes. The high-resolution anatomical information provided by MRI can also be exploited to reduce partial volume effect (PVE) in PET images due to the limited spatial resolution of current clinical PET scanners [11]. To compensate for the blurring that degrade PET image resolution, point spread function (PSF) modeling and resolution recovery techniques have been extensively explored. However, PSF PET reconstruction is known to produce Gibbs over- and undershoots near tissue boundaries. In simultaneous PET/MRI with perfect spatial registration, the exquisite MRI anatomical information can be incorporated into PET image reconstruction algorithms in order to reduce

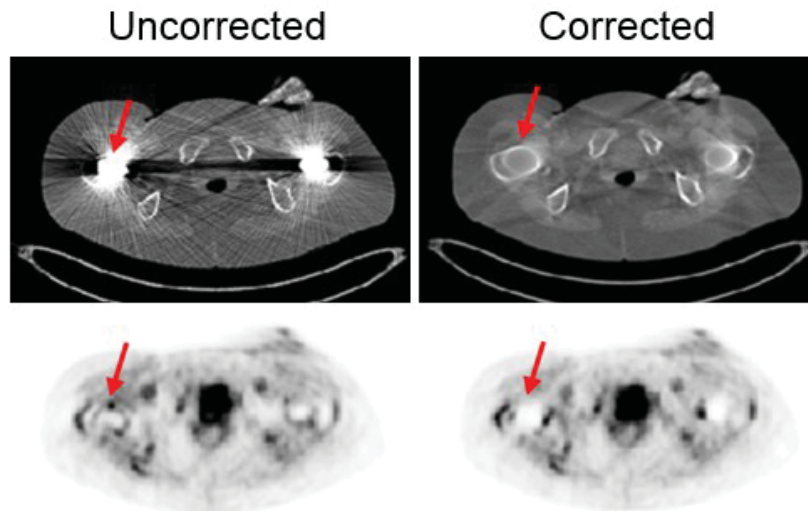


Fig. 1 The metallic artifacts in CT-based attenuation correction of PET data can induce pseudo uptake of tracers. The correction of CT artifacts therefore increase the confidence of the PET findings. Reprinted with permission from [9].

PVE and PSF Gibbs artifacts [12]. These reconstruction methods promote the formation of edges by enforcing smoothness within organs/tissues but not across boundaries or using mutual information between MRI morphological and PET physiological information. Additionally, the presence of MRI magnetic field during PET acquisition can reduce positron range in the direction perpendicular to the magnetic field and therefore improves PET image resolution [13]. The blurring introduced by moving organs during PET acquisition can also significantly degrade the effective resolution of PET systems. Another advantage of simultaneous PET/MRI is that the MRI can provide the motion vector fields required in motion-compensation PET image reconstruction [14].

In spite of all these advantages, MRI data acquisition is considerably more time-consuming than CT, especially when complementary MR sequences are performed [15]. Fast MRI data acquisition is therefore of particular importance in PET/MRI where anatomical, motion-tracking and supplementary functional sequences are desired. Emerging trends for accelerating MR acquisitions focus on compressed sensing (CS) and parallel MRI techniques [16], which are based on the under-sampling of MR data space (k -space) and estimation of missing data using the redundant information available in the acquired data or prior knowledge about the underlying image. Moreover, in PET/MRI, the PET attenuation map should ideally be derived from MR images. In contrary to CT, MRI image intensities are related to hydrogen proton density, relaxation time properties of tissues and the selected pulse timing parameters. Therefore, there is no a unique global mapping technique to convert MR images to PET attenuation maps. Additionally, lung tissue and cortical bone, which are two important tissue types in attenuation maps, exhibit no signal on images acquired with conventional MRI sequences; owing to their low water content and short transverse relaxation time. Therefore, the lungs, bones and the air inside some organs, which also produces a void signal, cannot be well differentiated from each other in images acquired with conventional MRI sequences [17]. Ultra-short echo time (UTE) MR pulse sequences have also been investigated for the detection and visualization of lung parenchyma [18] as well as bones [19]. However, UTE pulse sequences are timing-consuming and sensitive to magnetic field inhomogeneities and therefore are not yet clinically feasible in whole-body MRI-based attenuation correction (MRAC) of PET data [20]. Currently, commercial PET/MRI systems employ MRI segmentation-based approaches as the standard attenuation correction method [17, 21]. In these methods, MR images are segmented into 3- or 4-tissue classes (background air, lung, fat and non-fat soft tissues) followed by assignment of predefined constant linear attenuation coefficients at 511-keV to each tissue class. However, the inter/intra-patient heterogeneity of attenuation coefficients in different tissue classes is ignored by these techniques. Moreover, since bones and air cavities cannot be well differentiated when using conventional clinically feasible MR sequences, these tissue classes are often ignored and replaced by soft-tissue, which can lead to significant bias in PET tracer uptake quantification in different organs [22, 23].

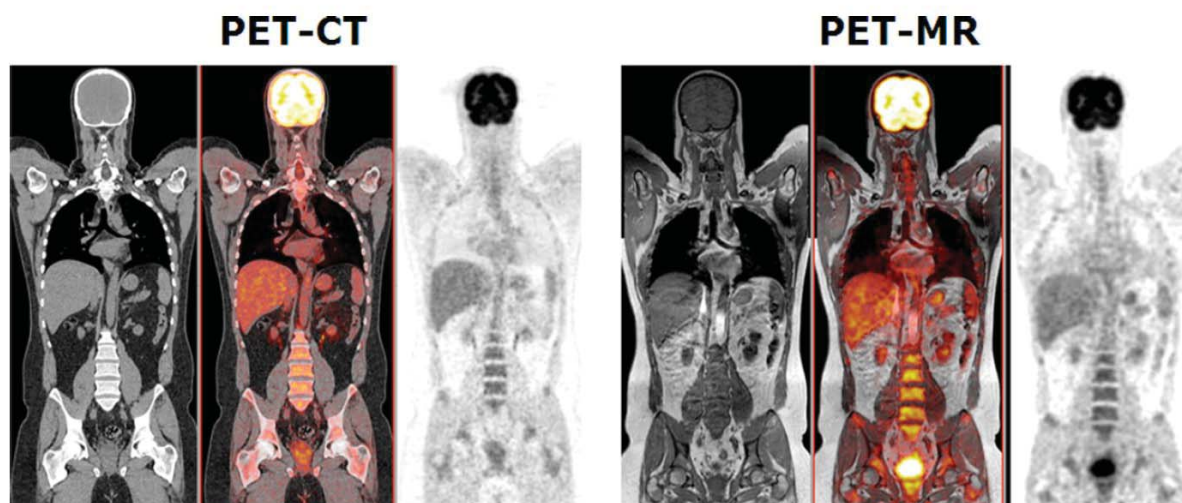


Fig. 2 Representative clinical PET/CT (left) and PET/MR (right) whole-body images of the same patient acquired sequentially (60 min time difference) on two combined systems (Siemens Biograph Hirez TrueV and Philips Ingenuity TF PET/MRI, respectively) following injection of 370 MBq of ^{18}F -FDG. Reprinted with permission from [8].

For this reason, other attenuation map generation techniques based on atlas registration [24, 25], external transmission sources [26, 27] and PET emission data [28, 29] have been explored and revisited in PET/MRI. In atlas registration-based approaches, co-registered MR-CT atlas datasets are used to derive a pseudo CT image from the patient's MR image or to learn a mapping function that predicts a pseudo CT image. These methods can solve the MRAC problem, particularly in brain imaging, provided that a perfect registration between the atlas and different patients can be achieved. However, such a registration is rarely possible in whole-body PET/MRI, owing to the limitations of registration algorithms and substantial anatomical differences between patients. With advances in PET detector technology, time-of-flight (TOF) PET capability has been recently introduced in clinical PET/CT and PET/MRI scanners with the aim of improving lesion detectability and image quality, as well as reducing acquisition time and/or patient's administrated dose [30, 31]. Following this rebirth of TOF PET, transmission and emission-based methods have been revisited for deriving patient-specific attenuation maps in PET/MRI and hence to circumvent the uncertainties and obstacles of the standard and UTE MRAC methods. In transmission-based approaches, attenuation coefficients are directly measured using external positron-emitting sources in a simultaneous transmission and emission acquisition. TOF information is then used to separate transmission from emission data. The major issue is the low count statistics of the transmission scan limited by emission scan time per bed position as well as additional patient dose [32]. In contrast, emission-based approaches do not require external transmission sources and only rely on TOF emission data for simultaneous estimation of activity and attenuation. The overall performance of these approaches depends on TOF timing resolution, count statistics of emission data and spatial distribution of the radiotracer in the body. In fact, it has been shown that TOF-PET image reconstruction can reduce the artifacts induced by attenuation correction errors [33, 34]. Emission-based attenuation correction methods are promising in TOF PET/MRI scanners, where MRI anatomical information can be exploited to impose prior information on the estimation of attenuation and therefore improve the performance of these emerging attenuation correction methods [28].

Dual-modality PET/CT and PET/MR imaging techniques has gained a tremendous interest during the last decade, not only in research but particularly in the clinical arena. The combination of CT or MRI anatomical information with PET has increased the clinical utility of PET physiological information and also triggered an emerging paradigm toward multi-modality and multi-parametric imaging techniques. Numerous active research groups in academia and industry have therefore focused on the development of innovative techniques and solutions for further development and addressing the challenges associated with multimodal molecular imaging.

II. Aim and outline of thesis

In the work presented in this dissertation, we aimed at developing new CT, MRI and PET image reconstruction and data correction techniques to address some prevalent challenges encountered in hybrid PET/CT and PET/MR imaging, as summarized in the previous section. Along these lines, we summarize the aims of this thesis in the following items:

- i) The development and evaluation of efficient metal artifact reduction algorithms in x-ray CT imaging to improve the clinical value of diagnostic CT images as well as the accuracy of CT-based attenuation correction in PET/CT.
- ii) The development of efficient and convergent image reconstruction algorithms in PET and MRI to facilitate the application of anatomical priors for MR-guided PET image reconstruction as well as compressed sensing techniques for sub-Nyquist MRI image reconstruction.
- iii) The development and evaluation of novel MRI-guided emission-based attenuation correction methods in TOF PET/MRI and comparison with current state-of-the-art algorithms with the aim of paving the way toward the adoption of these techniques in clinical PET/MRI.

In chapter 2, we introduce a novel MAR algorithm by formulating the recovery of corrupted CT projection data as a regularized inverse problem, in which we exploit two types of prior information: i) the sparsity of CT sinograms in the wavelet domain and ii) the wavelet coefficients of a prior CT sinogram. The optimization problem is solved using the Douglas-Rachford splitting algorithm and the resulting MAR algorithm is then compared with standard and current state-of-the-art MAR algorithms using both simulated and clinical studies with different metallic implants.

In chapter 3, we introduce a 3D projection completion MAR algorithm for the maximum a posteriori (MAP) completion of missing projections. Motivated by the concept of subtraction sparsification in the context of compressed sensing and prior image application in metal artifact reduction, we propose a new prior function to exploit i) the sparsity of a residual sinogram obtained from the subtraction of the unknown target sinogram and a prior CT sinogram and ii) a sparsity-promoting diffusivity function defined on the prior sinogram for the recovery of missing projections. The optimization problem is solved using an accelerated projected gradient algorithm and the resulting MAR method is compared with current state-of-the-art MAR algorithms for fan-beam and cone-beam CT using simulated and clinical datasets with different metallic implants.

Chapter 4 compares the performance of five different MAR techniques for metal artifact reduction using a sizable number of simulated and clinical datasets of patients with hip prostheses. The ability of the algorithms in restoring the radiological manifestations of tissues and abnormalities in the vicinity of metallic implants are evaluated qualitatively by experienced radiologists and quantitatively using realistic simulation studies.

In chapter 5, we propose an accelerated optimization algorithm for penalized weighted least-squares (PWLS) PET image reconstruction using edge-preserving and anatomically guided penalty functions. The optimization of PWLS cost function with such penalty functions has two challenges: i) ill-conditioning of its Hessian matrix and therefore slow convergence and ii) non-differentiability of non-smooth penalty functions. To address these challenges and to provide a framework for incorporating anatomical side boundary information in the reconstruction, we proposed a proximal preconditioned gradient algorithm accelerated with ordered subsets and compared its performance with state-of-the-art algorithm with three different preconditioners.

In chapter 6, a new sparsity-promoting regularization technique is introduced for iterative MR image reconstruction from highly undersampled k -space data. In fact, compressed sensing (CS) MRI allows for reducing MR data acquisition time while obtaining images with comparable quality to those obtained with fully sampled k -spaces. The proposed regularization is obtained by the iterative linearization of the non-convex smoothly clipped absolute deviation (SCAD) norm with the aim of reducing the sampling rate even lower than it is required by the conventional L_1 norm while approaching an L_0 norm. The CS-MR image reconstruction is formulated as a constrained optimization problem using a variable splitting technique and solved using an augmented Lagrangian (AL) method. The performance of the resulting SCAD-based algorithm is evaluated for

discrete gradients and wavelet sparsifying transforms and compared with its L_1 -based counterpart using phantom and clinical studies.

Quantitative PET necessitates a long chain of data corrections among which attenuation correction is an essential part. The development of combined PET/MRI systems stimulated the widespread interest in developing novel strategies for deriving accurate attenuation maps with the aim to improve the quantitative accuracy of these emerging hybrid imaging systems. In chapter 7, we reviewed the past and current state-of-the-art developments and latest advances in PET/MRI attenuation correction including the methods developed and evaluated in this thesis. The advantages and drawbacks of each approach for addressing the challenges of MR-based attenuation correction is comprehensively described. Future prospects and potential clinical applications of these techniques and their integration in commercial systems is also discussed.

In TOF PET/CT imaging, it has been demonstrated that TOF PET image reconstruction is less sensitive to inconsistencies between emission and correction data compared to non-TOF reconstructions. In chapter 8, we conduct, for the first time a clinical study to evaluate the impact of TOF image reconstruction on PET quantification errors induced by MRI-based attenuation correction using simulation and clinical PET/CT studies. The impact of TOF on reducing the errors induced by metal-susceptibility and respiratory-phase mismatch artifacts is also evaluated using clinical and simulation studies.

It has recently been shown that the attenuation map at 511 keV can be estimated from TOF PET emission data using joint maximum likelihood reconstruction of attenuation and activity (MLAA). In chapter 9, we propose a novel MRI-guided MLAA algorithm for emission-based attenuation correction in whole-body TOF PET/MR imaging. The algorithm imposes MR spatial and CT statistical constraints on the MLAA estimation of attenuation maps using a constrained Gaussian mixture model and a Markov random field smoothness prior. Thereby, the dependency of the MLAA algorithm on TOF timing resolution, count statistics and activity distribution as well as the scale problem of the algorithm is effectively reduced. The proposed MLAA algorithm is then compared with the MLAA algorithms proposed previously in the literature using simulation and clinical studies for two different PET tracers.

In standard segmentation-based MRI-guided attenuation correction in PET/MRI systems, the inter/intra-patient variability of linear attenuation coefficients (LACs) is ignored by assigning constant LACs to each tissue class, which can lead to PET quantification errors, especially in the lung regions. In chapter 10, we aim at deriving continuous and patient-specific lung LACs from TOF PET emission data using a simplified version of the MLAA algorithm proposed in chapter 9. The algorithm is constrained for estimation of lung LACs only in the standard 4-class MR attenuation map using Gaussian lung tissue preference. The performance of the proposed algorithm is evaluated using clinical PET/CT datasets. PET quantification accuracy of MRAC and MLAA methods is compared against the reference CT-based AC method in the lungs, lesions located in/near the lungs and neighboring tissues.

In chapter 11, the performance of the proposed MLAA-GMM algorithm is evaluated against the standard 4-class MRAC method using clinical whole-body PET/MRI/CT studies with the aim of highlighting the potentials of the emission-based AC methods in TOF PET/MRI imaging and pave the way for their translation into clinic.

Chapter 12 concludes this work and discusses future perspectives in this field along with possible scenarios for the continuation of the studies conducted on this dissertation.

References

- [1] D. A. Torigian, H. Zaidi, T. C. Kwee, B. Saboury, J. K. Udupa, Z.-H. Cho, and A. Alavi, "PET/MR Imaging: Technical aspects and potential clinical applications," *Radiology*, vol. 267, no. 1, pp. 26-44, 2013.
- [2] J. F. Valliant, "A bridge not too far: linking disciplines through molecular imaging probes," *J Nucl Med*, vol. 51, no. 8, pp. 1258-68, Aug, 2010.
- [3] O. Israel, M. Mor, D. Gaitini, Z. Keidar, L. Guralnik, A. Engel, A. Frenkel, R. Bar-Shalom, and A. Kuten, "Combined functional and structural evaluation of cancer patients with a hybrid camera-based PET/CT system using (18)F-FDG," *J Nucl Med*, vol. 43, no. 9, pp. 1129-36, Sep, 2002.
- [4] R. Bar-Shalom, N. Yefremov, L. Guralnik, D. Gaitini, A. Frenkel, A. Kuten, H. Altman, Z. Keidar, and O. Israel, "Clinical performance of PET/CT in evaluation of cancer: additional value for diagnostic imaging and patient management," *J Nucl Med*, vol. 44, no. 8, pp. 1200-9, Aug, 2003.
- [5] M. Abdoli, R. A. Dierckx, and H. Zaidi, "Metal artifact reduction strategies for improved attenuation correction in hybrid PET/CT imaging," *Med Phys*, vol. 39, no. 6, pp. 3343-60, Jun, 2012.
- [6] T. Pan, and H. Zaidi, "Attenuation correction strategies for positron emission tomography/computed tomography and 4-Dimensional positron emission tomography/computed tomography," *PET Clin*, vol. 8, no. 1, pp. 37-50, 2013.
- [7] T. Beyer, A. Bockisch, H. Kuhl, and M. J. Martinez, "Whole-body 18F-FDG PET/CT in the presence of truncation artifacts," *J Nucl Med*, vol. 47, no. 1, pp. 91-9, Jan, 2006.
- [8] H. Zaidi, and A. D. Guerra, "An outlook on future design of hybrid PET/MRI systems," *Med Phys*, vol. 38, no. 10, pp. 5667-5689, 2011.
- [9] M. Abdoli, J. R. de Jong, J. Pruijm, R. A. Dierckx, and H. Zaidi, "Reduction of artefacts caused by hip implants in CT-based attenuation-corrected PET images using 2-D interpolation of a virtual sinogram on an irregular grid," *European Journal of Nuclear Medicine and Molecular Imaging*, vol. 38, no. 12, pp. 2257-68, Dec, 2011.
- [10] A. R. Padhani, and K. A. Miles, "Multiparametric imaging of tumor response to therapy," *Radiology*, vol. 256, no. 2, pp. 348-64, Aug, 2010.
- [11] C. C. Meltzer, P. E. Kinahan, P. J. Greer, T. E. Nichols, C. Comtat, M. N. Cantwell, M. P. Lin, and J. C. Price, "Comparative evaluation of MR-based partial-volume correction schemes for PET," *J Nucl Med*, vol. 40, no. 12, pp. 2053-65, Dec, 1999.
- [12] K. Vunckx, A. Atre, K. Baete, A. Reilhac, C. M. Deroose, K. Van Laere, and J. Nuyts, "Evaluation of three MRI-based anatomical priors for quantitative PET brain imaging," *IEEE Trans Med Imaging*, vol. 31, no. 3, pp. 599-612, Mar, 2012.
- [13] J. Cal-González, J. L. Herraiz, S. España, P. M. G. Corzo, J. J. Vaquero, M. Desco, and J. M. Udias, "Positron range estimations with PeneloPET," *Physics in Medicine and Biology*, vol. 58, no. 15, pp. 5127, 2013.
- [14] S. Y. Chun, T. G. Reese, J. Ouyang, B. Guerin, C. Catana, X. Zhu, N. M. Alpert, and G. El Fakhri, "MRI-based nonrigid motion correction in simultaneous PET/MRI," *J Nucl Med*, vol. 53, no. 8, pp. 1284-91, Aug, 2012.
- [15] G. K. von Schulthess, and P. Veit-Haibach, "Workflow Considerations in PET/MR Imaging," *J Nucl Med*, vol. 55, no. Supplement 2, pp. 19S-24S, May 1, 2014.
- [16] M. Lustig, D. Donoho, and J. M. Pauly, "Sparse MRI: The application of compressed sensing for rapid MR imaging," *Magn Reson Med*, vol. 58, no. 6, pp. 1182-95, Dec, 2007.
- [17] A. Martinez-Möller, M. Souvatzoglou, G. Delso, R. A. Bundschuh, C. Chefd'hotel, S. I. Ziegler, N. Navab, M. Schwaiger, and S. G. Nekolla, "Tissue classification as a potential approach for attenuation correction in whole-body PET/MRI: evaluation with PET/CT data," *J Nucl Med*, vol. 50, no. 4, pp. 520-526, 2009.
- [18] K. Zeimpekis, G. Delso, F. Wiesinger, P. Veit-Haibach, G. von Schulthess, and R. Grimm, "Investigation of 3D UTE MRI for lung PET attenuation correction," *J Nucl Med*, vol. 55, no. Supplement 1, pp. 2103, 2014.
- [19] V. Keereman, Y. Fierens, T. Broux, Y. De Deene, M. Lonneux, and S. Vandenberghe, "MRI-based attenuation correction for PET/MRI using ultrashort echo time sequences," *J Nucl Med*, vol. 51, no. 5, pp. 812-8, 2010.
- [20] A. P. Aitken, D. Giese, C. Tsoumpas, P. Schleyer, S. Kozierke, C. Prieto, and T. Schaeffter, "Improved UTE-based attenuation correction for cranial PET-MR using dynamic magnetic field monitoring," *Med Phys*, vol. 41, no. 1, pp. -, 2014.
- [21] Z. Hu, S. Renisch, B. Schweizer, T. Blaffert, N. Ojha, T. Guo, J. Tang, C. Tung, J. Kaste, V. Schulz, I. Torres, and L. Shao, "MR-based attenuation correction for whole-body PET/MR system," *IEEE Nucl Sci Symp Conf Record*, pp. 2119-2122, 2010.

- [22] I. Bezrukov, H. Schmidt, F. Mantlik, N. Schwenzer, C. Brendle, B. Schölkopf, and B. J. Pichler, "MR-based attenuation correction methods for improved PET quantification in lesions within bone and susceptibility artifact regions," *J Nucl Med*, vol. 54, no. 10, pp. 1768-1774, 2013.
- [23] J. Ouyang, C. Se Young, Y. Petibon, A. A. Bonab, N. Alpert, and G. El Fakhri, "Bias Atlases for Segmentation-Based PET Attenuation Correction Using PET-CT and MR," *IEEE Trans Nuc Sci*, vol. 60, no. 5, pp. 3373-3382, 2013.
- [24] M. Hofmann, I. Bezrukov, F. Mantlik, P. Aschoff, F. Steinke, T. Beyer, B. J. Pichler, and B. Scholkopf, "MRI-based attenuation correction for whole-body PET/MRI: quantitative evaluation of segmentation- and atlas-based methods," *J Nucl Med*, vol. 52, no. 9, pp. 1392-9, Sep, 2011.
- [25] A. Johansson, M. Karlsson, and T. Nyholm, "CT substitute derived from MRI sequences with ultrashort echo time," *Med Phys*, vol. 38, no. 5, pp. 2708-2714, 2011.
- [26] P. Mollet, V. Keereman, E. Clementel, and S. Vandenberghe, "Simultaneous MR-compatible emission and transmission imaging for PET using time-of-flight information," *Medical Imaging, IEEE Transactions on*, vol. PP, no. 99, pp. 1-1, 2012.
- [27] H. Rothfuss, V. Panin, A. Moor, J. Young, I. Hong, C. Michel, J. Hamill, and M. Casey, "LSO background radiation as a transmission source using time of flight," *Phys Med Biol*, vol. 59, no. 18, pp. 5483-500, 2014.
- [28] A. Salomon, A. Goedicke, B. Schweizer, T. Aach, and V. Schulz, "Simultaneous reconstruction of activity and attenuation for PET/MR," *IEEE Trans Med Imaging*, vol. 30, no. 3, pp. 804-813, 2011.
- [29] A. Rezaei, M. Defrise, G. Bal, C. Michel, M. Conti, C. Watson, and J. Nuyts, "Simultaneous reconstruction of activity and attenuation in Time-of-Flight PET," *IEEE Trans Med Imaging* vol. 31, no. 12, pp. 2224-33, 2012.
- [30] M. Conti, "Focus on time-of-flight PET: the benefits of improved time resolution," *Eur. J. Nucl. Med. Mol. Imag*, vol. 38, no. 6, pp. 1147-57, Jun, 2011.
- [31] G. El Fakhri, S. Surti, C. M. Trott, J. Scheuermann, and J. S. Karp, "Improvement in lesion detection with whole-body oncologic time-of-flight PET," *J Nucl Med*, vol. 52, no. 3, pp. 347-353, March 1, 2011, 2011.
- [32] P. Mollet, V. Keereman, J. Bini, D. Izquierdo-Garcia, Z. A. Fayad, and S. Vandenberghe, "Improvement of attenuation correction in time-of-flight PET/MR imaging with a positron-emitting source," *J Nucl Med*, vol. 55, no. 2, pp. 329-36, Feb, 2014.
- [33] T. G. Turkington, and J. M. Wilson, "Attenuation artifacts and time-of-flight PET." pp. 2997-2999.
- [34] M. Conti, "Why is TOF PET reconstruction a more robust method in the presence of inconsistent data?," *Phys Med Biol*, vol. 56, no. 1, pp. 155-68, Jan 7, 2011.

Chapter 2

X-ray CT metal artifact reduction using wavelet domain L_0 sparse regularization

Abolfazl Mehranian, Mohammad Reza Ay , Arman Rahmim and Habib Zaidi

IEEE Trans Med Imaging Vol. 32, No. 9, pp 1707-1722 (2013)

© 2013 IEEE.

Abstract

Purpose: X-ray computed tomography (CT) imaging of patients with metallic implants usually suffers from streaking metal artifacts. In this paper, we propose a new projection completion metal artifact reduction (MAR) algorithm by formulating the completion of missing projections as a regularized inverse problem in the wavelet domain.

Methods: The Douglas-Rachford splitting (DRS) algorithm was used to iteratively solve the problem. Two types of prior information were exploited in the algorithm: i) the sparsity of the wavelet coefficients of CT sinograms in a dictionary of translation-invariant wavelets and ii) the detail wavelet coefficients of a prior sinogram obtained from the forward projection of a segmented CT image. A pseudo- L_0 synthesis prior was utilized to exploit and promote the sparsity of wavelet coefficients. The proposed L_0 -DRS MAR algorithm was compared with standard linear interpolation and the normalized metal artifact reduction (NMAR) approach proposed by Meyer et al using both simulated and clinical studies including hip prostheses, dental fillings, spine fixation and EEG electrodes in brain imaging.

Results and conclusion: The qualitative and quantitative evaluations showed that our algorithm substantially suppresses streaking artifacts and can outperform both linear interpolation and NMAR algorithms.

I. Introduction

The non-linear absorption of polychromatic x-ray beams used in x-ray computed tomography (CT) often results in beam hardening and the selective absorption of x-ray photons [1]. In the presence of strongly attenuating objects such as metallic implants, beam hardening and scattering is usually so strong that the detectors sensing the implants experience severe photon starvation and, as such, the relevant log-processed projection data become corrupted and inconsistent [2, 3]. Consequently, the data inconsistency appears as dark and bright streaking artifacts during image reconstruction, which can obscure crucial diagnostic information in tissues surrounding the implants [4-6]. Moreover, non-linear partial volume effects and noise can also give rise to data corruption and hence streaking artifacts [7]. Over the years, the prevalence of CT imaging in clinical practice and the need for improved image quality in patients bearing metallic implants have spurred continuous efforts towards the development of metal artifact reduction (MAR) algorithms to compensate for corrupted and missing projections, thus mitigating metal artifacts. MAR algorithms fall into two classes: projection completion and iterative image reconstruction algorithms.

In the projection completion approach, which is often followed by filtered-back-projection (FBP) image reconstruction, the missing projections are synthesized from neighboring projections using linear and polynomial interpolation [4, 8-10], wavelet interpolation [11], adaptive filtering [12, 13] and inpainting [14-17] techniques. Other approaches aim at replacing the missing projections with those available in opposite view angles or adjacent CT slices [18-20] or the projections obtained from forward projection of tissue-segmented CT images [21-24]. The efficiency of these algorithms in the recovery of missing projections hinges on how robustly they can exploit the available projection data or utilize *a priori* information about missing projections. In fact, if not appropriately developed, these methods might induce new artifacts. Recently, Meyer *et al.* [25] proposed a very promising projection-based normalized MAR (NMAR) algorithm to facilitate the interpolation of missing projections without introducing new severe artifacts. In this algorithm, the original sinogram is first normalized by a sinogram obtained from a tissue-segmented CT image, called *prior* image, and then the missing data are linearly interpolated. Finally, the resulting sinogram is de-normalized. In general, projection completion algorithms should be preceded by a metal trace identification step, in which projections running through metallic implants (i.e. corrupted or missing projections) are identified. This is achieved by either (i) segmentation of CT images for metallic implants and forward projection of the resulting *metal-only* image into an artificial sinogram domain [4, 26, 27], or (ii) direct segmentation of raw sinogram data for corrupted projections [10, 13, 16].

During the last decade, iterative model-based image reconstruction methods enabled the implementation of a novel class of algorithms: these techniques originate from statistical methods that estimate missing or incomplete data [28]. They can be easily adapted to truncated and missing sinogram data by ignoring or reducing statistical contributions of corrupted projections, and by imposing constraints and prior knowledge on the images being reconstructed [27, 29-31]. In this class of algorithms, the missing projections are identified by either image- and sinogram-based approaches used in projection completion [29, 32] or a hybrid of both involving iterative metal-only image reconstruction and metal-trace segmentation [27, 33, 34]. However, these algorithms cannot entirely compensate for severe data corruptions [35], and hence, their initiation and combination with projection completion algorithms has also been investigated [32, 36]. Compared to projection completion methods, model-based iterative image reconstruction is computationally intensive. Recently, Van Slambrouck *et al.* [37] proposed a region-based iterative reconstruction method to reduce the computational complexity of this class of MAR algorithms. In this method, the regions containing metals are reconstructed using a fully polychromatic spectral model, while other regions are reconstructed using a simpler model that only considers the spectral behavior of water attenuation. Although this approach tends to preserve structures near metallic implants, the reconstructed images still suffer from streaking artifacts in comparison with linear interpolation and Meyer's NMAR approaches.

In this work, we propose a new projection completion MAR algorithm in which the recovery of missing projections is formulated as a regularized inverse problem and some prior information about the underlying complete sinogram is exploited during the optimization process. Specifically, we propose a sparse synthesis regularization for the estimation of missing projections in the wavelet domain and exploit two types of prior information: i) the sparsity of a CT sinogram in a dictionary of translation-invariant wavelets and ii) the detail wavelet coefficients of a prior sinogram obtained by a tissue-segmented CT image. The Douglas-Rachford Splitting (DRS) algorithm is used for the optimization of the problem. The sparsity of sinograms in the wavelet

domain is promoted by a pseudo L_0 norm based on the homotopic approximation of an L_0 norm. We also compare the performance of the proposed MAR algorithm with standard linear interpolation and NMAR algorithms using simulation and clinical studies to assess its potential and demonstrate its outperformance over these MAR approaches.

II. Materials and methods

II.A. problem formulation

We denote the 2D log-processed sinogram of a CT slice as a vector in \mathbb{R}_+^N , where N is the number of detector channels times the number of projection angles. Let \mathbf{f} be an observed sinogram with metal traces that corrupt the projection data at the locations indexed by the set $\Omega \subset \{1, \dots, N\}$. In the recovery of missing projections, we formulate the following forward model:

$$\mathbf{y} = \Phi \mathbf{f} + \mathbf{n} \quad (1)$$

where $\mathbf{y} \in \mathbb{R}^M$, $M < N$, is an incomplete sinogram, $\Phi \in \mathbb{R}^{M \times N}$ is a lossy matrix that removes the projections of \mathbf{f} over the set Ω and \mathbf{n} represents data perturbations due to white Gaussian noise (with variance of σ^2). The matrix Φ can be thought of as an $N \times N$ identity matrix that has been downsized along $r = N - M$ rows, indexed by the set Ω . To estimate a sinogram with complete data, one approach is to invert the problem (1) by minimizing the cost function $\frac{1}{2\sigma^2} \sum_{i=1}^M (y_i - [\Phi \mathbf{f}]_i)^2$, which is derived by considering Gaussian noise. However, this minimization has an infinite number of possible solutions. To regularize the solution space and penalize unsatisfactory solutions, one can impose *a priori* knowledge about the solution through a *regularizer* or *prior* $R(\mathbf{f})$. Therefore, the solution can be obtained by the following optimization problem:

$$\hat{\mathbf{f}} = \operatorname{argmin}_{\mathbf{f} \in \mathbb{R}_+^N} \left\{ \frac{1}{2\sigma^2} \|\mathbf{y} - \Phi \mathbf{f}\|^2 + \lambda R(\mathbf{f}) \right\} \quad (2)$$

where $\|\mathbf{x}\|$ stands for the Euclidean (L_2) norm of the vector \mathbf{x} , which is a special case ($p = 2$) of the L_p norm defined as $\|\mathbf{x}\|_p = (\sum_{i=1}^N |x_i|^p)^{1/p}$, and λ is a regularization parameter that controls the balance between the fidelity of the solution to the observations and its regularity to prior knowledge.

In the context of compressed sensing and sparse signal recovery, the prior knowledge that an expected signal or solution is sparse (i.e. having many zero components) is exploited to recover it from its samples or incomplete measurements. When \mathbf{f} is not sparse directly (e.g. in the sinogram domain), it is possible to explore its sparsity or compressibility in an appropriate sparse representation dictionary [38]. By definition, if \mathbf{f} is sparse (or compressible) in the dictionary $\mathbf{W} = [w_1, \dots, w_N]^T \in \mathbb{R}^{N \times K}$, most of its energy is represented by and compressed in a few large magnitude coefficients. In other words, when \mathbf{f} is expressed as a linear combination of $K \geq N$ elementary functions, $\mathbf{f} = \mathbf{W}\boldsymbol{\theta} = \sum_{i=1}^K w_i \theta_i$, the majority of the decomposition coefficients, θ_i , are (close to) zero. The dictionary \mathbf{W} , namely *synthesis* (or reconstruction) operator, often consists of $K = N$ concatenated orthonormal bases or $K > N$ tight frames. In the case of a basis, \mathbf{W} is a square full-rank matrix that satisfies, $\mathbf{W}\mathbf{W}^* = \mathbf{W}^*\mathbf{W} = \mathbf{I}$ where \mathbf{W}^* is its conjugate transpose, namely an *analysis* (or decomposition) operator and \mathbf{I} is the identity matrix. In the case of a tight frame, \mathbf{W} is a non-square matrix and a redundant dictionary that only satisfies $\mathbf{W}\mathbf{W}^* = \mathbf{I}$ while $\mathbf{W}^*\mathbf{W} \neq \mathbf{I}$ [39, 40]. Given an appropriate sparse dictionary, the solution of the problem (2) can be alternatively obtained through synthesis from its representation coefficients, i.e. $\hat{\mathbf{f}} = \mathbf{W}\hat{\boldsymbol{\theta}}$, where

$$\hat{\boldsymbol{\theta}} = \operatorname{argmin}_{\boldsymbol{\theta} \in \mathbb{R}} \left\{ \frac{1}{2\sigma^2} \|\mathbf{y} - \Phi \mathbf{W}\boldsymbol{\theta}\|^2 + \lambda R(\boldsymbol{\theta}) \right\}, \quad \boldsymbol{\theta} = \{\theta_i \mid \theta_i \in \mathbb{R}, \mathbf{W}\boldsymbol{\theta} \in \mathbb{R}_+^N\}. \quad (3)$$

This formulation is referred to as a synthesis approach, whereas the formulation of the problem (2) with the prior $R(\mathbf{W}^*\mathbf{f})$ is called an analysis approach [41]. Unless the dictionary is a basis, the two formulations do not result in the same solution. In fact, the synthesis approach emphasizes more on the sparsity of the solution, while the analysis approach emphasizes a balance between the sparsity of decomposition coefficients and the smoothness of the solution [40]. In this study, we made use of a tight frame of translation-invariant wavelets and followed the synthesis approach for the completion of missing projections. We employed Daubechies 7/9 biorthogonal (D7/9) wavelets with four resolution levels and implemented by undecimated discrete wavelet transforms and a lifting scheme. It is worth mentioning that these wavelets are used in the JPEG-2000 image compression standard [42]. Figure 1 shows a 512×512 block of a typical CT sinogram and its two representative

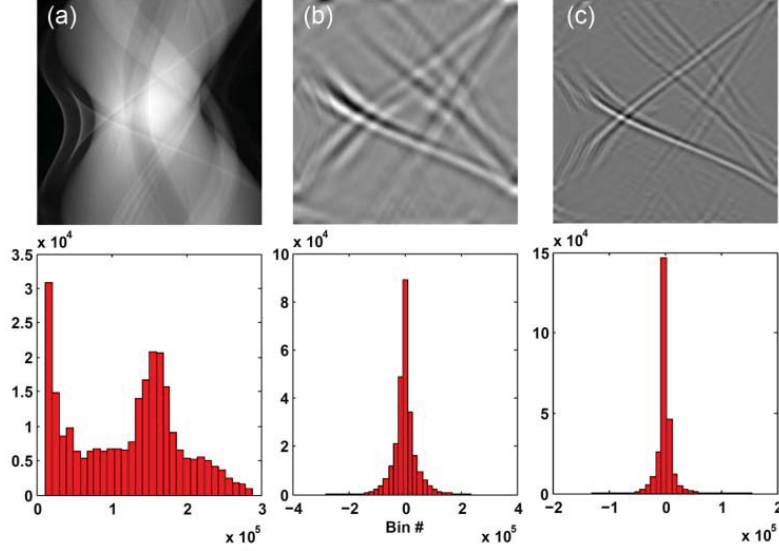


Figure 1 Top: (a) A 512×512 block of a typical CT sinogram and (b–c) its two representative detail wavelet coefficients at two different resolution levels. Bottom: The corresponding histograms of the images shown in (a–c) over 30 bins.

detail wavelet coefficients at two different resolution levels. As seen in the histograms, a CT sinogram is not directly sparse, but can have a sparse representation in the wavelet domain. One of the most successful priors in describing the usually heavy-tailed density of wavelet coefficients is the generalized Gaussian distribution [43], whose logarithm is the p -th power of an L_p norm for $0 < p \leq 2$:

$$R(\boldsymbol{\theta}) = \sum_{i=1}^p |\theta_i|^p = \|\boldsymbol{\theta}\|_p^p \quad (4)$$

The L_p norm can be utilized to promote the sparsity of the wavelet coefficients. An ideal sparsity-promoting prior is the L_0 norm, $\|\mathbf{x}\|_0$, which counts the number of non-zero components of \mathbf{x} . However, this non-convex prior results in an intractable optimization problem and requires global search optimization techniques such as simulated annealing. There exist convex L_p norms or priors for $p \geq 1$, among which the L_1 norm favors the highest degree of sparsity and hence, as a proxy to L_0 norm, has garnered significant attention in compressed sensing and sparsity regularization [44–46]. The L_0 norm can, however, be homotopically approximated by a pseudo L_0 norm as follows:

$$R(\boldsymbol{\theta}) = \lim_{\rho \rightarrow 0} \sum_{i=1} \psi(\theta_i, \rho) \quad (5)$$

where ψ is a quasi-convex potential function with a homotopic parameter ρ . As ρ approaches zero, the pseudo L_0 norm approaches the L_0 norm. In this study, we employed the following log potential function [46, 47]:

$$\psi(\theta, \rho) = \nu \ln \left(1 + \frac{|\theta|}{\rho} \right), \quad \nu = \frac{1}{\ln(1+1/\rho)} \quad (6)$$

where ν is a normalization factor. As shown in figure 2(a), for large values of ρ , this potential function approaches an absolute value function (associated with L_1 norm) and becomes convex, while for small values of ρ it becomes non-convex and approaches a zero-one potential function (associated with L_0 norm).

II.B. Optimization

To solve the optimization problem defined in Eq. (3), we follow the DRS algorithm, which is targeted for solving the following general minimization problem [48]:

$$\min_{\boldsymbol{\theta} \in \mathcal{H}} \{F_1(\boldsymbol{\theta}) + F_2(\boldsymbol{\theta})\} \quad (7)$$

where F_1 and F_2 are proper, convex and lower semi-continuous (l.s.c) functions in a Hilbert space \mathcal{H} . To describe the DRS algorithm, we first need to define the proximity operator $prox_F(\cdot)$ of a proper, convex and l.s.c function F that maps \mathcal{H} to \mathbb{R} . For every $\mathbf{z} \in \mathcal{H}$, the minimum energy of the envelope of F is achieved at a unique point, $prox_F(\boldsymbol{\theta})$, called proximal map or proximum, i.e. ([49]):

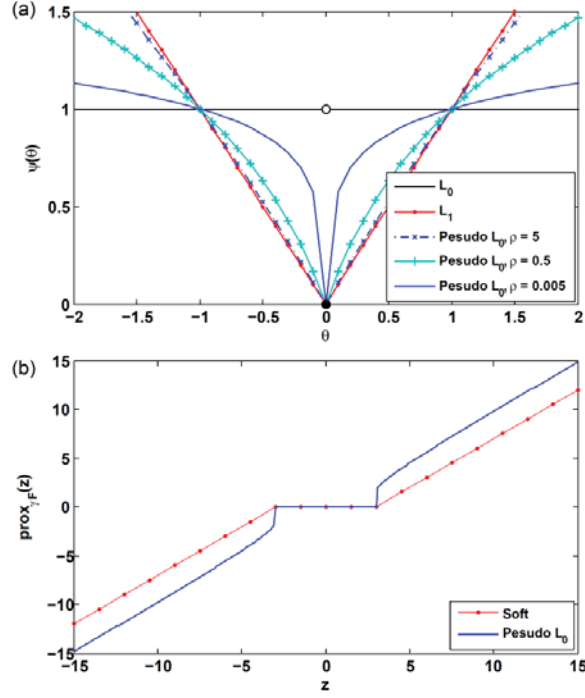


Figure 1. (a) Comparison of the potential functions of L_1 , pseudo L_0 and L_0 norms. (b) The thresholding rules induced by L_1 and pseudo L_0 norms.

$$\text{prox}_F(\boldsymbol{\theta}) = \underset{\mathbf{z} \in \mathcal{H}}{\text{argmin}} \left\{ \frac{1}{2} \|\mathbf{z} - \boldsymbol{\theta}\|^2 + F(\mathbf{z}) \right\} \quad (8)$$

By this definition, the DRS algorithm iteratively estimates the minimizer $\widehat{\boldsymbol{\theta}}$ of the problem (7) as follows:

$$\widehat{\boldsymbol{\theta}}^k = \text{prox}_{F_1}(\boldsymbol{\theta}^k) + a^k \quad (9)$$

$$\boldsymbol{\theta}^{k+1} = \boldsymbol{\theta}^k + \gamma^k (\text{prox}_{F_2}(2\widehat{\boldsymbol{\theta}}^k - \boldsymbol{\theta}^k) - \widehat{\boldsymbol{\theta}}^k + b^k) \quad (10)$$

where $\text{prox}_{F_1}(\cdot)$ and $\text{prox}_{F_2}(\cdot)$ are the proximity operators of the functions F_1 and F_2 , γ^k is a (variable) relaxation parameter in the range (0, 2) and a^k and b^k are two sequences associated with the proximity operators allowing for approximations in their calculation and inexact implementation. The existence and uniqueness conditions of a solution to the optimization problem defined in Eq. (7) using the DRS algorithm are discussed in [48]. For theoretical discussions on the convergence of the DRS algorithm for non-convex problems, interested readers should consult ref. [50]. To apply the DRS to the problem (3), we need to obtain the proximity operator of the data fidelity term $D(\boldsymbol{\theta}) = \frac{1}{2\sigma^2} \|\mathbf{y} - \Phi\mathbf{W}\boldsymbol{\theta}\|^2$, (i.e. F_1) and the operator of the prior $R(\boldsymbol{\theta})$ for a pseudo L_0 norm (i.e. F_2). In the following subsections, we derive closed-form solutions for these operators and discuss the incorporation of prior wavelet coefficients into the DRS algorithm. As we obtain a closed-form solution for the proximity maps, we can simply set the a^k and b^k terms to zero in Eqs. (9) and (10).

1) The proximal map of data fidelity

The proximal map of the data fidelity term, i.e.

$$\text{prox}_{\sigma D}(\boldsymbol{\theta}) = \underset{\mathbf{z} \in \mathbb{R}^K}{\text{argmin}} \left\{ \frac{1}{2} \|\mathbf{z} - \boldsymbol{\theta}\|^2 + \frac{1}{2\sigma^2} \|\mathbf{y} - \Phi\mathbf{W}\mathbf{z}\|^2 \right\} \quad (11)$$

is obtained by equating the derivative of its objective to zero, thereby the solution is given by: $\widehat{\mathbf{z}} = (\mathbf{W}^* \Phi^T \Phi \mathbf{W} + \sigma^2 \mathbf{I})^{-1} (\sigma^2 \boldsymbol{\theta} + \mathbf{W}^* \Phi^T \mathbf{y})$. To calculate the inverse term in this equation, we follow the matrix inversion lemma and make use of the fact that $\Phi \Phi^T = \mathbf{W} \mathbf{W}^* = \mathbf{I}$, thereby the proximal mapping is given by:

$$\text{prox}_{\sigma D}(\boldsymbol{\theta}) = \boldsymbol{\theta} + \frac{1}{1+\sigma^2} \mathbf{W}^* \Phi^T (\mathbf{y} - \Phi \mathbf{W} \boldsymbol{\theta}). \quad (12)$$

In this study, we consider that the operator Φ in Eq. (1) removes the projections of \mathbf{f} without introducing noise. As a result, the variance of noise, σ^2 , in Eq. (12) is set to zero.

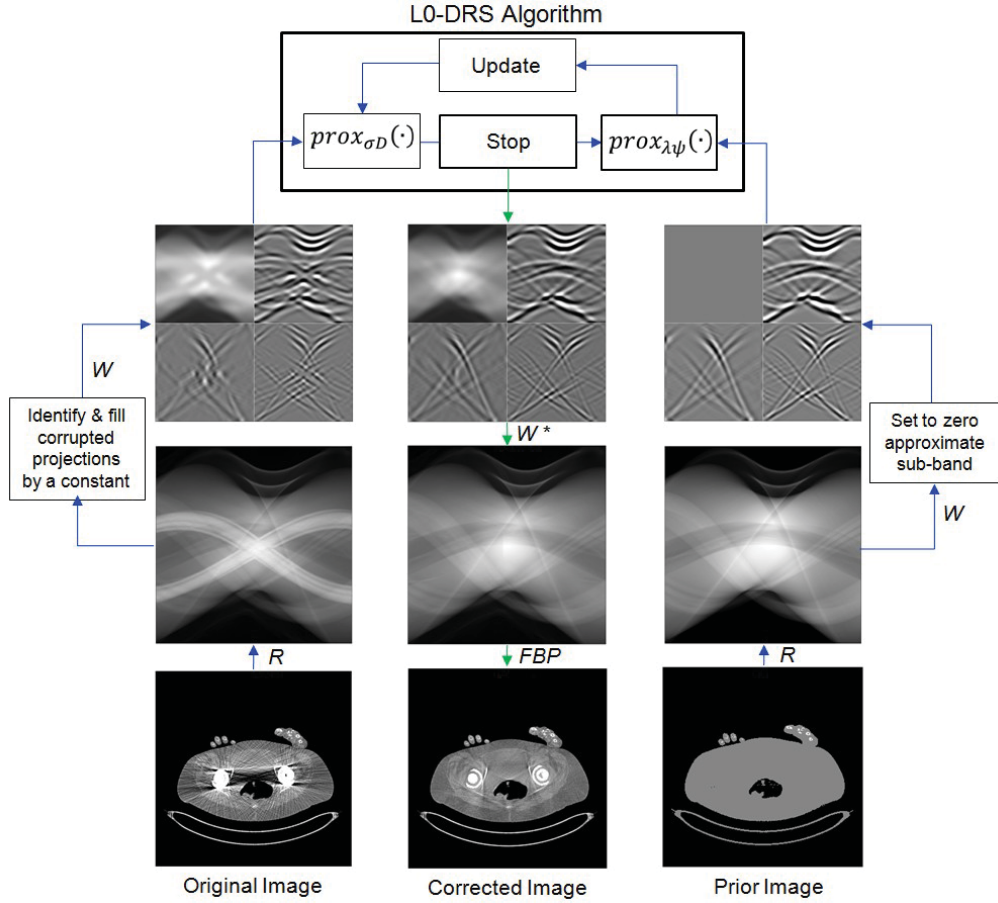


Figure 3. Flowchart of the proposed wavelet-based L_0 -DRS algorithm. In this algorithm, the uncorrected image is segmented to produce metallic implants and a prior image. The images are then forward projected by the operator R . The corrupted projections are identified and filled with a constant value. The resulting sinograms are transformed into the wavelet domain by the operator W . The approximate sub-band of the prior wavelet coefficients is set to zero. The wavelet coefficients are fed into the DRS algorithm, which estimates the wavelet coefficients of missing projections according to Algorithm 1. The estimated coefficients are transformed back into the sinogram domain by the operator W^* and the corrected images are reconstructed using filtered back-projection (FBP) and superimposed by the implants.

2) The proximal map of the prior

The pseudo L_0 norm defined in Eq. (5) is separable and follows the form $R(\mathbf{z}) = \sum_i \psi(z_i)$, where $\psi(z) = \nu \ln(1 + |z|/\rho)$. The proximal map of such a separable function can therefore be obtained separately with respect to each component as follows:

$$\text{prox}_{\lambda\psi}(\theta_i) = \underset{z_i \in \mathbb{R}}{\text{argmin}} \left\{ \frac{1}{2} (z_i - \theta_i)^2 + \lambda\psi(z_i) \right\} \quad (13)$$

One can obtain a closed-form solution to the above problem by the following thresholding rule (see Appendix A for more details):

$$\text{prox}_{\lambda\psi}(\theta_i) = \begin{cases} \frac{1}{2} (\theta_i - \rho + \sqrt{(\theta_i + \rho)^2 - 4\lambda\nu}), & \theta_i > T \\ 0, & |\theta_i| \leq T \\ \frac{1}{2} (\theta_i + \rho - \sqrt{(\theta_i - \rho)^2 - 4\lambda\nu}), & \theta_i < -T \end{cases} \quad (14)$$

where $T = 2\sqrt{\lambda\nu} - \rho$. In this rule, as $\rho \rightarrow 0$, the threshold T is slowly decreased. It can therefore play a role similar to the cooling parameter of simulated annealing techniques, allowing the solution to escape from local minima. As shown in Appendix A, when $\rho \rightarrow \infty$ the solution of problem (13) is given by a *soft* thresholding rule [51], which is in fact the proximity operator of an L_1 norm. Figure 2(b) compares the derived thresholding rule with a soft thresholding rule. It can be seen that the pseudo L_0 rule tends to linearly shrink the coefficients θ_i in $|\theta_i| > T$.

3) Incorporation of prior wavelet coefficients

To improve the accuracy of the restored wavelet coefficients and hence the missing sinogram projections, we modify the DRS algorithm in order to incorporate some prior wavelet coefficients obtained from the sinogram of a prior image. For this purpose, we introduce the detail sub-bands of such prior wavelet coefficients, θ_p , into Eq. (10) as follows:

$$\theta^k = \theta^{k+1} + \gamma^k (\text{prox}_{E_2}(2\hat{\theta}^k - \theta^k - \theta_p) - \hat{\theta}^k + \theta_p) \quad (15)$$

where θ_p is in fact the wavelet coefficients with zeroed approximate sub-band. In this modification, the thresholding of wavelet coefficients is disturbed by subtracting the energy corresponding to the prior coefficients, and then the removed energy is added back. The rationale behind this modification is motivated by the observation that the algorithm can properly restore the approximate sub-band of the wavelet coefficients of missing projections from adjacent coefficients. However, as usual a large area of sinogram projections is corrupted by metallic implants, the detail coefficients are not properly restored. Therefore, the introduction of prior detail coefficients can improve the accuracy of the estimation. To this end, Algorithm 1 summarizes the proposed algorithm in the recovery of missing projections.

Algorithm 1: L_0 -DRS Algorithm

Choose: $\mu, \gamma^k, \lambda, \eta$ and initialize: $\theta_p, \theta^0 = W^*f^0, \rho^0 = 1, v^0 = \ln(1 + 1/\rho^0), k = 0$

While ($\|\theta^{k+1} - \theta^k\|/\|\theta^k\| < \eta$) **do**,

1. Compute the proximal map, $\hat{\theta}^k$, of data fidelity for θ^k according to Eq. (12).
2. Threshold the coefficients $2\hat{\theta}^k - \theta^k - \theta_p$ according to Eq. (14).
3. Compute θ^{k+1} according to Eq. (15).
4. Impose non-negativity constraint: $\theta^{k+1} = W^*[W\theta^{k+1}]_+$.
5. Update the variables: $\rho^{k+1} = \mu\rho^k, v^{k+1} = \ln(1 + 1/\rho^{k+1}), k = k + 1$.

Output: $\hat{f} = W\hat{\theta}^k$.

In this algorithm, we let ρ iteratively approaching zero using the relaxation parameter $0 < \mu < 1$ and set $\gamma^k = 1$. The regularization parameter λ should be large enough to ensure the thresholding of the wavelet coefficients. Therefore, we set it to the maximum projection value of \mathbf{y} . A global convergence was declared when the normalized L_2 error of two successive iterates falls below a tolerance of $\eta = 1 \times 10^{-3}$. The initial guess of the wavelet coefficient, θ^0 , is obtained from the forward wavelet transform of a sinogram, in which missing projections have been filled with a non-zero constant value. Figure 3 shows the flow chart of the proposed algorithm. The missing projections are identified by the forward projection (or Radon transform, R) of a metal only image, obtained from the segmentation of metallic implants in the uncorrected image. The prior image was obtained by the approach proposed by Meyer *et al.* [52] (see next section for details). In this work, we followed a block-wise approach in the recovery of missing projections, using two overlapping 512×512 blocks, automatically portrayed on missing regions of the sinograms (see next section for the specifications of sinograms). This approach favors the fact that discrete wavelet transforms are typically implemented for dyadic- and square-sized matrices.

II.C. Simulation and clinical studies

In this study, the performance of the proposed MAR algorithm was evaluated using artificial sinograms (raw data) obtained from the forward projection of original uncorrected CT images. To acquire such data in conditions closely matching actual data acquisition, we consider the fan-beam geometry of a simulated single-slice CT scanner with 888 detector channels, 984 angular samples over a 360 orbit, detector pitch of 1 mm, 949 mm source to detector distance, 541 mm source to iso-center distance, 408 mm iso-center to detector distance. The geometric system matrix describing this scanner was generated by the MATLAB-based Image Reconstruction Toolbox [53] and line integrals were employed during forward projection to obtain the Radon transform.

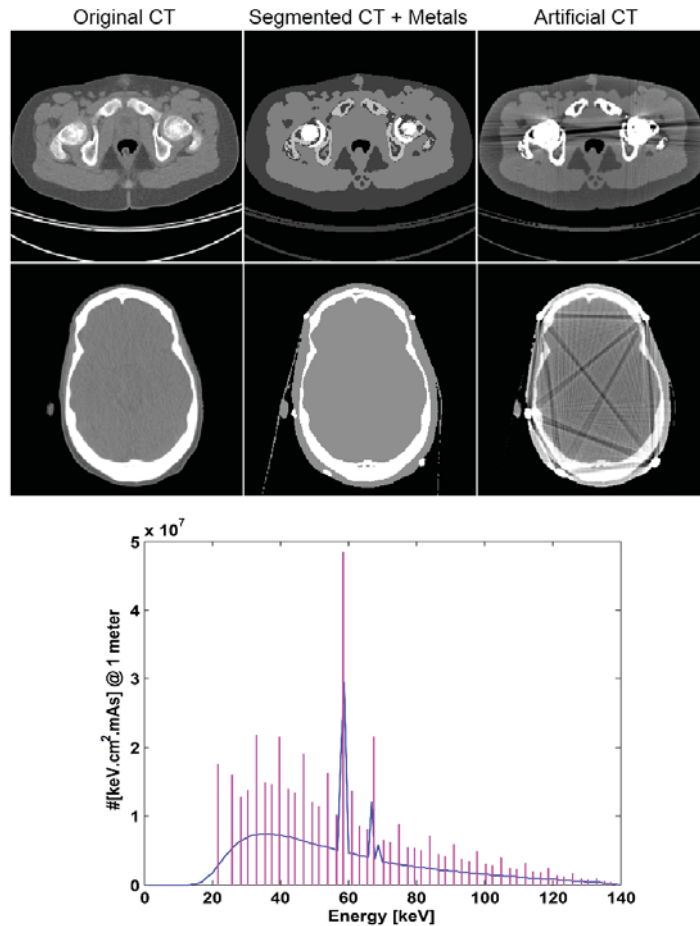


Figure 4. Simulation of metal artifacts based on the polychromatic propagation of x-ray beams. The original CT images are segmented into different tissue classes and superimposed on metallic implants. The x-ray spectrum is sampled for a finite number of energies. The attenuation coefficients of each class are then calculated for each energy and the Poisson noise realization of their sinograms summed up and log-processed. The resulting sinograms are then reconstructed using the FBP algorithm, which produces CT images presenting with streaking artifacts. (Display window/level in 1st and 2nd row: 700/90 and 800/50 HU, respectively).

Following the correction of the sinograms for corrupted projections, the corrected images were reconstructed using the FBP algorithm, with Ram-Lak filter, for a resolution of 512×512 , pixel size of 0.97 mm and a 500-mm field-of-view. The Ram-Lak filter was chosen to best preserve the sharpness of the reconstructed images. Algorithm 1 together with undecimated discrete wavelet transforms were implemented in MATLAB 2010a, running on a 12-core workstation with 2.4 GHz Intel Xeon processors and 32 GB memory. In this study, we followed Meyer's approach [52] to define the prior image. In this approach, the original CT image, contaminated by streaking artifacts is segmented into three tissue types: air, bone and soft tissue. For this purpose, we used simple thresholding to segment CT images. Soft tissues were segmented using a threshold of 624 HU, while bone tissues were segmented at 1300-1400 HU, depending on the organ or slice being examined. Note that dark and bright streak artifacts can be falsely segmented as air and bone in the segmented soft and bone images, respectively. These false segmentations were respectively eliminated by close and open morphological filtering. As suggested by Meyer *et al.* [52], an alternative way in such cases can be the segmentation of an image pre-corrected using a linear interpolation MAR algorithm. Following segmentation, the CT numbers of air and soft tissue regions were set to -1000 and 0 HU, respectively, and the numbers of bone regions were kept the same as the original image because of the variation of bone density and CT numbers. In the obtained prior image, we assigned the CT number of soft tissue to metal implants. The performance of the proposed MAR algorithm was evaluated using a number of simulated and clinical studies of patients with hip prostheses, electroencephalogram (EEG) electrodes, dental fillings and spine fixation. As mentioned earlier, the missing projections and thereby the metal trace set Ω , were identified by forward projection of a segmented metal only image. The segmentation of metallic implants was performed using simple thresholding at about 3000 HU for dental fillings and 2000 HU

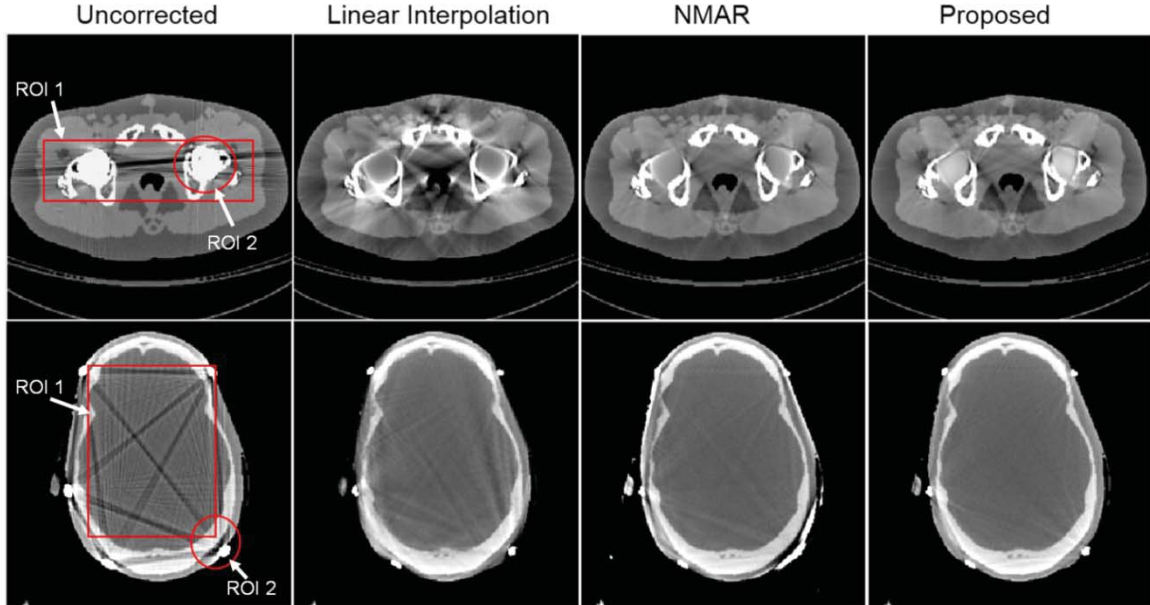


Figure 5. Illustration of metal artifact reduction of simulated hip prostheses (top) and head EEG CT studies (bottom) (WW/WL = 500/50 HU).

Table I. Summary of CT scanning parameters used for acquisition of the clinical studies.

	Siemens Biograph 64 TP PET/CT			Siemens Sensation 16 CT	
	Hip prostheses	Dental fillings	Spine fixation	ECG electrodes	Dental fillings
Tube voltage (kVp)	100/120	120	120	140/120	120
Tube current (mA)	40/32	116/91	95	179/175	166
Exposure time (ms)	500	500	500/500	1500/1000	750
Slice thickness (mm)	2-2	5	5	3	5

for other implants. In some cases, a morphological dilation was performed on the segmented implants to include more accurately all pixels belonging to the implants. To objectively evaluate the performance of the proposed MAR algorithm with respect to a ground truth CT image (i.e. without metal artifacts), we retrospectively generated metal artifacts in the artifact-free CT image of two patients with simulated bilateral hip prostheses and head EEG electrodes (Figure 4). To simulate beam hardening and the resulting streaking artifacts, we modeled the polychromatic propagation of x-ray beams through the patient body. For this purpose, the original CT images were segmented into 3 classes (air, soft tissue, and bone) and were superimposed on iron implants. A polyenergetic x-ray spectrum was generated by SpekCal software [54] for a tube voltage of 140 kVp, 2.5 mm aluminum filtration, 30 degrees anode angle and a tube output of $\sim 200 \mu\text{Gy}/\text{mAs}$ at 1 meter. As shown in Figure 4, the spectrum was uniformly sampled for 51 monoenergetic x-ray beams with an intensity and average energy calculated over each energy interval. For each beam, the energy-dependent linear attenuation coefficients of biological tissues were calculated using the NIST XCOM photon cross section library [55]. The attenuation maps were forward projected and then the Poisson noise realizations of the resulting sinograms summed up to obtain a sinogram acquired under the conditions of polychromatic propagation of x-ray beams. The resulting sinogram was log-processed and reconstructed using the FBP algorithm. As shown in figure 4, the reconstructed artificial CT images suffer from streaking artifacts. In this simulation, Compton scattering and non-linear partial volume effect were not modeled. From artificially degraded images, we obtained prior images, metallic implants, and missing projections in the sinograms resulting from the polychromatic propagation of x-ray beams. In addition, for each dataset a ground truth image was obtained using the above-mentioned procedure by considering the metallic implants as bony structures.

The performance of the proposed L_0 -DRS algorithm was evaluated using the simulated datasets through comparison to the conventional linear interpolation approach and the NMAR algorithm proposed by Meyer *et al.* [52]. For the objective comparison of MAR algorithms, two regions of interest (ROIs) were drawn on uncorrected images and the normalized root mean square difference (NRMSD) and mean absolute deviation

(MAD) between corrected images (x^{MAR}) and their ground truth (x^{True}) were calculated for each ROI as follows:

$$\text{NRMSD}(\%) = 100 \times \sqrt{\frac{\sum_{i \in \text{ROI}} (x_i^{MAR} - x_i^{True})^2}{\sum_{i \in \text{ROI}} (x_i^{True})^2}} \quad (16)$$

$$\text{MAD}(\text{HU}) = \frac{1}{N} \sum_{i \in \text{ROI}} |x_i^{MAR} - x_i^{True}| \quad (17)$$

For the clinical evaluation of the MAR algorithms, the CT datasets of 8 patients were used. The data were acquired in helical mode on the Biograph 64 True Point PET/CT and Sensation 16 CT scanners (Siemens Healthcare, Erlangen, Germany), equipped with 40- and 24-row detectors, respectively. The clinical studies include: uni- and bi-lateral hip prostheses (2 patients), dental fillings (3 patients), spine fixation (1 patient) and EEG electrodes (2 patients). Table I summarizes scanning parameters used for CT data acquisition. For quantitative evaluation of the MAR algorithms using clinical studies, we calculated the absolute mean deviation (AMD) between mean CT numbers of two ROIs defined on uncorrected and corrected CT images over streaking artifacts. Owing to the absence of a ground truth for the clinical studies, we defined a same-sized ROI on uncorrected images far from streaking artifacts and used it as a reference ROI.

III. Results

III.A. Simulation studies

Figure 5 shows the results of metal artifact reduction of the simulated bilateral hip and EEG head datasets using the studied MAR algorithms. In both datasets, the algorithms have noticeably reduced streaking artifacts. However, linear interpolation was unable to effectively reduce the artifacts, since new artifacts have been introduced in the corrected images. The NMAR and proposed algorithms have noticeably reduced the artifacts, thereby improving the quality of the corrected images. In the hip dataset, the two algorithms depict nearly the same level of artifact reduction; however, as can be seen, the proposed algorithm tends also to restore the regions of metallic implants. In the head dataset, the proposed algorithm shows less residual artifacts in comparison with NMAR. Moreover, in this simulated dataset and also the clinical datasets with EEG electrodes, we noticed that the NMAR algorithm introduces wide and severe bright streaking artifacts at the borders near the electrodes (see figure 5), which are due to the normalization of projection bins by small values at these regions. To practically reduce this effect in clinical studies, we expanded the soft tissue region of prior images for this algorithm. Furthermore, to avoid division by zero during normalization, we thresholded zero bins in the sinogram of the prior image at a threshold value $t = 1$. Small values of t have been suggested by Meyer *et al.* [52]; however, these values can result in highly inaccurate values in the normalized sinograms, and hence, can contribute to the appearance of severe bright streaking artifacts in the EEG datasets.

For the quantitative comparison of the algorithms with respect to the ground truth image, two ROIs were defined on the degraded CT images (see figure 5, 1st column): one large rectangular ROI (ROI 1) to cover the largest part of affected areas, and one circular ROI (ROI 2) for local evaluations near the implants. Table II summarizes the NRMSD and MAD results for the two datasets. In the ROI-based evaluation, the regions of metallic implants were excluded from the ROIs of (un-)corrected and ground truth images, since the implants are finally added back to the corrected images. The results of both datasets show that the proposed algorithm outperforms both linear interpolation and NMAR algorithms globally (in ROI 1) and locally (in ROI 2) by achieving lower NRMSD and MAD estimates. To further evaluate the algorithms, figure 6(a–c) shows three projection profiles on the sinograms of the hip dataset completed by the studied MAR algorithms along the dash lines shown in figure 6(d). As can be seen, the proposed MAR algorithm has more accurately estimated the missing projections toward the true projections. For both simulated datasets, the relaxation parameter μ in Algorithm 1 was set to 0.8. To obtain this heuristically optimal value and also to evaluate the impact of μ on MAR performance and convergence rate of the proposed algorithm, we performed a set of experiments with different values of μ and monitored the variations of NRMSD in the defined ROIs. Figure 7(a–b) show NRMSD versus different values of μ in the range 0.65–0.95, with an increment value of 0.05, for ROIs 1 and 2, respectively.

Table II. ROI-based quantitative evaluation of the studied MAR algorithms using simulated hip and EEG CT studies in terms of normalized root mean square difference (NRMSD) and mean absolute deviation (MAD).

Phantom	ROI	Uncorrected		Linear interpolation		NMAR		L_0 -DRS	
		NRMSD (%)	MAD (HU)	NRMSD (%)	MAD (HU)	NRMSD (%)	MAD (HU)	NRMSD (%)	MAD (HU)
Hip prosthesis	1	56.96	197.29	13.43	109.12	7.53	54.78	7.27	55.50
	2	86.89	367.26	17.05	145.57	12.52	97.17	11.51	95.67
EEG electrodes	1	11.92	20.02	1.27	7.58	0.87	5.46	0.73	4.65
	2	73.03	145.73	8.83	43.49	31.07	151.94	3.58	19.79

Table III. ROI-based quantitative evaluation of the studied MAR algorithms using clinical studies, shown in figures 9–11, in terms of absolute mean deviation (AMD) between the mean CT number of two ROIs, drawn on artifactual regions (ROIs 1 and 2), and that of a reference ROI, drawn on a background region far from artifacts (ROI B). For each dataset, the CT images of cases 1–3 are shown in the 1st–3rd rows of the figures, respectively.

Dataset	Case #	ROI #	Uncorrected	Linear interpolation	NMAR	L_0 -DRS
Hip prosthesis	1	1	347.41	87.62	73.57	52.18
		2	576.97	178.94	181.00	173.41
	2	1	153.08	104.53	145.78	124.44
		2	303.30	247.32	113.45	108.81
	3	1	146.73	14.73	26.11	53.14
		2	145.59	5.95	22.33	7.55
Dental fillings	1	1	89.60	99.17	155.86	46.91
		2	73.51	6.65	12.23	0.00
	2	1	54.53	52.48	56.55	36.64
		2	187.25	81.55	73.93	66.11
	3	1	76.54	78.54	22.58	60.65
		2	59.94	54.56	15.92	1.01
Spine fixation	1	1	92.39	98.75	4.22	4.90
		2	43.68	15.03	42.60	6.04
	2	1	200.96	67.98	21.13	19.88
		2	4.05	82.41	76.78	56.96
	3	1	113.42	92.40	59.41	52.01
		2	134.91	64.89	25.42	20.59
EEG electrodes	1	1	0.16	3.69	11.45	8.90
		2	2.29	13.16	10.32	0.49
	2	1	54.02	19.34	23.54	20.51
		2	27.13	74.45	38.05	3.14
	3	1	54.38	121.40	88.09	62.94
		2	12.95	40.10	24.09	18.83

The results show that an optimal value of μ for these datasets is in the range 0.75–0.85. Thereby, we chose a mid value of 0.8 as an optimal value. The visual comparison of corrected images using different values of μ did not reveal a significant difference. The small variations of NRMSD in ROIs for both datasets, whose standard deviations are 0.01–0.2 in ROI 1 and 0.04–0.3 in ROI 2, reflect this observation. Figure 7(c) shows the number of elapsed iterations for different values of the relaxation parameter. It turns out that as μ increases, the number of iterations also increases. In fact, for lower values of μ , the homotopic parameter ρ in Eq. (6) decays faster to zero, thereby the pseudo L_0 norm approaches an L_0 norm after fewer number of iterations. It should be emphasized that these results were obtained for a tolerance $\eta = 1 \times 10^{-3}$ in Algorithm 1. Therefore, the algorithm was stopped when the relative difference between two successive wavelet coefficients is less than 1%. It was found that smaller tolerance values have no a significant effect on the quality of corrected images but can potentially increase the number of iterations and computation time. The average computational time of our MATLAB-based implementation of the proposed L_0 -DRS algorithm was found to be around 5.1 seconds per iteration. Therefore, our simulation results show that higher values of μ and η might not be prudent in terms of image quality and computational time.

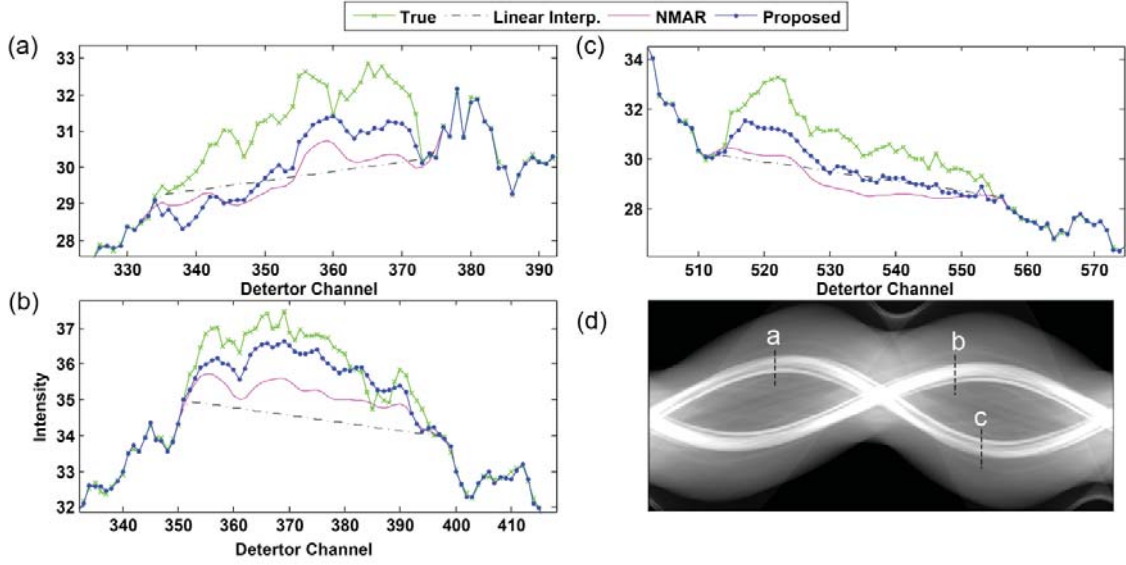


Figure 6. Comparison of projection profiles completed by the evaluated MAR algorithms with the true profiles of the hip prosthesis data along the dash lines shown in (d).

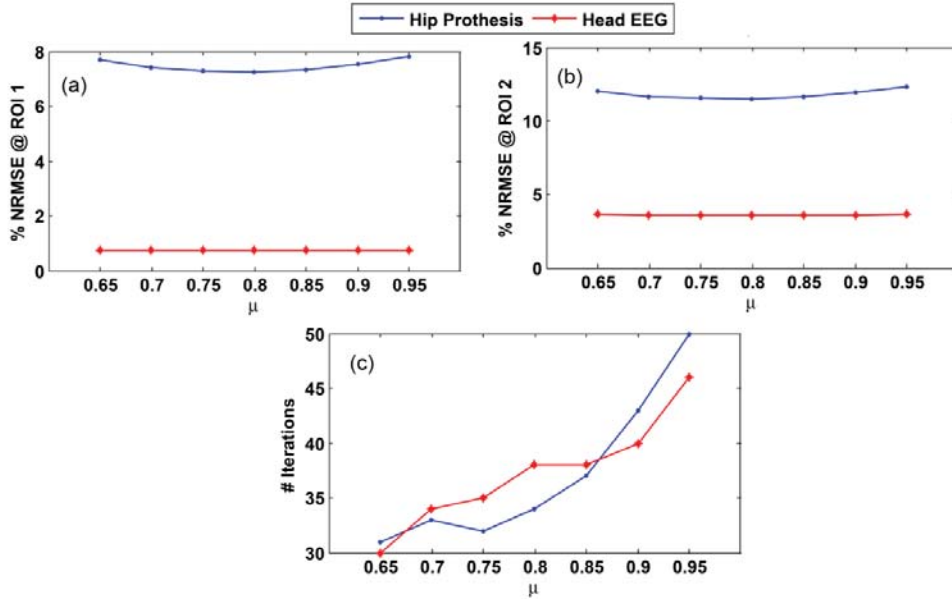


Figure 7. Objective performance of the proposed L_0 -DRS MAR algorithm for different relaxation parameters μ using the simulated hip and head CT data in terms of (a–b) NRMSE in ROIs 1 and 2, and (c) the number of required iterations to reach convergence.

III.B. Clinical studies

The simulated hip and EEG studies, which had different numbers and sizes of metallic implants, showed that the proposed algorithm achieves its best performance in terms of improvement of image quality and the required number of iterations when using $\mu = 0.8$ and $\eta = 1 \times 10^{-3}$. In our clinical studies, we initialized the proposed L_0 -DRS algorithm using the above values and, similar to simulation studies, compared its performance against linear interpolation and NMAR algorithms. As mentioned earlier, four different categories of metallic implants, including hip prostheses, dental fillings, spine fixation and EEG electrodes were considered in this work. In each category, we selected three CT slices for qualitative evaluations. For each slice, three ROIs were defined on artifactual regions near metallic implants (ROIs 1 and 2) and on a background region far away from artifacts

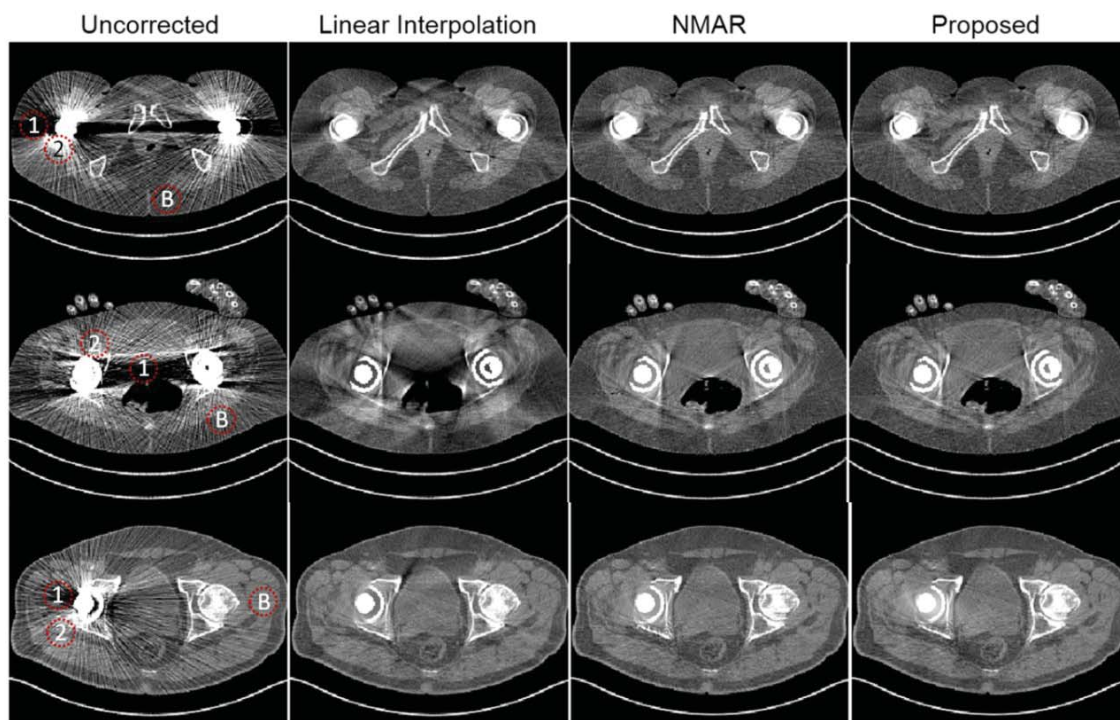


Figure 8. Illustration of metal artifact reduction of the clinical hip prosthesis datasets (W W /WL= 700/40 HU).

(ROI B) and the absolute deviation between the mean CT number of ROIs 1 and 2 and that of ROI B was calculated.

1) Hip prostheses

Figure 8 shows the results of metal artifact reduction in CT slices of two patients with uni- and bi-lateral hip prostheses. As summarized in Table I, these patients have undergone a low-dose CT scan for attenuation correction as part of clinical PET/CT examinations. As can be seen, the metallic implants resulted in severe bright and streaking artifacts mostly due to beam hardening and photon starvation. The MAR algorithms have substantially reduced streaking artifacts. However, linear interpolation has introduced new artifacts, especially in the 2nd-row dataset in which there are two large hip prostheses that corrupt a large number of projections, which makes pure interpolation inefficient. The NMAR algorithm improves the performance of linear interpolation by normalization with a prior sinogram. In comparison, it has remarkably improved image quality; however, there are still residual dark and new bright artifacts in the 1st- and 2nd-row images. The proposed wavelet-based MAR algorithm, which incorporates the same prior sinogram as in NMAR, has also improved image quality and visually achieved the same level of artifact reduction as NMAR. However, a close inspection revealed that the proposed algorithm has reduced more effectively the residual dark streaking artifacts in the 1st-row image and introduced less bright artifacts in the 2nd-row located around the implants. For the quantitative evaluation of the algorithms, we delineated ROIs 1, 2 and B on the uncorrected image as shown in figure 8 (1st column). The ROIs are of the same size (30 mm in diameter). Since in this case, ROI B contains streaking artifacts, we used the NMAR image as a reference for this background ROI. The quantitative results are presented in Table III. Note that in this table, the cases 1–3 correspond to the images shown in 1st–3rd rows. The results show that the proposed algorithm generally achieves lower AMD values compared to NMAR algorithm in both ROIs defined in regions impaired with dark streaking artifacts. It should be noted that the 3rd case linear interpolation outperforms the other algorithms. However, in terms of overall image quality, the proposed and NMAR algorithms have a better performance.

2) Dental fillings

The reduction of artifacts arising from dental fillings is a challenging task because there are often multiple high-density implants that severely corrupt projection data and thereby the resulting streaking artifacts obscure diagnostically important information in the dental arch area. Figure 9 shows the results of artifact reduction in

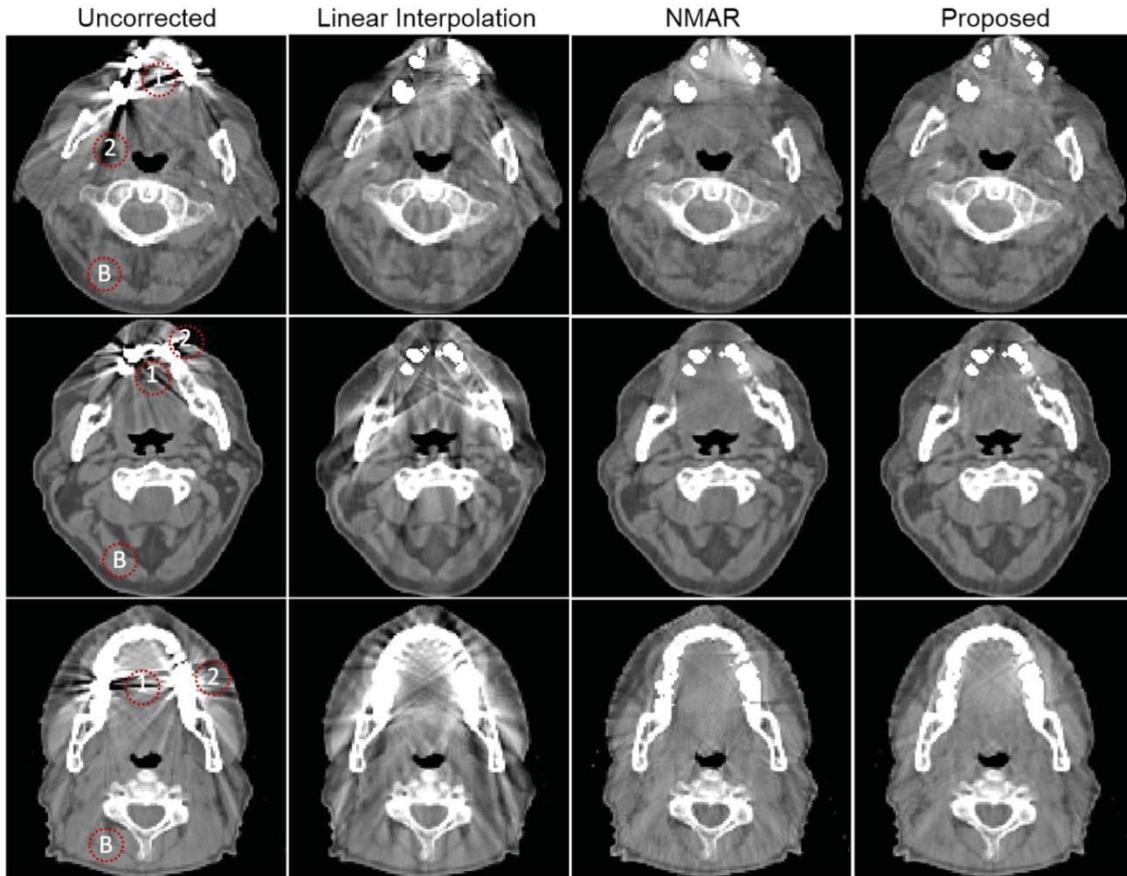


Figure 9. Illustration of metal artifact reduction of clinical dental filling CT images (WW/WL = 600/40 HU).

CT data of three patients presenting with dental fillings. As can be seen, linear interpolation introduced new streaking artifacts in all three cases. Because, as mentioned above, in such cases there are multiple closely-seated dental fillings, which makes pure interpolation of corrupted projections from neighboring projections inefficient and even inaccurate. The images corrected by NMAR and the proposed algorithm show a substantial improvement in terms of artifacts reduction without introducing new severe ones. Note that in the case of the 1st and 2nd row datasets, we applied a dilation morphological filtering (with disk-shaped structuring element of 1.94 mm radius) to the segmented metallic implants in order to completely remove residual artifacts in the images corrected by NMAR and proposed MAR algorithms. Afterwards, the original segmented metals were added back to the images. The comparison of results in the 1st-row dataset, acquired with arms up, shows that the proposed algorithm outperforms its NMAR counterpart by the reduction of artifacts without introducing new blurring-like artifacts in the palatine area. In the 2nd-row dataset, the same trend is also observed, although the performance of the algorithms is more comparable. In the 3rd-row dataset, the proposed algorithm has, however, slightly introduced new bright streaking artifacts in the area between the implants. For quantitative comparison of the algorithms, three ROIs (20 mm in diameter) were defined on the uncorrected images, as shown in figure 9. The results of ROI analysis show that the L_0 -DRS algorithm outperforms the NMAR algorithm by achieving lower values of absolute mean deviation with respect to the background ROI B.

3) Spine fixation

Figure 10 shows the results of metal artifact reduction in three CT slices of a patient with spine fixation undergoing low-dose CT imaging in the context of a PET/CT examination. The results show that the reduction of artifacts in this localization is somehow challenging, since the implants are seated close to each other and several bony structures surround the implants. In all three cases, linear interpolation is not efficient and introduces new streaking artifacts. In the 1st-row dataset, the NMAR and proposed algorithms substantially suppress dark streaking artifacts; however, both of them have introduced blurring and new artifacts around and beneath the implants. In the 2nd- and 3rd-row datasets, both algorithms have noticeably reduced the artifacts in

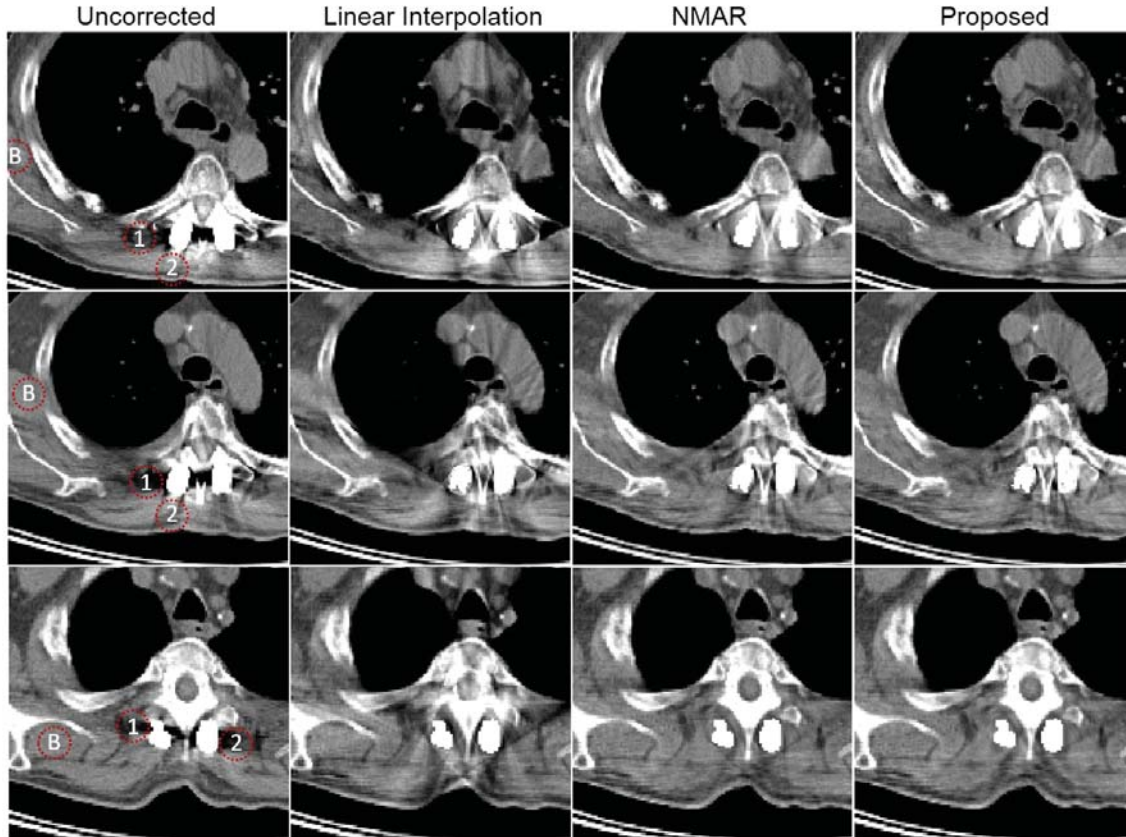


Figure 10. Illustration of metal artifact reduction of clinical spine fixation CT images (WW/WL = 500/40 HU).

comparison with linear interpolation, particularly in the last one, where both algorithms have almost eradicated the artifacts. The quantitative evaluation of the algorithms was performed using the same-sized (20 mm in diameter) ROIs. The results are summarized in Table III. It turns out that the proposed algorithm can generally outperform NMAR, which can be verified by visual interpretation of the corrected images in, for e.g. ROI 2 of the 1st-row dataset. As can be seen, the proposed algorithm has comparably introduced less dark artifacts in that region.

4) EEG electrodes

Figure 11 shows the results of metal artifact reduction of the CT data presenting with EEG electrodes. As expected, linear interpolation lags behind NMAR and the proposed algorithm since they make use of some prior information during projection completion. In the 1st- and 2nd-row datasets, a morphological dilation filtering (with a disk element of radius 1.94 mm) was applied on the segmented metallic implants, because our preliminary results showed that simple thresholding cannot guarantee the identification of all corrupted projections and thereby, dark streaking artifacts reappear in the reconstructed images. As mentioned earlier, in the case of NMAR algorithm, the soft tissue portion of the prior images of the datasets was expanded by a dilation filtering since this algorithm results in extremely severe bright artifacts at the borders. The results show that in all three datasets, the proposed algorithm outperforms its counterparts. The outperformance of this algorithm is more noticeable in the amount of residual artifacts in the cranium area. More accurate artifact reduction in regions close to electrodes is achieved by the proposed algorithm. As can be seen, linear interpolation and NMAR algorithms have respectively distorted and under-estimated soft tissues around the electrodes. The quantitative analysis was performed for same-sized ROIs (30 mm in diameter) shown in figure 11 (1st column). The results presented in Table III show that the proposed algorithm achieves lower metric values, reflecting the introduction of less artifacts in this region.

To further assess the performance of the studied algorithms in the sinogram domain, figure 12 compares the sinograms of uncorrected and corrected images of two datasets. The 1st row shows the sinograms of the bilateral hip dataset shown in figure 8 (middle row), while the second one shows those of the EEG electrode dataset shown in figure 11 (middle row). In both cases, the sinograms with missing projections (metal traces) have also

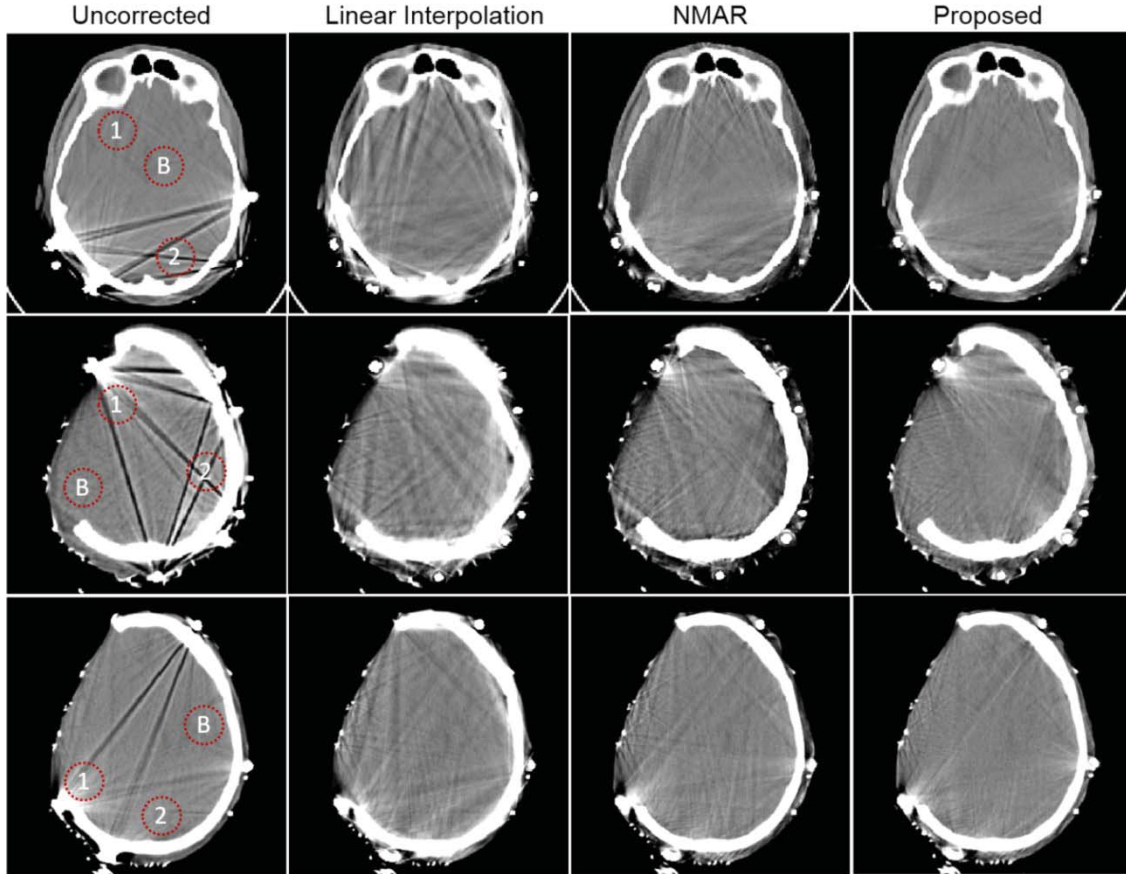


Figure 11. Illustration of metal artifact reduction of clinical head EEG studies (WW/WL = 500/40 HU). The results show that the proposed algorithm results in the lowest residual artifacts, especially at the borders near to the electrodes.

been shown. As can be seen, linear interpolation simply bridges the missing area and results in discontinuities. This inaccurate projection completion also appears in the NMAR algorithm, especially in the 2nd-row sinogram, where in some projection angles, the missing projections are close to the border of the head. In both datasets, the proposed algorithm has more accurately and continuously estimated the missing projections.

IV. Discussion

The presence of permanent metallic implants in patients undergoing x-ray CT examinations can induce streaking metal artifacts that impair the diagnostic quality and clinical usefulness of CT images. In this work, we proposed a new projection completion-based MAR algorithm by formulating the recovery of missing projections as a regularized inverse problem and employed a pseudo L_0 sparsity-promoting prior to impose the prior knowledge of the sparsity CT sinograms in a dictionary of translation invariant wavelets. Furthermore, we exploited the detail sub-bands of the wavelet coefficients of a prior sinogram to improve the efficiency of the proposed algorithm.

We compared the proposed algorithm with linear interpolation and Meyer's NMAR algorithms. The NMAR algorithm uses prior sinogram for normalizing and flattening the neighboring projections of missing regions, thus facilitating the interpolation task. In contrast, our proposed algorithm is based on solving an optimization problem in which the missing projections are iteratively estimated. In this algorithm, the prior sinograms are exploited in a very different approach. The detail wavelet coefficients of a prior sinogram are iteratively introduced into this algorithm during the pseudo L_0 -based thresholding of intermediate wavelet coefficients (see Algorithm 1). Following the convergence of the algorithm, declared by a stopping criterion, an inverse wavelet transform is applied on the estimated coefficients and the completed sinogram is obtained. Zhao *et al.* [11] proposed a related projection completion MAR algorithm in the wavelet domain. In this algorithm, the missing projections are one-dimensionally interpolated by a weighted sum of the wavelet coefficients of the corrupted

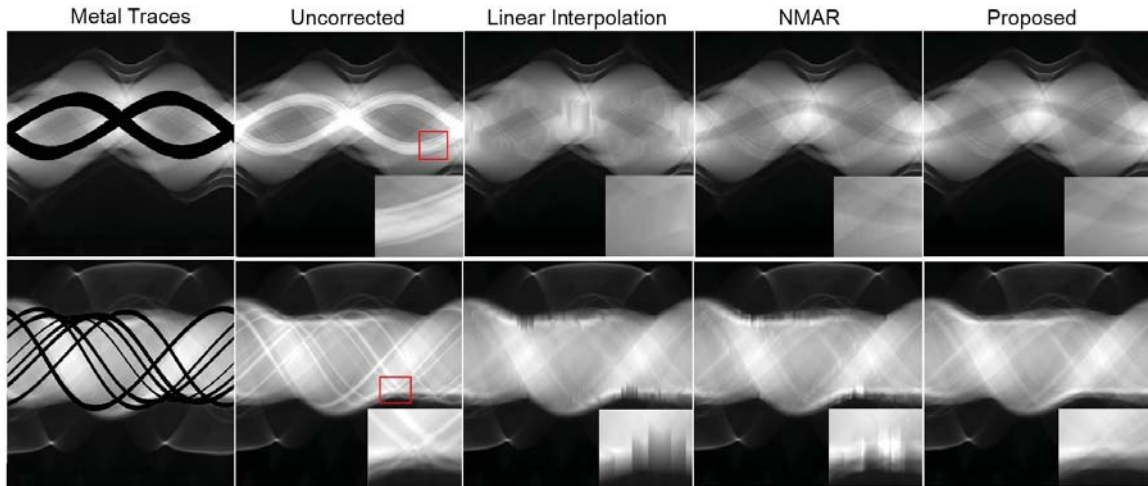


Figure 12. Comparison of the sinograms completed by the studied MAR algorithms. Top to bottom: the sinograms of the images shown in the middle row of figures 8 and 11, respectively. In the first column, the missing projections (metal traces) are shown with zero-intensity.

projections and the wavelet coefficients of linearly interpolated projections. Although theoretically well-founded, this algorithm did not significantly reduce metal artifacts compared to standard linear interpolation. In contrast, the proposed algorithm is an iterative wavelet-based algorithm in which missing projections are two-dimensionally optimally estimated by thresholding and proximal mapping schemes. To objectively assess the efficacy of the proposed algorithm with respect to a ground truth, we simulated metal artifacts in tissue-segmented CT datasets by considering the polychromatic propagation of x-ray beams. As can be seen in figure 4, the resulting streaking artifacts impair the tissues in the same way as a real CT acquisition. Although in this simulation the generation of streaking artifacts due to scatter and non-linear partial effect was not modeled, it provided a ground truth and an artificially degraded image. Thereby, the performance of the algorithms was evaluated for a data recovery problem in which the amount of missing data and the source of available data are the same. Moreover, as the simulations were performed on phantoms derived from clinical studies, the impact of the relaxation parameter μ on the performance of the proposed algorithm could be objectively optimized and used in our clinical studies. Despite the absence of ground truth for clinical studies with metallic implants, we also followed an ROI-based quantitative evaluation approach for the assessment of MAR algorithms using clinical datasets and reference ROIs defined on uncorrected images. It is worth nothing that there are few reference-free criteria such as band-pass filtered gradient (BPG) [56] and regression without truth (RWT) [57], which can be respectively used to evaluate the performance of MAR algorithms in the sinogram domain and on images of a population of patients [26]. However, these methods complicate the evaluation procedure since BPG compares the performance of MAR algorithms in the sinogram domain and RWT needs an optimization task over a large number of CT images.

In both simulated and clinical studies, the segmentation of uncorrected images to produce metallic implants and prior images were performed using simple thresholding. The dark and bright artifacts falsely segmented as air and bone regions were eliminated by close and open morphological filtering. The accuracy of the prior image is of great importance for the performance of both NMAR and the proposed algorithm, since segmentation errors in prior image can reappear in the final reconstructions. For accurate segmentation of artifacts from anatomy in a prior image, automatic procedures through adaptive and knowledge-based thresholding have been described in [58] and [59], respectively.

The evaluation of the proposed L_0 -DRS algorithm against linear interpolation and NMAR algorithms using a number of simulated and clinical datasets showed that our algorithm can outperform its counterparts objectively and subjectively and therefore reduce metal artifacts in a more efficient way. Its improved performance should be ascribed to the facts that this wavelet-based MAR algorithm decomposes a sinogram into several resolution levels and estimate the missing projections in approximate and detail sub-bands through a thresholding scheme guided by prior wavelet coefficients. One of the current limitations of the proposed algorithm in comparison with NMAR is the computational time. In this study, we exploited translation invariant wavelets implemented by undecimated discrete wavelet transform (UDWT). In this implementation, the decimation (down sampling) is

eliminated in favor of invariance to the shifts of an input image, thus avoiding the star-like artifacts usually induced by the standard decimated wavelet transform. However, due to its redundancy, the UDWT is of higher computational complexity and renders the computational cost of our iterative MAR algorithm relatively expensive. The average computation time of the algorithm for the clinical datasets was found to be about 5 minutes. In this work, the performance of the proposed algorithm was evaluated for 4 resolution levels yielding a redundancy factor of 1:13, since there are three detail sub-bands for each resolution level (in horizontal, vertical and diagonal directions) and one approximation sub-band for all levels. In addition, we followed a block-wise recovery of missing projections in the wavelet domain. For each sinogram, two overlapping 512×512 blocks were considered; therefore the matrix size of UDWTs became $512 \times 512 \times 13 \times 2$, which obviously calls for an increased number of arithmetic operations. Future work will focus on decreasing the computational burden of the algorithm by: i) performance and trade-off assessment of the algorithm for lower resolutions and use of other wavelets such as Daubechies wavelets with a vanishing moment of 4, ii) employing smaller block sizes, and iii) implementation of UDWT in MATLAB MEX file or C/C++. In addition, future work will concentrate on improving the performance of the proposed algorithm by utilizing modified sub-bands of the corrupted sinograms to better preserve the edge information around metallic implants.

V. Conclusion

In this study, an L_0 wavelet-based projection completion algorithm was proposed for metal artifact reduction in x-ray CT imaging. In this algorithm, the completion of missing projections was formulated as a regularized inverse problem which was solved using the Douglas-Rachford splitting algorithm. The sparsity of the wavelet coefficients of CT sinograms as well as the detail wavelet coefficients obtained from the segmentation of the uncorrected images were exploited in the algorithm as prior information. The performance of the proposed L_0 -DRS MAR algorithm was compared with conventional linear interpolation and the normalized MAR algorithm proposed by Meyer *et al* [52]. It was demonstrated, using simulated and clinical studies, that the proposed algorithm can outperform its counterparts based on objective and subjective metrics. In conclusion, the proposed MAR algorithm proved to be promising in reducing metal artifacts in x-ray CT imaging.

Acknowledgements

This work was supported by the Swiss National Science Foundation under grant SNSF 31003A-135576, Geneva Cancer League, the Indo-Swiss Joint Research Programme ISJRP 138866, and Geneva University Hospital under grant PRD 11-II-1.

Appendix A

To solve the problem in Eq. (13) for the quasi-convex log function, we follow the proof of proposition 1 in [60]. When $z_i = 0$, it is clear that the unique minimizer $\hat{z}_i \triangleq \text{prox}_{\lambda\psi}(\theta_i)$ is zero. Moreover, as the log potential function $\psi(z_i) = \nu \ln(1 + |z_i|/\rho)$, $\nu = \ln(1 + 1/\rho)^{-1}$, is even-symmetric, therefore the minimizer of this problem is odd, i.e. $\text{prox}_{\lambda\psi}(-\theta_i) = -\text{prox}_{\lambda\psi}(\theta_i)$, and one can only consider $z_i > 0$. By equating the derivative of the objective of the problem to zero, i.e.

$$z_i - \theta_i + \lambda\nu(z_i + \rho)^{-1} = 0,$$

a quadratic equation is obtained, whose real positive root is given by:

$$\text{prox}_{\lambda\psi}(\theta_i) = \frac{1}{2}(\theta_i - \rho + \sqrt{(\theta_i + \rho)^2 - 4\lambda\nu}) \quad (\text{A.1})$$

if $\theta_i > (2\sqrt{\lambda\nu} - \rho)$. For $z_i < 0$, one can exploit the oddness property of this solution, thereby the minimizer of the problem reads: $-\text{prox}_{\lambda\psi}(-\theta_i)$ if $\theta_i < -(2\sqrt{\lambda\nu} - \rho)$. From above, it is deduced that in the interval $|\theta_i| < (2\sqrt{\lambda\nu} - \rho)$, z_i and thus $\text{prox}_{\lambda\psi}(\theta_i)$ are zero. Hence, the solution is obtained as in Eq. (14). When $\rho \rightarrow \infty$, the equation in (A.1) asymptotically approaches $\text{prox}_{\lambda\psi}(\theta_i) = \theta_i - \lambda$ with real positive values for $\theta_i > \lambda$, which gives rise to a *soft* thresholding rule as follows:

$$\text{prox}_{\lambda\psi}(\theta_i) = \begin{cases} \theta_i - \lambda, & \theta_i > \lambda \\ 0, & |\theta_i| \leq \lambda \\ \theta_i + \lambda, & \theta_i < -\lambda \end{cases} . \quad (\text{A.2})$$

References

- [1] W. R. Hendee, and E. R. Ritenour, *Medical Imaging Physics*, 4th ed.: Wiley-Liss, Inc., 2002.
- [2] J. Hsieh, *Computed tomography: principles, design, artifacts, and recent advances*, 2nd ed., Bellingham, WA: SPIE, , 2009.
- [3] M. Abdoli, R. A. J. O. Dierckx, and H. Zaidi, "Metal artifact reduction strategies for improved attenuation correction in hybrid PET/CT imaging.," *Med Phys*, vol. 39, no. 6, pp. 3343-3360, 2012.
- [4] W. A. Kalender, R. Hebel, and J. Ebersberger, "Reduction of CT artifacts caused by metallic implants.," *Radiology*, vol. 164, no. 2, pp. 576-577, 1987.
- [5] J. Wei, G. A. Sandison, W.-C. Hsi, M. Ringor, and X. Lu, "Dosimetric impact of a CT metal artefact suppression algorithm for proton, electron and photon therapies.," *Phys Med Biol*, vol. 51, no. 20, pp. 5183-5197, 2006.
- [6] M. R. Ay, A. Mehranian, M. Abdoli, P. Ghafarian, and H. Zaidi, "Qualitative and quantitative assessment of metal artifacts arising from implantable cardiac pacing devices in oncological PET/CT studies: A phantom study.," *Mol Imaging Biol*, vol. 13, no. 6, pp. 1077-1087, 2011.
- [7] B. De Man, J. Nuyts, P. Dupont, G. Marchal, and P. Suetens, "Metal streak artifacts in X-ray computed tomography: a simulation study." *IEEE Trans Nucl Sci*, vol. 46, pp. 691-696, 1999 .
- [8] J. Wei, L. Chen, G. A. Sandison, Y. Liang, and L. X. Xu, "X-ray CT high-density artefact suppression in the presence of bones.," *Phys Med Biol*, vol. 49, no. 24, pp. 5407-5418, 2004.
- [9] M. Abdoli, M. R. Ay, A. Ahmadian, and H. Zaidi, "A virtual sinogram method to reduce dental metallic implant artefacts in computed tomography-based attenuation correction for PET.," *Nucl Med Commun*, vol. 31, no. 1, pp. 22-31, 2010.
- [10] C. Xu, F. Verhaegen, D. Laurendeau, S. A. Enger, and L. Beaulieu, "An algorithm for efficient metal artifact reductions in permanent seed," *Med Phys*, vol. 38, no. 1, pp. 47-56, 2011.
- [11] S. Zhao, D. D. Robertson, G. Wang, B. Whiting, and K. T. Bae, "X-ray CT metal artifact reduction using wavelets: an application for imaging total hip prostheses.," *IEEE Trans Med Imaging*, vol. 19, no. 12, pp. 1238-1247, 2000.
- [12] E. M. Abu Anas, S. Y. Lee, and M. K. Hasan, "Removal of ring artifacts in CT imaging through detection and correction of stripes in the sinogram.," *Phys Med Biol*, vol. 55, no. 22, pp. 6911-6930, 2010.
- [13] W. J. H. Veldkamp, R. M. S. Joemai, A. J. van der Molen, and J. Geleijns, "Development and validation of segmentation and interpolation techniques in sinograms for metal artifact suppression in CT.," *Med Phys*, vol. 37, no. 2, pp. 620-628, 2010.
- [14] J. Gu, L. Zhang, G. Yu, Y. Xing, and Z. Chen, "X-ray CT metal artifacts reduction through curvature based sinogram inpainting.," *Journal of X-Ray Science and Technology*, vol. 14, pp. 73-82, 2006.
- [15] X. Duan, L. Zhang, Y. Xiao, J. Cheng, Z. Chen, and Y. Xing, "Metal artifact reduction in CT images by sinogram TV inpainting." *IEEE Nuclear Science Symposium Conference Record*, 2008, pp. 4175-4177.
- [16] H. Xue, L. Zhang, Y. Xiao, Z. Chen, and Y. Xing, "Metal artifact reduction in dual energy CT by sinogram segmentation based on active contour model and TV inpainting." *IEEE Nuclear Science Symposium Conference Record (NSS/MIC)*, 2009, pp. 904-908.
- [17] Y. Zhang, Y. F. Pu, J. R. Hu, Y. Liu, and J. L. Zhou, "A new CT metal artifacts reduction algorithm based on fractional-order sinogram inpainting," *J Xray Sci Technol*, vol. 19, no. 3, pp. 373-384, 2011.
- [18] M. Yazdi, M. A. Lari, G. Bernier, and L. Beaulieu, "An opposite view data replacement approach for reducing artifacts due to metallic dental objects.," *Med Phys*, vol. 38, no. 4, pp. 2275-2281, 2011.
- [19] S. Tohnak, A. J. H. Mehnert, M. Mahoney, and S. Crozier, "Dental CT metal artefact reduction based on sequential substitution.," *Dentomaxillofac Radiol*, vol. 40, no. 3, pp. 184-190, 2011.
- [20] B. Kratz, I. Weyers, and T. M. Buzug, "A fully 3D approach for metal artifact reduction in computed tomography," *Med Phys*, vol. 39, no. 11, pp. 7042-7054, 2012.
- [21] M. Bal, and L. Spies, "Metal artifact reduction in CT using tissue-class modeling and adaptive prefiltering.," *Med Phys*, vol. 33, no. 8, pp. 2852-2859, 2006.
- [22] H. Yu, K. Zeng, D. K. Bharkhada, G. Wang, M. T. Madsen, O. Saba, B. Policeni, M. A. Howard, and W. R. Smoker, "A segmentation-based method for metal artifact reduction.," *Acad Radiol*, vol. 14, no. 4, pp. 495-504, 2007.

- [23] D. Prell, Y. Kyriakou, M. Beister, and W. A. Kalender, "A novel forward projection-based metal artifact reduction method for flat-detector computed tomography.," *Phys Med Biol*, vol. 54, no. 21, pp. 6575-6591, 2009.
- [24] M. Meilinger, C. Schmidgunst, O. Schutz, and E. W. Lang, "Metal artifact reduction in cone beam computed tomography using forward projected reconstruction information," *Z Med Phys*, vol. 21, no. 3, pp. 174-182, 2011.
- [25] E. Meyer, R. Raupach, M. Lell, B. Schmidt, and M. Kachelriess, "Normalized metal artifact reduction (NMAR) in computed tomography," *Med Phys*, vol. 37, no. 10, pp. 5482-93, 2010.
- [26] M. Abdoli, M. Ay, A. Ahmadian, R. Dierckx, and H. Zaidi, "Reduction of dental filling metallic artefacts in CT-based attenuation correction of PET data using weighted virtual sinograms optimized by a genetic algorithm.," *Med Phys*, vol. 37, no. 12, pp. 6166-6177, 2010.
- [27] X. Zhang, J. Wang, and L. Xing, "Metal artifact reduction in x-ray computed tomography (CT) by constrained optimization.," *Med Phys*, vol. 38, no. 2, pp. 701-711, 2011.
- [28] A. P. Dempster, N. M. Laird, and D. B. Rubin, "Maximum likelihood from incomplete data via the EM algorithm.," *J Royal Stat Soc B*, vol. 38, pp. 1-38, 1977.
- [29] B. De Man, "Iterative Reconstruction for Reduction of Metal Artifact in Computed Tomography," PhD Thesis, Morfologie En Medische, Katholieke Universiteit Leuven, Leuven, 2001.
- [30] M. Oehler, and T. M. Buzug, "Statistical image reconstruction for inconsistent CT projection data.," *Methods Inf Med*, vol. 46, pp. 261-269, 2007.
- [31] L. Ritschl, F. Bergner, C. Fleischmann, and M. Kachelrieß, "Improved total variation-based CT image reconstruction applied to clinical data.," *Phys Med Biol*, vol. 56, pp. 1545-1561, 2011.
- [32] H. Xue, L. Zhang, Y. Xing, and Z. Chen, "An iterative reconstruction technique for metal artifact reduction," Proc. of the 11th Fully Three-dimensional Image Reconstruction in Radiology and Nuclear Medicine, Potsdam, Germany, 2011, pp. 199-202.
- [33] B. Meng, J. Wang, and L. Xing, "Sinogram preprocessing and binary reconstruction for determination of the shape and location of metal objects in computed tomography (CT)," *Med. Phys.*, vol. 37, no. 11, pp. 5867-5875, 2010.
- [34] J. Choi, K. S. Kim, M. W. Kim, W. Seong, and J. C. Ye, "Sparsity driven metal part reconstruction for artifact removal in dental CT.," *J X-Ray Sci Tech*, vol. 19, pp. 457-475, 2011.
- [35] J. F. Williamson, B. R. Whiting, J. Benac, R. J. Murphy, G. J. Blaine, J. A. O'Sullivan, D. G. Politte, and D. L. Snyder, "Prospects for quantitative computed tomography imaging in the presence of foreign metal bodies using statistical image reconstruction.," *Med Phys*, vol. 29, no. 10, pp. 2404-2418, 2002.
- [36] C. Lemmens, D. Faul, and J. Nuyts, "Suppression of metal artifacts in CT using a reconstruction procedure that combines MAP and projection completion.," *IEEE Trans Med Imaging*, vol. 28, no. 2, pp. 250-260, 2009.
- [37] K. Van Slambrouck, and J. Nuyts, "Metal artifact reduction in computed tomography using local models in an image block-iterative scheme," *Med Phys*, vol. 39, no. 11, pp. 7080-93, 2012.
- [38] M. Elad, *Sparse and Redundant Representations, From Theory to Applications in Signal and Image Processing*, New York: Springer, 2010.
- [39] I. Daubechies, B. Han, A. Ron, and Z. Shen, "Framelets: MRA-based constructions of wavelet frames.," *Appl Comput Harmon Anal*, vol. 14, no. 1, pp. 1-46, 2003.
- [40] H. Ji, Z. Shen, and Y. Xu, "Wavelet frame based image restoration with missing/damaged pixels.," *East Asia Journal on Applied Mathematics*, vol. 1, pp. 108-131, 2011.
- [41] M. Elad, P. Milanfar, and R. Rubinstein, "Analysis versus synthesis in signal priors.," *Inverse Problems*, vol. 23, no. 3, pp. 947-968, 2007.
- [42] A. Skodras, C. Christopoulos, and T. Ebrahimi, "The JPEG 2000 still image compression standard.," *IEEE Signal Processing Magazine*, vol. 18, no. 5, pp. 36-58, 2001.
- [43] P. Moulin, and J. Liu, "Analysis of multiresolution image denoising schemes using generalized-Gaussian and complexity priors.," *IEEE Trans Inf Theory*, vol. 45, pp. 909-919, 1999
- [44] S. S. Chen, D. Donoho, L. and M. Saunders, A, "Atomic decomposition by basis pursuit.," *SIAM J Sci Comput*, vol. 20, no. 1, pp. 33-61, 1998.
- [45] D. L. Donoho, "Compressed sensing.," *IEEE Trans Inf Theory*, vol. 52, no. 4, pp. 1289-1306, 2006.

- [46] E. Candes, M. Wakin, and S. Boyd, "Enhancing sparsity by reweighted ℓ_1 Minimization.." *J Fourier Anal Appl*, no. 14, pp. 877-905, 2007.
- [47] J. Trzasko, and A. Manduca, "Highly undersampled magnetic resonance image reconstruction via homotopic ℓ_0 -minimization.." *IEEE Trans Med Imaging*, vol. 28, no. 1, pp. 106-121, 2009.
- [48] P. L. Combettes, and J. C. Pesquet, "A Douglas-Rachford splitting approach to nonsmooth convex variational signal recovery.," *IEEE Journal of Selected Topics in Signal Processing*, vol. 1, no. 4, pp. 564-574, 2007.
- [49] I. Ekeland, and R. Temam, *Convex Analysis and Variational Problems:* , Amsterdam: North-Holland, 1976
- [50] F. J. A. Artacho, and J. Borwein, "Global convergence of a non-convex Douglas-Rachford iteration.," *Journal of Global Optimization*, vol 57, no 3, pp 753-769, 2013.
- [51] D. L. Donoho, and J. M. Johnstone, "Ideal spatial adaptation by wavelet shrinkage.," *Biometrika*, vol. 81, no. 3, pp. 425-455, 1994.
- [52] E. Meyer, R. Raupach, M. Lell, B. Schmidt, and M. Kachelrie, "Normalized Metal Artifact Reduction (NMAR) in Computed Tomography," *Med. Phys.*, vol. 37, pp. 5482-5493, 2010.
- [53] J. Fessler. "Image reconstruction toolbox, <http://www.eecs.umich.edu/~fessler/code/index.html>, University of Michigan."
- [54] G. Poludniowski, G. Landry, F. DeBlois, P. M. Evans, and F. Verhaegen, "SpekCalc : a program to calculate photon spectra from tungsten anode x-ray tubes," *Phys Med Biol*, vol. 54, no. 19, pp. N433, 2009.
- [55] M. J. Berger, and J. H. Hubbell, "XCOM: Photon Cross Sections on a Personal Computer," *Center for Radiation Research, National Bureau of Standards*, 1987.
- [56] B. Kratz, S. Ens, J. Muller, and T. M. Buzug, "Reference-free ground truth metric for metal artifact evaluation in CT images," *Med Phys*, vol. 38, no. 7, pp. 4321-4328, 2011.
- [57] J. W. Hoppin, M. A. Kupinski, G. A. Kastis, E. Clarkson, and H. H. Barrett, "Objective comparison of quantitative imaging modalities without the use of a gold standard.," *IEEE Trans Med Imaging*, vol. 21, no. 5, pp. 441-449, 2002.
- [58] S. Karimi, P. Cosman, C. Wald, and H. Martz, "Segmentation of artifacts and anatomy in CT metal artifact reduction," *Med Phys*, vol. 39, no. 10, pp. 5857-68, 2012.
- [59] M. Bal, and L. Spies, "Metal artifact reduction in CT using tissue-class modeling and adaptive prefiltering," *Med. Phys.*, vol. 33, no. 8, pp. 2852- 2859, 2006.
- [60] M. J. Fadili, J.-L. Starck, and F. Murtagh, "Inpainting and Zooming Using Sparse Representations," *The Computer Journal*, vol. 52, no. 1, pp. 64-79, 2009.

Chapter 3

3D prior image constrained projection completion for x-ray CT metal artifact reduction

Abolfazl Mehranian, Mohammad Reza Ay, Arman Rahmim *and* Habib Zaidi

IEEE Trans Nucl Sci Vol. 60, No. 5, pp 1-15 (2013)

© 2013 IEEE.

Abstract

Purpose: The presence of metallic implants in the body of patients undergoing x-ray computed tomography (CT) examinations often results in severe streaking artifacts that degrade image quality. In this work, we propose a new metal artifact reduction (MAR) algorithm for 2D fan-beam and 3D cone-beam CT based on the maximum *a posteriori* (MAP) completion of the projections corrupted by metallic implants.

Methods: In this algorithm, the prior knowledge obtained from a tissue-classified prior image is exploited in the completion of missing projections and incorporated into a new prior potential function. The prior is especially designed to exploit and promote the sparsity of a residual projection (sinogram) dataset obtained from the subtraction of the unknown target dataset from the projection dataset of the tissue-classified prior image. The MAP completion is formulated as an equality-constrained convex optimization and solved using an accelerated projected gradient algorithm. The performance of the proposed algorithm is compared with two state-of-the-art algorithms, namely 3D triangulated linear interpolation (LI) and normalized metal artifact reduction (NMAR) algorithm using simulated and clinical studies.

Results and conclusion: The simulations targeting artifact reduction in 2D fan-beam and 3D cone-beam CT demonstrate that our algorithm can outperform its counterparts, particularly in cone-beam CT. In the clinical datasets, the performance of the proposed algorithm was subjectively and objectively compared in terms of metal artifact reduction of a sequence of 2D CT slices. The clinical results show that the proposed algorithm effectively reduces metal artifacts without introducing new artifacts due to erroneous interpolation and normalization as in the case of LI and NMAR algorithms.

I. Introduction

X-ray computed tomography (CT) has experienced considerable technical advances over the past two decades and has now emerged as a leading cross-sectional imaging technique for various diagnostic and therapeutic applications. However, the appearance of streaking metal artifacts in CT images of patients bearing metallic implants can obscure crucial diagnostic information and therefore reduce image quality and the clinical relevance of this valuable imaging modality. As polychromatic x-ray beams used in CT pass through a patient, low energy (soft) x-ray photons, which are often of little importance to image formation, are preferentially absorbed to a greater extent than high energy photons. The outcome of this selective absorption is that patient's absorbed dose increases and the x-ray beam get richer in high energy photons and thus becomes harder [1]. Due to this so-called beam hardening effect, the log-processed transmission data will no longer be a linear function of tissue thickness. In the presence of strongly attenuating objects, such as metallic implants, beam hardening and Compton scattering become so severe that the detectors sensing the implants get starved of photons, and thus the relevant projection data become corrupted and inconsistent. The filtered backprojection (FBP) reconstruction algorithm, which is widely used in CT image reconstruction, assumes a linear or monochromatic propagation model for the detected photons and, as such fails to consider the non-linear beam hardening and scattering effects [2]. Consequently, the reconstructed images exhibit cupping artifacts, declined CT numbers behind bony structures [3] and contrast-enhanced regions [4], and streaking artifacts around metallic objects [5]. Most current generation commercial CT scanners, however, apply first-order beam hardening correction (water correction) algorithms to compensate for beam hardening, but due to the incapability of these algorithms to calibrate the beam hardening of high-Z materials, streaking artifacts still appear in the reconstructed images. The dark and bright streaking artifacts can harbor pathologic lesions and degrade the radiological manifestation of the surrounding tissues. Consequently, since the past three decades, extensive efforts have been directed toward developing efficient metal artifact reduction (MAR) algorithms in order to compensate for the corrupted and missing projection data and hence to improve the diagnostic quality and confidence of CT imaging.

Typically, MAR algorithms comprise two steps: a) metal trace identification, in which the projections corrupted by metallic implants are identified and b) artifact reduction, through which the identified missing projections are compensated for or treated in such a way that the associated streaking artifacts are mitigated. Metal traces are conventionally identified by segmentation of metallic implants in FBP reconstructed images using thresholding [5-7] or clustering techniques [8, 9] followed by reprojection of the obtained *metal-only* images onto the projection or sinogram domain. Other approaches are based on segmentation of metal traces directly in raw sinogram data using active contours [10], curve detection [11] and Markov random field (MRF) [12] techniques. More recently, hybrids of these two approaches have also been proposed using iterative metal-only image reconstruction and segmentation [13-16]. The second step of MAR methods has been mainly explored by two classes of algorithms: projection completion and iterative image reconstruction.

Projection completion aims at interpolating the missing projections from their neighbors through linear [5], cubic spline [6, 17], and wavelet [18] interpolations or iterative inpainting techniques using curvature-driven diffusion [19, 20], total variation (TV) [10, 21, 22] and wavelet regularization [23]. Other approaches rely on replacing the missing projections with the projections from nearby slices or opposite side angles [24, 25]. Bal and Spies proposed to replace the missing projections by the projections obtained from the forward projection of a tissue-classified CT image, namely tissue-class model or *prior* image [8]. The problem with this approach is that the prior sinogram projections over missing regions (metal traces) are not well fitted with the projections of the original sinogram in immediate neighboring regions and hence, there is always a risk for discontinuities and generation of new artifacts. Recently, Meyer *et al* [26] proposed a promising method to solve this fitness problem. In this method, referred to as normalized MAR (NMAR), the original sinogram is normalized by the sinogram of prior image, thereby flattening neighboring projections. Then, the missing data are linearly interpolated and the resulting sinogram is de-normalized. Projection completion has also been combined with algorithms that exploit the information hidden in low- and high-pass filtered sinograms [27] or low- and high-pass filtered reconstructed images [28]. This class of algorithms is often fast and computationally appealing; however, if not efficiently implemented, these techniques might produce new artifacts. In fact, their efficiency depends on how robustly they can exploit the still available projection data or even a prior knowledge in the recovery of missing data.

On the other hand, iterative reconstruction algorithms establish another class of algorithms that, unlike FBP, attempt to frame the reconstruction problem in a way that more closely resembles reality. In their evolution from algebraic to model-based statistical reconstruction techniques, these algorithms have allowed for a rich description of physical and statistical mechanisms involved in the imaging process and also for incorporating a priori knowledge of the images to be reconstructed [29]. They can be adapted to missing data situations by down-weighting [30, 31] or ignoring [13, 32, 33] the contribution of the corrupted projections, or can be tailored to polychromatic propagation models in order to reduce both beam hardening and metallic artifacts [34, 35]. However, this class of algorithms cannot entirely eradicate severe metallic artifacts [36], hence their initiation [31, 37] and combination [38] with projection completion techniques have also been investigated. Despite their advantages and the development of GPU-based and parallelizable algorithms [2], iterative image reconstruction techniques are still memory-demanding and computationally intensive. Interested readers are referred to a recent review on MAR algorithms [39]. To reduce the computational complexity of this class of MAR algorithms, Van Slambrouck *et al* [40] proposed a region-based iterative reconstruction method. In this method, a fully polychromatic reconstruction model is used for metallic regions, while a simpler monochromatic model is used for other regions. It is worth noting that model-based iterative algorithms have also been successfully applied for sinogram restoration and beam hardening correction [41, 42].

In this study, we propose a three-dimensional (3D) projection completion MAR algorithm in a Bayesian framework for the maximum *a posteriori* (MAP) completion of missing projections. In this framework, we systematically exploit the side information obtained from a tissue-classified prior image and also prior knowledge about the unknown projections based on previous works in the framework of compressed sensing and sparse signal recovery. In this context, the prior knowledge that a target signal or solution is sparse (i.e. having many zero components) or has a sparse and/or compressible representation in a given transform domain is exploited to recover it from its samples or incomplete measurements. Chen *et al* proposed a prior image constrained compressed sensing technique for reducing streaking artifacts in CT image reconstruction from undersampled projection angles [43]. In this technique, the target image is sparsified by subtraction from a prior image and then the subtracted image is further sparsified using a discrete gradient operator. Motivated by the concept of subtraction sparsification in the context of compressed sensing [43, 44] and prior image application in metal artifact reduction [8, 26, 45], we propose a new prior function to exploit i) the sparsity of a residual sinogram obtained from the subtraction of a target sinogram and a prior sinogram and ii) a sparsity-promoting diffusivity function defined on the prior sinogram for the recovery of missing projections. Furthermore, we extend the proposed MAP projection completion to three dimensions in order to interpolate the missing projections from all available projection data. The idea of 3D interpolation has previously been studied for recovery of missing projections in flat-panel cone beam CT [45] and in a sequence of 2D CT slices [46]. In the present work, we evaluate the performance of the proposed MAR algorithm in comparison with NMAR and a 3D linear interpolation algorithm implemented on a triangulated mesh grid using simulation and clinical studies and demonstrate that our MAR approach can potentially outperform the above state-of-the-art algorithms.

II. Materials and Methods

II.A. Problem Formulation

Let $\mathbf{x}_o \in \mathbb{R}^N$ denote an observed CT projection (sinogram) dataset with projections corrupted by metallic implants over the set $\Omega \subset \{1, \dots, N\}$, namely missing or metal-trace set. In the recovery of the underlying uncorrupted projection dataset, \mathbf{x} , we formulate the following forward model:

$$\mathbf{y} = \mathbf{H}\mathbf{x} + \mathbf{n} \quad (1)$$

where $\mathbf{H} \in \mathbb{R}^{M \times N}$, $M < N$, is a lossy operator that removes the projections of \mathbf{x} over the set Ω . $\mathbf{y} \in \mathbb{R}^M$ is the observed dataset with removed or missing projections and \mathbf{n} represents zero-mean Gaussian white noise with variance σ^2 . The matrix \mathbf{H} is constructed in two steps: i) an $N \times N$ diagonal matrix is defined with zero and one diagonal values. The rows and columns along which this matrix is zero are indexed by the set Ω . ii) The zero-rows of the matrix are then removed. In effect, the resulting $M \times N$ matrix removes the elements of \mathbf{x} over the set Ω .

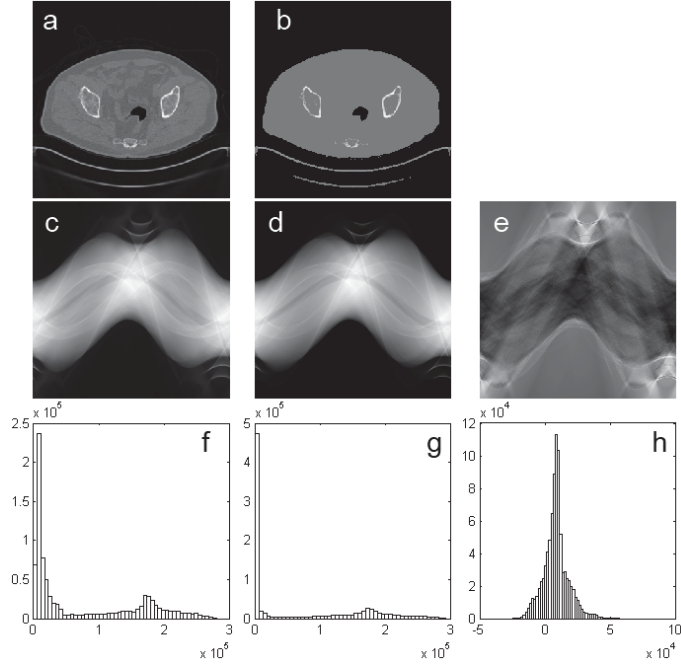


Figure 1. Illustration of subtraction sparsification. (a–d) A target CT image and its tissue-classified prior image and their corresponding sinograms, respectively. (e) The sinogram obtained from the subtraction of the target and prior sinograms. (f–h) The histograms of the sinograms shown in (c–e) in 30 bins. The histograms show that sinogram subtraction gives rise to the compressibility of the target sinogram.

In Eq. (1), the system of equations is underdetermined and therefore has an infinite number of solutions. In order to regulate and confine the solution space, we follow a Bayesian estimation approach. In this approach, one aims at finding a solution that maximizes the *a posteriori* probability density of \mathbf{x} given \mathbf{y} , which according to Bays' rule is given by:

$$P(\mathbf{x}|\mathbf{y}) \propto P(\mathbf{y}|\mathbf{x})P(\mathbf{x}) \quad (2)$$

where r.h.s densities are respectively the probability density of \mathbf{y} given \mathbf{x} and the prior probability density of \mathbf{x} . Since the density probability for the observation of \mathbf{y} given \mathbf{x} is the density for $\mathbf{n} = \mathbf{y} - \mathbf{H}\mathbf{x}$, we have:

$$P(\mathbf{y}|\mathbf{x}) \sim e^{-\frac{1}{2\sigma^2}\|\mathbf{y}-\mathbf{H}\mathbf{x}\|^2} \quad (3)$$

where $\|\mathbf{z}\| = \sqrt{\sum_i z_i^2}$. In this framework, the unknown \mathbf{x} is treated as a stochastic quantity with a prior probability density, $P(\mathbf{x}) \sim e^{-U(\mathbf{x})}$, where $U(\mathbf{x})$ is Gibbs or prior energy. This density is in fact used to impose our prior knowledge on the estimation. The MAP estimation is then obtained by maximizing $P(\mathbf{x}|\mathbf{y})$ or equivalently minimizing the following a posteriori energy:

$$\hat{\mathbf{x}} = \underset{\mathbf{x}}{\operatorname{argmin}} \left\{ \frac{1}{2\sigma^2} \|\mathbf{y} - \mathbf{H}\mathbf{x}\|^2 + U(\mathbf{x}) \right\} \quad (4)$$

In the above equation, the first term measures the proximity of \mathbf{x} to \mathbf{y} if observed through \mathbf{H} , while the second term enforces the compliance of \mathbf{x} to our prior knowledge. Generally, as the variance of noise decreases, the proximity of $\mathbf{H}\mathbf{x}$ to \mathbf{y} increases. In the limit where no noise is introduced as \mathbf{H} operates on \mathbf{x} (as is the case in this work), the problem defined in Eq. (4) asymptotically reduces to the following constrained optimization problem:

$$\hat{\mathbf{x}} = \underset{\mathbf{x} \in \Theta}{\operatorname{argmin}} U(\mathbf{x}), \quad \Theta = \{\mathbf{x} \in \mathbb{R}^N | \mathbf{y} = \mathbf{H}\mathbf{x}\} \quad (5)$$

where Θ is a constraint set inside which the linear set of equations $\mathbf{y} = \mathbf{H}\mathbf{x}$ defines the feasible set of solutions. Geometrically speaking, this set appears as a hyperplane whose intersection with the ball of the prior $U(\mathbf{x})$ defines the solution. Solving Eq. (5) is in fact achieved by decreasing the prior's energy until its ball last touches the hyperplane. To impose our prior knowledge about the unknown \mathbf{x} , we employ a prior function whose gradient at point \mathbf{x} is defined as follows:

$$U'(\mathbf{x}) = \nabla^T (g(\|\nabla \mathbf{x}_p\|) \nabla (\mathbf{x} - \alpha \mathbf{x}_p))$$

$$g(t) = \frac{1}{1 + \alpha \left(\frac{t}{\delta}\right)^2} \quad (6)$$

where $\nabla \in \mathbb{R}^{3N \times N}$ is a 3D derivative matrix (with symmetric boundary conditions) that approximates the gradient using first-order finite differences in horizontal, vertical and axial directions, \mathbf{x}_p is the sinogram of a tissue-classified prior image (prior sinogram), $g(t), \delta > 0$, is a modified Perona–Malik diffusivity function [47] and $\alpha \in [0,1]$ is a relaxation parameter to weight the impact of the prior sinogram.

The proposed prior function exploits two types of side information i) the diffusion directions into missing regions obtained from the prior sinogram and ii) the sparsity or compressibility of the subtraction sinogram. Figure 1 further illustrates the idea of subtraction sparsification. Figures. 1(a–e) show a target image and its tissue-classified prior image, their sinograms as well as the subtraction sinogram, respectively. In figures. 1(f–h), the corresponding histograms of the sinograms are shown in 30 bins. As can be seen, the subtraction gives rise to the compressibility of the target sinogram. Therefore, the application of discrete gradient operator ∇ can promote the sparsity of the subtraction sinogram. In Eq. (6), when α tends toward zero, the problem in Eq. (5) reduces to a constrained Tikhonov energy minimization. In section II.C, we will elaborate the derivation of a prior image from an observed CT image with metal artifacts.

II.B. The Optimization Algorithm

To solve the problem in Eq. (5), we follow an optimization transfer technique within the context of convex programming [48]. In this technique, the original objective function is iteratively substituted by a convex, easy-to-optimize surrogate function, which transfers its optimization to the objective function. Let us recast the problem in Eq. (5) into the following unconstrained problem:

$$\min_{\mathbf{x}} \{U(\mathbf{x}) + \iota_{\Theta}(\mathbf{x})\}, \quad \iota_{\Theta}(\mathbf{x}) = \begin{cases} 0, & \mathbf{x} \in \Theta \\ \infty, & \mathbf{x} \notin \Theta \end{cases} \quad (7)$$

where ι_{Θ} is the indicator function of the set Θ . To obtain a convex surrogate, we approximate the function $U(\mathbf{x})$ at point $\mathbf{x}^{(k)}$ using second-order Taylor expansion. Thus, the resulting surrogate reads:

$$S(\mathbf{x}, \mathbf{x}^{(k)}) = U(\mathbf{x}^{(k)}) + U'(\mathbf{x}^{(k)}) (\mathbf{x} - \mathbf{x}^{(k)})^T + \frac{L}{2} \|\mathbf{x} - \mathbf{x}^{(k)}\|^2 + \iota_{\Theta}(\mathbf{x}) \quad (8)$$

where L is the Lipschitz constant of the gradient of the prior function. By completing the square, dropping terms independent of \mathbf{x} in Eq. (8) and letting $\tau = 1/L$, the solution then iteratively reads:

$$\mathbf{x}^{(k+1)} = \underset{\mathbf{x}}{\operatorname{argmin}} \left\{ \frac{1}{2\tau} \|\mathbf{x} - \mathbf{u}^{(k)}\|^2 + \iota_{\Theta}(\mathbf{x}) \right\} \triangleq \operatorname{prox}_{\iota_{\Theta}}(\mathbf{u}^{(k)}) \quad (9)$$

where $\mathbf{u}^{(k)} = \mathbf{x}^{(k)} - \tau U'(\mathbf{x}^{(k)})$ is a gradient descent with step size τ and $\operatorname{prox}_{\iota_{\Theta}}(\cdot)$ is a proximal mapping associated with the function $\iota_{\Theta}(\mathbf{x})$. This algorithm is referred to as a proximal gradient algorithm [49]. Since $\iota_{\Theta}(\mathbf{x})$ is an indicator function, the proximal mapping reduces to a projection onto the convex set (POCS) Θ . For the constraint sets that are hyperplanes, the POCS step is achieved by the following algebraic reconstruction technique [50]:

$$\operatorname{proj}_{\iota_{\Theta}}(\mathbf{u}^{(k)}) = \mathbf{u}^{(k)} + \mathbf{H}^T (\mathbf{y} - \mathbf{H} \mathbf{u}^{(k)}). \quad (10)$$

The above projector, in effect, inserts the already known projections from \mathbf{y} into $\mathbf{u}^{(k)}$. The Lipschitz constant L plays an important role in the convergence of gradient-based algorithms. According to Theorem 8.3 in [50], for a fixed step size, τ , a gradient descent algorithm converges to the minimizer of a function if $0 < \tau \leq 2/L$. As mentioned above, as $\alpha \rightarrow 0$ in Eq. (6), the prior function becomes a Tikhonov function, whose Lipschitz constant is given by $L_T = \lambda_{\max}(\nabla^T \nabla)$, where λ_{\max} is the largest eigenvalue. This implies that the L constant of the proposed functional should be larger than L_T . Using the power iteration method or the result presented in Appendix B in [51], one can show that $L_T \leq 8$ for 2D datasets and $L_T \leq 12$ for 3D datasets. In this work, we improved the convergence rate of the optimization algorithm using Nesterov's acceleration [52]. To this end, Algorithm 1 summarizes the employed optimization algorithm whereas figure 2 shows the flowchart of the algorithm. In this algorithm, we declare the convergence of the algorithm when the relative difference between $\mathbf{x}^{(k+1)}$ and $\mathbf{x}^{(k)}$ falls below a tolerance ($\eta = 1 \times 10^{-4}$). In this work, we set $\delta = 5 \times 10^{-4}$ and $\alpha = 0.95$ in Eq. (6) for all the datasets presented in the Results section.

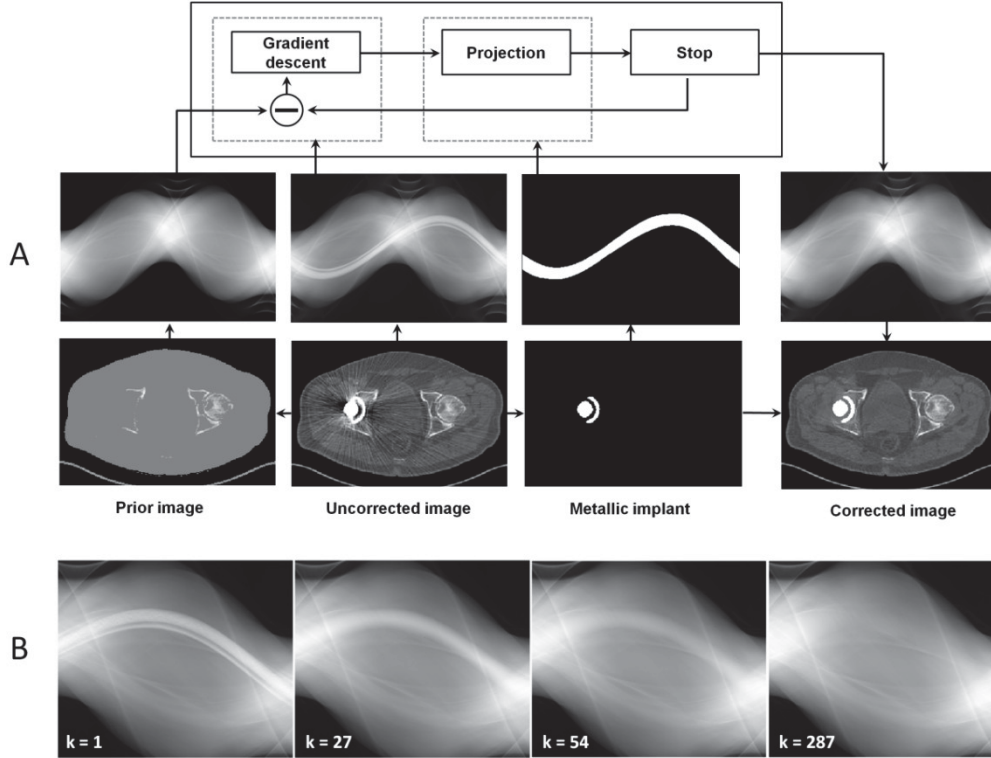


Figure 2. A) Flowchart of the proposed algorithm. The uncorrected CT image is segmented to extract metallic implants and tissue-prior image. The sinogram of the images are fed into the algorithm, which consists of two main steps: i) gradient descent of a subtraction sinogram, obtained by subtracting the prior sinogram and estimated sinogram, and ii) a projection step in which the already known projections are inserted into the estimated sinogram. The corrected image is obtained by FBP reconstruction of the estimated sinogram and then metallic implants are added back to the image. Panel B) illustrates the recovery of corrupted projections as a function of the number of iterations (k).

Algorithm 1 Prior image constrained projection completion.

Choose: δ , τ , α and η ; initialize: $\mathbf{x}^{(-1)} = \mathbf{x}^{(0)} = \mathbf{x}_u$, $t^{(0)} = 1$, $k = 0$ and $\mathbf{g} = (1 + \alpha(\|\nabla_{\mathbf{x}_p}\|/\delta)^2)^{-1}$.*

While ($\|\mathbf{x}^{(k+1)} - \mathbf{x}^{(k)}\|/\|\mathbf{x}^{(k)}\| < \eta$) **do**,

1. $t^{(k+1)} = \frac{1}{2} \left(1 + \sqrt{1 + 4(t^{(k)})^2} \right)$.
2. $\tilde{\mathbf{x}} = \mathbf{x}^{(k)} + \frac{t^{(k)} - 1}{t^{(k+1)}} (\mathbf{x}^{(k)} - \mathbf{x}^{(k-1)})$.
3. $\mathbf{x}^{(k+1)} = \text{proj}_{t_{\Theta}} \left(\tilde{\mathbf{x}} - \tau \nabla^T (\mathbf{g} \nabla (\mathbf{x}^{(k)} - \mathbf{x}_p)) \right)$.
4. $k = k + 1$.

Output: $\mathbf{x}^{(k+1)}$.

* \mathbf{x}_u and \mathbf{x}_p are uncorrected and prior sinograms.

II.C. Prior and metal-only images

To obtain a tissue-classified prior image from CT images with streaking dark and bright artifacts, Bal and Spies [8] applied 2D filtering to uncorrected CT images, tailored to reduce noise and streaking artifacts, and classified them into air, soft tissue, normal tissue, bone, and metal regions using K-means clustering. An average CT number was then assigned to each region. In this work, we segmented the uncorrected CT images into air, bone, soft tissue and lung (if present in the field-of-view) using a simple thresholding technique [26, 45]. Following tissue classification, CT numbers of air and soft tissue regions were set to -1000 and 0 HU, respectively, and the numbers of bone as well as lung regions were kept the same as the original image because of the inherent variability of bone and lung tissue densities and as such the corresponding CT numbers. In the segmentation of

uncorrected CT images into different tissues, severe dark and bright streaking artifacts can be falsely classified as air and bone in the segmented soft tissue and bone images, respectively. Following the work of Karimi *et al* [53] on the derivation of a prior image, we applied a 3D close and open morphological filtering on the segmented classes to reduce these errors. In cases with severe artifacts, the residual misclassifications were interactively reduced using a graphical user interface. As suggested by Prell *et al* [45], an alternative way would be to segment an image pre-corrected using a linear interpolation MAR algorithm. However, in some cases, we noticed that linear interpolation and its improved 3D triangulated version fail to effectively reduce streaking artifacts. The segmentation of metallic implants and thus generation of a metal-only image was performed by simple thresholding at about 3000 HU for dental fillings and 2000 HU for other implants. In the obtained prior image, we assigned the CT number of soft tissue to the segmented metal implants. Following the generation of prior and metal-only images, a prior sinogram as well as metal traces (missing projections) were obtained by line-integral forward projections.

II.D. Simulation and clinical studies

The performance of the proposed MAR algorithm was compared with 3D linear interpolation (LI) implemented on a Delaunay triangulated grid and the normalized metal artifact reduction (NMAR) algorithms using simulated and clinical studies. To objectively evaluate the performance of algorithms with respect to a reference CT image (i.e. without metal artifacts), we retrospectively generated metal artifacts in artifact-free images of two simulated phantoms i) a patient with bilateral hip prostheses and ii) a jaw phantom with dental fillings. These phantoms were designed to evaluate the performance of the algorithm for both 2D fan-beam and 3D cone-beam geometries, respectively. As shown in figure 3, the hip phantom was constructed by segmenting an original CT image into 3 classes, i.e. air, soft tissue and bone plus iron prostheses. The jaw phantom was analytically modeled from several spheroids, simulating teeth with radii ranging from 8 to 20 mm, and a large sphere simulating the head. For this phantom, we considered two dental fillings.

To simulate beam hardening and the resulting streaking artifacts, we modeled the polychromatic propagation of x-ray beams for the bilateral hip and jaw phantoms, according to the following model [54]:

$$\mathbf{g}_i = \sum_{k=1}^K \text{Poisson} \left\{ I_k^{(i)} \exp \left[- \int_{\mathcal{L}_i} \mu(\mathbf{l}, E_k) dl \right] + S_k^{(i)} \right\} \quad (11)$$

where \mathbf{g}_i is the measured number of photons in projection bin i , $I_k^{(i)}$ is the number of incident photons at k th energy along projection line i , $\mu(\mathbf{l}, E_k)$ is the energy-dependent attenuation map for different tissue classes and $S_k^{(i)}$ accounts for the contribution of scatters. A polyenergetic x-ray spectrum was generated using SpekCal software [55] for a tube voltage of 120 kVp, 2.5 mm aluminum filtration, 10 degrees anode angle and a tube output of 123.8 $\mu\text{Gy}/\text{mAs}$ at 1 meter. The spectrum was uniformly sampled for $K = 35$ monoenergetic x-ray beams with an intensity and average energy calculated over each energy interval. For each tissue class, energy-dependent linear attenuation coefficients were derived and interpolated from the NIST XCOM photon cross section library [56]. The attenuation maps were forward projected and then according to Eq. (11), the Poisson noise realization of the transmission and scatter sinograms were summed up to get a sinogram acquired under the conditions of polychromatic propagation of x-ray beams. In this work, we considered a constant-level scatter for non-zero projection bins [57]. The resulting sinogram was log-processed and reconstructed by FBP and FDK algorithms. As shown in figure 3, the reconstructed artificial CT images suffer from beam hardening and streaking artifacts in a similar way as in real CT acquisitions. In our simulations, non-linear partial volume effect was not modeled.

Following the generation of an artificially degraded image, we obtained a prior image, metallic implants, missing projections in the sinograms resulting from the polychromatic propagation of x-ray beams. In addition, for each dataset a reference image was obtained using the above-mentioned procedure by considering the metallic implants as bony structures and ignoring scatter. For metal artifact reduction in the hip phantom and clinical datasets, we evaluated the performance of the proposed algorithm using artificial sinograms obtained from the fan-beam forward projection of uncorrected CT images. To acquire artificial projection data under conditions closely matching actual acquisition, we considered the fan-beam geometry of a simulated single-slice CT scanner with 888 detector channels, 984 angular samples over a 360 orbit, detector pitch of 1 mm, 949 mm source to detector distance, 541 mm source to iso-center distance, 408 mm iso-center to detector distance. The geometric system matrix describing this scanner was generated by the Image Reconstruction Toolbox (IRT) [58],

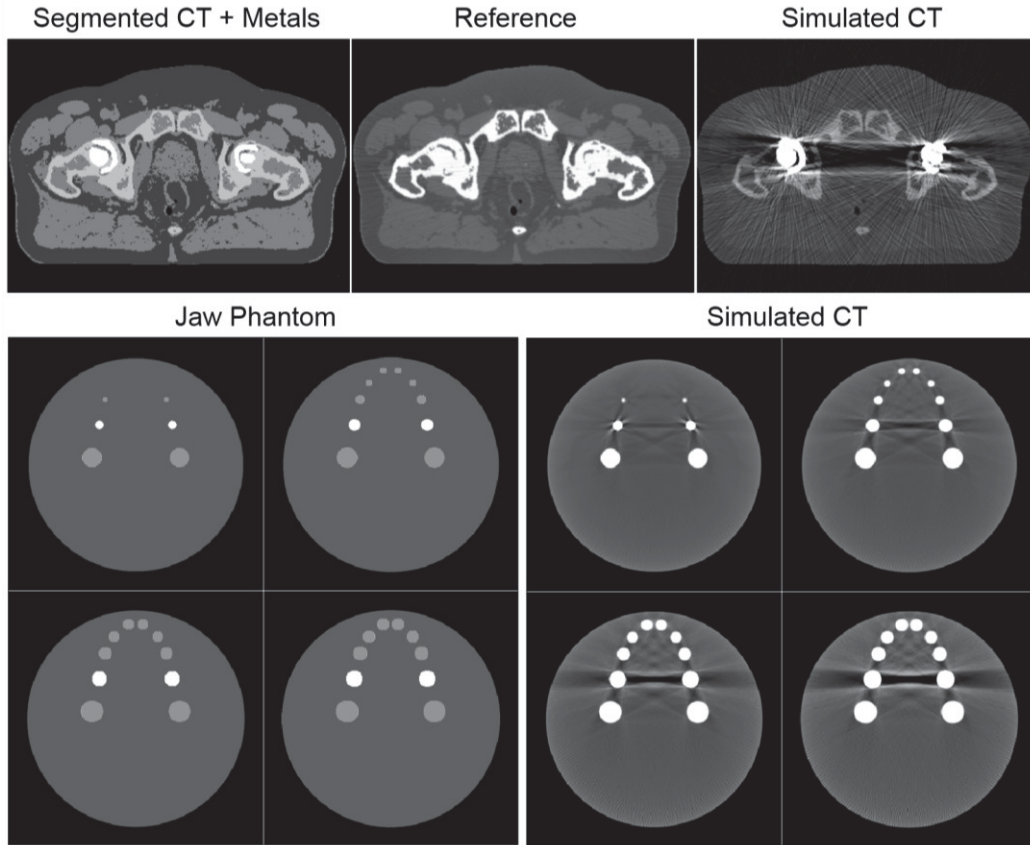


Figure 3. Simulation of metal artifacts in a 2D bi-lateral hip prostheses phantom (top panel) and a 3D jaw phantom (bottom panel) based on the polychromatic propagation of x-ray beams. In the hip phantom, an original CT image was segmented into bone, soft and normal tissues. A polychromatic data acquisition was performed on the segmented image to obtain an artifact-free reference image. To simulate metal artifacts, two metallic implants were superimposed on the segmented CT image and the transmission data were acquired using a polychromatic x-ray CT transmission model considering the scattering due to metallic implants. The jaw phantom was designed for 3D cone-beam CT and consists of several spheroids representing teeth and two simulated dental fillings within a large spheroidal soft tissue region. In this phantom, the metal artifacts were also simulated by considering a polychromatic CT model.

Table I. Summary of CT scanning parameters used in the clinical studies.

	Hip prostheses	ECG electrodes	Dental fillings	Spine fixation	Hip prosthesis
Tube voltage (kVp)	100/120	140/120	120	120	120
Tube current (mA)	40/32	179/175	166/116	95	99
Exposure time (ms)	500	1500/1000	750/500	500	500
Slice thickness (mm)	2	3	5	5	2

Table II. Quantitative evaluation of the mar algorithms for the simulated hip and jaw phantoms in terms of normalized root mean square difference (nrmsd) and mean absolute deviation (mad) metrics.

Phantom	ROI/VOI	Uncorrected		LI		NMAR		Proposed	
		NRMSE (%)	MAD (HU)	NRMSE (%)	MAD (HU)	NRMSE (%)	MAD (HU)	NRMSE (%)	MAD (HU)
Hip	1	69.20	92.76	20.02	42.47	20.56	41.37	18.62	40.30
	2	118.29	190.29	19.76	65.53	21.29	68.39	19.55	64.95
Jaw	1	18.28	18.69	5.95	18.59	3.40	7.81	3.23	4.64
	2	8.72	28.56	1.35	4.66	1.13	4.62	0.60	2.50

running in MATLAB 2010a (The MathWorks, Inc., Natick, MA) on a 12-core workstation with 2.4 GHz Intel Xeon processors and 32 GB memory. Line integrals were employed during forward projection to obtain the Radon transform. For the evaluation of the algorithm for the jaw phantom, we simulated a cone-beam flat-panel CT scanner with the following specifications: a flat panel detector with a matrix size of 384×320 and crystal size

of $1.56 \times 1.56 \text{ mm}^2$, 800 mm source to iso-center distance, 470 mm iso-center to detector distance and 360 projection angles. The $384 \times 320 \times 360$ projection dataset of the jaw phantom was obtained using the IRT toolbox. Following the correction of the sinograms of the hip phantom and clinical studies, the corrected images were reconstructed using the FBP algorithm with Ram-Lak filter, for a resolution of 512×512 with pixel size of 0.97 mm and a 500-mm field-of-view. The Ram-Lak filter was chosen to best preserve the sharpness of the reconstructed images. The corrected images of the jaw phantom were reconstructed using the FDK algorithm with a matrix size of $512 \times 512 \times 20$ and voxel size of $1 \times 1 \times 2 \text{ mm}^3$. For the clinical evaluation of the MAR algorithm, CT datasets of 8 patients were used. The data were acquired in helical mode on the Biograph 64 True Point PET/CT and Sensation 16 CT scanners (Siemens Healthcare, Erlangen, Germany), equipped with 40- and 24-row detectors, respectively. The datasets include uni- and bi-lateral hip prostheses, dental fillings, EEG electrodes, shoulder prosthesis and spine fixation with pedicle screws. Table I summarizes CT scanning parameters of the datasets.

II.E. Evaluation Metrics

The performance of the proposed algorithm was subjectively and objectively compared with 3D linear interpolation and NMAR algorithms. In simulation studies, the performance of the algorithms in terms of reducing streaking artifacts was objectively evaluated with respect to a reference using region of interest (ROI) analysis. For this purpose, two ROIs were drawn on uncorrected images and the normalized root mean square difference (NRMSD) and mean absolute deviation (MAD) between corrected images (f^{MAR}) and their reference image (f^{Ref}) were calculated for each ROI as follows:

$$\text{NRMSD}(\%) = 100 \times \sqrt{\frac{\sum_{i \in \text{ROI}} (f_i^{MAR} - f_i^{Ref})^2}{\sum_{i \in \text{ROI}} (f_i^{Ref})^2}} \quad (12)$$

$$\text{MAD}(\text{HU}) = \frac{1}{N} \sum_{i \in \text{ROI}} |f_i^{MAR} - f_i^{Ref}| \quad (13)$$

For quantitative evaluation of the MAR algorithms for the clinical datasets, we calculated mean and standard deviation of CT numbers in volumes of interests (VOI) defined on uncorrected and corrected CT images over streaking artifacts. Owing to the absence of a reference artifact-free image in the clinical datasets, we defined a reference VOI on uncorrected images far from streaking artifacts.

III. Results

III.A. Simulation Studies

Figure 4 compares the performance of MAR algorithms for the simulated bilateral hip study. In this dataset, the algorithms have noticeably reduced streaking artifacts. However, the visual comparison reveals that the proposed algorithm results in the production of less new artifacts as pointed by the arrows. It should be noted that both NMAR and the proposed algorithm depict a similar dark streak over the bladder because both use the same prior image. However, the proposed algorithm shows noticeable reduction of this artifact. For the objective comparison of the algorithms with respect to the reference image shown in figure 3, two ROIs were defined on the uncorrected CT image (see figure 4): one large rectangular ROI, namely ROI 1, to capture a large affected area, and one circular ROI, namely ROI 2, for local evaluation near the implants.

Table II summarizes the NRMSD and MAD results. In the ROI-based evaluations, the regions of metallic implants were excluded from the ROIs of (un-)corrected and reference images, since the implants are finally added back to the corrected images. The results show that the proposed algorithm achieves a better local and global performance, which is consistent with the subjective evaluation.

Figure 5 compares the performance of MAR algorithms for the cone-beam CT study. The figure also shows the simulated reference and uncorrected images. As mentioned in Section II.D, in the reference image, the metallic implants were replaced by bones and the projection data were analytically acquired using the polychromatic x-ray propagation model defined in Eq. (11). As can be seen, the reference reconstructed images suffer from streaking artifacts between teeth and an overall cupping artifact due to beam hardening effect and the incapability of the FDK algorithm in considering the non-linear and selective absorption of the x-ray photons.

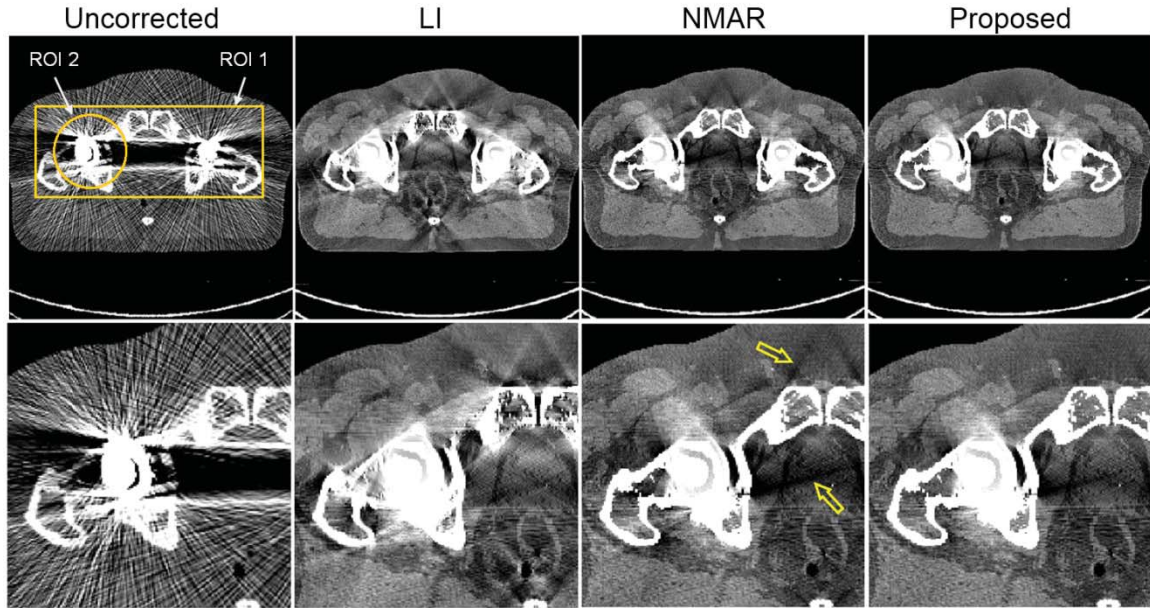


Figure 4. Comparison between the proposed and other MAR algorithms for the simulated bi-lateral hip prostheses dataset (WW/WL=450/50 HU).

The subjective comparison of the corrected images demonstrates that, contrary to 3D linear interpolation and NMAR, the proposed 3D MAR algorithm has remarkably reduced metallic artifacts without introducing new artifacts. Note that the images were only corrected for metal artifacts and as such, beam hardening artifacts between teeth are still present. In this dataset, we performed the interpolation step of the NMAR algorithm on sinogram views of the 3D projections of the jaw phantom. A volumetric prior image was constructed by replacing the metallic implants of the jaw phantom with soft tissue and its corresponding projection obtained using a monochromatic x-ray model at 80 kVp. The same prior sinogram was then employed for both NMAR and the proposed algorithm. As shown in figure 5, two VOIs were defined on the uncorrected images and the NRMSE and MAD metrics calculated. The results presented in Table II show that the proposed algorithm also outperforms its counterparts when using objective metrics.

III.B. Clinical Studies

Figure 6 compares the performance of MAR algorithms for the clinical hip studies with uni- and bi-lateral prosthesis. As summarized in Table I, the patients have undergone a low-dose CT scan for PET attenuation correction and therefore metallic implants have resulted in severe dark and noisy streaking artifacts mainly due to beam hardening and photon starvation. In the uni-lateral hip prosthesis dataset, the studied algorithms have noticeably reduced the artifacts; however, LI and NMAR algorithms have introduced new artifacts (follow the arrows). As can be seen, the NMAR algorithm has particularly introduced flare at the borders and around the prosthesis, which should be attributed to the propagation of interpolation errors during (de-)normalization. While the proposed algorithm has effectively reduced the artifacts, it has harbored the details of the hip prosthesis in the axial direction (see sagittal view). This is due to the fact that the projection data of the studied clinical studies were obtained by stacking the 2D sinograms of a sequence of CT slices, which might not be fully correlated in the third dimension as in cone-beam CT. Hence, the proposed MAR algorithm shows slightly axial detail degradation in the displayed window setting. For objective assessment of the algorithms, a VOI was drawn on the area suffering from dark artifacts, as shown in the coronal slice. Note that in this and the following figures, we only show VOIs in one dimension. A background VOI was also defined on a region far away from the artifacts. The mean and standard deviation of CT numbers of the reconstructed image over the VOIs are summarized in Table III. The results show that the proposed algorithm gives rise to a closer mean value to the background mean value, while NMAR shows a noticeable difference with respect to background. In the bi-lateral hip prostheses dataset (shown in figure 6 bottom panel), both NMAR and the proposed algorithm have substantially reduced the artifacts, while linear interpolation has reduced new artifacts. The subjective evaluation

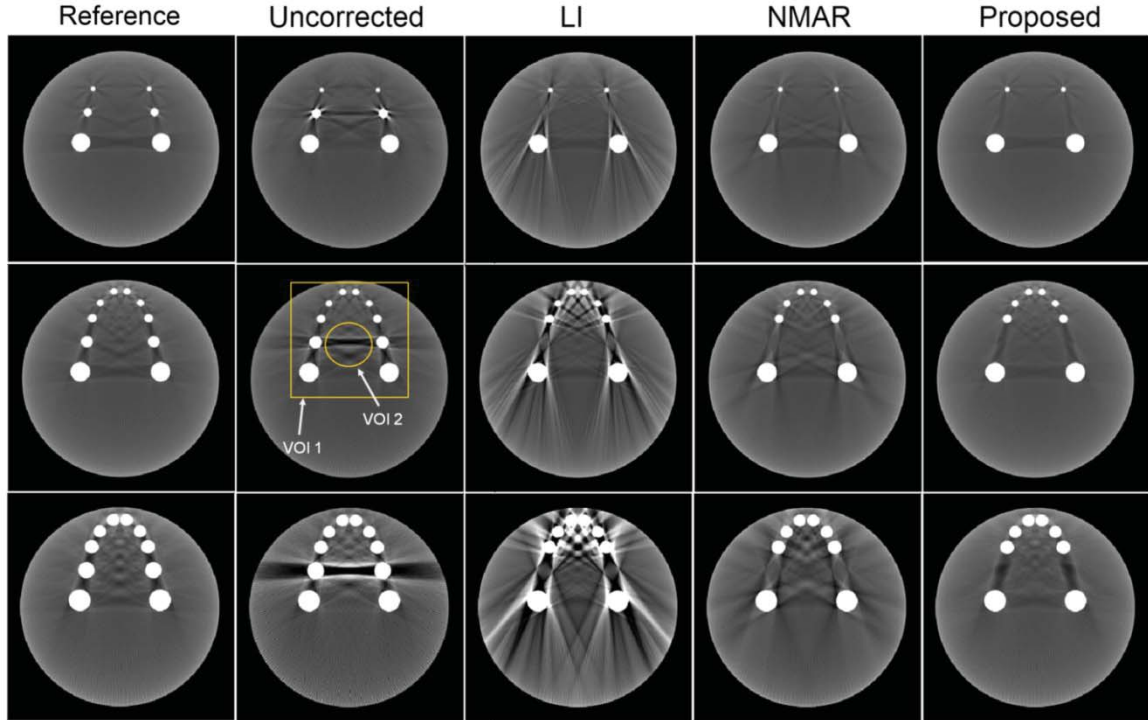


Figure 5. Comparison between the proposed and other MAR algorithms for the jaw phantom simulated for 3D cone-beam CT imaging (The display window is the same for all images).

Table III. Quantitative evaluation of the studied mar algorithms for the clinical datasets, shown on the top (T) and bottom (B) panels of figures 6–9, in terms of mean and standard deviation of CT numbers within a volume of interest drawn on artifactual regions (see the figures) and on a background reference region far away from the artifacts.

Dataset (Figure)	Panel	Background	Uncorrected	LI	NMAR	Proposed
Hip prostheses (6)	T	36.0 ± 39.0	-53.5 ± 209.0	30.26 ± 181.4	72.0 ± 150.8	39.4 ± 171.2
	B	0.78 ± 36.8	-184.1 ± 272.2	-114.0 ± 190.4	-14.0 ± 185.9	-34.39 ± 189.0
EEG electrodes (7)	T	32.6 ± 12.9	38.7 ± 25.4	36.9 ± 17.1	45.3 ± 14.2	33.9 ± 13.4
	B	36.4 ± 30.8	48.4 ± 134.5	44.7 ± 124.6	43.2 ± 120.8	40.2 ± 119.9
Dental filling (8)	T	20.8 ± 19.2	34.7 ± 74.7	34.5 ± 69.2	66.0 ± 40.3	23.0 ± 38.2
	B	21.2 ± 25.3	64.3 ± 235.6	108.3 ± 102.6	111.2 ± 105.3	75.8 ± 91.3
Shoulder prosthesis (9)	T	0.8 ± 44.2	-94.1 ± 145.7	-30.4 ± 82.2	-8.0 ± 75.2	-10.85 ± 88.0
Spin fixation (9)	B	29.6 ± 18.8	-83.7 ± 154.5	-43.2 ± 106.8	-41.9 ± 102.1	-52.7 ± 105.7

of corrected images shows that the proposed algorithm has reduced the artifacts without introducing bright streaking emanating from the prosthesis (see arrow). The VOI analysis (Table III), however shows that NMAR has more effectively reduced the dark streaks between the hips (over the region shown in figure 6 on the coronal slice). The sizes of the projection data of these datasets were $888 \times 984 \times 103$ and $\times 99$. In the recovery of missing projections, the proposed algorithm converged, on average, after 95 iterations with elapsed computation time of 657 seconds. In order to reduce computation time, we trimmed the radial bins of the projection data to those passing through the patient body. This procedure reduces the matrix size of projection datasets and therefore reduces the number of arithmetic operations during the calculation of 3D finite differences.

Figure 7 compares the performance of MAR algorithms for two patients with EEG electrodes. As can be seen in these datasets, the proposed algorithm has more effectively reduced the artifacts in comparison with LI and NMAR algorithms. In these datasets for which the metallic implants are outside the skull, we noticed that the NMAR algorithm introduces wide and severe bright and dark streaking artifacts at the borders near the electrodes, which are due to the normalization of projection bins by small values at these regions. To practically reduce this effect, we expanded the soft tissue region of prior images for this algorithm and also thresholded the very high-valued projections of de-normalized sinograms to a normal value. Furthermore, to avoid division by zero during normalization, we set zero bins in the sinogram of the prior image to 1. Small threshold values have been suggested by Meyer *et al* [26]; however, these values can result in highly inaccurate values in the normalized sinograms and hence can contribute to the appearance of severe bright streaking artifacts in the EEG

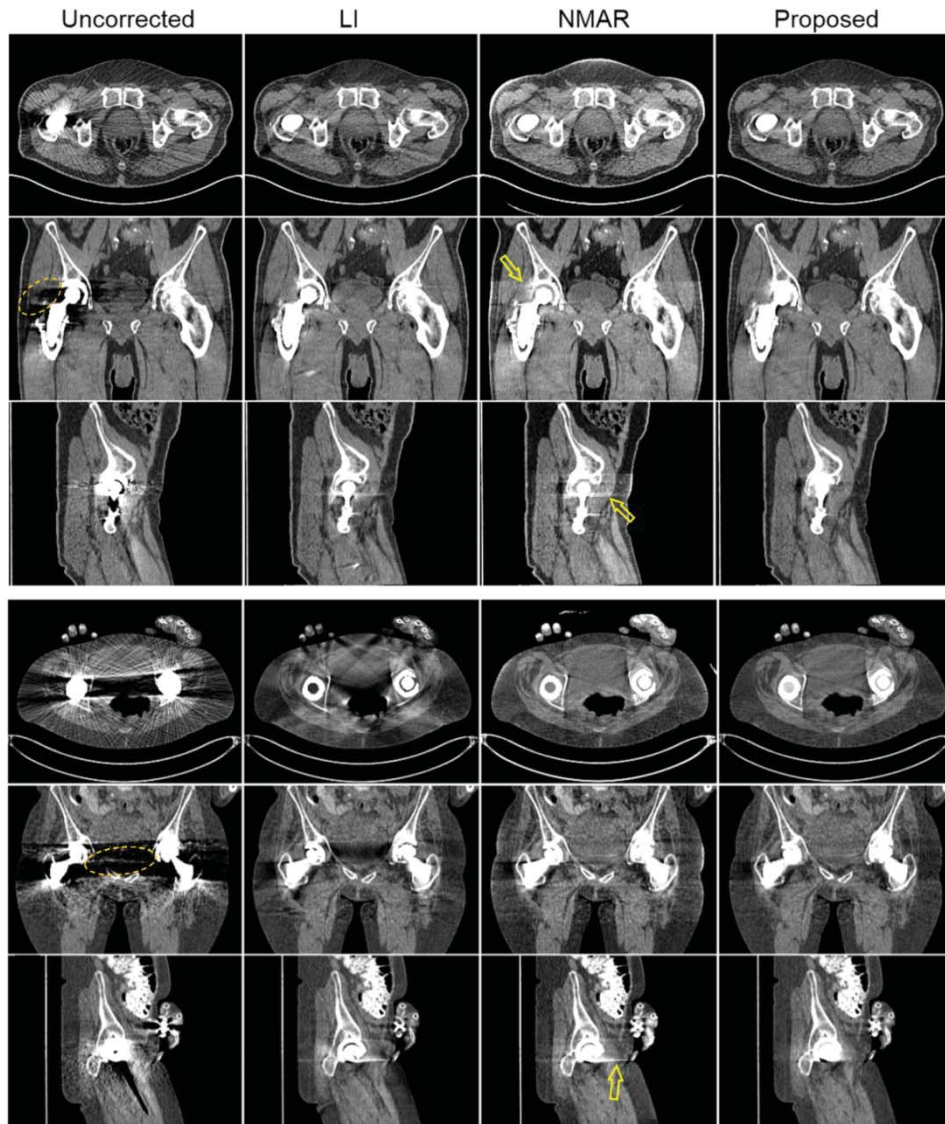


Figure 6. Comparison between the proposed and other MAR algorithms for the clinical uni- and bi-lateral hip prostheses datasets (WW/WL = 500/50 HU).

datasets. As indicated by the arrows in figure 7, the improved NMAR still give rise to new artifacts, particularly in the bottom dataset which has more electrodes. The reduced streaks artifacts in the regions close to the electrodes is of importance in CT-based attenuation correction of PET data, specifically in patients with epileptic foci [59].

For quantitative evaluation of the algorithms, two large VOI were defined in the cranium covering most of the streaks, as shown in figure 7. The results for both datasets (Table III) demonstrate that the proposed algorithm depicts an improved performance over LI and NMAR algorithms by achieving a mean CT number close to the background VOI. These datasets had 82 and 83 slices and the proposed algorithm converged, on average, after 194 iterations within 776 seconds. Figure 8 compares the performance of MAR algorithms for two clinical head datasets with multiple dental fillings. The reduction of metallic artifacts arising from multiple dental fillings is somewhat a challenging task, since their metal traces in the sinogram domain are usually unified in some angles and result in a large missing region. As can be seen in both datasets, linear interpolation has introduced dark streaking artifacts, while NMAR and the proposed algorithm have more effectively reduced the artifacts. As mentioned earlier, these two algorithms exploit some prior information for the interpolation of missing projections. However, the images shown in figure 8 show that the NMAR algorithm depicts a flare in the lip region of the top dataset and in the palatine region of the bottom dataset (see arrows). Conversely, the proposed algorithm, which uses the same image prior, does not result in such new artifacts, which should be

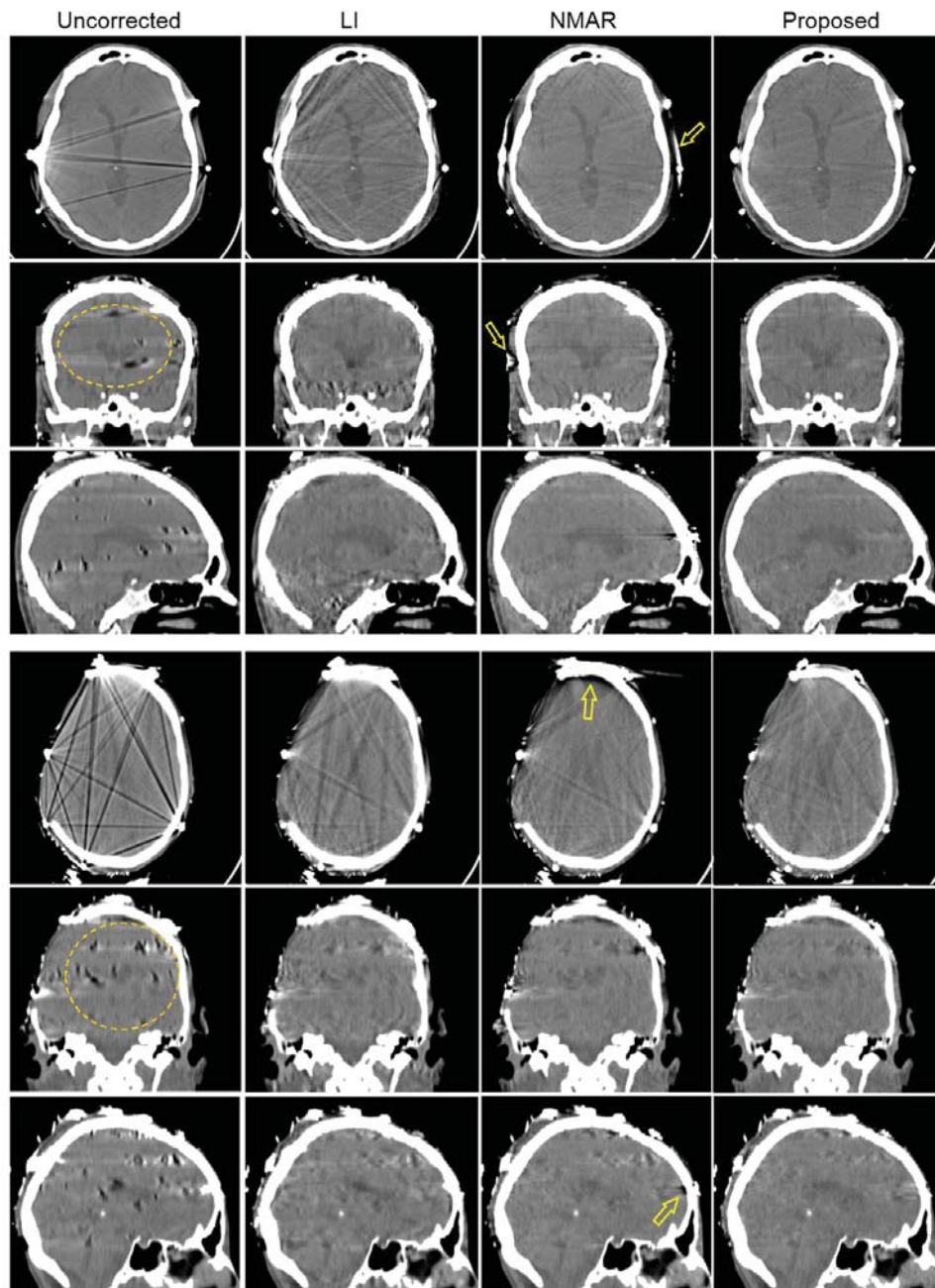


Figure 7. Comparison between the proposed and other MAR algorithms for the clinical head EEG datasets (WW/WL = 350/50 HU).

ascribed to error propagation during de-normalization. As shown in the sagittal slices shown in figure 8, two VOIs were defined in the oral cavity for objective comparison of the algorithms. Consistent with the subjective observations, the results in Table III show that the NMAR algorithm overestimates CT numbers in comparison with the background VOI. The results also confirm the outperformance of the proposed algorithm in the oral cavity region. These datasets had 13 and 16 slices and the proposed algorithm has converged, on average, after 169 Iterations within 129 seconds. Figure 9 (top panel) compares the performance of MAR algorithms for a clinical study with unilateral shoulder prosthesis. The uncorrected images suffer from severe dark streaks radiating from the implant. The results show that the algorithms have substantially reduced the dark streaking artifacts; however, LI has introduced new bright artifacts while NMAR depicts some residual bright artifacts

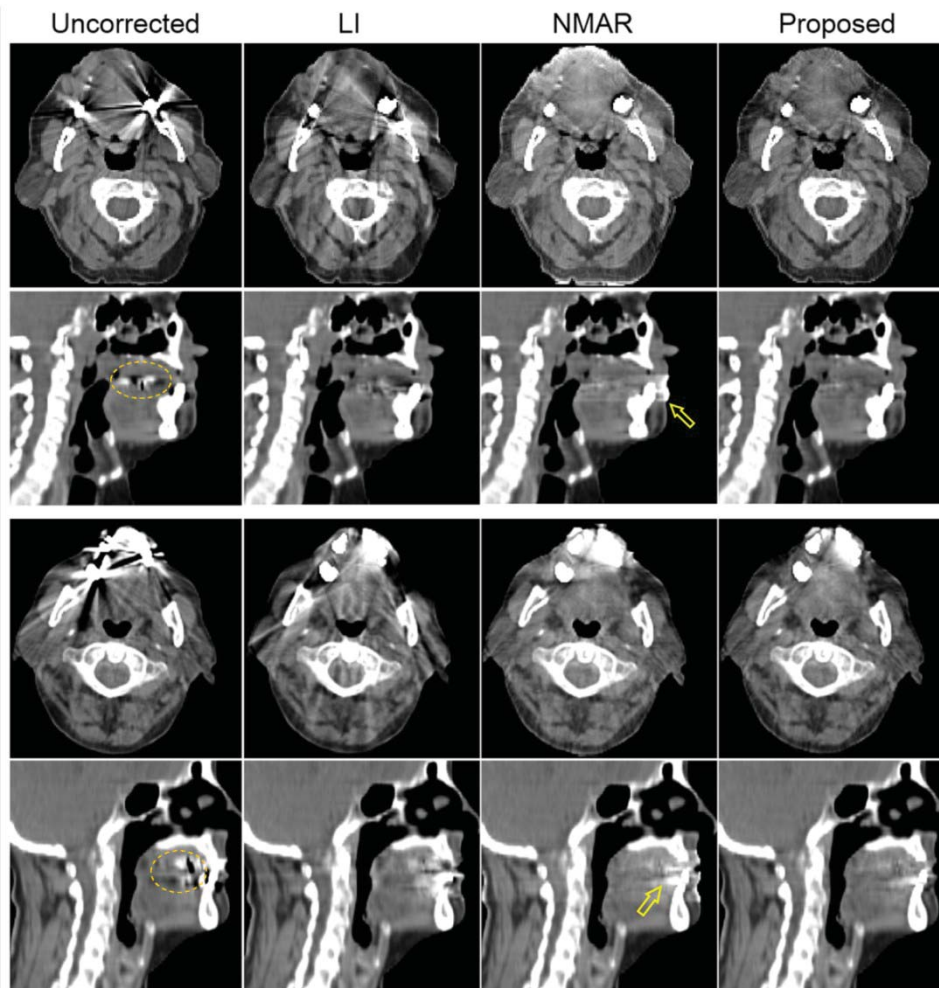


Figure 8. Comparison between the proposed and other MAR algorithms for the clinical dental filling datasets (WW/WL = 500/50 HU).

(see arrows). The performance of the proposed algorithm is comparable with NMAR but with reduced bright artifacts. For quantitative comparison of the different MAR algorithms, a VOI was drawn over regions affected by dark streaks (as shown in the transverse slice) and the mean and standard deviation of CT numbers were calculated. The results shown in Table III portray that NMAR and the proposed algorithms achieve comparable performance in terms of artifacts reduction in the selected volume of interest. Figure 9 (bottom panel) compares the performance of MAR algorithms for a clinical study with spine fixation. For this challenging case where the metallic implants are located close together and surrounded by several bony structures, linear interpolation has limited performance. This makes the pure interpolation of missing projections from adjacent projections inefficient and even inaccurate.

As can be seen, both NMAR and the proposed algorithm have substantially reduced the dark streak artifacts; however, as can be observed in the sagittal views, the residual dark artifacts in the image corrected using the proposed algorithm are more pronounced in front of the vertebrae in comparison with LI and NMAR. At the same time, as shown by the black arrow, the proposed algorithm shows less artifacts in the rear of the vertebrae. The quantitative performance of the algorithms in reducing the dark artifacts in the VOI shown on the sagittal slice reveals that in this region, LI and NMAR perform better. In these datasets, the number of slices were 99 and 101 and the proposed algorithm converged, on average, after 195 iterations within 996 seconds.

Figure 10 compares the performance of the evaluated algorithms in the projection domain. The top panel shows the zoomed-in scout and sinogram views of the bilateral hip dataset shown in figure 6. Similarly, the bottom panel compares the same views of the EEG head dataset shown in figure 7 (top panel). As can be seen, the LI algorithm, implemented in a 3D triangulated grid, cannot effectively interpolate the missing projections,

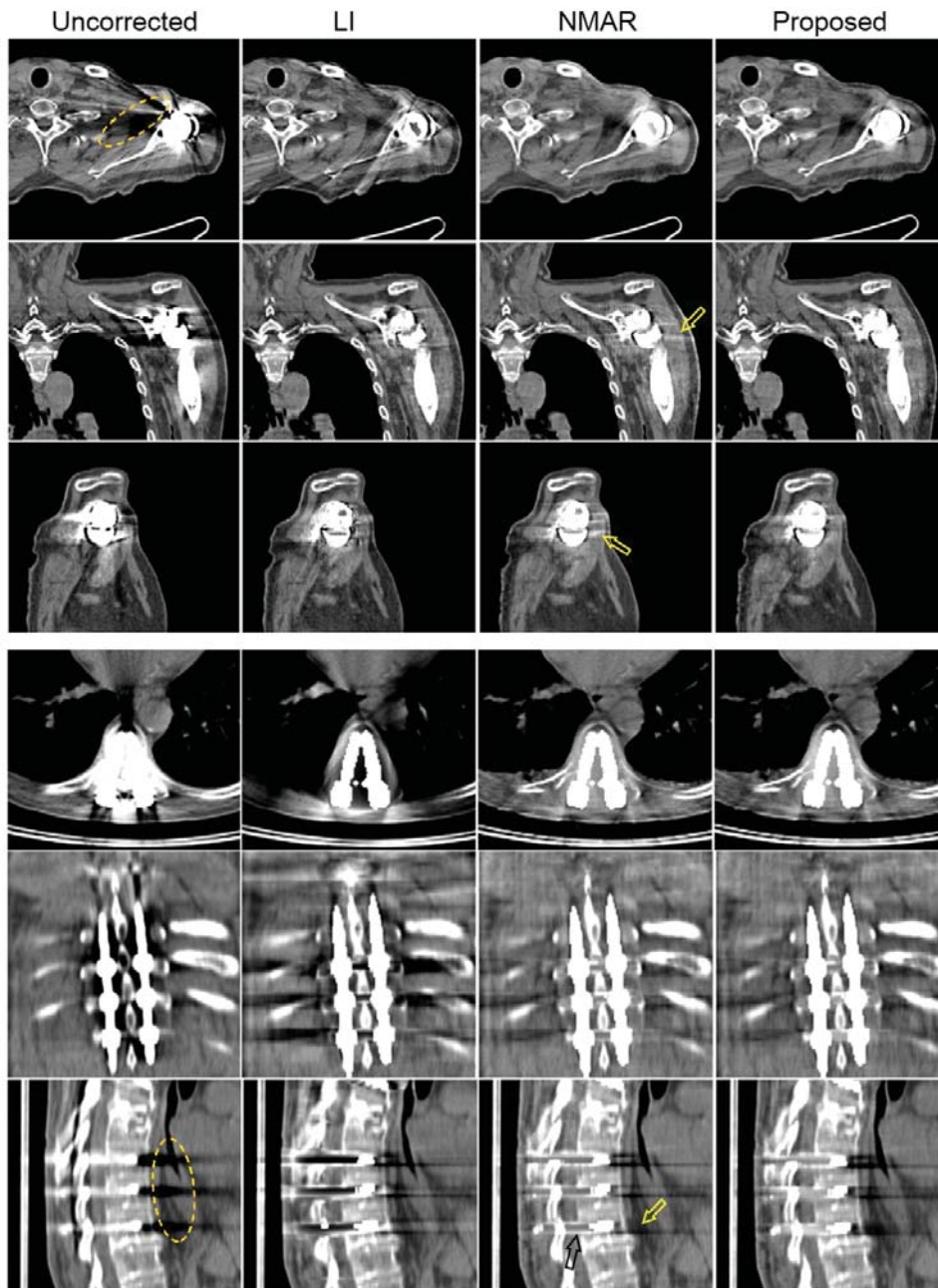


Figure 9 Comparison between the proposed and other MAR algorithms for the clinical shoulder and spine datasets (WW/WL = 500/50 HU).

particularly in the case of hip prostheses where a large number of projections have been corrupted and the neighboring projections are not so much informative. The comparisons between NMAR and our algorithm for the hip dataset show that both algorithms have similar performance; however, as shown by the arrow, NMAR is susceptible to the propagation of error during linear interpolation which simply bridges the missing projections in the radial direction. The comparison of these algorithms for the EEG dataset shows that the proposed algorithms restore the missing projections more accurately than NMAR. As pointed by the arrow, the NMAR algorithm results in high-value false projections near the electrodes, which are due to erroneous normalization. As mentioned earlier, we substantially reduced these errors by expanding the soft tissue component of the prior image. The inspection of the sinogram views also show that the proposed algorithm more accurately and smoothly restores the missing projections compared to its counterparts.

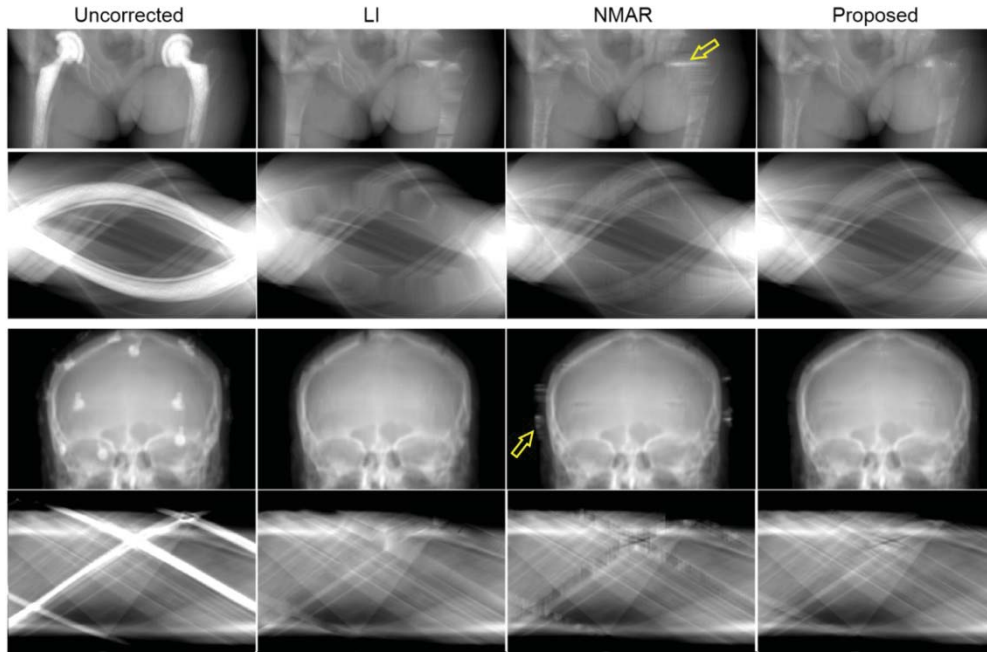


Figure 10. Comparison of the scout scans and sinogram views of projection data completed by the studied MAR algorithms. Top to bottom panels: Projection data of the bi-lateral hip prosthesis study (shown in figure 6, top panel) and the data of the EEG electrode study (shown in figure 7, top panel). As indicated by the arrows, the proposed algorithm is not susceptible to interpolation and normalization errors of LI and NMAR algorithms.

IV. Discussion

Streaking artifacts arising from metallic implants can degrade the quality of CT images and impact the clinical relevance of this diagnostic procedure by obscuring the radiological manifestation of tissues surrounding the implants. In this work, we introduce a 3D MAR algorithm for reducing metal artifacts in a fan-beam and cone-beam CT scanners. In this algorithm, the recovery and completion of missing projections was formulated as a maximum a posteriori (MAP) estimation, in which our expectations and prior knowledge about the missing projections was imposed using a novel prior potential function. This function was developed to interpolate the missing projections from available projection data and at the same time, to exploit prior projection (sinogram) data obtained from the forward projection of a tissue-classified CT image. As elaborated in Section II. A, we exploit the compressibility of a residual sinogram, obtained from the subtraction of the target (unknown) and prior sinograms, as a prior knowledge. The compressibility or sparsity of the residual sinogram is further promoted using discrete gradients, which is known as a sparsifying transform, and a modified Perona-Malik diffusivity function defined on the prior sinogram. We compared the performance of the proposed algorithm with two popular and state-of-the-art MAR algorithms, namely a 3D linear interpolation implemented on an irregular grid and Meyer's NMAR algorithm using simulation and clinical studies. Based on subjective and objective evaluations, it was found that the proposed algorithm can generally outperform its counterparts for both 2D fan-beam and 3D cone-beam CT imaging. In the implementation of NMAR and the proposed algorithm, we used the same prior image obtained by the procedure described in Section II.C. As demonstrated in our results, the proposed algorithm is not susceptible to interpolation and normalization errors encountered in the NMAR algorithm, particularly when metallic implants are at the surface of the body as in epileptic patients presenting with EEG electrodes. However, both algorithms are susceptible to segmentation errors of the prior image. These errors are mostly due to the classification of dark streak artifacts as air within the soft tissue component of the prior image. As shown in [8], these errors can reappear in the reconstructed images. Recently, several studies focused on accurate segmentation of different tissues from metal artifacts in uncorrected CT images. Chen et al [60] used non-local filtering and mutual information maximized segmentation to improve the performance of Bal and Spies' method [8] for the classification of biological tissues. Karimi et al [53] proposed to

apply close and open morphological operations on uncorrected images in order to reduce dark and bright artifacts. This procedure is then followed by a region growing segmentation guided by a distance-dependent threshold that limits the grouping of artifacts as anatomy. However, these approaches might fail in cases with large or multiple closely-seated implants [53]. To more practically reduce segmentation errors, Prell et al [45] suggested tissue classification on a CT image corrected by linear interpolation. This idea has recently motivated some recent attempts to iteratively improve the derivation of an initial prior image [61, 62]. There are also other approaches enabling to avoid segmentation errors and possibly to improve the accuracy of recovered projections by defining a prior image from statistical anatomical atlases [63].

In the proposed prior function defined in Eq. (6), we introduce a relaxation parameter α which can be used to control the impact of the prior image in the recovery of missing projections. In cases with severe segmentation errors in the prior image, this parameter can be set to a small value or zero, thereby the errors are reduced or eliminated in the reconstructed image. However, as mentioned earlier, as α decreases to zero, the proposed prior reduces to a Tikhonov quadratic prior. Therefore, the performance of the algorithm degrades to that of conventional MAR algorithms. The Perona–Malik diffusivity function defined in Eq. (6) includes the contrast parameter δ , which controls the amount of edge-enhancement. Since CT projection data are usually smooth, we set $\delta = 5 \times 10^{-4}$ in this work for all used datasets and found that this value is fairly small in order to guide the completion of missing projections. Generally, smaller values of δ have a negative impact on the convergence of the employed projected gradient algorithm. Nevertheless, we improved the convergence rate and thus the computation time of the optimization algorithm using Nesterov's acceleration, as formulated in Algorithm 1. In terms of computation time, our results show that the 3D linear interpolation on a triangulated mesh and NMAR are the most time-consuming and fastest MAR algorithms, respectively. In a dataset having size of $888 \times 984 \times 103$, the elapsed computation times are about 1630 and 25 seconds, respectively, on our MATLAB-based implementations. Note that since the 3D LI algorithm is memory demanding for such a dataset, it was implemented for every 10 slices. For the clinical studies used in this work, the performance of the various MAR algorithms was evaluated using artificial projection data obtained from the forward projection of uncorrected images, whereas for simulation studies, the algorithms were evaluated on the original projection data. Joemai et al reported that the correction of corrupted projections on original scanner-specific raw data is more effective than corrections performed on artificial data [64]. However, we followed the latter generic method for the clinical studies while considering the geometry of a realistic fan-beam CT scanner and put more emphasis on the development of a new MAR algorithm that reduces metal artifacts as efficiently as or better than current state-of-the-art MAR algorithms.

V. Conclusion

In this study, a 3D MAR algorithm was proposed in the maximum *a posteriori* completion of missing projections in a sequence of 2D CT slices and 3D cone-beam CT. In this algorithm, we exploit side information about missing projections, obtained from a tissue-classified prior CT image using a novel prior potential function. The prior was designed to exploit and promote the sparsity of a residual projection dataset (sinogram) obtained from the subtraction of the unknown target dataset from the projection dataset of the tissue-classified prior image. The formulated MAP problem was casted as a constrained optimization problem and solved using an accelerated projected gradient algorithm. The proposed algorithm was compared with two state-of-the-art algorithms using simulation and clinical studies. In 2D fan-beam and 3D cone-beam simulations, it was demonstrated that the proposed 3D algorithm outperforms its counterparts, particularly in cone-beam CT. In the clinical studies, the performance of the evaluated MAR algorithms was evaluated using artificial sinograms of a sequence of 2D CT slices. It was found that the proposed algorithm effectively reduces metal artifacts without introducing new ones owing to more accurate utilization of prior information in comparison with its state-of-the-art counterparts. Future work will focus on the application of the proposed MAR algorithm in clinical 3D cone beam CT imaging.

Acknowledgements

This work was supported by the Swiss National Science Foundation under grant SNSF 31003A-135576, the Indo-Swiss Joint Research Programme ISJRP 138866, and Geneva University Hospital under grant PRD 11-II-1.

References

- [1] W. R. Hendee, and E. R. Ritenour, *Medical Imaging Physics*, 4th ed.: Wiley-Liss, Inc., 2002.
- [2] X. Pan, E. Y. Sidky, and M. Vannier, "Why do commercial CT scanners still employ traditional, filtered back-projection for image reconstruction?," *Inverse Probl.*, vol. 25, no. 12, pp. 1230009, 2009.
- [3] G. T. Herman, "Demonstration of beam hardening correction in computed tomography of the head," *J. Comput. Assist. Tomogr.*, vol. 3, no. 3, pp. 373-378, 1979.
- [4] K. Kitagawa, R. T. George, A. Arbab-Zadeh, J. A. Lima, and A. C. Lardo, "Characterization and correction of beam-hardening artifacts during dynamic volume CT assessment of myocardial perfusion," *Radiology*, vol. 256, no. 1, pp. 111-118, 2010.
- [5] W. A. Kalender, R. Hebel, and J. Ebersberger, "Reduction of CT artifacts caused by metallic implants," *Radiology*, vol. 164, no. 2, pp. 576-7, 1987.
- [6] M. Bazalova, L. Beaulieu, S. Palefsky, and F. Verhaegen, "Correction of CT artifacts and its influence on Monte Carlo dose calculations," *Med. Phys.*, vol. 34, pp. 2119-2132, 2007.
- [7] M. Abdoli, J. R. de Jong, J. Pruim, R. A. J. O. Dierckx, and H. Zaidi, "Reduction of artefacts caused by hip implants in CT-based attenuation-corrected PET images using 2-D interpolation of a virtual sinogram on an irregular grid," *Eur. J. Nucl. Med. Mol. Imaging*, vol. 38, pp. 2257-2268, 2011.
- [8] M. Bal, and L. Spies, "Metal artifact reduction in CT using tissue-class modeling and adaptive prefiltering," *Med. Phys.*, vol. 33, no. 8, pp. 2852- 2859, 2006.
- [9] H. Yu, K. Zeng, D. K. Bharkhada, G. Wang, M. T. Madsen, O. Saba, B. Policeni, M. A. Howard, and W. R. K. Smoker, "A segmentation-based method for metal artifact reduction," *Acad. Radiol.*, vol. 14, no. 4, pp. 495-504, 2007.
- [10] H. Xue, L. Zhang, Y. Xiao, Z. Chen, and Y. Xing, "Metal Artifact Reduction in Dual Energy CT by Sinogram Segmentation Based on Active Contour Model and TV Inpainting," *IEEE Nuclear Science Symposium Conference Record (NSS/MIC)*, 2009, pp. 904- 908.
- [11] C. Xu, F. Verhaegen, D. Laurendeau, S. A. Enger, and L. Beaulieu, "An algorithm for efficient metal artifact reductions in permanent seed implants," *Med. Phys.*, vol. 38, no. 1, pp. 47- 56, 2011.
- [12] W. J. H. Veldkamp, R. M. S. Joemai, A. J. van der Molen, and J. Geleijns, "Development and validation of segmentation and interpolation techniques in sinograms for metal artifact suppression in CT," *Med. Phys.*, vol. 37, no. 2, pp. 620-628, 2010.
- [13] X. Zhang, J. Wang, and L. Xing, "Metal artifact reduction in x-ray computed tomography (CT) by constrained optimization," *Med. Phys.*, vol. 38, no. 2, pp. 701-711, 2011.
- [14] B. Meng, J. Wang, and L. Xing, "Sinogram preprocessing and binary reconstruction for determination of the shape and location of metal objects in computed tomography (CT)," *Med. Phys.*, vol. 37, no. 11, pp. 5867-5875, 2010.
- [15] J. Choi, K. S. Kim, M. W. Kim, W. Seong, and J. C. Ye, "Sparsity driven metal part reconstruction for artifact removal in dental CT," *J. X-Ray Sci. Tech.*, vol. 19, pp. 457-475, 2011.
- [16] M. Meilinger, E. W. Lang, C. Schmidgunst, and O. Schutz, "Projective segmentation of metal implants in Cone Beam computed tomographic images," *7th International Symposium on Image and Signal Processing and Analysis (ISPA)*, Dubrovnik, 2011, pp. 507 - 512.
- [17] M. Abdoli, M. R. Ay, A. Ahmadian, R. Dierckx, and H. Zaidi, "Reduction of dental filling metallic artefacts in CT-based attenuation correction of PET data using weighted virtual sinograms optimized by a genetic algorithm," *Med. Phys.*, vol. 37, pp. 6166-6177, 2010.
- [18] S. Zhao, D. Robertson, G. Wang, and B. Whiting, "X-ray CT metal artifact reduction using wavelets: An application for imaging total hip prostheses," *IEEE Trans. Med. Imaging*, vol. 19, pp. 1238-1247, 2000.
- [19] J. Gu, L. Zhang, G. Yu, Y. Xing, and Z. Chen, "X-ray CT metal artifacts reduction through curvature based sinogram inpainting," *J. X-Ray Sci. Tech.*, vol. 14, no. 2, pp. 73-82, 2006.
- [20] Y. Zhang, Y. F. Pu, J. R. Hu, Y. Liu, Q. L. Chen, and J. L. Zhou, "Efficient CT Metal Artifact Reduction Based on Fractional-Order Curvature Diffusion," *Comput. Math. Methods Med.*, 173748, 2011.
- [21] X. Duan, L. Zhang, Y. Xiao, J. Cheng, Z. Chen, and Y. Xing, "Metal artifact reduction in CT images by sinogram TV inpainting," *IEEE Nuclear Science Symposium Conference Record (NSS/MIC)*, 2008, pp. 4175-4177.

- [22] Y. Zhang, Y. F. Pu, J. R. Hu, Y. Liu, and J. L. Zhou, "A new CT metal artifacts reduction algorithm based on fractional-order sinogram inpainting," *J. X-Ray Sci. Tech.*, vol. 19, no. 3, pp. 373-384, 2011.
- [23] A. Mehranian, M. R. Ay, A. Rahmim, and H. Zaidi, "X-ray CT metal artifact reduction using wavelet domain sparse regularization.," *IEEE Trans Med Imaging*, vol. 32, no. 9, pp. 1707-22, 2013.
- [24] M. Yazdi, M. A. Lari, G. Bernier, and L. Beaulieu, "An opposite view data replacement approach for reducing artifacts due to metallic dental objects," *Med. Phys.*, vol. 38, no. 4, pp. 2275-2281, 2011.
- [25] S. Tohnak, M. A. J, M. Mahoney, and S. Crozier, "Dental CT metal artefact reduction based on sequential substitution," *Dentomaxillofac Radiol.*, vol. 40, no. 3, pp. 184-190, 2011.
- [26] E. Meyer, R. Raupach, M. Lell, B. Schmidt, and M. Kachelrieß, "Normalized metal artifact reduction (NMAR) in Computed Tomography," *Med. Phys.*, vol. 37, pp. 5482-5493, 2010.
- [27] K. Y. Jeong, and J. B. Ra, "Metal artifact reduction based on sinogram correction in CT," *IEEE Nuclear Science Symposium Conference Record (NSS/MIC)*, 2009, pp. 3480-3483.
- [28] E. Meyer, R. Raupach, M. Lell, B. Schmidt, and M. Kachelrieß, "Frequency split metal artifact reduction (FSMAR) in computed tomography," *Med. Phys.*, vol. 39, no. 4, pp. 1904-1916, 2012.
- [29] J. Hsieh, *Computed tomography : principles, design, artifacts, and recent advances*, 2 ed., Bellingham, WA: SPIE, , 2009.
- [30] J. Nuyts, and S. Stroobants, "Reduction of attenuation correction artifacts in PET-CT," *IEEE Nuclear Science Symposium Conference Record (NSS/MIC)*, 2005, pp. 1895-1899.
- [31] M. Oehler, and T. M. Buzug, "Statistical image reconstruction for inconsistent CT projection data," *Methods Inf. Med.*, vol. 46, pp. 261-269, 2007.
- [32] B. De Man, J. Nuyts, P. Dupont, G. Marchal, and P. Suetens, "Reduction of metal streak artifacts in x-ray computed tomography using a transmission maximum a posteriori algorithm," *IEEE Trans. Nucl. Sci.*, vol. 47, no. 3, pp. 977-981, 2000.
- [33] L. Ritschl, F. Bergner, C. Fleischmann, and M. Kachelrieß, "Improved total variation-based CT image reconstruction applied to clinical data," *Phys. Med. Biol.*, vol. 56, pp. 1545-1561, 2011.
- [34] G. Van Gompel, K. Van Slambrouck, M. Defrise, K. J. Batenburg, J. de Mey, J. Sijbers, and J. Nuyts, "Iterative correction of beam hardening artifacts in CT," *Med. Phys.*, vol. 38, pp. S36, 2011.
- [35] B. De Man, J. Nuyts, P. Dupont, G. Marchal, and P. Suetens, "An iterative maximum-likelihood polychromatic algorithm for CT," *IEEE Trans. Med. Imaging.*, vol. 20, pp. 999-1008, 2001.
- [36] J. F. Williamson, B. R. Whiting, J. Benac, R. J. Murphy, G. J. Blaine, J. A. O'Sullivan, D. G. Politte, and D. L. Snyder, "Prospects for quantitative computed tomography imaging in the presence of foreign metal bodies using statistical image reconstruction," *Med. Phys.*, vol. 29, no. 10, pp. 2404-2418, 2002.
- [37] H. Xue, L. Zhang, Y. Xing, and Z. Chen, "An Iterative Reconstruction Technique for Metal Artifact Reduction," *11th International Meeting on Fully Three-dimensional Image Reconstruction in Radiology and Nuclear Medicine*, 2011, pp. 199-202.
- [38] C. Lemmens, D. Faul, and J. Nuyts, "Suppression of metal artifacts in CT using a reconstruction procedure that combines MAP and projection completion," *IEEE Trans. Med. Imaging*, vol. 28, pp. 250-260 2009.
- [39] M. Abdoli, R. A. Dierckx, and H. Zaidi, "Metal artifact reduction strategies for improved attenuation correction in hybrid PET/CT imaging," *Med. Phys.*, vol. 39, no. 6, pp. 3343-3360, 2012.
- [40] K. Van Slambrouck, and J. Nuyts, "Metal artifact reduction in computed tomography using local models in an image block-iterative scheme," *Med. Phys.*, vol. 39, no. 11, pp. 7080-93, 2012.
- [41] J. La Riviere, J. Bian, and P. A. Vargas, "Penalized-likelihood sinogram restoration for computed tomography," *IEEE Trans. Med. Imaging*, vol. 25, pp. 1022-1036, 2006.
- [42] G. V. Gompel, K. V. Slambrouck, M. Defrise, K. J. Batenburg, J. d. Mey, J. Sijbers, and J. Nuyts, "Iterative correction of beam hardening artifacts in CT," *Med. Phys.*, vol. 38, no. S1, pp. S36-S49, 2011.
- [43] G. H. Chen, J. Tang, and S. Leng, "Prior image constrained compressed sensing (PICCS): a method to accurately reconstruct dynamic CT images from highly undersampled projection data sets," *Med. Phys.*, vol. 35, no. 2, pp. 660-3, 2008.
- [44] V. Cevher, A. Sankaranarayanan, M. F. Duarte, D. Reddy, R. G. Baraniuk, and R. Chellappa, "Compressive sensing for background subtraction," *Proceedings of the 10th European Conference on Computer Vision: Part II, Marseille, France, 2008*, pp. 155-168.

- [45] D. Prell, Y. Kyriakou, M. Beister, and W. A. Kalender, "A novel forward projection-based metal artifact reduction method for flat-detector computed tomography," *Phys. Med. Biol.*, vol. 54, no. 21, pp. 6575, 2009.
- [46] B. Kratz, I. Weyers, and T. M. Buzug, "A fully 3D approach for metal artifact reduction in computed tomography," *Med. Phys.*, vol. 39, no. 11, pp. 7042-7054, 2012.
- [47] P. Perona, and J. Malik, "Scale-space and edge detection using anisotropic diffusion," *IEEE Trans. Pattern Anal. Mach. Intell.*, vol. 12, pp. 629-639, 1990.
- [48] K. Lange, D. R. Hunter, and I. Yang, "Optimization transfer using surrogate objective functions," *J. Comput. Graph. Stat.*, vol. 9, pp. 1-20, 2000.
- [49] A. Beck, and M. Teboulle, "Gradient-Based Algorithms with Applications in Signal Recovery Problems", *Convex Optimization in Signal Processing and Communications*, D. Palomar and Y. Eldar, eds., pp. 33-88: Cambridge University Press, 2010.
- [50] E. P. Chong, and S. H. Zak, *An Introduction to Optimization*, 2 ed.: John Wiley & Sons, 2001.
- [51] J. Dahl, P. C. Hansen, S. H. Jensen, and T. L. Jensen, "Algorithms and software for total variation image reconstruction via first-order methods," *Numer. Algo.*, vol. 53, pp. 67-92, 2010.
- [52] A. Beck, and M. Teboulle, "A fast iterative shrinkage-thresholding algorithm for linear inverse problems," *SIAM J. Imaging Sci.*, vol. 2, no. 1, pp. 183-202, 2009.
- [53] S. Karimi, P. Cosman, C. Wald, and H. Martz, "Segmentation of artifacts and anatomy in CT metal artifact reduction," *Med. Phys.*, vol. 39, no. 10, pp. 5857-68, 2012.
- [54] P. J. La Rivière, "Penalized-likelihood sinogram smoothing for low-dose CT," *Med. Phys.*, vol. 32, no. 6, pp. 1676-1683, 2005.
- [55] G. Poludniowski, G. Landry, F. DeBlois, P. M. Evans, and F. Verhaegen, "SpekCalc : a program to calculate photon spectra from tungsten anode x-ray tubes," *Phys. Med. Biol.*, vol. 54, no. 19, pp. N433, 2009.
- [56] M. J. Berger, and J. H. Hubbell, "XCOM: Photon Cross Sections on a Personal Computer," *Center for Radiation Research, National Bureau of Standards*, 1987.
- [57] B. De Man, J. Nuyts, P. Dupont, G. Marchal, and P. Suetens, "Metal streak artifacts in X-ray computed tomography: a simulation study," *IEEE Nuclear Science Symposium Conference Record (NSS/MIC)*, 1998, pp. 1860-1865.
- [58] J. Fessler. "Image reconstruction toolbox, <http://www.eecs.umich.edu/~fessler/code/index.html>, University of Michigan, Accessed 2012."
- [59] C. Lemmens, M.-L. Montandon, J. Nuyts, O. Ratib, P. Dupont, and H. Zaidi, "Impact of metal artefacts due to EEG electrodes in brain PET/CT imaging," *Phys. Med. Biol.*, vol. 53, no. 16, pp. 4417-4429, 2008.
- [60] Y. Chen, Y. Li, H. Guo, Y. Hu, L. Luo, X. Yin, J. Gu, and C. Toumoulin, "CT metal artifact reduction method based on image segmentation and sinogram in-painting," *Math. Prob. Eng.*, vol. 2012, Article ID 786281, 18 pages, 2012.
- [61] F. Morsbach, S. Bickelhaupt, G. A. Wanner, A. Krauss, B. Schmidt, and H. Alkadhi, "Reduction of metal artifacts from hip prostheses on CT images of the pelvis: Value of iterative reconstructions," *Radiology*, vol. 268, no. 1, 237-44, 2013.
- [62] Y. Zhang, H. Yan, X. Jia, J. Yang, S. B. Jiang, and X. Mou, "A hybrid metal artifact reduction algorithm for x-ray CT," *Med. Phys.*, vol. 40, no. 4, pp. 041910-17, 2013.
- [63] O. Sadowsky, L. Junghoon, E. G. Sutter, S. J. Wall, J. L. Prince, and R. H. Taylor, "Hybrid cone-beam tomographic reconstruction: Incorporation of prior anatomical models to compensate for missing data," *IEEE Trans. Med. Imaging*, vol. 30, no. 1, pp. 69-83, 2011.
- [64] R. M. S. Joemai, P. W. d. Bruin, W. J. H. Veldkamp, and J. Geleijns, "Metal artifact reduction for CT: Development, implementation, and clinical comparison of a generic and a scanner-specific technique," *Med. Phys.*, vol. 39, no. 2, pp. 1125-1132, 2012.

Chapter 4

Comparative methods for hip prosthesis metal artifact reduction in pelvic CT

Mehrsima Abdoli, Abolfazl Mehranian, Angeliki Ailianou, Minerva Becker and Habib Zaidi

Phys Med Biol (2015) under revision

Abstract

Purpose: Metal artifact reduction (MAR) produces images with improved quality potentially leading to confident and reliable clinical diagnosis and therapy planning.

Methods: In this work, we evaluate the performance of five MAR techniques for the assessment of computed tomography (CT) images of patients with hip prostheses. Five MAR algorithms were evaluated using simulation and clinical studies. The algorithms included one-dimensional linear interpolation (LI) of the corrupted projection bins in the sinogram, two-dimensional interpolation (2D), a normalized metal artifact reduction (NMAR) technique, a metal deletion technique (MDT), and a 3D prior image constrained projection completion approach (MAPC). The algorithms were applied to 10 simulated datasets as well as 30 clinical studies of patients with metallic hip implants. Qualitative evaluations were performed by two blinded who assigned scores from 0 to 5, experienced radiologists, who ranked overall artifact severity, as well as pelvic organ recognition for each algorithm, respectively.

Results: Simulation studies revealed that 2D, NMAR and MAPC techniques performed almost equally well in all regions. LI falls behind the other approaches in terms of reducing dark streaking artifacts as well as preserving unaffected regions ($p < 0.05$). Visual assessment of clinical datasets revealed the superiority of NMAR and MAPC in the evaluated pelvic organs and in terms of overall image quality.

Conclusion: Overall, all methods, except LI, performed equally well in artifact-free regions. Considering both clinical and simulation studies, 2D, NMAR and MAPC seem to outperform the other techniques.

I. Introduction

Over the past few decades, x-ray computed tomography (CT) has emerged as one of the leading cross-sectional imaging modalities offering a broad range of clinical applications in diagnostic radiology, radiation oncology and multimodal molecular imaging [1, 2]. Despite the acknowledged value of this imaging modality, CT image quality and quantitative accuracy can be impaired by a number of physical degrading factors [3], mainly artifacts arising from the presence of metallic objects in the field-of-view, such as dental fillings, hip or knee prostheses, cardiac pacemakers, and spinal cages [4]. The appearance of streaking artifacts often obscure the anatomical structures surrounding the implants, leading to reduced diagnostic CT confidence and potentially equivocal findings [5-7]. Moreover, severe dark and bright streaking artifacts can result in imperfect dose calculation due to impaired organ boundary delineation in radiation therapy treatment planning [8] and over/under-estimation of activity concentration in CT-based attenuation correction of positron emission tomography data [9, 10]. As a result, many attempts have been directed toward developing metal artifacts reduction (MAR) techniques capable of reducing the artifacts and thus enhancing CT image quality [11].

Since polychromatic x-ray beams used in x-ray CT pass through the patient, soft and low energy x-rays are preferentially absorbed to a great extent compared to high-energy photons. A direct consequence of this selective absorption is an increase in patient's absorbed dose, compared to an ideal monoenergetic beam, and a non-linear increase in the beam's average energy, which is often referred to as beam hardening effect [12]. The metallic objects with a high atomic number strongly attenuate the crossing x-ray photons resulting in severe beam hardening and thus photon starvation at the detectors. This non-linear propagation of x-ray beams over metallic objects renders the corresponding transmission projection data inconsistent and corrupted. The filtered backprojection (FBP) algorithm, which still is the most widely used algorithm in CT image reconstruction, however, assumes a linear propagation model for the detected photons and as such, is susceptible to data inconsistencies leading to dark and bright streaking artifacts in the reconstructed images. The beam hardening, scatter and streaking metal artifacts can be intrinsically suppressed to an acceptable diagnostic level using polychromatic statistical iterative image reconstruction algorithms [13]. However, such algorithms are memory demanding and computationally intensive. As a result, MAR algorithms have been mostly developed for FBP and algebraic/monochromatic iterative image reconstruction algorithms with the aim of correcting for sinogram corruption and data inconsistency. In this regard, metal artifact reduction techniques can generally be divided into five categories: (i) interpolation-based sinogram correction, (ii) non-interpolation-based sinogram correction, (iii) hybrid sinogram correction, (iv) iterative image reconstruction and (v) image-based approaches [11]. Most these MAR techniques possess some advantages and drawbacks in terms of computational simplicity, accuracy and efficiency in reducing the artifacts produced by different metallic objects and introducing new artifacts. The different characteristics and potential performance of these algorithms, therefore, calls for a comprehensive comparative evaluation in order to understand the benefits and shortcomings of each algorithm.

In this study, five MAR techniques, belonging to different categories, were compared and evaluated using clinical studies of patients with primary hip replacement. Hip replacement is the second most common joint replacement surgery with an increasing number of procedures in the aging population [14]. This comparative study aimed to compare the performance of various MAR algorithms for the assessment of adjacent and distant pelvic organs and global image quality.

II. Materials and Methods

II.A. Metal artefact reduction approaches

In this study, we selected representative MAR techniques from the three most commonly used MAR categories, namely three interpolation-based sinogram correction techniques, one non-interpolation-based method and one hybrid sinogram correction approach. These techniques are described in the following subsection. In all MAR techniques used in this work, a virtual sinogram was utilized rather than the original raw CT data to overcome the challenges associated with the usage of proprietary raw data, usually encrypted by the manufacturers. The virtual sinogram is generated by forward projection of the reconstructed images [15].

1) Interpolation-based sinogram correction

The majority of the proposed MAR approaches employ this category of techniques due to simplicity and easy and fast implementation. These techniques consist of two steps: (i) metal trace identification, in which the corrupted sinogram bins, namely missing projection bins, are identified and (ii) missing projection bin interpolation [16-18]. The missing projection bins can be either identified directly in the sinogram domain using dedicated segmentation techniques [18, 19] or through forward-projection of segmented metallic objects on the image space [6, 20]. Kalender *et al.* [6] proposed a simple linear interpolation (LI) based MAR algorithm in which missing projection bins are identified by forward-projection of manually segmented metallic objects and interpolated along projection profiles using a one-dimensional (1D) linear interpolation algorithm. In the current study, we slightly modified this approach by using a simple thresholding technique to delineate the metallic objects. Since the Hounsfield units (HU) corresponding to high atomic number objects, such as metals, are considerably higher than that of human body tissues, they can be easily distinguished. However, in regions where the bright streaking artifacts are quite intense, their CT values might be very high, in which case the differentiation, by any means, becomes a challenge.

1D interpolation is, however, known to generate new artifacts in the reconstructed CT images, mainly due to the discontinuity of the interpolated bins along the second dimension of the sinogram matrix [15]. In an attempt to improve the smoothness and continuity of the sinogram, two-dimensional (2D) interpolation techniques were proposed [21, 22]. The challenge associated with application of 2D interpolation schemes is that the corrupted projection bins are eliminated from the sinogram grid, and as such, the sinogram grid (which is originally a square-based grid) is not regular anymore. Such irregular grid is not compatible with any 2D interpolation method. To tackle this issue, the irregular sinogram grid was rearranged into a triangle-based grid, known as Delaunay triangulated grid [23]. This 2D interpolation approach, compatible with such triangle-based grid, is referred to as Clough-Tocher interpolation [24].

Another attempt to improve the performance of the simple linear interpolation approach was investigated by Meyer *et al.* [25]. In their approach, known as normalized metal artifact reduction (NMAR), a normalized sinogram is generated by forward projection of a tissue-classified prior image. A multi-threshold segmentation is applied to the original CT image in order to obtain the prior image. A linear interpolation is then performed on the normalized sinogram and the corrected image is generated by reconstruction of the de-normalized sinogram. The prior images were derived by segmentation of the corrected CT images using the linear interpolation method into two tissue classes, bones and soft tissues using thresholding-based segmentation. As reported in [25], this would result in a more accurate prior image compared to the segmentation of uncorrected CT images. For the identification of the missing projections, the metallic implant was segmented by the thresholding of the uncorrected CT image at threshold of 2500 HU, and the resulting metal-only image was forward projected. To obtain the prior image, the LI corrected CT images were then segmented for soft tissues (body contour) at threshold on -501 HU was employed. The bones were identified from the LI CT image by a threshold of 200 HU. The metallic implants were excluded from the identified bones using a binary masking. The prior image was then obtained by assigning the CT values of 1070 HU to the soft tissue label, followed by superimposition of the identified bones (having the same CT values as the uncorrected images). Finally, the prior image was smoothed by 8 mm FWHM Gaussian filter.

2) Non-interpolation based sinogram correction

Alongside the presented MAR approaches, which make use of interpolation methods to correct for the artifacts in the sinogram domain, a number of sinogram-based strategies aiming at correcting the affected projection bins using methods other than interpolation were investigated. In this context, Mehranian *et al.* proposed a MAR technique based on maximum *a posteriori* completion of the corrupted projection bins (MAPC) [26]. In this technique, a tissue-classified prior image, which is incorporated into a novel prior potential function, serves as a prior knowledge about the missing projection bins. Subtraction of the unknown target and the prior sinograms, which is a measure of sparsity of the residual sinogram, provides a prior knowledge. The MAPC problem was solved as a constrained optimization problem using an accelerated projected gradient algorithm. In this study, for the MAPC, we used the same prior image as used for NMAR. The MAPC method aims to iteratively estimate the missing projections from neighboring projections, and adjacent slices (in 3D case) and also the prior projections obtained from the forward projection of the prior image. In this algorithm, the impact of the prior projections are controlled by a weighting factor α , which in this study was set to 1, since

in the case of hip prosthesis a large amount of projection data are corrupted and therefore the prior images play an importance rule in the recovery of the corrupted data. In this algorithm there are two more parameters, including convergence parameters $\eta = 1 \times 10^{-4}$ and the diffusivity contrast parameter $\delta = 5 \times 10^{-5}$. These parameters were selected according to previous results in [26].

3) Hybrid sinogram correction

Many correction strategies combine various techniques to achieve an improved performance. In this context, a combination of interpolation- and non-interpolation-based sinogram correction was proposed [27]. This method builds on the well-established metal deletion technique (MDT) to substitute the corrupted projection bins in an iterative filtered backprojection process. An initial image is generated using the linear interpolation approach. Thereafter, four iterations of FBP are conducted in each of which, the corrupted bins are replaced by their value in the previous iteration. In this study, the CT images corrected by LI MAR methods, were filtered using a 3D median filtering, as an edge-preserving filter. The filtered images were forward projected and the corrupted projections of the original sinograms (identified following the forward projection of the metal only images) were then replaced by the projection of the resulting sinograms. This procedure was repeated four times as described in [27].

II.B Simulation and clinical studies

The above referenced MAR techniques (LI, 2D, NMAR, MAPC and MDT) were evaluated using simulated and clinical studies. Since the ground truth is not available in clinical setting, we followed a simulation procedure described by Mehranian *et al.* for the simulation of metal artifacts on clinical artifact-free CT images [26]. In this procedure, the image is segmented into three classes: air, soft tissue and bone and is superimposed by metallic prostheses (figure 1.a). A polychromatic x-ray spectrum was generated using the SpekCal software for a tube voltage of 120 kVp, 2.5 mm aluminum filtration, 10 degrees anode angle and a tube output of 123.8 $\mu\text{Gy/mAs}$ at 1 meter. The spectrum was then uniformly sampled into 35 mono-energetic beams, with intensities and average energies calculated over each energy interval to preserve the tube output. For each tissue class, 35 different attenuation values were obtained based on the NIST XCOM photon cross section library. Thereafter, the attenuation map is forward projected and Poisson noise is added to the resulting sinogram to obtain projection data acquired using polychromatic x-ray beams. The amount of added noise mimics the typical noise level observed in clinical studies. The projection data are then log-processed and reconstructed utilizing a FBP algorithm. Figures 1.b and 1.c show a sample of simulated CT image produced according to the above described procedure. In this study, we simulated metal artifacts in 10 patients with hip replacements (5 bilateral and 5 unilateral hip implants).

The various MAR approaches were further evaluated using 30 clinical studies of patients with single or double hip implants (13 males and 17 females with age range, 42-90 years, and average age 65 years). These patients were scanned on a 64-slice Biograph mCT scanner (Siemens Healthcare, Erlangen, Germany), using the following parameters: 100 kVp, 30 mAs (using CARE Dose4D automatic tube current modulation), 16×1.2 collimation and a pitch of 1.5.

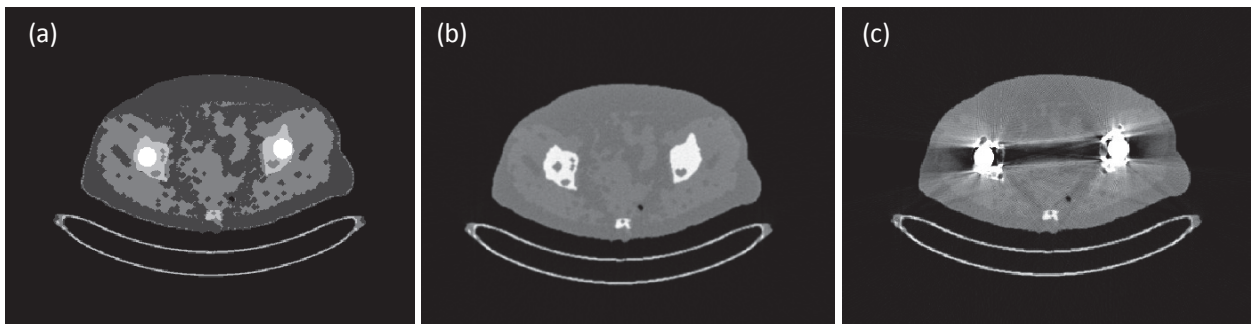


Figure 1. Artifact simulation process: (a) The CT image is segmented into three classes: air, soft tissue and bone; (b) Artifact-free CT image (ground truth). (c) Simulated image containing metallic artifacts. The metal is

inserted in the segmented image when the artefacted image is to be reconstructed (a), and is excluded otherwise. Window width/window level = 2100/1200.

II.C. Evaluation strategy and statistical analysis

Using the ground truth artifact-free CT image, the impact of MAR can be accurately evaluated using quantitative metrics. Therefore, for the simulated datasets, three metrics were calculated using region of interest (ROI)-based analysis. Six ROIs were defined on each image, two on regions corresponding to bright streaking artifacts, two on regions corresponding to dark streaking artifacts, and two on artifact-free regions (figure 4.a). The same ROIs were used on both ground truth images and corrected images. The evaluation metrics include the mean relative error (MRE), normalized root mean square difference (NRMSD) and mean absolute deviation (MAD) between the corrected ($I^{corrected}$) and ground truth image (I^{true}):

$$\% MRE = \frac{I^{corrected} - I^{true}}{I^{true}} \times 100\% \quad (1)$$

$$\% NRMSD = \sqrt{\frac{\sum_{i \in ROI} (I_i^{corrected} - I_i^{true})^2}{\sum_{i \in ROI} (I_i^{true})^2}} \times 100\% \quad (2)$$

$$MAD = \frac{1}{N} \sum_{i \in ROI} |I_i^{corrected} - I_i^{true}| \quad (3)$$

$I^{corrected}$ and I^{true} represent the mean intensity (original HU + 1024 to prevent zero denominator) within each ROI and i the index of pixels belonging to each ROI. N is the number of voxels in a given ROI.

The difference between mean intensities within the defined regions of interest on the corrected and ground truth images were also statistically analyzed using a two-tailed paired t-test.

For the clinical datasets, where the ground truth is not available, a blind qualitative evaluation of the original anonymized CT images and those produced using the 5 MAR techniques was performed by two experienced radiologists (10 and 25 years of experience) separately who ranked the distinction of five organs in the pelvic area: bladder, rectum, prostate (if applicable), seminal vesicles (if applicable) and vagina (if applicable). The ranking was performed by assigning scores from 0 to 5, with rank 0 indicating totally obscured organs, with no structures identifiable and 5 indicating recognition with high confidence [27]. The overall quality of the images was also similarly scored. Typical windowing adopted in clinical pelvic organ evaluation was used to evaluate the datasets.

Interobserver agreement regarding ratings for organ evaluation and for overall image quality was assessed using the kappa statistics, kappa values ranging from 0 – 1 (slight agreement: 0.01 – 0.2; fair agreement: 0.21 – 0.4; moderate agreement: 0.41 – 0.6; good agreement: 0.61 – 0.8; excellent agreement: 0.81 – 1). All statistical analyses (t-test and kappa) were performed using SPSS for windows (SPSS Inc., Version 14.0).

III. Results

III.A. Quantitative analysis

Figure 2 illustrates an example of a simulated artefacted CT image together with the corresponding ground truth and corrected images. It can be observed that all MAR approaches reduce the apparent streaking artifacts to some extent. However, since the simulated datasets contain less diverse assortment of soft tissue compartments compared to real clinical studies, there is less information to be retrieved through the artifact reduction process.

Figure 3 presents the quantitative analysis of the simulated images using the three defined metrics. Each metric is presented in a separate graph where every MAR technique is plotted as a bar with a different gray level. Looking at the three plots, it can be observed that three methods (2D, NMAR and MAPC) seem to share the highest performance in correcting for dark streaking artifacts, while LI fall behind the other methods in all regions.

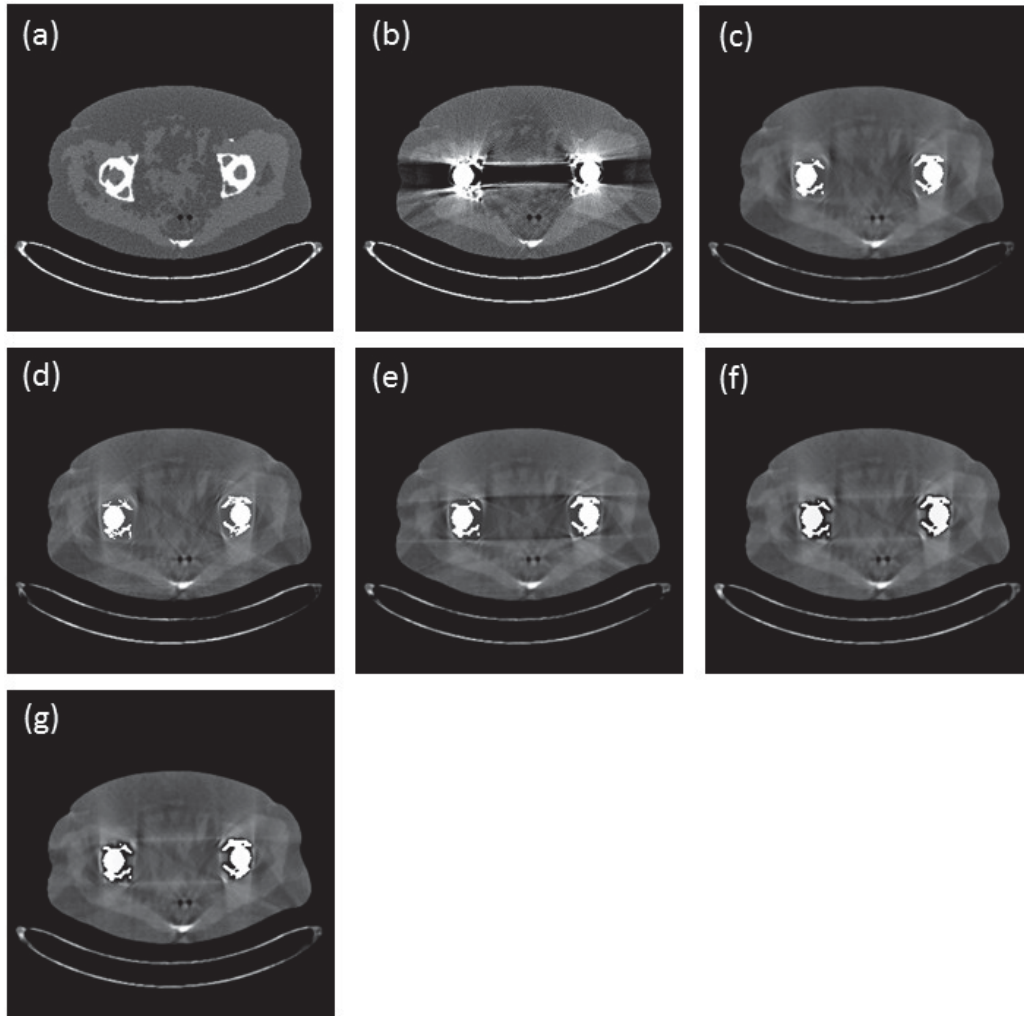


Figure 2. (a) Representative artifact-free CT image without metal implants, (b) artefacted CT image with simulated metal implants, and same image shown in (b) corrected using the different MAR techniques: (c) LI, (d) 2D, (e) MDT, (f) NMAR and (g) MAPC. Window width/window level = 2100/1200.

In regions with no artifacts, the errors and deviations associated with all MAR methods remain similarly low, except LI which presents a slightly higher error. Table 1 summarizes the results of the statistical analysis of these datasets in different regions using on a 2-tailed paired t-test. As the results presented in Table 1 suggest, the differences in regions corresponding to dark streaking artifacts are all significant (P -value < 0.05). However, there is no proof of statistical significance between regions corresponding to bright streaking artifacts and artifact-free areas for all five correction techniques (P -value > 0.05).

Table 1. P-values obtained by statistical analysis of the different MAR techniques in dark, bright and unaffected regions for the simulated studies using paired 2-tailed t-test.

Region	MAR method				
	LI	2D	MDT	NMAR	MAPC
Dark	<0.005	<0.001	<0.001	<0.002	<0.002
Bright	0.79	0.57	0.38	0.22	0.40
Unaffected	0.06	0.24	0.23	0.08	0.14

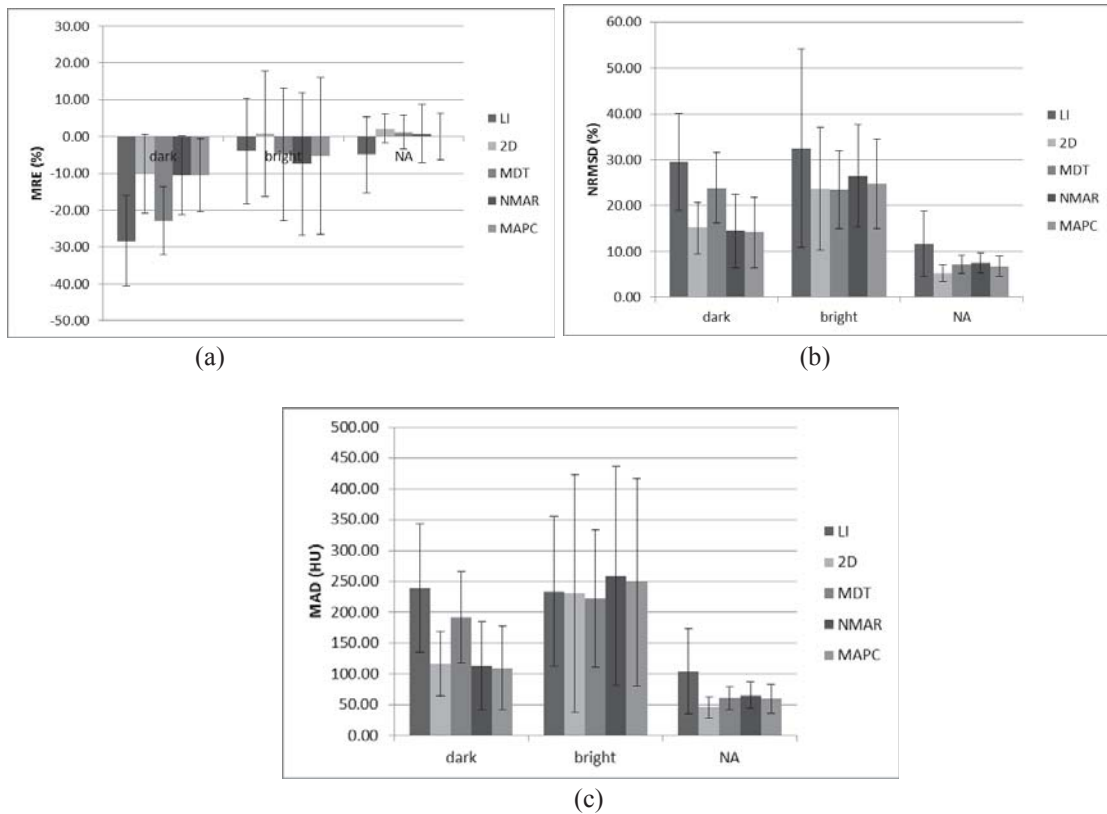


Figure 3. Quantitative analysis of the simulated CT images using three metrics: (a) mean relative error (MRE), (b) normalized root mean square difference (NRMSD) and (c) mean absolute deviation (MAD). Error bars represent the standard deviation.

III.B. Qualitative data analysis

A representative clinical study is shown in figure 4, where the original image and the corresponding corrected images using the five MAR methods are presented. It can be noticed that almost all methods leave a trace of the streaking artifacts after correction. However, they all enhance the quality of the images to a great extent. Since the ground truth for the clinical datasets is not known, the images were independently analyzed by two expert radiologists and scored from 0 to 5 for five organs in the pelvic area based on how the organ can be recognized. The different organs used for scoring are marked with an arrow (In figure 4f). The overall quality of the images was also ranked to reflect the severity of the remaining artifacts. Figure 5 illustrates the average scores and standard deviations assigned to each organ, as well as the ranking reflecting overall image quality.

A representative clinical study is shown in figure 6 where the streaking artifacts in the original image (figure 6.a) completely obscure the prostate, seminal vesicles and bladder. The average scores assigned by the radiologists to these organs are 0, 0 and 0.5, respectively. As can be seen in figure 6 (b-f), all five MAR techniques have considerably improved the diagnostic value of CT images and the pelvic organs are clearly recognizable after image processing, with scores varying between 4 and 5. Interobserver agreement for scoring of each organ, as well as for overall image quality were excellent with kappa values as follows: 0.87 for the prostate, 0.89 for the seminal vesicles, 0.86 for the vagina, 0.80 for the bladder and 0.83 for overall image quality. Although that there is a very good agreement between the observations of the two raters, the calculation of kappa was not possible for the rectum since the results did not meet the kappa statistics criteria given that the ranges of scores for both observers were different (one radiologist ranked it in the range of 2 to 5, while the second ranked it between 4 and 5).

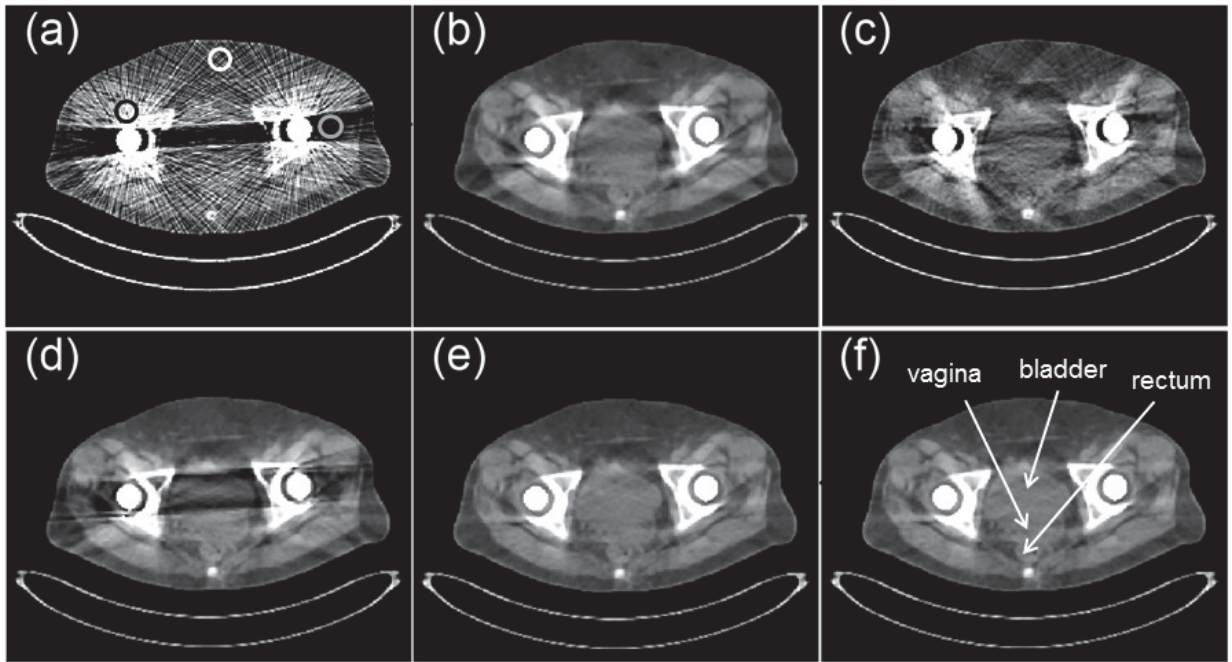


Figure 4. Representative clinical case showing (a) the original artifacted CT image and the corrected images using the various MAR approaches: (b) LI, (c) 2D, (d) MDT, (e) NMAR and (f) MAPC. The ROIs used for the quantitative analysis are shown in (a), where the black ROI corresponds to the bright region, the grey ROI to the dark region and the white ROI to the unaffected region. The organs used for scoring are also depicted in (f). Window width/window level = 500/20.

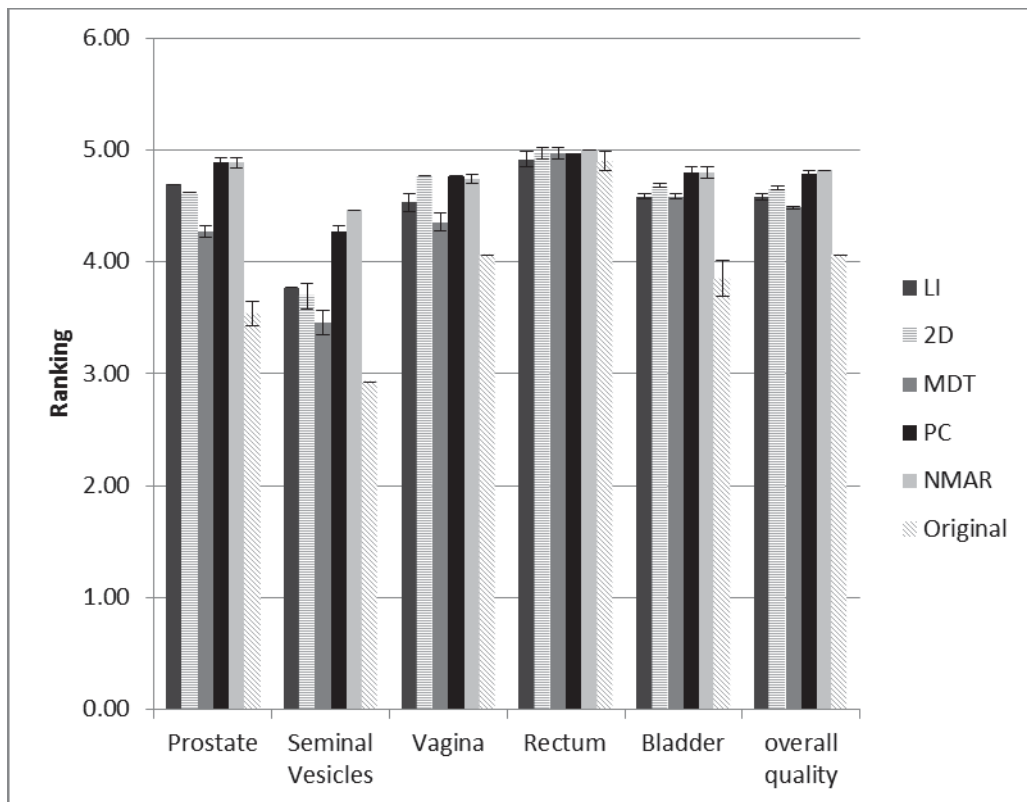


Figure 5. Average scoring of the clinical studies in five selected organs of the pelvic area and overall image quality (observations of the two radiologists are averaged). Error bars represent the standard deviation.

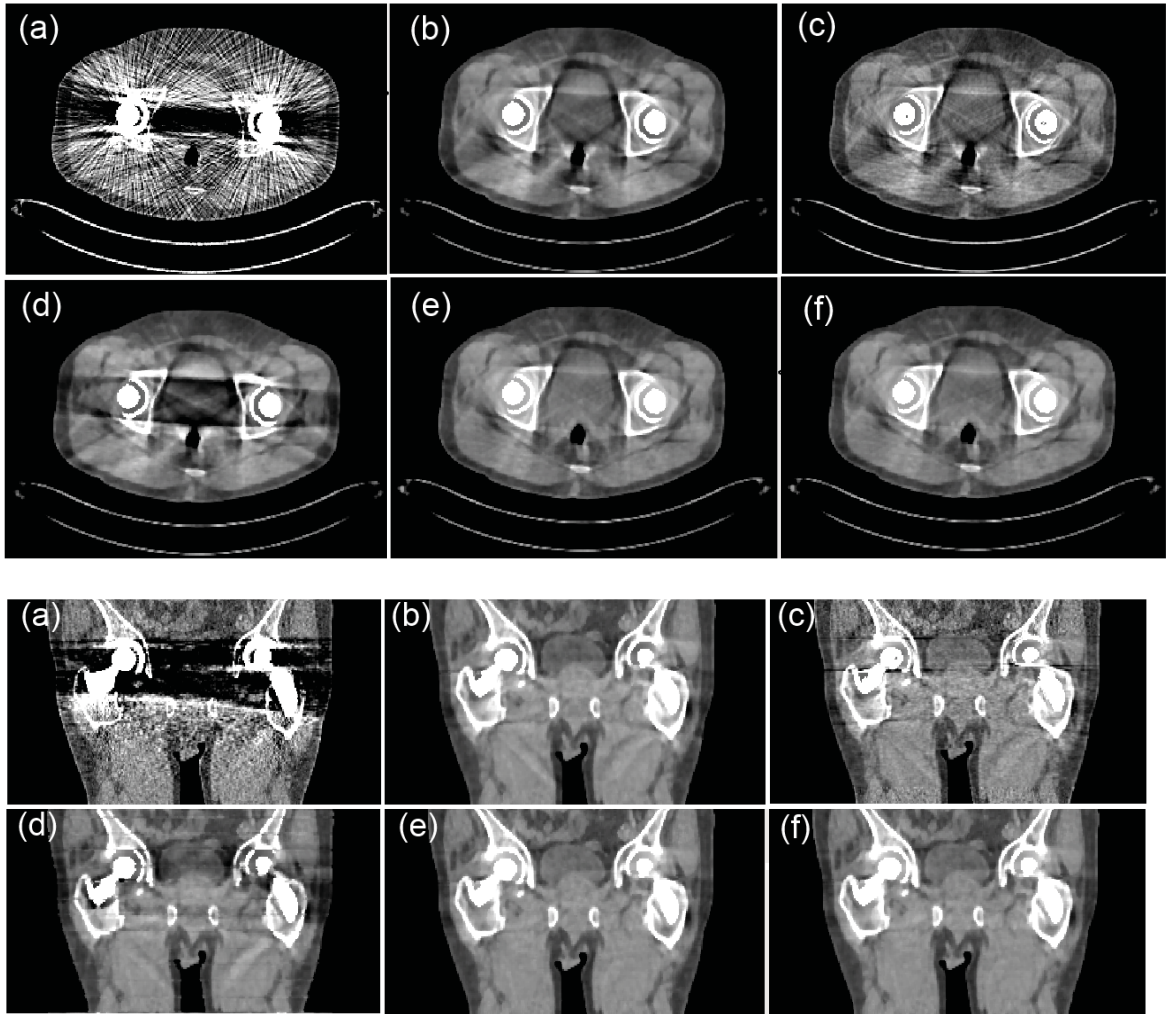


Figure 6. Representative clinical study showing in two planes (top: axial and bottom: coronal) the considerable enhancement of the diagnostic value of CT examinations contributed by metal artifact reduction. (a) The original artifacted CT image and the corrected images generated using the various MAR approaches: (b) LI, (c) 2D, (d) MDT, (e) NMAR and (f) MAPC. Window width/window level = 500/20.

IV. Discussion

The reduction of metallic streaking artifacts on CT images proved to play a significant role in improving diagnostic image quality and quantitative capability of this imaging modality. The confident usage of x-ray CT in a broad range of clinical applications requires proper correction for image degrading factors to reduce the artifacts they produce. Several correction approaches have been proposed during the past few decades [11], which motivated the comparison of their performance in an attempt to highlight their advantages and drawbacks. In this paper, we compared five different MAR techniques belonging to different categories of MAR approaches using simulated and clinical studies of patients bearing hip metallic implants. All selected MAR methods operate in the sinogram domain, which proved to be superior to image-based approaches [11].

The results obtained using simulated studies demonstrated that the performance of the selected MAR algorithms alters in different regions of the images. In regions corresponding to dark streaking artifacts, two interpolation-based approaches (i.e. 2D and NMAR) and a non-interpolation based approach (i.e. MAPC) perform almost equally well. A lower MAD is the evidence of a lower deviation in the intensity of the pixels (in HU) in the investigated regions. Since the ROIs were carefully defined in areas where only one tissue type is present, a low MAD was expected. MRE and NRMSD are two measures of relative error (in percentage) and as such, lower values are desired. As a consequence, all three quantitative validation metrics confirm that 2D,

NMAR and MAPC outperform the other methods in terms of correcting for dark streaking artifacts. LI appears to have the lowest performance in these regions.

In regions corresponding to bright streaking artifacts, all methods have comparable performance. However, LI has slightly inferior performance in terms of NRMSD. NMAR appears to fall slightly behind the other three methods in correcting the bright streaking artifacts. The performance of all selected methods, except LI, is approximately similar in artifact-free regions. MRE and NRMSD remain within about $\pm 5\%$ and deviations of intensities are less than 50 HU, which is quite acceptable. The average HU deviation in artifact-free regions goes up to 100 HU when using LI and NRMSD. MRE measures are also higher relative to other four methods. The results of the statistical analysis revealed that the mean differences between the corrected images and the corresponding ground truth are not statistically significant in regions corresponding to bright streaking artifacts and artifact-free regions. On the other hand, all techniques seem to have a poor performance in dark streaking areas.

The results of the clinical studies enabled to observe that, except the rectum, which is almost never influenced by streaking artifacts and as such is ranked close to 5 in all image sets, the other organs have been scored approximately between 3 and 4 before correction (Fig. 5). This means that all organs in the pelvic area are more or less recognizable, with different levels of certainty.

Although the differences between the ranking of the different MAR techniques were not considerable, NMAR and MAPC appear to outperform the other techniques, particularly for the prostate, where the ranking is very close to the maximum rank. These observations are in agreement with the simulated studies in the regions corresponding to dark streaking artifacts. In this analysis, the LI algorithm does not outperform the other techniques, neither in the five different organs nor the overall image quality. The 2D approach achieves an intermediate ranking among other approaches. LI and MDT techniques have shown the lowest performance using both simulation and clinical studies.

The inconsistent performance of MAR techniques belonging to the same category (e.g. NMAR and LI) indicates that the approaches cannot be ranked based on the category they belong to. Since the more complicated MAR techniques, such as NMAR and MAPC, are able to outperform simple interpolation schemes, such as LI, it seems advisable to invest in more complex approaches. On the other hand, there is still room for improvement of the more sophisticated approaches, such as NMAR and MAPC, which might enable them to achieve improved performance in the regions corresponding to bright streaking artifacts. On the other hand, the potential of rather simple approaches, such as 2D, must not be overlooked. Hybrid approaches enabling to combine various techniques taking the advantages of each one into account seem to be the way to go to achieve an ultimate solution addressing the shortcomings of each technique. Recent studies reporting on the evaluation of this type of techniques seem to confirm their strength and robustness in clinical setting [28].

The scope of this study was limited to metal hip implants. Further investigation of other common sources of streaking artifacts, such as dental fillings, is required to generalize the conclusions of these findings regarding the performance of various MAR approaches. It should however be noted that metallic hip implants have been chosen in this work since they produce the most severe streaking artifacts and, as such, this work is deemed to be a proper representative sample of various sources of metallic artifact.

Another known limitation of this work is that artificial sinograms are used rather than the original sinograms produced by the CT scanners. Although previous studies demonstrated that the use of virtual sinograms does not bring in significant bias in the outcome of MAR techniques [11, 15], it is worthwhile to compare the performance of the various MAR algorithms on the original sinograms using a larger number of clinical studies to increase the statistical power of the study.

V. Conclusion

In this work, we compared the performance of five MAR techniques for the reduction of metal artifacts in CT images of patients presenting with hip prostheses using simulation and clinical studies. The simulation studies demonstrated that the 2D, NMAR and MAPC methods achieved the best performance in reducing dark streak artifacts, which are dominant in patients with bilateral hip implants. In regions contaminated with bright streaking artifacts, all five methods exhibited comparable performance. The results of the clinical studies showed that NMAR and MAPC methods outperform the other techniques, particularly for the prostate, which is usually obscured in dark streaking artifacts. It was concluded that the reduction of artifacts induced by hip prosthesis,

enabling improved diagnostic confidence in CT images, can be reliably achieved by NMAR and MAPC techniques.

Acknowledgments

This work was supported by the Swiss National Science Foundation under grants SNSF 31003A-149957 and 320030_135728/1 and the Indo-Swiss Joint Research Programme ISJRP-138866.

References

- [1] W. A. Kalender, "X-ray computed tomography.," *Phys Med Biol*, vol. 51, no. 13, pp. R29-43, Jul 7, 2006.
- [2] A. Bockisch, L. S. Freudenberg, D. Schmidt, and T. Kuwert, "Hybrid imaging by SPECT/CT and PET/CT: Proven outcomes in cancer imaging.," *Sem Nucl Med*, vol. 39, no. 4, pp. 276-289, 2009.
- [3] J. F. Barrett, and N. Keat, "Artifacts in CT: recognition and avoidance.," *Radiographics*, vol. 24, no. 6, pp. 1679-1691, Nov-Dec, 2004.
- [4] E. Klotz, W. A. Kalender, R. Sokiransky, and D. Felsenberg, "Algorithms for the reduction of CT artifacts caused by metallic implants." pp. 642-650.
- [5] D. D. Robertson, J. Yuan, G. Wang, and M. W. Vannier, "Total hip prosthesis metal-artifact suppression using iterative deblurring reconstruction.," *J Comput Assist Tomogr*, vol. 21, no. 2, pp. 293-298, Mar-Apr, 1997.
- [6] W. A. Kalender, R. Hebel, and J. Ebersberger, "Reduction of CT artifacts caused by metallic implants.," *Radiology*, vol. 164, no. 2, pp. 576-577, Aug, 1987.
- [7] A. Mehranian, M. R. Ay, A. Rahmim, and H. Zaidi, "X-ray CT metal artifact reduction using wavelet domain L0 sparse regularization.," *IEEE Trans Med Imaging*, vol. 32, no. 9, pp. 1707-1722, Sep, 2013.
- [8] C. C. Watson, "Supplemental transmission method for improved PET attenuation correction on an integrated MR/PET.," *Nucl Instr Meth A*, vol. 734, Part B, pp. 191-5, 2014.
- [9] P. E. Kinahan, D. W. Townsend, T. Beyer, and D. Sashin, "Attenuation correction for a combined 3D PET/CT scanner.," *Med Phys*, vol. 25, no. 10, pp. 2046-2053, Oct, 1998.
- [10] H. Zaidi, and B. H. Hasegawa, "Determination of the attenuation map in emission tomography.," *J Nucl Med*, vol. 44, no. 2, pp. 291-315, 2003.
- [11] M. Abdoli, R. A. J. O. Dierckx, and H. Zaidi, "Metal artifact reduction strategies for improved attenuation correction in hybrid PET/CT imaging.," *Med Phys*, vol. 39, no. 6, pp. 3343-3360, 2012.
- [12] W. R. Hendee, and E. R. Ritenour, *Medical Imaging Physics*, 4th Edition ed., New York: Wiley-Liss, Inc., 2002.
- [13] J. Nuyts, B. De Man, J. A. Fessler, and e. al, "Modelling the physics in the iterative reconstruction for transmission computed tomography.," *Phys Med Biol*, vol. 58, no. 12, pp. R63-96, 2013.
- [14] H. Rothfuss, V. Panin, I. Hong, and e. al, "LSO background radiation as a transmission source using time of flight information." pp. 1-5.
- [15] M. Abdoli, M. Ay, A. Ahmadian, R. Dierckx, and H. Zaidi, "Reduction of dental filling metallic artefacts in CT-based attenuation correction of PET data using weighted virtual sinograms optimized by a genetic algorithm.," *Med Phys*, vol. 37, no. 12, pp. 6166-6177, Jan, 2010.
- [16] G. H. Glover, and N. J. Pelc, "An algorithm for the reduction of metal clip artifacts in CT reconstructions.," *Med Phys*, vol. 8, no. 6, pp. 799-807, Nov-Dec, 1981.
- [17] T. Hinderling, P. Ruegsegger, M. Anliker, and C. Dietschi, "Computed tomography reconstruction from hollow projections: an application to in vivo evaluation of artificial hip joints.," *J Comput Assist Tomogr*, vol. 3, no. 1, pp. 52-57, Feb, 1979.
- [18] C. Xu, F. Verhaegen, D. Laurendeau, S. A. Enger, and L. Beaulieu, "An algorithm for efficient metal artifact reductions in permanent seed.," *Med Phys*, vol. 38, no. 1, pp. 47-56, Jan, 2011.
- [19] W. J. H. Veldkamp, R. M. S. Joemai, A. J. van der Molen, and J. Geleijns, "Development and validation of segmentation and interpolation techniques in sinograms for metal artifact suppression in CT.," *Med Phys*, vol. 37, no. 2, pp. 620-628, 2010.
- [20] M. Bazalova, L. Beaulieu, S. Palefsky, and F. Verhaegen, "Correction of CT artifacts and its influence on Monte Carlo dose calculations.," *Med Phys*, vol. 34, no. 6, pp. 2119-2132, 2007/06/00/, 2007.
- [21] M. Abdoli, J. R. de Jong, J. Pruijm, R. A. Dierckx, and H. Zaidi, "Reduction of artefacts caused by hip implants in CT-based attenuation-corrected PET images using 2-D interpolation of a virtual sinogram on an irregular grid.," *Eur J Nucl Med Mol Imaging*, vol. 38, no. 12, pp. 2257-2268, Dec, 2011.
- [22] D. Prell, Y. Kyriakou, M. Beister, and W. A. Kalender, "A novel forward projection-based metal artifact reduction method for flat-detector computed tomography.," *Phys Med Biol*, vol. 54, no. 21, pp. 6575-6591, 2009.
- [23] P. Delaunay, "Sur la sphere vide.," *Bulletin of Academy of Sciences of the USSR*, vol. 6, pp. 793-800, 1934.

- [24] R. Clough, and J. Tocher, "Finite element stiffness matrices for analysis of plates in blending." pp. 515-545.
- [25] E. Meyer, R. Raupach, M. Lell, B. Schmidt, and M. Kachelriess, "Normalized metal artifact reduction (NMAR) in computed tomography," *Med Phys*, vol. 37, no. 10, pp. 5482-93, Oct, 2010.
- [26] A. Mehranian, M. R. Ay, A. Rahmim, and H. Zaidi, "3D prior image constrained projection completion for x-ray CT metal artifact reduction," *IEEE Trans Nuc Sci*, vol. 60, no. 5, pp. 3318-32, 2013.
- [27] F. E. Boas, and D. Fleischmann, "Evaluation of two iterative techniques for reducing metal artifacts in computed tomography.," *Radiology*, vol. 259, no. 3, pp. 894-902, Jun, 2011.
- [28] M. Axente, A. Paidi, R. Von Eyben, C. Zeng, A. Bani-Hashemi, A. Krauss, and D. Hristov, "Clinical evaluation of the iterative metal artifact reduction algorithm for CT simulation in radiotherapy," *Med Phys*, vol. 42, no. 3, pp. 1170-83, Mar, 2015.

Chapter 5

An ordered-subsets proximal preconditioned gradient algorithm for edge-preserving PET image reconstruction

Abolfazl Mehranian, Arman Rahmim, Mohammad Reza Ay, Fotis Kotasidis, Habib Zaidi

Med Phys Vol. 40, No. 5, pp 052503-14 (2013)

Abstract

Purpose: In iterative PET image reconstruction, the statistical variability of the PET data pre-corrected for random coincidences or acquired in sufficiently high count rates can be properly approximated by a Gaussian distribution, which can lead to a penalized weighted least-squares (PWLS) cost function. In this study, we propose a proximal preconditioned gradient algorithm accelerated with ordered subsets (PPG-OS) for the optimization of the PWLS cost function and develop a framework to incorporate boundary side information into edge-preserving total variation (TV) and Huber regularizations.

Methods: The PPG-OS algorithm is proposed to address two issues encountered in the optimization of PWLS function with edge-preserving regularizers. First, the second derivative of this function (Hessian matrix) is shift-variant and ill-conditioned due to the weighting matrix (which includes emission data, attenuation and normalization correction factors) and the regularizer. As a result, the paraboloidal surrogate functions (used in the optimization transfer techniques) end up with high curvatures and gradient-based algorithms take smaller step-sizes toward the solution, leading to a slow convergence. In addition, preconditioners used to improve the condition number of the problem, and thus to speed up the convergence, would poorly act on the resulting ill-conditioned Hessian matrix. Second, the PWLS function with a non-differentiable penalty such as TV is not amenable to optimization using gradient-based algorithms. To deal with these issues and also to enhance edge-preservation of the TV and Huber regularizers by incorporating adaptively or anatomically derived boundary side information, we followed a proximal splitting method. Thereby, the optimization of the PWLS function is split into a gradient descent step (upgraded by preconditioning, step size optimization and ordered subsets) and a proximal mapping associated with boundary weighted TV and Huber regularizers. The proximal mapping is then iteratively solved by dual formulation of the regularizers.

Results: The convergence performance of the proposed algorithm was studied with three different diagonal preconditioners and compared with the state-of-the-art separable paraboloidal surrogates accelerated with ordered-subsets (SPS-OS) algorithm. In simulation studies using a realistic numerical phantom, it was shown that the proposed algorithm depicts a considerably improved convergence rate over the SPS-OS algorithm. Furthermore, the results of bias-variance and signal to noise evaluations showed that the proposed algorithm with anatomical edge information depicts an improved performance over conventional regularization. Finally, the proposed PPG-OS algorithm is used for image reconstruction of a clinical study with adaptively derived boundary edge information, demonstrating the potential of the algorithm for fast and edge-preserving PET image reconstruction.

Conclusions: The proposed PPG-OS algorithm shows an improved convergence rate with the ability of incorporating additional boundary information in regularized PET image reconstruction.

I. Introduction

Positron Emission Tomography (PET) is one of the leading molecular imaging modalities for the detection, staging and monitoring of metabolically active lesions in oncology[1], the diagnosis and risk stratification of cardiovascular diseases in cardiology[2], functional brain imaging in a wide variety of clinical neurological applications [3] and many other medical disciplines. Over the years, PET imaging has experienced considerable advances in data acquisition and image reconstruction [4, 5]. The development of model-based statistical image reconstruction techniques has substantially increased the quantitative accuracy of PET images. These reconstruction techniques can explicitly account for the physical and statistical processes involved in the image formation procedure and allow for the incorporation of prior knowledge and side information about the PET activity distribution [6, 7]. In the Bayesian estimation framework (under zero-one loss function), statistical reconstruction techniques are formulated as the maximum a posteriori (MAP) estimation of the underlying PET image given the acquired emission data. Specifically, MAP reconstruction attempts to estimate an image that has the maximal statistical consistency with measured data (expressed as maximum Poisson or Gaussian likelihood) and at the same time is in conformance with a priori knowledge (expressed as a prior distribution or penalty function) [8].

The statistical variability of prompt PET measurements is best described by the Poisson distribution; however, when the measurements are corrected for accidental coincidences or acquired at sufficiently high count rates, the Poisson distribution can be approximated to the Gaussian distribution [9]. Making use of the Gaussian model or likelihood leads to a weighted least squares data-consistency term, which when augmented by a prior or penalty function results in a penalized weighted least-squares (PWLS) cost function [9]. In the PWLS reconstruction, the mean and variance of the measured data are assumed to be known following the correction for attenuation, detector normalization and accidental coincidences. The minimization of the resulting cost function maximizes the posterior probability of the underlying activity distribution given the measured data. The penalty function penalizes deviations from an *a priori* knowledge and in fact imposes our expectations about the image being estimated. For this purpose, quadratic Tikhonov-based penalty functions have been widely used to suppress noise and impose smoothness during reconstruction [10]. These priors effectively suppress noise on the assumption that sharp transitions between adjacent voxels are probably due to noise [8]. However, as a compromise, the sharp edges at the boundaries of organs or lesions are blurred. To avoid the smoothing of boundaries, a variety of edge-preserving non-quadratic penalty functions have been studied in the literature [11-17], among which Huber [18] and total variation (TV) [19] have garnered significant attention. These penalty functions or regularizers emphasize on the smoothing or regularization of neighboring voxels with small intensity differences, while retaining edges between the voxels with large intensity differences. In most of the above approaches, boundaries are detected based on the short-range and local interactions of neighboring voxels. In an attempt to encourage the formation and preservation of continuous boundaries, various penalty functions have been proposed to exploit the non-local features captured from the image itself [20-22] or from other side information [23, 24]. Yu *et al* [20] proposed a boundary weighted quadratic prior which adaptively derives boundary weights (curves) between organs and thereby penalizes local differences inside each region more than those across boundaries. With the advent of dual modality PET/CT and more recently PET/MR scanners, the penalty functions exploiting anatomical side information, known as anatomical priors, have gained attention in PET image reconstruction [25-28]. Anatomical priors are commonly used to encourage spatial smoothness within organs in PET images while discouraging it across organ boundaries. For this purpose, some groups incorporated anatomical labels and boundaries into the quadratic priors [24, 25, 29, 30]. The mutual information and joint entropy prior between the anatomical and functional images have also been used further to regulate the global distribution of activity within organs during the reconstruction task [27, 31].

To optimize the PWLS cost function with anatomically weighted quadratic penalty function, Comet *et al* [32] used successive over-relaxation (SOR) algorithm, while Drawaja *et al* [29] used separable paraboloidal surrogates accelerated with ordered-subsets (SPS-OS) for a similar penalty function. In general, several efficient algorithms have been proposed for the optimization of PWLS cost function, mostly in the context of transmission tomography, such as SPS-OS [33], block coordinate descent [34] and preconditioned conjugate gradient (PCG) methods [35]. However, there are some issues and considerations in developing optimization algorithms for the PWLS cost function. First issue is the ill-conditioning and shift-variance of its second-order derivative (Hessian) due to its weighting matrix (see section II) and the penalty function, particularly with edge-

preserving penalties [36]. As a result, the paraboloidal surrogate functions end up with high curvatures [33] and gradient-based algorithms with small step-sizes, leading to slow convergence. In addition, preconditioners used to improve the condition number of the Hessian, and thus to speed up the convergence, would act poorly on the resulting ill-conditioned Hessian matrix [36]. Some special shift-invariant weighting matrices and preconditioners have been proposed to deal with this issue, however, through making a number of assumptions and introducing computational complexities [35, 37]. Another issue arises when employing non-continuously differentiable penalty functions such as TV. As a result, the PWLS cost function would not be amenable to optimization using conventional gradient-based algorithms. A conventional approach to address the non-differentiability and the so-called staircasing effect of the TV penalty is to smooth it with a Huber norm [38]. Staircasing refers to the formation of artificially flat regions in the reconstructed images. Another approach is variable splitting and dual formulation of TV prior as proposed by Chambolle [39]. Recently, Ramani *et al* [40] employed variable splitting and augmented Lagrangian methods to reduce the PWLS problem into independent sub-problems toward addressing the above issues.

In this study, we describe an approach to improve the convergence rate of existing gradient-based algorithms for the PWLS cost function and also for the first time to enhance the edge-preserving effect of the Huber and TV functions by incorporating additional anatomical boundary information (as weights) into their dual formulations. To address the ill-conditioning of the Hessian matrix due to the penalty function, and also to provide a framework for the dual formulation of weighted TV and Huber priors, we followed a proximal point technique to surrogate the PWLS cost function with a proxy function. The proxy or surrogate was split into a gradient descent and a proximal mapping associated with the priors or regularizers. The convergence rate of the gradient descent step was improved by preconditioning, step size optimization and ordered subsets; thereby a proximal preconditioned gradient algorithm accelerated with ordered-subsets (PPG-OS) was derived. The performance of the proposed algorithm was studied for three different preconditioners and compared with the SPS-OS algorithm in a simulation study. Finally, the proposed image reconstruction algorithm with boundary weighted regularization was assessed using simulation and clinical studies.

II. Theory

II.A The PWLS cost function

Let $x \in \mathbb{R}^N$ be the true activity distribution being observed by a PET imaging system, described by the geometric system matrix $G \in \mathbb{R}^{M \times N}$. Under Poisson photon counting statistics (no deadtime or data correction), the negative Poisson log-likelihood for observing the measured prompt coincidences $y^p \in \mathbb{Z}^M$ given x is described by:

$$\Phi(x) = \sum_{j=1}^M (n_j a_j [Gx]_j + \bar{r}_j) - y_j^p \log(n_j a_j [Gx]_j + \bar{r}_j) \quad (1)$$

where $[Gx]_j = \sum_{i=1}^N G_{ji} x_i$ is the expected number of counts in j^{th} line-of-response (LOR), and n_j , a_j , \bar{r}_j account for detector efficiency, photon attenuation, and expected random and scatter coincidences in the j^{th} LOR, respectively. The quadratic approximation of $\Phi(x)$ in Eq. (1) around an estimate of the trues at the j^{th} LOR, i.e. \hat{y}_j , yields a weighted least-squares (WLS) cost function:

$$\phi(x) = \frac{1}{2} \sum_{j=1}^M w_j ([Gx]_j - \hat{y}_j)^2, \quad w_j = \frac{n_j^2 a_j^2}{\max(1, y_j^p)}, \quad \hat{y}_j = \frac{y_j^p - \bar{r}_j}{n_j a_j} \quad (2)$$

where \hat{y} is a pre-corrected emission sinogram. The details of the above derivation are given in Appendix A. To penalize estimates of x deviating from *a priori* knowledge, the cost function in Eq. (2) can be augmented by a penalty or regularizer, $R(x)$, which results in the following penalized WLS cost function [9]:

$$\psi(x) = \frac{1}{2} \|Gx - \hat{y}\|_W^2 + \beta R(x) \quad (3)$$

where $W = \text{diag}\{w_1, \dots, w_M\}$ and $\beta > 0$ is a regularization parameter that controls the balance between the fidelity of Gx to the data and the regularity of x to a prior knowledge. In this study, we describe an algorithm for the optimization of PWLS cost function which: i) allows for efficient implementation of an edge-preserving regularization capable of incorporating anatomical edge information and ii) possesses an improved convergence rate. We consider a 3D regularizer of the general form:

$$R(x) = \sum_{i=1}^{3N} \omega_i \varphi([Dx]_i) \quad (4)$$

where $D = [D_v^T, D_h^T, D_a^T]^T \in \mathbb{R}^{3N \times N}$ is a derivative matrix, composed of first-order finite difference matrices in horizontal, vertical and axial directions, $\varphi: \mathbb{R} \rightarrow \mathbb{R}$ is a non-convex potential function, differentiable on $\mathbb{R} \setminus \{0\}$ and the ω_i s are weighting factors that control the strength of regularization between voxels. The conventional quadratic regularization uses $\varphi_Q(t) = t^2/2$, which tends to blur edges by assigning high penalties on large voxel differences. The anisotropic total variation (TV) regularizer makes use of an absolute value potential function $\varphi_{TV}(t) = |t|$ to preserve sharp edges while suppressing noise [19]. There are, however, two issues with the TV regularizer. First, as this regularizer (with unit weights) is locally edge preserving, it sometimes results in staircasing in the reconstructed images. Second, it is not continuously differentiable because of the non-differentiability of the absolute value function at points $[Dx]_i = 0$. As a result, the PWLS cost function is not amenable to optimization using conventional gradient-based approaches. To address these issues, the absolute value function is usually smoothed to $|t| \approx \sqrt{t^2 + \epsilon}$ or an anisotropic Huber potential function is employed, which is given by [18]:

$$\varphi_H(t) = \begin{cases} |t| - \frac{\delta}{2}, & |t| \geq \delta \\ \frac{1}{2\delta} |t|^2, & |t| < \delta \end{cases} \quad (5)$$

where $\epsilon > 0$ and $\delta > 0$ control the smoothing and thus the edge-preserving effects. Note that when ϵ or $\delta = 0$, the smoothed TV penalty reduces to a non-smooth TV penalty. TV and Huber regularizations with unit weights detect and preserve edges based on information derived from short-range interactions between neighboring voxels. In this study, we describe an approach to improve the global edge-preservation property of these regularizers using the weights, ω_i , based on the information captured from the images being regularized [20] or from side information of CT or MRI [23, 29].

II.B The Proposed Algorithm

As mentioned earlier, there are two issues in the optimization of PWLS cost function making use of a (weighted) TV or Huber regularization, i) the ill-conditioning of its Hessian matrix, which ends up with the slow convergence of optimization algorithms and ii) the non-continuous differentiability of TV regularizer. The presence of weighting factors can introduce additional shift-variance into the Hessian matrix and thus make the optimization of this cost function more challenging.

To optimize the PWLS function in Eq. (3), we follow a proximal point method [41, 42] wherein, one iteratively adds a proximal penalty term to an original cost function $\psi(x)$. As a result, an easy-to-optimize proxy or surrogate function, $\psi(x, x^k)$, can be obtained whose optimization guarantees that of the original cost function. In this sense, the proximal point technique follows the same idea of optimization transfer techniques [43]. Therefore, we iteratively estimate the solution of the problem (3) by:

$$x^{k+1} = \operatorname{argmin}_{x \geq 0} \psi(x, x^k), \quad \psi(x, x^k) \triangleq \psi(x) + \frac{1}{2} \|x - x^k\|_L^2 \quad (6)$$

where $L = \pi I_N - G^T W G$ is a positive definite matrix, in which I_N is an $N \times N$ identity matrix, $G^T W G$ is the Fisher information term of the Hessian, $\mathcal{H} = G^T W G + \beta \nabla^2 R(x)$, of the PWLS functional and π satisfies $\pi \geq \lambda_{\max}(G^T W G)/2$. $\lambda_{\max}(\cdot)$ denotes the largest eigenvalue. Note that the surrogate function in Eq. (6) satisfies the monotonicity conditions for surrogates [43, 44]. i.e., it i) coincides with $\psi(x)$ at point $x = x^k$, ii) has a matched gradient as $\psi(x)$ at that point and iii) lies above this function at other points. By some algebra, the surrogate can be written as:

$$\psi(x, x^k) = \frac{\pi}{2} \left\| x - \left(x^k - \frac{1}{\pi} \nabla \phi(x^k) \right) \right\|^2 - \frac{1}{2\pi} \|\nabla \phi(x^k)\|^2 + \nabla \phi(x^k) + \beta R(x) \quad (7)$$

where $\nabla \phi(x^k) = G^T W (G x^k - \hat{y})$. Hence, we split the optimization problem in Eq. (6) into two steps i) a gradient descent:

$$\tilde{x} = x^k - \tau \nabla \phi(x^k) \quad (8)$$

where $\tau = 1/\pi$ is a step size, and ii) a proximal mapping associated with the regularizer $R(x)$:

$$x^{k+1} = \operatorname{argmin}_{x \geq 0} \frac{1}{2} \|x - \tilde{x}\|^2 + \tau \beta R(x) + C \quad (9)$$

where C is a constant. This algorithm is known as the proximal gradient algorithm [45, 46]. To improve the convergence rate of this algorithm for PET image reconstruction, we propose to upgrade the step in Eq. (8) to a proximal preconditioned gradient algorithm accelerated with i) ordered subsets (PPG-OS) and ii) step size optimization.

1) Preconditioning and step size optimization

Generally, an ideal preconditioner, $P \in \mathbb{R}^{N \times N}$, for PG-type algorithms, that aims to optimize the PWLS objective function, would be the inverse of the Hessian matrix such that $P\mathcal{H} = I_N$, where the condition number of the matrix $P\mathcal{H}$, i.e. the ratio of its largest to smallest eigenvalues, is minimal (unity). However, because of the ill-conditioning of the Hessian due to the weighting matrix W and the penalty $R(x)$ [35] the exact computation of the inverse of the Hessian is impractical and thus approximations are used. In the applied splitting technique, the Hessian matrix is reduced to $G^T W G$, which is better conditioned than \mathcal{H} , particularly when the regularizer is non-quadratic and edge-preserving. In this work, we employed three different diagonal preconditioners including: $P_1 = \text{diag}\{(G^T W G)_{ii}\}^{-1}$, which uses the inverse of the diagonal elements of the Hessian matrix, [47] $P_2 = \text{diag}\{G^T W G \mathbf{1}\}^{-1}$, where $\mathbf{1} \in \mathbb{R}^N$ and $P_3^k = \text{diag}\{(x^k + \epsilon)/G^T \mathbf{1}\}^{-1}$, where $\epsilon > 0$ ensures the positivity of this EM-type preconditioner and $\mathbf{1} \in \mathbb{R}^M$. [48] The preconditioner P_2 has been inspired from De Pierro's convexity method to the data fidelity term in Eq. (4) (see Ref.[49]). As we extended the step in Eq. (8) to a preconditioned gradient descent, the step size τ should satisfy: $0 < \tau \leq 2/\lambda_{\max}(P G^T W G)$. Proof follows from Theorem 8.3 in Ref.[50]. To achieve the maximum amount of decrease of the cost function, the step size can be obtained by the following maximization:

$$\tau^k = \arg\max_{\tau \geq 0} \{\phi(x^k - \tau P \nabla \phi(x^k))\} \quad (10)$$

whereby, an optimal step size is obtained by:

$$\tau^k = \frac{(P \nabla \phi(x^k))^T \nabla \phi(x^k)}{(P \nabla \phi(x^k))^T G^T W G (P \nabla \phi(x^k))} \quad (11)$$

2) Proximal mapping

To solve the *primal* problem (9) for a (non-differentiable) weighted TV and weighted Huber and penalty functions, we cast it into its *dual* problem by making use of an extended dual formulation of these penalty functions. First, we notice that the weighted absolute value of a scalar $x \in \mathbb{R}$ with the weight $\omega > 0$ can be defined as:

$$\omega |x| = \max\{zx : |z| \leq \omega\} \quad (12)$$

Hence, using the above fact, one can define a weighted TV function in its dual formulation by: $R_{TV}^\omega(x) = \sum_{i=1}^{3N} \max_{z \in Q_i} \{z [Dx]_i\}$, where $Q_i = \{z \in \mathbb{R} : |z| \leq \omega_i\}$ is a dual feasible set. Since the Huber penalty function generalizes the TV one, we define the weighted version of Huber regularizer in duality context by [51, 52]:

$$R_H^\omega(x) = \max_{z \in Q} \left\{ z^T D x - \frac{\delta}{2} z^T z \right\} \quad (13)$$

$$Q = \{z \in \mathbb{R}^{3N} : |z_i| \leq \omega_i, \forall i = 1, \dots, 3N\}$$

where the quadratic term $(\delta/2)z^T z$ accounts for the smoothness of the Huber penalty such that $\delta = 0$ reduces it to a weighted TV penalty. Using this formulation, the non-differentiability of the TV function is transferred to the set Q , which can be easily addressed during the proximal mapping. By plugging Eq. (13) into Eq. (9), one arrives at the following primal-dual problem, which is convex in the primal variable x and concave in the dual variable z :

$$\min_{x \geq 0} \max_{z \in Q} \left\{ \frac{1}{2} \|x - \tilde{x}\|^2 + \tau \beta (z^T D x - \frac{\delta}{2} z^T z) \right\} \quad (14)$$

To solve this problem, we exchange the order of the maximization and minimization using the min-max property, reduce $\tau \beta$ to β , and minimize the problem with respect to x . Substituting the resulting solution $x = \tilde{x} - \beta D^T z$ into the max problem gives:

$$\max_{z \in Q} \left\{ -\frac{\beta^2}{2} z^T D D^T z + \beta z^T D \tilde{x} - \frac{\beta \delta}{2} z^T z \right\} \quad (15)$$

We address the non-negativity on this solution later within the body of the algorithm (Algorithm 1, step 6a). The above problem is then cast into the following minimization by multiplying its objective with $-1/\beta^2$ and completing the square:

$$\min_{z \in Q} \left\{ \frac{1}{2} \|D^T z - \tilde{x}/\beta\|^2 + \frac{\delta}{2\beta} \|z\|^2 + C \right\} \quad (16)$$

To find the solution of the above constrained problem, we follow the proximal point method by adding the proximal penalty $\frac{1}{2} \|z - z^n\|_\Sigma^2$ to its objective, where $\Sigma = \alpha I_{3N} - DD^T$, I_{3N} is a $3N \times 3N$ identity matrix and the parameter α should satisfy $\alpha \geq \lambda_{\max}(DD^T)/2$. By some algebra, dropping constant terms and letting $\sigma = \beta/\alpha$, the minimizer of the problem then reads:

$$\begin{aligned} z^{n+1} &= \operatorname{argmin}_{z \in Q} \left\{ \frac{1}{2} z^T z - b^T z \right\} \\ b &= \frac{1}{\delta + \sigma} (\sigma z^n + D(\tilde{x} - \beta D^T z^n)) \end{aligned} \quad (17)$$

As the above problem is separable, one can solve it component-wise subjected to the constraint $|z_i| \leq \omega_i$. One can show that for $|b_i| \leq \omega_i$, the solution is $z_i^{n+1} = b_i$, and for $|b_i| > \omega_i$, the solution reads $z_i^{n+1} = \omega_i \operatorname{sign}(b_i)$. As a result, the solution of Eq. (19) is vector b projected to the subset Q as follows:

$$z_i^{n+1} = \operatorname{proj}_Q(b_i) = \begin{cases} \omega_i \operatorname{sign}(b_i), & |b_i| > \omega_i \\ b_i, & |b_i| \leq \omega_i \end{cases} \quad (18)$$

To this end, Algorithm 1 summarizes the proposed PPG algorithm, whose convergence rate was improved by ordered subsets. Note that subsetization is employed within steps 1 through 4 and hence step size optimization is carried out for each subset.

Algorithm 1: PPG-(OS) Algorithm

Initialize: $x^0 = x^1 = \mathbf{0}$, $z^0 = Dx^0$, $\delta, \alpha, \beta, \sigma = \frac{\beta}{\alpha}, T, k = n = 0$

While (stopping criterion is not met) **do**

1. $\nabla\Phi = G^T W(Gx^k - \hat{y})$
2. $p^k = P\nabla\Phi$
3. $\tau^k = (p^k)^T \nabla\Phi / (p^k)^T G^T W G(p^k)$
4. $x^{k+1} = x^k - \tau^k p^k$.
5. $\tilde{x} \leftarrow x^{k+1}$.
6. **While** $n \leq T$ **do**
 - a. $x^n = [\tilde{x} - \beta D^T z^n]_+$.
 - b. $b = \frac{1}{\delta + \sigma} (\sigma z^n + Dx^n)$.
 - c. $z_i^{n+1} = \operatorname{proj}_Q(b_i), i = 1, \dots, N$.
 - d. $n = n + 1$
7. $x^{k+1} \leftarrow x^n$
8. $k = k + 1$.

Output: $\hat{x} \leftarrow x^{k+1}$

In this algorithm the non-negativity constraint declared in problem (14) is imposed on the primal variable x^n on step 6a, where $[t]_+ = \max(0, t)$ is a non-negativity operator. In this study, we approximated the largest eigenvalue of the matrix DD^T using power iteration method [53], which was found to be less than 8 in 2D regularization and 12 in the 3D case. Therefore, in the Algorithm 1, one can initialize the parameter $\alpha \geq 4$ in 2D and 6 in 3D cases. In the thresholding scheme in Eq. (18), the boundary weights $\{\omega_1, \dots, \omega_{3N}\} \in [a, 1], 0 < a < 1$, are chosen such that lower weights are assigned to the smoothing of boundary regions and thereby the global edge-preserving effect of the resulting algorithm is improved. The weights can be derived from anatomical side information or from the image being regularized. In this study, we derived weighting factors by the following equation [54]:

$$\omega_i = S_a \left\{ \frac{1}{1 + \operatorname{Edge}(x)} \right\}, i = 1, \dots, N \quad (19)$$

where $S_a(t)$ is a scaling function that maps the range of t to $[a, 1]$ and $\operatorname{Edge}(\cdot)$ is an edge detector. We used 2D Canny edge detector [55] using MATLAB's *edge* function with automatic threshold selection. In Eq. (4), three weighting factors were defined for the gradient of each voxel in horizontal, vertical and axial directions. The weights given by Eq. (19) were therefore concatenated to obtain such directional weights at each voxel. In all experiments, we set $a = 0.01$, since noise can reside on edges and therefore non-zero weights are prudent to

suppress noise at edges. In this study, we compared the convergence rate of the proposed PPG-OS algorithm with the SPS-OS algorithm in the optimization of the PWLS cost function. The details of the implementation of SPS-OS algorithm are given in Appendix B.

III. Methods

The performance of the proposed algorithm was evaluated using simulated and clinical studies. In this section, we describe the evaluation procedure of the algorithm and provide the methods and definitions relevant to the studies.

III.A Simulation study

For the purpose of realistic simulations, we simulated a typical activity distribution with several metabolically active regions and a lesion using a 256×256 T1-weighted brain MR image. The activity concentration in the gyrus and the tumor were assigned an average tumor-to-background ratio of 1.6 and 1.9, respectively. The simulated activity distribution and the MR images together with a corresponding MR-derived attenuation map are shown in figures 1(a-c). The attenuation map is composed of linear attenuation coefficients of bone (0.120 cm^{-1}), soft tissue (0.096 cm^{-1}), and air (0 cm^{-1}). The MR image was further used to derive anatomical boundaries for the weighted regularization method elaborated in Section II.B.2. The projection data of the simulated activity distribution were computed analytically for a PET scanner with parallel strip-integral geometry (4.06 mm strip width, 258 radial samples, and 404 angular samples uniformly spaced over 180 degrees). The system matrix describing this scanner was generated using the Image Reconstruction Toolbox (IRT) developed by Fessler *et al.*[56] and the images reconstructed with image resolution of 256×256 and pixel size of $1.94 \times 1.94 \text{ mm}^2$. Following the attenuated forward projection of the simulated activity distribution, 10 Poisson noise realizations were simulated with a total count of 6×10^6 and 10% random coincidence rate.

Figure 1(d) shows the image reconstructed from a given noise realization using the standard OSEM (15 iterations and 6 subsets) algorithm. As expected, the conventional OSEM algorithm enforces maximal consistency between the reconstructed image and the noisy emission data; thereby the final image tends to be

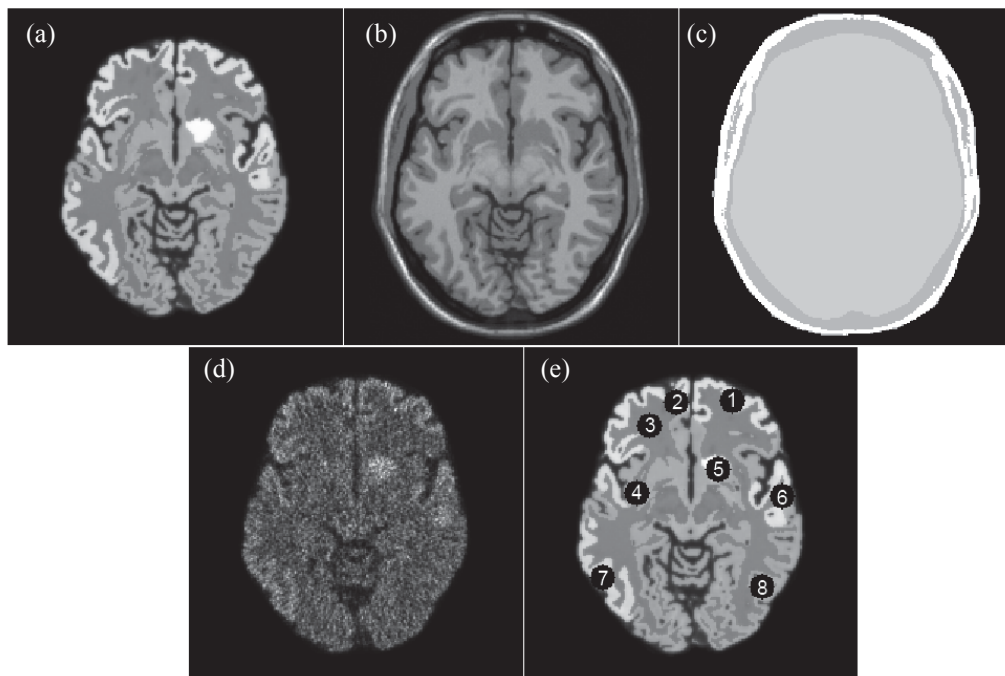


Figure 1. (a) The true activity distribution derived from (b) a transaxial T1-weighted brain MRI together with (c) its corresponding MR-derived attenuation map. (d) The image reconstructed from a given noise realization using the standard OSEM (15 iterations, 6 subsets) algorithm. (e) The regions of interest used for quantitative bias-variance evaluation of the proposed algorithm with anatomically-weighted regularization.

noisy. In the simulation study, we objectively compared the proposed PPG-OS algorithm (using the preconditioners P_1 , P_2 and P_3^k) with the SPS-OS algorithm for 6 ordered subsets. All reconstructions were initialized with a zero initial image. For the evaluation of the algorithms, we consider Huber regularization with the smoothing parameter $\delta = 0.5$ for two reasons: i) to avoid the staircasing artifacts resulting from non-smooth TV regularization and ii) to make the resulting PWLS cost function differentiable and thus amenable to optimization using the SPS-OS algorithm. In all reconstructions using the proposed algorithm, the proximal mapping of the regularizer (step 6 in Algorithm 1) was performed by $T = 5$ iterations, which was found to be enough for the regularization step. As presented in Algorithm 1, a global convergence was declared when the relative change of the image estimate between two successive iterations falls below a tolerance of $\eta = 5 \times 10^{-4}$.

To assess the convergence rate of the algorithms, we heuristically chose three regularization parameters that resulted in the highest signal-to-noise ratio (SNR) between the actual image, x^* , and the reconstructed image \hat{x} after convergence. The SNR is defined as:

$$\text{SNR} = -20 \log \left(\frac{\|\hat{x} - x^*\|}{\|x^*\|} \right) \quad (20)$$

In the next step, the impact of boundary-weighted regularization on the convergence rate of the PPG-OS algorithm as well as image quality was respectively evaluated in terms of SNR and bias-variance trade off over the simulated noise realizations. We followed a region-of-interest (ROI) based approach to assess the bias vs. variance performance of the proposed algorithm. As shown in figure 1 (e), 8 ROIs (~15 mm in diameter) were drawn over different regions of the designed brain phantom. For each ROI, bias was calculated by:

$$\text{Bias} = \frac{|\bar{x} - \bar{x}^*|}{\bar{x}^*} \times 100 \quad (21)$$

where $\bar{x} = \frac{1}{m} \sum_{j=1}^m \hat{x}^{(j)}$, $\hat{x}^{(j)} = \frac{1}{n} \sum_i x_i^{(j)}$ and $\bar{x}^* = \frac{1}{n} \sum_i x_i^*$, m is the number of noise realizations and n is the number of voxels in the ROI, $x^{(j)}$ is the image reconstructed from j^{th} noise realization and x^* is the true object distribution. The variance was also obtained by normalized standard deviation (NSD) for each ROI:

$$\text{NSD} = \frac{1}{n} \sum_{i=1}^n \sqrt{\frac{\frac{1}{m-1} \sum_{j=1}^m (x_i^{(j)} - \bar{x}_i)^2}{\bar{x}_i}} \quad (22)$$

where $\bar{x}_i = \frac{1}{m} \sum_{j=1}^m x_i^{(j)}$ represents the ensemble mean value of voxel i . For each ROI, bias was plotted against NSD values as a function of iteration number and the performance of weighted regularization was compared with the conventional regularization.

III.B Clinical PET study

The proposed PPG-OS-P2 algorithm was employed for image reconstruction of a clinical brain PET/CT scan. The patient was administrated with 205 MBq of ^{18}F -FDG and a dynamic study (60 min) was acquired on the Biograph 64 True Point PET/CT scanner scanner (Siemens Healthcare, Erlangen). The PET scanner operates in fully 3D mode and records prompt and random coincidences in 32-bit list-mode packets, which include the sinogram bin address of each event. Based on bin addresses, the data were histogrammed for a 15 min (0-15 min) static study (~78 million prompts) using an in-house list-mode histogrammer and thereby the prompts, randoms and net true sinograms were generated with a size of $336 \times 336 \times 313$. Standard corrections were applied on the net-true sinograms (attenuation, normalization and scatter) to obtain the pre-corrected sinogram \hat{y} . The data were then reconstructed in 3D mode using the PPG-OS-P2 algorithm with conventional Huber and weighted Huber regularizations. Siddon's algorithm [57] was used to derive a line integral-based geometric system matrix for the Biograph True Point scanner. A hybrid of system matrix pre-computation and in-plane and axial symmetry translations was utilized for a fast and memory efficient image reconstruction. At the end, the preconditioner P2 was pre-computed and an image volume of $336 \times 336 \times 81$ size was reconstructed using the proposed algorithm (8 iterations and 14 subsets). For weighted regularization, we followed an approach in which the boundary weights were iteratively derived from the image estimates during the reconstruction using Eq. (19).

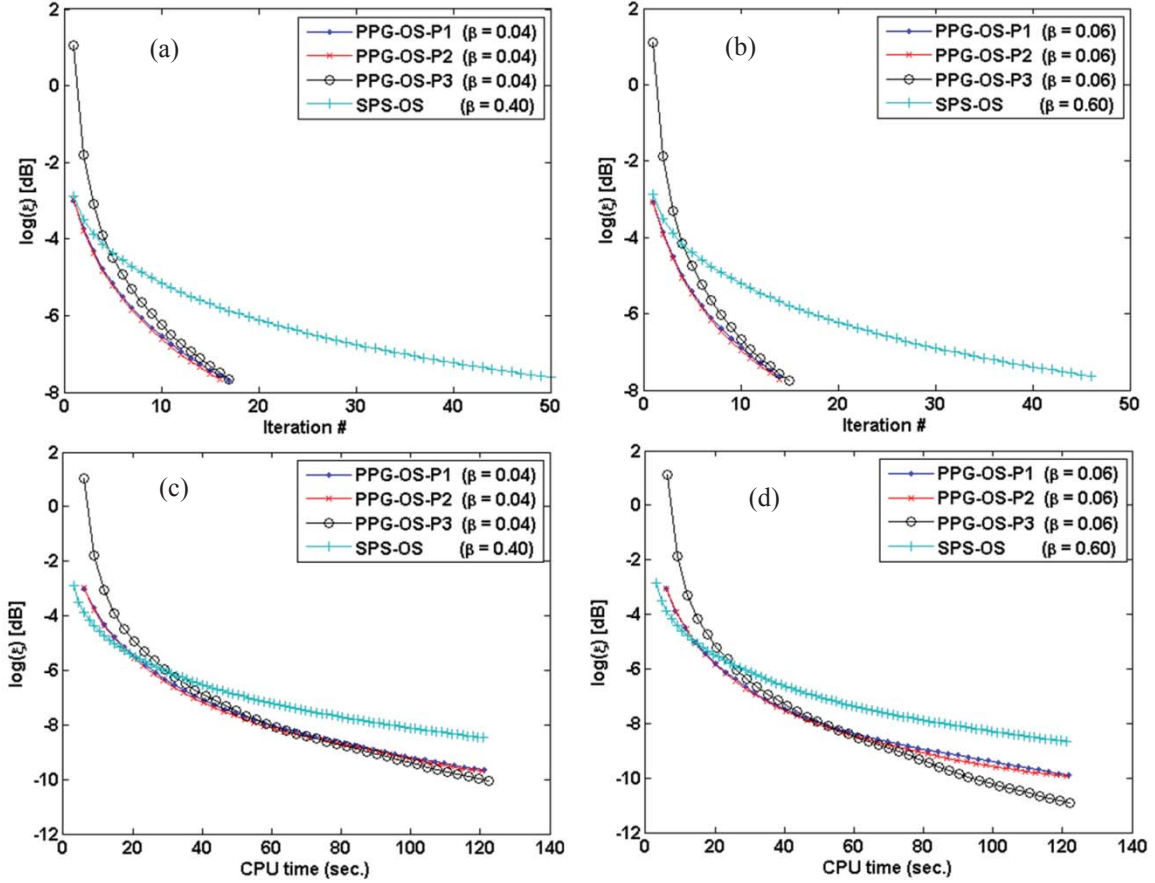


Figure 2. (a–b) The convergence of the studied algorithms for different regularization parameters as a function of iteration number and (c–d) computation (CPU) time. The vertical axis is in logarithmic scale.

IV. Results

IV.A Simulation studies

1) Convergence rate

Table 1 summarizes the SNR performance of the studied algorithms after their convergence as well as the number of required iterations for the 10 noise realizations (ten-trial) and a single noise realization (single-trial). As presented, the algorithms depict nearly similar SNR performance for the chosen regularization parameters; however, the proposed PPG-OS algorithm achieves its SNR performance in a considerably fewer number of iterations in comparison with the SPS-OS algorithm. Furthermore, the ten-trial average performance shows that the proposed algorithm with the preconditioner P_2 results in a higher SNR and a lower range of iterations in comparison with the other two preconditioners.

Figures 2a–b keep track of the convergence rate of the algorithms by the log of the relative error $\xi = \|x^{k+1} - x^k\| / \|x^k\|$, which was used as a stopping criterion for the algorithms meeting the tolerance of 5×10^{-4} . The convergence curves are shown for the single-trial results in Table I and for two different regularization parameters. It turns out that the proposed algorithm achieves a considerably improved convergence rate over the SPS-OS algorithm and depicts the fastest convergence rate with the preconditioner P_2 . The PPG-OS-P1 and PPG-OS-P2 algorithms present generally with similar convergence rates, while PPG-OS-P3 lags behind at early iterations and approaches them at the last iterations. The same trend was almost observed for the other noise realizations. It should be emphasized that the convergence behavior of the PPG-OS-P3 algorithm highly depends on the parameter ϵ used to ensure the positivity of the preconditioner. In this study, we set $\epsilon = 1 \times 10^{-4}$ and observed that larger values of ϵ improve the initial convergence of the resulting algorithm, however, they could not ensure a convergence rate as fast as smaller values. Figures 2c–d show the performance of the algorithms in

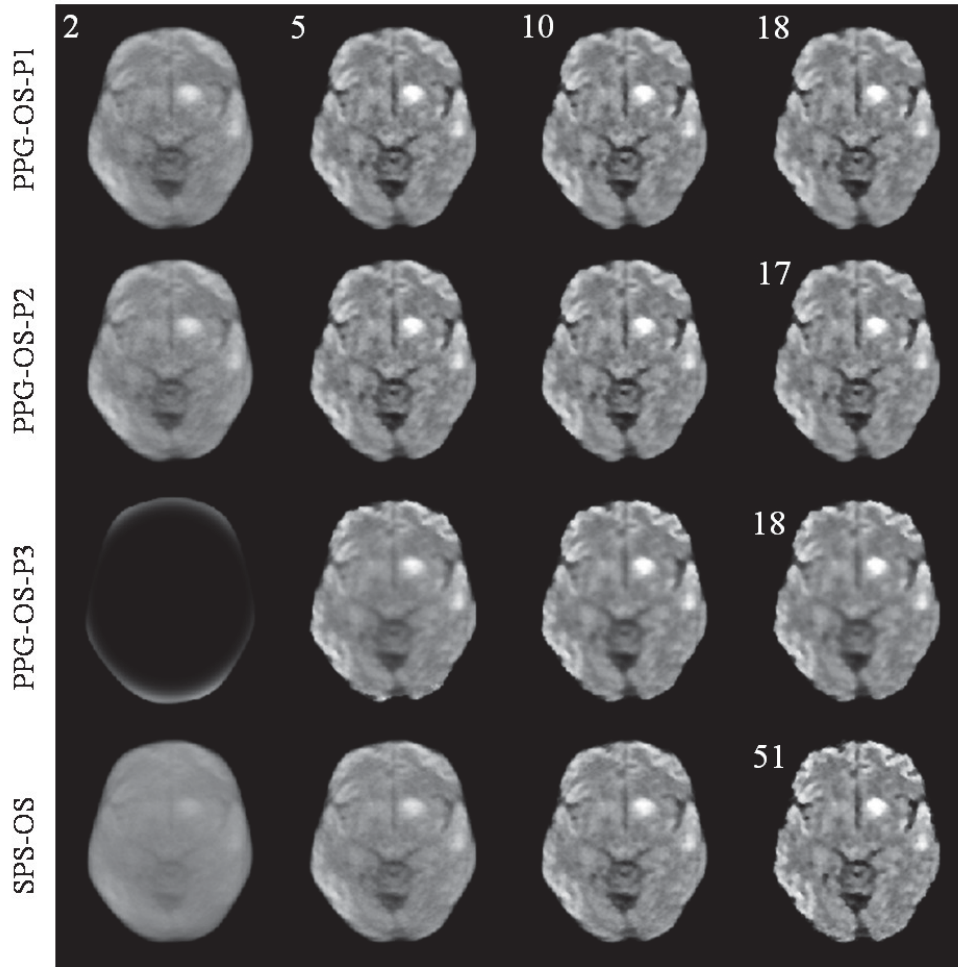


Figure 3. The evolution of images reconstructed by the studied algorithms as a function of iteration (for $\beta = 0.04$ and 0.4 for PPG-OS and SPS-OS, respectively). The last column shows the image estimates after convergence. As can be seen, the proposed algorithm with the preconditioners P1 and P2 show an improved initial and overall convergence. The display window is the same for all images.

terms of the relative error between two successive estimates as a function of computation (CPU) time. The results show that after a CPU time of 120 sec, the PPG-OS algorithm reduces the relative error more than the SPS-OS algorithm and hence provides a faster convergence. In the implementation and comparison of both algorithms, the same forward and backward projector as well as the same number of subsets were used. It was found that the average computation time per iteration of our algorithm is 2.92 sec while it is 1.45 sec in the case of SPS-OS. This increased computation time is mostly due to step size optimization and iterative proximal mapping.

Figure 3 shows the evolution of the image solution with iteration number for the studied algorithms. Consistent with Table I and figure 2, the results show the improved convergence rate of the proposed algorithm, particularly with the preconditioners P1 and P2, over the SPS-OS algorithm. It can be observed that after 2 iterations, PPG-OS-P1 and PPG-OS-P2 algorithms estimate the hot and cold spots faster than their counterpart. The last column in this figure shows the image estimates after convergence for the chosen regularization parameters. For image reconstruction of the clinical study presented in the next section, we utilized the proposed PPG-OS algorithm with the preconditioner P2 because i) it showed a higher SNR and better convergence rate in comparison with the other two preconditioners according to simulation results, and ii) contrary to preconditioner P1, preconditioner P2 does not need direct access to the Hessian matrix, and hence the pre-computation of the system matrix. For clinical datasets, the system matrix is a very large-sized matrix that raises memory shortage issues. As a result, P2 can be pre-computed using on-the-fly forward and back-projections. Generally, the computation of an optimal step size (Eq. 11) for large-sized clinical data increases remarkably the overall

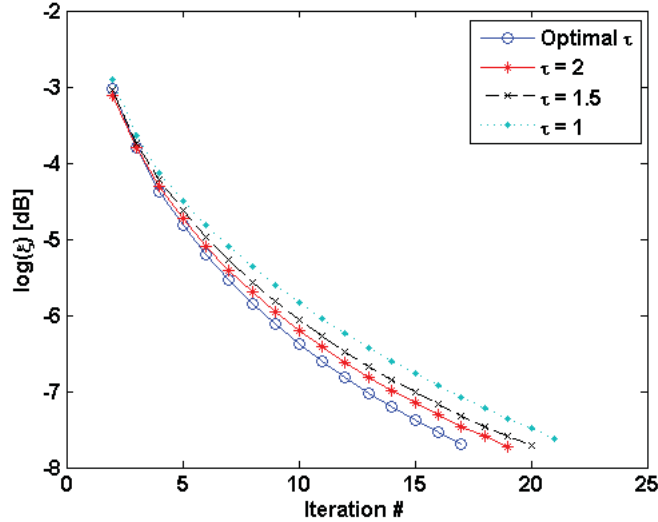


Figure 4. The convergence rate of the PPG-OS-P2 algorithm for optimal and fixed step lengths as a function of iteration number ($\beta = 0.04$). The results show that step size $\tau = 2$ is near to optimal for this algorithm.

Table I. The quantitative performance of the studied algorithms for ten noise realizations (ten-trial) and a single noise realization (single-trial) of simulated PET emission data.

Algorithm	β	Ten-trial		Single-trial	
		SNR [Average]	Iterations [Range]	SNR	Iterations
PPG-OS-P1	0.02	17.45	23–25	17.49	23
	0.04	16.76	17–18	16.85	18
	0.06	16.08	15–16	16.17	15
PPG-OS-P2	0.02	17.54	22–24	17.57	23
	0.04	16.87	17–18	16.97	17
	0.06	16.19	15	16.27	15
PPG-OS-P3	0.02	17.33	23–28	17.42	28
	0.04	16.45	18–19	16.52	18
	0.06	15.88	15–17	15.98	16
SPS-OS	0.2	17.77	57–59	17.92	59
	0.4	16.85	50–52	16.77	51
	0.6	16.75	46–48	16.36	47

reconstruction time of the proposed subsetized algorithm, because of additional forward projection of each descent direction, $P\nabla\phi(x^k)$, in each subset. To reduce computation time, we designed an experiment to find a fixed, near-to-optimal step size for the PPG-OS-P2 algorithm according to the condition $0 < \tau^k \leq 2/\lambda_{\max}(PG^TWG)$. Using the power iteration method, it was found that the largest eigenvalue of the P_2G^TWG matrix is close to unity for all noise realizations and for a strip- or line-integral geometry, i.e. $\lambda_{\max}(P_2G^TWG) \cong 1$. As a result, one can declare $0 < \tau \leq 2$. Figure 4 compares the convergence rate of the PPG-OS-P2 algorithm for optimal and fixed step sizes and the same noise realization and regularization parameter ($\beta = 0.06$). The results show that as the step size increases up to 2, the convergence rate of the resulting algorithm approaches the algorithm with optimal step sizes. The same trend was observed with other noise realizations and regularization parameters. As a result, with the step size $\tau = 2$, one can considerably save computation time, yet exploit a favorable convergence rate.

2) Regularization with boundary side information

To incorporate anatomical side information into Huber regularization in the form of weighting factors, we derived the anatomical boundaries from the MR image shown in figure 1(b) using Canny edge detector with

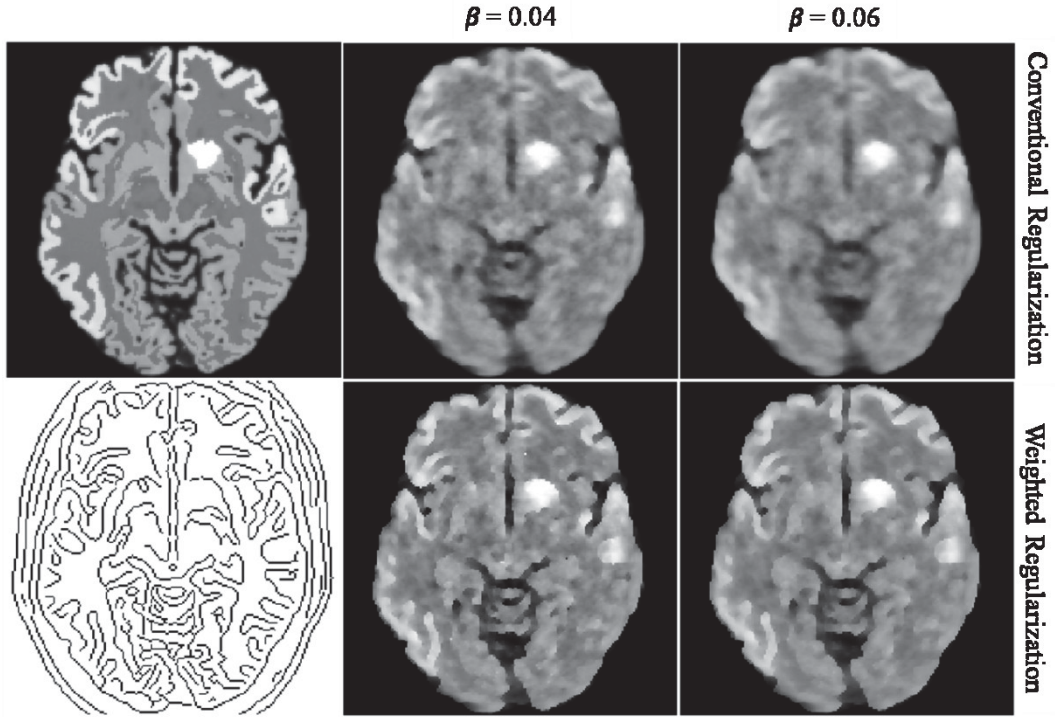


Figure 5. Huber regularization with anatomical boundary information. First row (from left to right) shows the true activity distribution and the images reconstructed using the PPG-OS-P2 with conventional regularization and regularization parameters of $\beta = 0.04$ and 0.06 . Second row (from left to right) shows the boundary weights used in the regularization and the images reconstructed using the PPG-OS-P2 algorithm with weighted regularization and the same β s. The display window is the same for all images.

Table II. The quantitative performance of the proposed algorithm with anatomically-weighted Huber regularization for ten noise realizations (ten-trial) and a single noise realization (single-trial) of simulated PET emission data.

Algorithm	β	Ten-trial		Single-trial	
		SNR [Average]	Iterations [Range]	SN R	Iterations
PPG-OS-P1	0.02	16.65	39–43	16.71	39
	0.04	17.24	26–27	17.26	27
	0.06	16.81	22–23	16.87	23
PPG-OS-P2	0.02	16.65	39–44	16.62	39
	0.04	17.38	25–26	17.41	26
	0.06	16.96	22–23	17.03	22
PPG-OS-P3	0.02	16.78	53–68	16.89	53
	0.04	17.10	35–62	17.21	35
	0.06	16.65	26–37	16.74	35

automatic threshold selection according to Eq. (19). The images reconstructed using the PPG-OS-P2 algorithm with and without boundary weighting are shown in figure 5. The first row shows the actual activity distribution and the images reconstructed using conventional Huber regularizer with regularization parameters $\beta = 0.04$ and 0.06 , respectively. The second row shows respectively the derived weighting factors and the image reconstructed using weighted Huber regularization with the above mentioned β parameters. The visual comparison of the images reveals that the incorporation of boundary information in the reconstruction process improves the accuracy of the estimated images. As can be seen, the weights tend to suppress the smoothing effect of the regularization across edges and therefore to increase image contrast.

Figure 6 compares line profiles through the true activity distribution and the images reconstructed with and without boundary weighted regularization. The profiles show that the weighted regularization (R_w) increases the contrast particularly in regions where the conventional unweighted regularization (R) reduces contrast.

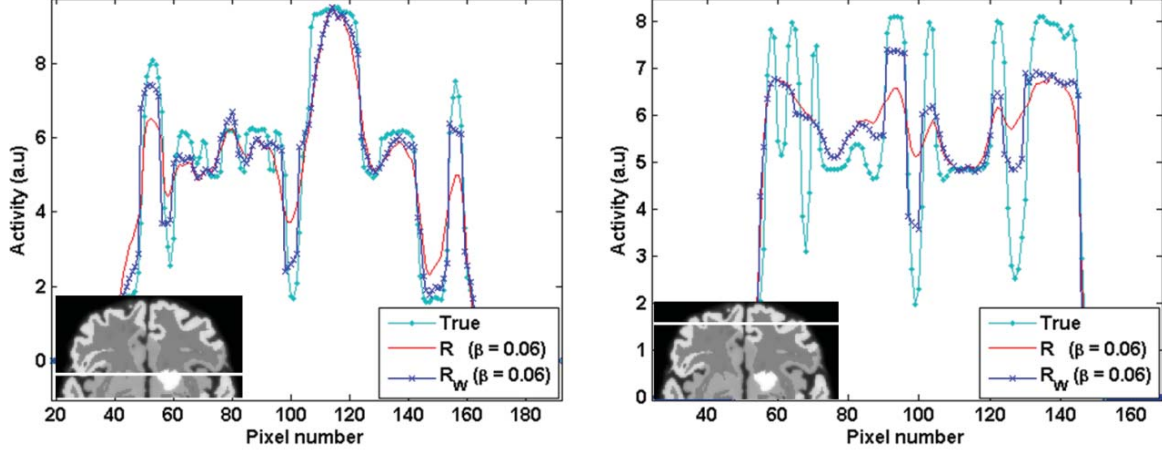


Figure 6. Activity line profiles through the true activity distribution and the images reconstructed using the PPG-OS-P2 algorithm with conventional regularization (R) and anatomically weighted regularization (R_w), along the lines shown in sub-figures.

Note that the metabolically active regions with weak boundary weights or without any corresponding anatomical boundary (e.g. the hot tumor) depict qualitatively nearly the same line profiles in the reconstructed images. Note that the edge enhancement in R_w profiles depends on the strength of edges, thereby; strong edges are more enhanced than the weak ones.

To further quantitatively compare the regularization techniques; we evaluated their bias-variance performance for the ROIs shown in figure 1(e) over 10 noise realizations of the emission data reconstructed using the PPG-OS-P2 algorithm. Figure 7 shows the bias-variance performance of the regularization techniques as a function of iteration number for regularization parameters of 0.04 and 0.06. Note that each point corresponds to 1 iteration and 6 subsets. The results show that the incorporation of the anatomical boundary information in the regularization substantially reduces the bias, thus allowing for more accurate estimation of the true activity distribution; however, it increases the noise. The regions with weak boundaries or without any corresponding anatomical boundaries (e.g. ROIs 3 and 5) show an improved bias-variance performance, while the regions with strong boundaries (e.g. ROIs 2 and 6) depict a substantial improvement in bias. The plots also show that in this simulation study, the regularization parameter $\beta = 0.06$ generally decreases the variance while increasing the bias. Therefore, it can be concluded that weighted regularization with a higher regularization parameter can give rise to a better bias-variance trade off.

We also evaluated the impact of the weighting scheme on the SNR and convergence performance of the proposed PPG-OS algorithm. Table II presents the results for the preconditioners P1, P2 and P3 and the 10 noise realizations (ten-trial) and a single noise realization (single-trial). In comparison with Table I, the results show that the incorporation of the anatomical boundary information in the regularization step reduces the convergence rate of the resulting algorithms, however, prudently improves their SNR performance for $\beta = 0.04$ and 0.06. In the case of $\beta = 0.02$, both SNR and convergence rate decrease, which should be attributed to the fact that the noise tends to reside on edges where regularization is suppressed (according to the lower bound a in Eq. (19)) and this low β is not sufficient to remove the noise and hence to establish the convergence path of the algorithm.

IV.B Clinical PET study

Figure 8 shows the transverse, coronal and sagittal planes of the clinical study reconstructed using the PPG-OS-P2 algorithm with conventional (unweighted) and weighted Huber regularizations ($\beta = 0.04$, $\delta = 0.08$) together with the weighting factors at the last iteration. The algorithm has successfully reconstructed this pre-corrected PET study at a typical noise level encountered in clinical setting. It can be observed that the incorporation of boundary weighting factors during reconstruction improves the contrast and hence the quality of the reconstructed images. As mentioned in section III.B, for this clinical study, the weighting factors were iteratively derived for each axial slice during reconstruction by means of MATLAB's 2D Canny edge detection operator. This operator has properly captured the in-plane topological features of the brain and thus resulted in contiguous

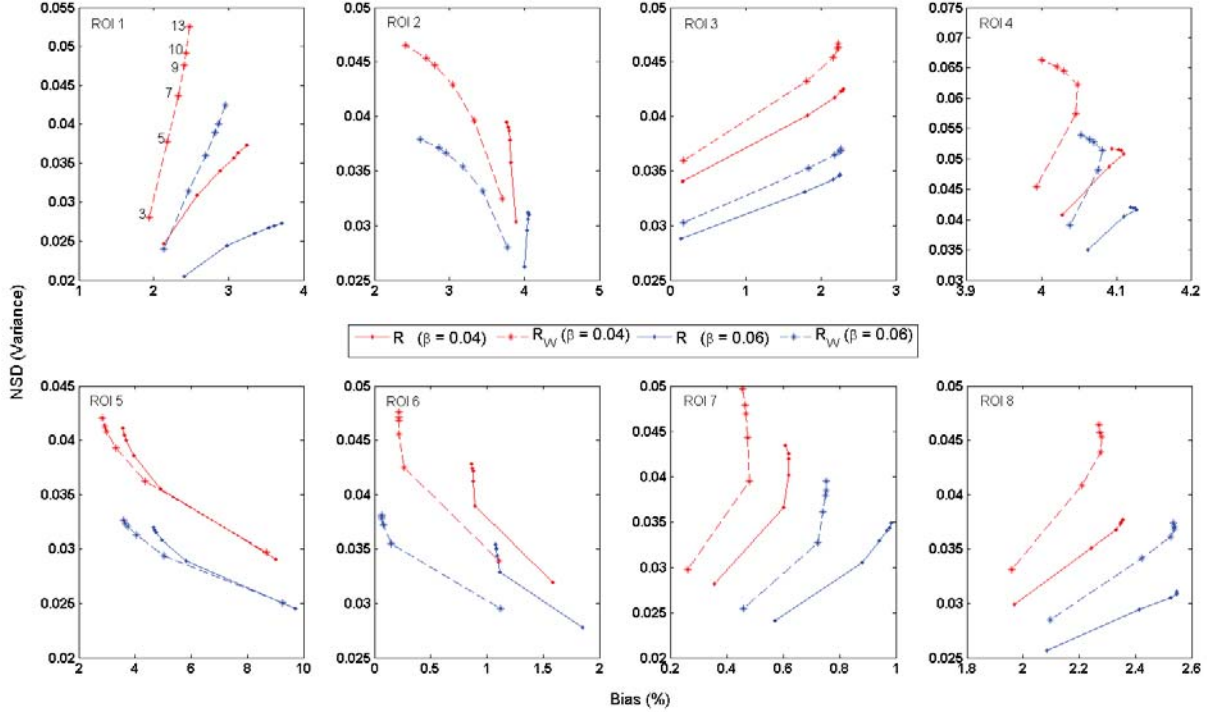


Figure 7. The bias versus variance trade-off of anatomically-weighted Huber regularization (R_W) in comparison with conventional Huber regularization (R) as a function of iteration number and regularization parameters. The trade-offs were obtained for 8 ROIs drawn on different regions of the brain phantom (see figure 1(e)) and calculated from 10 noise realizations of simulated PET emission data reconstructed using the PPG-OS-P2 algorithm.

boundaries mostly in the transverse plane. However, as can be seen in the coronal and sagittal planes displayed in figure 8, the derived weighting factors have also considerably improved the image contrast in these planes.

V. Discussion

In this study, we developed an algorithm for the optimization of PWLS cost function in PET image reconstruction with an improved convergence rate and described the capability of the algorithm to incorporate anatomical edge information into the regularization step exploiting total variation and Huber regularizations.

V.A Convergence Rate and Parameter Selection

In principle, an iterative algorithm is globally convergent if for any arbitrary initial estimate the algorithm is guaranteed to converge to a solution where the gradient of the cost function is zero[50]. However, in practice, an iterative algorithm is said to be convergent if it reaches a solution where the image estimates do not change (or practically change within a tolerance) with succeeding iteration [58]. The convergence rate is often referred to as the number of iterations it takes the algorithm to reach a convergent solution. In this study, it was shown that the proposed algorithm depicts a fast convergence rate in the optimization of PWLS cost function. The average SNR results in Table I show that for the same regularization parameter, the proposed algorithm and the SPS-OS algorithm converge roughly to the same solution. However, the range of iterations show that the proposed algorithm converges in a fewer number of iterations. Generally, the convergence rate of gradient-based algorithms depends highly on the condition number of the Hessian matrix of the cost function[50]. In this regard, preconditioners are used to improve the conditioning of the problem. The Hessian matrix of the PWLS cost function is ill-conditioned due to the weighting matrix and the penalty function. As elaborated in Section II.B, we split the optimization of PWLS into two steps. This procedure reduced the Hessian matrix of PWLS to its Fisher information matrix and hence removing the additional shift variance induced by the regularizer. As a result, the preconditioners can more effectively approximate the inverse of the resulting Hessian matrix, and therefore, the order of convergence of the resulting algorithm is improved. According to Eq. (B.1), in appendix B, the SPS-OS algorithm has also a preconditioned gradient form. In this algorithm, the Hessian matrix,

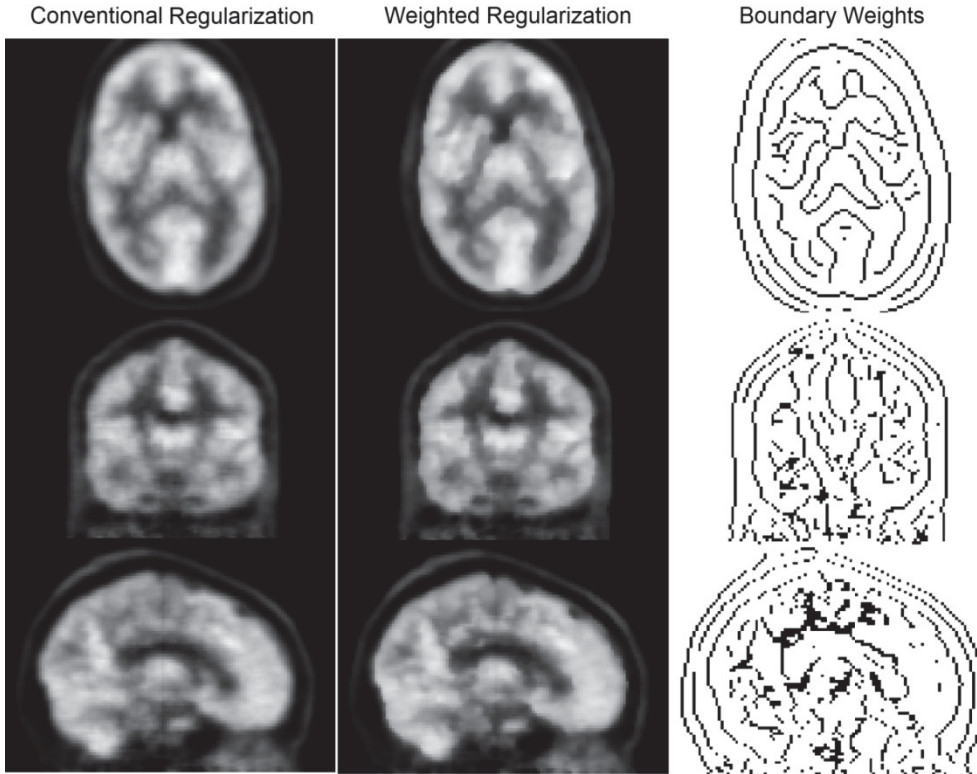


Figure 8. PET images (transverse, coronal and sagittal slices) of the clinical brain study reconstructed using the proposed PPG-OS-P2 algorithm with Huber and weighted Huber regularizations. The boundary weighting factors derived from the last iteration are also shown.

however, includes the second order derivative of the regularizer and therefore the preconditioner should approximate the inverse of this matrix with a comparatively higher condition number. Generally, the preconditioners increase the convergence rate of the algorithm and in principle should not have an effect on the final solution [35]. The results shown in Tables I and II show that the proposed algorithm with the studied preconditioners achieves nearly the same average SNR performance over 10 Poisson noise realizations. In accordance with figure 3 (right column), this implies that the proposed algorithm with the studied preconditioners converges to nearly the same solution. The results; however, show that the preconditioner P_2 , inspired by De Pierro's convexity trick, depicts the best convergence rate. It should be noted that the SPS-OS algorithm exploits a preconditioner with the same structure (see Eq. B.1).

The convergence properties of an optimization algorithm depend on the choice of involved parameters. The results presented in Table I show that by increasing the regularization parameter β , the convergence rate of the algorithms is improved. This is mainly due to a higher regularization and faster stabilization of the solution in terms of noise and fluctuations between two successive iterations. In this work, we studied the edge-preserving Huber prior, which reduces the staircasing of the TV prior. In the simulation study, we experimentally set the smoothing parameter $\delta = 0.5$ to avoid the staircasing while in the clinical dataset we used $\delta = 0.08$. Generally, this parameter should be chosen according to the level of noise and the intrinsic smoothing effect of basis functions used in the discretization of activity distribution. In noisy datasets, Huber regularization with lower values of δ tends to preserve false details formed by noise, particularly with rectangular basis functions (voxels) that do not possess an intrinsic smoothing effect. Hence, the parameter δ should be increased accordingly to effectively reduce noise and staircasing effect. The convergence rate of algorithms such as SPS-OS depends on δ , since the condition number of the problem is inversely related to this parameter (see Theorem 3.1 in Ref.[59]). This implies that the convergence rate of the proposed splitting based algorithm should, in principle, be independent of δ . The PPG-OS algorithm also includes two other parameters, α and T , which are respectively the largest eigenvalue of the DD^T matrix (see section II.B.2), and the number of sub-iterations in the proximal mapping (see Algorithm 1). The parameter α was set to 5 (larger than 4) in the 2D regularization in the simulation study and 7 (larger than 6) in the 3D regularization for clinical studies. It was found that setting the values of this parameter lower than the abovementioned limits results in artifacts and in some cases the

divergence of the algorithm. The number of sub-iterations T was set to 5 in both simulation and clinical studies. Generally, this parameter implicitly controls the amount of regularization and can potentially impact the convergence rate; however, we found that a higher number of sub-iterations has the same impact as the abovementioned value. Finally, the number of ordered subsets was set to 6 and kept constant in our comparisons. Increasing the number of subsets can in principle improve the convergence rate of the proposed algorithm and generally the algorithms exploiting the subsetization.

V.B Incorporation of Anatomical Edge Information

The major motivation for the incorporation of boundary information, derived from CT and MR images[28, 29] or from the emission/transmission image being regularized [20] into the regularization step is to promote the formation and preservation of continuous boundaries and therefore to improve image quantification and tumor delineation. In this study, we showed that the proposed algorithm can be extended to incorporate such information into the dual formulation of the edge-preserving TV and Huber regularizer according to our observations in Eq. (12). The Canny edge detection operator was used to derive such boundary information from an MR image, in our simulation study, and from the emission image, in our clinical study. The comparison of the results shown in Tables I and II demonstrates that the average SNR with weighted regularization is improved, however, at the expense of increased convergence rate. This is due to the fact that noise also resides in boundary regions and reduced values of α in Eq. (19) tend to preserve noise in those regions. The bias-variance evaluations in the simulation study showed that a boundary-weighted Huber regularization noticeably reduces bias; however, it can increase variance particularly in regions with strong boundaries. In general, an improved bias-variance trade-off can be achieved by adjusting the parameter α as well as the regularization parameter β . Canny's edge detection method is based on the assumption that in regions where the amplitude of image gradient is high, an edge probably exists. It exploits hysteresis thresholding to detect edges and thus is somewhat robust to noise. However; at higher noise levels, it might pick up false edges. To enhance the robustness of this edge detector, particularly for the task of simultaneous edge-detection and image reconstruction, the procedure can be improved by edge detection methods based on local mutual information [60]. In this study, we introduced the PPG-OS algorithm and demonstrated its improved convergence rate as well as its ability to incorporate the anatomical boundary information. Future work is therefore to evaluate the algorithm with more adaptive edge detection techniques in clinical PET/MR datasets.

VI. Conclusion

In this study, we proposed a splitting-based preconditioned conjugate gradient algorithm accelerated with ordered-subsets for the PWLS reconstruction of PET data. The splitting allowed for decoupling of the penalty function from the PWLS cost function, thereby i) the ill-conditioning of its Hessian and thus convergence rate of the resulting algorithm was improved and ii) a proximal sub-problem was obtained for implementing adaptively or anatomically weighted TV and Huber regularizations in their dual formulations. The proposed algorithm was studied for three different diagonal preconditioners and compared with the SPS-OS algorithm. In simulation studies, it was demonstrated that the proposed algorithm achieves a considerable improved convergence rate over its counterpart. The performance of the proposed algorithm with boundary-weighted regularization was also evaluated using both simulation and clinical studies. It was concluded that the proposed PPG-OS algorithm is efficient in terms of convergence rate and capable of incorporating boundary side information in the regularized PET image reconstruction.

Acknowledgment

This work was supported by the Swiss National Science Foundation under grant SNSF 31003A-135576, Geneva Cancer League, and the Indo-Swiss Joint Research Programme ISJRP 138866.

APPENDIX A

Derivation of weighted least-squares (WLS) cost function

Let us rewrite the negative Poisson log-likelihood in Eq. (1) as follows:

$$\Phi(x) = \sum_{j=1}^M h_j([Gx]_j) \quad (\text{A.1})$$

$$h_j(y_j) = (n_j a_j y_j + \bar{r}_j) - y_j^p \log(n_j a_j y_j + \bar{r}_j)$$

A quadratic approximation of the above objective function is obtained by applying a second-order Taylor's expansion to the marginal function $h(y_j)$ around an estimate of net-true coincidences at the j th line-of-response, \hat{y}_j , which yields:

$$h_j(y_j) \approx h_j(\hat{y}_j) + h'_j(\hat{y}_j)(y_j - \hat{y}_j) + \frac{1}{2} h''_j(\hat{y}_j)(y_j - \hat{y}_j)^2 \quad (\text{A.2})$$

where the first and second derivatives of h_j are given by:

$$h'_j(y_j) = n_j a_j \left(1 - \frac{y_j^p}{n_j a_j y_j + \bar{r}_j + \bar{s}_j} \right) \quad (\text{A.3})$$

$$h''_j(y_j) = y_j^p \left(\frac{n_j a_j}{n_j a_j y_j + \bar{r}_j + \bar{s}_j} \right)^2$$

Using the estimate $\hat{y}_j = (y_j^p - \bar{r}_j - \bar{s}_j)/n_j a_j$ into Eq. (A.2), we then arrive at:

$$h_j(y_j) \approx y_j^p - y_j^p \log(y_j^p) + \frac{1}{2} \frac{n_j^2 a_j^2}{y_j^p} (y_j - \hat{y}_j)^2 \quad (\text{A.4})$$

By dropping the terms independent of y_j in Eq. (A.4), the log-likelihood reduces to the following weighted least squares cost function:

$$\phi(x) = \frac{1}{2} \sum_{j=1}^M w_j ([Gx]_j - \hat{y}_j)^2, \quad w_j = \frac{n_j^2 a_j^2}{\max(1, y_j^p)} \quad (\text{A.5})$$

In the above equation, we add one count to the empty sinogram bins to avoid division by zero. Note when the prompt emission sinogram is not available, the prompt coincidences can be estimated from an available pre-corrected sinogram \hat{y} , which yields $y_j^p \approx n_j a_j \hat{y}_j + \bar{r}_j + \bar{s}_j$.

APPENDIX B

SPS-OS Algorithm

The one-subset version of the SPS-OS algorithm applied for the PWLS cost function with a continuously differentiable penalty function has the following preconditioned gradient descent from [29]:

$$x^{k+1} = x^k - P(\nabla\phi(x^k) + \beta\nabla R(x^k)), \quad P = \text{diag}\{G^T W G \mathbf{1} + \beta\nabla^2 R(x^k)\}^{-1} \quad (\text{B.1})$$

where $\nabla R(x^k) = \sum_{ij} d_{ji} \omega_i \phi'([Dx]_i)$, $\nabla^2 R(x^k) = \sum_{ij} |d_{ji}| \omega_i \sum_k |d_{ki}|$, where d_{ji} s are the elements of matrix D and ω_i are weighting factors to control the strength of regularization at voxel i .

References

- [1] J. Czernin, M. Allen-Auerbach, and H. R. Schelbert, "Improvements in cancer staging with PET/CT: Literature-based evidence as of september 2006.," *J Nucl Med*, vol. 48, no. 1_suppl, pp. 78S-88, January 1, 2007, 2007.
- [2] M. F. Di Carli, S. Dorbala, J. Meserve, G. El Fakhri, A. Sitek, and S. C. Moore, "Clinical myocardial perfusion PET/CT," *J. Nucl. Med.*, vol. 48, no. 5, pp. 783-793, 2007.
- [3] J. C. Price, "Molecular brain imaging in the multimodality era.," *J Cereb Blood Flow Metab*, vol. 32, pp.1377-139, 2012.
- [4] H. Zaidi, and A. Alavi, "Current trends in PET and combined (PET/CT and PET/MR) systems design.," *PET Clinics*, vol. 2, no. 2, pp. 109-123, 2007/4, 2007.
- [5] A. J. Reader, and H. Zaidi, "Advances in PET image reconstruction.," *PET Clinics*, vol. 2, no. 2, pp. 173-190, 2007/4, 2007.
- [6] R. M. Lewitt, and S. Matej, "Overview of methods for image reconstruction from projections in emission computed tomography.," *Proceedings of the IEEE*, vol. 91, no. 10, pp. 1588-1611, 2003.
- [7] J. Qi, and R. M. Leahy, "Iterative reconstruction techniques in emission computed tomography.," *Phys Med Biol*, vol. 51, no. 15, pp. R541-R578, Aug 7, 2006.
- [8] D. S. Lalush, and M. Wernick, "Iterative image reconstruction.," *Emission Tomography: The Fundamentals of PET and SPECT.*, M. Wernick and J. Aarsvold, eds., pp. 443-472, San Diego: Academic Press, 2004.
- [9] J. A. Fessler, "Penalized weighted least-squares image reconstruction for positron emission tomography.," *IEEE Trans Med Imaging*, vol. 13, no. 2, pp. 290-300, 1994.
- [10] W. C. Karl, "Regularization in Image Restoration and Reconstruction," *Handbook of Image and Video Processing*, A. Bovik, ed., San Diego: Academic Press, 2000.
- [11] P. J. Green, "Bayesian reconstructions from emission tomography data using a modified EM algorithm.," *IEEE Trans Med Imaging*, vol. 9, no. 1, pp. 84-93, 1990.
- [12] V. E. Johnson, W. H. Wong, X. Hu, and C. T. Chen, "Image restoration using Gibbs priors: Boundary modeling, treatment of blurring, and selection of hyperparameter," *IEEE Trans Pattern Anal Machine Intell*, vol. 13, pp. 413-425, 1991.
- [13] C. Bouman, and K. Sauer, "A generalized Gaussian image model for edge-preserving MAP estimation," *IEEE Trans Image Process*, vol. 2, pp. 296-310, 1993.
- [14] S. J. Lee, A. Rangarajan, and G. Gindi, "Bayesian image reconstruction in SPECT using higher order mechanical models as priors," *IEEE Trans Med Imaging*, vol. 14, pp. 669-680, 1995.
- [15] P. Perona, and J. Malik, "Scale-space and edge detection using anisotropic diffusion.," *IEEE Trans Patt Analysis Machine Intelligence*, vol. 12, no. 7, pp. 629-639, 1990.
- [16] F. Catte, P.-L. Lions, J.-M. Morel, and T. Coll, "Image selective smoothing and edge detection by nonlinear diffusion," *SIAM J Numer Anal*, vol. 29, pp. 182-193, 1992.
- [17] S. T. Acton, "Locally monotonic diffusion," *IEEE Trans Signal Process*, vol. 48, pp. 1379-1389, 2000.
- [18] P. J. Huber, *Robust Statistics*, New York: Wiley, 1981.
- [19] L. Rudin, S. Osher, and E. Fatemi, "Nonlinear total variation based noise removal algorithms," *Physica D*, vol. 60, pp. 259-268, 1992.
- [20] D. F. Yu, and J. A. Fessler, "Edge-preserving tomographic reconstruction with nonlocal regularization," *IEEE Trans Med Imaging*, vol. 21, no. 2, pp. 159-173, 2002.
- [21] H. H. Feng, W. C. Karl, and D. A. Castanon, "A curve evolution approach to object-based tomographic reconstruction," *IEEE Trans Image Process*, vol. 12, pp. 44-57, 2003.
- [22] A. Sawatzky, "(Nonlocal) Total Variation in Medical Imaging," Ph.D Thesis, Fachbereich Mathematik und Informatik der Mathematisch-Naturwissenschaftlichen Fakultät, Westfälischen Wilhelms-Universität Münster, Münster, Germany, 2011.
- [23] J. E. Bowsher, V. E. Johnson, T. G. Turkington, R. J. Jaszcak, C. E. Floyd, and R. E. Coleman, "Bayesian reconstruction and use of anatomical a priori information for emission tomography," *IEEE Trans Med Imaging*, vol. 15, pp. 673-686, 1996.

- [24] G. Gindi, M. Lee, A. Rangarajan, and I. G. Zubal, "Bayesian reconstruction of functional images using anatomical information as priors.," *IEEE Trans Med Imaging*, vol. 12, no. 4, pp. 670-680, 1993.
- [25] J. A. Fessler, N. H. Clinthorne, and W. L. Rogers, "Regularized emission image reconstruction using imperfect side information." pp. 1991-1995 vol.3.
- [26] K. Baete, J. Nuyts, W. Van Paesschen, P. Suetens, and P. Dupont, "Anatomical-based FDG-PET reconstruction for the detection of hypo-metabolic regions in epilepsy," *Medical Imaging, IEEE Transactions on*, vol. 23, no. 4, pp. 510-519, 2004.
- [27] J. Tang, and A. Rahmim, "Bayesian PET image reconstruction incorporating anato-functional joint entropy," *Phys. Med. Biol.*, vol. 54, pp. 7063-75, 2009.
- [28] K. Vunckx, A. Atre, K. Baete, A. Reilhac, C. M. Deroose, K. Van Laere, and J. Nuyts, "Evaluation of Three MRI-Based Anatomical Priors for Quantitative PET Brain Imaging," *Medical Imaging, IEEE Transactions on*, vol. 31, no. 3, pp. 599-612, 2012.
- [29] Y. K. Dewaraja, K. F. Koral, and J. A. Fessler, "Regularized reconstruction in quantitative SPECT using CT side information from hybrid imaging," *Phys. Med. Biol.*, vol. 55, pp. 2523-2539, 2010.
- [30] F. Bataille, C. Comtat, S. Jan, F. C. Sureau, and R. Trebossen, "Brain PET Partial-Volume Compensation Using Blurred Anatomical Labels," *Nuclear Science, IEEE Transactions on*, vol. 54, no. 5, pp. 1606-1615, 2007.
- [31] S. Somayajula, E. Asma, and R. M. Leahy, "PET image reconstruction using anatomical information through mutual information based priors." pp. 2722-2726.
- [32] C. Comtat, P. E. Kinahan, J. A. Fessler, T. Beyer, D. W. Townsend, M. Defrise, and C. Michel, "Clinically feasible reconstruction of 3D whole-body PET/CT data using blurred anatomical labels," *Phys. Med. Biol.*, vol. 47, pp. 1-20, 2002.
- [33] H. Erdogan, and J. A. Fessler, "Ordered subsets algorithms for transmission tomography," *Phys Med Biol*, vol. 44, no. 11, pp. 2835-2851, 1999.
- [34] T. M. Benson, B. K. B. De Man, F. Lin, and J. B. Thibault, "Block-based iterative coordinate descent." pp. 2856-2859.
- [35] J. A. Fessler, and S. D. Booth, "Conjugate-gradient preconditioning methods for shift-variant PET image reconstruction.," *IEEE Trans Image Process*, vol. 8, no. 5, pp. 688-699, 1999.
- [36] N. H. Clinthorne, and et al, "Preconditioning methods for improved convergence rates in iterative reconstructions," *IEEE Trans Med Imaging*, vol. 12, pp. 78-83, 1993.
- [37] A. H. Delaney, and Y. Bresler, "A fast and accurate Fourier algorithm for iterative parallel-beam tomography," *IEEE Trans Image Process*, vol. 5, no. 5, pp. 740-753, 1996.
- [38] J. Savage, and K. Chen, "On multigrids for Solving a Class of Improved Total Variation Based Staircasing Reduction Models," *Mathematics and Visualization*. pp. 60-94.
- [39] A. Chambolle, "An algorithm for total variation minimization and applications," *J Math Imaging Vis*, vol. 20, no. 1-2, pp. 89-97, 2004.
- [40] S. Ramani, and J. A. Fessler, "A Splitting-Based Iterative Algorithm for Accelerated Statistical X-Ray CT Reconstruction," *IEEE Trans. Med. Imaging*, vol. 31, no. 3, pp. 677-688, 2012.
- [41] J. Eckstein, and D. Bertsekas, "On the DouglasRachford splitting method and the proximal point algorithm for maximal monotone operators," *Math Program*, vol. 5, pp. 293-318, 1992.
- [42] S. Setzer, "Operator splittings, bregman methods and frame shrinkage in image processing," *Int J Comput Vision*, vol. 92, no. 3, pp. 265-280, 2011.
- [43] K. Lange, D. R. Hunter, and I. Yang, "Optimization transfer using surrogate objective functions," *J. Comput Graph Stat*, vol. 9, pp. 1-20, 2000
- [44] D. Hunter, and K. Lange, "A tutorial on MM algorithms," *The American Statistician*, vol. 58, pp. 30-37, 2004.
- [45] A. Beck, and M. Teboulle, "Gradient-based algorithms with applications in signal recovery problems," *Convex Optimization in Signal Processing and Communications*, D. Palomar and Y. Eldar, eds., pp. 33-88: Cambridge University Press, 2010.
- [46] W. Zuo, and Z. Lin, "A generalized accelerated proximal gradient approach for total-variation-based image restoration," *IEEE Trans Image Process*, vol. 20, no. 10, pp. 2748-2759, 2011.
- [47] C. A. Johnson, J. Seidel, and A. Sofer, "Interior-point methodology for 3-D PET reconstruction," *IEEE Trans Med Imaging*, vol. 19, pp. 271-285, 2000.

- [48] L. Kaufman, "Maximum likelihood, least squares, and penalized least squares for PET.," *IEEE Trans Med Imaging*, vol. 12, no. 2, pp. 200-214, 1993.
- [49] D. Kim, and J. A. Fessler, "Accelerated ordered-subsets algorithm based on separable quadratic surrogates for regularized image reconstruction in x-ray CT." pp. 1134-1137.
- [50] E. P. Chong, and S. H. Zak, *An Introduction to Optimization*, 2 ed., New York: John Wiley & Sons, 2001.
- [51] A. Chambolle, and T. Pock, "A first-order primal-dual algorithm for convex problems with applications to imaging," *J Math Imaging Vis*, vol. 40, no. 1, pp. 120-145, 2010.
- [52] S. Becker, J. Bobin, and E. J. Candes, "NESTA: A fast and accurate first-order method for sparse recovery," *SIAM J Imaging Sci*, vol. 4, pp. 1-39, 2011.
- [53] J. Kiusalaas, *Numerical Methods in Engineering with MATLAB*, 2 ed.: Cambridge University Press, 2010.
- [54] J. Cheng-Liao, and J. Qi, "PET image reconstruction with anatomical edge guided level set prior," *Physics in Medicine and Biology*, vol. 56, no. 21, pp. 6899, 2011.
- [55] J. F. Canny, "A computational approach to edge detection," *IEEE Trans Pattern Anal Machine Intell*, vol. 8, no. 6, pp. 679-698, 1986.
- [56] J. Fessler. "Image reconstruction toolbox, <http://www.eecs.umich.edu/~fessler/code/index.html>, University of Michigan."
- [57] F. Jacobs, E. Sundermann, B. D. Sutter, M. Christiaens, and I. Lemahieu, "A fast algorithm to calculate the exact radiological path through a pixel or voxel space," *J Comput Inform Technol*, vol. 6, no. 1, pp. 89-94, 1998.
- [58] D. S. Lalush, and B. M. W. Tsui, "A fast and stable maximum a posteriori conjugate gradient reconstruction algorithm," *Med. Phys.*, vol. 22, no. 8, pp. 1273-1284, 1995.
- [59] T. Jensen, J. Jørgensen, P. Hansen, and S. Jensen, "Implementation of an optimal first-order method for strongly convex total variation regularization," *BIT Numerical Mathematics*, vol. 52, no. 2, pp. 329-356, 2012.
- [60] W. Guo, and F. Huang, "A local mutual information guided denoising technique and its application to self-calibrated partially parallel imaging," in *Med. Image. Comput. Comput. Assist. Interv.*, Part II, LNCS 5242, 2008, pp. 939-947.

Chapter 6

Smoothly clipped absolute deviation (SCAD)
regularization for compressed sensing MRI using
an augmented Lagrangian scheme

Abolfazl Mehranian, Mohammad Reza Ay, Arman Rahmim and Habib Zaidi

Magn Reson Imaging 31(8), 1399-1411 (2013)

Abstract

Purpose: Compressed sensing (CS) provides a promising framework for MR image reconstruction from highly undersampled data, thus reducing data acquisition time. In this context, sparsity-promoting regularization techniques exploit the prior knowledge that MR images are sparse or compressible in a given transform domain. In this work, a new regularization technique was introduced by iterative linearization of the non-convex smoothly clipped absolute deviation (SCAD) norm with the aim of reducing the sampling rate even lower than it is required by the conventional l_1 norm while approaching an l_0 norm.

Methods: The CS-MR image reconstruction was formulated as an equality-constrained optimization problem using a variable splitting technique and solved using an augmented Lagrangian (AL) method developed to accelerate the optimization of constrained problems. The performance of the resulting SCAD-based algorithm was evaluated for discrete gradients and wavelet sparsifying transforms and compared with its l_1 -based counterpart using phantom and clinical studies. The k -spaces of the datasets were retrospectively undersampled using different sampling trajectories. In the AL framework, the CS-MRI problem was decomposed into two simpler sub-problems, wherein the linearization of the SCAD norm resulted in an adaptively weighted soft thresholding rule with a sparsity enhancing effect.

Results: It was demonstrated that the proposed regularization technique adaptively assigns lower weights on the thresholding of gradient fields and wavelet coefficients, and as such, is more efficient in reducing aliasing artifacts arising from k -space undersampling, when compared to its l_1 -based counterpart.

Conclusion: The SCAD regularization improves the performance of l_1 -based regularization technique, especially at reduced sampling rates, and thus might be a good candidate for some applications in CS-MRI.

I. Introduction

Magnetic resonance imaging (MRI) is one of the leading cross-sectional imaging modalities in clinical practice offering a great flexibility in representing the anato-functional characteristics of organs and soft tissues. However, MRI often suffers from long data acquisition time. Fast data acquisition is of particular importance for capturing temporal changes over whole organs in a short time. Beside ultra-fast imaging sequences [1], emerging trends focus on partial Fourier [2] and parallel MRI (pMRI) [3, 4], which are based on the undersampling of k -space and estimation of missing data using the redundant information available in the acquired data or prior knowledge about the underlying image.

One of the issues of the data acquisition techniques employing k -space undersampling is reduced signal to noise ratio (SNR), since SNR is directly proportional to the number of phase-encoding steps or the amount of acquired data. Furthermore, at high undersampling rates or acceleration factors, the reconstructed images can exhibit residual aliasing artifacts that further degrade image quality. The reduced SNR and residual artifacts, in fact, arise from the ill-conditioning of the inverse problems encountered in this context [5]. Regularization and explicit incorporation of prior knowledge during reconstruction of MR images is an efficient way to improve the conditioning of the problem and thus to penalize unsatisfactory and noisy solutions. Several regularization schemes have been assessed in this context. Tikhonov regularization suppresses noise and artifacts by favoring smooth image solutions [6-8]. The truncated singular value decomposition attempts to reduce noise by truncating small singular values on the assumption that noise amplification is associated with small singular values of solution [6, 9]. Both regularizations are based on l_2 norm minimization and tend to blur the details and edges in the estimated image [6, 10]. Recent developments in compressed sensing have introduced sparsity regularization techniques, which have garnered significant attention in MR reconstruction from highly undersampled k -spaces. In fact, CS-MRI reduces noise and aliasing artifacts by exploiting the prior knowledge that MR images are sparse or weakly sparse (compressible) in spatial and/or temporal domains [11, 12], in a given transform domain such as wavelets, Fourier, discrete gradients [11, 13] or in learned dictionaries [14, 15]. By establishing a direct link between sampling and sparsity, CS theory provides an alternative sampling criterion to conventional Shannon-Nyquist theory [16, 17]. According to this theory, it is possible to accurately recover the underlying signal or solution from the data acquired at sampling rates far below the Nyquist limit as long as i) it is sparse or has a sparse representation in a given transform domain and ii) the sampling pattern is random or such that the aliasing artifacts are incoherent (noisy-like) in that domain [17, 18].

Sparsity regularization aims at finding a solution that has the sparsest representation in a given sparse transform domain. In this regard, the l_0 norm is an ideal regularizer (or prior), which counts the number of non-zero elements of the solution [19]. However, this non-convex prior results in an intractable and non-deterministic polynomial-time hard (NP-hard) optimization problem. For this reason, the l_1 norm has been widely used as a convex surrogate to the l_0 norm and has gained popularity in conjunction with wavelet [20, 21] and discrete gradient transforms [22]. The latter is known as total variation (TV) regularization [23-26] and has been shown to outperform l_2 -based regularizations in CS-(p)MRI [27, 28]. The l_1 -based regularizations; however, show a lower limit in the required sampling rate and hence in the maximum achievable acceleration rate [29]. In addition, the l_1 norm is known to be biased due to over-penalizing large sparse representation coefficients [30]. To further reduce the sampling rate and approach l_0 norm minimization, Candes *et al.* [30] proposed a reweighted l_1 norm minimization in which the sparsity induced by the l_1 norm is enhanced by the weighting factors that are derived from the current estimate of the underlying solution. This approach has been successfully applied in CS-(p)MRI [31-33]. Furthermore, non-convex priors homotopically approximating the l_0 norm have also been studied showing the improved performance of the resulting regularization techniques in the recovery of strictly sparse signals [19, 34, 35]. However, MR images are usually compressible rather than sparse, hence it is desirable to exploit the sparsity-promoting properties of both l_1 and l_0 norm minimizations [36]. To improve the properties of l_1 and pseudo l_0 norms in terms of unbiasedness, continuity and sparsity, Fan and Li [37] proposed a non-convex prior called smoothly clipped absolute deviation (SCAD) norm in the context of statistical variable selection. This norm has been designed to not excessively penalize large valued coefficients as in the l_1 norm and at the same time approaching an l_0 norm. Teixeira, *et al.* [38] have previously studied the SCAD regularization for sparse signal recovery using a second-order cone optimization method. In this work, we employed, for the first time, the SCAD regularization with discrete gradients and wavelet transforms in the context of CS-MRI and solved the resulting problem using variable splitting and augmented Lagrangian (AL) methods. In the AL

framework, the optimization problem is reduced to simpler sub-problems, leading to an improved convergence rate in comparison with state-of-the-art and general purpose optimization algorithms [39, 40]. In this framework, the linearization of the SCAD norm resulted in a weighted soft thresholding rule that exploits the redundant information in image space to adaptively threshold the gradient fields and wavelet coefficients and to effectively reduce aliasing artifacts. In this study, we compared the performance of the proposed SCAD-based regularization with the conventional l_1 -based approach using simulation and clinical studies, where k -spaces were retrospectively undersampled using different sampling patterns to demonstrate the potential application of the proposed method in CS-MR image reconstruction.

II. Materials and methods

II.A. Theory

For a single-coil CS-MRI, we formulate the following CS acquisition model:

$$\mathbf{y} = \Phi \mathcal{F} \mathbf{x} + \mathbf{n} \quad (1)$$

where $\mathbf{y} \in \mathbb{C}^M$ is the undersampled k -space of the underlying MR image, $\mathbf{x} \in \mathbb{R}^N$, contaminated with additive noise $\mathbf{n} \in \mathbb{C}^M$. $\mathcal{F} \in \mathbb{C}^{N \times N}$ is a Fourier basis through which \mathbf{x} is being sensed and $\Phi \in \mathbb{R}^{M \times N}$ is a sampling matrix that compresses data to $M < N$ samples. The matrix $\mathbf{A} = \Phi \mathcal{F}$ is often referred to as sensing or Fourier encoding matrix. The direct reconstruction of \mathbf{x} from \mathbf{y} (by zero-filling the missing data and then taking its inverse Fourier transform) results in aliasing artifacts, which is attributed to the ill-conditioning of matrix \mathbf{A} . As a result, regularization is required to regulate the solution space according to a prior knowledge. The solution can therefore be obtained by the following optimization problem:

$$\hat{\mathbf{x}} = \underset{\mathbf{x}}{\operatorname{argmin}} \frac{1}{2} \|\Phi \mathcal{F} \mathbf{x} - \mathbf{y}\|^2 + R(\mathbf{x}) \quad (2)$$

where the first term enforces data consistency and the second one, known as regularizer, enforces data regularity. In the CS-MRI context, sparse l_1 -based regularizers have been widely used because the l_1 norm is a convex and sparsity promoting norm, thereby the resulting problem is amenable to optimization using convex programming. These regularizers are of the form $R(\mathbf{x}) = \|\Psi \mathbf{x}\|_1 = \lambda \sum_{i=1}^N (|\Psi \mathbf{x}|_i)$, where $\lambda > 0$ is a regularization parameter controlling the balance between regularization and data-consistency and Ψ is a sparsifying transform such as discrete wavelet, Fourier or gradient transform. The CS approach makes it possible to accurately reconstruct the image solution of problem (1), provided that i) the underlying image has a sparse representation in the domain of the transform Ψ , i.e. most of the decomposition coefficients are zero, while few of them have a large magnitude, ii) the sensing matrix \mathbf{A} should be sufficiently incoherent with the sparse transform Ψ , thereby the aliasing artifacts arising from k -space undersampling would be incoherent (noise like) in the domain of Ψ [11, 18].

II.B. Proposed Method

The sparsity or compressibility of an image solution induced by l_1 based regularizers can be increased by introducing a non-convex potential function, ψ_λ , as follows:

$$R(\mathbf{x}) = \sum_{i=1}^N \psi_\lambda(|\Psi \mathbf{x}|_i) \quad (3)$$

where ψ_λ assigns a higher penalty on the coefficients of small magnitude, therefore, they are being shrunk towards zero. In this study, the non-convex SCAD potential function is applied for CS-MRI regularization. The SCAD function, which has been widely and successfully used for linear regression with variable selection [37], is defined as:

$$\psi_\lambda(|t|) = \begin{cases} \lambda|t| & |t| \leq \lambda \\ (-|t|^2 + 2a\lambda|t| - \lambda^2)/2(a-1), & \lambda < |t| \leq a\lambda \\ (1+a)\lambda^2/2 & |t| > a\lambda \end{cases} \quad (4)$$

where $a > 2$. This potential function corresponds to a quadratic spline with knots at λ and $a\lambda$. Based on simulations and some Bayesian statistical arguments, Fan and Li [37] suggested $a = 3.7$.

In this study, 3D discrete gradient and 2D wavelet transforms were employed as sparsifying transforms. For discrete gradient, we define $\Psi = [\Psi^h, \Psi^v, \Psi^a] \in \mathbb{R}^{3N \times N}$, which is composed of directional first-order finite difference matrices (horizontal, vertical and axial) with periodic boundary conditions. By convention, we define

the magnitude of the gradient at voxel i by $|\Psi\mathbf{x}|_i = ([\Psi^h\mathbf{x}]_i^2 + [\Psi^v\mathbf{x}]_i^2 + [\Psi^a\mathbf{x}]_i^2)^{1/2}$, $[\Psi\mathbf{x}]_i \in \mathbb{R}^3$. The summation over the magnitude of the gradient at all voxels in Eq. (3) defines an isotropic TV regularizer, which is known to be edge-preserving in image processing and sparsity-promoting in compressed sensing. However, this is known to sometimes result in stair-casing artifacts, which are artificial flat regions in the image domain. For wavelet transforms, we make use of Daubechies 7/9 biorthogonal (D7/9) wavelets, with four resolution levels in a normalized tight (Parseval) frame of translation-invariant wavelets, implemented by undecimated discrete wavelet transforms (UDWT) and a lifting scheme. In UDWT, the decimation (downsampling) is eliminated in favor of invariance to the shifts of an input image, thus avoiding the star-like artifacts usually induced by the standard decimated wavelet transform. Note that in the case of a tight frame, $\Psi \in \mathbb{R}^{D \times N}$, which is called decomposition or forward wavelet transform, satisfies $\Psi^T\Psi = \mathbf{I}$, where Ψ^T is reconstruction or inverse wavelet transform and \mathbf{I} is the identity matrix.

To solve the problem defined in Eq. (2) using SCAD-based regularizer, we follow the augmented Lagrangian (AL) method, which has been originally developed for constrained optimization problems [41]. The AL method, also known as the method of multipliers [42], allows for the optimization of non-continuously differentiable regularizers through a variable splitting technique, in which auxiliary constraint variables are defined and the original optimization problem is decomposed to simpler sub-problems [39]. Hence, we define the auxiliary variable $\boldsymbol{\theta} = \Psi\mathbf{x}$ and cast the problem (2), with the regularizer defined by equations (3) and (4), into the following constrained problem:

$$\min_{\mathbf{x}, \boldsymbol{\theta}} \left\{ \Gamma(\mathbf{x}, \boldsymbol{\theta}) \triangleq \frac{1}{2} \|\Phi\mathbf{F}\mathbf{x} - \mathbf{y}\|^2 + \sum_{i=1}^N \psi_\lambda(|\theta_i|) \right\} \quad (5)$$

subject to $\boldsymbol{\theta} = \Psi\mathbf{x}$

The augmented Lagrangian for this problem is defined as:

$$\mathcal{L}(\mathbf{x}, \boldsymbol{\theta}, \boldsymbol{\gamma}) = \Gamma(\mathbf{x}, \boldsymbol{\theta}) - \boldsymbol{\gamma}^T(\boldsymbol{\theta} - \Psi\mathbf{x}) + \frac{\rho}{2} \|\boldsymbol{\theta} - \Psi\mathbf{x}\|^2 \quad (6)$$

where $\boldsymbol{\gamma}$ and $\rho > 0$ are respectively the Lagrange multipliers and the penalty parameter associated with the equality constrain $\boldsymbol{\theta} = \Psi\mathbf{x}$. The AL method aims at finding a saddle point $(\mathbf{x}^*, \boldsymbol{\theta}^*)$ minimizing \mathcal{L} . The classical approach to solve Eq. (6) alternates between a joint-minimization and an update step as follows:

$$(\mathbf{x}^{k+1}, \boldsymbol{\theta}^{k+1}) = \underset{\mathbf{x}, \boldsymbol{\theta}}{\operatorname{argmin}} \mathcal{L}(\mathbf{x}, \boldsymbol{\theta}, \boldsymbol{\gamma}^k) \quad (7)$$

$$\boldsymbol{\gamma}^{k+1} = \boldsymbol{\gamma}^k - \rho(\boldsymbol{\theta}^{k+1} - \Psi\mathbf{x}^{k+1}) \quad (8)$$

As joint-minimization in Eq. (7) is not trivial, an alternating minimization with respect to a given variable while fixing the other one can be followed. Using this approach, referred to as alternating direction method of multipliers (ADMM) [43], the optimization algorithm of Eq. (7) reads:

$$\mathbf{x}^{k+1} = \underset{\mathbf{x}}{\operatorname{argmin}} \frac{1}{2} \|\Phi\mathbf{F}\mathbf{x} - \mathbf{y}\|^2 - \boldsymbol{\gamma}_k^T(\boldsymbol{\theta}^k - \Psi\mathbf{x}) + \frac{\rho}{2} \|\boldsymbol{\theta}^k - \Psi\mathbf{x}\|^2 \quad (9)$$

$$\boldsymbol{\theta}^{k+1} = \underset{\boldsymbol{\theta}}{\operatorname{argmin}} \sum_{i=1}^N \psi_\lambda(|\theta_i|) - \boldsymbol{\gamma}_k^T(\boldsymbol{\theta} - \Psi\mathbf{x}^{k+1}) + \frac{\rho}{2} \|\boldsymbol{\theta} - \Psi\mathbf{x}^{k+1}\|^2 \quad (10)$$

Recently, Ramani *et al.* [40] studied the ADMM method for pMRI and demonstrated its outperformance over nonlinear conjugate gradient algorithms. In this work, we followed this method and derived solutions for the involved sub-problems as follows.

1) Minimization with respect to \mathbf{x}

The minimization in Eq. (9) is achieved by taking the derivative of the objective of the problem with respect to \mathbf{x} and equating it to zero, thereby one arrives at the following normal equations:

$$(\mathcal{F}^H \Phi^T \Phi \mathcal{F} + \rho \Psi^T \Psi) \mathbf{x}^{k+1} = \mathcal{F}^H \Phi^T \mathbf{y} + \Psi^T (\rho \boldsymbol{\theta}^k - \boldsymbol{\gamma}^k) \quad (11)$$

where $(\cdot)^H$ denotes the Hermitian transpose and $\Phi^T \Phi \in \mathbb{R}^{N \times N}$ is a diagonal matrix with zeros and ones on the diagonal entries. To solve this problem, one need to invert the matrix $\mathbf{G} = \mathcal{F}^H \Phi^T \Phi \mathcal{F} + \rho \Psi^T \Psi$. In the case of discrete gradients with periodic boundary conditions, the matrix $\Psi \in \mathbb{R}^{3N \times N}$ has a block-circulant structure and its directional derivatives can be achieved by circular convolutions with two-element kernels.

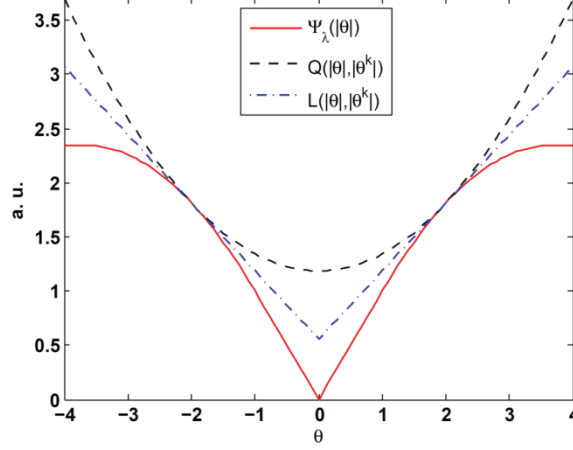


Figure 1. The non-convex SCAD potential function (ψ) together with its convex quadratic (Q) and linear (L) surrogates ($\theta^k = 2, a = 3.7, \lambda = 3.7$).

Therefore, Ψ can be efficiently diagonalized using 3D discrete Fourier transform (DFT) [44], i.e. $\Psi = \mathcal{F}\Lambda\mathcal{F}^H$, where Λ is a diagonal complex matrix containing the DFT coefficients of the convolution kernels of Ψ . Hence, one obtains $\Psi^T\Psi = \mathcal{F}^H|\Lambda|^2\mathcal{F}$, where $|\Lambda|^2 \in \mathbb{R}^{N \times N}$ is the modulus of Λ , also the eigenvalue matrix of $\Psi^T\Psi$. With this diagonalization, the solution of problem (9) is given by:

$$\mathbf{x}^{k+1} = \mathcal{F}^H \left[(\Phi^T\Phi + \rho|\Lambda|^2)^{-1} \mathcal{F} (\mathcal{F}^H\Phi^T\mathbf{y} + \Psi^T(\rho\theta^k - \gamma^k)) \right] \quad (12)$$

It should be noted that in the case of non-Cartesian MR data, the Fourier encoding matrix $\Phi\mathcal{F}$ is not diagonalizable using discrete Fourier transform. However, the solution can be obtained by regridding of data to Cartesian k -space or the use of iterative techniques such as the conjugate gradient algorithm for estimating the inverse of \mathbf{G} . Recently, Akcakaya *et al.* [45] proposed another approach to approximate the matrix $\Phi^T\Phi$, which is not diagonal in the case of non-Cartesian data acquisition, by a diagonal matrix which gives an approximate closed-form solution to this sub-problem.

In the case of wavelet frames, the inversion of matrix \mathbf{G} can be obtained by Sherman-Morrison-Woodbury matrix inversion formula and exploiting the fact that $\Psi^T\Psi = \Phi\Phi^T = \mathbf{I}$, as follows:

$$\mathbf{G}^{-1} = \frac{1}{\rho} \left(\mathbf{I} - \mathcal{F}^H\Phi^T(\Phi\Phi^T + \rho\mathbf{I})^{-1}\Phi\mathcal{F} \right) = \frac{1}{\rho} \left(\mathbf{I} - \frac{1}{1+\rho} \mathcal{F}^H\Phi^T\Phi\mathcal{F} \right) \quad (13)$$

By doing some algebra and knowing that $\mathcal{F}\mathcal{F}^H = \mathbf{I}$, one can show that the solution of Eq. (11) for wavelet transforms reads:

$$\mathbf{x}^{k+1} = \Psi^T \left(\theta^k - \frac{1}{\rho} \gamma^k \right) + \frac{1}{1+\rho} \mathcal{F}^H\Phi^T \left(\mathbf{y} - \Phi\mathcal{F}\Psi^T \left(\theta^k - \frac{1}{\rho} \gamma^k \right) \right) \quad (14)$$

2) Minimization with respect to θ

The SCAD potential function is non-convex; thereby the problem (10) might have multiple local minima. The minimization of non-convex problems often depends on the initial estimate and the choice of the optimization algorithm. Global search techniques, such as simulated annealing, can guarantee convergence to a global minimizer but they are impractical for routine use in image reconstruction. Hence, one can utilize an optimization transfer technique to iteratively surrogate the non-convex function by a convex function, which is amenable to optimization. Fan and Li [37] proposed a local quadratic approximation to the SCAD function near the point θ_i^k as follows:

$$Q(|\theta_i|, |\theta_i^k|) = \psi_\lambda(|\theta_i^k|) + \frac{1}{2} \frac{\psi'_\lambda(|\theta_i^k|)}{|\theta_i^k|} (|\theta_i|^2 - |\theta_i^k|^2) \quad (15)$$

where the first derivative of the SCAD function is given by:

$$\psi'_\lambda(|t|) = \begin{cases} \lambda, & |t| \leq \lambda \\ \max(0, a\lambda - |t|), & |t| > \lambda \end{cases} \quad (16)$$

The quadratic surrogate in Eq. (15) is, however, undefined at points $\theta_i^k = 0$. The denominator can be conditioned to $|\theta_i^k| + \epsilon$, where ϵ is a predefined perturbation parameter [46]. Since an ϵ erroneous potentially degrades the sparsity of the solution as well as the convergence rate of the optimization algorithm, Zou and Li [47] proposed the linear local approximation of the SCAD function near the point θ_i^k . As a result, the following convex surrogate is obtained:

$$Q(|\theta_i|, |\theta_i^k|) = \psi_\lambda(|\theta_i^k|) + \psi'_\lambda(|\theta_i^k|)(|\theta_i| - |\theta_i^k|) \quad (17)$$

Figure 1 compares the SCAD function with its quadratic and linear convex surrogates. Note that the linear surrogate is a non-smooth function and is similar to a scaled or weighted l_1 -norm. Given the superiority of linearization of SCAD, we adopted this convex surrogate and derived a closed-form solution to the problem (10). By dropping the terms independent of θ_i in Eq. (17), completing the square in Eq. (10) and defining the intermediate variable $\tilde{\theta} = \Psi \mathbf{x}^{k+1} + \frac{1}{\rho} \boldsymbol{\gamma}^k$, we can rewrite the problem (10) as follows:

$$\boldsymbol{\theta}^{k+1} = \underset{\boldsymbol{\theta}}{\operatorname{argmin}} \sum_{i=1}^N \psi'_\lambda(|\theta_i^k|) |\theta_i| + \frac{\rho}{2} \|\tilde{\boldsymbol{\theta}} - \boldsymbol{\theta}\|^2 \quad (18)$$

As the terms in the above optimization problem are separable, we obtain the solution by the following component-wise soft-thresholding estimator according to theorem 1 in [48]:

$$\theta_i^{k+1} = \begin{cases} 0 & |\tilde{\theta}_i| \leq \omega_i^k / \rho \\ \tilde{\theta}_i - \omega_i^k \operatorname{sign}(\tilde{\theta}_i) / \rho, & |\tilde{\theta}_i| > \omega_i^k / \rho \end{cases} \quad (19)$$

where $\omega_i^k = \psi'_\lambda(|\theta_i^k|)$ are iteratively derived weighting factors that promote or suppress the thresholding of the decomposition coefficients and in the case of discrete gradients, by convention, $|\tilde{\theta}_i| = \sqrt{|\tilde{\theta}_i^h|^2 + |\tilde{\theta}_i^v|^2 + |\tilde{\theta}_i^a|^2}$, where $|c| = c * c$ is the modulus of the complex variable c . Note that in the case of discrete gradients, ω_i^k is isotropically used for the gradient fields at a voxel in three directions, that is, the weighting factors are concatenated to obtain $\boldsymbol{\omega}^k = \in \mathbb{R}^{3N}$ and then are fed into Eq. (19).

As a result of linearization of the SCAD function, the regularizer $R(\boldsymbol{\theta}) = \sum_{i=1}^N \psi'_\lambda(|\theta_i^k|) |\theta_i|$ for $\boldsymbol{\theta}_i = [\Psi \mathbf{x}]_i$ in fact behaves as an iteratively weighted l_1 -based regularizer with improved performance (see Results section). Note that by setting the weights $\omega_i^k = \lambda$, the proposed regularization reduces to the conventional l_1 -based regularization. To this end, Algorithm 1 summarizes the proposed SCAD-ADMM algorithm for CS-MRI. A global convergence is declared when the relative difference between \mathbf{x}^{k+1} and \mathbf{x}^k falls below a tolerance (η).

Algorithm 1: SCAD-ADMM

Choose ρ, λ, η and initialize $\boldsymbol{\theta}^0, \boldsymbol{\gamma}^0 = \mathbf{0}$.

Pre-compute $|\Lambda|^2$ if Ψ is discrete gradients.

While ($\|\mathbf{x}^{k+1} - \mathbf{x}^k\| / \|\mathbf{x}^k\|$) $> \eta$ **do**

1. Compute \mathbf{x}^{k+1} according to Eq. (12) if Ψ is discrete gradients or Eq. (14) if Ψ is a wavelet transform.
2. Define the intermediate variable $\tilde{\boldsymbol{\theta}} = \Psi \mathbf{x}^{k+1} + \boldsymbol{\gamma}^k / \rho$.
3. Compute the weights $\boldsymbol{\omega}^k = \psi'_\lambda(|\boldsymbol{\theta}^k|)$ using Eq. (16).
4. Compute $\boldsymbol{\theta}^{k+1}$ by weighted soft-thresholding of $\tilde{\boldsymbol{\theta}}$ using Eq. (19) and the weights $\boldsymbol{\omega}^k$.
5. Update Lagrange multipliers according to Eq. (8).

Output: \mathbf{x}^{k+1} .

II.C. Experiments and evaluations

Several simulations and retrospective k -space undersampling in clinical datasets were performed to evaluate the performance of the proposed SCAD regularization with l_1 -based regularization. The variable density random sampling and Cartesian approximations of the radial and spiral Fourier trajectories were used for retrospective undersampling of the (fully sampled) Cartesian k -spaces of phantoms and clinical datasets. To demonstrate the performance of SCAD regularization for highly undersampled MR reconstruction, we first performed a set of simulated noisy data generated from the anthropomorphic XCAT phantom. In this experiment, the k -space of a

512×512 slice of the XCAT phantom was sampled by 8 equally spaced radial trajectories as well as a single-shot variable-density spiral trajectory, respectively corresponding to 98.33 and 98.30% undersampling, with 20 dB complex noise added to k -spaces. For the evaluation of the proposed SCAD-ADMM algorithm with 3D discrete gradients, an MR angiography (MRA) dataset in a patient with arterial bolus injection was obtained from Ref. [49]. The dataset has been synthesized from projection data collected for 3 frames per second for a total of 10 seconds (31 collected frames) and linearly interpolated into 200 temporal frames. In this study, 30 time frames of this dataset (with resolution of 256×256) were chosen and their 3D k -space was retrospectively undersampled using a stack of 2D single-shot variable-density spiral trajectories, yielding 78.7% undersampling. The performance of the algorithm was further evaluated with 2D translation-invariant wavelets using two brain datasets. A transverse slice of a 3D brain T1-weighted MRI dataset (of the size 181×217×181) were obtained from the BrainWeb database (McGill University, Montreal, QC, Canada) [50], which has been simulated for 1 mm slice thickness, 3% noise and 20% intensity non-uniformity. The image slice was zero-padded to 256×256 pixels and its k -space was retrospectively undersampled by a variable-density random sampling pattern with 85% undersampling. Finally in clinical patient study, a Dixon MRI dataset was acquired on a Philips Ingenuity TF PET/MRI scanner (Philips Healthcare, Cleveland, OH). The MRI subsystem of this dual-modality imaging system is equipped with the Achieva 3.0T X-series MRI system. A whole body scan was acquired using a 16-channel receiver coil and a 3D multi-echo 2-Point FFE Dixon (mDixon) technique with parameters: TR = 5.7 ms, TE1/TE2 = 1.45 / 2.6, flip angle = 10° and slice thickness of 2 mm, matrix size of 480 × 480 × 880 and in plane resolution of 0.67 mm × 0.67 mm. From this sequence, in-phase, out-of-phase, fat and water (IP/OP/F/W) images are reconstructed. For the comparison of SCAD- and l_1 -based wavelet regularizations, a representative image slice of OP image was zero-padded to 512×512 pixels and its k -space was retrospectively undersampled by the Cartesian approximation of radial trajectory with 83% undersampling. Note that in the k -spaces of the studied datasets were obtained by forward Fourier transform of the image slices.

All of our CS-MR reconstructions were performed in MATLAB 2010a, running on a 12-core workstation with 2.40 GHz Intel Xeon processors and 32 GB memory. The improvement of image quality was objectively evaluated using peak signal to noise ratio (PSNR) and mean structural similarity (MSSIM) index, [51] between the ground truth fully sampled image, \mathbf{x}^* , and the images reconstructed by l_1 - and SCAD-based regularizations, \mathbf{x} . The PSNR is defined as:

$$PSNR(\mathbf{x}, \mathbf{x}^*) = 20 \log_{10} \left(\frac{\max_{1 \leq i \leq N} |\mathbf{x}_i^*|^2}{\sqrt{\frac{1}{N} \sum_{i=1}^N |\mathbf{x}_i^* - \mathbf{x}_i|^2}} \right)$$

MSSIM, which evaluates both nonstructural (e.g., intensity) and structural (e.g., residual streaking artifacts) deviations of an image from its reference image, is given by:

$$SSIM(\mathbf{x}, \mathbf{x}^*) = \frac{(2\mu_x \mu_{x^*} + C_1)(2\sigma_{xx^*} + C_2)}{(\mu_x^2 + \mu_{x^*}^2 + C_1)(\sigma_x^2 + \sigma_{x^*}^2 + C_2)}$$

$$MSSIM(\mathbf{x}, \mathbf{x}^*) = \frac{1}{L} \sum_{l=1}^L SSIM(\mathbf{x}_l, \mathbf{x}_l^*)$$

where the mean intensity, μ , and standard deviation, μ , of \mathbf{x} and \mathbf{x}^* and their correlation coefficient, σ_{xx^*} , are calculated over L local image patches. The constants $C_1 = (K_1 D)^2$ and $C_2 = (K_2 D)^2$ are introduced to avoid instability issues, where D is the dynamic range of pixel values. $K_1 = 0.01$ and $K_2 = 0.03$ according to Ref. [51]. Based on this metric, a perfect score, i.e. $MSSIM(\mathbf{x}, \mathbf{x}^*) = 1$ is achieved only when the image \mathbf{x} is identical to the ground truth image \mathbf{x}^* . In addition, the reconstructed images were qualitatively compared through visual comparison and intensity profiles. In all reconstructions, a tolerance of $\eta = 1 \times 10^{-4}$ was used in Algorithm 1 to declare the convergence of the algorithms.

III. Results

III.A. CS-MR image reconstructions

Figure 2 shows the results of image reconstruction in XCAT phantom for radial and single-shot variable density spiral trajectories, in first and second rows, respectively, and compares the images reconstructed by zero-filing, l_1 - and SCAD-based ADMM algorithms with discrete gradient sparsifying transform. This figure also shows the

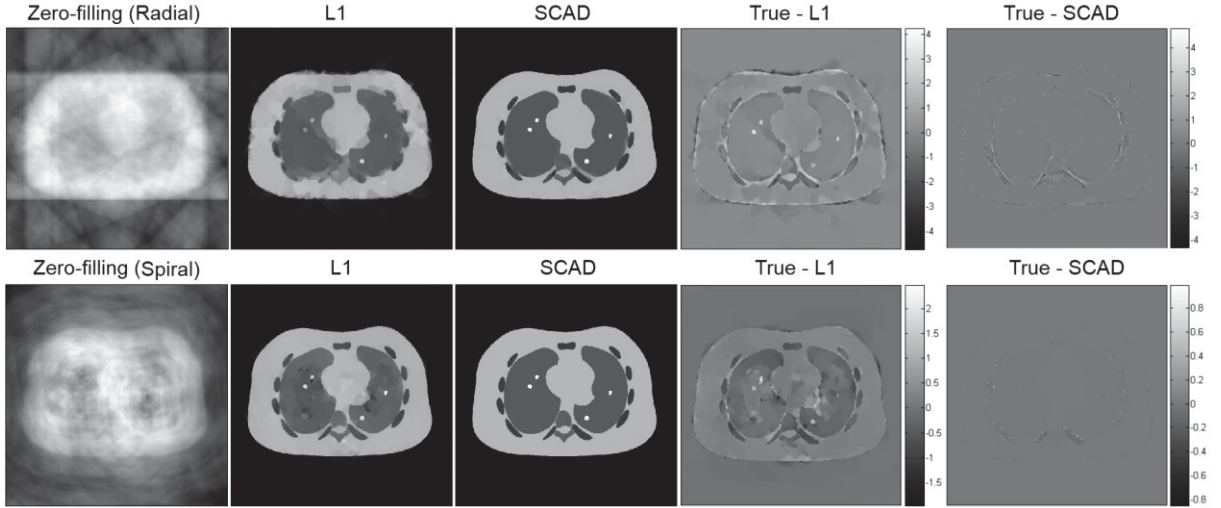


Figure 2. Reconstruction of the XCAT phantom through zero-filling, gradient-based l_1 and SCAD ADMM algorithms from the k -spaces sampled by 8 equally spaced radial Fourier trajectories (top) and a variable-density spiral trajectory (bottom), respectively, corresponding to 98.33 and 98.30 % undersampling. The difference images show the deviations of the reconstructed images from the true fully sampled image.

Table 1. Summary of the peak signal-to-noise ratio (PSNR) and mean structural similarity (MSSIM) performance of the studied algorithms in CS-MRI with respect to fully sampled (reference) images. The number of iterations and computation (CPU) time per iteration (in seconds) are also reported.

Dataset	PSNR (dB)			SSIM			Iterations CPU time/Iter. (sec.)			
	Zero-Filling	L1	SCAD	Zero-Filling	L1	SCAD	L1	SCAD	L1	SCAD
XCAT (Radial)	17.66	26.03	35.89	0.21	0.83	0.98	2130	0.06	2862	0.08
XCAT (Spiral)	14.21	31.41	52.66	0.16	0.84	0.99	2489	0.07	2745	0.08
MR Angiogram	24.65	28.32	28.60	0.64	0.69	0.70	94	0.83	138	0.97
BrainWeb	14.84	18.52	20.36	0.39	0.59	0.62	335	0.49	354	0.66
Brain mDixon	23.76	27.91	29.13	0.31	0.98	0.99	96	1.84	102	2.12

difference images between true and reconstructed images. As can be seen, the proposed regularization technique has efficiently recovered the true image and outperformed the its TV counterpart in both cases. In this simulation study with extremely high undersampling, the involved parameters, i.e. ρ , λ and a , were heuristically optimized to obtain the best case performance of the algorithms. For the radial sampling results, the optimized parameters were set to $\rho = 0.5$, $\lambda = 0.03$, $a = 3.7$ for SCAD and $\rho = 0.2$, $\lambda = 0.05$ for TV. Similarly, in the spiral sampling, the parameters were set to $\rho = 0.15$, $\lambda = 0.15$, $a = 3.7$ for SCAD and $\rho = 0.05$, $\lambda = 0.15$ for TV. The quantitative evaluation of the algorithms in terms of PSNR and SSIM index is presented in Table 1. The results show that the SCAD regularization significantly improves peak signal to noise ratio in the reconstructed images and also gives rise to a perfect similarity between the true and the reconstructed images. It should be noted that at sufficiently high sampling rate the l_1 -based TV regularization can restore the underlying image as faithfully as the SCAD regularization. However, we purposefully lowered the sampling rate to evaluate the ability of algorithms in CS-MRI from highly undersampled datasets.

In figure 3 (a), a representative slice of the reconstructed MRA images is compared with the fully sampled ground truth. The visual comparison of the regularized reconstructions shows that both l_1 -based TV and SCAD regularization have noticeably suppressed noise and undersampling artifacts in comparison with zero-filling, which is in fact an un-regularized reconstruction. However, a close comparison of the images reveals that the SCAD regularization results in a higher image contrast (see arrows), since it exploits the weighting factors that suppress regularization across boundaries. Figure 3 (b–c) also shows the k -space trajectory used for undersampling and the intensity profiles of the reconstructed images along the dashed line shown on the true image. The profiles also demonstrate that the SCAD regularization technique can improve the performance of its TV counterpart. The algorithms were also quantitatively evaluated based on PSNR and MSSIM metrics. The results summarized in Table 1 further demonstrate the outperformance of the proposed regularization technique. Note that during image reconstruction of this and the other two brain datasets, we first optimized the involved

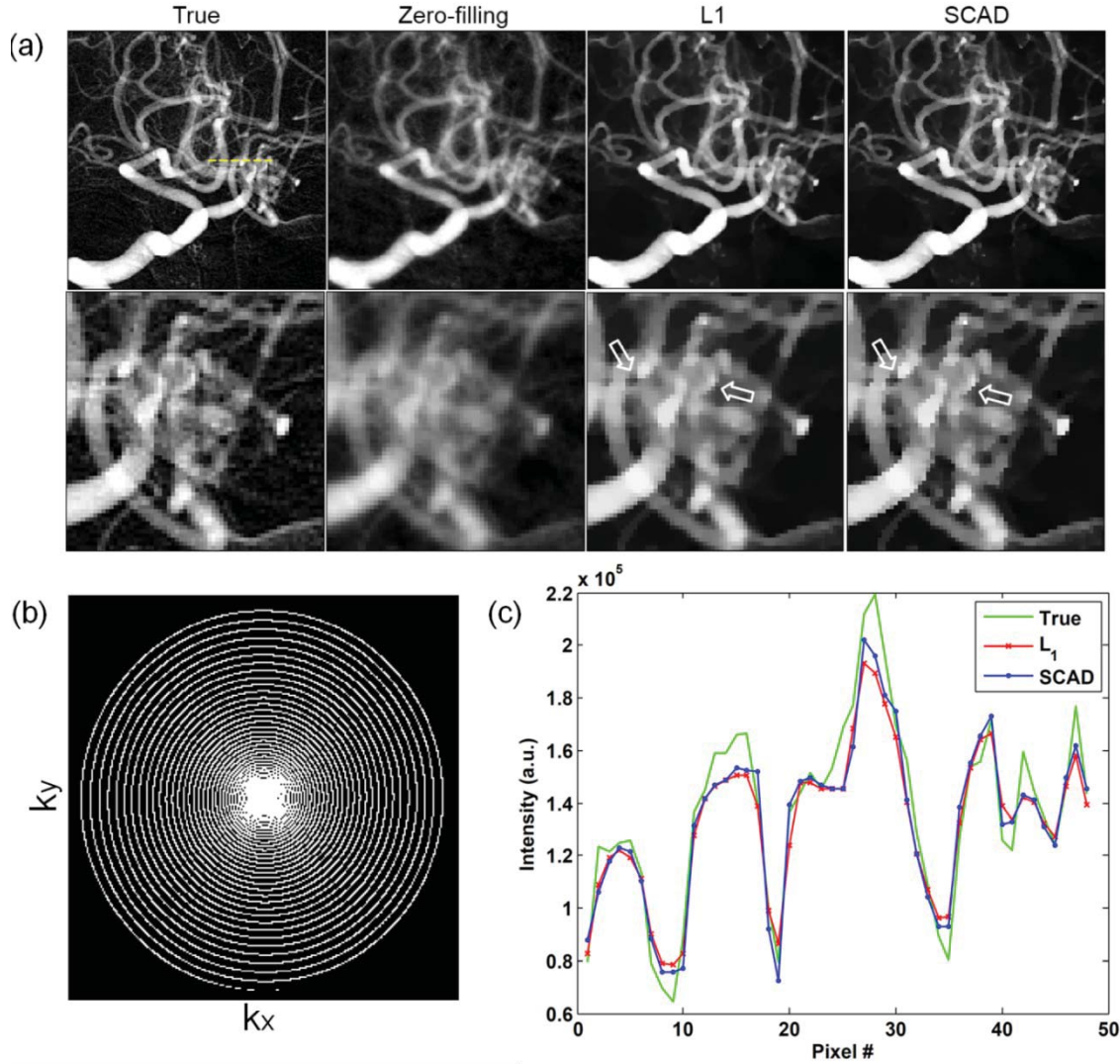


Figure 3. (a) Reconstruction of the MR angiogram dataset through zero-filling, gradient-based l_1 and SCAD ADMM algorithms using a 3D stack of a single-shot variable-density spiral trajectory (78.7% undersampling). The L1 and SCAD images are shown with the same display window. (b) The illustration of k -space undersampling pattern. (c) The comparison of intensity profiles of reconstructed images along the dash line shown on the true image.

parameters of the ADMM algorithm, i.e. λ and ρ , for l_1 -based regularizations to obtain the best case performance. Then, we optimized the performance of the SCAD regularization using the same values for the scale parameter a in Eq. (16). For this dataset, the optimal parameters were set to $\rho = 1.2$, $\lambda = 1800$, $a = 100$.

Figures 4(a) and 5(a) show the image reconstruction results of the simulated (BrainWeb) and clinical brain Dixon datasets, respectively. As mentioned earlier, translation-invariant wavelets were employed as sparsifying transforms. As can be seen in both cases, the proposed regularization technique depicts improved performance in reducing the aliasing artifacts and restoring the details in comparison with l_1 -based regularization (see arrows). In figures 4(b–c) and 5(b–c), k -space undersampling patterns as well as line profiles of the reconstructed images along the dash line in true images are shown. The line profiles demonstrate that the SCAD regularization can restore the true profiles more faithfully. As will be elaborated in the Discussion section, this regularizer exploits the redundant information in the image being reconstructed in order to suppress the thresholding of wavelet coefficients of image features and thereby to improve the accuracy of the reconstructed images. The quantitative evaluations of the l_1 -based and SCAD regularizations presented in Table 1 demonstrate that the proposed regularizer achieves an improved SNR and structural similarity over its counterpart. The optimal parameters obtained for the simulated (BrainWeb) and clinical brain Dixon datasets were set to $\rho = 0.2$, $\lambda = 3$ and $\rho = 0.5$, $\lambda = 3$, $a = 10$, respectively.

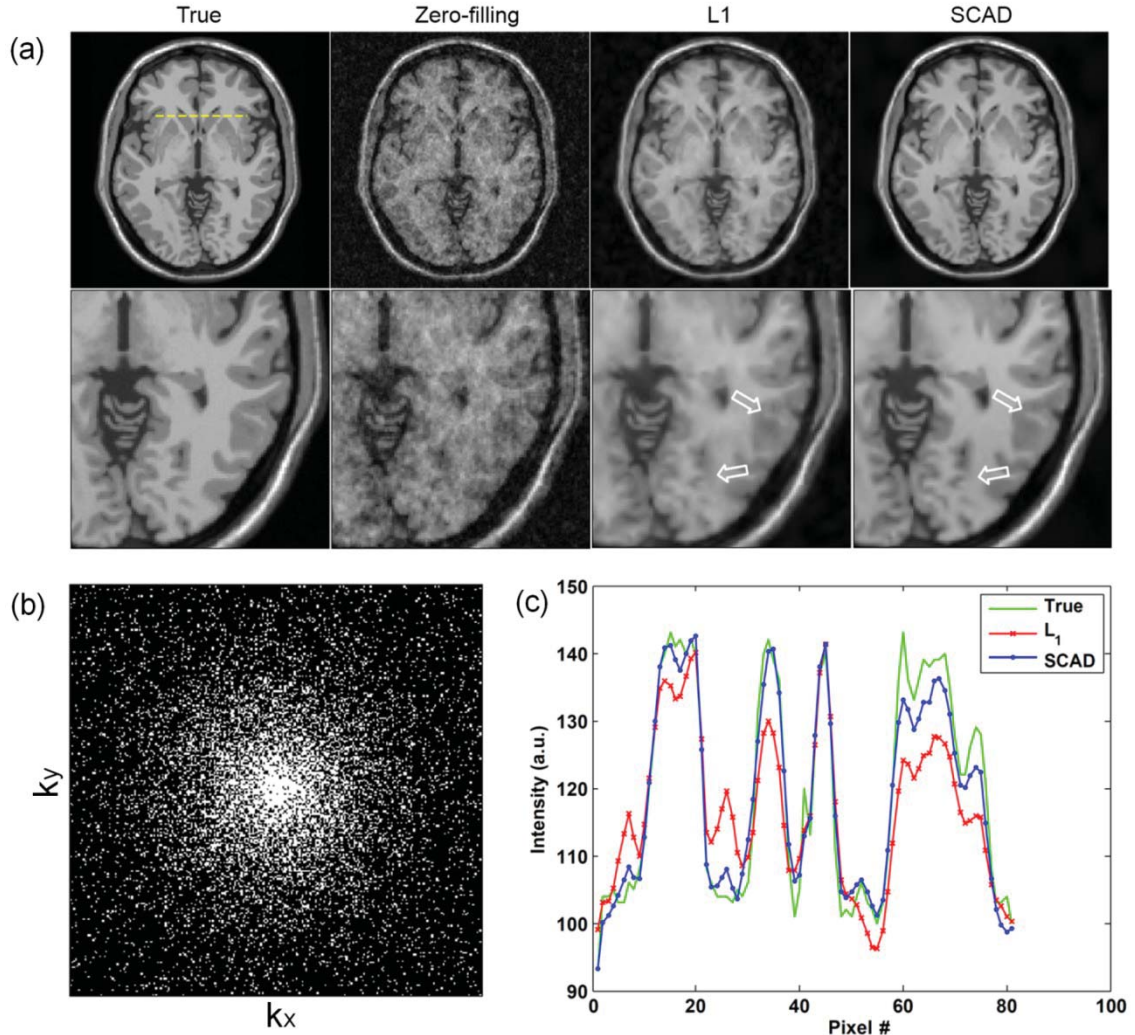


Figure 4. (a) Reconstruction of the BrainWeb phantom through zero-filling, wavelet-based l_1 and SCAD ADMM algorithms using a variable density random sampling (85% undersampling). The L1 and SCAD images are shown with the same display window. (b–c) As in figure 3.

III.B. Convergence rate and computation time

Table 1 summarizes the number of iterations and the computation (CPU) time per iteration for l_1 and SCAD-ADMM algorithms obtained for the studied datasets. Overall, for retrospective reconstruction of a dataset of size $256 \times 256 \times 30$, the TV and SCAD-ADMM algorithms require about 0.83 and 0.97 seconds per iteration in our MATLAB-based implementation. For the simulated (BrainWeb) and clinical brain Dixon datasets, which had matrix sizes of 256×256 and 512×512 and where wavelet transforms were used, the algorithms required an increased CPU time per iteration. This is due to the fact that wavelet transforms, particularly translation-invariant wavelets, require more arithmetic operations compared to finite differences (discrete gradients) and hence present with higher computational complexity. In practical settings, an iterative algorithm is said to be convergent if it reaches a solution where the image estimates do not change (or practically change within a certain tolerance determined by a stopping criterion) compared to the succeeding iteration [52]. As mentioned earlier, a tolerance of $\eta = 1 \times 10^{-4}$ was used in Algorithm 1 to declare the convergence of the algorithms. For the parameters optimally tuned, it was found that the l_1 -based ADMM algorithm generally converges after a fewer number of iterations in comparison with the SCAD-ADMM. In the MRA, BrainWeb and brain Dixon datasets, it converged after 94, 335 and 94 iterations, respectively, while the SCAD converged after 138, 354 and 102 iterations, respectively. The same trend was also observed for the XCAT phantom with radial and spiral undersampling patterns. This convergence behavior should be ascribed to the weighting scheme that SCAD

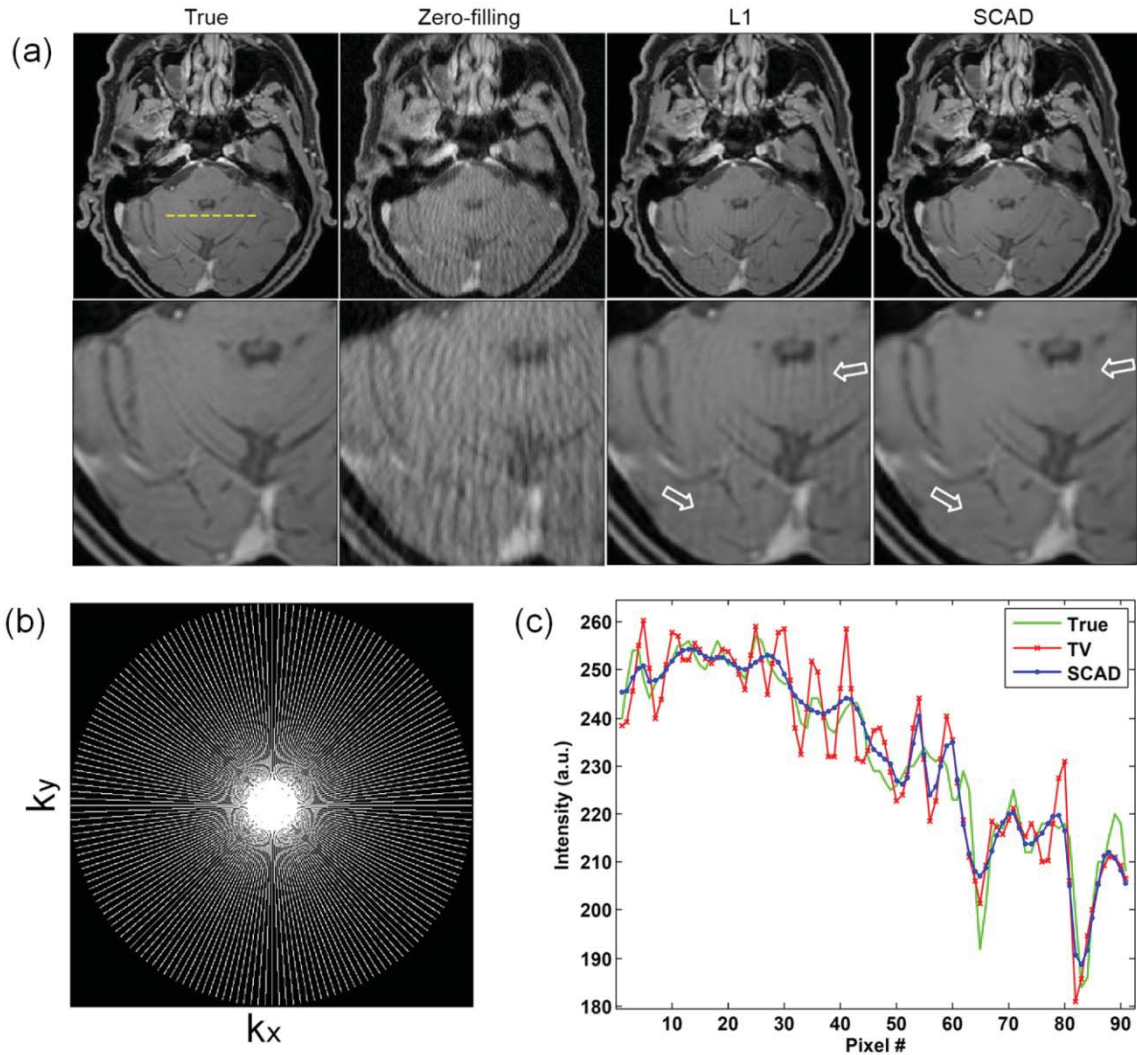


Figure 5. (a) Reconstruction of the clinical brain Dixon (out-of-phase) dataset through zero-filling, wavelet-based l_1 and SCAD ADMM algorithms using a radial trajectory (87.54% undersampling). The L1 and SCAD images are shown with the same display window. (b–c) As in figure 3.

regularization exploits. In fact, this weighting scheme attempts to iteratively recognize and preserve sharp edges. As a result, it takes the algorithm more iterations to identify true edges from those raising from aliasing and streaking artifacts. However, our results showed that the SCAD regularization achieves a higher PSNR at the same common iteration in comparison with the l_1 -based regularization. Figure 6 shows PSNR improvement with iteration number in CS-MR reconstruction of the MRA, BrainWeb and the brain Dixon datasets, respectively. As can be seen, the decreased convergence rate of (or the increased number iterations in) the proposed regularization technique is compensated with an overall increased PSNR.

IV. Discussion

Fast MRI data acquisition is of particular importance in applications such as dynamic myocardium perfusion imaging and contrast-enhanced MR angiography. Compressed sensing provides a promising framework for MR image reconstruction from highly undersampled k -spaces and thus enables a substantial reduction of acquisition time [11, 53]. In this study, we introduced a new regularization technique in compressed sensing MR image reconstruction based on the non-convex smoothly clipped absolute deviation norm with the aim of decreasing the

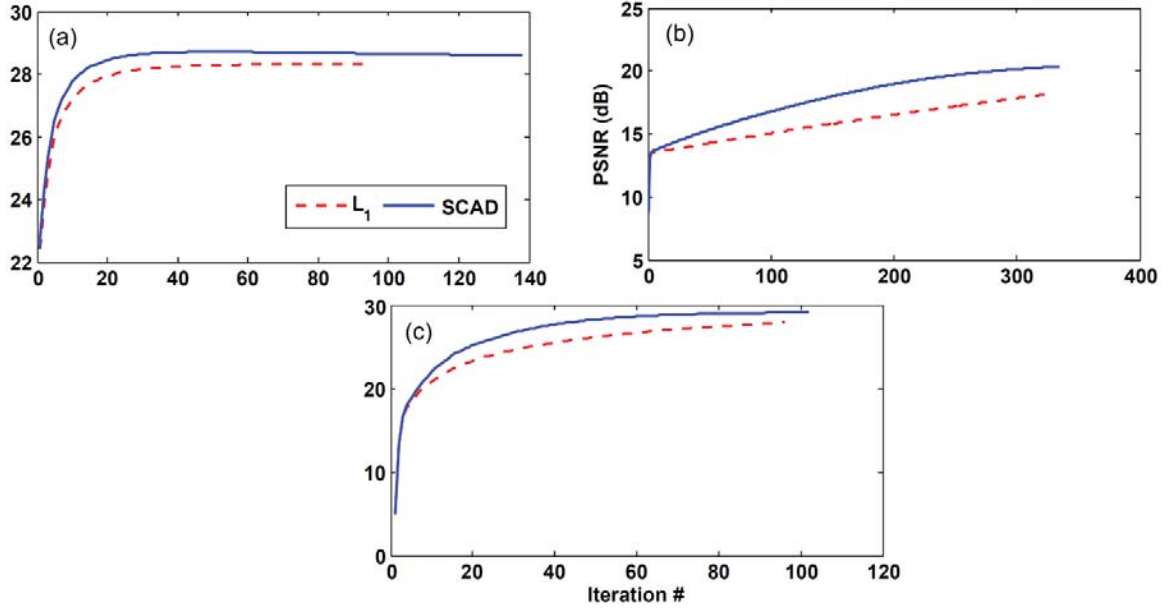


Figure 6. PSNR improvement as a function of iteration number for the CS-MR reconstruction of: (a) the MRA, (b) BrainWeb and (c) the brain Dixon datasets using l_1 and SCAD-based regularizations.

sampling rate even lower than it is required by the conventional l_1 norm. The CS-MRI reconstruction was formulated as a constrained optimization problem and the SCAD norm was iteratively convexified by linear local approximations within an augmented Lagrangian framework. We employed finite differences and wavelet transforms as a sparsifying transform and compared the proposed regularizer with its l_1 -based TV counterpart.

IV.A. Edge preservation and sparsity promotion

The linearization of the SCAD norm in effect gives rise to a reweighted l_1 norm. In general, our qualitative and quantitative results showed improved performance of the SCAD over the l_1 based regularization. This outperformance is due to the fact that the reweighted l_1 norm non-uniformly thresholds the gradient fields and wavelet coefficients of the image estimate according to adaptively derived weighting factors (Step 4 in Algorithm 1). In fact, these weighting factors, on one hand, suppress the smoothing (thresholding) of edges and features and on the other hand, enforce the smoothing of regions contaminated by noise and artifacts. Figures 7(a–b) show respectively the weighting factors associated with gradient fields of the MRA image (figure 3) and those with the wavelet coefficients of the brain Dixon image (figure 5) as a function of iteration number. Figure 7(b) only shows the weights of the detail coefficients at resolution 4 in the diagonal direction. It is worth mentioning that the wavelet transform decomposes an image into one approximate subband and several (horizontal, vertical and diagonal) detail subbands. It can be seen that as iteration number increases: i) the true anatomical boundaries are being distinguished from false boundaries arising from artifacts, especially in the case of the brain dataset where the radial sampling pattern results in streaking artifacts and ii) the emphasis on edge preservation (the wall of vessels or the border of structures) increases by assigning zero or close to zero weights (dark intensities) to edges and the suppression of in-between regions is continued by high-value weights (bright intensities). Furthermore, the dynamic range of the weighting factors is continuous and varies based on the importance and sharpness of the edges, which demonstrates the adaptive nature of this weighting scheme. The end result of this procedure is in fact the promotion of the sparsity of image estimate in the domain of the sparsifying transform. Figures 8(a–b) show the horizontal gradient field (θ^h) of the MRA frame shown in figure 3 at iteration number 5, thresholded respectively by soft-thresholding and weighted soft-thresholding with the same regularization and penalty parameters. The histograms of the images (20 bins) are shown in figures 8 (c–d). The results show that the SCAD weighting scheme promote the sparsity by zeroing or penalizing small value coefficients that appear as noise and incoherent (noisy-like) artifacts. This is also noticeable in the histograms

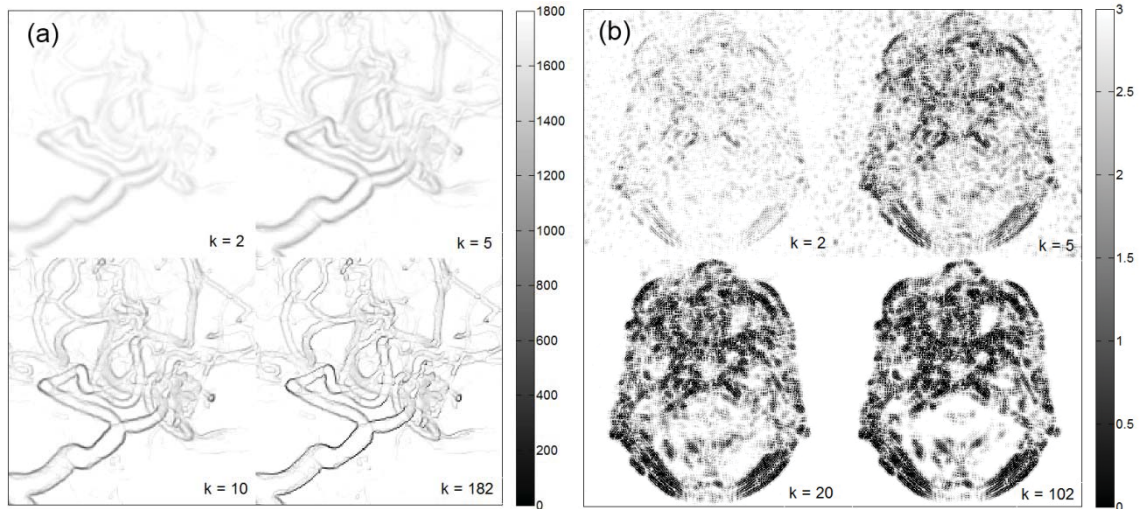


Figure 7. Evolution of the weights (ω^k) of (a) the MRA frame and (b) brain Dixon image shown in figures 3 and 6 with iteration number. The gray-color bar shows the dynamic range of the weights.

where the frequency of coefficients in close-to-zero bins has been reduced, while it has been increased in the zero-bin. To enhance sparsity, Candes *et al.* [30] proposed a reweighted l_1 norm by iterative linearization of a quasi-convex logarithmic potential function. They demonstrated that unlike the l_1 norm, the resulting reweighted l_1 norm (with the weights $\omega_i^k = \lambda(|\theta_i^k| + \epsilon)^{-1}$, in our notation in Eq. (19)) provides a more “democratic penalization” by assigning higher penalties on small non-zero coefficients while encouraging the preservation of larger coefficients. In this sense, a reweighted l_1 norm regularization resembles an l_0 norm, which is an ideal sparsity-promoting, but, intractable norm. Recently, Trzasko *et al.* [19] proposed a homotopic l_0 norm approximation by gradually reducing the perturbation parameter ϵ in quasi-convex norms (e.g. the logarithmic function) to zero. It has been shown that the solution of l_0 penalized least squares problems, such as the one in Eq. (18) with an l_0 regularizer, can be achieved with a hard thresholding rule [54, 55], which thresholds only the coefficients lower than a threshold $\sqrt{2\lambda}$. As observed by Trzasko *et al.*, the hard thresholding rule associated with l_0 regularization increases sparsity and offers strong edge retention in comparison with soft thresholding, which is associated with l_1 regularization. In comparison with the weighting scheme of Candes *et al.* and in connection with the homotopic l_0 approximations, the linearized SCAD regularization invokes a weighted soft-thresholding rule that in limit approaches hard thresholding rule. Figure 9(a) compares the standard hard and soft thresholding rules with the weighted soft-thresholding rule obtained from the linearization of the SCAD function (according to Eq. (17)), for different values of the scale parameter a and for $\lambda = 1$. Similarly, Figure 9(b) compares those standard rules with the weighted soft-thresholding rule by Candes’ weighting scheme for different values of the perturbation parameter ϵ and for $\lambda = 1$. As can be seen, for small values of ϵ , the weighted soft-thresholding rule of SCAD resembles hard thresholding, while for small values of ϵ the Candes’ weighted rule is at best between the standard hard and soft thresholding. On the other hand, for large values of a and ϵ , the SCAD and Candes’ rules respectively approach soft thresholding and an identity rule (which can be thought of as a soft-thresholding with zero threshold). In fact, Fan and Li [37] proposed the SCAD potential function to improve the properties of l_1 and hard thresholding penalty functions (those approximating l_0 norm) in terms of unbiasedness, continuity and sparsity. This function avoids the tendency of soft-thresholding on over-penalizing large coefficients and the discontinuity and thus instability of hard-thresholding and at the same time, promotes the sparsity of the solution [37]. Generalized l_p Gaussian norms, for $0 < p < 1$, have also been successfully used in the context of CS-MRI reconstruction [19, 56]. The sparsity induced by l_p norms is promoted as p approaches zero, since the resulting norm invokes a pseudo l_0 norm. In [57], Foucart and Lai showed that l_p norms give rise to a reweighted l_1 norm with weighting factors $\omega_i^k = \lambda(|\theta_i^k| + \epsilon)^{p-1}$ (in our notation), which reduces to Candes’ weights for $p = 0$. Chartrand [56] derived the so-called p -shrinkage rule for l_p norms, which is in fact a weighted soft thresholding rule with the weights $\omega_i^k = \lambda(|\theta_i^k|)^{p-1}$.

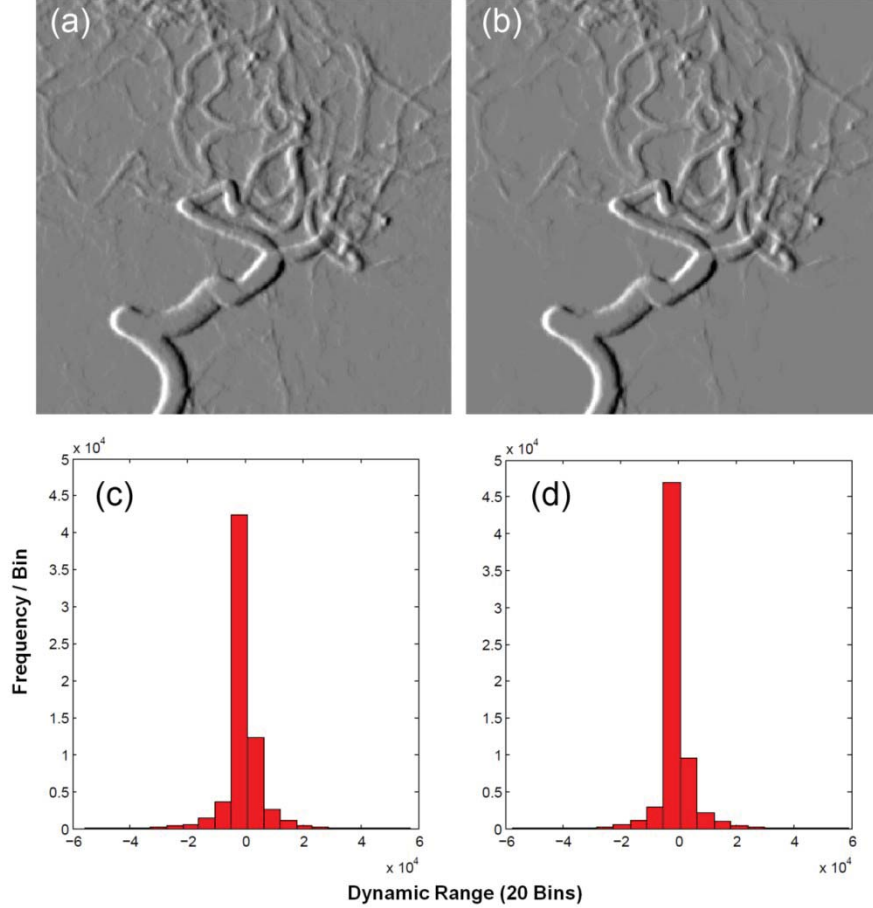


Figure 8. The sparsity promotion of SCAD regularizer. (a–b) The horizontal gradient field of the image frame shown in figure 3 (at iteration 5) thresholded respectively by soft and weighted soft thresholding with the same regularization and penalty parameters. (c–d) The histograms of the images shown in (a) and (b), respectively (with 20 bins). Similar display window is used for the images shown in (a) and (b).

Based on the asymptotic behavior of Candes' weighted soft thresholding (figure (9)), one can conclude that l_p norms (with $0 < p < 1$) best approaches a *semi-hard* thresholding rule for $p = 0$ and $\epsilon = 0$, while the thresholding rule invoked by linearized SCAD can well approach a hard thresholding rule. The results presented in figures 3–5 show that the images reconstructed by l_1 based-ADMM algorithm suffer from an overall smoothing in comparison with SCAD and show to some extent reduced stair-casing artifacts that are sometimes associated with TV regularization using gradient and time-marching based optimization algorithms. These artifacts, which are false and small patchy regions within a uniform region, are often produced by first-order finite differences and can be mitigated by second-order differences [23] or a balanced combination of both [58]. As noted by Trzasko *et al.* [19] and implied from the above discussion, the soft thresholding (associated with l_1 norm) in the ADMM algorithm tends to uniformly threshold the decomposition coefficients, thereby it leads to a global smoothing of the image (similar to wavelet-based reconstructions) and thus the reduction of false patchy regions.

IV.B. Computational complexity and parameter selection

In this study, we solved the standard CS-MRI image reconstruction defined in Eq. (2) using an augmented Lagrangian method. Recently, Ramani *et al* [40] studied AL methods for pMRI and showed that this class of algorithms is computationally appealing in comparison with nonlinear conjugate gradient and monotone fast iterative soft-thresholding (MFISTA) algorithms. In the minimization of the AL function with respect to \mathbf{x} they solved Eq. (11), which also included sensitivity maps of array coils, using a few iterations of the conjugate-gradient algorithm. In contrast, we derived a closed-form solution for this equation in Cartesian CS-MRI, which allowed speeding up the algorithm, particularly by the per-computation of the eigenvalue matrix of the discrete

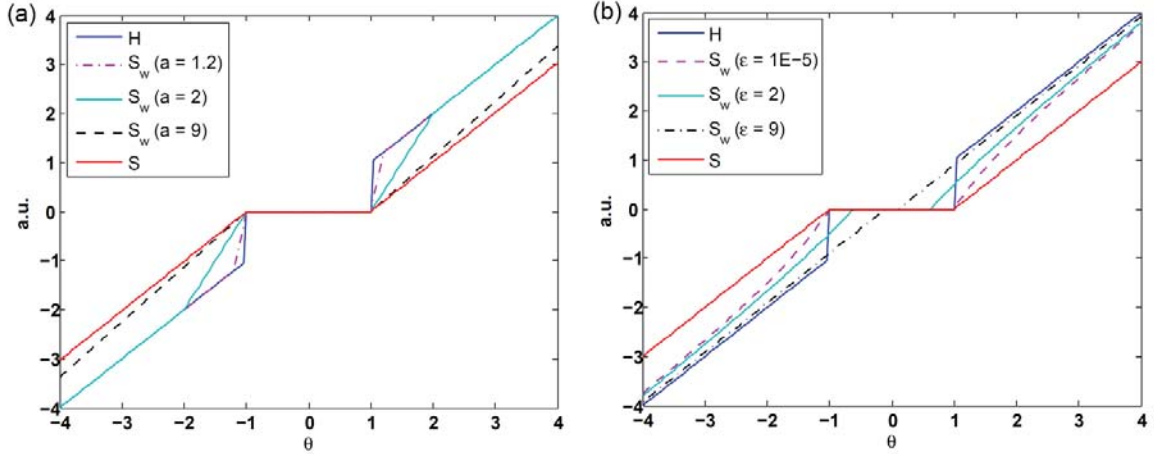


Figure 9. Comparison of hard (H) and soft (S) thresholding rules with soft thresholding (S_w) rules weighted by: (a) the linearization of SCAD function for different scale parameters a and (b) Candes' approach for different perturbation parameters ϵ .

gradient matrix Ψ . As mentioned earlier, this analytic solution can also be assessed by regridding the non-Cartesian data or using the approximation method proposed in [45].

The convergence properties of the proposed SCAD-ADMM algorithm, similar to other optimization algorithms, depends on the choice of the involved parameters, i.e. the penalty parameter ρ the regularization parameter λ and the SCAD's scale parameter a . The choice of these parameters in turn depends on a number of factors including the acquisition protocol, level of noise and the task at hand. As mentioned earlier in the clinical datasets, we optimized the parameter λ and ρ for l_1 regularization to obtain the best qualitative and quantitative results. Using the same parameters, the parameter a was optimized for SCAD regularization. In fact, we followed this parameter selection for an un-biased comparison of the l_1 and SCAD regularizations in order to demonstrate that the proposed technique can improve the performance of l_1 regularization by incorporating iteratively derived weighting factors. However, this parameter selection might not be optimal for SCAD and its convergence properties, since this regularizer tends to gradually and cautiously remove noisy-like artifacts. In particular, we found that higher values of λ improved the convergence rate of the l_1 - and hence SCAD-based algorithms, but at the same time, resulted in overall smoothing of image features, which in the case of SCAD regularization could be compensated by decreasing the scale parameter a . The latter parameter, in fact, controls the impact of weighting factors in SCAD regularization. The lower values of this parameter increase edge-preservation because, as can be seen in figure 9(a), the resulting weighted soft thresholding approaches a hard thresholding rule, which is akin to l_0 regularization. While higher values of a reduce edge preservation, since the weighting factors become uniform and approach the parameter λ . In other words, as seen in figure 9(a), the weighted soft thresholding approaches the standard soft thresholding with a uniform threshold value of λ . In general, it was observed that the parameter a is less data-dependent and shows a higher flexibility for its selection in comparison with λ . An alternative way to choose the pair parameters (a, λ) for SCAD could be two-dimensional grids search using some criteria such as cross validation and L-curve methods [6], which calls for future investigations.

IV.C. Future directions

As our results demonstrate, the SCAD regularization allows for more accurate reconstructions from highly undersampled data and hence reduced sampling rate for rapid data acquisitions. However, it is worth to mention the limitations and future outlook of the proposed SCAD-ADMM algorithm. In this study, we evaluated the proposed algorithm for Cartesian approximation of radial and spiral trajectories and compared its performance with l_1 -based ADMM. This approximation and synthetization of the k -spaces from magnitude images cannot accurately represent the actual data acquisition process in MRI. Nevertheless, our comparative results showed that the proposed regularization can improve the performance of l_1 -based regularization using adaptive identification and preservation of image features. Future work will focus on the evaluation of the proposed

regularization for non-Cartesian datasets and also parallel MR image reconstruction using AL methods [40]. Performance assessment of the SCAD norm in comparison with a family of reweighted l_1 norms and l_0 homotopic norms within the presented AL framework is also underway.

V. Conclusion

In this study, we proposed a new regularization technique for compressed sensing MRI through the linearization of the non-convex SCAD potential function in the framework of augmented Lagrangian methods. Using variable splitting technique, the CS-MRI problem was formulated as a constrained optimization problem and solved efficiently in the AL framework. We exploited discrete gradients and wavelet transforms as a sparsifying transform and demonstrated that the linearized SCAD regularization is an iteratively weighted l_1 regularization with improved edge-preserving and sparsity-promoting properties. The performance of the algorithm was evaluated using phantom simulations and retrospective CS-MRI of clinical studies. It was found that the proposed regularization technique outperforms the conventional l_1 regularization and can find applications in CS-MRI image reconstruction.

Acknowledgment

This work was supported by the Swiss National Science Foundation under grant SNSF 31003A-135576 and the Indo-Swiss Joint Research Programme ISJRP 138866.

References

- [1] S. Plein, T. N. Bloomer, J. P. Ridgway, T. R. Jones, G. J. Bainbridge, and M. U. Sivananthan, "Steady-state free precession magnetic resonance imaging of the heart: Comparison with segmented k-space gradient-echo imaging," *J Magn Reson Imaging*, vol. 14, pp. 230-236, 2001.
- [2] G. McGibney, M. R. Smith, S. T. Nichols, and A. Crawley, "Quantitative evaluation of several partial fourier reconstruction algorithms used in mri," *Magnetic Resonance in Medicine*, vol. 30, no. 1, pp. 51-59, 1993.
- [3] D. J. Larkman, and R. G. Nunes, "Parallel magnetic resonance imaging," *Phys. Med. Biol.*, vol. 52, pp. R15-55, 2007.
- [4] M. Blaimer, F. Breuer, M. Mueller, R. M. Heidemann, M. A. Griswold, and P. M. Jakob, "SMASH, SENSE, PILS, GRAPPA: how to choose the optimal method," *Top Magn Reson Imaging*, vol. 15, pp. 223-236, 2004.
- [5] K. P. Pruessmann, M. Weigher, M. B. Scheidegger, and P. Boesiger, "SENSE: Sensitivity encoding for fast MRI," *Magn Reson Med*, vol. 42, pp. 952-962, 1999.
- [6] W. C. Karl, "Regularization in Image Restoration and Reconstruction," *Handbook of Image and Video Processing*, A. Bovik, ed., San Diego: Academic Press, 2000.
- [7] Z.-P. Liang, R. Bammer, J. Jim, N. J. Pelc, and G. H. Glover, "Improved image reconstruction from sensitivity-encoded data by wavelet denoising and Tikhonov regularization." pp. 493-496.
- [8] F. H. Lin, F. N. Wang, S. P. Ahlfors, M. S. Hamalainen, and J. W. Belliveau, "Parallel MRI reconstruction using variance partitioning regularization," *Magn Reson Med*, vol. 58, pp. 735-744, 2007.
- [9] W. E. Kyriakos, L. P. Panych, D. F. Kacher, C. F. Westin, S. M. Bao, R. V. Mulkern, and F. A. Jolesz, "Sensitivity profiles from an array of coils for encoding and reconstruction in parallel (SPACE RIP)," *Magn Reson Med*, vol. 44, pp. 301-308, 2000.
- [10] L. Ying, B. Liu, M. C. Steckner, G. Wu, M. Wu, and S.-J. Li, "A statistical approach to SENSE regularization with arbitrary k-space trajectories," *Magn Reson Med*, vol. 60, no. 2, pp. 414-421, 2008.
- [11] M. Lustig, D. L. Donoho, and J. M. Pauly, "Sparse MRI: The Application of Compressed Sensing for Rapid MR Imaging," *Magn Reson Med*, vol. 58, pp. 1182-1195, 2007.
- [12] H. Jung, K. Sung, K. Nayak, S. , E. Kim, Yeop , and J. C. Ye, "k-t FOCUSS: A General Compressed Sensing Framework for High Resolution Dynamic MRI," *Magn Reson Med*, vol. 61, pp. 103-116, 2009.
- [13] U. Gamper, P. Boesiger, and S. Kozerke, "Compressed sensing in dynamic MRI," *Magn Reson Med*, vol. 59, no. 2, pp. 365-373, 2008.
- [14] M. Hong, Y. Yu, H. Wang, F. Liu, and S. Crozier, "Compressed sensing MRI with singular value decomposition-based sparsity basis," *Phys. Med. Biol.*, vol. 56, pp. 6311-6325, 2011.
- [15] S. Ravishankar, and Y. Bresler, "MR Image Reconstruction From Highly Undersampled k-Space Data by Dictionary Learning," *IEEE Trans Image Process*, vol. 30, no. 5, pp. 1028-1041, 2011.
- [16] E. Candes, J. Romberg, and T. Tao, "Robust uncertainty principles: exact signal reconstruction from highly incomplete frequency information," *IEEE Trans Inf Theory*, vol. 52, pp. 489-509, 2006.
- [17] D. Donoho, "Compressed sensing," *IEEE Trans Inf Theory*, vol. 52, no. 4, pp. 1289-1306, 2006.
- [18] E. Candès, and J. Romberg, "Sparsity and incoherence in compressive sampling," *Inverse Problems*, vol. 23, no. 3, pp. 969, 2007.
- [19] J. Trzasko, and A. Manduca, "Highly Undersampled Magnetic Resonance Image Reconstruction via Homotopic L0 Minimization," *IEEE Trans Med Imag*, vol. 28, no. 1, pp. 106-121, 2009.
- [20] S. J. M. Lustig M, Donoho D L and Pauly J M, "k-t SPARSE: high frame rate dynamic MRI exploiting spatio-temporal sparsity," in Proc. Intl. Soc. Mag. Reson. Med., Seattle, WA, 2006.
- [21] C. Hu, X. Qu, D. Guo, L. Bao, and Z. Chen, "Wavelet-based edge correlation incorporated iterative reconstruction for undersampled MRI," *Magnetic Resonance Imaging*, vol. 29, no. 7, pp. 907-915, 2011.
- [22] M. Lustig, D. L. Donoho, and J. M. Pauly, "Rapid MR imaging with compressed sensing and randomly under-sampled 3DFT trajectories," in Proc. Intl. Soc. Mag. Reson. Med., Seattle, WA, 2006.
- [23] K. T. Block, M. Uecker, and J. Frahm, "Undersampled radial MRI with multiple coils. Iterative image reconstruction using a total variation constraint," *Magn Reson Med*, vol. 57, no. 6, pp. 1086-1098, 2007.
- [24] G. Adluru, C. McGann, P. Speier, E. G. Kholmovski, A. Shaaban, and E. V. R. DiBella, "Acquisition and reconstruction of undersampled radial data for myocardial perfusion magnetic resonance imaging," *J Magn Reson Imaging*, vol. 29, no. 2, pp. 466-473, 2009.
- [25] L. Chen, G. Adluru, M. Schabel, C. McGann, and E. Dibella, "Myocardial perfusion MRI with an undersampled 3D stack-of-stars sequence," *Med Phys*, vol. 39, no. 8, pp. 5204-5211, 2012.
- [26] F. Knoll, C. Clason, K. Bredies, M. Uecker, and R. Stollberger, "Parallel imaging with nonlinear reconstruction using variational penalties," *Magn Reson Med*, vol. 67, no. 1, pp. 34-41, 2012.
- [27] J. X. Ji, Z. Chen, and L. Tao, "Compressed sensing parallel Magnetic Resonance Imaging," in Proc. IEEE EMBS, 2008, pp. 1671-1674.

- [28] B. Liu, K. King, M. Steckner, J. Xie, J. Sheng, and L. Ying, "Regularized sensitivity encoding (SENSE) reconstruction using bregman iterations," *Magn Reson Med*, vol. 61, no. 1, pp. 145-152, 2009.
- [29] R. Otazo, D. Kim, L. Axel, and D. K. Sodickson, "Combination of Compressed Sensing and Parallel Imaging for Highly Accelerated First-Pass Cardiac Perfusion MRI," *Magn Reson Med*, vol. 64, pp. 767-776, 2010.
- [30] E. J. Candès, M. B. Wakin, and S. P. Boyd, "Enhancing Sparsity by Reweighted L1 Minimization," *J Fourier Anal Appl*, vol. 14, pp. 877-905, 2008.
- [31] C.-H. Chang, and J. Ji, "Parallel Compressed Sensing MRI Using Reweighted L1 Minimization." p. 2866.
- [32] C. Hu, X. Qu, D. Guo, L. Bao, S. Cai, and Z. Chen, "Undersampled MRI reconstruction using edge-weighted L1 norm minimization." p. 2832.
- [33] M. Lustig, J. Velikina, A. Samsonov, C. Mistretta, J. M. Pauly, and M. Elad, "Coarse-to-fine Iterative Reweighted l1-norm Compressed Sensing for Dynamic Imaging." p. 4892.
- [34] D. S. Weller, J. R. Polimeni, L. Grady, L. L. Wald, E. Adalsteinsson, and V. K. Goyal, "Evaluating sparsity penalty functions for combined compressed sensing and parallel MRI." pp. 1589-1592.
- [35] R. Chartrand, "Exact Reconstruction of Sparse Signals via Nonconvex Minimization," *Signal Processing Letters, IEEE*, vol. 14, no. 10, pp. 707-710, 2007.
- [36] W. Yong, L. Dong, C. Yuchou, and L. Ying, "A hybrid total-variation minimization approach to compressed sensing." pp. 74-77.
- [37] J. Fan, and R. Li, "Variable selection via nonconcave penalized likelihood and its oracle properties," *J. Amer. Statistical Assoc.*, vol. 96, no. 456, pp. 1348-1360, 2001.
- [38] F. C. A. Teixeira, S. W. A. Bergen, and A. Antoniou, "Signal recovery method for compressive sensing using relaxation and second-order cone programming." pp. 2125-2128.
- [39] M. V. Afonso, J. M. Bioucas-Dias, and M. A. Figueiredo, "Fast image recovery using variable splitting and constrained optimization," *IEEE Trans Image Process*, vol. 19, no. 9, pp. 2345-56, Sep, 2010.
- [40] S. Ramani, and J. A. Fessler, "Parallel MR Image Reconstruction Using Augmented Lagrangian Methods," *IEEE Trans Med Imag*, vol. 30, no. 3, pp. 694-706, 2011.
- [41] J. Nocedal, and S. J. Wright, *Numerical Optimization*, 2th ed.: Springer, 2006.
- [42] M. Powell, "A method for nonlinear constraints in minimization problems," *Optimization*, R. Fletcher, ed., pp. 283-298, New York: Academic Press 1969.
- [43] J. Eckstein, and D. Bertsekas, "On the DouglasRachford splitting method and the proximal point algorithm for maximal monotone operators," *Mathematical Programming*, vol. 5, pp. 293-318, 1992.
- [44] Y. Wang, J. Yang, W. Yin, and Y. Zhang, "A New Alternating Minimization Algorithm for Total Variation Image Reconstruction," *SIAM J. Imaging Sciences*, vol. 3, pp. 248-272, 2008.
- [45] M. Akcakaya, S. Nam, T. Basha, V. Tarokh, W. J. Manning, and R. Nezafat, "Iterative Compressed Sensing Reconstruction for 3D Non-Cartesian Trajectories without Gridding & Regridding at Every Iteration." p. 2550.
- [46] D. Hunter, and R. Li, "Variable selection using mm algorithms," *Ann. Statist.*, vol. 33, pp. 1617-1642, 2005.
- [47] H. Zou, and R. Li, "One-step sparse estimates in nonconcave penalized likelihood models," *Ann. Stat.*, vol. 36, pp. 1509-1533, 2008.
- [48] A. Antoniadis, and J. Fan, "Regularization of wavelets approximations," *J. Am. Stat. Assoc.*, vol. 96, pp. 939-967, 2001.
- [49] *MRI UNBOUND*, http://www.ismrm.org/mri_unbound/simulated.htm.
- [50] *BRAINWEB*, <http://www.bic.mni.mcgill.ca/brainweb/>.
- [51] W. Zhou, A. C. Bovik, H. R. Sheikh, and E. P. Simoncelli, "Image quality assessment: from error visibility to structural similarity," *IEEE Trans Image Process*, vol. 13, no. 4, pp. 600-612, 2004.
- [52] D. S. Lalush, and B. M. W. Tsui, "A fast and stable maximum a posteriori conjugate gradient reconstruction algorithm," *Med Phys*, vol. 22, no. 8, pp. 1273-1284, 1995.
- [53] M. Lustig, D. L. Donoho, J. M. Santos, and J. M. Pauly, "Compressed Sensing MRI," *IEEE Signal Process Mag*, vol. 25, no. 2, pp. 72-82, 2008.
- [54] T. Blumensath, M. Yaghoobi, and M. E. Davies, "Iterative Hard Thresholding and L0 Regularisation." pp. III-877-III-880.
- [55] S. J. Wright, R. D. Nowak, and M. A. T. Figueiredo, "Sparse Reconstruction by Separable Approximation," *IEEE Trans Signal Process*, vol. 57, no. 7, pp. 2479-2493, 2009.
- [56] R. Chartrand, "Fast algorithms for nonconvex compressive sensing: MRI reconstruction from very few data." pp. 262-265.
- [57] S. Foucart, and M. Lai, "Sparsest solutions of underdetermined linear systems via Lq-minimization for $0 < q < 1$," *Appl. Comput. Harmon. Anal.*, vol. 26, pp. 395-407, 2009.
- [58] F. Knoll, K. Bredies, T. Pock, and R. Stollberger, "Second order total generalized variation (TGV) for MRI," *Magn Reson Med*, vol. 65, no. 2, pp. 480-491, 2011.

Chapter 7

Magnetic resonance imaging-guided attenuation correction in PET/MRI: challenges, solutions and opportunities

Abolfazl Mehranian, Hossein Arabi and Habib Zaidi

Med Phys (2015) submitted

Abstract

Attenuation correction is an essential component and is by far the most important among the long chain of data correction techniques required for quantitative PET imaging. The development of combined PET/MRI systems stimulated the widespread interest in developing novel strategies for deriving accurate attenuation maps with the aim to improve the quantitative accuracy of these emerging hybrid imaging systems. The attenuation map in PET/MRI should ideally be derived from anatomical MR images; however, MRI intensities reflect proton density and relaxation time properties of biological tissues rather than their electron density and photon attenuation properties. Therefore, in contrast to PET/CT, there is a lack of standardized global mapping between the intensities of MRI signal and linear attenuation coefficients at 511 keV. Moreover, in standard MRI sequences, bones and lung tissues do not produce measurable signals owing to their low proton density and short transverse relaxation times. MR images are also inevitably subject to artifacts that degrade their quality, thus compromising their applicability for the task of attenuation correction in PET/MRI. MRI-guided attenuation correction strategies can be classified in three broad categories; (i) segmentation-based approaches, (ii) atlas-registration and machine learning methods, and (iii) emission-based approaches. This paper summarizes past and current state-of-the-art developments and latest advances in PET/MRI attenuation correction. The advantages and drawbacks of each approach for addressing the challenges of MR-based attenuation correction is comprehensively described. The opportunities brought by both MRI and PET imaging modalities for deriving accurate attenuation maps and improving PET quantification will be elaborated. Future prospects and potential clinical applications of these techniques and their integration in commercial systems will also be discussed.

I. INTRODUCTION

Hybrid positron emission tomography/magnetic resonance imaging (PET/MRI) has emerged as a new imaging modality enabling concurrent morphological and molecular characterization of different organs/tissues and physiopathological conditions. Over the last decade, tremendous efforts have been directed toward addressing the challenges faced by PET/MRI systems from two perspectives: (i) instrumentation and conceptual system design and (ii) improvement of quantitative performance to achieve at least comparable accuracy to standard PET/computed tomography (PET/CT) systems. With the advent of solid-state photodetectors, such as avalanche photodiodes and silicon photomultipliers, the challenge of mutual compatibility between PET and MRI subsystems has now been well addressed, paving the way toward fully integrated clinical time-of-flight (TOF) PET/MR systems [1-3]. However, accurate attenuation correction (AC) of PET data has remained another major challenge in PET/MRI [4, 5]. A number of active research groups have focused on the development of innovative techniques for deriving accurate attenuation maps to improve the quantitative accuracy of PET/MR imaging. During the last decade, significant progress has been achieved in this field as thoroughly appraised in previous reviews by Hofmann *et al.* [6], Bezrukov *et al.* [4] and many others [7-9].

In this work, we examine the challenges and recent technical advances in the rapidly evolving field of attenuation correction in PET/MRI. Overall, AC methods in PET/MRI can be categorized into three main classes: (i) segmentation-based approaches, which segment MR images into different tissue classes and assign predefined attenuation coefficients to each class, (ii) atlas-based and machine learning techniques in which a co-registered MR-CT atlas dataset is used to derive a pseudo-CT image and/or to learn a mapping function that predicts the pseudo-CT image from patient-specific MR image and (iii) the recently revisited emission- and transmission-based methods, in which the attenuation map is estimated from TOF emission or transmission data. We first briefly review the problem of photon attenuation in PET and AC approaches used on standalone PET and PET/CT scanners, which constitute a basis for the development of AC methods in PET/MRI. We then discuss the challenges and technical considerations involved for attenuation map generation in PET/MRI and provide a detailed overview of MRAC methods with special emphasize on their pros and cons. A possible scenario of future developments and opportunities is also provided.

I.A Photon attenuation in PET

The radionuclides used in PET imaging constantly undergo nuclear transmutation through the emission of a positron and neutrino. After traveling a random and tortuous path and colliding with different atoms, the positron annihilates with an electron resulting in the coincident emission of two 511-keV photons in almost opposite directions. In PET imaging, these annihilation photons are recoded and the biodistribution and activity concentration of the radiotracer is then estimated through the tomographic reconstruction of the acquired data. Due to photoelectric and mostly Compton scattering interactions of 511-keV photons with biological tissues, only a fraction of the emitted photon pairs are recorded along each line of response (LOR). According to Beer-lambert law, $\exp(-\int_L \mu(x)dx)$, this fraction depends on the thickness of the attenuating material, L , and the energy-dependent linear attenuation coefficients (LAC), μ , of the tissues (Figure 1A).

The reconstruction of PET data without correcting for photon attenuation will therefore result in the under/over-estimation of tracer concentration (Figure 1B) and inaccurate measurements of tracer uptake. In fact, attenuation correction is crucial for accurate and reproducible measurements of standardized uptake value (SUV) for characterizing lesions (e.g. based on a maximum SUV threshold of 2.5) and monitoring response to chemo-radiation therapies. The task of attenuation correction is thus to derive the attenuation correction factors (ACF) and apply them to measured data either before reconstruction (pre-correction) for analytic filtered back-projection image reconstruction or during reconstruction for model-based iterative reconstruction, such as ordinary Poisson or attenuation-weighted ordered subsets expectation maximization (OSEM).

I.B Attenuation correction in PET

In standalone PET scanners, such as the Siemens high-resolution research tomograph (HRRT) dedicated for brain imaging, patient-specific ACFs are derived from the acquisition of a transmission scan using external

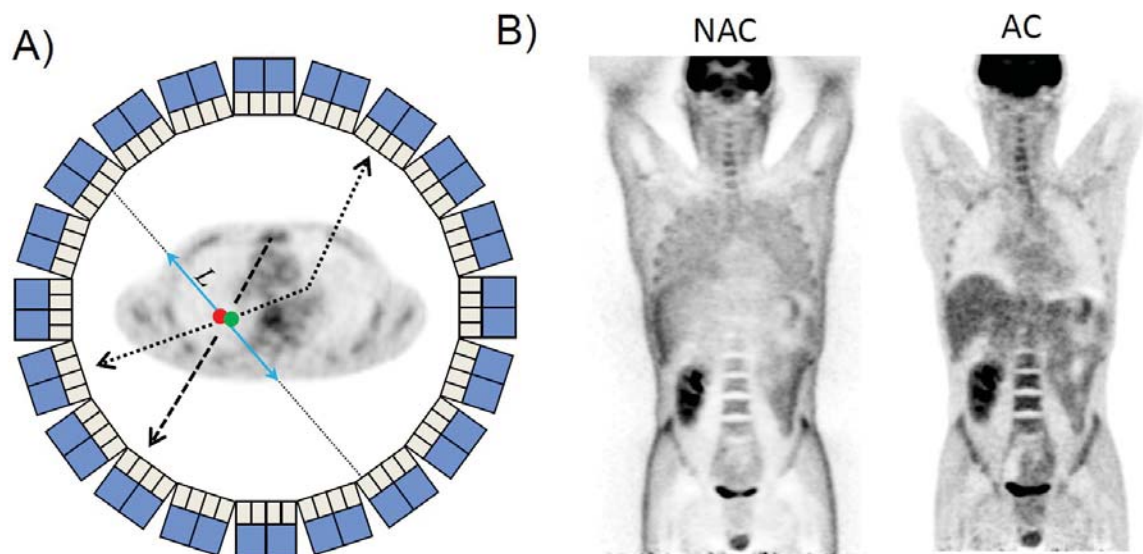


Figure 1. (A) Attenuation of annihilation photons due to photoelectric absorption (dash) and Compton scattering (dot). (B) PET images reconstructed without (NAC) and with (AC) attenuation correction.

positron-emitting ($^{68}\text{Ga}/^{68}\text{Ge}$) or single-photon (^{137}Cs)-emitting radionuclide sources before (pre-injection), during (simultaneous), or after (post-injection) the PET emission scan. Pre- or post-injection transmission scans increase substantially the total examination time, while simultaneous acquisition reduces the scan time at the expense of the contamination of transmission and emission data. To avoid noise and bias propagation from transmission to emission images, the resulting attenuation maps are usually segmented into different tissue classes such as air, lung, soft tissue and bone followed by assignment of predefined attenuation coefficients at 511-keV to each tissue class [10-12]. Another approach is to register a generic transmission attenuation map (template) to non-attenuation corrected (NAC) emission images and to exploit the aligned template for attenuation correction [13, 14].

With the advent of combined PET/CT scanners, anatomical CT images are used for proper AC of PET data, eliminating lengthy and noisy transmission scans on standalone PET scanners. Since CT units (Hounsfield units) are directly related to the attenuation properties of tissues at 70-140 kVp, the images can be directly converted into attenuation maps at a photon energy of 511 keV using a kVp-dependant bilinear mapping [15]. CT images are less noisy and acquired much faster than transmission scans. In addition, they facilitate substantially the task of lesion localization in PET images through image fusion. In PET/MRI system, MRI provides high spatial resolution anatomical images with superior soft-tissue contrast compared to CT. Therefore, combined PET/MRI is expected to be the method-of-choice in clinical oncology with neoplasms associated with soft-tissue regions, e.g. lesions in the pelvis, head-and-neck region, or brain. However, attenuation correction is challenging and not as straightforward as in PET/CT.

I.C Challenges of MRI-guided attenuation correction

In PET/MRI, the attenuation map at 511 keV should ideally be derived from the acquired MR images. However, contrary to x-ray CT, MRI signals are not correlated with electron density and photon attenuating properties of tissues, but rather to proton density and magnetic relaxation properties. Therefore, there is no unique global mapping technique to convert MRI intensities to attenuation coefficients. Similar to early transmission-based AC methods, the most straightforward way to derive attenuation maps in PET/MRI is to classify MR images for segmentation of different tissue classes and assign proper LACs to each tissue class. However, lung tissues and cortical bones, which are two important tissue types in attenuation maps, exhibit low signals on images acquired using conventional spin-echo or gradient-recalled echo (GRE) MR pulse sequences owing to their low water content and short transverse (T_2) relaxation time. Therefore, the lungs, bones and air pockets, which also produce a low MR signal intensity, cannot be well differentiated from each other for the generation of MRI segmentation-based attenuation maps. Ultra-short echo time (UTE) pulse sequences have also been investigated

for the detection and visualization of bones [16, 17] as well as lung parenchyma [18]. However, UTE MRI is prohibitively timing-consuming and sensitive to magnetic field inhomogeneities and, as such, it is not yet clinically feasible for whole-body MRI-guided attenuation correction (MRAC) of PET data. However, substantial progress has been recently achieved in accelerated sub-Nyquist MRI acquisitions using parallel MRI and compressed sensing techniques, which are particularly suited for UTE data acquisition [19, 20].

In contrary to PET/CT, in whole-body PET/MRI scans, the arms are positioned down mainly because of patient comfort and support as well as coil positioning compliance. However, the limited transaxial field-of-view (FOV) of MRI scanners (45-50 cm) can result in the truncation of the arms and shoulders in the acquired MRI images compared to the larger useful transaxial FOV of PET scanners (60-70 cm). The generation of attenuation maps from truncated MR images is another challenge in terms of deriving complete attenuation maps in whole-body scans. In patients having metallic implants, such as titanium prosthesis or dental fillings, the main magnetic field around the implants is usually locally distorted producing expansive signal voids with peripheral areas of high intensity known as blooming or magnetic susceptibility artifacts. These artifacts are more pronounced in fast GRE MRI sequences, often used for MRAC, due to the lack of 180° refocusing radio-frequency (RF) pulses. The void artifacts can be miss-segmented or lead to inaccurate LAC prediction by atlas-based learning techniques.

A further challenge arises from the attenuation and scattering of annihilation photons by MRI RF coils in integrated or insert-based PET/MRI systems as well as other attenuating objects present in the PET FOV including patient’s bed and patient positioning aids. In whole-body MRI imaging, integrated body coils are usually used for receiving MRI signals. Moreover, to improve signal-to-noise ratio, without compromising acquisition time, flexible surface RF coils or head and neck coils are employed during scanning. Similar to bony structures, short T₂ materials do not provide measurable signals in conventional MRI sequences and therefore remain invisible. The presence of such attenuating material especially flexible coils that can be placed in arbitrary positions and orientations can locally affect PET quantification and should therefore be included in the attenuation map. Several other challenges and problems specific to each category of MRAC methods are discussed in the following section together with recent advances in the field.

II. STRATEGIES FOR ATTENUATION CORRECTION IN PET/MRI

II.A Segmentation-based AC methods

The attenuating tissues in the body consist mainly of soft tissues, adipose (fat) tissue, lungs, air cavities (sinuses, abdominal air pockets) and cortical and spongy bones. Each tissue class has a different electron density and therefore different intra/inter-patient attenuation coefficients at 511 keV as summarized in Table 1. In segmentation-based MRAC methods, the aim is to segment MR images into as much tissue classes as possible and to assign representative, or if possible, patient-specific, linear attenuation coefficients at 511 keV to each tissue class. As mentioned earlier, in conventional MRI scans, bones cannot be well discriminated from air cavities in the head and most soft and fat tissues in whole-body imaging.

1) *Brain Imaging.* In brain PET imaging, the cortical bones of the skull substantially contribute to the attenuation and scattering of annihilation photons. For accurate PET quantification, the bones must therefore be accounted in the MRAC map. Otherwise if substituted by soft tissue, the tracer uptake might be underestimated by up to 25% in cortical regions and 5-10% in central regions of the cranium, as recently reported by Anderson *et al.* [21] using 19 brain clinical PET/MRI scans.

Table 1. Attenuation coefficients at 511-keV of different biological tissues (see Table 2 in Ref. [7] for relevant references).

Tissue	Linear attenuation coefficient (cm ⁻¹)
Lung	0.018–0.03
Adipose tissue	0.086–0.093
Soft tissue	0.094–0.100
Spongy bone	0.110
Cortical bone	0.130–0.172

In a comparative study between PET, PET/CT and PET/MR using an anatomical brain phantom, Teuho *et al.* [22] also reported the largest underestimations (11% to 17%) in the temporal cortex and orbito-frontal cortex.

To the best of our knowledge, the first segmentation-based MRAC method was reported by Le Goff *et al.* [23] for brain PET/MR imaging. MRI images were classified into background air, soft tissue and bones using thresholding, morphological filtering and connect component analysis. Despite the sinuses were not classified and the eyes were mis-classified, the local relative errors in tracer uptake did not exceed 12%. Zaidi *et al.* [24] improved upon this approach by using supervised fuzzy C-means clustering that could identify the sinus and thus segment T₁-weighted MR images into air, brain tissue, skull and nasal sinuses. Predefined tissue-dependent linear attenuation coefficients were then assigned to different tissue classes. Volume-of-interest (VOI)-based quantitative analyses showed a high correlation between MRAC and ¹³⁷Cs transmission-AC PET images in most regions of the brain. Wagenknecht *et al.* [25] proposed an automatic three-step approach in which neural network-based segmentation and prior knowledge about brain's anatomical regions and their relative positions are exploited to distinguish tissue classes. Although MR segmented regions showed a high correspondence with the CT segmented regions, this technique might result into mis- or over-segmentation of bones in the case of abnormal anatomy or presence of pathology, where the anatomical pre-assumptions will no longer hold true.

The above segmentation approaches attempt to indirectly segment bones from air-filled cavities. However, in the presence of anatomical abnormalities or MRI artifacts, the probability of miss-classification errors is irreducible. Therefore, UTE MRI-based methods were explored since 2010 for bone visualization and direct segmentation of bones in brain studies. Catana *et al.* [16] and Keereman *et al.* [17] used a dual-echo UTE MRI sequence to derive 3-class attenuation maps including air, soft tissue and bones. In this sequence, bone signal is present in the first ultrashort echo time (TE1) and absent in the second longer echo time (TE2), while the signal of other tissues remains the same in both echoes. As a result, in both studies, bones intensities were enhanced using arithmetical operations based on the difference of TE images. Catana *et al.* [16] used a morphological closing and arithmetical operations based on the sum of TE images to identify the air-filled regions, while Keereman *et al.* [17] used a region-growing and thresholding scheme to segment air cavities and outer head air. Despite the promising results, bone classification was subject to errors in bone/air or soft-tissue air interfaces due to diamagnetic susceptibility effects at these interfaces.

Berker *et al.* [26] proposed a UTE triple-echo MRI sequence, combining UTE and Dixon sequences for bone detection and fat separation in order to generate a 4-class PET attenuation map. In the Dixon sequence, the fact that fat and water protons precess at slightly different frequencies (chemical shift effect) is exploited to generate in- and out-phase images from which fat-only and water-only images are obtained. Bones were segmented from differential UTE images using empirical thresholding and multiple morphological filtering. The 4-class attenuation maps exhibited a high visual similarity to reference CT-based attenuation correction (CTAC) maps. Despite bone misclassifications at paranasal sinuses, over 80% of voxels in 6 studied patients were correctly classified.

Recently, Delso *et al.* [27] assessed the performance of dual-echo UTE imaging for bone segmentation in head and neck imaging of 20 patients scanned on a trimodality PET/CT-MR system [28]. Their results showed that the UTE segmented bones produce an acceptable overlap with reference CT bones over the skull, however, segmentation errors increase at (i) the base of the skull due to the presence of several unwanted structures with short echo times (e.g. facial and neck musculature), (ii) air interfaces due to diamagnetic susceptibility artifacts, (iii) posterior part of eyeballs due to eye motion during acquisition and (iv) dental arch region due to metallic artifacts. They concluded that the above artifacts can degrade the reconstructed PET images and, as such, more sophisticated approaches are necessary to compensate for these effects.

2) *Whole-body Imaging.* In whole-body imaging, MR images are similarly segmented into different tissue classes to which predefined LACs are assigned. Contrary to brain imaging, the segmentation of bones is much more challenging in whole-body imaging, especially the vertebra where the bones are spongy and contain either hematopoietic or fatty tissues with a moderate MR intensity. The application of UTE MRI sequences for whole-body bone segmentation is not feasible yet since it is time-consuming for routine clinical usage. Moreover, the radial k-space acquisition, used to reduce TE acquisition time as much as possible, results in a spherical reconstructed FOV, whereby the body contour can be truncated [17]. Fat/soft-tissue to bone miss-classifications and vice versa are also inevitable in whole-body UTE images [29]. Apart from the segmentation of bones, other challenges of segmentation-based MRAC methods in whole-body imaging include accurate segmentation of the lungs and the assignment of patient-specific attenuation coefficients to each tissue class, especially the lungs

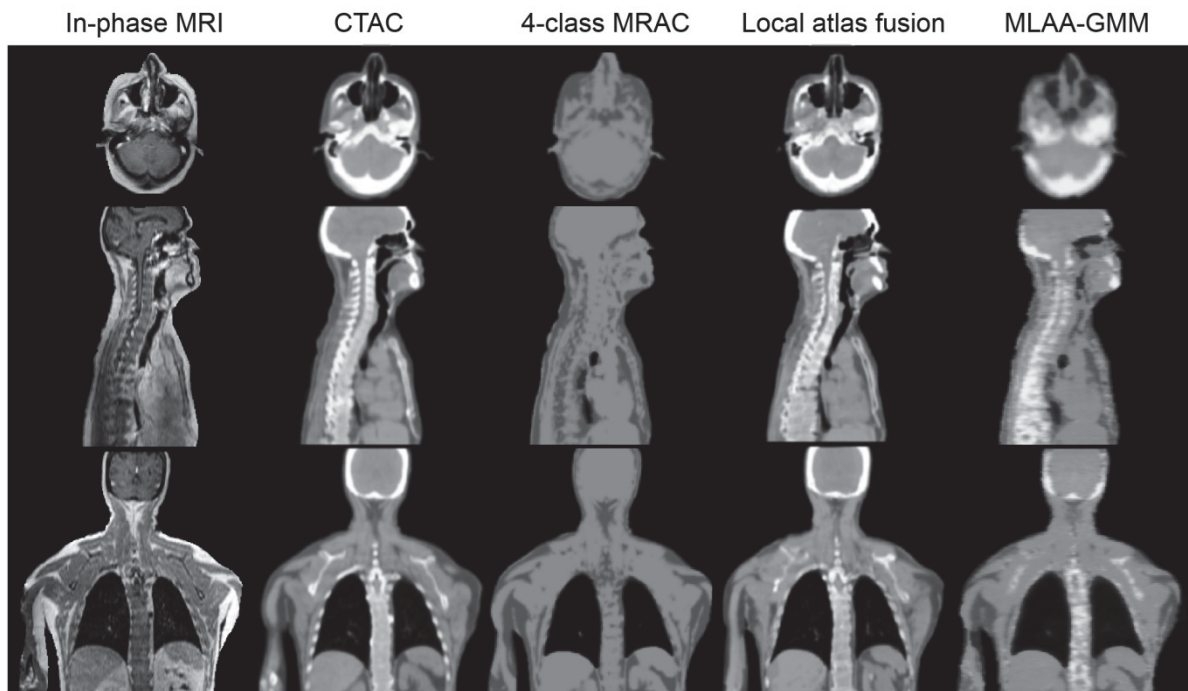


Figure 2. Comparison of the attenuation maps obtained by the 4-class segmentation based method [33], local weighted atlas fusion [34] and an MRI-guided emission based method [35]. Adopted with permission from Mehranian and Zaidi [36].

given their heterogeneity. The latter problem is elaborated below in the section *Inter/intra-patient variability of LACs*.

Current whole-body MRAC methods rely on the segmentation of the MR images into 3 or 4 tissue classes, where bones are substituted by soft-tissue. Hu *et al.* [30, 31] implemented a 3-class attenuation map on the Ingenuity TF PET/MR system [32] by segmenting MR images of a 3D T1-weighted spoiled gradient echo sequence (known as *atMR*) into background air, lungs and soft tissue. The *atMR* sequence, which takes about 3 min for a 100 cm axial coverage, is merely designed for the segmentation of body contour and lungs. The lungs are segmented using a deformable shape model initialized by an intensity-based region-growing segmentation technique. This lung-model adaptation prevents the leakage of the lungs into the stomach and intestine, and also allows for improved lung segmentation in the presence of cardiac and respiratory motion artifacts [31]. Using 15 patients, an overall underestimation of tracer uptake by up to 10% in malignant lesions was reported. [30]

Schulz *et al.* [37] also proposed a 3-class segmentation of MRI images obtained from a 3D gradient and spin echo sequence with a flip angle of 2° . This sequence, essentially yielding a proton-density weighting, was chosen to equalize fat and water signals and thus increase the reliability of automatic segmentation of the MR images into 3-classes. The external body contour and lungs were segmented using thresholding of the Laplace-weighted histogram of MR images and a region-growing technique, respectively. Using 15 whole-body PET-CT/MR patients, they reported a systematic over- and under-estimations of SUV in bony and fatty regions, respectively. Overall, the bias was $<7\%$ in most malignant lesions.

To include fat as 4th tissue class, Martinez-moller *et al.* [33] used a 2-point Dixon sequence for the separation of fat and water. In this proof-of-principle study, they used 35 clinical PET/CT scans to demonstrate the potential merit of 4-class MRAC attenuation map in PET/MRI imaging. They reported a mean SUV error of about -8% for bone lesions and concluded that this bias in SUV estimation is clinically irrelevant. In a follow-up study using 35 PET/CT and Dixon T1-weighted MR images, Eiber *et al.* [38] demonstrated that there is no statistically significant difference between PET/MRI and PET/CT for the anatomical localization of 81 PET positive lesions. Their quantitative results also showed that the 4-class MRAC PET images have a high SUV correlation to reference CTAC PET images. Figure 2 compares the attenuation maps of a representative study produced using the segmentation-based 4-class technique with atlas- and emission-based algorithms.

Hoffmann *et al.* [39] included a mixture of fat and soft tissues as 5th class (in addition to air, lung, fat and soft tissue classes) and evaluated this segmentation method and their proposed atlas-based approach using 11 PET/MRI/CT datasets. The in-phase, water and fat images were segmented in 5 classes using intensity-based thresholding, morphological filtering and connect component analysis. The authors reported mean absolute SUV errors of 8% and %14 in lesions and regions of normal uptake, respectively.

Wollenweber *et al.* [40] recently proposed a continuous fat/water (CFW) method allowing for the continuous variation of fat and soft tissue. A phase-field-based segmentation technique was employed to segment body contour, lungs and trachea in the thorax and air pockets in the abdomen. In this approach, fat and water fraction images are calculated and used to derive continuous fat and water attenuation coefficients within the interval 0.086 - 0.1 cm⁻¹. The quantitative analysis showed that the CFW and 4 discrete-class MRAC methods result in mean SUV errors of 10.4% and 5.7% in the liver and 1.7%, and -1.6% in malignant lesions, respectively.

To evaluate the importance of bones in whole-body MRAC attenuation maps, Hofmann *et al.* [39] substituted bones in CTAC attenuation maps of 11 PET/CT patients by soft tissues. Their results demonstrated that the substitution of bones with soft tissue results in mean SUV errors of 4% in 88 VOIs defined in soft tissues adjacent to bones in the pelvic region and 3% in 28 VOIs defined in soft-tissue lesions. A similar study was conducted by Samarini *et al.* [41] using 22 PET/CT patient datasets. Their results showed an underestimation of tracer uptake of 11% and 3% in osseous and soft tissue lesions adjacent to bones, respectively. For sclerotic and osteolytic spine lesions, mean SUV underestimations of 16% and 7% were reported, respectively.

3) *Segmentation of non-attenuation corrected PET images.* The segmentation of NAC PET images to define 3 tissue classes (i.e. background air, lung, and soft tissues) has also been investigated [42]. Recently, Chang *et al.* [43] proposed a three-step iterative PET segmentation method for whole-body ¹⁸F-FDG scans. In the first step, an initial attenuation map is produced by segmenting body contour from NAC PET images using an active contour method followed by reconstruction of PET images using this attenuation map. In the second step, the attenuation map is refined by segmenting the lungs from the resulting AC PET images using a thresholding approach. PET images are then reconstructed using this updated attenuation map. Finally, the heart and liver, mis-segmented as lung tissue, are removed using a manually-seeded region growing technique. However, tissue classification from NAC PET images is generally limited to radiotracers that distribute throughout the body such as ¹⁸F-FDG and will not work for specific tracers. These techniques have been extensively employed to reduce truncation and metal artifacts in MRI-derived attenuation maps, as discussed in the following sections.

II. B Atlas-based segmentation, registration and machine learning methods

To predict attenuation coefficients on a continuous scale, current methods rely on either atlas or template registration to the target subject or the use of machine learning techniques to train a classifier or mapping function to segment MR images or convert them into pseudo-CT images. Due to the reduced inter-patient variability and rigid structure of the head region, atlas-based and machine learning approaches can produce fairly accurate attenuation maps. However, in whole-body imaging where there is substantial inter-patient variability of anatomy and anomalies, these approaches still require further research and development efforts to be capable of producing accurate and cost-effective attenuation maps. In the following, we review the different atlas-based approaches with special emphasis on latest developments and advances in brain and whole-body imaging.

1) *Atlas-based and machine learning methods in brain imaging.* Montandon and Zaidi [44] proposed and applied a transmission atlas-guided attenuation correction in cerebral 3D PET imaging to reduce the acquisition time by eliminating transmission scanning. Patient-specific attenuation map is obtained by anatomic standardization through nonlinear warping of a stereotactic transmission template of normal subjects. Templates are usually created by taking the average of multiple co-registered brain attenuation maps to represent mean attenuation values and anatomical variability of a given population [45]. Rota Kops *et al.* [46, 47] proposed and evaluated a brain attenuation map generation technique using a reference template. The final attenuation map is created by registration of the template to the target patient's MR image. Wollenweber *et al.* [48] conducted a study to evaluate atlas-based PET attenuation correction in the head. An atlas-based pseudo-CT was generated based on a probabilistic head atlas using attenuation corrected CT images derived from 50 subjects. The method includes enhancement of bones in T1-weighted MR images using a combination of 3 mm Hessian operators to create a flatness measure followed by a local non-rigid registration between the bone-enhanced MR and the CT-based skull atlas. The resulting pseudo-CT images were compared to a 3-class segmentation of the CT (air, fat, soft tissue) and CT-based AC. PET activity concentration was systematically under-estimated on average by

4.9% when using the segmented CT-based AC. Conversely, the atlas-based method reduced the error to 0.2% on average. It was concluded that atlas-based AC in the head provides adequate PET quantification and image quality compared to methods that do not account for bone. Hofmann *et al.* [49] proposed a method combining prior knowledge available in the aligned atlas dataset with pattern recognition to generate patient-specific attenuation map in brain imaging. In the first step, a number of matched MR-CT pairs are registered to the target subject to create an atlas template. Then, a Gaussian regression process (GRP) is utilized to predict the substitute CT value for each voxel based on robust measurement of intensity similarity and spatial closeness of patches of voxels between the target image and atlas dataset. The GRP has been adopted to provide more patient-specific pseudo-CT estimation and to increase robustness to local miss-registration through selection of better local matches from the dataset for each voxel individually. The quantitative analysis of 17 clinical studies reported a mean relative error of 3.2% for predefined regions of interest [49]. Schreibmann *et al.* [50] developed a multimodality optical flow deformable model for registration of single patient CT as template to the target MR image to predict an attenuation map for PET AC. Malone *et al.* [51] used an average of 10 transmission images to create a template attenuation map and evaluated two different image registration algorithms, namely SPM2 [52] and CISG [53], for brain MRAC.

In an attempt to generate brain attenuation maps for PET AC without the need for atlas registration, Chan *et al.* [54] proposed a voxel-wise classification method for bone/air segmentation from MR images using random forest classifier. A supervised random forest scheme was realized and trained based on a bag of features (such as gradient correlation, gray level, edges, local image context) extracted from structural diffusion-weighted MR and uncorrected PET images. Using 10 patients, the Dice similarity score (DSC) between the segmentation results and the ‘ground truth’ obtained by thresholding CT images revealed an accuracy of 0.83 ± 0.08 and 0.98 ± 0.01 for air gaps and bone, respectively. The same idea was evaluated by Yang *et al.* [55] utilizing conditional random field and image fusion based on dual-tree complex wavelet transform and extracted features from uncorrected PET and T1 weighted MR image. The assessment of 20 clinical brain images using the DSC metric showed an accuracy of 72.90, 96.65 and 98.94 for bone, air and soft-tissue, respectively.

In a comparative study, Uh *et al.* [56] demonstrated that the method proposed by Hofmann [49] may not be able to provide significant improvement compared to other atlas methods such as arithmetic average of aligned CT atlas images, questioning its relevance given its high computation time. They concluded that arithmetic means process may be a reasonable choice for clinical practice considering performance and computational costs issues, while single atlas or template registration or assigning a bulk CT number to the entire patient volume introduced remarkable bias. To increase the robustness of atlas-based methods to miss-registration errors, Burgos *et al.* [57, 58] developed synthetic CTs through a multi-atlas information propagation scheme where the MRI-derived patient’s morphology is locally matched to the aligned dataset of MRI-CT pairs using a robust local image similarity measure based on local normalized cross-correlation (LNCC) criterion. The local matching through morphological similarity enables the algorithm to find local matches and similar anatomy across atlas dataset. Therefore, the poor matched atlases are discarded or at least given lower weights, thus leading to a more patient-specific pseudo-CT. The obtained pseudo-CT images were compared to a segmentation-based method using an UTE MRI sequence and to a simplified atlas-based method resulting in a mean brain PET quantification relative error of 0.17%, -11.78% and 0.78%, respectively. Examples of ground truth CT, proposed pseudo-CT, best-atlas CT, UTE CT and difference images are presented in Figure 3.

Izquierdo-Garcia *et al.* [59] presented an approach for AC of brain PET data using Statistical Parametric Mapping 8 software (SPM8) taking advantage of both segmentation and atlas-derived features to generate a robust attenuation map. Anatomic MR images of 15 subjects were first segmented into 6 distinct tissue classes and then non-rigidly co-registered using a diffeomorphic approach to generate MR-CT pair template. Thereafter, for a given subject, a similar procedure is carried out to co-register the target MR image to the template and the pseudo-CT image is constructed by applying the inverse transformations. In fact, the incorporated segmentation part enriched the available information in MR images allowing for a more accurate registration outcome. The quantitative analysis of the corresponding reconstructed PET images revealed mean relative errors of $3.87 \pm 5.0\%$ and $2.74 \pm 2.28\%$ for voxelwise- and region of interest-based analysis, respectively.

Chen *et al.* [60] developed an atlas-based brain attenuation map exploiting a probabilistic segmentation of air canal and sinus and sparse regression strategy for atlas fusion. The sparse regression has been designed to assign greater weights to atlas images exhibiting better local intensity match during the atlas fusion process.

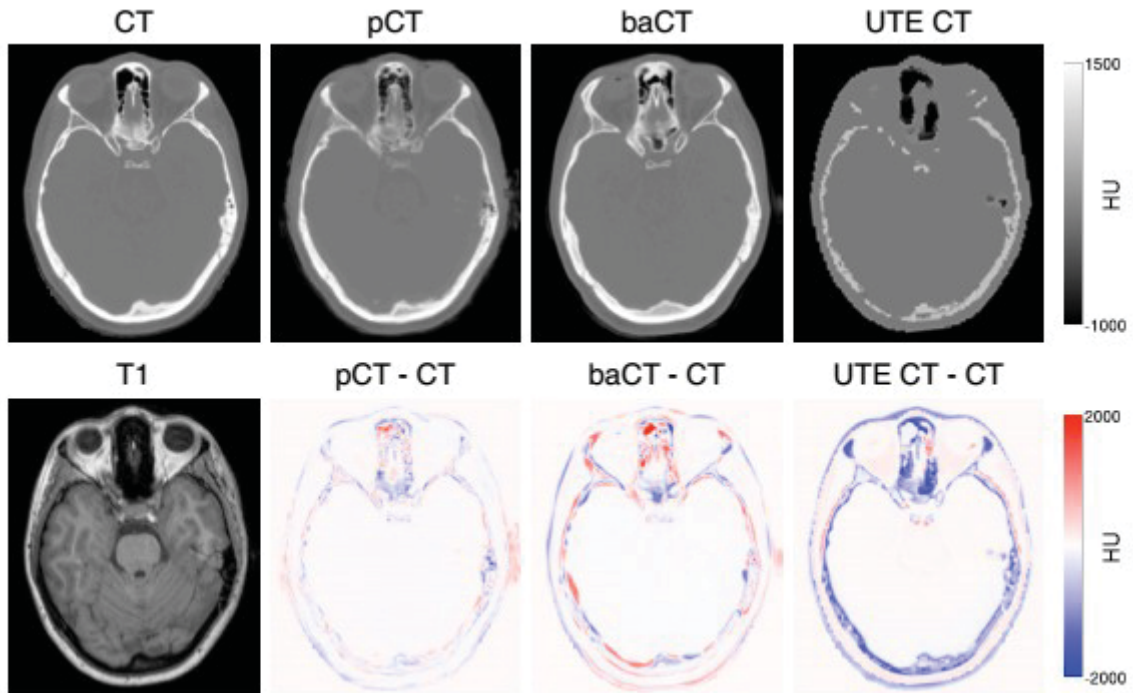


Figure 3. Top row (from left to right): The acquired CT, the pseudo-CT generated by the proposed method, the best atlas CT (baCT) and the UTE CT. Bottom row (from left to right): the acquired T1, the difference between pCT and CT, the difference between baCT and CT, and the difference between UTE CT and CT. Reprinted with permission from Burgos *et al.* [47].

The T1-weighted MR images of the target and atlas datasets are fed into the regression process within patches of images. The proposed method yielded a mean absolute relative error of $2.42 \pm 61.0\%$, $3.28 \pm 60.93\%$, and $2.16 \pm 61.75\%$ in the whole brain, gray and white matter, respectively, compared to PET-CT AC serving as reference.

To generate a pseudo-CT for the purpose of PET/MRI-guided radiotherapy planning, Sjölund *et al.* [61] realized a surrogate CT generation using a deformable registration algorithm, known as the Morphon, enhanced with a certainty mask that allows tailoring the influence of certain regions in the registration. Furthermore, for the atlas fusion part, the collection of deformed atlas CTs are iteratively registered to their joint mean to build a more similar pseudo-CT to the target CT. The authors concluded that voxel-wise atlas fusion using the median value provides better results. The proposed method yielded a mean absolute error in terms of pseudo-CT generation (in HUs) of 113.4 ± 17.6 and 117.9 ± 20.3 for median and iterated atlas fusion strategies compared to the corresponding CT images, respectively.

2) *UTE machine learning and atlas-based segmentation in brain imaging.* The capability of UTE sequences to provide additional information to ease the detection of bones along with machine learning techniques to classify new observations can potentially yield promising results in terms of attenuation map determination for brain imaging. Johansson *et al.* [62] developed a Gaussian mixture regression algorithm trained with features derived from 2 UTE and one 3D T2-weighted sequences to predict continuous LACs of the head. In a follow-up study, the same authors reduced the required MR images to only 2 UTE sequences to obviate the need for T2 weighted 3D spin echo based sequence (SPACE) acquisition, thus decreasing the acquisition time [63]. The clinical evaluation using 8 patients examined with ^{18}F -FLT PET showed an average relative difference between PET images corrected for attenuation using pseudo-CT images and those corrected using CT images of 1.9% in the brain [64]. Johansson *et al.* [65] also investigated the possibility to incorporate spatial information on a voxel-by-voxel basis in the Gaussian mixture regression, with the aim to improve the quality of resulting pseudo-CT. They concluded that the inclusion of spatial information enhanced the accuracy of the estimated pseudo-CT particularly in small complicated anatomical regions, such as the inner ear and post-nasal cavities. Ribeiro *et al.* [66] developed a feed forward neural network algorithm to predict non-linearly the attenuation coefficients based

on two UTE sequences. A 3-layer neural network was trained using patches of voxels extracted from UTE1 and UTE2 images and template-based AC map created by computing an average of 10 transmission PET scans [47]. The output of the neural network would be continuous attenuation coefficients predicted for each voxel. The bone tissue extracted from the resulting pseudo-CT showed an accuracy of 0.77 based on DSC segmentation metric and the attenuation corrected PET images using the neural network-based map revealed an overall relative difference of 3.90% with respect to CT-based AC used as the reference.

In brain imaging, UTE MRI segmentation is subject to artifacts and under-or over-segmentation of bones [27]. To improve the robustness of tissue classification in the head, Poynton *et al.* [67] employed an atlas-based classifier to segment T1-weighted MRI images into 3 tissue classes. A probabilistic air/soft-tissue/bone atlas was constructed from T1-weighted, dual-echo UTE and co-registered CT images of 13 patients and used to train the classifier that calculates the posterior class probability of each tissue class at each voxel of a new subject. The results showed an improvement over UTE-based segmentation, especially in the sinus and inferior regions of the skull. The percentage of misclassified voxels was considerably lower using the proposed method, especially for misclassification of bone as soft tissue. Delso *et al.* [68] proposed a similar approach for improved bone segmentation of UTE images. In their approach, the posterior class probability maps were obtained from a training set of 20 co-registered MRI and CT images and conditioned to certain empirical rules to reduce the impact of mis-registration errors and partial volume effects in MRI/CT training datasets as well as air/tissue interface and metal artifacts.

Roy *et al.* [69] proposed a patch-based method to obviate the need for atlas registration. In the first step, a reference dataset consisting of dual echo UTE images and a co-registered CT from the same subject is created. Then, patches of voxels extracted from the target image are used to find matched counterparts in the reference dataset. By matching patches between the reference and target images, corresponding patches from the reference CT are combined via a Bayesian framework. Even though the information from the reference dataset is utilized in this approach, there is no need that the reference dataset be aligned with the target image. PET/CT and UTE datasets of 5 patients were used for evaluation taking another patient's co-registered UTE and CT as reference. PET data were corrected for attenuation using the original CT, the proposed method, and Siemens' Dixon- and UTE-based μ -maps as well as a deformable registration based pseudo-CT generation technique. The PET images corrected for attenuation using the proposed method showed higher correlation (average $R^2=0.99$) with the reference PET-CT AC. Most of the above mentioned pseudo-CT generation methods tend to segment bone tissue from MR images followed by assignment of predefined attenuation coefficients.

Juttukonda *et al.* [70] demonstrated a correlation between bone intensities in MR and CT images. The scatter plot derived from 97 subjects, where each point represents the intensity of bone tissue in UTE image versus CT number, suggested a strong sigmoid relationship ($R^2=0.95$). This regression analysis was used to derive patient-specific bone attenuation coefficients for the target subject. The proposed pseudo-CT generation required dual echo UTE and two-point Dixon image acquisitions. Since UTE sequences provide signal distinction between air and bone, regions of the sinus cavities were segmented using thresholding of the voxelwise multiplicative inverse of the UTE echo 1 and UTE echo 2 images. Bony structures were extracted via thresholding of the R2 image generated from the UTE echo 1 and 2 images. Fat and soft-tissue were obtained through segmenting the Dixon images. Air, fat, and soft-tissue were assigned linear attenuation coefficient of 0, 0.092, 0.1 cm^{-1} , respectively. The proposed method produced mean Dice coefficients of 0.75 ± 0.05 across 98 subjects for bone and 0.60 ± 0.08 for sinus air cavities.

3) *Whole-body imaging.* The variability and complexity of human anatomy and the high level of noise and partial volume effect in MR sequences used for attenuation correction make the direct segmentation of bones from MR images a prohibitively difficult task. Furthermore, application of UTE sequences for whole-body imaging is not yet customary owing to the long acquisition time and susceptibility to artifacts when using a large FOV. Therefore, the use of atlas registration for prediction of bone tissue is common practice in whole-body MRI-guided attenuation generation.

Hofmann *et al.* [71] presented a methodology for incorporating prior knowledge on class probabilities into the registration process to improve the quality of inter-modality registration between CT and MR whole-body scans. For each image voxel, vectors of class probabilities were constructed using knowledge derived from the imaging modality, pre-segmentations, and/or probabilistic atlases based on which new image similarity measures were defined which outperformed standard and normalized mutual information-based registration techniques. To predict bone tissue in whole-body imaging and generate a continuous attenuation map, a combination of atlas-

based and pattern recognition methods was implemented [72]. The proposed method is a modified version of similar approaches developed for brain imaging described earlier [49]. Two major modifications were made to suite whole-body imaging applications. First, a 4-class segmented version of MR images (air, lung, water and fat) was used to augment the robustness of image registration process and the selection of patches of voxels from the atlas dataset for subsequent Gaussian process regression (GPR). Second, an automatic post-processing rule was applied to override the resulting pseudo-CT in cases where MRI intensity is sufficient to reliably determine the tissue class of water or fat. Voxels that have sufficiently low MRI intensity and none of the atlases predicted bone in a nearby location were mapped to air. Average errors of 8% for VOIs defined in regions of normal uptake and 6% in high focal uptake VOIs were reported compared with 14% and 8%, respectively, obtained for 5-class (air, lung, fat, fat/soft-tissue, soft-tissue) segmentation-based method.

Bezrukov *et al.* [73] modified Hofmann's method to increase its robustness to metal-induced artifacts present in MR images. A spatial bone probability map was developed to identify probable location of metal artifacts. In addition, this method used only the GPR step for prediction of bones in regions with non-zero bone probability to reduce the required processing time, while other regions with zero probability of bone presence were assigned corresponding fat or water attenuation coefficients. The clinical evaluation of PET data (10 patients) corrected for attenuation using the proposed pseudo-CT generation technique revealed quantification errors of $0.6 \pm 11.1\%$ in lesions affected by MR susceptibility artifacts compared to $-4.1 \pm 11.2\%$ achieved using Hofmann's approach.

Arabi and Zaidi [34] modified the method proposed by Hofmann to enhance the accuracy of bone identification and lung attenuation value estimation. To increase the robustness of the method to non-systematic registration bias and anatomical abnormalities, deformed atlas images were locally sorted based on morphological similarity to the target image through a robust similarity measurement using localized normal cross-correlation before being fed into the GPR step. In this way, the atlas images with locally gross misalignment errors would be discarded from training and pseudo-CT generation process. The evaluation of extracted bone on resulting pseudo-CTs considering 14 patients showed an accuracy of 0.65 ± 0.07 based on the DSC metric compared to 0.58 ± 0.09 achieved by Hofmann's method. The high computational time required for elaborating and training the GPR is thought to be the major drawback of this method.

Marshall *et al.* [74] proposed a scheme which required only one online image registration to incorporate bone tissue in whole-body attenuation map. A database of 121 CT images was created to match the target MRI via weighted heuristic measures to find the most similar CT in terms of body geometry before the atlas registration step. The similarity metrics consist of factors such as sex, weight, age, fat to lean tissue ratio, body and lung volume. Then the most similar CT in the atlas database was non-rigidly aligned to the target subject. Thereafter, the bones from the aligned CT were added to a four-class whole-body attenuation map (air, lung, fat and lean tissue). The obtained attenuation map was compared with standard four-class attenuation map without bone. The MRI-based attenuation correction ignoring bone (standard 4-class attenuation map) resulted in relative errors ranging from -37% to -8% in VOIs containing bone while the inclusion of bone reduced these errors to -3% to 4% .

More recently, Arabi and Zaidi [75] implemented and compared a wide range of atlas-based attenuation map generation and bone segmentation methods of whole-body MR images. The accuracy of extracted whole-body bone was evaluated for different algorithms, including Hofmann method [72], arithmetic mean of whole aligned atlas dataset,[76] single template,[46, 47] most similar atlas,[77] global[78] and local[79] weighting atlas fusion strategies, using PET/CT and MR Dixon images of 23 clinical studies through leave-one-out cross validation. Local weighting atlas fusion strategies based on standard image similarity measures such as the mean square distance, LNCC and normalized mutual information outperformed other methods resulting in bone extraction accuracy of 0.92 ± 0.06 based on Dice metric while Hofmann, arithmetic mean of whole aligned dataset and global weighting schemes yielded 0.61 ± 0.02 , 0.60 ± 0.02 and 0.65 ± 0.05 , respectively. A representative slice of extracted whole-body bone along with error distance map obtained for the aforementioned methods is illustrated in Figure 4.

II.C Emission- and transmission-based AC methods

With advances in PET detector technology, TOF PET capability has recently been introduced in clinical PET/CT and PET/MRI scanners, with the aim of improving image quality through the higher signal to noise ratio and lesion detectability. Following the rebirth of TOF-PET, transmission- and emission-based methods have been revisited for deriving patient-specific attenuation maps in PET/MRI.

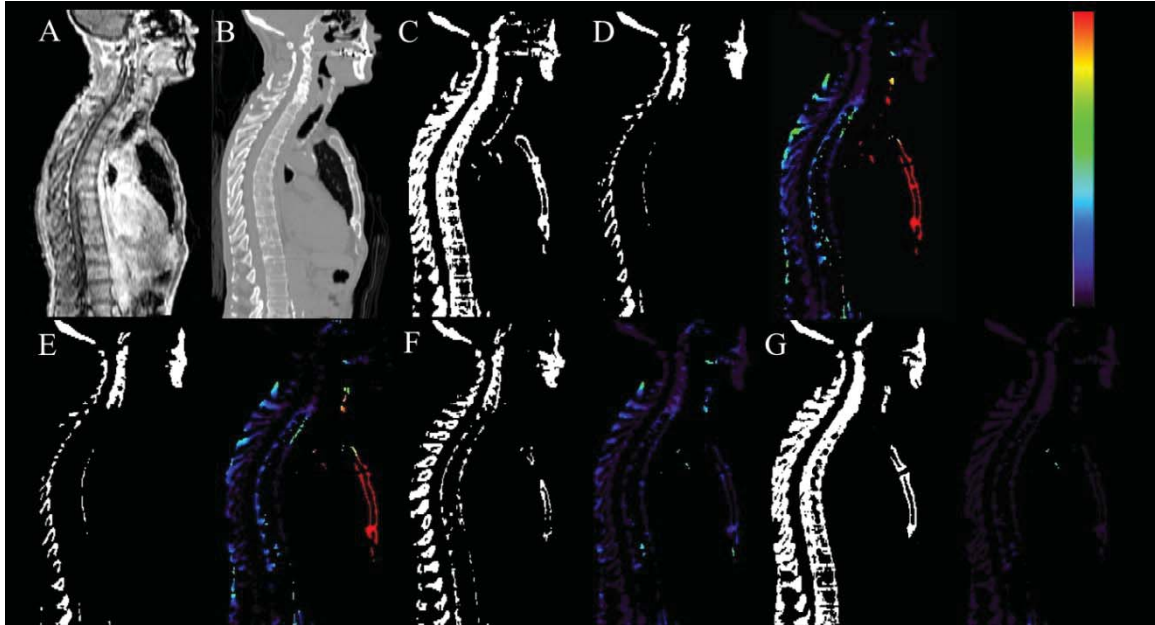


Figure 4. Representative slice of bone segmentation from MR image along with corresponding error distance map. (A) In-phase MR image, (B) corresponding CT image, (C) binary image of reference bone, (D) Hofmann's method, (E) arithmetic mean of whole aligned dataset, (F) global weighting atlas fusion, and (G) local weighting atlas fusion. Reprinted with permission from Arabi and Zaidi [34].

In the following, we briefly review current state-of-the-art algorithms proposed so far for attenuation estimation.

1) *Attenuation estimation using the consistency conditions of the attenuated Radon transform.* Early attempts focused on the direct estimation of attenuation coefficients from emission data without using any estimate of the activity map based on the Helgason-Ludwig consistency conditions for emission data [80]. These conditions state that, in the absence of noise, a given emission data can only arise under certain attenuation conditions, or conversely for a given attenuation map; only certain emission data are possible. However, the resulting system of equations is highly ill-posed and, as such, it is not sufficient to completely determine the attenuation map. Therefore, consistency conditions were mainly exploited to refine an initial attenuation map [81], usually an attenuation template [82] or an attenuation map obtained from segmentation of NAC PET images and an atlas [83] or a transmission attenuation map [84], in such a way that the resulting attenuation map becomes most consistent with the emission data.[85] To facilitate the estimation of attenuation maps from arbitrary scanning geometries and to provide stable numerical implementation, Bronnikov *et al.* [86] formulated the discrete consistency conditions (DCC) for the range of the attenuated Radon transform. Welch *et al.* [84] used DCC to choose optimal threshold values for segmentation of transmission attenuation maps whereas Panin *et al.* [87] employed DCC to select regularization parameters for statistical transmission reconstruction of attenuation maps in 3D PET. However, DCC-based approaches had a limited success in terms of achieving solution stability and thus did not find their way for usage in clinical settings. Fortunately, TOF PET technology recently opened new opportunities for deriving accurate attenuation information from emission data.

Based on the range of consistency conditions of the TOF attenuated Radon transform, Defrise *et al.* [88] recently showed that attenuation correction factors can be determined from TOF-PET data up to a constant scaling factor. They demonstrated that for all LORs containing activity, emission data determine the angular and radial derivatives of the Radon transform of the attenuation map. The stability of this method was illustrated numerically by means of a 2D simulation. Rezaei *et al.* [89] extended this work to 3D TOF PET and only made use of the radial derivatives to estimate the attenuation volume. They studied different rebinning techniques of the derivative sinograms and found that these techniques result in different levels of accuracy. Li *et al.* [90] recently improved upon this approach by incorporating prior MR sinograms into the maximum a posteriori estimation of the attenuation sinogram from TOF emission data.

2) *Attenuation estimation from only emission data.* Emission-based estimation of attenuation coefficients was first proposed by Censor *et al.* [91] where an algebraic reconstruction technique (ART) was used to simultaneously reconstruct attenuation and activity maps. To account for the statistical variability of emission data, Wu *et al.* [92] proposed the joint Poisson-log-likelihood maximization of emission data for the simultaneous reconstruction of activity and attenuation. An alternating optimization was followed, in which the activity was reconstructed using a maximum likelihood expectation maximization (MLEM) algorithm, while the attenuation map was reconstructed using a variant of the ART algorithm.

Nuyts *et al.* [93] further refined the concept of simultaneous maximum likelihood reconstruction of activity and attenuation (MLAA), in which the activity and attenuation were alternatively reconstructed using an MLEM and a scaled gradient ascent algorithm. The MLAA algorithm had limited success owing to: (i) inherent cross-talk artifacts, i.e. the propagation of activity features into the attenuation map and vice versa, (ii) the limitations of activity support, i.e. the LORs that are out of the support of activity distribution (those without prompt coincidences) provide no information about the attenuation, and (iii) count statistics, which determine the level of noise in the estimated attenuation and activity maps. To reduce the cross-talk and noise artifacts, Nuyts *et al.* imposed Gaussian tissue preference and Gibbs smoothness priors on the attenuation estimation. Moreover, they assumed that the activity fairly supports the estimation of attenuation, as it is the case in ^{18}F -FDG PET imaging. Consequently, for LORs with zero counts, they assumed zero attenuation since those LORs are probably out of the body contour. The performance of the algorithm was found to be sensitive to a number of hyperparameters that should be heuristically selected.

Krol *et al.* [94] formulated a unified statistical model for simultaneous activity and attenuation estimation in the framework of expectation maximization. Landmann *et al.* [95] proposed the alternating maximization of joint Poisson-log-likelihood using a one-dimensional Newton optimization algorithm. Median root prior smoothing was also iteratively imposed on activity and attenuation maps. However, these algorithms had a limited success for cross-talk suppression. To reduce these artifacts, Crepaldi and De Pierro [96] proposed an algorithm that alternates between an iterative data refinement (IDR) and alternating reconstruction of activity and attenuation distributions. IDR is used to enforce data consistency conditions within the range of the nonlinear PET attenuated Radon transform. A multiplicative factor was iteratively applied to the MLEM step of the algorithm in order to guarantee the convergence of this non-linear problem. Using simulation studies, the authors demonstrated that the proposed method can reduce cross-talk artifacts.

With the advent of TOF PET/MRI scanners, Salomon *et al.* [97] imposed the inherent spatial constraint of TOF on activity estimation and MR anatomical information on attenuation map estimation within the MLAA algorithm. Thereby, the noise and cross-talk artifacts were substantially reduced. As reported earlier by the same authors, the incorporated TOF information enables the reduction of the source influence (cross-talk artifacts) even at the relatively limited TOF time resolution of current generation PET scanners (~ 580 ps FWHM) [98]. Moreover, in their modified MLAA algorithm, the attenuation coefficients were estimated over many anatomical regions obtained from the segmentation of T1-weighted MRI. Therefore, the reduced number of the unknown attenuation coefficients also allowed for further reduction of cross-talk. However, the segmentation of anatomical MR images is subject to errors, especially between bones and air in paranasal sinuses, or soft tissue close to the ribs and vertebrae. Moreover, depending on the number of regions, the region-wise estimation also might not consider the local variability of attenuation coefficients, especially in the lungs and vertebrae.

Using Fisher information-based analysis, Rezaei *et al.* [99] demonstrated that TOF can suppress cross-talks in the MLAA algorithm, consequently stabilizing the joint estimation problem. In addition, consistent with theoretical findings reported earlier [88], they demonstrated experimentally that the reconstructed activity maps are globally scaled, while the attenuation maps show a position dependent scaling. To solve the scale problem, the authors suggested to use some a priori knowledge about the expected values of attenuation coefficients or to combine this emission-based AC method with full or partial transmission information obtained from transmission scanning. Later, Rezaei *et al.* [100], proposed a maximum likelihood algorithm that jointly estimates the activity distribution and the attenuation correction factors (MLACF). This method avoids the reconstruction of the attenuation image. If additive contributions (such as scatter and randoms) can be ignored, the algorithm does not even require storage of the attenuation correction factors, and becomes very similar to the standard MLEM algorithm. They demonstrated that the algorithm is robust to errors in the detector pair sensitivities. Since MLACF does not estimate the attenuation map, the authors suggested using prior knowledge about the tracer distribution to correct for the scale problem. Bal *et al.* [101] studied the scale corrected MLACF

algorithm using 57 FDG-PET/CT brain studies in comparison with the CTAC method serving as reference. They concluded that MLACF-based reconstruction can provide images that are both qualitatively and quantitatively equivalent to CT-based reconstructions, thus opening the door to potential applications in low-dose brain PET imaging.

Recently, Mehranian and Zaidi [35] proposed an MRI-guided MLAA algorithm for AC in whole-body PET/MR imaging. The algorithm imposes MRI spatial and CT statistical constraints on the estimation of attenuation maps using a constrained Gaussian mixture model (GMM) and Markov random field smoothness prior. In contrary to Salomon *et al.* [97], they employed Dixon water and fat MR images, which were segmented into 4 known tissue classes, including outside air, lung, fat and soft-tissue and an unknown MR low-intensity class corresponding to air cavities, cortical bone and susceptibility artifacts. A co-registered bone probability map was used to indicate the possible position of bones and thus to include misclassified spongy bones into the unknown class. The estimation of attenuation coefficients over the unknown class was regularized using a mixture of 4 Gaussians, and over the known tissue classes using uni-modal Gaussians, parameterized over a representative patient population. The constrained GMM in fact penalizes the large deviations of attenuation coefficients from their expected value in each known tissue class and their distribution from a histogram parameterized over a patient population. Therefore, as demonstrated by the authors, the modified MLAA algorithm effectively suppresses noise, cross-talk and scaling problems of the joint estimation problem. It was also concluded that the LACs of regions located out of the support of activity but are in a known tissue class can be recovered more accurately. In a companion clinical study [36], the authors showed that the 4-class MRAC and their proposed MLAA-AC methods resulted in average SUV errors of -5.4% and -3.5% in lungs and -18.4% and -10.2% in bones, respectively.

3) *Attenuation estimation from emission and transmission data.* The attenuation maps obtained from short transmission scans are often contaminated with noise [12]. To suppress noise in such attenuation maps, Clinthorne *et al.* [102] proposed the joint maximum likelihood (ML) reconstruction of attenuation and activity images. Since the activity and attenuation maps are coupled in the joint ML objective function, an alternating maximization was followed. Erdogan and Fessler [103] applied paraboloidal surrogates to form a monotonic algorithm for joint ML and used an alternating-maximization approach with paraboloidal surrogates coordinate descent algorithm. They also modeled the contamination of transmission data by emission data. Glatting *et al.* [104] formulated a similar joint ML for emission and transmission reconstruction. A one-dimensional Newton optimization method was used for alternating estimation of activity and attenuation. The contamination of transmission data by emission data, scatter and randoms was ignored.

One of the advantages of TOF technology is to separate emission and transmission data during simultaneous data acquisition [105]. Based on this capability, Mollet *et al.* [106] implemented a simultaneous transmission and emission acquisition on the Philips Ingenuity TF PET/MRI scanner [29] using an annulus-shaped transmission source. The annulus was filled with ^{18}F -FDG and mounted into the gantry of the scanner. In this approach, blank and examination (emission and transmission) scans are acquired without and with the patient in the FOV. Subsequently, TOF information is used to separate the transmission and emission data. The attenuation map is then reconstructed from the blank and transmission data. The same authors demonstrated that the limited TOF resolution of current PET scanners does not allow for perfect separation of transmission data from emission data [107]. Therefore, the calculated attenuation coefficients might be non-uniformly scaled and different from their expected values.

As demonstrated by Rezaei *et al.* [108], the MLAA algorithm can estimate both activity and attenuation distributions up to a scaling factor which depends on the initial guess of the activity and attenuation maps. Furthermore, it was emphasized that the emission data do not provide information about the attenuation along the LORs that do not intersect a region containing a significant amount of the radiotracer (LORs located out-of-activity support). For example, attenuation of the patient's bed and coils cannot be completely recovered using MLAA. Panin *et al.* [109] proposed to make use of simultaneous emission and rotating rod sources transmission TOF data acquisitions to more accurately estimate the attenuation map during MLAA reconstruction. Therefore, the additional transmission data establish the solution and solve the scaling and out-of-activity support problems. Similarly, Watson [110] proposed to use sparse line sources for transmission scanning in combination with emission data. It was concluded that the use of supplemental transmission data can significantly improve the accuracy of the estimated LACs in truncated regions as well as the quantitative performance of the emission-only MLAA algorithm. More recently, Rothfuss *et al.* [111] studied the feasibility of using the inherent

background radiation of LSO crystals as transmission sources, where TOF information is employed to separate emission and LSO transmission data. The utilization of this additional information has pertinent implications when combined with emission data to stabilize and improve the MLAA algorithm.

4) *Attenuation estimation from scattered coincidences.* For the task of estimating activity and attenuation distributions from emission data of locally accumulating radiotracers, the projections that are out of the support of the activity distribution (i.e. those without prompt coincidences but intersecting the patient's body) do not directly provide information about photon attenuation. However, these LORs might contain scattered coincidences that can provide additional information about the attenuation they have experienced. In addition, with improving the energy resolution of PET detectors, the scattered coincidences can also be employed to better estimate the activity distribution and therefore to stabilize the joint estimation of activity and attenuation. Recently, Conti *et al.* [112] demonstrated that scattered coincidences can be used to reconstruct activity distributions using TOF and energy information. Sun and Pistorius [113] proposed a generalized scatter reconstruction algorithm to extract the activity distribution using both true and scattered coincidences by considering the limited energy resolution of PET detectors used in clinical practice. Zhang *et al.* [114] developed a scatter model to estimate attenuation coefficients from scattered coincidences by ignoring the attenuation of scattered coincidences. Based on this simplified model, an MLEM algorithm was derived to iteratively estimate attenuation considering the differential Klein-Nishina cross-section and the expected number of scattered events between detector pairs during forward and backprojection. Their simulation results showed that an acceptable attenuation map can be estimated with reduced cross-talk. More recently, Berker *et al.* [115] proposed a scatter-to-attenuation backprojection to reconstruct PET attenuation coefficients from scattered-photon energies in the range of 248–478 keV. Their simulation results suggested that the attenuation map can be derived in the case of perfect spherical symmetry of attenuation and activity distributions as well as attenuation outside of the activity support.

III. CHALLENGES AND POTENTIAL SOLUTIONS

III. A MRI truncation compensation

The MRI transaxial FOV is limited owing to the deterioration of the homogeneity of the main magnetic field (B₀) and linearity of gradient field, especially at the edge of the FOV. Therefore, the truncation of body organs at the edge of the FOV can occur in obese patients, which if not compensated for, can adversely affect MRAC of PET data. Delso *et al.* [116] used 10 PET/CT datasets to reproduce MR FOV truncation and demonstrated that with completely truncated arms, SUV errors ranging between 20% and 30% occur in the heart and spine regions, with maximum errors of up to 50% in the rib near the edge of the FOV. More recently, Schramm *et al.* [117] reported that arm truncation artifacts in 19 PET/MRI patient datasets led to an average SUV underestimation of less than 6% for VOIs defined in the trunk, while over the arms the errors were in the range of 16% to 57%. Overall, three general approaches have been proposed to compensate for MRI FOV truncation including: PET image segmentation, emission-based and pure MRI-based approaches.

1) *PET image segmentation.* Hu *et al.* [118] proposed to compensate for truncation artifacts of attenuation maps generated using the 3-class MRAC technique using the body contour delineated from uncorrected PET images. In their approach, possible truncated regions were identified slice-by-slice within a disk with predefined inner and outer radii. For these regions, the patient contour is extracted from the uncorrected PET images and the missing regions are filled with soft-tissue as shown in Figure 5. To better delineate the body contour, Delso *et al.* [116] proposed to segment PET images preliminary corrected for attenuation using truncated attenuation maps. Schramm *et al.* [117] followed a similar approach and employed a 3D contour identification using an automatically determined threshold. Using a TOF PET/MRI system, Qian *et al.* [119] demonstrated that the segmentation of NAC TOF PET images results in more accurate body contour delineation, actually enabling to avoid overestimating truncated regions. However, thresholding-based separation of body contour and background air even when using NAC TOF PET images is sensitive to intensity variations and threshold selection. Blaffert *et al.* [120] compared threshold-based and gradient-based segmentation of body contour. They concluded that gradient-based segmentation using a watershed algorithm results in better separation of the arms from the body and, thus leading to more accurate truncation compensation. However, they found that the correction of truncated breasts is still challenging since in most NAC TOF PET images, air-breast tissue contrast is lower than air-to-arms tissue contrast.

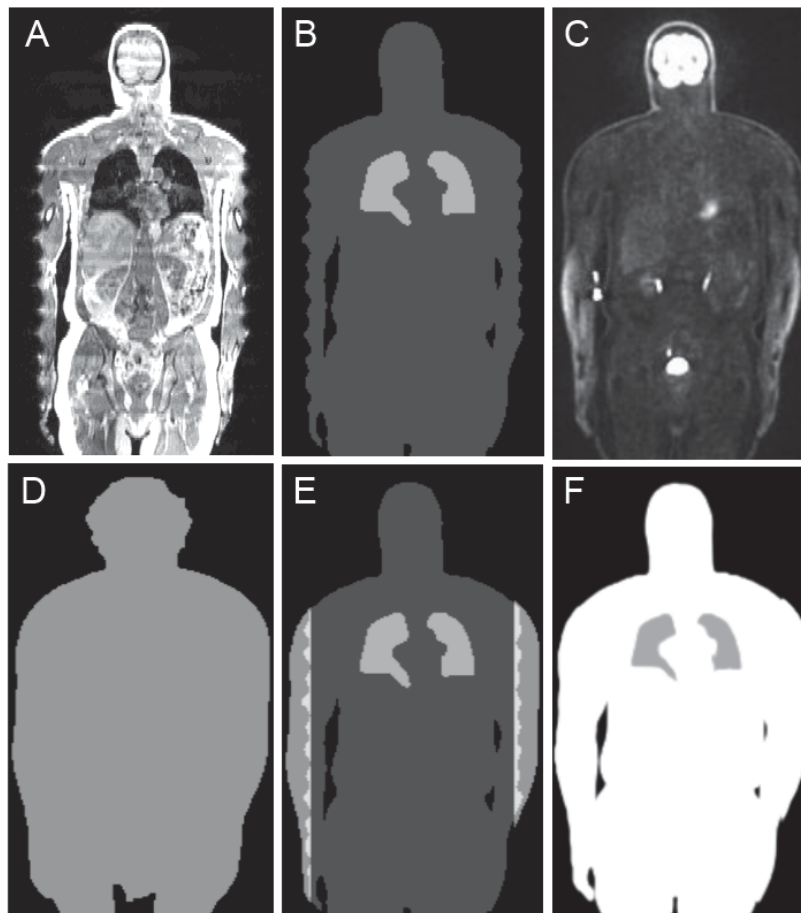


Figure 5. PET/MRI truncation compensation using PET segmentation. (A) truncated atMR image, (B) 3-class MRAC map, (C) NAC TOF PET image, (D) body contour derived from segmentation of NAC TOF PET image, (E) overlap of the attenuation map and the identified truncation regions, and (F) final truncation compensated attenuation map. Adapted with permission from Blaffert *et al.* [120].

2) *Emission-based truncation compensation.* Nuyts *et al.* [121] proposed to compensate the missing part of the MRI-derived attenuation map from non-TOF emission data using a constrained MLAA algorithm. In this algorithm, only the truncated region of the MRI-based attenuation map is estimated under the influence of a bi-modal tissue preference prior (i.e. air and soft tissue) and a relative difference edge preserving prior. The authors evaluated this method using five artificially truncated ^{18}F -FDG PET/CT studies and demonstrated that the SUV underestimation errors were reduced from 20% to 7% for all voxels with SUVs larger than 1. In the MRI-guided MLAA algorithms described in [35], the authors suggested to segment the uncorrected or preliminary corrected PET images to identify the truncated regions in MR images. However, as mentioned earlier, the performance of the MLAA algorithm is dependent on the tracer biodistribution. For specific tracers with local uptake, emission-based techniques might have limited success.

3) *Extended FOV MRI.* The B0 inhomogeneities and gradient nonlinearities at the edges of large MRI FOVs usually result in geometrically distorted or truncated body contours. Recently, Blumhagen *et al.* [122] proposed a pure MRI-based truncation compensation method referred to as B0 homogenization using gradient enhancement (HUGE). This method extends the FOV by determining an optimal readout gradient field which locally compensates B0 inhomogeneities and gradient nonlinearities. The distortion artifacts outside the normal MRI FOV was noticeably reduced by this approach without any hardware modifications. The authors compared the performance of the HUGE algorithm with the MLAA algorithm using 12 PET/MRI clinical studies [123]. The conventional AC map was generated using a 2-point Dixon technique. For the compensation of truncated arms, a multislice 2D spin-echo sequence was implemented to automatically apply HUGE depending on the slice position. Applying the HUGE method extended the FOV of the Dixon MRI from 50 to 60 cm, but at the expense

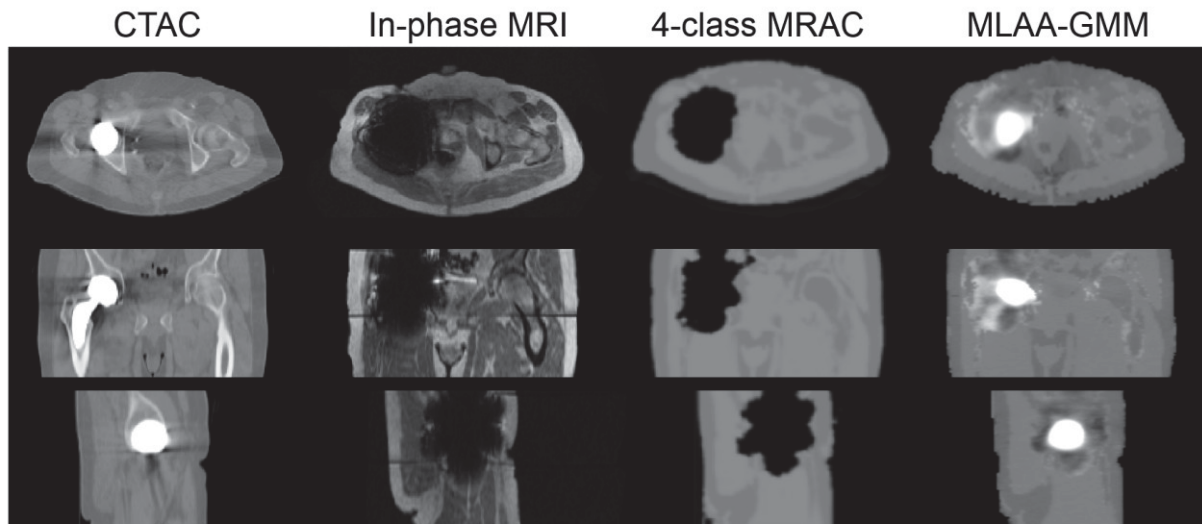


Figure 6. The compensation of metal induced susceptibility artifacts in MRAC maps using the MRI-guided MLAA algorithm described in Ref [35].

of increased MRI data acquisition time. Overall, both truncation compensation methods improve the accuracy of derived attenuation maps with a trade-off of increased scanning time using the HUGE method and increased post-processing time using the MLAA algorithm. The main advantage of HUGE over MLAA is that MRI-based FOV extension is independent of tracer distribution and kinetics.

III. B MR susceptibility and respiratory artifact reduction

Signal voids due to magnetic field distortions caused by metallic implants (blooming artifacts) can give rise to segmentation errors in segmentation-based MRAC methods as well as imperfect LAC prediction of atlas-based learning techniques. Signal voids might erroneously be identified as air cavities, for example, in the case of hip prostheses, dental fillings and spine-fixation screws, or complicate lung segmentation, as in the case of sternal fixations, pacemakers, ICD leads ... etc [124-126]. It has been reported that the resulting erroneous attenuation map can lead to substantial SUV underestimations by about 50% in the case of hip prosthesis [73] and >100% in dental filling cases [127]. The correction of MR susceptibility artifacts has been explored using the following approaches.

1) *Void segmentation.* Ladefoged *et al.* [125] proposed a semi-automatic algorithm to identify the signal voids caused by endoprotheses in the 4-class MRAC attenuation maps of 4 PET/CT/MR patient datasets. In this study, the segmented void artifacts were filled with soft-tissue attenuation coefficient. Ideal segmented AC maps were also obtained by superimposing the co-registered metallic implant on the MRAC maps. It was demonstrated that the resulting attenuation maps can substantially reduce the underestimation of the SUVs. Schramm *et al.* [128] proposed an automatic metal artifact reduction technique using 3-class MRAC maps. In this approach, the body contour is identified from the preliminary attenuation-corrected PET images and the atMR image. The resulting body contour is filled by soft tissue, thereby isolated signal voids and particularly the artifacts connecting the background air to soft tissues and lungs are corrected. The lungs are then identified based on the axial position of the shoulders and are segmented using an intensity thresholding approach. Although the simple filling of voids by soft-tissue attenuation coefficient is a first-line correction method, the authors reported a residual SUV bias of about -13% on average.

2) *Atlas-based registration and emission-based estimation.* For the reduction of metal artifacts in MRAC maps, Bezrukov *et al.* [73] proposed an atlas-based susceptibility artifact correction technique. In this approach, the possible position of artifacts in 4-class MRAC maps is identified using an atlas of artifact regions. Artifactual regions are then filled by soft-tissue attenuation coefficients. To account for the attenuation coefficients of bones inside void regions, i.e. in the case of hip prostheses, the resulting attenuation maps were further improved by predicting bones over the regions indicated by a bone probability map using an atlas-based registration and pattern recognition method. Their results indicated that filling the voids with soft-tissue reduces the

quantification errors of lesions located within or near artifacts from about -50% to -15% , while accounting for bones in the artifactual regions reduces the errors to $<1\%$.

Another approach for proper correction of artifacts that also accounts for the attenuation coefficients of metallic implants is the emission-based estimation of the attenuation coefficients using MLAA type of algorithms. Figure 6 shows the performance of the MLAA-GMM algorithm [35] in terms of estimating attenuation maps at 511 keV of a patient with unilateral hip prosthesis. As shown, the in-phase MR image and the resulting 4-class MRAC attenuation map suffer substantially from the blooming artifacts. The MLAA algorithm, initialized with the 4-class MRAC map, however, is capable of not only filling the void regions in an acceptable way but also estimating the attenuation coefficients of the metallic implant. Therefore, the results demonstrate that emission-based AC methods are promising for proper attenuation correction of PET images in the presence of extensive MR metallic artifacts.

3) *Optimized MRI data acquisition.* Many factors affect the appearance of metal artifacts in MR images, including the composition of metallic implants, their orientation with respect to the direction of the main magnetic field, the MR pulse sequence and data acquisition parameters (voxel size, section thickness, and echo train length) [128, 129]. It has been shown that the careful selection of pulse sequence and acquisition parameters can be effective in mitigating metal-induced susceptibility artifacts, thus enabling to improve the diagnostic value and clinical relevance of MRI used separately or in combination with PET. The direct effect of magnetic field inhomogeneity caused by metallic implants is the fast dephasing of net magnetization and therefore signal loss. This phenomenon is more pronounced when using the fast gradient-echo sequence for MRAC, specifically in Dixon fat and water separation. The dephasing can, however, be partially avoided using (fast) spin-echo and UTE sequences. In spin-echo sequences, 180° refocusing RF pulses are applied to reverse the dephasing induced by magnetic field inhomogeneity, while in UTE sequences, the MR signal is sampled immediately after RF excitation, so that the magnetization does not have enough time to be dephased. Several techniques have also been developed for minimizing metal artifacts for fast spin-echo sequences, such as slice encoding for metal artifact correction (SEMAC) and multi-acquisition with variable resonance image combination (MAVRIC) [130]. For a detailed comparison of these techniques, interested readers are referred to [128]. Chen *et al* [131] compared the performance of SEMAC and MAVRIC and a 2D fast spin-echo sequence in MR imaging of 14 patients having knee replacement implants. It was demonstrated that SEMAC and MAVRIC both significantly reduced the artifact extent compared to fast spin-echo, allowing accurate measurement of the implant dimensions and rotation. Recently, Burger *et al.* [132] utilized diagnostic MAVRIC images to compensate for dental metal artifacts induced in Dixon-based MRAC attenuation maps using 8 PET/CT/MRI patient datasets. They demonstrated that accurate attenuation maps can be derived using this technique, yet at the expense of a considerably increased acquisition time.

Respiratory phase mismatch between PET and MRI/CT attenuation maps is known to be another source of error in PET quantification. Owing to this mismatch, white-band banana artifacts usually occur around the heart and liver dome due to undercorrection for attenuation [133]. It has been shown that these artifacts result in errors of up to 24% in tracer uptake of liver tumors [134]. Methodologies for the correction of this type of artifacts can be classified into two categories which are briefly discussed below.

1) *4D attenuation map generation.* Buerger *et al.* [134] explored the possibility of deriving 4D MRAC maps for AC of respiratory gated PET data. Respiratory synchronized MRI acquisitions were used to gate PET data acquisition and to derive motion vector fields. The gated data were then reconstructed with their corresponding phase-matched attenuation maps with respect to a reference respiratory phase. Using static PET images obtained from time-weighted averaging of images corresponding to different respiratory phases, the authors demonstrated that banana-shaped artifacts were substantially reduced. However, the acquisition of 4D MRI datasets is time-consuming and this remains a major issue for clinical adoption of these techniques. Fayad *et al.* [135] proposed to derive motion fields from gated non-attenuation corrected PET images and to generate 4D MRI attenuation maps from end-expiration static MRI volumes. They demonstrated the potential of using 4D NAC PET images to derive 4D MRAC attenuation maps from a single static MRI volume.

2) *Emission-based attenuation/motion estimation.* Recently, Mehranian and Zaidi [136] investigated the potential of emission-based estimation of lung attenuation coefficients of 4-class MRAC attenuation maps. They demonstrated that the proposed constrained MLAA algorithm can compensate for respiratory-phase mismatch as well as lung mis-segmentation errors, thus improving SUV quantification of the liver and lung lesions. Rezaei and Nuyts [137] proposed a joint reconstruction and registration framework of gated PET data. In this

framework, the gated PET activity and attenuation images are jointly reconstructed using the MLAA algorithm and registered to a reference frame using Demons registration algorithm. Using simulations, the authors demonstrated that this approach reduces the inter-frame registration error between activity and attenuation maps.

III. C MR coils and other attenuating devices

Besides patient's body, several other objects present in the FOV of PET/MRI systems can contribute to photon attenuation and scattering. This includes the RF coils, patient bed and patient positioning and immobilization devices. Although these devices are invisible when using conventional MRI sequences, the attenuation of these devices should be estimated and accounted for in the attenuation maps to achieve accurate PET quantification. MacDonald *et al.* [138] and Tellmann *et al.* [139] reported 19% and 13-19% underestimation of tracer uptake in the brain, respectively, when the attenuation map did not include head surface RF coils. Likewise, Kartmann *et al.* [140] reported local underestimation of activity concentration up to 15.5% if surface body coil is not accounted for in attenuation maps. Delso *et al.* [141] reported that head and neck RF coils can reduce the number of prompt counts by 17% while Fürst *et al.* [142] found that the patient's table results in 19% count loss of true coincidences on the integrated Biograph mMR PET/MR system.

On this latter system, the RF body coils are placed in front of the PET detectors for uniform RF transmission and efficient signal acquisition [143]. However, the signal received from the body coil suffers from noise since the coil is far from the patient. For the same acquisition time, higher signal-to-noise ratio can be achieved by using dedicated receiver coils placed on the surface of the body. All coils and objects present in the FOV attenuate the emission data to some degree; therefore their corresponding attenuation should be included in the attenuation maps. The attenuation of fixed objects, such as patient bed, body and rigid coils (i.e. head/neck, spine, torso and etc.) can be measured using transmission sources (^{68}Ge or ^{137}Cs) [141] or CT scans [144] and incorporated into attenuation maps as templates. Zhang *et al.* [145] concluded that the patient table and coil templates generated from transmission scans are artifact-free and more accurate than those generated from CT scans. In fact, the high-density metallic components of the bed or RF coils often result in streaking artifacts on CT images [146], which can propagate into attenuation corrected PET images [138, 144]. Moreover, as demonstrated by MacDonald *et al.* [138], the bi-linear energy mapping of CT to attenuation coefficients at 511 keV for non-biological materials might not be valid. Therefore, additional quantification errors of up to 28% can be induced in PET images. To reduce the artifacts, the authors suggested redesigning the MR coils by rearranging the placement of the most attenuating materials.

Paulus *et al.* [147] optimized the CT bi-linear energy mapping procedure of hardware PET/MR components to PET attenuation coefficients at 511 keV through the calibration of CT numbers of these components using transmission scanning. The authors also investigated the impact of spatial misregistration of a body matrix RF coil, placed on the top of the NEMA phantom, on PET quantification by shifting the attenuation map in different directions. Attenuation correction neglecting the presence of the coil resulted in 11% underestimation of activity in the upper volume of the phantom close to the coil. Considering the attenuation of the coil using the standard bilinear mapping resulted in an average overestimation of 3.1% (without extended CT scale) and 4.2% (with extended CT scale). Using the optimized bilinear mapping procedure, the bias in the top volume of the phantom was reduced to -0.5% . The simulation of misregistration of a flexible surface RF coil showed acceptable results for shifts of the coil below 5 mm. Previously, Delso *et al.* [141] also reported that the placement of the coil templates in attenuation maps by itself is also an important issue. An axial misalignment of the coils of more than 1-2 mm results in image artifacts and incorrect quantification.

The inclusion of flexible surface coils is more challenging because of their patient-specific application, positioning and orientation. As mentioned above, ignoring surface coils in attenuation maps can lead to local quantification errors of up to 20%. Tellmann *et al.* [139] reported that the spatial misalignment of body surface coils due to involuntary patient motion can result in 9% bias maximum in tracer uptake quantification.

To determine the position of body matrix coil, Paulus *et al.* [148] applied two approaches: (i) cod liver oil capsules were attached to the surface of the coil as MR visible makers and (ii) UTE sequence was employed to image the coil. In the first approach, MR markers were rigidly registered to the same markers in the CT image of the coil using landmark-based registration. In the second approach, UTE images showed only parts of the coil's plastic housing and image registration to CT template was more difficult to achieve.

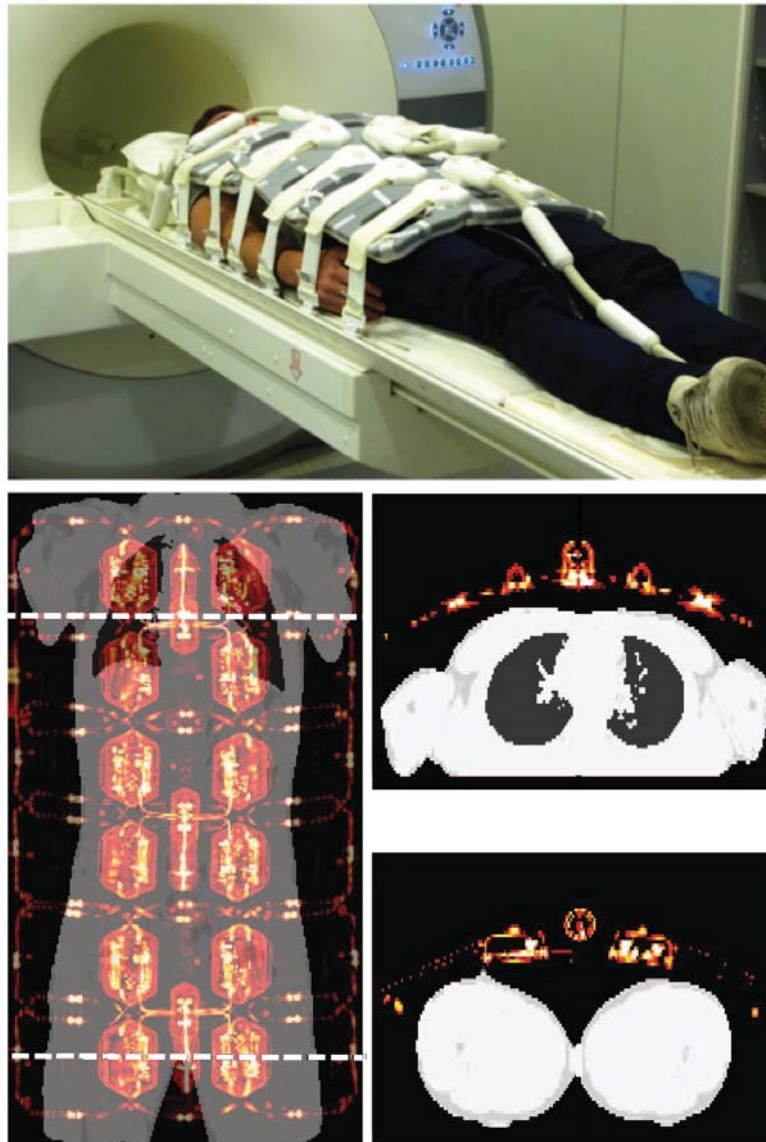


Figure 7. Attenuation correction of flexible RF coils. Top: MR imaging setup of an exemplary volunteer with three overlapping RF surface coils. Bottom: Combined 4-class attenuation map of the volunteer with the registered CT-based attenuation maps of the overlapping RF coils. Adapted with permission from Kartmann *et al.* [140].

They reported that using template-based CTAC of coils reduces the count loss, but slightly overestimates the activity concentration due to inappropriate conversion of coil's Hounsfield units to attenuation coefficients at 511 keV. Similarly, Eldib *et al.* [149] studied the application of UTE for visualization of flexible carotid coils. The same authors also studied several non-rigid registration algorithms to correctly deform CT templates to match MR coil markers [150]. They found that the V-spline registration algorithm produced the most accurate registration compared to B-spline, thin-plate spline and elastic body spline methods. Kartmann *et al.* [140] presented an approach for automatic localization of multiple RF surface coils in whole-body PET/MRI. In this approach, different marker patterns were used to distinguish multiple partly overlapping RF surface coils. Non-rigid B-spline registration was used to register the corresponding markers on the CTAC template to the identified MR markers. The presented algorithm reliably reduced PET quantification errors due to overlooking the coils in the attenuation maps from 15.5% to 4.3%. Figure 7 shows the MR imaging setup of a subject with three overlapping RF surface coils together with coil CT templates overlaid on the 4-class MARC map [140]. Mantlik *et al.* [151] studied the attenuation effect of patient positioning aids on PET quantification. Evaluation of a

head/neck patient data showed an SUV underestimation of a maximum of 9% when patient positioning aids was not accounted for in the attenuation map. It was concluded that patient positioning aids did not produce significant attenuation in the lower extremities.

Another approach for estimating the attenuation of MR invisible objects present in the FOV of PET/MRI scanners is to use emission- or transmission-based methods. As demonstrated by Nuyts *et al.* [121], the MLAA algorithm can potentially estimate cold attenuating objects present in the FOV. In a simulation study, they demonstrated that the MLAA algorithm not only compensated for MR truncation artifacts but also retrieved 6 rods placed in the front of a torso phantom. In an experimental study, Rezaei *et al.* [99] showed that the MLAA algorithm can partially estimate the patient table. These approaches are promising; however, their robustness still needs to be characterized in different situations using large clinical databases.

The standard coils currently employed on clinical PET/MRI systems have not been designed to have low or zero photon attenuation but to provide the maximum signal-to-noise ratio in MR imaging. The PET/MR coils can be redesigned to have low photon attenuation without compromising their performance. RF coil optimization for PET/MRI is an active research topic and the initial results obtained so far are promising. In standard whole-body RF transmit/receive coils, various RF components, such as diodes, capacitors, inductors, cables ... etc, are placed throughout the coil for optimal MR performance. To remove such components from the FOV of the PET subsystem, Saha [152] redesigned the coil in a 3T simultaneous PET/MR system with minimal use of high density RF components, thereby producing a zero PET attenuation whole-body coil. Stickle *et al.* [153] described a PET optimized 16-element anterior array coil for acquiring high-sensitive cardiac/torso PET and MR images in a 3T simultaneous PET/MRI system. In this coil, PET transparent material was used for coil formers, the arrangement of attenuating components (i.e. internal cables, feed and decoupling boards) was optimized and a new mechanical feedboard and decoupling housing design was developed. Dregely *et al.* [154] developed a dedicated breast MR coil for the mMR scanner in which PET attenuation was reduced by moving the high-density components, such as preamplifiers away from the imaging FOV. However, to account for the overall photon attenuation and scattering in the coil, a CT-based template of the coil was acquired and co-registered to the coil's position for incorporation in 4-class MRAC maps.

III. D Tissue classification

1) *Number of tissue classes.* In segmentation-based MRAC methods currently employed on clinical PET/MRI scanners, standard 3- or 4-tissue classes are considered [33, 37]. However, as discussed in Section II, substantial efforts have been directed toward segmenting bones as 5th class, especially in brain imaging. Additional tissue classes such as mixture of fat and soft tissue and internal air cavities have also been considered for reducing the bias and artifacts in MRAC PET images. In 3-class attenuation maps, the LAC of adipose tissues (0.0864 cm^{-1}) is substituted by that of soft tissue (0.0975 cm^{-1}), which can result in overestimation of tracer uptake in fatty tissue lesions such as lipomas. In 4-class attenuation maps, the fat tissue class, obtained from 2-point echo Dixon sequence, is added as a separate tissue class and in 5-class maps, the bones identified using UTE sequences or atlas-based segmentation are considered as another tissue class. Ouyang *et al.* [155] compared PET quantification accuracy of 3-, 4- and 5-tissue class MRAC methods using 23 PET/CT datasets with the reference CTAC method. Voxel-wise evaluation of bias in tissue classes showed that as the number of tissue classes increase absolute quantification errors in different tissue classes, except the lungs, decrease. It was found that even with 5-tissue class MRAC, where bones are included; bias is still present with overestimation of tracer uptake in the vertebrae. They concluded that one possible solution to reduce the bias in the lungs and bones is to segment the lungs into more than one class and the bones into low- and high-density bones. However, more refined segmentation of the lungs and bones is technically challenging when using conventional MRI or even UTE sequences. Using Monte Carlo simulations, Keereman *et al.* [156] also concluded that at least 6-tissue classes (air, lung, soft tissue, fat, spongy and cortical bones) should be identified in MRAC maps in order to reduce quantification errors to less than 5%. Akbarzadeh *et al.* [157] evaluated the effect of different tissue classes on PET quantification by segmenting air, lung, soft tissue, spongy and cortical bones using simulations and clinical studies. They showed that by ignoring bones the mean SUV error in lesions located in bones reaches up to 30.7%. It was also found that a higher number of bone tissue classes improves the accuracy of the attenuation correction procedure.

2) *Erroneous tissue identification.* The miss-classification of different tissue classes in MRAC maps can lead to quantification errors and complicate the interpretation of PET images. The lung and bones are the most difficult tissue classes to identify when using conventional MRI sequences and as such, miss-classification is expected to occur most likely in these tissues. Moreover, the accuracy of tissue segmentation depends on the quality of MR images in terms of signal to noise ratio and partial volume effect, the type and robustness of the segmentation algorithm used (i.e. simple thresholding, contour-based, atlas-based and etc.) and the presence of image artifacts (i.e. metal artifacts, respiratory motion, intensity inhomogeneities, ...etc.).

Keereman *et al.* [156] evaluated the effect of errors in the segmentation of lungs and cortical bones due to high level of noise and partial volume effect. Overall, the results showed that the higher the percentage of misclassifications, the higher the PET quantification errors in malignant lesions. However, it was found that up to 20% tissue misclassification from bone to soft tissue yielded errors below 5%. A similar range was reached for up to 10% misclassification of lung to air. It has also been reported that the mis-segmentation of air cavities to skull [124] and soft-tissue in the abdomen [158] can noticeably affect the visual interpretation of PET images. Catana *et al.* [159] reported that substituting the internal air cavities with soft-tissue can introduce large overestimations (>20%) in adjacent structures. Choi *et al.* [160] evaluated the impact of 3-class UTE-based attenuation correction on quantification of dopamine transporter binding ratio in 16 patients suspected of having Parkinson disease. It was found that the mis-segmentation of brain's ventricles as air during the generation of the MRAC maps resulted in significant underestimation of binding ratio in the periventricular regions.

More recently, Brendle *et al.* [161] evaluated the frequency and impact of tissue misclassifications, caused by MR image artifacts on PET quantification and interpretation. Attenuation maps of 100 patients scanned on the Biograph mMR system were inspected for appearance of artifacts. The artifacts were categorized into 9 groups: (i) FOV edge artifacts, mis-segmentation of tissue as air at the edges of the axial FOV, (ii) metal artifacts, (iii) lung border artifacts, misclassification of lung border as soft tissue, fat, or air, (iv) body contour artifact, expanded or recessed areas of body contour, (v) flip fat water, complete change of fat and soft-tissue attenuation coefficients, (vi) fatty brain artifacts, misclassification of the brain and partially the soft tissue of the neck as fat, (vii) paranasal sinus misclassification, (viii) respiratory artifacts, and (ix) trachea misclassification. In this study, transaxial FOV truncation artifacts were not included as these artifacts are corrected on the mMR scanner using the MLAA algorithm. It was found that the 276 identified artifacts are mostly located around metal implants (16%), in the lungs (19%), and outer body contours (31%). Twenty-one percent of all PET-avid lesions (38 of 184 lesions) were affected by artifacts; nevertheless, the majority of the artifacts did not complicate the visual interpretation of PET images. Yet, in 4 lung artifacts, false-positive lesions were excluded only by means of NAC PET and MRI images. Quantitatively, their results showed that attenuation artifacts led to significant SUV changes in areas with misclassification of air as soft tissue (i.e. metal artifacts) and soft tissue as lung.

III. E Inter/intra-patient variability of LACs

In segmentation-based Dixon and UTE MRAC methods, constant predefined attenuation coefficients are assigned to each tissue class. Therefore, intra- and inter-patient variability of the attenuation coefficients is ignored, which can lead to non-negligible SUV errors especially in the lungs and bones. Atlas-based machine learning and emission-based AC methods are capable of providing more accurate estimates of patient-specific LACs of lungs and bones using the additional information hidden in atlas and emission data.

1) *Lungs.* Among the various tissue classes defined in segmentation-based MRAC methods, the lungs have the largest inter-patient LAC variability with a standard deviation of 0.004 cm^{-1} [37, 157, 163]. In fact, the pulmonary parenchyma and vasculature vary considerably among patients by as much as 30%, depending on gender, body height, pathological conditions [163], breathing patterns [164] and body positioning [165]. As such, different LACs have been assigned to lung tissue class, ranging from 0.018 to 0.035 cm^{-1} [33, 166]. Keereman *et al.* [156] showed that if patient-specific lung LACs are not considered in MRAC maps, PET quantification errors of up to 26% might occur. It was reported that the assignment of a LAC of 0.024 cm^{-1} to the lungs produces relative errors of $13.5 \pm 10.7\%$ [72] and $7.7 \pm 3.0\%$ [74], respectively. Conversely, the assignment of a LAC of 0.018 cm^{-1} to the lungs produces PET quantification bias of $1.9 \pm 2.3\%$ [33] and $-0.5 \pm 13.3\%$ [158] in lung lesions and normal lung tissues. Ouyang *et al.* [155] reported a relative error of $4.4 \pm 14.4\%$ for SUV estimates in the lungs using a lung LAC of 0.0276 cm^{-1} . A small number of studies have focused on the derivation of patient-specific lung LACs considering lung tissue heterogeneity. The techniques reported so far

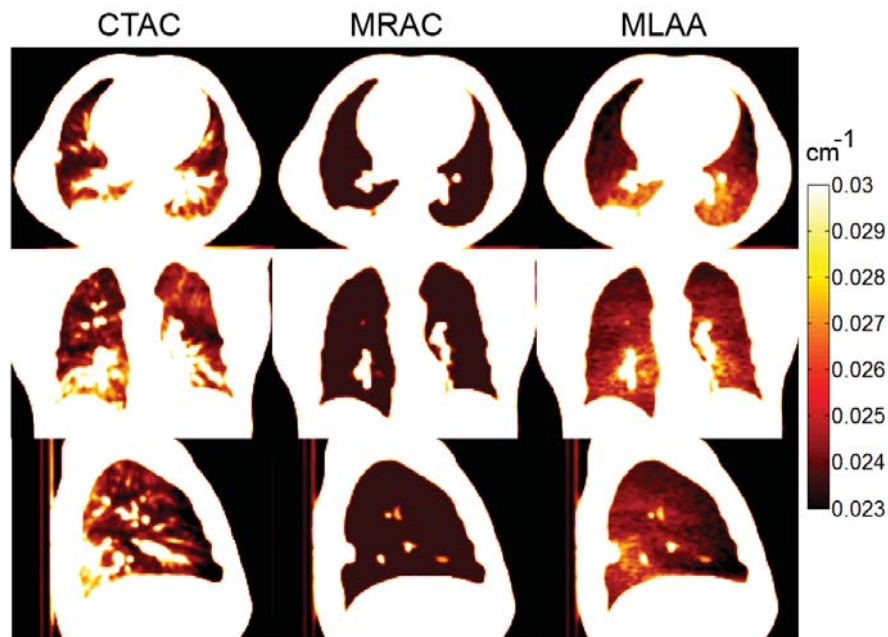


Figure 8. Comparison of the attenuation maps of the standard 4-class MRAC and the MRAC improved by the MLAA algorithm over the lungs with the reference CTAC maps in lung displaying windows. Adapted with permission from Ref [136].

can be classified into 3 categories: (i) prediction of mean lung LACs from MRI intensity and/or lung volume, (ii) atlas-based registration and learning, and (iii) emission-based estimation of lung LACs.

Marshall *et al.* established a linear mapping function between MRI and CT image intensities of the lungs of 5 dogs, as human surrogates, to predict the mean of lung LACs [167]. Lonn *et al.* [169] derived a linear relationship between lung volume and mean LACs. Both studies proved the improved performance of these approaches in terms of lung LAC prediction. However, as a general rule, the MRI-to-CT mapping function requires a standardized MRI protocol and is influenced by the presence of respiratory motion, diamagnetic susceptibility and flow-related artifacts. The volume-to-LAC prediction model does not take into account the impact of other factors such as gender, age, pathological conditions and body positioning. Moreover, these approaches do not account for intra-patient variability of lung attenuation coefficients.

Atlas-based registration and machine learning techniques can in principle predict intra-patient variability of lung LACs based on comprehensive training sets and reinforced learning models. In the technique proposed by Hofmann *et al.* [72], local structures of MR images and their corresponding CT atlases are incorporated into a GPR for prediction of LACs. In spite of promising results achieved for soft-tissue and bony structures, this method exhibited large errors in the lungs owing to the insufficient signal produced by the lungs when using conventional MRI sequences. Recently, Arabi and Zaidi [34] embedded the correlation between lung volume and lung mean LACs into the GPR kernels and demonstrated that their improved method reduces the lung SUV bias from 8.9% (using Hofmann's approach) to 4.1%.

Emission-based derivation of lung LACs has also been explored by various groups. Madsen and Lee [83] used consistency conditions to refine an initial lung contour obtained from a lung atlas and the MLAA framework to estimate the attenuation coefficients. Berker *et al.* [169] proposed a constrained TOF-MLAA algorithm for the estimation of mean lung LACs in 5-class MRAC maps (including bone as the 5th class). The results obtained using Monte Carlo simulated PET/CT studies showed a high PET quantification bias, probably because of out-of-field (OOF) accidental coincidences, error propagation into the lungs and the unsolved scaling problem of the MLAA algorithm. Later, the same authors quantified the influence of OOF accidental coincidences using simulations. A bias of 15% was found in the estimation of mean lung LACs, which was significantly reduced by removing OOF accidentals from the data, suggesting that accidental OOF coincidences are the major contributor to the bias. [170] An alternative approach was investigated by Mehranian and Zaidi [136] using an MLAA algorithm constrained by a lung tissue preference prior for patient-specific lung LACs estimation of 19 PET/CT clinical studies. Their results showed that the standard 4-class MRAC method resulted

in an average SUV error of $-5.2 \pm 7.1\%$ in the lungs, while the proposed MLAA algorithm reduced the error to $-0.8 \pm 6.3\%$. Figure 8 compares the CTAC, MRAC and MLAA attenuation maps of a patient whose lungs have a congested structure and high density gradients. As shown, the MLAA algorithm can accurately retrieve the lung density gradient in a continuous fashion, thus providing more accurate attenuation correction.

2) *Bones*. In segmentation-based methods, where bones are segmented as an additional tissue class using either UTE sequences or atlas-based approaches, the selection of appropriate bone tissue LAC is a subject of debate (see Table 2 in Ref [171] for details) as different LACs have been used for the skull (range of 0.116 - 0.172 cm^{-1}) and whole-body cortical and spongy bones (range of 0.11 - 0.15 cm^{-1}). Schleyer *et al.* [172] studied the impact of inaccurate bone LAC assignment using 9 whole-body PET/CT datasets. In their study, the bones in CT images were replaced by three patient-specific bone LACs (mean, peak and maximum values) and three generic LACs values of air (0 cm^{-1}), soft tissue (0.095 cm^{-1}) and bone (0.13 cm^{-1}). They found that the assignment of the mean bone LAC of each patient resulted in the lowest error (5% on average) in the lung tissue. Replacing bones with soft-tissue LAC also produced a lower error than the assignment of bone LACs, mainly because of assigning higher LACs to spongy bones having in principle a LAC of 0.11 cm^{-1} [156]. In brain UTE imaging, Catana *et al.* [159] evaluated the impact of 8 different bone LACs ranging from 0.136 to 0.180 cm^{-1} on PET quantification. Their results suggested that the LACs producing the smallest bias and smallest variability were 0.171 cm^{-1} and 0.136 cm^{-1} , respectively. They also concluded that the best bias-variability trade-off in PET quantification was achieved by assigning bone LACs of 0.143 cm^{-1} and 0.151 cm^{-1} , as previously reported in Ref [24].

Atlas-based registration and machine learning can potentially estimate intra-patient variability of bone LACs by for example differentiating cortical bone in the skull from spongy bone in the vertebrae. Making use of the best atlas or local weighting of sorted atlases [34, 58] can in principle capture the inter-patient variability of the predicted bones. Navalpakkam *et al.* [29] employed a UTE-based machine learning technique to predict continuous bone LACs in 10 PET/CT/MRI datasets and compared their proposed method with standard 4-class and the 5-class (including bone) MRAC. Their results showed SUV underestimations of 11% close to cortical bones when excluding bones. On the other hand, assigning a constant LAC value of 0.151 cm^{-1} to bone tissue class resulted in 4.2% SUV overestimation in the same regions. Conversely, the continuously predicted LACs resulted in errors of 2.16%. Emission-based approaches are also promising for estimation of patient-specific bone attenuation coefficients. A recent study reported a mean LAC for bone derived from CT images of 5 PET/CT/MRI datasets of 0.118 cm^{-1} , while the MLAA-GMM algorithm estimated a mean value of 0.104 cm^{-1} , which reduced the bias compared to the standard 4-class MRAC method neglecting bone [36].

3) *MRI contrast agents*. In contrast-enhanced MR imaging, the administration of small molecular weight paramagnetic contrast agents allows for tumor grading, characterization of the functional integrity of tumor microvasculature and evaluation of other pathophysiological conditions. The high-atomic number, rare-earth elements used in these agents (e.g. Gadolinium and Dysprosium) can; however, have an impact on PET attenuation correction in PET/MRI. In experimental phantom studies, Lee *et al.* [173] evaluated the effects of MR contrast agents on PET quantification using different concentrations of a Gadolinium-based contrast agent. Clinical evaluations were also conducted on 8 breast-cancer patients who underwent sequential FDG PET/CT (pre), dynamic contrast-enhanced MRI and FDG PET/CT (post) scans. In the presence of MRI contrast agent, the SUV slightly increased ($\sim 5\%$ for a maximum contrast agent concentration of 1.7 mmol). However, there was no correlation between the magnitude of SUV increase and the concentration of the agent. SUV_{max} measurements on pre- and post-PET scans in malignant tumors and the liver showed significant over- and underestimation, respectively, while no significant difference was observed in SUV_{max} of normal regions in the breast. It was concluded that clinically relevant concentrations of MRI contrast media ($< 0.2 \text{ mmol}$) have negligible effects on the interpretation and quantification of PET images.

Lois *et al.* [174] also evaluated the effect of oral and intravenous MRI contrast media on PET quantification in PET/MRI. The results of CT and PET transmission measurements showed that clinically relevant concentrations of MRI contrast media have similar mean linear PET attenuation coefficients as water. Therefore, the administered contrast agents did not result in noticeable quantification errors in the corresponding PET images. However, it was demonstrated that attenuation map miss-segmentation errors might occur after ingestion of superparamagnetic iron oxide-based contrast agents.

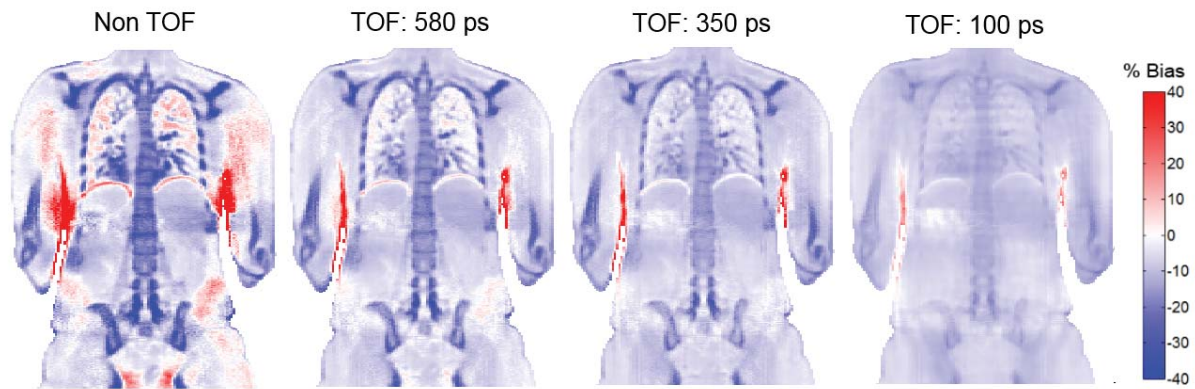


Figure 9. Bias maps between PET image reconstructed by the 4-class MRAC and CTAC maps without TOF and with different TOF resolutions in a whole-body phantom simulated from a clinical study. Adapted with permission from Ref [184].

IV. CURRENT TRENDS AND OPPORTUNITIES

IV. A Impact of time of flight on erroneous attenuation correction

With the advent of clinical TOF-PET systems, several studies reported that TOF can improve PET image quality in terms of signal-to-noise ratio, lesion detectability, convergence rate [175, 176] and tolerance to inconsistencies between emission and correction data (including attenuation) compared to non-TOF reconstructions [177, 178]. With TOF capability, the detection time differences of the coincident annihilation photons are measured, with a temporal uncertainty governed by the timing resolution of the PET detectors, and exploited during image reconstruction. The image voxels are locally updated based on the spatial uncertainty associated with the TOF resolution of the scanner and therefore the intra-voxel dependencies and therefore error propagations are reduced. Recently, Ahn *et al.* [179] developed analytical methods for the evaluation of attenuation error propagation in TOF and non-TOF PET image reconstructions. They demonstrated that the propagated errors in TOF PET are proportional to TOF timing resolution, while in the case of non-TOF PET, they are proportional to the patient size.

Wollenweber *et al.* [180] evaluated the effect of excluding a surface coil from the MRAC maps on PET quantification using TOF and non-TOF reconstructions. They found that with TOF information, the SUV errors due to neglecting the coil attenuation are slightly reduced from -8.2% to -7.3% . Davison *et al.* [181] evaluated the impact of TOF on reduction of PET quantification errors induced by metal artifact voids in MRAC maps. In this work, artificial signal voids were simulated in different regions of the attenuation maps of 7 patients undergoing sequential PET/CT and simultaneous TOF PET/MRI using the Signa system (GE Healthcare, Waukesha, WI) with nominal TOF time resolution of <400 ps [182] scans. It was found that the TOF capability significantly reduces the artifacts. The percentage error reduction with TOF ranged from 21% to 60% for medium-sized artifacts simulated in the maxilla and the sternum, respectively. For artifacts located in the chest, sternum, and pelvic regions, the most significant error reduction achieved was at least 40%. Using the same PET/MRI system referenced above, the influence of TOF on improving the image quality and diagnostic interpretation of PET images in the presence of attenuation artifacts was evaluated using 25 clinical studies [183]. It was concluded that PET/MR reconstructions benefit from TOF information in terms of recovery of pathologies missed on non-TOF PET images and artifact reduction especially around metallic implants.

Mehranian and Zaidi [184] also studied the impact of TOF PET image reconstruction on the reduction of quantification errors induced by the standard 4-class MRAC and the presence of metal and respiratory-phase mismatch related artifacts. In this work, 27 whole-body FDG PET/CT datasets acquired on the Siemens mCT scanner (with nominal TOF resolution of 580 ps) were analyzed. The results showed that non-TOF MRAC method resulted in an average error of -3.4% and -21.8% in the lungs and bones, respectively, whereas the TOF reconstructions reduced the errors to -2.9% and -15.3% , respectively. Simulation results also showed that as TOF resolution improves, the visual artifacts and quantification errors are substantially reduced (Figure 9). It was concluded that MRI-guided attenuation correction should be less of a concern on future TOF PET/MR scanners with improved timing resolution.

IV. B Advances in ultrashort and zero echo time MRI

Ultra-short echo time MRI sequences have been developed to depict tissues with low proton density and short T2 relaxation time, such as the lung and cortical bone. The transverse relaxation of hydrogen protons is mainly governed by their bonding status and chemical environment. In compactly structured tissues, the spin-spin interactions are high leading to fast dephasing and T2 shortening, while in liquid water such as cerebrospinal fluid, the free and bound-water molecules are sparsely distributed leading to less spin-spin interactions and longer T2. The MR signal of short T2 tissues decay quickly even during RF excitation. The UTE pulse sequence has therefore been developed to start signal acquisition as quickly as possible. It differs from conventional sequences in three aspects [185]:

- (i) Free induction decay (FID) signal sampling: In conventional spin- and gradient-echo sequences, the FID signal is refocused by a 180° pulse and its echo is sampled at time TE or spoiled and recalled at time TE by a bi-polar gradient pulse, respectively. While in UTE, the FID signal is directly sampled after RF excitation with only a delay from hardware transmit/receive switching time.
- (ii) Short RF pulse: The signal of short T2 components can decay during the application of long RF pulses, therefore in UTE short or half RF excitation pulses are employed. This, however, requires high bandwidth pulses which results in small flip angles for the same RF power.
- (iii) Radial center-out sampling of k-space: In UTE sequences, the k-space is sampled using radial trajectories starting from the center of k-space moving outward by synchronized application of gradient coils. Therefore, in contrast to conventional Cartesian trajectories, there is no need for applying a rewinder-type gradient to return to the beginning of each k-space line.

However, the acquisition of high-resolution UTE images is time-consuming, typically around 6 mins in 3T brain imaging [17]. The acquisition time can be reduced by acquiring data with a coarser resolution, but this would lead to segmentation and learning errors for the task of attenuation correction. Recent attempts for accelerating UTE data acquisition focus on k-space under-sampling in the context of compressed sensing (CS) and parallel MR imaging (pMRI), or the combination of both. Du *et al.* [186] proposed to combine UTE with a highly undersampled interleaved multi-echo variable-TE acquisition scheme. The progressively increasing TEs of this technique allowed for spectroscopic imaging of short T2 tissues ranging from 8 μ s to 1.5 ms in clinically acceptable scan times. Li *et al.* [187] described a 3D CS UTE sequence with hybrid-radial encoding strategy and demonstrated the feasibility of their technique for achieving an acceleration factor of 10. Hu *et al.* [188] studied the acceleration of UTE scans through k-space sampling optimization. In this work, the angular sampling rate of 3D radial k-space trajectories was reduced from 100% to 25% for a series of UTE sequences with TEs in the range 0.1-2.3 ms. The resulting scan times on the Philips 3T Achieva MRI system were in the range 172-43 sec. They demonstrated that high-quality bone-enhanced images can be generated using the UTE sequence with k-space undersampling as low as 25% (acceleration factor of 4) while preserving bone-air contrast at the cost of a minimal increase of noise level. Although radial undersampling violates the Nyquist criterion, spherical symmetry of this sampling pattern helps to preserve the spatial resolution. However, higher undersampling rate can give rise to aliasing artifacts that degrade image quality.

Aitken *et al.* [19] proposed to combine CS and sensitivity encoding (SENSE) pMRI for accelerating dual-echo UTE. To investigate undersampling limits, the full radially sampled MRI data of a volunteer (acquired for about 7.5 min on a 3T MRI scanner) was retrospectively sampled by factors of 2-16. Fully sampled images were reconstructed by gridding, while the undersampled echo images were reconstructed by model-based iterative reconstruction incorporating coils' sensitivity and an L1-sparsity prior. The results showed that there is a good agreement between the fully sampled and undersampled maps with undersampling factors of up to 8 (scan time of 53 sec.). For higher acceleration, the contrast between bone and soft tissue was deteriorated leading to bone-air misclassification during the generation of MRAC maps. MR images of 5 volunteers were prospectively undersampled by an acceleration factor of 8. Similarly, the results were in good agreement with fully sampled images. The sampling pattern in radial UTE sequences; however, does not meet sampling requirements of pMRI techniques, such as SENSE. Therefore, advanced non-Cartesian image reconstruction algorithms are required at the expense of increased reconstruction time. Johansson *et al.* [20] studied two non-Cartesian parallel image reconstruction algorithms for the reconstruction of undersampled radial UTE and GRE data of 23 head datasets. The k-spaces were retrospectively undersampled by factors of 3-30 and reconstructed using conventional re-gridding and non-Cartesian iterative algorithms. The authors reported that for acceleration of up to 5, the acceptable pseudo-CT images can be obtained by the reconstruction methods. The authors concluded that non-

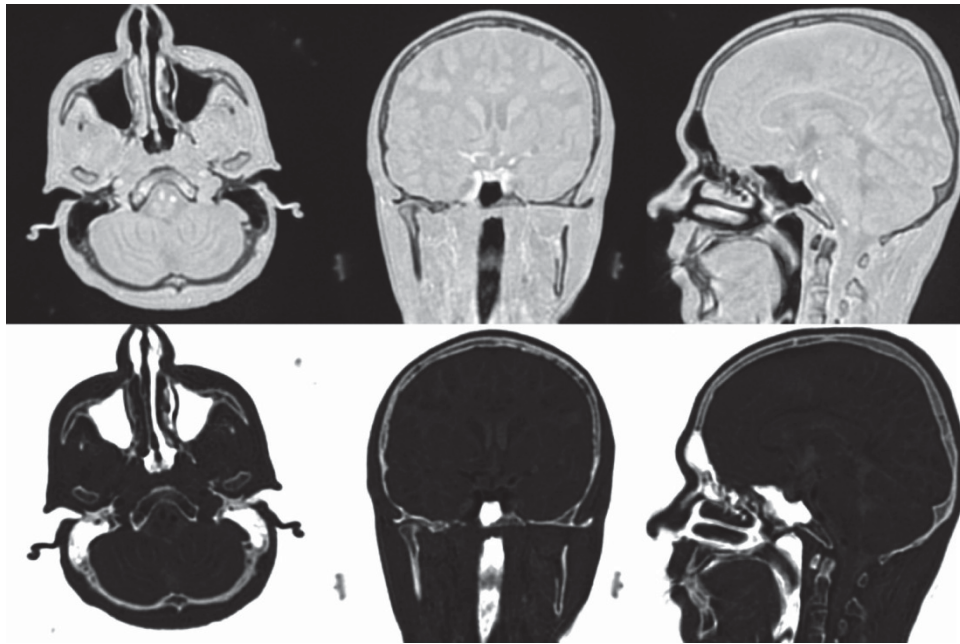


Figure 10. High-resolution zero TE image of the head in linear (Top) and inverse logarithmic (Bottom) scale. Reprinted with permission from Ref [191].

Cartesian parallel reconstruction methods slightly improved image quality at the expense of increased computational time. As such, gridding reconstruction is sufficient for moderate k-space sub-sampling by which the scan time can be decreased by a factor of 3 (from 6 to 2 min).

In UTE imaging, the suppression of long T2 components is necessary to separate the bone signal from soft tissue, which is performed by echo subtraction, saturation prepulses, multiple sequences, ...etc [189]. As mentioned earlier, the most widely used approach is echo subtraction using a dual-echo UTE. Recently, there has been promising advances in zero time echo (ZTE) sequences for imaging of short T2 structures without the need for time-consuming long T2 suppression methods [190]. Unlike UTE and most MR pulse sequences, in ZTE the frequency-encoding (readout) gradients are set before spin excitation and not ramped down between pulse repetitions. As a result, signal readout starts instantaneously upon excitation leading to a nominal TE of zero. The gradients are in fact slightly ramped between repetitions, which in turn minimizes eddy currents and the artifacts thereof. In ZTE, RF excitation pulse with very short duration and thus high bandwidth is employed which leads to small flip angles and therefore native proton-density (PD) weighted image contrasts.

Wiesinger *et al.* [191] investigated a PD-weighted ZTE sequence for visualization and segmentation of the skull. They developed and optimized a rotating ultra-fast imaging sequence (RUFIS) of type ZT pulse sequence for efficient bone signal enhancement and flat PD response of soft-tissues. An inverse logarithmic image scaling was used to highlight bone and differentiate it from surrounding soft-tissue and air. The flat PD response of soft tissue is in fact important to avoid T1 saturation that would result in the misclassification of long T1 soft-tissues (i.e., CSF and eyes) as bone or air. In contrast to most UTE sequences which mostly explore T2 relaxation time differences, the presented PD-weighted ZTE takes advantage of PD differences. Therefore, it eliminates the application of long T2 suppression methods. The authors studied standard and high-resolution protocols with acquisition times of about 3 and 6 min, respectively. Figure 10 shows a representative high-resolution ZTE and log-scaled images of the head.

Delso *et al.* [192] evaluated the feasibility of PD-weighted ZTE imaging for skull segmentation of 15 clinical studies acquired on a trimodality PET/CT-MR system. Quantitative evaluation based on the Jaccard distance between ZTE and corresponding CT bone masks showed improved performance of ZTE over dual-echo UTE by achieving overlap distances over the entire head of 38-63% compared to 47-79%. It was found that contrary to UTE, the presence of tendons on bone masks obtained with ZTE was minor. However, they reported remaining mis-classifications at air/tissue interfaces, i.e. nasal cartilage and inner ear as in UTE.

Lung tissues are characterized by low PD and fast decaying signal due to local magnetic inhomogeneities induced at air-tissue interfaces. Recently, Johnson *et al.* [193] demonstrated the feasibility of free-breathing 3D

radial UTE whole lung imaging by optimizing this sequence for improved SNR and reduced T2*-induced blurring in conjunction with respiratory gating motion rejection. Radial undersampling and 8-channel pMRI were also used to reduce scan time to 5.5 min. Gibiino *et al.* [194] studied a free-breathing 3D RUFIS zero-TE approach for visualization of lung parenchyma and vessels, including prospective and retrospective motion correction. They also demonstrated that high-quality images of lung parenchyma free from blurring and eddy-current artifacts can be obtained using ZTE in less than 6 min.

V. CONCLUDING REMARKS AND OUTLOOK

The generation of accurate and patient-specific attenuation maps in whole-body PET/MRI proved to be a challenging task. In this work, we reviewed the tremendous efforts carried out during the last decade for developing solutions and algorithms to address these challenges. We categorized the MRAC algorithms into three generic groups: segmentation, atlas registration and learning and emission-based methods. The principles, algorithmic implementations, characteristics and recent advances and achievements of each category of methods were then elaborated. Each category of techniques has its own advantages and disadvantages from different standpoints and considering the various aspects. Table 2 (inspired from Ref [8]) compares the general advantages, drawbacks and potential of these techniques. Owing to their time-efficacy, simplicity and robustness, segmentation-based MRAC is currently the method of choice implemented on current commercial PET/MRI scanners. In fact, robustness is one of the main prerequisites for the clinical adaptation of an attenuation correction technique to guarantee accurate diagnosis and interpretation of PET findings. Since the introduction and wide adoption of segmentation-based MRAC methods on hybrid clinical PET/MRI systems, a number of studies have shown that their use on commercial PET/MRI systems provides images with similar or even improved diagnostic accuracy as PET/CT imaging.[195, 196] However, these methods have some limitations and drawbacks, including reduced PET quantification accuracy in lesions located in/close to bones, lungs and in regions presenting with artifacts.

On the other hand, atlas-based and emission-based methods show promise in terms of deriving more accurate attenuation maps, thus improving PET quantification. However, these methods are still in their infancy and require more detailed investigation and additional research to improve their robustness and efficacy. For instance, the performance of atlas registration-based methods depends on the collectivity of the MRI/CT training set and the efficiency of the learning algorithm. The performance of emission-based methods depends on TOF timing resolution and the PET tracer biodistribution. In brain imaging, several studies demonstrated that atlas-based segmentation or registration techniques can properly segment or predict bones [58, 68]. In whole-body imaging the combination of segmentation-based and atlas-based registration showed promising performance compared to that achieved by each method alone [73]. The combination of segmentation-based and lung emission-based attenuation correction has also been investigated showing a high potential of emission-based methods in deriving patient specific lung LACs [136]. The results of comprehensive comparative evaluation studies can be exploited to come up with novel MRAC strategies taking advantage of the advantages of each technique.

Table 2. Comparison of the pros and cons of the different categories of MRAC techniques used in PET/MRI.

	Segmentation-based	Atlas-based	Emission-based
Computation speed	+++	+	-
Simplicity and robustness	+++	+	+
Patient-specificity of lung LACs	-	+	++
Patient-specificity of bone LACs	-	++	+
Specific data requirement	-	+	+
MR Truncation compensation	-	-	++
Coil attenuation estimation	-	-	+
MR Susceptibility artifact reduction	-	+	++
Respiratory artifact reduction	-	-	+

MRI transaxial FOV truncation compensation through TOF NAC PET image segmentation or the MLAA algorithm are among the most promising approaches. Further investigation is still required to evaluate the efficiency and computational complexity of the two approaches. The attenuation coefficients of fixed and flexible objects (patient table, body coils, surface coils, etc.) is currently best accounted for using pre-measured attenuation maps of fixed parts and deformable registration of templates for flexible parts [140]. Although emission-based algorithms can in principle estimate such attenuating objects, it remains to be demonstrated whether these techniques can accurately and completely estimate these objects given that they might have partial support of activity. As elaborated in this work, emission-based methods look promising for the correction of metal susceptibility artifacts by estimating the high attenuation coefficients of the metallic implants, which is not feasible using atlas-based registration techniques. On the MRI side, there have been some promising pulse sequence developments that can mitigate and reduce the extent of metal blooming artifacts. For the compensation of respiratory-phase mismatch between MRAC maps and PET images, currently two approaches are possible, (i) acquisition of 4D attenuation maps and (ii) simultaneous reconstruction of activity and attenuation. Emission-based methods are, however, as computationally intensive as atlas-based registration methods or even more. This further motivates the combination of these advanced methods with fast segmentation-based techniques. However, additional investigation is still required to further improve the accuracy and robustness of these attenuation correction methods to pave the way for their translation into clinical PET/MRI systems.

As futuristic outlook, we believe that potential exciting developments to achieve accurate PET attenuation correction in PET/MRI, thus enabling improved PET quantification, can be broadly summarized in the following items: (i) The most promising attenuation correction methods will likely be achieved by hybrid techniques combining the three categories of MRAC methods to take advantage of the positive aspects of each class of methods. (ii) Technological advances in time-of-flight PET as well as U/ZTE MRI sequences will progressively continue to respectively provide opportunities in mitigating the adverse effects of inaccurate attenuation correction and deriving more accurate attenuation maps to render future research in this field worthless.

During the following decade, we are witnessing further developments in PET detector technology and translation of digital silicon photomultipliers with new scintillators (such as monolithic crystals [196]) from laboratory and preclinical settings into the clinical arena, assuring improved TOF capability and thus attenuation correction errors to an acceptable level. In addition, emission-based AC methods, which rely on hidden information in PET data to estimate attenuation maps, will show more promise as the TOF time resolution of PET scanners improves. With ongoing developments in instrumentation, we believe that a TOF PET time resolution of less than 100 ps might be possible in the future [197, 198]. Thereby, one can anticipate improved robustness and availability of this type of attenuation correction methods in the near future, given their high potential compared to other techniques (Table 2). With ongoing progress in array processing technology [199] and feasibility of real-time image reconstruction [200], emission-based AC methods will also be certainly computationally appealing in clinical setting.

There have been remarkable advances in fast MRI data acquisition through parallel MRI and k-space undersampling to make the acquisition time of UTE MRI sequences clinically feasible. Moreover, the same trend is followed by the recent emergence of ZTE MRI sequence with promising characteristics for bone and lung parenchyma visualization in the context of PET/MRI. Certainly, these pulse sequences will continue to undergo further developments and improvements and will be made available in the clinic not only for attenuation correction but also for musculoskeletal and pulmonary disease evaluation.

Moving from the present to the future will involve tremendous evaluation and further development of the three main classes of attenuation correction techniques discussed in this work both in academic and corporate settings to achieve the best compromise. The assessment and comparison of the various attenuation correction methods should continue in the context of multicentric clinical trials supported and implemented by manufacturers involving the use of large databases to assure the reproducibility and robustness of the developed algorithms. The outcomes of these trials will be vital for clinical adoption of the most promising approaches meeting the high-level standards required for their translation into clinical settings.

ACKNOWLEDGMENTS

This work was supported by the Swiss National Science Foundation under Grant SNSF 31003A-149957 and the Indo-Swiss Joint Research Programme ISJRP-138866.

REFERENCES

- [1] H. Zaidi, and A. D. Guerra, "An outlook on future design of hybrid PET/MRI systems," *Med Phys*, vol. 38, no. 10, pp. 5667-5689, 2011.
- [2] J. A. Disselhorst, I. Bezrukov, A. Kolb, C. Parl, and B. J. Pichler, "Principles of PET/MR imaging," *J Nucl Med*, vol. 55, pp. 2S-10S, 2014.
- [3] S. Vandenberghe, and P. K. Marsden, "PET-MRI: a review of challenges and solutions in the development of integrated multimodality imaging.," *Phys Med Biol*, vol. 60, no. 4, pp. R115-54, Feb 21, 2015.
- [4] I. Bezrukov, F. Mantlik, H. Schmidt, B. Scholkopf, and B. J. Pichler, "MR-Based PET attenuation correction for PET/MR imaging," *Semin Nucl Med*, vol. 43, no. 1, pp. 45-59, Jan, 2013.
- [5] H. Zaidi, "Is MR-guided attenuation correction a viable option for dual-modality PET/MR imaging?," *Radiology*, vol. 244, no. 3, pp. 639-642, 2007.
- [6] M. Hofmann, B. Pichler, B. Schölkopf, and T. Beyer, "Towards quantitative PET/MRI: a review of MR-based attenuation correction techniques," *Eur. J. Nucl. Med. Mol. Imaging*, vol. 36, no. 1, pp. 93-104, 2009/03/01, 2009.
- [7] G. Wagenknecht, H.-J. Kaiser, F. Mottaghy, and H. Herzog, "MRI for attenuation correction in PET: methods and challenges," *Magn Reson Mat Phys Biol Med*, vol. 26, no. 1, pp. 99-113, 2013/02/01, 2013.
- [8] A. Martinez-Moller, and S. G. Nekolla, "Attenuation correction for PET/MR: problems, novel approaches and practical solutions," *Z Med Phys*, vol. 22, no. 4, pp. 299-310, Dec, 2012.
- [9] V. Keereman, P. Mollet, Y. Berker, V. Schulz, and S. Vandenberghe, "Challenges and current methods for attenuation correction in PET/MR," *Magn Reson Mat Phys Biol Med*, vol. 26, no. 1, pp. 81-98, 2013.
- [10] E. Z. Xu, N. A. Mullani, K. L. Gould, and W. L. Anderson, "A Segmented Attenuation Correction for PET," *J Nucl Med*, vol. 32, no. 1, pp. 161-165, January 1, 1991, 1991.
- [11] H. P. v. V. Floris, W. K. Reina, N. M. v. B. Bart, F. M. M. Carla, W. A. M. d. J. Hugo, A. L. Adriaan, and B. Ronald, "Impact of attenuation correction strategies on the quantification of High Resolution Research Tomograph PET studies," *Phys Med Biol*, vol. 53, no. 1, pp. 99, 2008.
- [12] H. Zaidi, M. Diaz-Gomez, A. E. Boudraa, and D. O. Slosman, "Fuzzy clustering-based segmented attenuation correction in whole-body PET imaging.," *Phys Med Biol*, vol. 47, no. 7, pp. 1143-1160, 2002.
- [13] R. Z. Stodilka, B. J. Kemp, F. S. Prato, A. Kertesz, D. Kuhl, and R. L. Nicholson, "Scatter and Attenuation Correction for Brain SPECT Using Attenuation Distributions Inferred from a Head Atlas," *J Nucl Med*, vol. 41, no. 9, pp. 1569-1578, September 1, 2000, 2000.
- [14] H. Zaidi, M.-L. Montandon, and D. O. Slosman, "Attenuation compensation in cerebral 3D PET: effect of the attenuation map on absolute and relative quantitation.," *Eur. J. Nucl. Med. Mol. Imaging*, vol. 31, no. 1, pp. 52-63, 2004.
- [15] J. P. Carney, D. W. Townsend, V. Rappoport, and B. Bendriem, "Method for transforming CT images for attenuation correction in PET/CT imaging.," *Med Phys*, vol. 33, no. 4, pp. 976-983, Apr, 2006.
- [16] C. Catana, A. van der Kouwe, T. Benner, C. J. Michel, M. Hamm, M. Fenchel, B. Fischl, B. Rosen, M. Schmand, and A. G. Sorensen, "Toward implementing an MRI-based PET attenuation-correction method for neurologic studies on the MR-PET brain prototype.," *J Nucl Med*, vol. 51, no. 9, pp. 1431-1438, Sep, 2010.
- [17] V. Keereman, Y. Fierens, T. Broux, Y. De Deene, M. Lonneux, and S. Vandenberghe, "MRI-based attenuation correction for PET/MRI using ultrashort echo time sequences," *J Nucl Med*, vol. 51, no. 5, pp. 812-8, 2010.
- [18] K. Zeimpekis, G. Delso, F. Wiesinger, P. Veit-Haibach, G. von Schulthess, and R. Grimm, "Investigation of 3D UTE MRI for lung PET attenuation correction," *J Nucl Med*, vol. 55, no. Supplement 1, pp. 2103, 2014.
- [19] A. Aitken, C. Kolbitsch, T. Schaeffter, and C. Prieto Vasquez, "Rapid Acquisition of PET Attenuation Maps from Highly Undersampled UTE Images Using Sparse-SENSE Reconstruction," *Proc. Intl. Soc. Mag. Reson. Med.*, Proceedings of the Annual Meeting of ISMRM, p. 0769: ISMRM, 2013.
- [20] A. Johansson, A. Garpebring, T. Asklund, and T. Nyholm, "CT substitutes derived from MR images reconstructed with parallel imaging," *Med Phys*, vol. 41, no. 8, pp. 082302, 2014.

- [21] F. L. Andersen, C. N. Ladefoged, T. Beyer, S. H. Keller, A. E. Hansen, L. Hojgaard, A. Kjaer, I. Law, and S. Holm, "Combined PET/MR imaging in neurology: MR-based attenuation correction implies a strong spatial bias when ignoring bone," *Neuroimage*, vol. 84, pp. 206-16, Jan 1, 2014.
- [22] J. Teuho, J. Johansson, J. Linden, V. Saunavaara, T. Tolvanen, and M. Teras, "Specification and estimation of sources of bias affecting neurological studies in PET/MR with an anatomical brain phantom," *Nucl Instrum Methods Phys Res A*, vol. 734, pp. 179-184, 2014.
- [23] R. Le Goff, V. Frouin, J.-F. Mangin, and B. Bendriem, "Segmented MR images for brain attenuation correction in PET," in Proc. SPIE, Image Processing, 1994, pp. 725-736.
- [24] H. Zaidi, M. L. Montandon, and D. O. Slosman, "Magnetic resonance imaging-guided attenuation and scatter corrections in three-dimensional brain positron emission tomography," *Med Phys*, vol. 30, no. 5, pp. 937-48, May, 2003.
- [25] G. Wagenknecht, E. R. Kops, L. Tellmann, and H. Herzog, "Knowledge-based segmentation of attenuation-relevant regions of the head in T1-weighted MR images for attenuation correction in MR/PET systems," in IEEE Nuclear Science Symposium and Medical Imaging Conference (NSS/MIC), 2009, pp. 3338-3343.
- [26] Y. Berker, J. Franke, A. Salomon, M. Palmowski, H. C. Donker, Y. Temur, F. M. Mottaghy, C. Kuhl, D. Izquierdo-Garcia, Z. A. Fayad, F. Kiessling, and V. Schulz, "MRI-based attenuation correction for hybrid PET/MRI systems: a 4-class tissue segmentation technique using a combined ultrashort-echo-time/Dixon MRI sequence," *J Nucl Med*, vol. 53, no. 5, pp. 796-804, 2012.
- [27] G. Delso, M. Carl, F. Wiesinger, L. Sacolick, M. Porto, M. Hüllner, A. Boss, and P. Veit-Haibach, "Anatomic evaluation of 3-dimensional ultrashort-echo-time bone maps for PET/MR attenuation correction," *J Nucl Med*, vol. 55, no. 5, pp. 780-785, May 1, 2014, 2014.
- [28] P. Veit-Haibach, F. Kuhn, F. Wiesinger, G. Delso, and G. von Schulthess, "PET-MR imaging using a tri-modality PET/CT-MR system with a dedicated shuttle in clinical routine.," *Magn Reson Mat Phys Biol Med*, vol. 26. no.1, pp. 25-35, 2013.
- [29] B. K. Navalpakkam, H. Braun, T. Kuwert, and H. H. Quick, "Magnetic resonance-based attenuation correction for PET/MR hybrid imaging using continuous valued attenuation maps," *Invest Radiol*, vol. 48, no. 5, pp. 323-32, May, 2013.
- [30] Z. Hu, N. Ojha, S. Renisch, V. Schulz, I. Torres, D. Pal, G. Muswick, J. Penatzer, T. Guo, P. Boernert, C.-H. Tung, J. Kaste, L. Shao, M. Morich, T. Havens, P. Maniawski, W. Schaefer, R. Guenther, and G. Krombach, "MR-based attenuation correction for a whole-body sequential PET/MR system," in IEEE Nuclear Science Symposium and Medical Imaging Conference (NSS/MIC), 2009, pp. 3508-3512.
- [31] Z. Hu, S. Renisch, B. Schweizer, T. Blaffert, N. Ojha, T. Guo, J. Tang, C. Tung, J. Kaste, V. Schulz, I. Torres, and L. Shao, "MR-based attenuation correction for whole-body PET/MR system," in IEEE Nuclear Science Symposium and Medical Imaging Conference (NSS/MIC), 2010, pp. 2119-2122.
- [32] H. Zaidi, N. Ojha, M. Morich, J. Griesmer, Z. Hu, P. Maniawski, O. Ratib, D. Izquierdo-Garcia, Z. A. Fayad, and L. Shao, "Design and performance evaluation of a whole-body Ingenuity TF PET-MRI system," *Phys Med Biol*, vol. 56, no. 10, pp. 3091-106, May 21, 2011.
- [33] A. Martinez-Möller, M. Souvatzoglou, G. Delso, R. A. Bundschuh, C. Chefd'hotel, S. I. Ziegler, N. Navab, M. Schwaiger, and S. G. Nekolla, "Tissue classification as a potential approach for attenuation correction in whole-body PET/MRI: evaluation with PET/CT data," *J Nucl Med*, vol. 50, no. 4, pp. 520-526, 2009.
- [34] H. Arabi, and H. Zaidi, "MRI-based pseudo-CT generation using sorted atlas images in whole-body PET/MRI," in IEEE Nuclear Science Symposium and Medical Imaging Conference (NSS/MIC), 2014, *in press*.
- [35] A. Mehranian, and H. Zaidi, "Joint estimation of activity and attenuation in whole-body TOF PET/MRI using constrained Gaussian mixture models," *IEEE Trans Med Imaging*, vol. in press, 2015.
- [36] A. Mehranian, and H. Zaidi, "Clinical assessment of emission- and segmentation-based MRI-guided attenuation correction in whole body TOF PET/MRI.," *J Nucl Med*, vol. 56, no. 6, pp. 877-883, 2015.
- [37] V. Schulz, I. Torres-Espallardo, S. Renisch, Z. Hu, N. Ojha, P. Börnert, M. Perkuhn, T. Niendorf, W. M. Schäfer, H. Brockmann, T. Krohn, A. Buhl, R. W. Günther, F. M. Mottaghy, and G. A. Krombach, "Automatic, three-segment, MR-based attenuation correction for whole-body PET/MR data," *Eur. J. Nucl. Med. Mol. Imaging*, vol. 38, no. 1, pp. 138-152, 2011.

- [38] M. Eiber, A. Martinez-Möller, M. Souvatzoglou, K. Holzapfel, A. Pickhard, D. Löffelbein, I. Santi, E. Rummeny, S. Ziegler, M. Schwaiger, S. Nekolla, and A. Beer, "Value of a Dixon-based MR/PET attenuation correction sequence for the localization and evaluation of PET-positive lesions," *Eur. J. Nucl. Med. Mol. Imaging*, vol. 38, no. 9, pp. 1691-1701, 2011/09/01, 2011.
- [39] M. Hofmann, I. Bezrukov, F. Mantlik, P. Aschoff, F. Steinke, T. Beyer, B. J. Pichler, and B. Scholkopf, "MRI-based attenuation correction for whole-body PET/MRI: Quantitative evaluation of segmentation- and Atlas-based methods.," *J Nucl Med*, vol. 52, no. 9, pp. 1392-1399, Sep, 2011.
- [40] S. D. Wollenweber, S. Ambwani, A. R. Lonn, D. D. Shanbhag, S. Thiruvankadam, S. Kaushik, R. Mullick, H. Qian, G. Delso, and F. Wiesinger, "Comparison of 4-class and continuous fat/water methods for whole-body, MR-based PET attenuation correction," *IEEE Trans Nuc Sci*, vol. 60, no. 5, pp. 3391-3398, 2013.
- [41] A. Samarin, C. Burger, S. Wollenweber, D. Crook, I. Burger, D. Schmid, G. von Schulthess, and F. Kuhn, "PET/MR imaging of bone lesions – implications for PET quantification from imperfect attenuation correction," *Eur. J. Nucl. Med. Mol. Imaging*, vol. 39, no. 7, pp. 1154-1160, 2012/07/01, 2012.
- [42] Y. C. Tai, K. P. Lin, M. Dahlbom, and E. J. Hoffman, "A hybrid attenuation correction technique to compensate for lung density in 3-D total body PET," *IEEE Trans Nuc Sci*, vol. 43, no. 1, pp. 323-330, 1996.
- [43] T. Chang, R. H. Diab, J. W. Clark, and O. R. Mawlawi, "Investigating the use of nonattenuation corrected PET images for the attenuation correction of PET data," *Med Phys*, vol. 40, no. 8, pp. 082508, 2013.
- [44] M.-L. Montandon, and H. Zaidi, "Atlas-guided non-uniform attenuation correction in cerebral 3D PET imaging.," *Neuroimage*, vol. 25, no. 1, pp. 278-286, 2005.
- [45] H. Zaidi, M.-L. Montandon, and S. Meikle, "Strategies for attenuation compensation in neurological PET studies.," *Neuroimage*, vol. 34, no. 2, pp. 518-541, 2007.
- [46] E. R. Kops, and H. Herzog, "Alternative methods for attenuation correction for PET images in MR-PET scanners," in *IEEE Nuclear Science Symposium and Medical Imaging Conference (NSS/MIC)*, 2007, pp. 4327-4330.
- [47] E. R. Kops, and H. Herzog, "Template based attenuation correction for PET in MR-PET scanners," in *IEEE Nuclear Science Symposium and Medical Imaging Conference (NSS/MIC)*, 2008, pp. 3786-3789.
- [48] S. D. Wollenweber, S. Ambwani, G. Delso, A. H. R. Lonn, R. Mullick, F. Wiesinger, Z. Piti, A. Tari, G. Novak, and M. Fidirich, "Evaluation of an atlas-based PET head attenuation correction using PET/CT & MR patient data," *IEEE Trans Nuc Sci*, vol. 60, no. 5, pp. 3383-3390, 2013.
- [49] M. Hofmann, F. Steinke, V. Scheel, G. Charpiat, J. Farquhar, P. Aschoff, M. Brady, B. Schölkopf, and B. J. Pichler, "MRI-based attenuation correction for PET/MRI: a novel approach combining pattern recognition and atlas registration," *J Nucl Med*, vol. 49, no. 11, pp. 1875-1883, 2008.
- [50] E. Schreibmann, J. A. Nye, D. M. Schuster, D. R. Martin, J. Votaw, and T. Fox, "MR-based attenuation correction for hybrid PET-MR brain imaging systems using deformable image registration," *Med Phys*, vol. 37, no. 5, pp. 2101-2109, 2010.
- [51] I. B. Malone, R. E. Ansorge, G. B. Williams, P. J. Nestor, T. A. Carpenter, and T. D. Fryer, "Attenuation Correction Methods Suitable for Brain Imaging with a PET/MRI Scanner: A Comparison of Tissue Atlas and Template Attenuation Map Approaches," *J Nucl Med*, vol. 52, no. 7, pp. 1142-1149, July 1, 2011, 2011.
- [52] W. D. Penny, K. J. Friston, J. T. Ashburner, S. J. Kiebel, and T. E. Nichols, *Statistical parametric mapping: the analysis of functional brain images: the analysis of functional brain images*: Academic press, 2011.
- [53] T. Hartkens, D. Rueckert, J. A. Schnabel, D. J. Hawkes, and D. L. Hill, "VTK CISG registration toolkit: An open source software sackage for affine and non-rigid registration of single-and multimodal 3D images," *Bildverarbeitung für die Medizin 2002*, pp. 409-412: Springer, 2002.
- [54] S.-L. Chan, Y. Gal, R. L. Jeffree, M. Fay, P. Thomas, S. Crozier, and Z. Yang, "Automated Classification of Bone and Air Volumes for Hybrid PET-MRI Brain Imaging," in *IEEE International Conference on Digital Image Computing: Techniques and Applications (DICTA)*, 2013, pp. 1-8.
- [55] Z. Yang, J. Choupan, F. Sepehrband, D. Reutens, and S. Crozier, "Tissue classification for PET/MRI attenuation correction using conditional random field and image fusion," *International journal of machine learning and computing*, vol. 3, no. 1, 2013.

- [56] J. Uh, T. E. Merchant, Y. Li, X. Li, and C. Hua, "MRI-based treatment planning with pseudo CT generated through atlas registration," *Med Phys*, vol. 41, no. 5, pp. 051711, 2014.
- [57] N. Burgos, M. J. Cardoso, M. Modat, S. Pedemonte, J. Dickson, A. Barnes, J. S. Duncan, D. Atkinson, S. R. Arridge, and B. F. Hutton, "Attenuation correction synthesis for hybrid PET-MR scanners," *Medical Image Computing and Computer-Assisted Intervention—MICCAI*, pp. 147-154: Springer, 2013.
- [58] N. Burgos, M. J. Cardoso, K. Thielemans, M. Modat, S. Pedemonte, J. Dickson, A. Barnes, R. Ahmed, C. J. Mahoney, J. M. Schott, J. S. Duncan, D. Atkinson, S. R. Arridge, B. F. Hutton, and S. Ourselin, "Attenuation correction synthesis for hybrid PET-MR scanners: application to brain studies," *IEEE Trans Med Imaging*, vol. 33, no. 12, pp. 2332-41, Dec, 2014.
- [59] D. Izquierdo-Garcia, A. E. Hansen, S. Forster, D. Benoit, S. Schachoff, S. Furst, K. T. Chen, D. B. Chonde, and C. Catana, "An SPM8-based approach for attenuation correction combining segmentation and nonrigid template formation: application to simultaneous PET/MR brain imaging," *J Nucl Med*, vol. 55, no. 11, pp. 1825-30, Nov, 2014.
- [60] Y. Chen, M. Juttukonda, Y. Su, T. Benzinger, B. G. Rubin, Y. Z. Lee, W. Lin, D. Shen, D. Lalush, and H. An, "Probabilistic air segmentation and sparse regression estimated pseudo ct for PET/MR attenuation correction," *Radiology*, 2014.
- [61] J. Sjölund, D. Forsberg, M. Andersson, and H. Knutsson, "Generating patient specific pseudo-CT of the head from MR using atlas-based regression," *Phys Med Biol*, vol. 60, no. 2, pp. 825, 2015.
- [62] A. Johansson, M. Karlsson, and T. Nyholm, "CT substitute derived from MRI sequences with ultrashort echo time," *Med Phys*, vol. 38, no. 5, pp. 2708-2714, 2011.
- [63] A. Johansson, M. Karlsson, J. Yu, T. Asklund, and T. Nyholm, "Voxel-wise uncertainty in CT substitute derived from MRI," *Med Phys*, vol. 39, no. 6, pp. 3283-3290, 2012.
- [64] A. Larsson, A. Johansson, J. Axelsson, T. Nyholm, T. Asklund, K. Riklund, and M. Karlsson, "Evaluation of an attenuation correction method for PET/MR imaging of the head based on substitute CT images," *Magn Reson Mat Phys Biol Med*, vol. 26, no. 1, pp. 127-136, 2013.
- [65] A. Johansson, A. Garpebring, M. Karlsson, T. Asklund, and T. Nyholm, "Improved quality of computed tomography substitute derived from magnetic resonance (MR) data by incorporation of spatial information-potential application for MR-only radiotherapy and attenuation correction in positron emission tomography," *Acta Oncologica*, vol. 52, no. 7, pp. 1369-1373, 2013.
- [66] A. S. Ribeiro, E. R. Kops, H. Herzog, and P. Almeida, "Hybrid approach for attenuation correction in PET/MR scanners," *Nucl Instrum Methods Phys Res A*, vol. 734, pp. 166-170, 2014.
- [67] C. B. Poynton, K. T. Chen, D. B. Chonde, D. Izquierdo-Garcia, R. L. Gollub, E. R. Gerstner, T. T. Batchelor, and C. Catana, "Probabilistic atlas-based segmentation of combined T1-weighted and DUTE MRI for calculation of head attenuation maps in integrated PET/MRI scanners," *Am J Nucl Med Mol Imaging*, vol. 4, no. 2, pp. 160-171, 2014.
- [68] G. Delso, K. Zeimpekis, M. Carl, F. Wiesinger, M. Hüllner, and P. Veit-Haibach, "Cluster-based segmentation of dual-echo ultra-short echo time images for PET/MR bone localization," *EJNMMI Physics*, vol. 1, no. 1, pp. 1-13, 2014/06/04, 2014.
- [69] S. Roy, W.-T. Wang, A. Carass, J. L. Prince, J. A. Butman, and D. L. Pham, "PET Attenuation Correction Using Synthetic CT from Ultrashort Echo-Time MR Imaging," *J Nucl Med*, vol. 55, no. 12, pp. 2071-2077, 2014.
- [70] M. R. Juttukonda, B. G. Mersereau, Y. Chen, Y. Su, B. G. Rubin, T. L. Benzinger, D. S. Lalush, and H. An, "MR-based attenuation correction for PET/MRI neurological studies with continuous-valued attenuation coefficients for bone through a conversion from R2* to CT-Hounsfield units," *NeuroImage*, 2015.
- [71] M. Hofmann, B. Schölkopf, I. Bezrukov, and N. D. Cahill, "Incorporating prior knowledge on class probabilities into local similarity measures for intermodality image registration," in Proceedings of the MICCAI, Workshop on Probabilistic Models for Medical Image Analysis (PMMIA), 2009.
- [72] M. Hofmann, I. Bezrukov, F. Mantlik, P. Aschoff, F. Steinke, T. Beyer, B. J. Pichler, and B. Scholkopf, "MRI-based attenuation correction for whole-body PET/MRI: quantitative evaluation of segmentation- and atlas-based methods," *J Nucl Med*, vol. 52, no. 9, pp. 1392-9, Sep, 2011.

- [73] I. Bezrukov, H. Schmidt, F. Mantlik, N. Schwenzer, C. Brendle, B. Schölkopf, and B. J. Pichler, "MR-based attenuation correction methods for improved PET quantification in lesions within bone and susceptibility artifact regions," *J Nucl Med*, vol. 54, no. 10, pp. 1768-1774, 2013.
- [74] H. R. Marshall, J. Patrick, D. Laidley, F. S. Prato, J. Butler, J. Théberge, R. T. Thompson, and R. Z. Stodilka, "Description and assessment of a registration-based approach to include bones for attenuation correction of whole-body PET/MRI," *Med Phys*, vol. 40, no. 8, pp. 082509, 2013.
- [75] H. Arabi, and H. Zaidi, "Comparison of atlas-based bone segmentation methods in whole-body PET/MRI," *IEEE Nuclear Science Symposium and Medical Imaging Conference (NSS/MIC)*, 2014, *in press*.
- [76] J. Uh, T. E. Merchant, Y. Li, X. Li, and C. Hua, "MRI-based treatment planning with pseudo CT generated through atlas registration.," *Med Phys*, vol. 41, no. 5, pp. 051711-8, 2014.
- [77] H. R. Marshall, J. Patrick, D. Laidley, F. S. Prato, J. Butler, J. Theberge, R. T. Thompson, and R. Z. Stodilka, "Description and assessment of a registration-based approach to include bones for attenuation correction of whole-body PET/MRI.," *Med Phys*, vol. 40, no. 8, pp. 082509, Aug, 2013.
- [78] Y. Xia, J. Fripp, S. S. Chandra, R. Schwarz, C. Engstrom, and S. Crozier, "Automated bone segmentation from large field of view 3D MR images of the hip joint.," *Phys Med Biol*, vol. 58, no. 20, pp. 7375-7390, 2013.
- [79] N. Burgos, M. Cardoso, K. Thielemans, M. Modat, J. Schott, J. Duncan, D. Atkinson, S. Arridge, B. Hutton, and S. Ourselin, "Attenuation correction synthesis for hybrid PET-MR scanners: Application to brain studies.," *IEEE Trans Med Imaging*, vol. 33, no. 12, pp. 2332-2341, Jul 17, 2014.
- [80] F. Natterer, "Determination of Tissue Attenuation in Emission Tomography of Optically Dense Media," *Inverse Probl*, vol. 9, no. 6, pp. 731-736, 1993.
- [81] A. Welch, C. Campbell, R. Clackdoyle, F. Natterer, M. Hudson, A. Bromiley, P. Mikecz, F. Chillcot, M. Dodd, P. Hopwood, S. Craib, G. T. Gullberg, and P. Sharp, "Attenuation correction in PET using consistency information.," *IEEE Trans Nucl Sci*, vol. 45, no. 6, pp. 3134-3141, 1998.
- [82] A. Bromiley, A. Welch, F. Chilcott, S. Waikar, S. McCallum, M. Dodd, S. Craib, L. Schweiger, and P. Sharp, "Attenuation correction in PET using consistency conditions and a three-dimensional template.," *IEEE Trans Nucl Sci*, vol. 48, no. 4, pp. 1371-1377, 2001.
- [83] M. T. Madsen, and J. R. Lee, "Emission based attenuation correction of PET images of the thorax," in *IEEE Nuclear Science Symposium and Medical Imaging Conference (NSS/MIC)*, 1999, pp. 967-971 vol.2.
- [84] A. Welch, W. Hallett, P. Marsden, and A. Bromiley, "Accurate attenuation correction in PET using short transmission scans and consistency information," *IEEE Trans Nuc Sci*, vol. 50, no. 3, pp. 427-432, 2003.
- [85] G. Allali, V. Garibotto, I. C. Mainta, S. Armand, R. Camicioli, O. Ratib, H. Zaidi, F. R. Herrmann, and F. Assal, "Dopaminergic denervation is not necessary to induce gait disorders in atypical parkinsonian syndrome.," *J Neurol Sci*, vol. 351, no. 1-2, pp. 127-132, Apr 15, 2015.
- [86] A. V. Bronnikov, "Reconstruction of attenuation map using discrete consistency conditions," *IEEE Trans Med Imaging*, vol. 19, no. 5, pp. 451-462, May, 2000.
- [87] V. Y. Panin, F. Kehren, J. J. Hamill, and C. Michel, "Application of discrete data consistency conditions for selecting regularization parameters in PET attenuation map reconstruction," *Phys Med Biol*, vol. 49, no. 11, pp. 2425-36, Jun 7, 2004.
- [88] M. Defrise, A. Rezaei, and J. Nuyts, "Time-of-flight PET data determine the attenuation sinogram up to a constant," *Phys Med Biol*, vol. 57, no. 4, pp. 885-899, Feb, 2012.
- [89] A. Rezaei, J. Nuyts, and M. Defrise, "Analytic Reconstruction of the Attenuation from 3D Time-of-Flight PET Data," in *IEEE Nuclear Science Symposium and Medical Imaging Conference (NSS/MIC)*, 2012.
- [90] H. Li, G. El Fakhri, and Q. Li, "Direct MAP Estimation of Attenuation Sinogram using TOF PET Data and Anatomical Information," in *Fully 3D Image Recon. in Rad. and Nuc. Med*, 2013, pp. 404-407.
- [91] Y. Censor, D. E. Gustafson, A. Lent, and H. Tuy, "A New Approach to the Emission Computerized Tomography Problem: Simultaneous Calculation of Attenuation and Activity Coefficients," *IEEE Trans Nuc Sci*, vol. 26, no. 2, pp. 2775-2779, 1979.
- [92] W. Chen-Hsien, J. M. M. Anderson, M. Rao, and B. Mair, "Iterative methods for correcting attenuation in positron emission tomography," in *Proc Int Conf Image Processing 1998*, pp. 700-705 vol.2.

- [93] J. Nuyts, P. Dupont, S. Stroobants, R. Benninck, L. Mortelmans, and P. Suetens, "Simultaneous maximum a posteriori reconstruction of attenuation and activity distributions from emission sinograms," *IEEE Trans Med Imaging*, vol. 18, no. 5, pp. 393-403, 1999.
- [94] A. Krol, J. E. Bowsher, S. H. Manglos, D. H. Feiglin, M. P. Tornai, and F. D. Thomas, "An EM algorithm for estimating SPECT emission and transmission parameters from emission data only," *IEEE Trans Med Imaging*, vol. 20, no. 3, pp. 218-232, 2001.
- [95] M. Landmann, S. N. Reske, and G. Glattig, "Simultaneous iterative reconstruction of emission and attenuation images in positron emission tomography from emission data only," *Med Phys*, vol. 29, no. 9, pp. 1962-7, Sep, 2002.
- [96] F. Crepaldi, and A. De Pierro, R. , "Activity and Attenuation Reconstruction for Positron Emission Tomography Using Emission Data Only Via Maximum Likelihood and Iterative Data Refinement," *IEEE Trans Nuc Sci*, vol. 54, no. 1, pp. 100-106, 2007.
- [97] A. Salomon, A. Goedicke, B. Schweizer, T. Aach, and V. Schulz, "Simultaneous reconstruction of activity and attenuation for PET/MR," *IEEE Trans Med Imaging*, vol. 30, no. 3, pp. 804-813, 2011.
- [98] A. Salomon, A. Goedicke, and T. Aach, "Simultaneous reconstruction of activity and attenuation in multi-modal ToF-PET.." pp. 339-342.
- [99] A. Rezaei, M. Defrise, G. Bal, C. Michel, M. Conti, C. Watson, and J. Nuyts, "Simultaneous reconstruction of activity and attenuation in Time-of-Flight PET," *IEEE Trans Med Imaging* vol. 31, no. 12, pp. 2224-33, 2012.
- [100] A. Rezaei, M. Defrise, and J. Nuyts, "ML-reconstruction for TOF-PET with simultaneous estimation of the attenuation factors," *IEEE Trans Med Imaging*, vol. 33, no. 7, pp. 1563-1572, 2014.
- [101] G. Bal, F. Kehren, C. Michel, C. Watson, D. Manthey, and J. Nuyts, "Clinical evaluation of MLAA for MR-PET," *J Nucl Med Meeting Abstracts*, vol. 52, no. 1_MeetingAbstracts, pp. 263-, May 1, 2011, 2011.
- [102] N. H. Clinthorne, J. A. Fessler, G. D. Hutchins, and W. L. Rogers, "Joint maximum likelihood estimation of emission and attenuation densities in PET," in *IEEE Nuclear Science Symposium and Medical Imaging Conference (NSS/MIC)*, 1991, pp. 1927-1932 vol.3.
- [103] H. Erdogan, and J. A. Fessler, "Joint estimation of attenuation and emission images from PET scans," in *IEEE Nuclear Science Symposium and Medical Imaging Conference (NSS/MIC)*, 1999, pp. 1672-1675 vol.3.
- [104] G. Glattig, M. Wuchenauer, and S. N. Reske, "Simultaneous iterative reconstruction for emission and attenuation images in positron emission tomography," *Med Phys*, vol. 27, no. 9, pp. 2065-71, Sep, 2000.
- [105] W. W. Moses, "Time of flight in PET revisited," *IEEE Trans Nuc Sci*, vol. 50, no. 5, pp. 1325-1330, 2003.
- [106] P. Mollet, V. Keereman, E. Clementel, and S. Vandenberghe, "Simultaneous MR-compatible emission and transmission imaging for PET using time-of-flight information," *IEEE Trans Med Imaging*, vol. PP, no. 99, pp. 1-1, 2012.
- [107] P. Mollet, V. Keereman, J. Bini, D. Izquierdo-Garcia, Z. A. Fayad, and S. Vandenberghe, "Improvement of attenuation correction in time-of-flight PET/MR imaging with a positron-emitting source," *J Nucl Med*, vol. 55, no. 2, pp. 329-36, Feb, 2014.
- [108] A. Rezaei, M. Defrise, G. Bal, C. Michel, M. Conti, C. Watson, and J. Nuyts, "Simultaneous reconstruction of activity and attenuation in time-of-flight PET.," *IEEE Trans Med Imaging*, vol. 31, no. 12, pp. 2224-2233, 2012.
- [109] V. Y. Panin, M. Aykac, and M. E. Casey, "Simultaneous reconstruction of emission activity and attenuation coefficient distribution from TOF data, acquired with external transmission source," *Phys Med Biol*, vol. 58, no. 11, pp. 3649-69, 2013.
- [110] C. C. Watson, "Supplemental transmission method for improved PET attenuation correction on an integrated MR/PET," *Nucl Instrum Methods Phys Res A*, vol. 734, Part B, pp. 191-195, 2014.
- [111] H. Rothfuss, V. Panin, A. Moor, J. Young, I. Hong, C. Michel, J. Hamill, and M. Casey, "LSO background radiation as a transmission source using time of flight," *Phys Med Biol*, vol. 59, no. 18, pp. 5483-500, 2014.
- [112] M. Conti, I. Hong, and C. Michel, "Reconstruction of scattered and unscattered PET coincidences using TOF and energy information," *Phys Med Biol*, vol. 57, no. 15, pp. N307-17, Aug 7, 2012.

- [113] H. Sun, and S. Pistorius, "A generalized scatter reconstruction algorithm for limited energy resolution PET detectors," in IEEE Nuclear Science Symposium and Medical Imaging Conference (NSS/MIC), 2014.
- [114] G. Zhang, H. Sun, and S. Pistorius, "Feasibility of scatter based electron density reconstruction for attenuation correction in positron emission tomography," in IEEE Nuclear Science Symposium and Medical Imaging Conference (NSS/MIC), 2014.
- [115] Y. Berker, F. Kiessling, and V. Schulz, "Scattered PET data for attenuation-map reconstruction in PET/MRI," *Med Phys*, vol. 41, no. 10, pp. 102502, Oct, 2014.
- [116] G. Delso, A. Martinez-Möller, R. A. Bundschuh, S. G. Nekolla, and S. I. Ziegler, "The effect of limited MR field of view in MR/PET attenuation correction," *Med Phys*, vol. 37, no. 6, pp. 2804-2812, 2010.
- [117] G. Schramm, J. Langner, F. Hofheinz, J. Petr, A. Lougovski, B. Beuthien-Baumann, I. Platzek, and J. van den Hoff, "Influence and Compensation of Truncation Artifacts in MR-Based Attenuation Correction in PET/MR," *IEEE Trans Med Imaging*, vol. 32, no. 11, pp. 2056-2063, 2013.
- [118] Z. Hu, N. Ojha, S. Renisch, V. Schulz, I. Torres, A. Buhl, D. Pal, G. Muswick, J. Penatzer, T. Guo, P. Bonert, C. Tung, J. Kaste, M. Morich, T. Havens, P. Maniawski, W. Schafer, R. W. Gunther, G. A. Krombach, and L. Shao, "MR-based attenuation correction for a whole-body sequential PET/MR system." IEEE Nuclear Science Symposium and Medical Imaging Conference (NSS/MIC), pp. 3508-3512.
- [119] R. Qian, R. M. Manjeshwar, S. Ambwani, and S. D. Wollenweber, "Truncation completion of MR-based PET attenuation maps using time-of-flight non-attenuation-corrected PET images," in IEEE Nuclear Science Symposium and Medical Imaging Conference (NSS/MIC), 2012, pp. 2773-2775.
- [120] T. Blaffert, S. Renisch, J. Tang, M. Narayanan, and Z. Hu, "Comparison of threshold-based and watershed-based segmentation for the truncation compensation of PET/MR images," in Proc. SPIE, Medical Imaging, 2012, pp. 831403-831403-12.
- [121] J. Nuyts, G. Bal, F. Kehren, M. Fenchel, C. Michel, and C. Watson, "Completion of a Truncated Attenuation Image from the Attenuated PET Emission Data," *IEEE Trans Med Imaging*, vol. 32, no. 2, pp. 237-46, 2013.
- [122] J. O. Blumhagen, R. Ladebeck, M. Fenchel, and K. Scheffler, "MR-based field-of-view extension in MR/PET: B0 homogenization using gradient enhancement (HUGE)," *Magn Reson Med*, vol. 70, no. 4, pp. 1047-57, Oct, 2013.
- [123] J. O. Blumhagen, H. Braun, R. Ladebeck, M. Fenchel, D. Faul, K. Scheffler, and H. H. Quick, "Field of view extension and truncation correction for MR-based human attenuation correction in simultaneous MR/PET imaging," *Med Phys*, vol. 41, no. 2, pp. 022303, 2014.
- [124] S. Keller, S. Holm, A. Hansen, B. Sattler, F. Andersen, T. Klausen, L. Højgaard, A. Kjær, and T. Beyer, "Image artifacts from MR-based attenuation correction in clinical, whole-body PET/MRI," *Magnetic Resonance Materials in Physics, Biology and Medicine*, vol. 26, no. 1, pp. 173-181, 2013/02/01, 2013.
- [125] C. Ladefoged, F. Andersen, S. Keller, J. Löfgren, A. Hansen, S. Holm, L. Højgaard, and T. Beyer, "PET/MR imaging of the pelvis in the presence of endoprostheses: reducing image artifacts and increasing accuracy through inpainting," *Eur. J. Nucl. Med. Mol. Imaging*, vol. 40, no. 4, pp. 594-601, 2013/04/01, 2013.
- [126] G. Schramm, J. Maus, F. Hofheinz, J. Petr, A. Lougovski, B. Beuthien-Baumann, I. Platzek, and J. van den Hoff, "Evaluation and automatic correction of metal-implant-induced artifacts in MR-based attenuation correction in whole-body PET/MR imaging," *Phys Med Biol*, vol. 59, no. 11, pp. 2713-26, Jun 7, 2014.
- [127] C. Ladefoged, T. Beyer, S. Keller, I. Law, L. Højgaard, A. Kjær, F. B. Lauze, and F. Andersen, "PET/MR imaging of head/neck in the presence of dental implants: reducing image artifacts and increasing accuracy through inpainting," in Annual Congress of the European Association of Nuclear Medicine, 2013.
- [128] B. A. Hargreaves, P. W. Worters, K. B. Pauly, J. M. Pauly, K. M. Koch, and G. E. Gold, "Metal-Induced Artifacts in MRI," *Am J Roentgenol*, vol. 197, no. 3, pp. 547-555, 2011/09/01, 2011.
- [129] M. J. Lee, S. Kim, S. A. Lee, H. T. Song, Y. M. Huh, D. H. Kim, S. H. Han, and J. S. Suh, "Overcoming artifacts from metallic orthopedic implants at high-field-strength MR imaging and multi-detector CT," *Radiographics*, vol. 27, no. 3, pp. 791-803, May-Jun, 2007.

- [130] K. M. Koch, J. E. Lorbiecki, R. S. Hinks, and K. F. King, "A multispectral three-dimensional acquisition technique for imaging near metal implants," *Magn Reson Med*, vol. 61, no. 2, pp. 381-90, Feb, 2009.
- [131] I. Hong, W. Luk, V. Panin, C. Watson, F. Kehren, and M. Casey, "Real-time PET reconstruction." 2015. *in press*.
- [132] I. A. Burger, M. C. Wurnig, A. S. Becker, D. Kenkel, G. Delso, P. Veit-Haibach, and A. Boss, "Hybrid PET/MR Imaging: An Algorithm to Reduce Metal Artifacts from Dental Implants in Dixon-Based Attenuation Map Generation Using a Multiacquisition Variable-Resonance Image Combination Sequence," *J Nucl Med*, vol. 56, no. 1, pp. 93-7, Jan, 2015.
- [133] T. Pan, and H. Zaidi, "Attenuation Correction Strategies for Positron Emission Tomography/Computed Tomography and 4-Dimensional Positron Emission Tomography/Computed Tomography," *PET Clinics*, vol. 8, no. 1, pp. 37-50, 2013.
- [134] C. Buerger, A. Aitken, C. Tsoumpas, A. P. King, V. Schulz, P. Marsden, and T. Schaeffter, "Investigation of 4D PET attenuation correction using Ultra-short Echo Time MR," in IEEE Nuclear Science Symposium and Medical Imaging Conference (NSS/MIC), 2011, pp. 3558-3561.
- [135] H. Fayad, H. Schmidt, C. Wuerslin, and D. Visvikis, "4D attenuation map generation in PET/MR imaging using 4D PET derived motion fields," in IEEE Nuclear Science Symposium and Medical Imaging Conference (NSS/MIC), 2013, pp. 1-4.
- [136] A. Mehranian, and H. Zaidi, "Emission-based estimation of lung attenuation coefficients for attenuation correction in PET/MR," *Phys Med Biol*, vol., 2015, *under revision*.
- [137] A. Rezaei, and J. Nuyts, "Joint registration of attenuation and activity images in gated TOF-PET," in IEEE Nuclear Science Symposium and Medical Imaging Conference (NSS/MIC), 2013, pp. 1-4.
- [138] L. R. MacDonald, S. Kohlmyer, C. Liu, T. K. Lewellen, and P. E. Kinahan, "Effects of MR surface coils on PET quantification," *Med Phys*, vol. 38, no. 6, pp. 2948-2956, 2011.
- [139] L. Tellmann, H. H. Quick, A. Bockisch, H. Herzog, and T. Beyer, "The effect of MR surface coils on PET quantification in whole-body PET/MR: Results from a pseudo-PET/MR phantom study," *Med Phys*, vol. 38, no. 5, pp. 2795-2805, 2011.
- [140] R. Kartmann, D. H. Paulus, H. Braun, B. Aklan, S. Ziegler, B. K. Navalpakkam, M. Lentschig, and H. H. Quick, "Integrated PET/MR imaging: Automatic attenuation correction of flexible RF coils," *Med Phys*, vol. 40, no. 8, pp. 082301, 2013.
- [141] G. Delso, A. Martinez-Möller, R. A. Bundschuh, R. Ladebeck, Y. Candidus, D. Faul, and S. I. Ziegler, "Evaluation of the attenuation properties of MR equipment for its use in a whole-body PET/MR scanner," *Phys Med Biol*, vol. 55, no. 15, pp. 4361, 2010.
- [142] S. Furst, M. Souvatzoglou, A. Martinez-Moller, M. Schwaiger, S. G. Nekolla, and S. I. Ziegler, "Impact of flexible body surface coil and patient table on PET quantification and image quality in integrated PET/MR," *Nuklearmedizin*, vol. 53, no. 3, pp. 79-87, 2014.
- [143] G. Delso, S. Furst, B. Jakoby, R. Ladebeck, C. Ganter, S. G. Nekolla, M. Schwaiger, and S. I. Ziegler, "Performance Measurements of the Siemens mMR Integrated Whole-Body PET/MR Scanner," *J Nucl Med*, vol. 52, no. 12, pp. 1914-1922, 2011.
- [144] B. Aklan, D. H. Paulus, E. Wenkel, H. Braun, B. K. Navalpakkam, S. Ziegler, C. Geppert, E. E. Sigmund, A. Melsaether, and H. H. Quick, "Toward simultaneous PET/MR breast imaging: Systematic evaluation and integration of a radiofrequency breast coil," *Med Phys*, vol. 40, no. 2, pp. 024301, 2013.
- [145] B. Zhang, D. Pal, H. Zhiqiang, N. Ojha, T. Guo, G. Muswick, T. Chi-Hua, and J. Kaste, "Attenuation correction for MR table and coils for a sequential PET/MR system," in IEEE Nuclear Science Symposium and Medical Imaging Conference (NSS/MIC), 2009, pp. 3303-3306.
- [146] M. Abdoli, R. A. J. O. Dierckx, and H. Zaidi, "Metal artifact reduction strategies for improved attenuation correction in hybrid PET/CT imaging.," *Med Phys*, vol. 39, no. 6, pp. 3343-3360, 2012.
- [147] D. H. Paulus, L. Tellmann, and H. H. Quick, "Towards improved hardware component attenuation correction in PET/MR hybrid imaging," *Phys Med Biol*, vol. 58, no. 22, pp. 8021, 2013.
- [148] D. H. Paulus, H. Braun, B. Aklan, and H. H. Quick, "Simultaneous PET/MR imaging: MR-based attenuation correction of local radiofrequency surface coils," *Med Phys*, vol. 39, no. 7, pp. 4306-15, Jul, 2012.

- [149] M. Eldib, J. Bini, P. M. Robson, D. Faul, and Z. A. Fayad, "Attenuation correction for flexible MRI coils using the ultra-short echo time sequence in MR/PET imaging," in Proc. Intl. Soc. Mag. Reson. Med., 2014, pp. 784.
- [150] M. Eldib, J. Bini, C. Calcagno, P. M. Robson, V. Mani, and Z. A. Fayad, "Attenuation correction for flexible magnetic resonance coils in combined magnetic resonance/positron emission tomography imaging," *Invest Radiol*, vol. 49, no. 2, pp. 63-9, Feb, 2014.
- [151] F. Mantlik, M. Hofmann, M. K. Werner, A. Sauter, J. Kupferschlager, B. Scholkopf, B. J. Pichler, and T. Beyer, "The effect of patient positioning aids on PET quantification in PET/MR imaging," *Eur. J. Nucl. Med. Mol. Imaging*, vol. 38, no. 5, pp. 920-9, May, 2011.
- [152] S. Saha, "Whole body RF coil design for a simultaneous PET-MR system," in Proc. Intl. Soc. Mag. Reson. Med., Milan, Italy, 2014.
- [153] Y.-J. Stickle, T.-Y. Yang, T. E. Zink, S. Bhatia, V. Taracila, F. Robb, B. K. Shah, and D. M. Goldhaber, "A PET optimized 16-element anterior array coil for 3T simultaneous MR/PET System " in Proc. Intl. Soc. Mag. Reson. Med., 2013.
- [154] I. Dregely, T. Lanz, S. Metz, M. F. Mueller, M. Kuschan, M. Nimbalkar, R. A. Bundschuh, S. I. Ziegler, A. Haase, S. G. Nekolla, and M. Schwaiger, "A 16-channel MR coil for simultaneous PET/MR imaging in breast cancer," *Eur Radiol*, vol. 25, no. 4, pp. 1154-61, Apr, 2015.
- [155] J. Ouyang, C. Se Young, Y. Petibon, A. A. Bonab, N. Alpert, and G. El Fakhri, "Bias atlases for segmentation-based PET attenuation correction using PET-CT and MR," *IEEE Trans Nuc Sci*, vol. 60, no. 5, pp. 3373-3382, 2013.
- [156] V. Keereman, R. V. Holen, P. Mollet, and S. Vandenberghe, "The effect of errors in segmented attenuation maps on PET quantification," *Med Phys*, vol. 38, no. 11, pp. 6010-9, Nov, 2011.
- [157] A. Akbarzadeh, M. R. Ay, A. Ahmadian, N. Riahi Alam, and H. Zaidi, "MRI-guided attenuation correction in whole-body PET/MR: assessment of the effect of bone attenuation," *Ann Nucl Med*, vol. 27, no. 2, pp. 152-162, 2013/02/01, 2013.
- [158] H. Arabi, O. Rager, A. Alem, A. Varoquaux, M. Becker, and H. Zaidi, "Clinical Assessment of MR-Guided 3-Class and 4-Class Attenuation Correction in PET/MR," *Mol Imaging Biol*, vol. 17, no. 2, pp. 264-76, Apr, 2015.
- [159] C. Catana, A. van der Kouwe, T. Benner, C. J. Michel, M. Hamm, M. Fenchel, B. Fischl, B. Rosen, M. Schmand, and A. G. Sorensen, "Toward implementing an MRI-based PET attenuation-correction method for neurologic studies on the MR-PET brain prototype," *J Nucl Med*, vol. 51, no. 9, pp. 1431-8, Sep, 2010.
- [160] H. Choi, G. J. Cheon, H.-J. Kim, S. H. Choi, J. S. Lee, Y.-i. Kim, K. W. Kang, J.-K. Chung, E. E. Kim, and D. S. Lee, "Segmentation-Based MR Attenuation Correction Including Bones Also Affects Quantitation in Brain Studies: An Initial Result of 18F-FP-CIT PET/MR for Patients with Parkinsonism," *Journal of Nuclear Medicine*, vol. 55, no. 10, pp. 1617-1622, October 1, 2014, 2014.
- [161] C. Brendle, H. Schmidt, A. Oergel, I. Bezrukov, M. Mueller, C. Schraml, C. Pfannenber, C. la Fougere, K. Nikolaou, and N. Schwenzer, "Segmentation-Based Attenuation Correction in Positron Emission Tomography/Magnetic Resonance: Erroneous Tissue Identification and Its Impact on Positron Emission Tomography Interpretation," *Invest Radiol*, Jan 12, 2015.
- [162] D. Izquierdo-Garcia, S. Sawiak, K. Knesaurek, J. Narula, V. Fuster, J. Machac, and Z. Fayad, "Comparison of MR-based attenuation correction and CT-based attenuation correction of whole-body PET/MR imaging," *Eur J Nucl Med Mol Imaging*, vol. 41, no. 8, pp. 1574-1584, 2014/08/01, 2014.
- [163] R. Karimi, G. Tornling, H. Forsslund, M. Mikko, A. Wheelock, S. Nyren, and C. M. Skold, "Lung density on high resolution computer tomography (HRCT) reflects degree of inflammation in smokers," *Respir Res*, vol. 15, pp. 23, 2014.
- [164] P. J. Robinson, and L. Kreel, "Pulmonary tissue attenuation with computed tomography: comparison of inspiration and expiration scans," *J Comput Assist Tomogr*, vol. 3, no. 6, pp. 740-8, Dec, 1979.
- [165] L. Gattinoni, P. Pelosi, G. Vitale, A. Pesenti, L. D'Andrea, and D. Mascheroni, "Body position changes redistribute lung computed-tomographic density in patients with acute respiratory failure," *Anesthesiology*, vol. 74, no. 1, pp. 15-23, Jan, 1991.

- [166] J. H. Kim, J. S. Lee, I. C. Song, and D. S. Lee, "Comparison of segmentation-based attenuation correction methods for PET/MRI: evaluation of bone and liver standardized uptake value with oncologic PET/CT data," *J Nucl Med*, vol. 53, no. 12, pp. 1878-82, Dec, 2012.
- [167] H. R. Marshall, F. S. Prato, L. Deans, J. Théberge, R. T. Thompson, and R. Z. Stodilka, "Variable lung density consideration in attenuation correction of whole-body PET/MRI," *J Nucl Med*, vol. 53, no. 6, pp. 977-984, June 1, 2012, 2012.
- [168] A. H. R. Lonn, and S. D. Wollenweber, "Estimation of mean lung attenuation for use in generating PET attenuation maps," in IEEE Nuclear Science Symposium and Medical Imaging Conference (NSS/MIC), 2012, pp. 3017-3018.
- [169] Y. Berker, A. Salomon, F. Kiessling, and V. Schulz, "Lung attenuation coefficient estimation using Maximum Likelihood reconstruction of attenuation and activity for PET/MR attenuation correction," in IEEE Nuclear Science Symposium and Medical Imaging Conference (NSS/MIC), 2012, pp. 2282-2284.
- [170] Y. Berker, A. Salomon, F. Kiessling, and V. Schulz, "Out-of-field activity in the estimation of mean lung attenuation coefficient in PET/MR," *Nucl Instrum Methods Phys Res A*, vol. 734, Part B, no. 0, pp. 206-209, 2014.
- [171] G. Wagenknecht, H.-J. Kaiser, F. Mottaghy, and H. Herzog, "MRI for attenuation correction in PET: methods and challenges," *Magn Reson Mat Phys Biol Med*, vol. 26, no. 1, pp. 99-113, 2013/02/01, 2013.
- [172] P. J. Schleyer, T. Schaeffter, and P. K. Marsden, "The effect of inaccurate bone attenuation coefficient and segmentation on reconstructed PET images," *Nucl Med Commun*, vol. 31, no. 8, pp. 708-16, Aug, 2010.
- [173] W. Lee, J.-A. Park, K. M. Kim, I.-O. Ko, I. Lim, J. S. Kim, J. Kim, S.-K. Woo, J. h. Kang, and S. M. Lim, "Effects of MR contrast agents on PET quantitation in PET-MRI study," *J Nucl Med Meeting Abstracts*, vol. 52, no. 1_MeetingAbstracts, pp. 53-, May 1, 2011, 2011.
- [174] C. Lois, I. Bezrukov, H. Schmidt, N. Schwenzer, M. Werner, J. Kupferschläger, and T. Beyer, "Effect of MR contrast agents on quantitative accuracy of PET in combined whole-body PET/MR imaging," *Eur. J. Nucl. Med. Mol. Imaging*, vol. 39, no. 11, pp. 1756-1766, 2012/11/01, 2012.
- [175] S. Surti, "Update on Time-of-Flight PET Imaging," *J Nucl Med*, vol. 56, no. 1, pp. 98-105, Jan, 2015.
- [176] G. El Fakhri, S. Surti, C. M. Trott, J. Scheuermann, and J. S. Karp, "Improvement in lesion detection with whole-body oncologic time-of-flight PET," *J Nucl Med*, vol. 52, no. 3, pp. 347-353, March 1, 2011, 2011.
- [177] T. G. Turkington, and J. M. Wilson, "Attenuation artifacts and time-of-flight PET," in IEEE Nuclear Science Symposium and Medical Imaging Conference (NSS/MIC), 2009, pp. 2997-2999.
- [178] M. Conti, "Why is TOF PET reconstruction a more robust method in the presence of inconsistent data?," *Phys Med Biol*, vol. 56, no. 1, pp. 155-68, Jan 7, 2011.
- [179] S. Ahn, L. Cheng, and R. M. Manjeshwar, "Analysis of the effects of errors in attenuation maps on PET quantitation in TOF PET," in IEEE Nuclear Science Symposium and Medical Imaging Conference (NSS/MIC), 2015.
- [180] S. Wollenweber, G. Delso, T. Deller, D. Goldhaber, M. Hüllner, and P. Veit-Haibach, "Characterization of the impact to PET quantification and image quality of an anterior array surface coil for PET/MR imaging," *Magn Reson Mat Phys Biol Med*, vol. 27, no. 2, pp. 149-159, 2014/04/01, 2014.
- [181] H. Davison, E. E. Ter Voert, F. de Galiza Barbosa, P. Veit-Haibach, and G. Delso, "Incorporation of Time-of-Flight Information Reduces Metal Artifacts in Simultaneous Positron Emission Tomography/Magnetic Resonance Imaging: A Simulation Study," *Invest Radiol*, Mar 11, 2015.
- [182] T. W. Deller, A. M. Grant, M. M. Khalighi, S. H. Maramraju, G. Delso, and C. S. Levin, "PET NEMA performance measurements for a SiPM-based time-of-flight PET/MR system," in IEEE Nuclear Science Symposium and Medical Imaging Conference (NSS/MIC), Seattle, WA, 8-15 November 2014, 2014, pp. *in press*.
- [183] ter Voert E, Delso G, Ahn S, Wiesinger F, Huellner M, and V.-H. P, "The effect of TOF on PET reconstructions in patients with (metal) implants in simultaneous TOF PET/MR scanning," in Radiological Society of North America Scientific Assembly and Annual Meeting Chicago IL, 2014
- [184] A. Mehranian, and H. Zaidi, "Impact of time-of-flight PET on quantification errors in MRI-based attenuation correction," *J Nucl Med*, vol. 56, no. 4, pp. 635-641, 2015.
- [185] J. E. Holmes, and G. M. Bydder, "MR imaging with ultrashort TE (UTE) pulse sequences: Basic principles," *Radiography*, vol. 11, no. 3, pp. 163-174, 2005.

- [186] J. Du, G. Hamilton, A. Takahashi, M. Bydder, and C. B. Chung, "Ultrashort echo time spectroscopic imaging (UTESI) of cortical bone," *Magn Reson Med*, vol. 58, no. 5, pp. 1001-9, Nov, 2007.
- [187] C. Li, J. Magland, and F. Wehrli, "Compressed sensing 3D ultrashort echo time (COMPUTE) imaging," in *Proc. Intl. Soc. Mag. Reson. Med.*, 2012, pp. 1402.
- [188] L. Hu, K.-H. Su, G. C. Pereira, A. Grover, B. Traugber, M. Traugber, and R. F. Muzic, "k-space sampling optimization for ultrashort TE imaging of cortical bone: Applications in radiation therapy planning and MR-based PET attenuation correction," *Med Phys*, vol. 41, no. 10, pp. 102301, 2014.
- [189] J. Du, and G. M. Bydder, "Qualitative and quantitative ultrashort-TE MRI of cortical bone," *NMR in Biomedicine*, vol. 26, no. 5, pp. 489-506, 2013.
- [190] M. Weiger, D. O. Brunner, B. E. Dietrich, C. F. Muller, and K. P. Pruessmann, "ZTE imaging in humans," *Magn Reson Med*, vol. 70, no. 2, pp. 328-32, Aug, 2013.
- [191] F. Wiesinger, L. I. Sacolick, A. Menini, S. S. Kaushik, S. Ahn, P. Veit-Haibach, G. Delso, and D. D. Shanbhag, "Zero TE MR bone imaging in the head," *Magn Reson Med*, 2015, *in press*.
- [192] G. Delso, F. Wiesinger, L. I. Sacolick, S. S. Kaushik, D. D. Shanbhag, M. Hüllner, and P. Veit-Haibach, "Clinical evaluation of zero-echo-time MR imaging for the segmentation of the skull," *J Nucl Med*, vol. 56, no. 3, pp. 417-422, March 1, 2015, 2015.
- [193] K. M. Johnson, S. B. Fain, M. L. Schiebler, and S. Nagle, "Optimized 3D ultrashort echo time pulmonary MRI," *Magn Reson Med*, vol. 70, no. 5, pp. 1241-1250, 2013.
- [194] F. Gibiino, L. Sacolick, A. Menini, L. Landini, and F. Wiesinger, "Free-breathing, zero-TE MR lung imaging.," *Magn Reson Mat Phys Biol Med*, pp. *in press*, Sep 9, 2015.
- [195] J. Czernin, L. Ta, and K. Herrmann, "Does PET/MR imaging improve cancer assessments? Literature evidence from more than 900 patients," *J Nucl Med*, vol. 55, no. Supplement 2, pp. 59S-62S, June 1, 2014, 2014.
- [196] M. Becker, and H. Zaidi, "Imaging in head and neck squamous cell carcinoma: the potential role of PET/MRI," *Br J Radiol*, vol. 87, no. 1036, pp. 20130677, 2014.
- [197] H. T. van Dam, G. Borghi, S. Seifert, and D. R. Schaart, "Sub-200 ps CRT in monolithic scintillator PET detectors using digital SiPM arrays and maximum likelihood interaction time estimation.," *Phys Med Biol*, vol. 58, no. 10, pp. 3243-3257, May 21, 2013.
- [198] K. Doroud, A. Rodriguez, M. C. S. Williams, K. Yamamoto, A. Zichichi, and R. Zuyewski, "Systematic study of new types of Hamamatsu MPPCs read out with the NINO ASIC.," *Nucl Instrum Methods Phys Res A*, vol. 753, no. 0, pp. 149-153, 7/21/, 2014.
- [199] J.-y. Cui, G. Prax, S. Prevrhal, and C. S. Levin, "Fully 3D list-mode time-of-flight PET image reconstruction on GPUs using CUDA," *Med Phys*, vol. 38, no. 12, pp. 6775-6786, 2011.
- [200] I. Hong, W. Luk, V. Panin, C. Watson, F. Kehren, and M. Casey, "Real-time PET reconstruction," in *IEEE Nuclear Science Symposium and Medical Imaging Conference (NSS/MIC)*, 2014.

Chapter 8

Impact of time-of-flight PET on quantification errors in MRI-based attenuation correction

Abolfazl Mehranian and Habib Zaidi

J Nuc Med Vol. 56, No. 4, pp 635-641 (2015)

Abstract

Purpose: Time-of-flight (TOF) PET/MRI is an emerging imaging technology with great capabilities offered by TOF to improve image quality and lesion detectability. We assess, for the first time, the impact of TOF image reconstruction on PET quantification errors induced by MRI-based attenuation correction (MRAC) using simulation and clinical PET/CT studies.

Methods: Standard 4-class attenuation maps were derived by segmentation of CT images of 27 patients undergoing PET/CT examinations into background air, lung, soft tissue and fat tissue classes, followed by the assignment of predefined attenuation coefficients to each class. For each patient, 4 PET images were reconstructed: non-TOF and TOF both corrected for attenuation using reference CT-based attenuation correction (CTAC) and the resulting 4-class MRAC maps. The relative errors between non-TOF and TOF MRAC reconstructions were compared with their reference CTAC reconstructions. The bias was locally and globally evaluated using volumes of interest (VOIs) defined on lesions and normal tissues and CT-derived tissue classes containing all voxels in a given tissue, respectively. The impact of TOF on reducing the errors induced by metal-susceptibility and respiratory-phase mismatch artifacts was also evaluated using clinical and simulation studies.

Results: Our results show that TOF-PET can remarkably reduce attenuation correction artifacts and quantification errors in the lungs and bone tissues. Using class-wise analysis, it was found that the non-TOF MRAC method results in an error of $-3.4 \pm 11.5\%$ in the lungs and $-21.8 \pm 2.9\%$ in bones, whereas its TOF counterpart reduced the errors to $-2.9 \pm 7.1\%$ and $-15.3 \pm 2.3\%$, respectively. The VOI-based analysis revealed that the non-TOF and TOF methods resulted in an average overestimation of 7.5% and 3.9% in/near lung lesions ($n = 23$) and underestimation of $<5\%$ for soft tissue and in/near bone lesions ($n = 91$). Simulation results showed that as TOF resolution improves, artifacts and quantification errors are substantially reduced.

Conclusion: TOF-PET substantially reduces artifacts and improves significantly the quantitative accuracy of standard MRAC methods. Therefore, MRI-based attenuation correction should be less of a concern on future TOF PET/MR scanners with improved timing resolution.

I. Introduction

Hybrid PET/MR imaging has recently emerged as a new modality enabling simultaneous molecular and morphological assessment of a variety of physiopathological conditions [1]. Over the last two decades, PET/MR technology has experienced considerable technical advances toward addressing the challenges encountered in system design and quantitative performance. With the advent of avalanche photodiodes and silicon photomultipliers (SiPMs), the challenge of mutual compatibility between PET and MR subsystems has now been well addressed, thus paving the way toward fully integrated time-of-flight (TOF) PET/MR systems [2]. However, accurate PET quantification using MRI-based attenuation correction (MRAC) remains a major challenge [3].

MR signals are related to proton density, relaxation time properties of tissues and the selected pulse parameters. Therefore, there is no a unique mapping between MR intensities and attenuation coefficients at 511 keV, as in PET/CT. Moreover, bones cannot be well delineated on conventional MR sequences because of their low water content and short transverse relaxation time. Truncation of MRI field-of-view (FOV) and metal-induced susceptibility artifacts are other problems encountered in MRAC [4]. Generally, MRAC methods can be categorized in 3 groups: segmentation-based approaches, which segment MR images into different tissue classes (background air, lung, fat, and soft tissue) and assign predefined attenuation coefficients to each class [5], atlas registration based approaches, in which a co-registered MR-CT atlas dataset is used to derive a pseudo CT image from the patient's MR image [6] and emission-based approaches in which the attenuation map is directly estimated from TOF-PET emission data with MR anatomical prior information [7, 8]. Currently, segmentation-based MRAC is the standard approach on commercial PET/MR scanners.

In 3- or 4-class MRAC methods, bones are replaced by soft tissue and the inter/intra-patient heterogeneity of attenuation coefficients in different tissue classes is ignored, which leads to quantification errors in the estimation of standardized uptake value (SUV) ranging between 4 and 25% in different organs [9-13]. Using PET/CT datasets of 35 patients, Martinez-Möller et al. reported an average SUV error of $8.0 \pm 3.3\%$ in 21 bone lesions and $<5\%$ in all other lesions [5]. Schulz et al. reported, using 15 whole-body PET-CT/MR patient scans, an average error of $6.5 \pm 4.1\%$ in 7 bone lesions and a maximum error of -13.4% in a pelvic bone lesion [14]. Ouyang et al demonstrated that if the bones can be identified in MR images to produce a 5-class MRAC map, SUV errors in all bones are reduced to $<10\%$ [10]. Ultra-short echo time (UTE) pulse sequences have been extensively explored to include bones as 5th class and reduce PET quantification errors [15]. Despite the promising results, UTE sequences are time-consuming and not yet clinically feasible.

With the advent of clinical TOF-PET systems, several studies reported that TOF can improve PET image quality in terms of signal-to-noise ratio, lesion detectability, convergence rate and tolerance to inconsistencies between emission and correction data compared to non-TOF reconstructions [16]. Using 2D phantom simulations, Boellaard et al. showed that TOF-PET reconstruction can reduce PET quantification errors when using MR-based attenuation correction [17]. In fact, in TOF-PET, the difference in arrival times of coincident annihilation photons are measured with an uncertainty governed by the timing resolution of the detectors. During PET image reconstruction, the additional TOF information is exploited to update image voxels only along segment of responses, defined by TOF resolution, instead of the whole line of response. Consequently, the cross-dependencies between image voxels are reduced, which results in reduced noise propagation, fast and space-invariant convergence, thus improving the detectability of lesions located near large hot regions (e.g. the liver), and reduced sensitivity to errors in normalization, attenuation and scatter corrections.

Considering the fast development of TOF-PET detectors toward sub-100 ps coincidence timing resolutions [18] and the lack of clinical studies highlighting the importance of TOF in MRAC PET, we aim at systematically evaluating the impact of TOF on PET quantification errors induced by 4-class MRAC. In addition, we evaluate the performance of TOF-PET in the presence of metal susceptibility and respiratory mismatch artifacts in MRAC maps. To explore the trend of bias reduction in future generation PET/MR scanners with improved timing resolution, we conduct realistic 3D simulations using different TOF resolutions in phantoms derived from clinical FDG examinations.

II. Materials and methods

II.A. Data acquisition and image reconstruction

PET/CT datasets were acquired on the Siemens Biograph mCT Flow scanner (Siemens Healthcare, Erlangen). The PET subsystem of the scanner consists of 4 rings of 48 detector blocks, covering axial and transaxial FOVs of 218 and 700 mm, respectively. PET data were acquired with an effective TOF resolution of 580 ps and reconstructed using an ordinary Poisson ordered subset expectation maximization (OSEM) algorithm with point spread function (PSF) and TOF. The default manufacturer-provided reconstruction parameters for OSEM+PSF with and without TOF were 2 iterations and 21 subsets, and 2 iterations and 24 subsets, respectively. The whole-body image matrix size was 200×200 with $4 \times 4 \times 2$ mm³ voxels. The CT subsystem is a 128-slice CT scanner (SOMATOM Definition AS+) with an extended transaxial FOV of 780 mm.

1) Clinical Studies

A total number of 27 patients (13 women, 14 men; average age 58.8 ± 18.2 years) referred for ¹⁸F-FDG ($n = 25$) and ¹⁸F-Choline ($n = 2$) PET/CT examinations were included in this study. The institutional ethics committee approved this retrospective study. The patients had an average body mass index (BMI) of 25.1 ± 4.2 kg/m². They were injected by a standard dose of ¹⁸F-FDG (250.5 ± 44.4 MBq) and ¹⁸F-Choline (329.1 ± 1.2 MBq). After an uptake time of 60 and 10 minutes for FDG and FCH administrations, whole-body PET/CT FlowMotion™ scanning was performed for two scan ranges, from the toes to the mid thigh with bed speed of 1.1 mm/sec. and from the mid thigh to the vertex with speed of 0.7 mm/sec. The average acquisition time was 24.9 ± 5.4 minutes. A whole-body CT scan protocol was performed for PET attenuation correction using 100-120 kVp, 150 mAs, and 5 mm slice thickness.

2) Simulation Studies

To explore the limiting impact of TOF on MRAC PET quantification errors, we conducted a series of 3D analytic simulations with different TOF timing resolutions using an in-house TOF-PET simulator, developed for the native geometry of the Siemens mCT system using MATLAB with SPMD parallel processing. The software was validated using the experimental NEMA phantom. Effective timing resolutions of 580, 350 and 100 ps were modeled to respectively represent typical TOF resolution of first generation of clinical TOF-PET/MR scanners, introduced since 2010 [19], current generation of SiPM-based TOF-PET scanners [2] and future generation PET scanners with the best possible timing resolution currently achievable in the laboratory [18]. Realistic whole-body phantoms were derived from clinical FDG PET/CT studies to simulate the biodistribution of FDG, patient-specific CTAC map, the respiratory-phase mismatch between PET and MRAC images. TOF sinogram data and actual attenuation factors were obtained by forward projection of activity and attenuation maps. Poisson noise realizations were simulated for 80 M counts. The contribution of scattered and random coincidences was ignored. The PET activity maps were reconstructed for 4 overlapping beds with a matrix size of $200 \times 200 \times 109$ per bed, using an ordinary Poisson OSEM algorithm with 3 iterations and 28 subsets for non-TOF, and 3 iterations and 21 subsets for TOF reconstructions.

II.B. Attenuation map generation

To derive MRAC maps, CT images of patients were segmented into 4 tissue classes: background air, lung, fat, and non-fat soft tissues. Background air and lungs were segmented using a seeded region growing technique implemented in the ITK-SNAP software [20]. The fat tissue class was segmented by thresholding CT intensity values between -470 and -53 Hounsfield units (corresponding to attenuation coefficients at 511 keV between 0.05 and 0.095 cm⁻¹). The soft tissue class was then defined as the complement of the segmented classes. In this procedure, bones and air pockets are assigned to soft tissue class. Mean attenuation coefficients of 0 , 0.0221 , 0.0864 and 0.0975 cm⁻¹ were assigned to background air, lungs, fat and non-fat soft tissue classes, respectively. Owing to intrinsic differences in image contrast between CT and MR imaging, the resulting 4-class attenuation maps might differ from the scanner's 4-class MRAC maps in tissue content. Supplemental Figure 1 compares both attenuation maps of a patient who underwent a PET/MRI scan on the Philips Ingenuity PET/MR scanner [19] and a complementary PET/CT scan where an excellent coregistration was achieved. As can be seen, both attenuation maps are in good agreement with sparse differences in fat content.

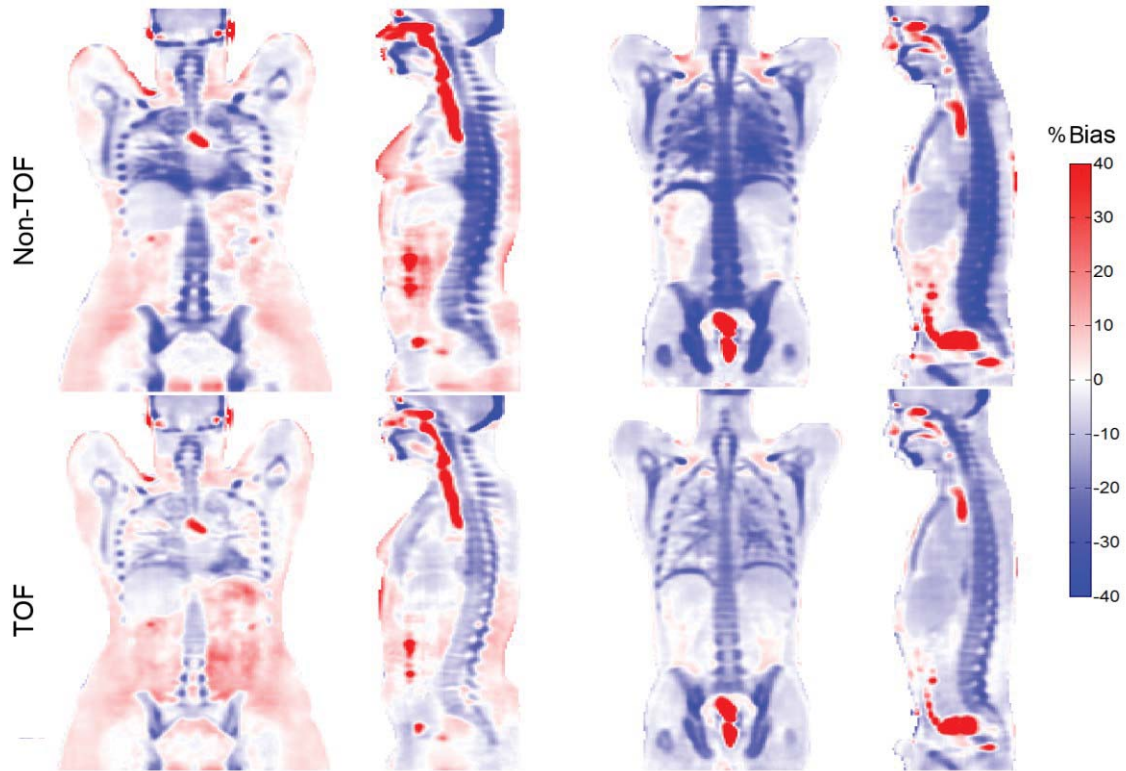


Figure 1. Representative bias maps between PET images corrected for attenuation using 4-class MRAC and CTAC techniques obtained using non-TOF and TOF reconstructions for two patients with large (left panel) and low (right panel) BMIs.

II.C. Data analysis

Four PET image reconstructions were performed for each patient: reference CTAC-PET and MRAC-PET with and without TOF. The relative quantification error (bias) in tracer uptake was calculated on a voxel-by-voxel basis (i) for each patient as follows:

$$Bias_i^m = 100 \times \frac{(SUV_{MRAC}^m)_i - (SUV_{CTAC}^m)_i}{(SUV_{CTAC}^m)_i}$$

where m is the reconstruction method (non-TOF or TOF). The difference in bias of the non-TOF and TOF methods was then evaluated using volume of interest (VOI) and class-wise analyses. For each patient, 13 VOIs were defined on normal tissues including the lungs (upper, middle and lower portions of left and right lungs), liver, aorta, cerebrum, 3rd thoracic (T3), 4th lumbar (L4) and illia of pelvis (left and right). Moreover, 80% isocontour VOIs were defined on the lesion locations in TOF CTAC-PET images. Lesions were classified into 3 groups: soft tissue ($n = 44$), bones and/or near bone ($n = 47$) and lungs and/or near lung ($n = 23$). For class-wise analyses, the original CT images were down-sampled to the resolution of PET images and segmented using region-growing and thresholding techniques into lungs, fat, soft tissue and bones. The distributions of some VOIs and tissue classes for a representative patient are shown in Supplemental Figure 2. For the defined VOIs, the mean (μ), standard deviation (σ) and root-mean-squared error (RMSE) of bias ($\sqrt{\mu^2 + \sigma^2}$) was calculated. The correlation between MRAC-PET and CTAC-PET with and without TOF was determined on scatter plots using Pearson correlation analysis. The concordance between the SUVs was evaluated using Bland-Altman plots. The limits of agreement were calculated from logarithmically transformed values. The statistical significance of differences in SUV bias was also evaluated using the Wilcoxon signed-rank test. The differences were considered statistically significant for P -values < 0.05 .

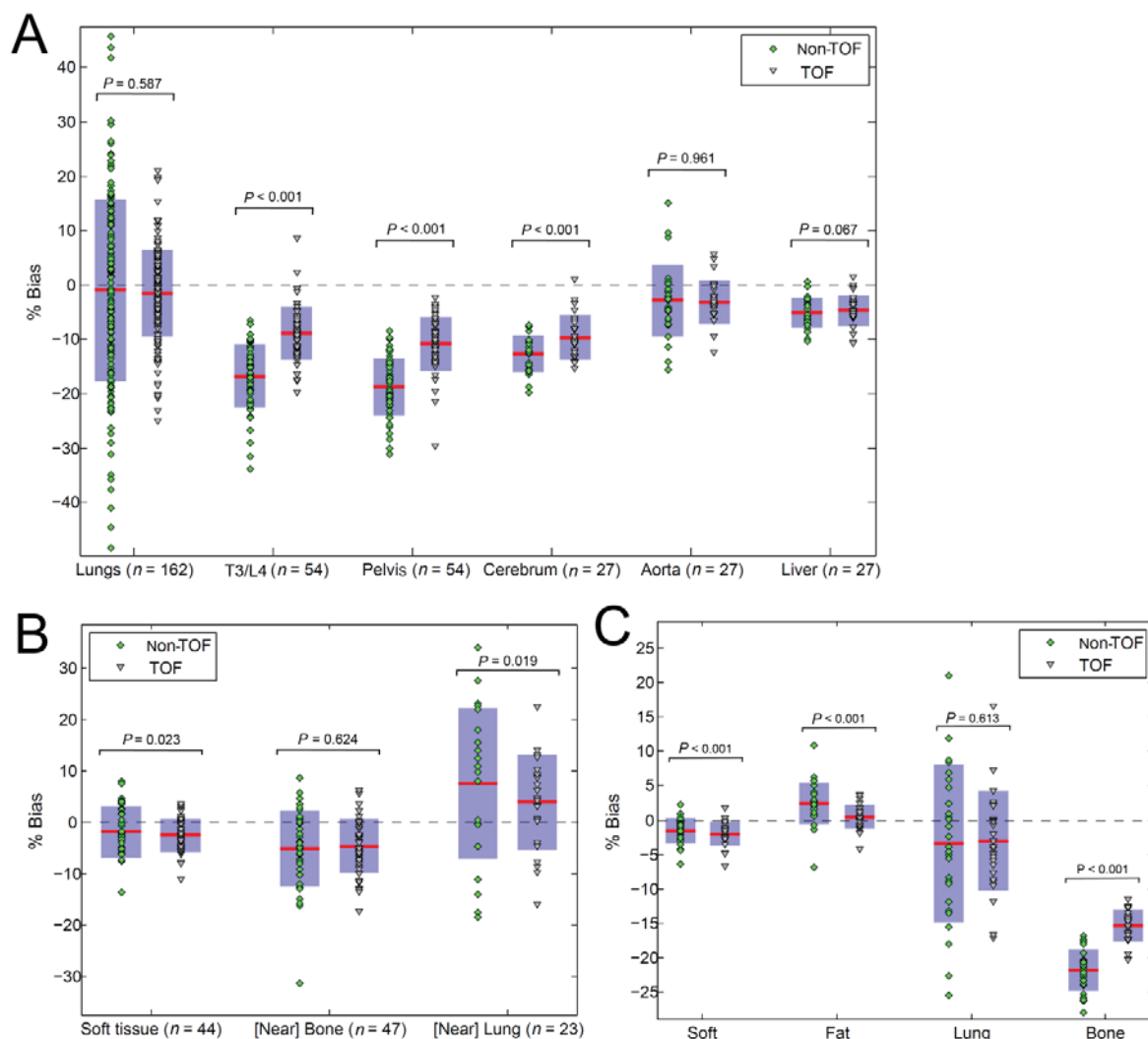


Figure 2. Relative errors of mean SUV estimations between MRAC-PET and reference CTAC-PET images reconstructed with and without TOF in (A) normal tissues, (B) lesions and (C) various tissue classes. Means and 2 standard deviations are indicated by horizontal bars and vertical boxes, respectively.

III. Results

III.A. Clinical studies

Figure 1 shows the bias maps of PET images reconstructed using non-TOF and TOF MRAC for two patients with different BMIs. The maps show that the maximum errors occur over the bones, lungs and air gaps. They are substantially reduced by TOF-PET reconstruction. Table 1 summarizes the mean, standard deviation (SD) and RMSE of SUV_{mean} bias between non-TOF MRAC-PET and CTAC-PET, and TOF MRAC-PET and CTAC-PET images in different VOIs located in normal regions and lesions, and defined tissue classes.

Figure 2A compares the mean and SD of SUV_{mean} bias between non-TOF and TOF PET images in VOIs defined on different tissues with normal tracer uptake. In this figure, the marker points show the mean of bias in each VOI, whereas the horizontal bars and vertical boxes indicate the mean and 2 SDs of bias between VOIs in each region. For the VOIs defined on the lungs ($n = 162$), the non-TOF MRAC resulted in an underestimation of $-1.0 \pm 16.6\%$ with a RMSE of 16.7%, while its TOF counterpart yielded an error of $-1.5 \pm 8.0\%$ with a RMSE of 8.1% (Table 1). For the total VOIs defined on T3/L4 vertebra, pelvis and cerebrum ($n = 135$), non-TOF and TOF methods resulted in an average bias error of $-16.7 \pm 5.6\%$ with a RMSE of 17.6% and $-9.8 \pm 4.8\%$ with a RMSE of 10.9%, respectively. Similarly, for all VOIs defined on soft tissues, aorta and liver ($n = 54$), non-TOF and TOF methods showed an average bias of $-3.9 \pm 5.2\%$ with 6.5% RMSE and $-3.4 \pm 3.5\%$ with 5.3% RMSE, respectively. The statistical analysis of the results revealed that the difference in the bias performance of non-

Table 1. PET quantification bias [Mean \pm SD, (RMSE)] of non TOF vs. TOF in different VOIs and tissue classes.

		non TOF	TOF
Normal regions (VOI)	Lung	-1.0 \pm 16.6% (16.7%)	-1.5 \pm 8.0% (8.1%)
	T3/L4	-16.8 \pm 5.8% (17.7%)	-8.8 \pm 4.9% (10.1%)
	Pelvis	-18.7 \pm 5.2% (19.4%)	-10.8 \pm 5.0% (11.9%)
	Cerebrum	-12.5 \pm 3.3% (13.0%)	-9.7 \pm 4.1% (10.5%)
	Aorta	-2.8 \pm 6.7% (7.3%)	-3.2 \pm 3.9% (5.1%)
	Liver	-5.2 \pm 2.8% (5.8%)	-4.7 \pm 2.9% (5.5%)
Lesions (VOI)	Soft tissue	-1.8 \pm 4.9% (5.3%)	-2.5 \pm 3.2% (4.1%)
	(Near) Bone	-5.2 \pm 7.2% (8.8%)	-4.6 \pm 5.2% (7.0%)
	(Near) Lung	7.5 \pm 14.6% (16.4%)	3.9 \pm 9.2% (10.0%)
Tissue classes	Soft	-1.5 \pm 1.8% (2.4%)	-2.0 \pm 1.7% (2.6%)
	Fat	2.4 \pm 3.0% (3.8%)	0.5 \pm 1.7% (1.7%)
	Bone	-21.8 \pm 2.9% (21.9%)	-15.3 \pm 2.3% (15.5%)
	Lung	-3.4 \pm 11.5 (11.9%)	-2.9 \pm 7.1% (7.7%)

TOF and TOF MRAC methods is significant over the vertebra, pelvis and cerebrum ($P < 0.001$), while there is no proof of statistically significant differences in the lungs ($P = 0.587$), aorta ($P = 0.961$) and liver ($P = 0.067$).

Figure 2B shows the mean \pm SD of bias between non-TOF and TOF-PET images in VOIs defined on lesions, grouped into 3 categories depending on their location: soft tissue, for lesions seated in fat and non-fat tissues ($n = 44$), (near) bone, for lesions located on bones or on soft tissues close to bone ($n = 47$) and (near) lungs, for lesions located in the lungs or in the immediate vicinity of the lungs, mainly the mediastinal lymph nodes ($n = 23$). The results presented in Table 1 show that in soft tissue and (near) bone lesions the non-TOF and TOF MRAC methods result in underestimation of SUV_{mean} with comparable RMSE biases of 5.3 vs. 4.1% and 8.8 vs. 7.0%, respectively. For lesions located in/near lungs, the methods overestimate the SUV_{mean} . TOF MRAC method, however, showed an improved performance by achieving a bias of $3.9 \pm 9.2\%$ (10.0% RMSE) compared to its non-TOF counterpart with a bias of $7.5 \pm 14.6\%$ (16.4% RMSE). The statistical analysis showed that there is a significant difference in bias performance of the methods in soft tissue ($P = 0.023$) and in/near lungs ($P = 0.019$) lesions, while there is no proof of statistically significant differences in/near bone lesions ($P = 0.624$).

The MRAC PET images were further analyzed for SUV correlation and concordance with respect to CTAC PET images. Figure 3 (top panel) shows the scatter plots of SUV_{mean} in all normal tissues and lesions in PET images reconstructed using MRAC and CTAC with and without TOF, with correlation coefficients and corresponding regression equations. Overall, there is a good correlation between non-TOF MRAC and non-TOF CTAC SUV values with $R^2 = 0.980$, which is improved by TOF reconstruction ($R^2 = 0.993$). Figure 3 (bottom panel) shows the Bland-Altman concordance analysis of the MRAC methods. Differences and limits of agreement (LA) are expressed as a function average SUVs of PET/MR and PET/CT. The regression lines of the difference (indicated with percent slope) shows a systematic underestimation of SUV for both non-TOF and TOF MRAC methods (-8.1% and -7.5% , respectively). The results show that the TOF reconstruction can reduce the bias and the SD of bias.

Figure 4 compares the non-TOF and TOF PET images of a patient presenting with metal-induced susceptibility artifacts in MRAC maps. The patient had a PET/MRI and a complementary PET/CT scan. The MR and CT images were non-rigidly registered. The void regions induced by the metal implant were then transferred to the derived 4-class CTAC map. As can be seen, the TOF reconstruction can substantially reduce the artifacts close to the hip implant. Figure 5 compares PET images of a patient with respiratory-phase mismatch between PET and MRAC maps. As pointed by the arrows, one of the lesions is indiscernible in non-TOF PET image due to the under-correction caused by respiratory-phase mismatch artifacts. However, the TOF reconstruction has effectively suppressed the artifacts, thus improving lesion detectability.

III.B. Simulation studies

Figure 6 shows the PET, actual CTAC and MRAC images used in our non-TOF and TOF simulations, together with the bias maps corresponding to non-TOF and TOF images with timing resolutions of 580, 350 and 100 ps.

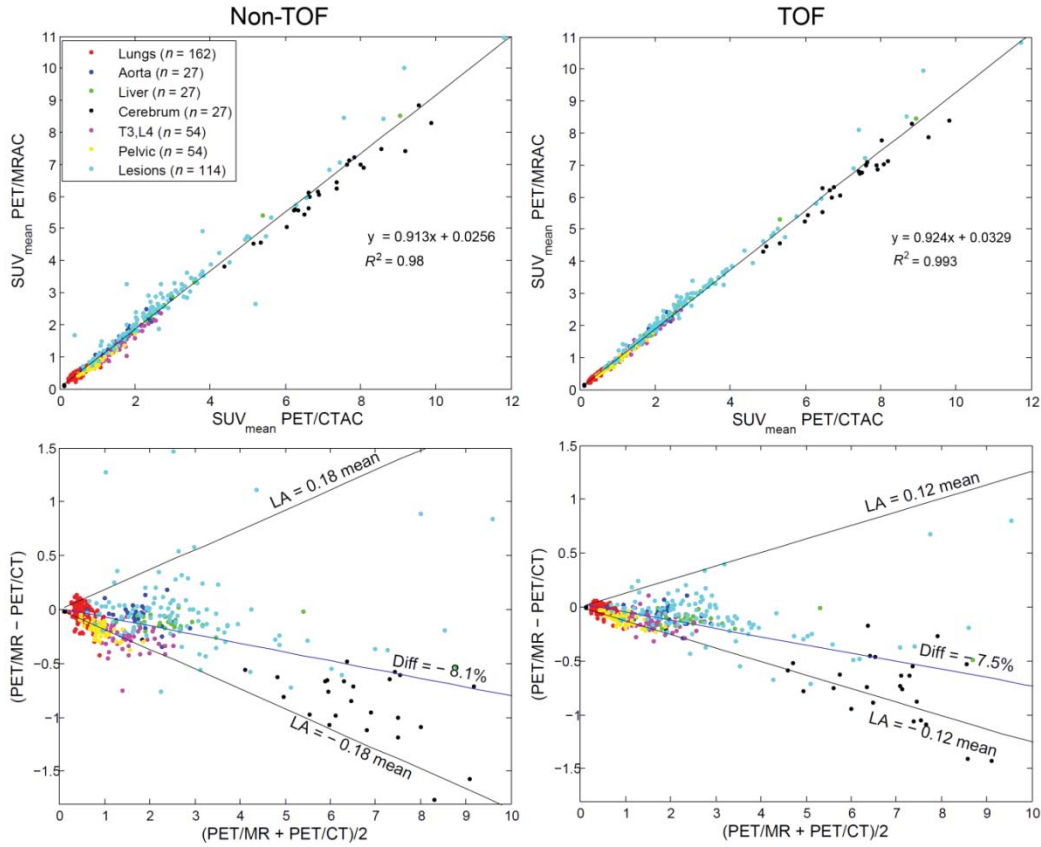


Figure 3. Top panel: Scatter plots showing results of linear regression analysis between SUV_{mean} in different VOIs of MRAC-PET and reference CTAC-PET with and without TOF. Bottom panel: Bland-Altman plots of SUV_{mean} for MRAC-PET and reference CTAC-PET with and without TOF. Differences and limits of agreement (LA) are expressed as a function of average SUVs of PET/MR and PET/CT.

Note that for each simulated TOF resolution, two PET images were reconstructed (using reference CTAC and 4-class MRAC maps). The results clearly show that PET quantification errors induced by the 4-class maps are reduced as the timing resolution is improved, especially over the bones. Class-wise analyses showed that over bones, the non-TOF reconstruction results in an underestimation of -25.15 ± 9.8 (27.0% RMSE), which is reduced to -19.3 ± 6.66 (20.42% RMSE), -16.63 ± 5.4 (17.51% RMSE) and -12.47 ± 3.23 (12.88% RMSE) using TOF reconstructions with timing resolutions of 580, 350 and 100 ps, respectively. For the non-TOF and TOF with 580, 350, 100 ps resolutions, RMSEs of bias averaged over all tissue classes except bones, were 13.11%, 9.15%, 8.61% and 8.28%, respectively. The impact of TOF reconstruction on respiratory-phase mismatch artifacts was further evaluated in a simulated clinical FDG scan (Figure 7). A respiratory-phase mismatch was simulated between the actual CTAC and MRAC maps with 12-mm displacement of diaphragm as if the MRI was acquired at the end of inspiration. A 4-mm spherical tumor was also inserted in the PET image to simulate a case where respiratory-phase mismatch impaired the detectability of a liver lesion. As shown in the figure, the activity of the tumor and superior border of liver were suppressed due to white-band banana artifacts. As the timing resolution improves, the tumor and liver lobe become more discernible and lean toward their actual uptake. The bias maps also demonstrate that improved TOF resolution reduces quantification errors.

IV. Discussion

To the best of our knowledge, this is the first clinical study highlighting the impact and importance of time-of-flight in MRAC PET image reconstruction. Using VOI-based and class-wise analyses, we demonstrated that TOF can reliably compensate for erroneous MRAC maps especially over the bone and lungs where the maximum errors occur. The results of 135 VOIs defined in/near bone regions with normal tracer uptake showed an average underestimation of 16.7% and 9.8% for non-TOF and TOF MRAC reconstructions, respectively.

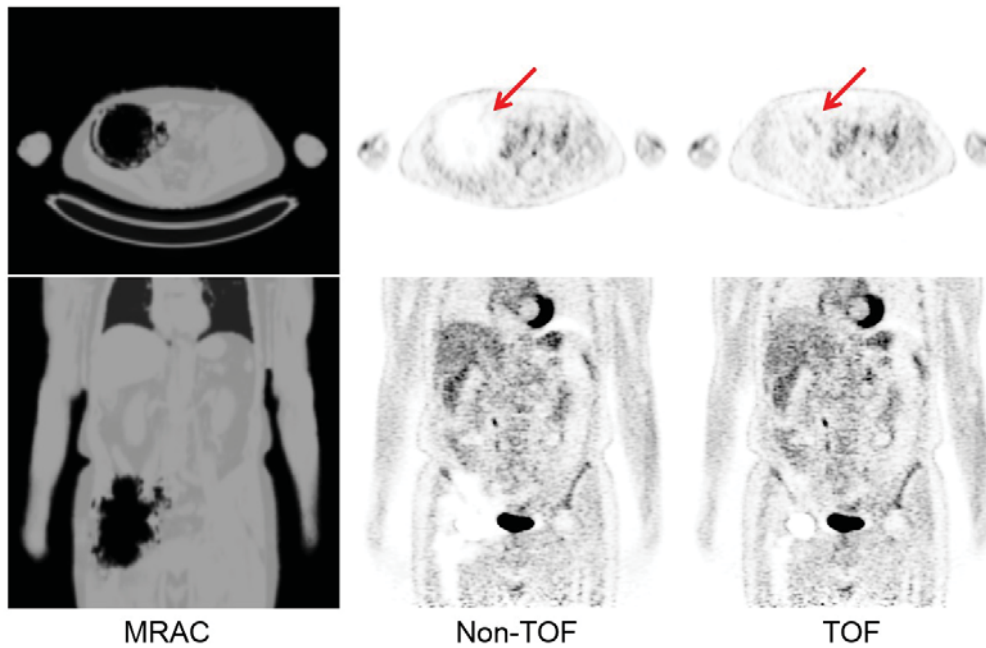


Figure 4. Comparison of non-TOF and TOF PET images in the presence of metal-induced susceptibility artifacts on MRAC attenuation map.

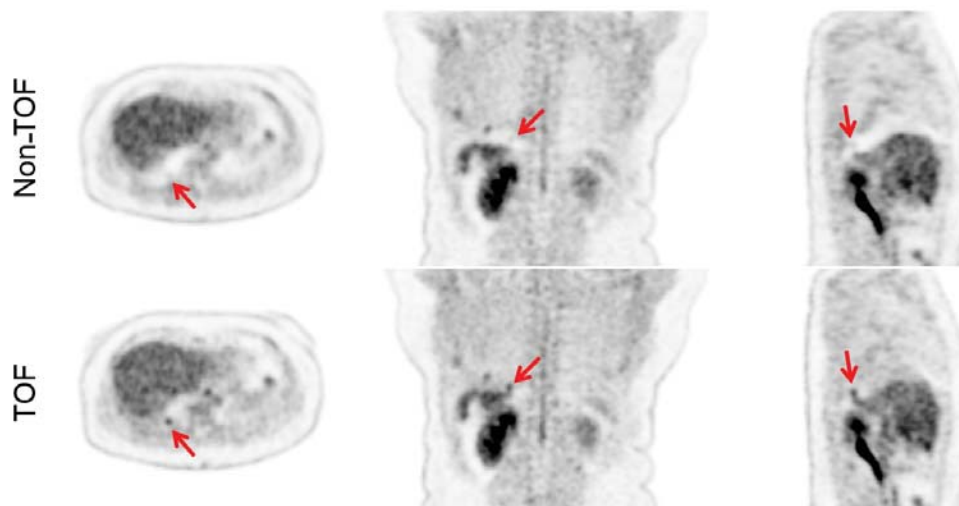


Figure 5. Comparison of non-TOF and TOF PET images in the presence of respiratory-phase mismatch between MRAC attenuation map and corresponding PET images.

Class-wise evaluations showed that these methods result in maximum underestimation of 21.8% and 15.3% over the bones, respectively. Our non-TOF results are consistent with the >15% errors reported in [9] using PET/MR datasets. The VOI-based evaluation of 47 in/near bone lesions showed an average 5% error for both methods, which is in agreement with the 8% and 6% errors reported in [5, 14]. Consistent with observations made in [5, 11], the results of 164 VOIs in normal tissues of the lungs showed an average SUV underestimation <2% for non-TOF and TOF methods. However, non-TOF MRAC showed a large standard deviation (16.6%), which was substantially reduced by TOF (8.1%). The reason for this large SD is that the standard MRAC methods do not take the intra/inter-patient variability of lung attenuation coefficients into account and assign a constant value for the lungs in all patients. Our results showed that non-TOF MRAC results in 7.5% overestimation of in/near lung lesions, which is reduced to 3.9% by TOF image reconstruction. For soft tissue lesions, the results showed that both methods give rise to <5% errors, which is in agreement with previous studies [5, 14]. Our study also demonstrated a strong correlation between PET/MR and PET/CT SUVs in normal tissues and lesions. It was found that using TOF PET image reconstruction, the dispersion of data points around the regression line is reduced, especially for lesions, resulting in a higher coefficient of determination. The Bland-Altman plots

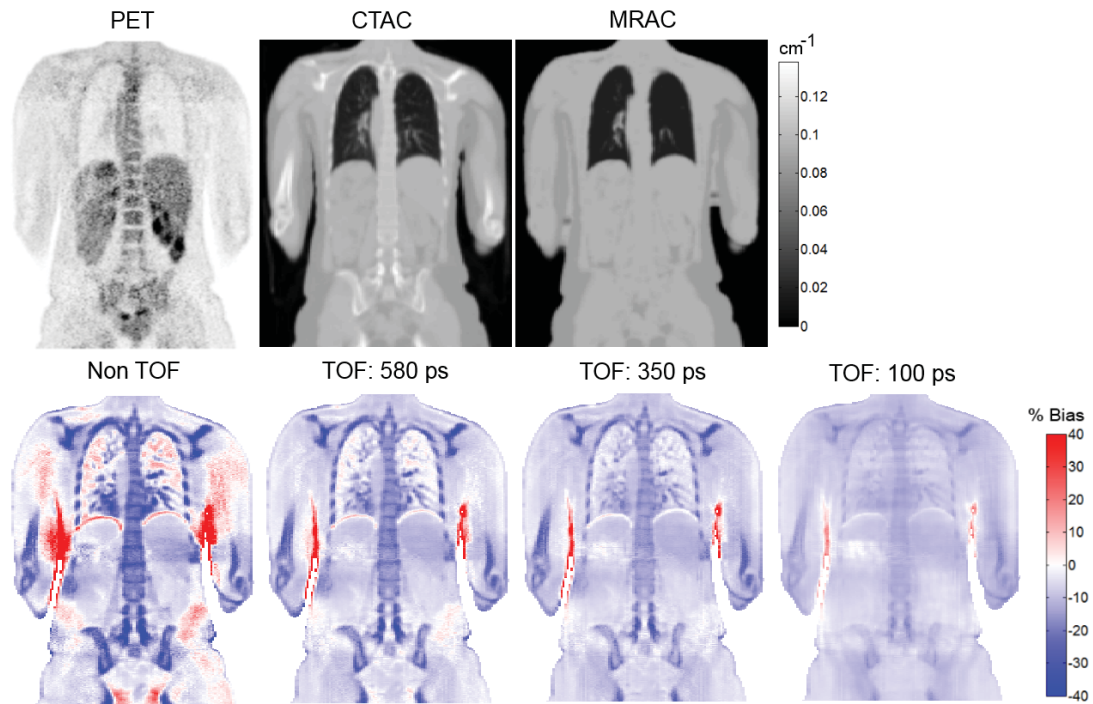


Figure 6. Simulation of the impact of TOF reconstruction on PET quantification errors of MRAC method. Top panel: The PET activity, CTAC and 4-class MRAC maps derived from a whole-body FDG-PET scan. Bottom panel: The bias maps between MRAC-PET and CTAC-PET images for different timing resolutions.

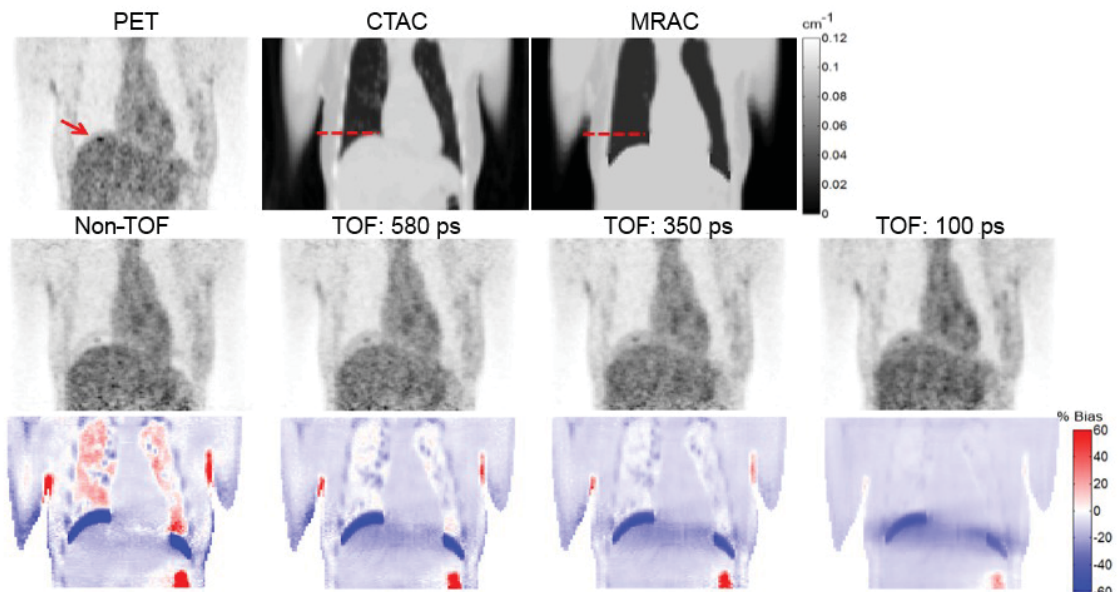


Figure 7. Simulation of the impact of TOF reconstruction on the reduction of artifacts induced by respiratory-phase mismatch between PET and MRAC images. Top: PET activity, CTAC and 4-class MRAC maps derived from a whole-body FDG-PET scan. Middle: the PET image reconstructed using different TOF timing resolutions. Bottom: the corresponding bias maps between MRAC-PET and CTAC-PET images.

revealed a limited concordance between PET/MR and PET/CT measurements in particular for lesions with high SUVs. As a result, both non-TOF and TOF methods showed a systematic bias, proportional to average SUVs. Nonetheless, the limit-of-agreement results showed that TOF can reduce the standard deviation of errors.

In this study, we used the default vendor-provided reconstruction parameters of 2/24 and 2/21 iterations/subsets for the non-TOF and TOF reconstructions, respectively. Indeed, the non-TOF reconstruction do not result in the same convergence rate achieved by TOF reconstruction. Achieving the same convergence

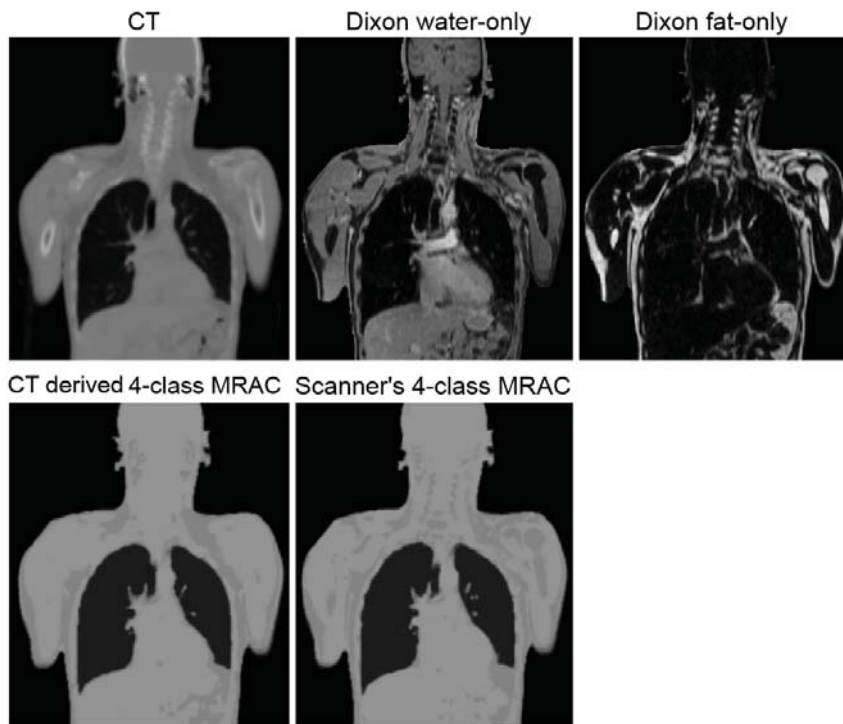
rate for lesions using both reconstruction methods is hardly accomplished in clinical setting, since it depends on the size and location of the lesions and lesion-to-background ratio, which varies for different lesions and patients. However, we evaluated SUV quantification errors of non-TOF and TOF MRAC methods using different iterations for one clinical study. As shown in Supplemental Figure 3, the bias changes with iteration number, especially in bones with non-TOF reconstruction. The results show that the bias introduced by TOF MRAC is almost steady for all tissue classes except bones. Consequently, the TOF MRAC method resulted in significantly less bias compared to its non-TOF counterpart for each iteration. Our simulation results demonstrated that as TOF timing resolution improves toward 100 ps, targeted for future TOF-PET/MR scanners, SUV quantification errors induced by inaccurate MRAC maps are substantially reduced, thereby improving the level of accuracy of PET quantification.

V. Conclusion

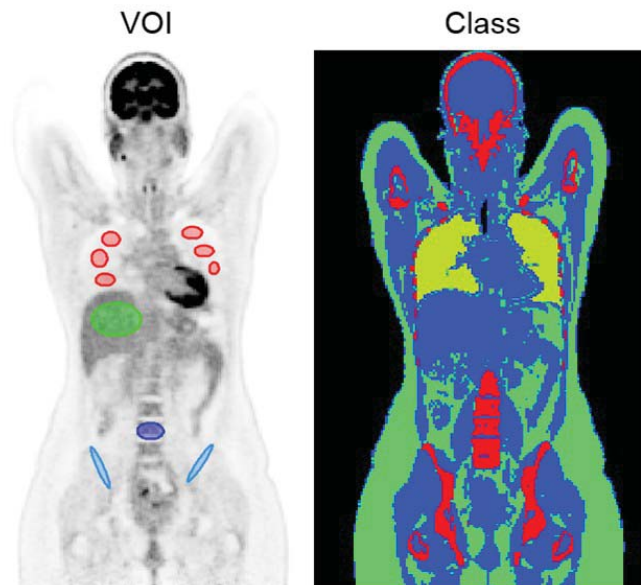
In this work, we evaluated the impact of TOF PET image reconstruction on SUV quantification errors caused by standard MR segmentation-based attenuation correction of PET data using simulation and clinical studies. Our results demonstrated that TOF capability can substantially reduce the mean and standard deviation of bias over the lungs and bones. It was found that non-TOF MRAC results in 11.9% and 21.9% root-mean-squared errors in the lungs and bones, respectively. These errors are reduced to 7.7% and 15.5%, respectively, when using TOF. The results showed that the root-mean-square errors of non-TOF and TOF methods in soft tissue and fat regions are less than 5%. From a clinical perspective, our study suggests that as the timing resolution of TOF-PET/MR scanners improves, PET quantitative accuracy for bone and lung lesions increases.

Acknowledgments

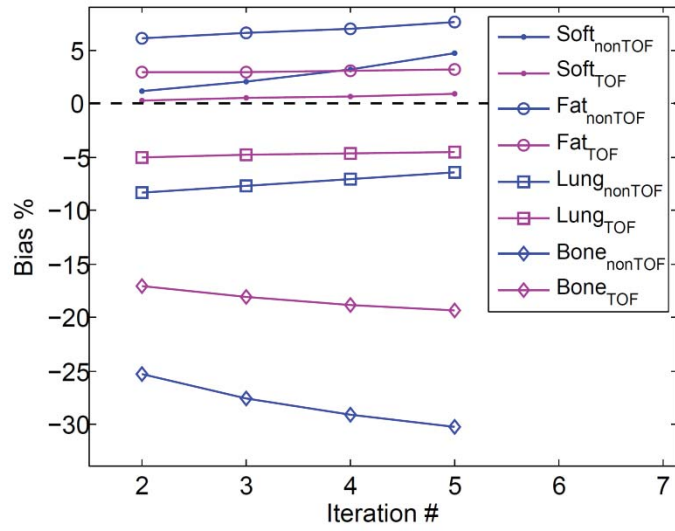
This work was supported in part by the Swiss National Science Foundation under Grant SNSF 31003A-149957 and the Indo-Swiss Joint Research Programme ISJRP 138866



SUPPLEMENTAL FIGURE 1. Comparison between attenuation maps derived from segmenting the CT and Dixon MR images into 4 tissue class attenuation maps of a patient that underwent both PET/CT and PET/MR examinations.



SUPPLEMENTAL FIGURE 2. Illustration of VOIs defined on organs with normal tracer uptake (shown here for lungs, liver, L4 and pelvis) and the defined four different tissue classes (fat, soft tissue, lungs and bones).



SUPPLEMENTAL FIGURE 3. PET quantification errors in non-TOF and TOF MRAC methods in different tissues classes as a function of iteration number in a single patient dataset.

References

- [1] D. A. Torigian, H. Zaidi, T. C. Kwee, B. Saboury, J. K. Udupa, Z.-H. Cho, and A. Alavi, "PET/MR Imaging: Technical aspects and potential clinical applications," *Radiology*, vol. 267, no. 1, pp. 26-44, 2013.
- [2] C. Levin, G. Glover, T. Deller, D. McDaniel, W. Peterson, and S. H. Maramraju, "Prototype time-of-flight PET ring integrated with a 3T MRI system for simultaneous whole-body PET/MR imaging [abstract]," *J Nucl Med*, no. 2_MeetingAbstracts, pp. 54 (Suppl 2):148, May 1, 2013, 2013.
- [3] H. Zaidi, "Is MRI-guided attenuation correction a viable option for dual-modality PET/MR imaging?," *Radiology*, vol. 244, no. 3, pp. 639-642, September 1, 2007, 2007.
- [4] S. Keller, S. Holm, A. Hansen, B. Sattler, F. Andersen, T. Klausen, L. Højgaard, A. Kjær, and T. Beyer, "Image artifacts from MR-based attenuation correction in clinical, whole-body PET/MRI," *Magn Reson Mater Phy*, vol. 26, no. 1, pp. 173-181, 2013/02/01, 2013.
- [5] A. Martinez-Möller, M. Souvatzoglou, G. Delso, R. A. Bundschuh, C. Chefd'hotel, S. I. Ziegler, N. Navab, M. Schwaiger, and S. G. Nekolla, "Tissue classification as a potential approach for attenuation correction in whole-body PET/MRI: evaluation with PET/CT data," *J Nucl Med*, vol. 50, no. 4, pp. 520-526, 2009.
- [6] M. Hofmann, I. Bezrukov, F. Mantlik, P. Aschoff, F. Steinke, T. Beyer, B. J. Pichler, and B. Schölkopf, "MRI-Based Attenuation Correction for Whole-Body PET/MRI: Quantitative Evaluation of Segmentation- and Atlas-Based Methods," *J Nucl Med*, vol. 52, no. 9, pp. 1392-1399, 2011.
- [7] A. Salomon, A. Goedicke, B. Schweizer, T. Aach, and V. Schulz, "Simultaneous reconstruction of activity and attenuation for PET/MR," *IEEE Trans Med Imaging*, vol. 30, no. 3, pp. 804-813, 2011.
- [8] A. Mehranian, and H. Zaidi, "Joint estimation of activity and attenuation in TOF-PET/MR using constrained Gaussian mixture models [abstract]. SNMMI Annual Meeting," *J Nucl Med*, vol. 55, no. Suppl, pp. (Suppl 1):645, 2014.
- [9] I. Bezrukov, H. Schmidt, F. Mantlik, N. Schwenzer, C. Brendle, B. Schölkopf, and B. J. Pichler, "MR-based attenuation correction methods for improved PET quantification in lesions within bone and susceptibility artifact regions," *J Nucl Med*, vol. 54, no. 10, pp. 1768-1774, 2013.
- [10] J. Ouyang, C. Se Young, Y. Petibon, A. A. Bonab, N. Alpert, and G. El Fakhri, "Bias Atlases for Segmentation-Based PET Attenuation Correction Using PET-CT and MR," *IEEE Trans Nuc Sci*, vol. 60, no. 5, pp. 3373-3382, 2013.
- [11] H. Arabi, O. Rager, A. Alem, A. Varoquaux, M. Becker, and H. Zaidi, "Clinical assessment of MR-guided 3-class and 4-class attenuation correction in PET/MR," *Mol Imaging Biol*, vol. 7, no. 2, pp. 264-276, 2015.
- [12] V. Keereman, R. V. Holen, P. Mollet, and S. Vandenberghe, "The effect of errors in segmented attenuation maps on PET quantification," *Med Phys*, vol. 38, no. 11, pp. 6010-9, Nov, 2011.
- [13] A. Samarin, C. Burger, S. Wollenweber, D. Crook, I. Burger, D. Schmid, G. von Schulthess, and F. Kuhn, "PET/MR imaging of bone lesions – implications for PET quantification from imperfect attenuation correction," *Eur. J. Nucl. Med. Mol. Imag*, vol. 39, no. 7, pp. 1154-1160, 2012/07/01, 2012.
- [14] V. Schulz, I. Torres-Espallardo, S. Renisch, Z. Hu, N. Ojha, P. Börner, M. Perkuhn, T. Niendorf, W. M. Schäfer, H. Brockmann, T. Krohn, A. Buhl, R. W. Günther, F. M. Mottaghy, and G. A. Krombach, "Automatic, three-segment, MR-based attenuation correction for whole-body PET/MR data," *Eur. J. Nucl. Med. Mol. Imag*, vol. 38, no. 1, pp. 138-152, 2011.
- [15] C. Catana, A. van der Kouwe, T. Benner, C. J. Michel, M. Hamm, M. Fenchel, B. Fischl, B. Rosen, M. Schmand, and A. G. Sorensen, "Toward implementing an MRI-based PET attenuation-correction method for neurologic studies on the MR-PET brain prototype," *J Nucl Med*, vol. 51, no. 9, pp. 1431-8, Sep, 2010.
- [16] M. Conti, "Why is TOF PET reconstruction a more robust method in the presence of inconsistent data?," *Phys Med Biol*, vol. 56, no. 1, pp. 155-68, Jan 7, 2011.
- [17] R. Boellaard, M. B. Hofman, O. S. Hoekstra, and A. A. Lammertsma, "Accurate PET/MR quantification using time of flight MLAA image reconstruction," *Mol Imaging Biol*, vol. 16, no. 4, pp. 469-77, Aug, 2014.
- [18] H. T. van Dam, G. Borghi, S. Seifert, and D. R. Schaart, "Sub-200 ps CRT in monolithic scintillator PET detectors using digital SiPM arrays and maximum likelihood interaction time estimation," *Phys Med Biol*, vol. 58, no. 10, pp. 3243-57, May 21, 2013.
- [19] H. Zaidi, N. Ojha, M. Morich, J. Griesmer, Z. Hu, P. Maniawski, O. Ratib, D. Izquierdo-Garcia, Z. A. Fayad, and L. Shao, "Design and performance evaluation of a whole-body Ingenuity TF PET-MRI system," *Phys Med Biol*, vol. 56, no. 10, pp. 3091-106, May 21, 2011.

- [20] P. A. Yushkevich, J. Piven, H. C. Hazlett, R. G. Smith, S. Ho, J. C. Gee, and G. Gerig, "User-guided 3D active contour segmentation of anatomical structures: significantly improved efficiency and reliability," *Neuroimage*, vol. 31, no. 3, pp. 1116-28, 2006.

Chapter 9

Joint estimation of activity and attenuation in whole-body TOF PET/MRI using constrained Gaussian mixture models

Abolfazl Mehranian and Habib Zaidi

IEEE Trans Med Imaging (2015) in press

© 2015 IEEE.

Abstract

Purpose: It has recently been shown that the attenuation map can be estimated from time-of-flight (TOF) PET emission data using joint maximum likelihood reconstruction of attenuation and activity (MLAA). In this work, we propose a novel MRI-guided MLAA algorithm for emission-based attenuation correction in whole-body PET/MR imaging. The algorithm imposes MR spatial and CT statistical constraints on the MLAA estimation of attenuation maps using a constrained Gaussian mixture model (GMM) and a Markov random field smoothness prior.

Methods: Dixon water and fat MR images were segmented into outside air, fat and soft-tissue classes and an MR low-intensity (unknown) class corresponding to air cavities, cortical bone and susceptibility artifacts. The attenuation coefficients over the unknown class were estimated using a mixture of 4 Gaussians, and those over the known tissue classes using unimodal Gaussians, parameterized over a patient population. To eliminate misclassification of spongy bones with surrounding tissues, and thus include them in the unknown class, we heuristically suppressed fat in water images and also used a co-registered bone probability map. The proposed MLAA-GMM algorithm was compared with the MLAA algorithms proposed by Rezaei *et al* and Salomon *et al* using simulation and clinical studies with two different tracer distributions.

Results and conclusion: The results showed that our proposed algorithm outperforms its counterparts in suppressing the cross-talk and scaling problems of activity and attenuation and thus produces PET images of improved quantitative accuracy. It can be concluded that the proposed algorithm effectively exploits the MR information and can pave the way toward accurate emission-based attenuation correction in TOF PET/MRI.

I. Introduction

Hybrid PET/MR systems have recently been introduced in clinical practice as a new diagnostic imaging modality offering the capability to combine molecular and morphological assessment of a variety of physiopathological conditions [1]. Thanks to advances in radiation detectors and PET instrumentation, PET/MR has now adequately addressed the mutual compatibility challenge between PET and MRI components. However, MRI-based attenuation correction (MRAC) remains as another major challenge owing to the lack of bone signal in conventional MR sequences and a unique global mapping between MR image intensities and corresponding attenuation coefficients [2, 3].

Overall, MRAC methods can be categorized into three classes: i) segmentation-based approaches, in which MR images are segmented into different tissue classes followed by assignment of predefined attenuation coefficients to each class [4, 5], ii) atlas registration-based approaches, in which a co-registered MR-CT atlas dataset is used to derive a pseudo CT image from the patient's MR image or to learn a mapping function that predicts the pseudo CT [6-9] and iii) emission-based approaches in which the attenuation map is estimated from PET emission data. Segmentation-based approaches usually do not take into account the presence of bones and the inter/intra-patient variability of attenuation coefficients, especially in the lungs. On the other hand, atlas registration based methods can solve the MRAC problem, particularly in brain imaging, provided that a perfect registration between the atlas and different patients can be achieved. However, a perfect whole-body registration is rarely possible owing to substantial anatomical differences between patients and their postures during scanning and current limitations of registration algorithms. Emission-based methods attempt to derive attenuation coefficients from emission data without using any estimate of the activity map, based on the consistency conditions of the attenuated Radon transform [10-12], or to simultaneously estimate activity and attenuation maps in a maximum likelihood (ML) framework [13-16]. The consistency conditions state that, in the absence of noise, a given emission data can only arise under certain attenuation conditions, or conversely for a given attenuation map, only certain emission data are possible. These conditions do not account for the statistical nature of emission data and generally cannot completely determine attenuation coefficients.

In the ML framework, the Poisson distribution of data is properly modeled and the joint likelihood is alternatively maximized with respect to activity and attenuation using a maximum likelihood reconstruction of attenuation and activity (MLAA) algorithm [14]. However, the estimated activity/attenuation pair often suffers from the so-called cross-talk artifacts, where the activity features propagate into the attenuation map and vice versa, reflecting the non-uniqueness of the solution. Therefore, some constraints on attenuation and activity maps have to be defined in order to confine the solution space and to suppress cross-talks. The tissue preference priors [14], local smoothness priors [14, 17] and range constraints [18] were therefore used for attenuation estimation. With the advent of time-of-flight (TOF) PET/MR scanners [19], Salomon *et al* [20, 21] imposed the inherent spatial constraint of TOF on activity estimation and the MR anatomical information on attenuation map estimation. Thereby, the noise and cross-talk artifacts were substantially reduced. In fact, it has been shown that TOF-PET image reconstruction can reduce the artifacts induced by attenuation correction errors [22, 23]. Using Fisher information-based analysis, Rezaei *et al* [24] demonstrated that TOF can suppress cross-talks in the MLAA algorithm, however, they found that the reconstructed activity maps are globally scaled, while the attenuation maps show a position dependent scaling. Based on the range consistency conditions of the TOF attenuated Radon transform, Defrise *et al* [25] also showed that attenuation correction factors can be determined from TOF-PET data up to a constant scaling factor. Overall, the performance of MLAA depends on (i) TOF timing resolution in order to suppress cross-dependencies between activity and attenuation maps, (ii) the count statistics of emission data for suppressing noisy estimations and (iii) the spatial distribution of the radiotracer in the body to support the estimation of attenuation map, which in turn depends on the injected radiotracer. Salomon *et al* [21] proposed a region-wise estimation of attenuation coefficients over MRI-derived anatomical regions to reduce noise and crosstalk artifacts. However, in conventional MR sequences, bones cannot be discriminated from air and the images usually suffer from partial volume effect (PVE) leading to misclassification of bones with surrounding tissues, especially over the ribs and vertebrae. Moreover, depending on the number of regions, the region-wise estimation also might not allow for the local variability of attenuation values, especially in the lungs and vertebrae.

In this work, we aim at improving the performance of MLAA by exploiting segmented Dixon MR images and a co-registered bone probability map in order to define spatial and statistical constraints on the estimation of

attenuation values using a constrained Gaussian mixture model (GMM) and Markov random field (MRF) smoothness prior. The proposed algorithm was compared with the original MLAA and Salomon's MLAA (MLAA-Salomon) algorithms.

II. Material and methods

II.A. Objective function

The measured TOF PET data, g_{it} , in LOR i and TOF bin t are best modeled as Poisson random variables with an expected value:

$$\bar{g}_{it} = n_i e^{-\sum_{k=1}^J l_{ik} \mu_k} \sum_{j=1}^J c_{ijt} \lambda_j + n_i \bar{s}_{it} + \bar{r}_{it} \quad (1)$$

where λ_j and μ_k are activity and attenuation values at voxels j and k , c_{ijt} is the geometric probability detection of annihilation events emitted from voxel j along LOR i in TOF bin t , n_i is detector normalization factors, l_{ik} is the intersection length of LOR i with voxel k , and \bar{s}_{it} and \bar{r}_{it} are the expected estimates of scatter and random events, estimated by model-based methods and delayed coincidence window measurements, respectively. In the maximum a posteriori (MAP) framework, the unknowns λ and μ are also modeled as random variables with prior densities, by which the solution space can be constrained. We exploited *a priori* knowledge about attenuation in the following joint MAP estimation:

$$(\hat{\lambda}, \hat{\mu}) = \operatorname{argmax}_{\lambda \geq 0, \mu \geq 0} \left\{ \sum_{it} \{g_{it} \log(\bar{g}_{it}) - \bar{g}_{it}\} + \beta R_{MRF}(\mu) + \gamma R_{GMM}(\mu) \right\} \quad (2)$$

where R_{MRF} and R_{GMM} are MRF and Gaussian mixture penalties to favor attenuation maps that are smooth, based on local intensity differences between adjacent voxels, and belong to a few distinct tissue classes according to the histogram of attenuation maps. β and γ are hyper-parameters, weighting the impact of the priors. $R_{MRF}(\mu)$ is defined as:

$$R_{MRF}(\mu) = - \sum_{j=1}^J \sum_{k \in N_j} \omega_{jk} \psi(\mu_k - \mu_j) \quad (3)$$

$$\psi(t) = \frac{1}{2} t^2$$

where N_j denotes a second-order neighborhood around the j^{th} voxel with 26 nearest neighbors, ω_{jk} is inversely proportional to the distance between voxel j and k , and $\psi(t)$ is a quadratic potential function penalizing large differences between voxels. In $R_{GMM}(\mu)$, it is assumed that the attenuation coefficients are independent random variables with a density function that is a mixture of H known Gaussian density functions:

$$R_{GMM}(\mu) = \sum_{j=1}^J \log \left\{ \sum_{h=1}^H \pi_h \mathcal{N}(\mu_j | \bar{\mu}_h, \sigma_h) \right\} \quad (4)$$

$$\mathcal{N}(\mu_j | \bar{\mu}_h, \sigma_h) = \frac{1}{\sqrt{2\pi}\sigma_h} \exp \left(-\frac{1}{2} \left(\frac{\mu_j - \bar{\mu}_h}{\sigma_h} \right)^2 \right).$$

where $\mathcal{N}(\mu_j | \bar{\mu}_h, \sigma_h)$ is the Gaussian density function associated with the h^{th} component with mean $\bar{\mu}_h$ and standard deviation σ_h , $\{\pi_h\}$ are mixture proportions that are assumed to be known and $\sum_h \pi_h = 1$. The mixture of Gaussians is used to reflect the fact that the histogram of the attenuation map consists of a few distinct peaks corresponding to air, lung, fat, soft-tissue and bone [26] (Figure1). In the proposed algorithm, we incorporate anatomical information derived from MR images into the GMM using a tissue prior map.

II.B. Tissue prior map and GMM parameters

In this work, Dixon MR images, which are widely used in 4-class segmentation-based MRAC methods, were used to derive a tissue prior map. The Dixon pulse sequence was developed for separation of fat and water by producing in-phase, out-of-phase, fat and water images from gradient-echo T1-weighted MR images [4]. The fat and water images are segmented into four classes (lung, fat soft-tissue, and outer air) and an additional unknown class indicating regions of low MR intensity corresponding to air cavities, cortical bones and susceptibility artifacts. A co-registered bone map indicating the possible position of bones is also added to the unknown class

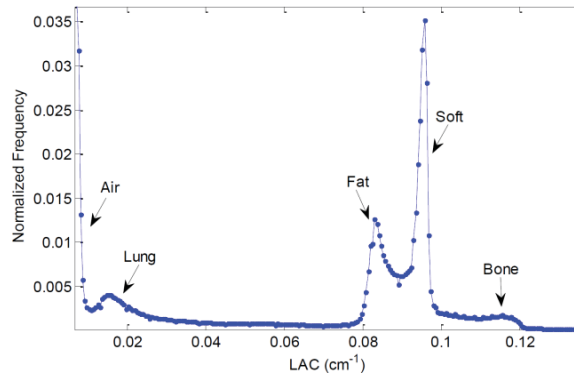


Figure1. The histogram of attenuation maps consists of a few distinct peaks corresponding to air, lung, fat, soft-tissue and bone.

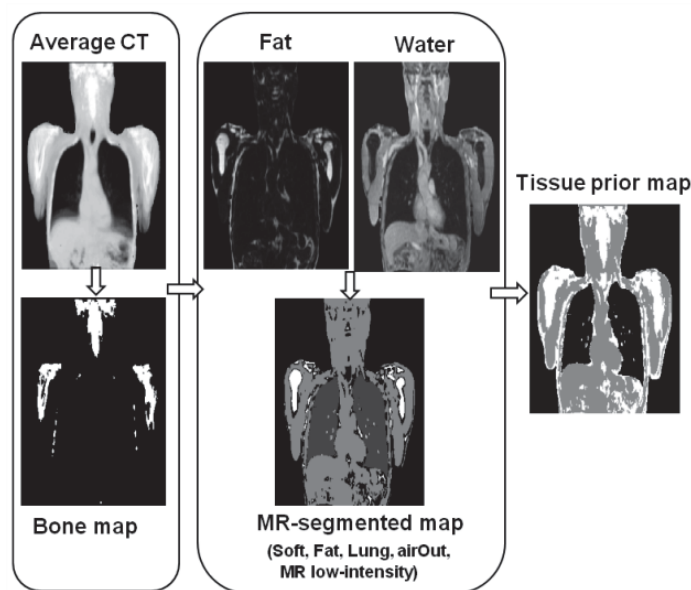


Figure 2. Derivation of tissue prior map from Dixon MR and co-registered CT images.

to include both cortical and spongy bones. Figure 2 summarizes the procedure. In the proposed method, a mixture of Gaussians (GMM) is used for the estimation of attenuation coefficients over the unknown class of the resulting tissue prior map, while uni-modal Gaussians (constrained GMM) are used over the known tissue classes. In the case of MR truncation artifacts, the outside air, as well as, unknown classes are expanded based on the contour of the estimated TOF activity at the first iteration. The segmentation of non-attenuation corrected TOF activity images has been shown to provide an accurate estimate of external body contour suitable for MR truncation compensation [27]. The MLAA's attenuation corrected TOF activity images can therefore be reliably used for body contour segmentation.

Due to partial volume averaging effect and incomplete fat suppression in the Dixon water images (because of phase errors induced by magnetic field inhomogeneities [28]), spongy bones containing either hematopoietic or fatty tissues can show a moderate MR intensity and therefore might be misclassified as surrounding soft-tissue and fat tissue classes. To eliminate this effect, we heuristically suppressed the fat signal in water images by the subtraction of water and fat images subjected to a non-negativity constraint. As shown in Figure 3, the spongy bones in the resulting image (e.g. the body and spinous processes of vertebrae) show a zero-intensity and therefore are segmented as belonging to the unknown class. Furthermore, we used a bone probability map, obtained from a co-registered average CT, to insure the inclusion of bones into the unknown class. The soft-tissue class was segmented by thresholding the subtraction image at the threshold point corresponding to the local minimum of its histogram (Figure 3). The voxels of the fat image whose intensity was 50% larger than the water image were assigned to fat tissue class. The lungs and background air were segmented from in-phase

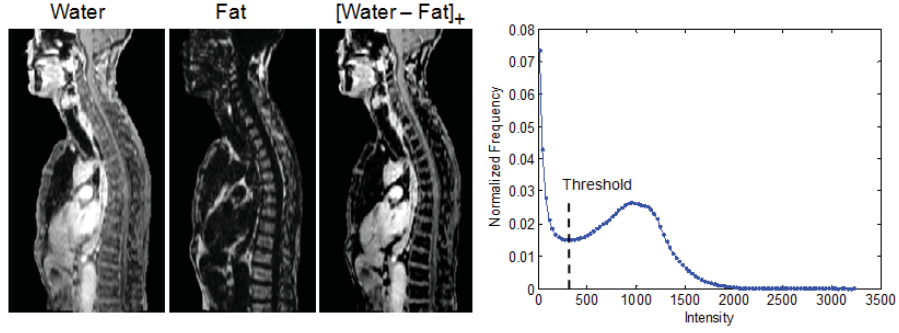


Figure 3. Soft-tissue segmentation. The fat image is subtracted from the water image (left panel). The resulting image is subjected to a non-negativity constraint and then segmented for soft-tissue at the threshold point corresponding to the local minimum of its histogram (right panel).

Table I. Estimated parameters of the constrained GMM over 10 whole-body CT images.

Mixture of Gaussians			Uni-modal Gaussians		
$\bar{\mu}$	σ	π		$\bar{\mu}$	σ
0.1205	0.0242	0.5661	Lung	0.0261	0.0107
0.0980	0.0051	0.2597	Fat	0.0834	0.0013
0.0278	0.0330	0.1150	Soft	0.0954	0.0012
0.0023	0.0019	0.0592			

images using a supervised seeded region-growing method implemented in the ITK-SNAP software [29]. Several seeds were manually placed on the regions targeted for segmentation. CT images used to derive the bone map were first converted to a pseudo-MR by setting the intensity of bones to a small value followed by non-rigid registration to the in-phase MR image using the Elastix software [30]. The resulting transformation fields were finally applied to the original CT images. The images were then segmented to extract bones and averaged. A bone map was derived by identifying voxels with a probability larger than 30%. Whole-body CT images of 10 patients (5 females, 5 males, mean age: 68.2 yr, range: 38–79 yr) were used to estimate the parameters of uni-modal Gaussians that best fit the histogram of attenuation coefficients in known tissue classes. For the estimation of the GMM parameters over the unknown class, bones and air gaps were segmented from CT images and the resulting masks were dilated using a morphological operator to mimic the unknown class in tissue prior maps. The distribution of CT attenuation coefficients over the masks were then estimated using a mixture of 4 Gaussians representing inside air, fat/soft mixture and bone using the expectation maximization (EM) algorithm. Table I summarizes the estimated parameters for uni-modal and mixture of Gaussians.

II.C. Optimization

The joint MAP in Eq. (2) is not necessarily strictly concave [31], thus the simultaneous estimation of activity and attenuation is not guaranteed to reach a global maximizer. Alternating optimization, i.e. maximization w.r.t. λ while keeping μ constant and vice versa was used to solve Eq. (2) [14]. Similar to the original MLAA algorithm [14, 24], the λ and μ optimization steps were solved using ordered subset EM (OSEM) and maximum likelihood for transmission tomography (MLTR) algorithms. Both algorithms are based on optimization transfer, which iteratively defines an easy-to-optimize surrogate for the problem. MLTR uses De Pierro’s additive trick and Jensen inequality to surrogate the log-likelihood function [32, 33]. The R_{MRF} prior is a strictly concave function and can be easily optimized during the μ optimization step. Since the R_{GMM} prior is not concave, we used the Jensen inequality of a log function to define the following surrogate for R_{GMM} in Eq. (4):

$$S_{GMM}(\mu, \mu^n) = \sum_j \sum_h z_{jh}^n \log \left(\frac{\mathcal{N}(\mu_j | \bar{\mu}_h, \sigma_h)}{\mathcal{N}(\mu_j^n | \bar{\mu}_h, \sigma_h)} \sum_h \pi_h \mathcal{N}(\mu_j^n | \bar{\mu}_h, \sigma_h) \right) = -\frac{1}{2} \sum_j \sum_h z_{jh}^n \left(\frac{\mu_j^n - \bar{\mu}_h}{\sigma_h} \right)^2 + C$$

$$z_{jh}^n = \frac{\pi_h \mathcal{N}(\mu_j^n | \bar{\mu}_h, \sigma_h)}{\sum_q \pi_q \mathcal{N}(\mu_j^n | \bar{\mu}_q, \sigma_q)}$$
(5)

where z_{jh}^n is obtained from the expectation maximization of GMM and in fact defines the membership probability of μ_j^n to class or component h and C is a constant value. Note that in a known tissue class $z_{jh}^n = 1$ and 0 elsewhere; therefore GMM is reduced to a uni-modal Gaussian in that class. As a result, the large deviation of attenuation coefficients from the expected values in each known class is penalized and thus estimations with noise and cross-talk artifacts are effectively suppressed. To this end, the proposed MLAA-GMM algorithm reads as follows:

$$\forall i, a_i^n = e^{-\sum_j l_{ij} \mu_j^n} \quad (6)$$

$$\forall j, \lambda_j^{n+1} = \frac{\lambda_j^n}{\sum_i c_{ij} n_i a_i^n} \sum_{it} c_{ijt} n_i a_i^n \frac{g_{it}}{n_i a_i^n \sum_k c_{ikt} \lambda_k^n + n_i \bar{s}_{it} + \bar{r}_{it}} \quad (7)$$

$$\forall i, \psi_i^n = n_i a_i^n \sum_{jt} c_{ijt} \lambda_j^{n+1} \quad (8)$$

$$\forall j, h, z_{jh}^n = \frac{\pi_h \mathcal{N}(\mu_j^n | \bar{\mu}_h, \sigma_h)}{\sum_q \pi_q \mathcal{N}(\mu_j^n | \bar{\mu}_q, \sigma_q)} \quad (9)$$

$$\forall j, \mu_j^{n+1} = \mu_j^n + \alpha \left(\frac{\sum_i l_{ij} \frac{\psi_i^n}{\psi_i^n + b_i} (\psi_i^n + b_i - g_i) - \gamma \sum_h z_{jh}^n \frac{\mu_j^n - \bar{\mu}_h}{(\sigma_h)^2} - \beta \frac{\partial R_{MRF}(\mu^n)}{\partial \mu_j}}{\sum_j l_{ij} \frac{(\psi_i^n)^2}{\psi_i^n + b_i} \sum_k l_{ik} - \gamma \sum_h \frac{z_{jh}^n}{(\sigma_h)^2} + \beta \frac{\partial^2 R_{MRF}(\mu^n)}{\partial^2 \mu_j}} \right) \quad (10)$$

where $b_i = n_i \bar{s}_i + \bar{r}_i$, $c_{ij} = \sum_t c_{ijt}$, $g_i = \sum_t g_{it}$ and $\bar{s}_i = \sum_t \bar{s}_{it}$ are TOF-integrated quantities and $\alpha > 0$ is a step size parameter. Algorithm 1 summarizes the detailed implementation of the proposed method. For both simulation and clinical studies reported in this work, we set $\alpha = 1.5$, $\beta = 50$, $\gamma = 0.015$.

Algorithm 1: MLAA-GMM

Initialize: $\mu^0, \lambda^0, \alpha, \beta, \gamma$ and GMM parameters $\pi, \bar{\mu}, \sigma$ according to Table I.

For global iterations, $n = 0, \dots, N$, **do**

Calculate attenuation factors from μ^n in Eq. (6).

For activity sub-iterations, **do**

Reconstruct λ^{n+1} using a TOF-OSEM in Eq. (7), initialized by λ^n .

End

For attenuation sub-iterations, **do**

Calculate the attenuated and normalized non-TOF forward projection of the estimated activity in Eq. (8).

Calculate the constrained membership probability of μ^n in Eq. (9).

Update μ^{n+1} using a non-TOF OS-MLTR in Eq. (10).

End

End

Return: μ^{n+1}, λ^{n+1}

II.C. Experiments

We evaluated the performance of the proposed MLAA-GMM algorithm using both simulated and clinical studies in comparison with the original MLAA proposed by Rezaei *et al* [24] and the MLAA approach proposed by Salomon *et al* [21]. For simulations studies, phantoms were derived from real clinical studies acquired on PET/CT and PET/MRI scanners installed at our institution.

II.C.1 Clinical PET/CT and PET/MRI data acquisition

PET/CT and MRI datasets of a patient with head and neck carcinoma were acquired on the Biograph mCT flow scanner (Siemens Healthcare) and Ingenuity TF PET/MRI scanner (Philips Healthcare) as part of the clinical workup. The TOF-PET data of the Biograph PET/CT scanner were used for reconstruction of activity and attenuation maps and the anatomical MR images acquired on the Ingenuity PET/MRI scanner were used for the MLAA algorithm. The patients were injected with 280 MBq of ^{18}F -FDG and underwent a 12 minute PET

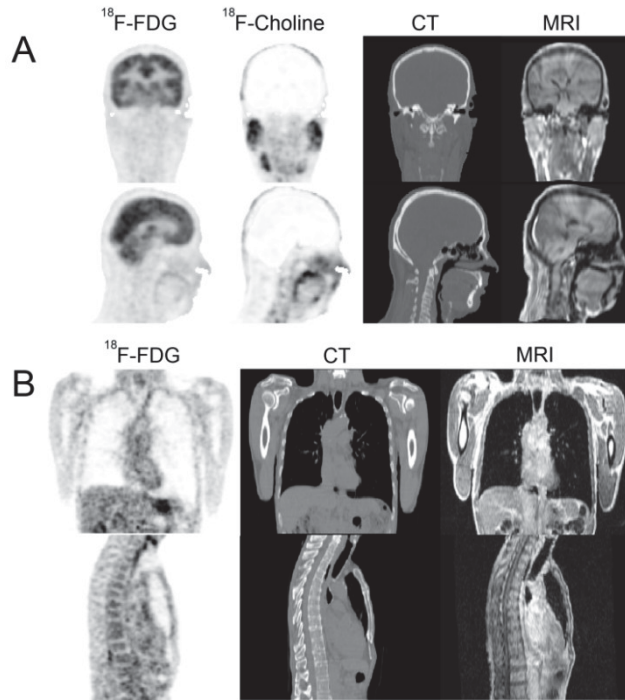


Figure 4. (A) The head PET/CT/MRI phantom emulating the biodistribution of ^{18}F -FDG and ^{18}F -Choline derived from real clinical studies. (B) PET/CT/MRI thorax phantom simulated from an ^{18}F -FDG clinical study.

scan about 60 minutes post-injection with arms-down position. The MR acquisition was performed on the Achieva 3T MRI subsystem of the Ingenuity TF PET/MRI scanner [19]. A whole-body scan was acquired in breath hold mode using a 3D 2-point multi-echo fast field echo Dixon (mDixon) technique using the following parameters: TR = 5.7 ms, TE1/TE2 = 1.45/2.6, flip angle = 10° and slice thickness of 3 mm, matrix size of 680×680 and in plane resolution of $0.67 \text{ mm} \times 0.67 \text{ mm}$. The acquisition time was limited to about 20 seconds to minimize breath hold time. The Dixon MR images were deformably registered to patient's CT images using the Elastix software.

II.C. 2 Experimental phantom measurements and simulations

The NEMA IEC body phantom was scanned on the mCT scanner to evaluate the quantitative performance of the MLAA algorithm with regard to the missing scaling factor [24]. About 100 MBq of ^{18}F -FDG were injected in the phantom followed by scanning for 30 minutes. In this experiment, a pseudo MR image was obtained from the corresponding CT images, by reducing the intensity of hollow glass spheres and their acrylic holders, and used to derive a tissue prior map and anatomical regions for MLAA-GMM and MLAA-Salomon algorithms, respectively. For MLAA-Salomon, the pseudo MR image was segmented into ~ 300 regions using a hybrid k -means and Markov random field clustering algorithm by means of the VolView software (Kitware, Inc., Clifton Park, NY), followed by connected component labeling. Regions with less than 10 voxels were assigned to their nearest populated regions.

Clinical PET/CT/MRI datasets were used to simulate noisy TOF data acquisitions on the mCT scanner. Two realistic head and thorax phantoms were derived from clinical studies to evaluate the performance the MLAA algorithms for different activity distributions, noise levels and body regions. In the head phantom shown in Figure 4(A), typical biodistribution of ^{18}F -FDG and ^{18}F -Choline (FCH), 60 min and 20 min post-injection were simulated, respectively. ^{18}F -FDG has an enhanced uptake in the brain and a background uptake over soft-tissues while ^{18}F -Choline (FCH) has an enhanced uptake in malignant tumors, i.e. glioma, salivary glands (parotids) and a negligible uptake in the brain [34]. The thorax phantom shown in Figure 4(B) was also derived from an ^{18}F -FDG PET scan, 60 min post-injection. An in-house TOF-PET simulator was developed for the native geometry of the Siemens Biograph mCT system, with an effective timing resolution of 580 ps and a coincidence window width of 4 ns, using MATLAB with SPMD parallel processing (MathWorks Inc., Natick, MA). The 4D TOF sinograms had 400 radial bins, 168 azimuthal angles, 621 planes (in 9 segments with span 11) and 13 time bins

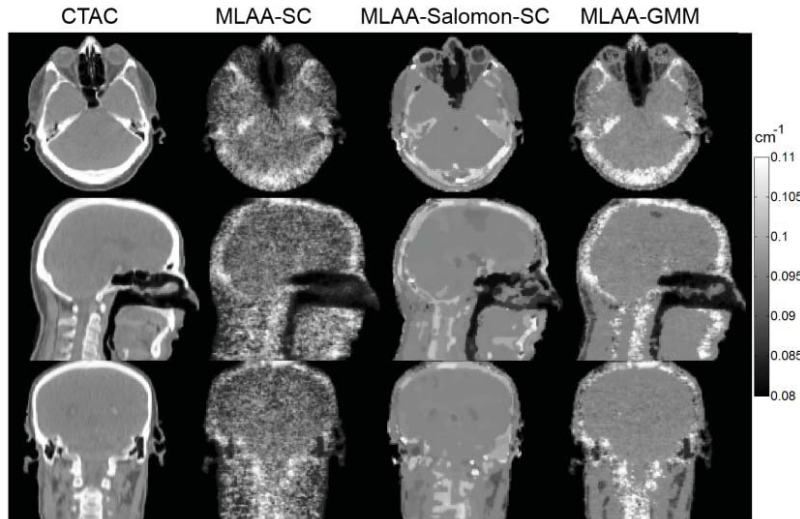


Figure 5. The estimated attenuation maps using the different MLAA algorithms in the ^{18}F -FDG head phantom compared with the corresponding reference CTAC map used as reference.

of 312 ps width. The attenuation and activity were reconstructed for a single bed. Projection data were attenuated by actual attenuation factors obtained from the forward projection of CT-based (CTAC) attenuation maps. Poisson noise realizations were simulated for 85 M and 40 M counts in the FDG and FCH head phantoms, respectively, and 40 M counts in the thorax phantom. In the simulations, the contribution of scattered and random coincidences was ignored. For the MR-constrained MLAA algorithms, MR images were coregistered to CT images using the Elastix software, with mutual information similarity measure and 5 resolution levels, and then down-sampled to the resolution of attenuation maps. For the proposed MLAA-GMM algorithm, a tissue prior map was derived from MR images and a co-registered bone map. For MLAA-Salomon algorithm, the T1-weighted in-phase MR images were segmented into many regions for each PET bed position using the above mentioned segmentation method

III. Results

III.A. Head and thorax phantom simulations

To evaluate the impact of activity distribution on the performance of the algorithms in estimating attenuation coefficients, the numerically simulated FDG and FCH head phantoms, presented in Section. II.D.2, were employed. In the FDG and FCH phantoms, 85 M and 40 M Poisson-distributed counts were respectively simulated from the attenuated forward projection of the true activity distributions. In the FDG data simulation case, the maximum number of counts in the TOF and non-TOF sinograms was 21 and 39, respectively, while in the FCH simulation, it was 19 and 35 for TOF and non-TOF sinograms, respectively. The activity/attenuation pair images were reconstructed with a matrix size of $400 \times 400 \times 109$ per bed using 40 global iterations, 1 iteration and 2 subsets for activity updates followed by 1 iteration and 3 subsets for attenuation updates.

The MLAA activity and attenuation reconstructions are scaled as reported earlier. To solve the scaling problem, Rezaei *et al* [24] iteratively imposed the known value of tissue attenuation to the 75th percentile of the LACs within the body contour. In this work, we evaluated MLAA and MLAA-Salomon algorithms with and without the scale correction (SC) factor proposed in [24]. In addition, we used the same MRF smoothing prior for the MLAA algorithm as for the proposed algorithm. For the studied algorithms, a background mask was imposed on the attenuation maps to set to zero the image voxels outside of CT support.

Figure 5 compares the estimated attenuation maps of the FDG phantom for the proposed MLAA-GMM and the scale corrected versions of MLAA and MLAA-Salomon algorithms. The results show that the MLAA-SC algorithm distinguishes well air gaps from soft-tissue; however, the estimated attenuation map suffers from noise, especially at the edge of the axial field-of-view, where the sensitivity and thus the support of activity is lower. The MLAA-Salomon-SC algorithm effectively suppresses noise; however, since MR images acquired

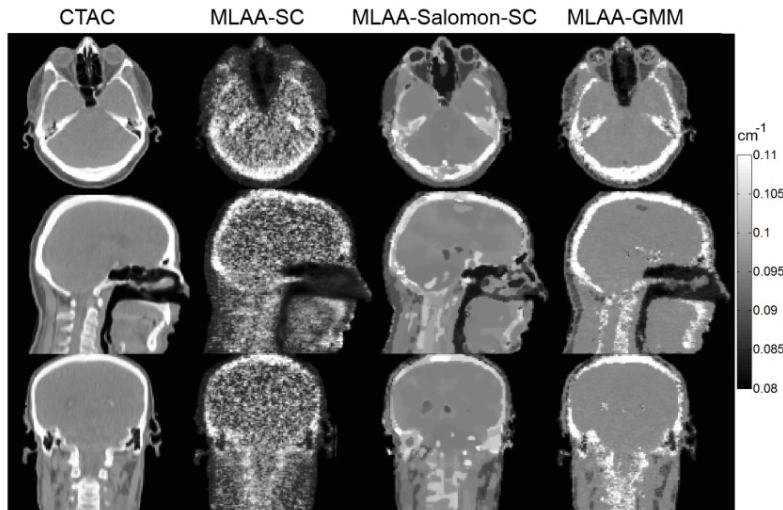


Figure 6. Same as figure 5 for the ^{18}F -Choline head phantom.

Table II. PET quantification bias (in percent) in different ROIs with respect to reference CTAC-PET images.

ALGORITHM		CEREBRUM	FRONTAL	C4
FDG	MLAA	-7.3 ± 2.7	-7.7 ± 3.2	-4.1 ± 7.7
	MLAA-SC	-15.7 ± 2.4	-15.7 ± 2.8	-11.4 ± 5.6
	MLAA-SALOMON	-7.7 ± 1.4	-7.4 ± 1.8	-7.4 ± 6.5
	MLAA-SALOMON-SC	-5.6 ± 1.5	-5.4 ± 1.8	-6.2 ± 6.5
	MLAA-GMM	-7.3 ± 1.1	-7.0 ± 1.5	-6.4 ± 4.5
FCH	MLAA	-0.4 ± 6.5	-1.0 ± 6.0	-3.4 ± 10.4
	MLAA-SC	31 ± 37.5	20.5 ± 34.0	54.2 ± 55.2
	MLAA-SALOMON	-0.3 ± 1.1	-0.3 ± 1.1	-6.4 ± 7.6
	MLAA-SALOMON-SC	41.2 ± 42.9	28.9 ± 39.7	68.0 ± 63.4
	MLAA-GMM	-2.5 ± 1.1	-1.6 ± 1.2	-6.2 ± 7.3

using conventional MR sequences cannot distinguish bone from air gaps, it cannot accurately differentiate the paranasal and petrous air cavities (see sagittal and coronal slices). For this algorithm, in-phase MR images were segmented into about 4500 distinct regions. Furthermore, because of the region-wise update, the estimated attenuation coefficients of bones are underestimated, indicating the slower convergence of this algorithm. In contrast, the MLAA-GMM algorithm outperforms its counterparts by effective noise suppression, air cavity differentiation and bone derivation. However, the algorithm cannot highlight all bony structures, e.g. temporal and parietal bones in the transverse and coronal slices, respectively, which should be ascribed to count level, convergence rate and activity distribution.

Figure 6 shows the estimated attenuation map of the FCH head phantom where the corresponding PET images have a more asymmetric distribution than the FDG head phantom (Figure 4) and provide less support for attenuation estimation, given the lower number of simulated counts. As can be seen, the MLAA-SC results in overwhelmingly noisy estimates, while both Salomon's and our algorithm suppress noise effectively. Because of the axially asymmetric distribution of activity or the high uptake of scalp, the algorithm estimates the bones more completely and accurately compared to the FDG phantom. Overall, the proposed MLAA algorithm shows an improved performance over its counterparts in the derivation of the attenuation map. Figure 7 compares the mean and standard deviation of the estimated attenuation maps for the FDG and FCH head phantoms with the reference CTAC maps for soft and bone tissue classes, respectively.

The linear attenuation coefficients (LACs) estimated by MLAA show a high standard deviation, which is considerably reduced when using MLAA-Salomon and MLAA-GMM algorithms. In soft-tissue, MLAA-GMM estimates the same attenuation coefficients for both phantoms, while the performance of the other algorithms depends on the activity distribution. The results show that the scale correction of the MLAA and Salomon's algorithms underestimate the attenuation coefficients, underlining the non-robustness of the scale correction approach proposed in [24].

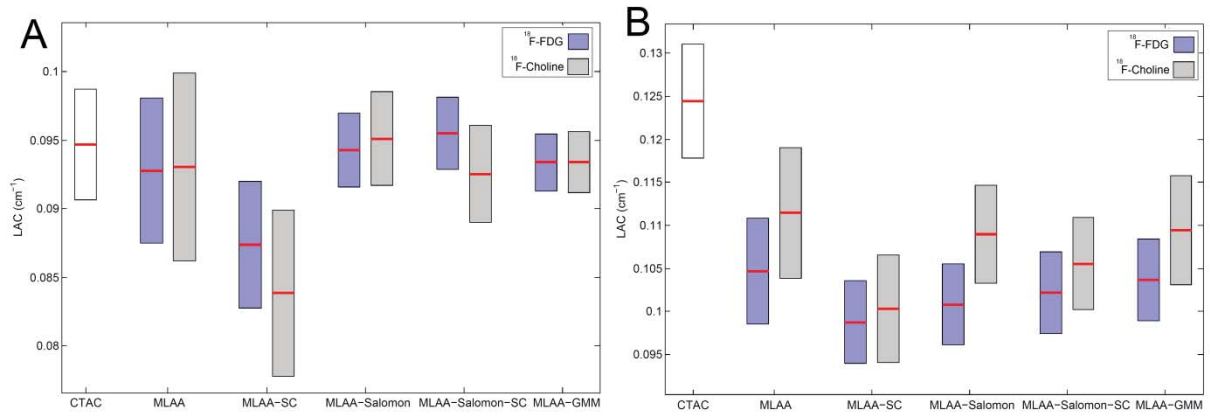


Figure 7. Comparison between the estimated attenuation maps using the different MLAA algorithms and the reference CTAC map in (A) soft tissue and (B) bone tissue classes for ^{18}F -FDG and ^{18}F -Choline head phantoms. The horizontal bars and vertical boxes indicate the mean and standard deviation (1σ) of attenuation coefficients.

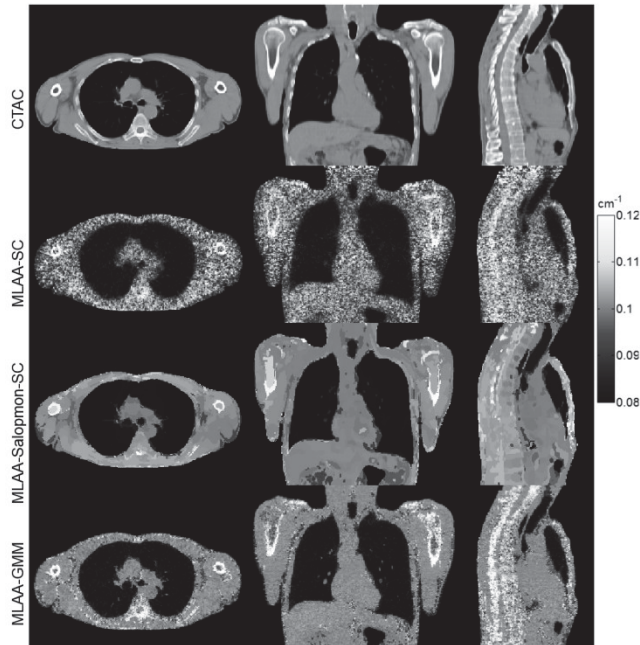


Figure 8. The estimated attenuation maps using the various MLAA algorithms in the ^{18}F -FDG thorax phantom compared with their corresponding reference CT-based attenuation map.

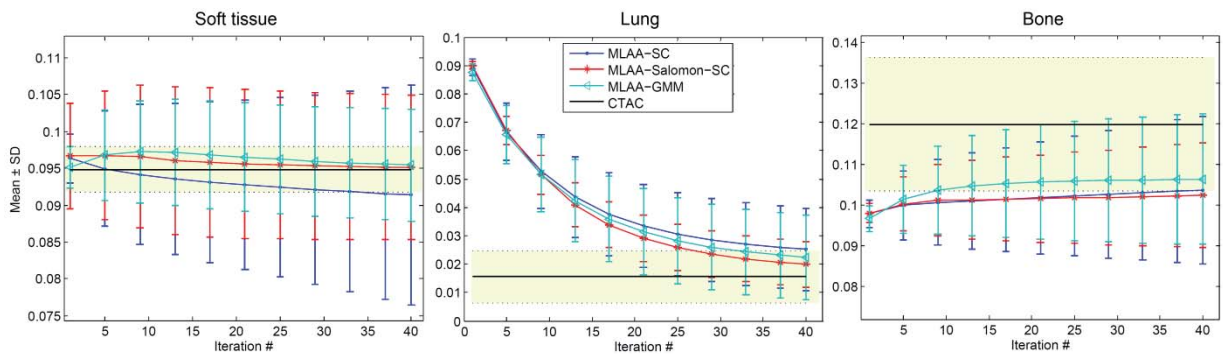


Figure 9. The mean \pm standard deviation of the estimated attenuation coefficients vs. the global iteration number in soft-tissue, lung and bone tissue classes of the thorax phantom using 40 M counts simulations. The horizontal solid lines and yellow bars indicate the expected value and the 2σ variation of LACs in the reference CTAC map.

In bony structures, the algorithms present almost the same quantitative performance and underestimate the mean bone attenuation coefficients; however, as shown in Figure 6, they can better estimate the bone LACs in the FCH phantom. The quantitative performance of the algorithms was further evaluated with respect to PET images reconstructed using CTAC attenuation maps. Table II summarizes the PET quantification bias of the algorithm for the FDG and FCH studies in three different ROIs (cerebrum, frontal lobe of brain and 4th cervical vertebra, C4). The results show that the algorithms present with similar performance, which is dependent on the activity distribution. However, the results also show that the scale corrected version of the MLAA and MLAA-Salomon algorithms results in very high bias.

Figure 8 compares the reconstructed attenuation maps of the thorax phantom with the CTAC attenuation map over 2 overlapping bed positions with 40 M counts per bed. In this simulation, the maximum number of counts in the TOF and non-TOF sinograms was 13 and 26, respectively. The images were reconstructed with the same resolution and number of iterations as the head phantom. For Salomon's algorithm, in-phase MR images corresponding to each bed were segmented into about 5000 distinct regions. As can be seen, MLAA differentiates well the lungs and air pockets; however, the estimated attenuation map suffers from noise. MLAA-Salomon-SC substantially reduces noise by region-wise averaging of the correction matrix (descent direction) during the estimation of attenuation; however, this algorithm is not able to estimate accurately bone attenuation, mainly because of the misclassification of bones with surrounding soft-tissues owing to i) the inherent partial volume averaging effect in the original MR images and the averaging effect induced during down-sampling to 400×400 resolution of the mCT images, ii) MR field inhomogeneities, and iii) the limitations of the segmentation algorithm. In contrast, the proposed algorithm outperforms its counterparts in reducing noise and potential cross-talk artifacts and in deriving bony structures.

Figure 9 shows the mean and standard deviation of the estimated LACs at each global iteration for soft-tissue, lung and bone classes of the thorax phantom. The mean and two-sigma deviation of the true attenuation coefficients are shown by the horizontal solid lines and yellow bars, respectively. Salomon's algorithm overestimates soft-tissue class, mainly because of the scaling problem of the joint estimation of activity and attenuation. MLAA-Salomon-SC algorithm estimates reasonably well the soft-tissue class, while MLAA-SC algorithm underestimates the mean soft-tissue attenuation coefficients because of inaccurate scale correction. However, the proposed algorithm correctly estimates the mean values with an acceptable standard deviation. In the lungs, as the number of iterations increases, the bias in the mean of estimated lung LACs decreases. Both Salomon and our approach outperform the MLAA algorithm. The algorithms show a monotonic convergence toward the expected value of lung LACs. However, they have not converged and reached a plateau after 40 global iterations, which results in 80 and 120 updates for activity and attenuation maps, respectively. The algorithms have almost the same convergence in the estimation of mean attenuation coefficients of bone, but the proposed algorithm tends to estimate more accurately the mean of bone LACs at earlier iterations, although at later iterations, it approaches the other algorithms.

III.B. Experimental NEMA phantom

In this experiment, the NEMA phantom was located at the center of the field-of-view of the mCT scanner and scanned for 15 minutes using step and go mode. A total number of about 200 M and 100 M prompt and accidental coincidences were recorded in the resulting TOF sinograms. In this phantom, the activity and attenuation maps were reconstructed with a matrix size of $200 \times 200 \times 109$ for 20 global iterations and the same update schedule as in the simulations. An initial attenuation map was derived by filling the body contour with water attenuation coefficient (0.0957 cm^{-1}). The CTAC attenuation map was used to enforce bed attenuation values as well as to estimate TOF scatter sinograms using Siemens e7 tools.

Figure 10 shows the activity and CTAC attenuation maps together with the attenuation maps estimated using MLAA-SC, MLAA-Salomon-SC and MLAA-GMM techniques. The algorithms differentiate well the body attenuating materials from the central cavity of the phantom, which contains lung equivalent density. The MLAA's attenuation map; however, suffers from noise and over-estimation of attenuation coefficients on the top of the phantom, which has an imperfect support of activity. Salomon's algorithm effectively reduces noise, since it updates the attenuation maps on a region-wise basis, while the MLAA-SC and MLAA-GMM algorithms update them on a pixel-wise basis. The region-wise update is efficient provided that an accurate segmentation

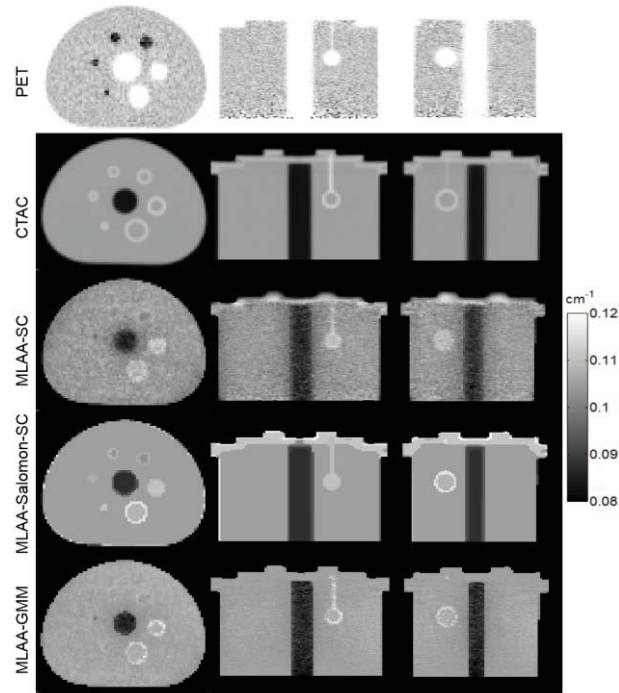


Figure 10. The NEMA PET activity and corresponding CT-based attenuation map together with the attenuation maps estimated using the various MLAA algorithms with the scale correction (SC) proposed in [24].

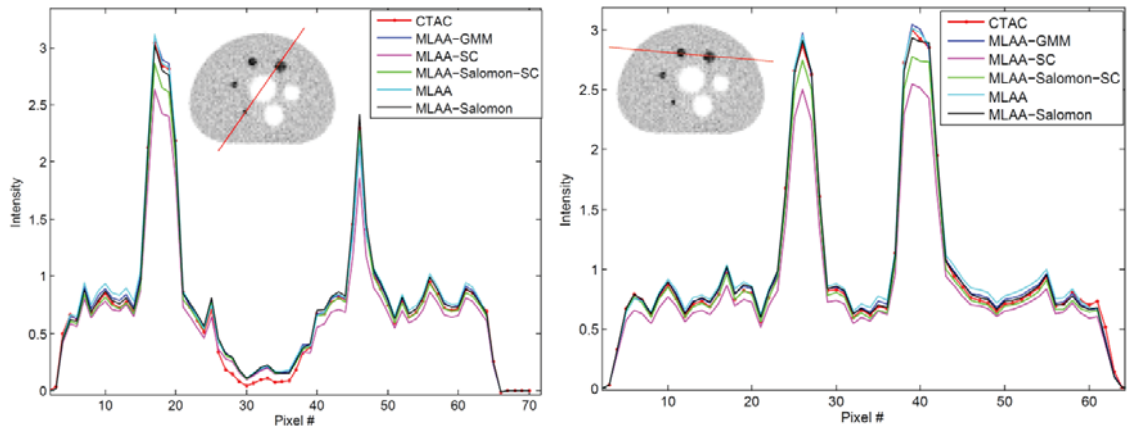


Figure 11. Activity profiles of the NEMA phantom reconstructed using the studied MLAA algorithms compared with reference CTAC-OSEM.

can be achieved. For this reason, the MLAA- Salomon-SC algorithm performs well over the body of the phantom; however, on the top of the phantom and the 28-mm sphere, it overestimates the attenuation coefficients. The proposed algorithm reduces noise and overestimation by penalizing the large deviation of attenuation coefficients from their expected values. Figure 11 compares the activity profiles of the estimated activity maps using the different MLAA-algorithms with the reference CTAC activity profiles. The results show that the MLAA-GMM, MLAA and MLAA-Salomon algorithms have almost the same performance since the scaling issue is not raised in this phantom study. Consequently, the scale correction of the two latter algorithms results in underestimation of the hot spots activity values. The quantitative performance of the algorithms was further evaluated. In this experimental and the following clinical studies, the mean (m^h) and standard deviation (σ^h) of the activity quantification errors (bias) was evaluated in each tissue class (h) as follows:

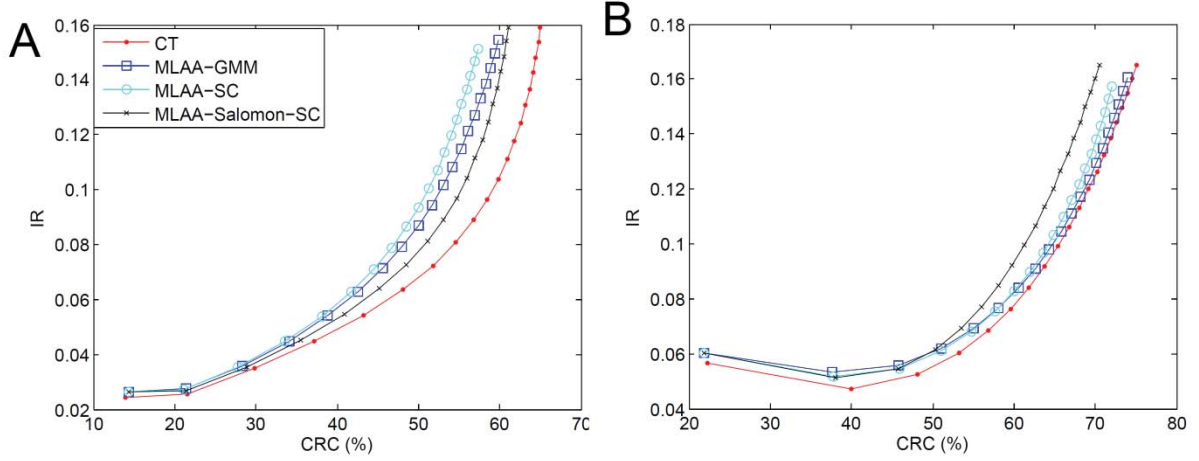


Figure 12. Image roughness (IR) versus contrast recovery coefficient (CRC) as a function of iteration number for different reconstructions of the NEMA phantom, weighted for (A) all of hot spheres and (B) all of cold spheres according to the size of spheres.

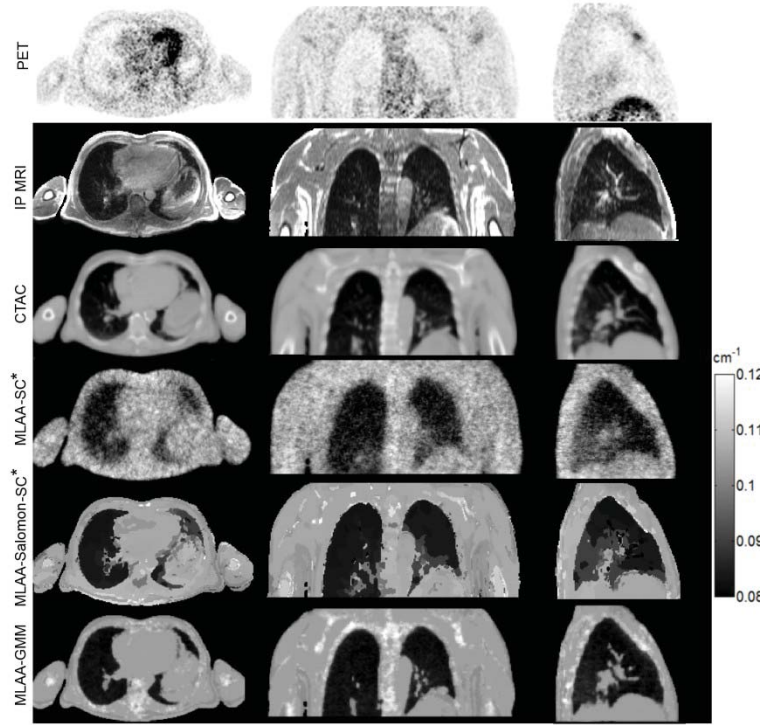


Figure 13. Comparison of the estimated attenuation maps for the ^{18}F -FDG clinical study with the reference CT-based attenuation map and the corresponding PET and MR images.

$$m^h = \frac{\sum_{i \in h} B_i}{N_h}, \quad \sigma^h = \sqrt{\frac{\sum_{i \in h} (B_i - m^h)^2}{N_h}}, \quad B_i = \frac{\lambda_i - \lambda_i^{CT}}{\lambda_i^{CT}} \quad (11)$$

where N_h is the number of voxels in class h . In the NEMA phantom, a soft tissue class was derived from the reconstructed CTAC PET images, while for the clinical studies, the classes of the tissue prior map were used for bias evaluation. The results show that the MLAA-GMM algorithm gives rise to -0.4 ± 3.2 % bias, while the MLAA and MLAA-Salomon result in a bias of 3.1 ± 5.2 % and 3.1 ± 4.7 %, respectively. The scale corrected version of the algorithms, i.e. MLAA-SC and MLAA-Salomon-SC, resulted in a bias of -8.4 ± 6.2 % and -0.9 ± 3.6 %, respectively. These results show that the heuristic scale correction method proposed by Rezaei *et al*, improves the overall quantitative performance of the Salomon's algorithm, while it adversely affects the original MLAA algorithm. The NEMA phantom was further used to evaluate the bias-variance performance of the

algorithms in terms of contrast recovery coefficient (CRC) as a metric of bias and image roughness (IR) as a metric of variance, according to the International Atomic Energy Agency (IAEA) protocol [35]. In order to assess the overall quantitative performance, we averaged the IR and CRC values of the hot spheres as well as the cold spheres, based on the size of the spheres (number of voxels in ROIs corresponding to each sphere). Fig. 12 shows the results for hot and cold spheres. For the same noise level in the hot spheres, the MLAA algorithm results in a lower CRC than the reference CTAC-OSEM algorithm. The MLAA-Salomon-SC and MLAA-GMM achieve a slightly better bias-variance performance than MLAA-SC. On the other hand, in the cold spheres, MLAA-Salomon-SC achieves the worst bias-variance trade-off, probably because of an inappropriate scale correction over the cold spot, where cross-talk artifacts can occur (see Fig. 10 middle column).

III.C. Clinical study and quantitative evaluation

A patient presenting with head and neck cancer, injected with 280 MBq ^{18}F -FDG, underwent a 12 min PET scan on the mCT Flow scanner using continuous bed motion mode. Dixon MR images were acquired on the Ingenuity TF PET/MRI scanner as described in Section II.D.1. PET data of an axial length of about 22 cm corresponding to a single bed position were used for joint reconstruction. The total number of prompts and net trues were about 47 and 30M counts, respectively.

The MLAA algorithms were initialized with water-equivalent attenuation map and CTAC-simulated scatter. The activity and attenuation maps were reconstructed with a matrix size of $400 \times 400 \times 109$ using 35 global iterations and the same update schedule as in the simulations. In our simulation and NEMA results, the applied scale correction was not robust, therefore for this dataset, as in [36], we assumed that the total amount of activity is known from the reference CTAC PET image and the activity reconstructions were scaled during reconstructions. We refer to this scale correction as SC*.

Figure 13 compares the reconstructed attenuation maps with the reference CTAC attenuation map as well as the corresponding in-phase MR image used in MLAA-Salomon-SC* and MLAA-GMM algorithms. In this comparison, the attenuation maps were smoothed using a 5 mm FWHM 3D Gaussian filter. The results show that the MLAA-SC* attenuation map suffers from noise. Salomon's algorithm effectively reduces the noise and artifacts; however, it suffers from MR segmentation errors, especially in the backbone area due to MR field inhomogeneities. In contrast, the proposed algorithm estimates more accurately the attenuation map through effective suppression of noise, artifacts and the scaling of attenuation.

Figure 14(A) illustrates the normalized histograms of the reconstructed attenuation maps in comparison with the reference CTAC maps. The peak LACs of the lung and soft-tissue have been shifted toward higher values in the attenuation maps estimated by MLAA and MLAA-Salomon algorithms, while the scale correction of the algorithms reduces the LAC scaling. The soft-tissue peak has been underestimated by MLAA-GMM, mainly because of the high value of the γ parameter of the GMM for this patient dataset. Figure 14(B) shows the mean \pm standard deviation of attenuation coefficients in soft-, lung and bone tissue classes obtained from segmentation of the CTAC map. The mean of CTAC and estimated LACs using MLAA-SC*, MLAA-Salomon-SC* and MLAA-GMM were 0.095, 0.094, 0.096, 0.095 cm^{-1} in soft tissues, 0.034, 0.04, 0.037 and 0.031 cm^{-1} in the lungs and, 0.112, 0.106, 0.101 and 0.106 cm^{-1} in bones, respectively.

Figure 15 compares the profiles of the estimated activity maps in this patient with respect to reference CTAC activity map along the depicted lines. As can be seen, the activity profiles of the MLAA and MLAA-Salomon algorithms are scaled and overestimate the hot and background regions. The scale correction of these algorithms using Rezaei's method (SC) tends to suppress the overestimation and improves the performance of the algorithms, however, the activity profile of the lesion tends to be underestimated. On the other hand the scale correction using the know tissue activity (SC*) can more robustly improve the performance of the algorithms. The results also show that the proposed method can reliably solve the scaling problem of the joint activity/attenuation estimation. The bias performance of the algorithms over soft-tissue, lung and bone classes was also evaluated. Table III summarizes the results of the bias in different tissue classes.

Contrary to the NEMA phantom study, the results demonstrate that MLAA and MLAA-Salomon suffer from the scaling problem. The scale correction using SC method improves the results, but the bias is still high, while the SC* method considerably improves the quantitative performance of the algorithms in soft tissues and bones except in the lungs where the amount tracer uptake is lower. In comparison, the results of MLAA-GMM are quite satisfactory and demonstrate the potential outperformance of the proposed emission- based method

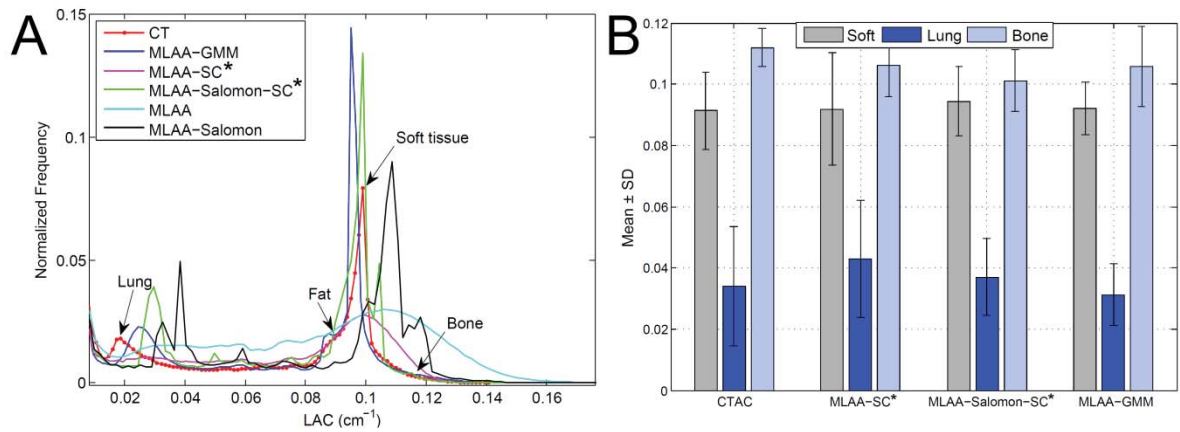


Figure 14. (A) The normalized histogram of the estimated attenuation maps of the ^{18}F -FDG clinical study with reference CTAC histograms. (B) The mean \pm standard deviation of the estimated attenuation coefficients of soft-tissue, lung and bone tissue classes.

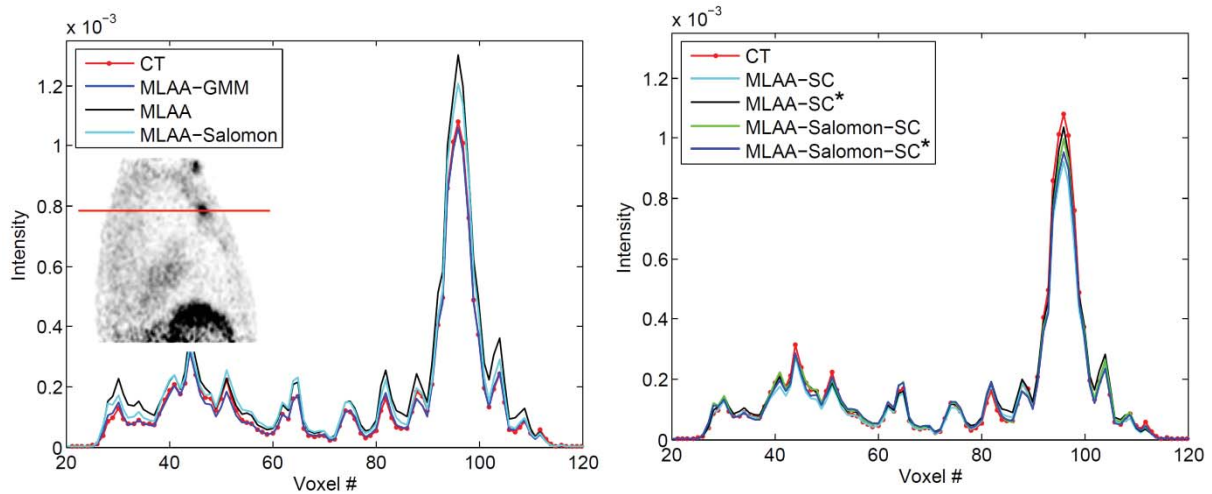


Figure 15. The activity profiles of the MLAA activity maps for the ^{18}F -FDG clinical study compared to their reference CTAC-OSEM profiles across an active tumor.

Table III. Percent error (bias) in the estimated activity of the FDG clinical study in different tissue classes.

ALGORITHM	FAT + SOFT TISSUE	LUNGS	BONES
MLAA	51.8 ± 104.1	98.4 ± 148.2	38.4 ± 75.5
MLAA-SC	-10.4 ± 19.0	19.9 ± 38.9	-17.8 ± 15.5
MLAA-SC*	-0.1 ± 25.1	30.3 ± 45.5	-6.5 ± 21.0
MLAA-SALOMON	24.9 ± 32.3	47.3 ± 40.6	8.6 ± 22.7
MLAA-SALOMON-SC	-2.1 ± 21.6	18.2 ± 32.2	-17.4 ± 14.9
MLAA-SALOMON-SC*	0.9 ± 21.6	16.3 ± 35.2	-13.1 ± 19.1
MLAA-GMM	-0.8 ± 20.2	1.97 ± 22.9	-5.5 ± 19.2

SC: SCALE CORRECTED USING THE METHOD PROPOSED IN [24].

SC*: SCALE CORRECTED USING KNOWN CTAC ACTIVITY [36].

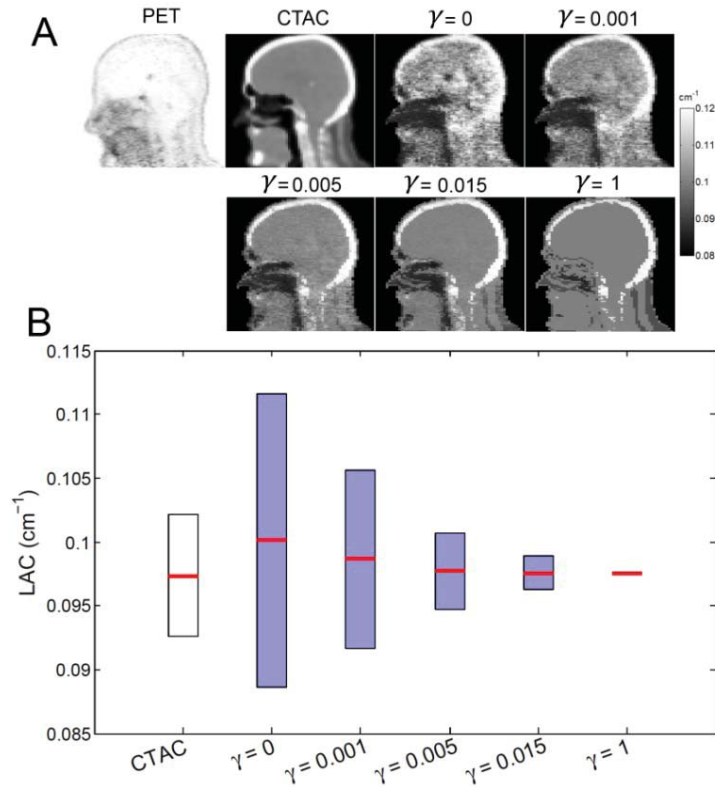


Figure 16. (A) The impact of the GMM weighting parameter on the performance of the MLAA-GMM algorithm in a clinical ^{18}F -FCH PET/CT dataset. (B) The estimated attenuation coefficients in soft tissue for the studied weights. The horizontal bars and vertical boxes indicate the mean and standard deviation (1σ) of attenuation coefficients.

over standard segmentation-based MRAC methods. However, any further conclusion necessitates a comparative study over a larger clinical database.

III.D. GMM weighting parameter and respiratory artifacts

In this section, we further evaluated the impact of the GMM weighting parameter, γ , on the performance of the proposed algorithm, as well as its behavior in the presence of respiratory-phase mismatch between MRI and PET images. A clinical ^{18}F -FCH PET/CT dataset was used to evaluate the impact of the γ parameter on the reduction of noise, cross-talk artifacts and the dependency on the activity distribution. A single bed scan covering the head was selected for the reconstruction. The sinogram contained a total number of about 80 M and 50 M prompt and accidental coincidences, respectively. The activity and attenuation maps were reconstructed with a matrix size of $200 \times 200 \times 109$ using 20 global iterations and the same update schedule as in the previous studies. For this dataset, MR images were not available. Therefore the tissue prior map was derived from the CTAC map. Fig. 16(A) compares the reconstructed attenuation maps with increasing values of the γ parameter from zero (corresponding to the original MLAA) to 1. Fig. 16(B) shows the mean \pm standard deviation of the estimated LACs in soft tissue in comparison with the reference CTAC. The proposed MLAA is in essence between the standard 4-class MRAC method and the original MLAA algorithm, depending on the GMM prior weight. Very low γ s reduce the algorithm to the original MLAA, while high-valued γ s ensure a 4-class MRAC method, where the deviation of attenuation coefficients from their expected 4-class values are penalized. The GMM prior effectively reduces noise and cross-talk artifacts (see the cranial area of the attenuation map with $\gamma = 0$). Consequently, the mean of the attenuation coefficients gets close to the expected values. However, the results show that high values of γ do not easily allow the differentiation of air attenuation coefficients in the unknown tissue class from their initial water attenuation coefficients.

In cases where the γ parameter is assigned a high value to benefit from the GMM prior and at the same time to avoid parameter optimization, a practical solution for this differentiation would be the gradual increase of the γ with iteration number (i.e. smooth forcing of the prior), where different tissues in the unknown class can be more accurately captured by Gaussian mixture model.

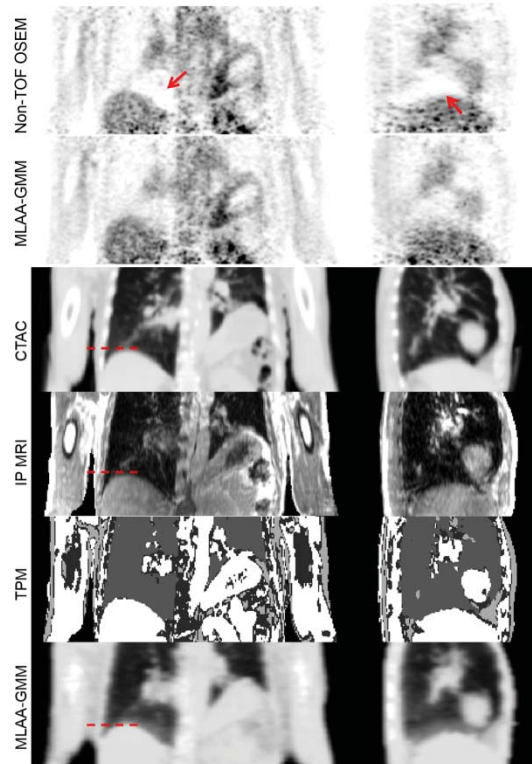


Figure 17. The non-TOF PET reconstruction of a clinical ^{18}F -FDG study, showing white-band respiratory artifacts, together with CTAC, IP MRI, tissue prior map (TPM) and MLAA-GMM attenuation map. The horizontal lines demonstrate that both CT and MR images are well co-registered. As pointed by the arrow, there is a respiratory-phase mismatch between PET and CT/MRI images; however, the MLAA-GMM algorithm has compensated for this mismatch. The display window for attenuation maps is $[0.07-0.10 \text{ cm}^{-1}]$.

In the case of respiratory-phase mismatch between MRI and PET images, the proposed algorithm should fairly compensate for this mismatch. Since patients spend more time in expiration than in inspiration during the respiratory cycle, the PET data, averaged over few minutes, are closer to the end of expiration than inspiration [37]. Therefore, if MR images are acquired near end-expiration, MR and PET images should be well aligned. However, if MR images are acquired at for example end-inspiration (severe mismatch), the proposed and original MLAA algorithms should be able to compensate for this mismatch. Fig. 17 compares the CT attenuation map of a clinical study over an axial length of 33 cm with the attenuation map estimated by the proposed algorithm. As the horizontal lines indicate, the two images correspond to the same respiratory phase because, as mentioned in Section II.B, MR images used in the MLAA-GMM algorithm were registered to reference CT images. However, a close examination of non-TOF PET images reveals the presence of respiratory-induced banana artifacts in the diaphragm region depicting a mismatch between PET and CT and thus PET and MR images. The TOF OSEM and MLAA-GMM PET images did not visually reveal the artifacts. Nonetheless, the results demonstrate that the proposed algorithm has well inherited the respiratory mismatch compensation from the original MLAA algorithm (cf. sagittal images) and therefore can reduce the resulting quantification errors.

III. Discussion

Accurate PET attenuation correction in quantitative PET/MRI examinations is of paramount importance. In this work, we proposed a novel approach to effectively employ MRI information in the joint estimation of activity and attenuation from emission data to pave the way toward accurate emission-based attenuation correction in whole-body PET/MR imaging.

Recently introduced commercial PET/MRI systems use standard 3- or 4-class segmentation-based MRAC methods. However, the inter/intra-patient heterogeneity of attenuation coefficients in different tissue classes is

ignored by these techniques. Moreover, since bone and air cannot be well differentiated on conventional MR sequences, owing to their low water content and short transverse relaxation time, they are often ignored and replaced by soft-tissue, which can lead to significant bias (4 to 25%) in PET tracer uptake quantification in different organs [38-41]. Ultra-short echo time (UTE) pulse sequences have been recently explored to include bones as a 5th class in order to reduce the bias [42, 43]. However, despite the promising results, UTE sequences are not yet clinically feasible in whole-body PET/MR imaging owing to long acquisition time. In addition, the images are also subject to misclassifications due to magnetic susceptibility artifacts at air/bone-soft-tissue interfaces [42] and eddy current artifacts [44].

Following the recent rebirth of time-of-flight PET, simultaneous estimation of activity and attenuation has regained popularity for attenuation correction on standalone PET [24] and hybrid PET/MRI systems [21] with spin-off applications in motion and misalignment correction between CTAC attenuation and PET activity maps [45]. The joint estimation is especially attractive for PET/MRI to circumvent the uncertainties and obstacles of the standard and UTE MRAC methods. However, as mentioned earlier, the quantitative accuracy of this estimation using the standard MLAA algorithm depends significantly on TOF timing resolution, count level and activity distribution. The latter supports the estimation of attenuation along LORs that intersect a region containing a substantial amount of activity and in fact determines the degree to which the attention maps can be accurately and completely estimated as demonstrated in our simulated FDG and FCH studies. It has been theoretically and experimentally shown that attenuation maps or attenuation correction factors can be estimated from TOF emission data up to a constant factor. Our experimental phantom and clinical studies showed that the scaling factor of the MLAA algorithm is also object-dependent. Several scenarios have been proposed to practically tackle this scaling issue by rescaling the estimated LACs [24], shifting the peak of the histogram of the estimated attenuation map to soft-tissue attenuation [46], or combining MLAA with full or partial transmission information [47, 48]. The scatter coincidences at a lower energy window [49], single events [50] and background radiation of LSO and LYSO crystals can also provide additional information about the attenuating material and hence a potential solution to this scaling factor [51].

In this work, a Gaussian mixture model was employed in the estimation of attenuation in order to reflect the prior knowledge that the histogram of the attenuation values generally consists of a few distinct peaks corresponding to fat, soft-tissue and bone. The spatial information derived from Dixon MR images is also incorporated into this model to favor known tissue types. A direct result of this spatially constrained tissue preference prior is the penalization of large deviations of attenuation coefficients from their expected value in each known tissue class and their distribution from a histogram parameterized over a patient population. Therefore, as our experimental and clinical results demonstrate, the scaling of attenuation and activity as well as noise and cross-talk artifacts in the attenuation map can be robustly suppressed. In addition, the LACs of regions that are out of the support of activity but are in a known tissue class are recovered more accurately. In comparison, Salomon's algorithm uses MR images to derive many distinct regions over which attenuation coefficients are estimated without additional information about their expected values.

As spongy bones, containing bone marrow, are usually misclassified as fat and soft-tissue in MR images, we proposed a simple way to suppress fat from water and thus enabling to estimate the voxels of bony structures using a GMM model. Moreover, we employed a co-registered bone probability map, obtained from several co-registered CT images, to indicate regions with possible bone occurrence. Bezrukov *et al* [38] recently used a bone and metal-artifact probability map to merge 4-class MRAC with an atlas- and pattern recognition-based MRAC algorithm. As mentioned earlier, a perfect atlas-to-patient registration can likely solve the MRAC problem. However, whole-body registration is subject to anatomical differences between subjects and the limitations of registration algorithms. The bone map registration used in our work is, in principle, not subject to such limitations owing to the inherent tolerance conveyed by averaging of CT images. Furthermore, since cortical bones (skull, body of vertebra, hips.. etc) in our heuristically fat suppressed water images are assigned to the low-intensity MR class, the attenuation coefficients of cortical bones are still guaranteed to be estimated with a mixture model in cases of severe mis-registration between MR and bone map. In the presence of MR susceptibility artifacts, MR void regions, which have no intensity, are included in the unknown class and therefore estimated using a GMM model.

Despite the capabilities of the proposed MLAA-GMM algorithm, it is worth to highlight some of its limitations and potential directions for future development to improve its performance. Similar to segmentation-based MRAC methods, the lungs must be segmented as accurately as possible, since the LAC of anatomical

structures that are either missed or incorrectly segmented can be wrongly estimated, depending on the user-defined weight, γ , of the GMM prior. Moreover, in the case of mis-registration between MRI and PET images over stomach air pockets, the proposed approach cannot compensate for this mismatch, similar to Salomon's algorithm. In a known tissue class, the objects or structures with an unexpected attenuation coefficient (i.e. misclassified spongy bone or small metallic objects that do not produce MR susceptibility artifacts) can be partially or completely suppressed, depending on the γ parameter.

Similar to other MAP image reconstruction strategies, the performance of the proposed algorithm depends on the choice of the hyper-parameters. In this proof-of-principle study, we tried to fix most of the involved parameters (schedule update, regularization parameters, activity and attenuation initializations) based on our simulation results. As shown in Fig. 16, the performance of the MLAA-GMM depends mainly on the γ parameter. In our experience, this parameter outweighs the β parameter of the MRF prior, therefore there is a flexibility in the selection of β . To avoid optimization of the γ over a large patient dataset, it can be chosen to a high value (based on few simulation or clinical results), which indeed enforces the algorithm toward the underlying 4-class MRAC method. To avoid the tissue differentiation of the unknown LACs with a high-valued γ , the parameter can be gradually increased to the desired value with iteration or update number. Similar to Salomon *et al*, we initialized the activity and attenuation with uniform maps and updated them using global and local iterations. In contrast, Rezaei *et al* used a different update schedule. They performed 3 iterations of 42 subsets for activity update whereas attenuation was updated 3 times after each update of activity for reconstruction of clinical studies. In fact, the MLAA algorithms are still in their infancy and require in-depth exploration of the impact of update schedules and initializations.

In the derivation of bone maps, CT registrations increase the number of preprocessing steps and the overall processing time, although in our experience, the most time consuming part is the TOF joint estimation of activity and attenuation. In brain studies where the skull is mainly cortical and presents with a low MR intensity, we believe that the bone map registration step of the algorithm can be skipped since the bones can be properly included in the unknown tissue class. Moreover, the combination of T1 and proton-density weighted imaging and MR sequences that provide bone-cartilage contrast (i.e. T2-weighted water-excitation dual-echo steady-state and T2-weighted multi-echo data image combination) might provide a solution to better distinguish fat and soft-tissue from spongy bones and thus to eliminate the bone probability map. Future work will focus on the evaluation of the algorithm in brain studies and comparison of its performance with the standard 4-class MRAC method using a large whole-body clinical database through 4-class attenuation initialization and scatter simulation.

V. Conclusion

In this work, an emission-based MRAC algorithm was proposed based on the maximum likelihood reconstruction of activity and attenuation with incorporation of prior MR information using a constrained Gaussian mixture model. The performance of the proposed MLAA-GMM algorithm was evaluated against current state-of-the-art MLAA algorithms using simulation, experimental and clinical studies. The results demonstrate that our algorithm is not susceptible to MR segmentation errors and provides a practical solution to the cross-talk and scaling problems of activity and attenuation estimates, through panelizing large deviations of attenuation coefficients from their expected values in each MR tissue class and overall attenuation distribution from its expected histogram.

Acknowledgements

This work was supported by the Swiss National Science Foundation under Grant SNSF 31003A-149957 and the Indo-Swiss Joint Research Programme ISJRP 138866. The authors would like to thank Mike Casey and Judson P. Jones (Siemens Healthcare) for providing and supporting VG50 e7 tools for the CBM mode reconstruction of the mCT Flow scanner.

References

- [1] D. A. Torigian, H. Zaidi, T. C. Kwee, B. Saboury, J. K. Udupa, Z.-H. Cho, *et al.*, "PET/MR Imaging: Technical aspects and potential clinical applications," *Radiology*, vol. 267, pp. 26-44, 2013.
- [2] I. Bezrukov, F. Mantlik, H. Schmidt, B. Scholkopf, and B. J. Pichler, "MR-based PET attenuation correction for PET/MR imaging.," *Semin Nucl Med*, vol. 43, pp. 45-59, 2013.
- [3] H. Zaidi, "Is MRI-guided attenuation correction a viable option for dual-modality PET/MR imaging?," *Radiology*, vol. 244, pp. 639-642, 2007.
- [4] A. Martinez-Moller, M. Souvatzoglou, G. Delso, R. A. Bundschuh, C. Chefd'hotel, S. I. Ziegler, *et al.*, "Tissue classification as a potential approach for attenuation correction in whole-body PET/MRI: Evaluation with PET/CT data.," *J Nucl Med*, vol. 50, pp. 520-526, 2009.
- [5] Z. Hu, S. Renisch, B. Schweizer, T. Blaffert, N. Ojha, T. Guo, *et al.*, "MR-based attenuation correction for a whole-body PET/MR system," *IEEE Nuclear Science Symposium & Medical Imaging Conference*, 2010, pp. 2119-2122.
- [6] M. Hofmann, F. Steinke, V. Scheel, G. Charpiat, J. Farquhar, P. Aschoff, *et al.*, "MRI-based attenuation correction for PET/MRI: A novel approach combining pattern recognition and Atlas registration.," *J Nucl Med*, vol. 49, pp. 1875-1883, 2008.
- [7] E. Schreibmann, J. A. Nye, D. M. Schuster, D. R. Martin, J. Votaw, and T. Fox, "MR-based attenuation correction for hybrid PET-MR brain imaging systems using deformable image registration.," *Med Phys*, vol. 37, pp. 2101-2109, 2010.
- [8] A. Johansson, M. Karlsson, and T. Nyholm, "CT substitute derived from MRI sequences with ultrashort echo time.," *Med Phys*, vol. 38, pp. 2708-2714, 2011.
- [9] B. K. Navalpakkam, H. Braun, T. Kuwert, and H. H. Quick, "Magnetic resonance-based attenuation correction for PET/MR hybrid imaging using continuous valued attenuation maps.," *Invest Radiol*, vol. 48, pp. 323-332, 2013.
- [10] F. Natterer, "Determination of tissue attenuation in emission tomography of optically dense media.," *Inverse Probl*, vol. 9, pp. 731-736, 1993.
- [11] A. Welch, C. Campbell, R. Clackdoyle, F. Natterer, M. Hudson, A. Bromiley, *et al.*, "Attenuation correction in PET using consistency information.," *IEEE Trans Nucl Sci*, vol. 45, pp. 3134-3141, 1998.
- [12] A. V. Bronnikov, "Reconstruction of attenuation map using discrete consistency conditions.," *IEEE Trans Med Imaging*, vol. 19, pp. 451-462, 2000.
- [13] C. H. Wu, J. M. M. Anderson, M. Rao, and B. Mair, "Iterative methods for correcting attenuation in positron emission tomography," *Proceedings of the International Conference on Image Processing*, 1998, pp. 700-705.
- [14] J. Nuyts, P. Dupont, S. Stroobants, R. Benninck, L. Mortelmans, and P. Suetens, "Simultaneous maximum a posteriori reconstruction of attenuation and activity distributions from emission sinograms.," *IEEE Trans Med Imaging*, vol. 18, pp. 393-403, 1999.
- [15] A. Krol, J. E. Bowsher, S. H. Manglos, D. H. Feiglin, M. P. Tornai, and F. D. Thomas, "An EM algorithm for estimating SPECT emission and transmission parameters from emissions data only.," *IEEE Trans Med Imaging*, vol. 20, pp. 218-232, 2001.
- [16] M. Landmann, S. N. Reske, and G. Glatting, "Simultaneous iterative reconstruction of emission and attenuation images in positron emission tomography from emission data only.," *Med Phys*, vol. 29, pp. 1962-1967, 2002.
- [17] M. S. Kaplan, D. R. Haynor, and H. Vija, "A differential attenuation method for simultaneous estimation of SPECT activity and attenuation distributions.," *IEEE Trans Nucl Sci*, vol. 46, pp. 535 -541, 1999.
- [18] F. Crepaldi and A. R. De Pierro, "Activity and attenuation reconstruction for positron emission tomography using emission data only via Maximum Likelihood and iterative data refinement.," *IEEE Trans Nucl Sci*, vol. 54, pp. 100-106, 2007.
- [19] H. Zaidi, N. Ojha, M. Morich, J. Griesmer, Z. Hu, P. Maniawski, *et al.*, "Design and performance evaluation of a whole-body Ingenuity TF PET-MRI system.," *Phys Med Biol*, vol. 56, pp. 3091-3106, 2011.

- [20] A. Salomon, A. Goedicke, and T. Aach, "Simultaneous reconstruction of activity and attenuation in multi-modal ToF-PET.," *10th International Meeting on Fully Three-Dimensional Image Reconstruction in Radiology and Nuclear Medicine (Fully3D)*, Beijing, China, 5-10 Sept. 2009, pp. 339-342.
- [21] A. Salomon, A. Goedicke, B. Schweizer, T. Aach, and V. Schulz, "Simultaneous reconstruction of activity and attenuation for PET/MR.," *IEEE Trans Med Imaging*, vol. 30, pp. 804-813, 2011.
- [22] T. G. Turkington and J. M. Wilson, "Attenuation artifacts and time-of-flight PET," *IEEE Nuclear Science Symposium Conference Record (NSS/MIC)*, 2009, pp. 2997-2999.
- [23] M. Conti, "Why is TOF PET reconstruction a more robust method in the presence of inconsistent data?," *Phys Med Biol*, vol. 56, pp. 155-168, 2011.
- [24] A. Rezaei, M. Defrise, G. Bal, C. Michel, M. Conti, C. Watson, *et al.*, "Simultaneous reconstruction of activity and attenuation in time-of-flight PET.," *IEEE Trans Med Imaging*, vol. 31, pp. 2224-2233, 2012.
- [25] M. Defrise, A. Rezaei, and J. Nuyts, "Time-of-flight PET data determine the attenuation sinogram up to a constant.," *Phys Med Biol*, vol. 57, pp. 885-899, 2012.
- [26] J. M. M. Anderson, K. Yoon-Chul, and J. T. Votaw, "Concurrent segmentation and estimation of transmission images for attenuation correction in positron emission tomography.," *IEEE Trans Nuc Sci*, vol. 56, pp. 136-146, 2009.
- [27] S. D. Wollenweber, S. Ambwani, A. R. Lonn, D. D. Shanbhag, S. Thiruvankadam, S. Kaushik, *et al.*, "Comparison of 4-class and continuous fat/water methods for whole-body, MR-based PET attenuation correction," *IEEE Trans Nuc Sci*, vol. 60, pp. 3391-3398, 2013.
- [28] J. Ma, "Dixon techniques for water and fat imaging.," *J Magn Reson Imaging*, vol. 28, pp. 543-558, 2008.
- [29] P. A. Yushkevich, J. Piven, H. C. Hazlett, R. G. Smith, S. Ho, J. C. Gee, *et al.*, "User-guided 3D active contour segmentation of anatomical structures: significantly improved efficiency and reliability.," *Neuroimage*, vol. 31, pp. 1116-1128, 2006.
- [30] S. Klein, M. Staring, K. Murphy, M. A. Viergever, and J. P. W. Pluim, "elastix: A toolbox for intensity-based medical image registration.," *IEEE Trans Med Imaging*, vol. 29, pp. 196-205, 2010.
- [31] N. H. Clinthorne, J. A. Fessler, G. D. Hutchins, and W. L. Rogers, "Joint maximum likelihood estimation of emission and attenuation densities in PET," *Conference Record of the IEEE Nuclear Science Symposium and Medical Imaging Conference*, 1991, pp. 1927-1932.
- [32] J. Nuyts, B. De Man, P. Dupont, M. Defrise, P. Suetens, and L. Mortelmans, "Iterative reconstruction for helical CT: a simulation study.," *Phys Med Biol*, vol. 43, pp. 729-737, 1998.
- [33] J. A. Fessler, E. P. Ficaro, N. H. Clinthorne, and K. Lange, "Grouped-coordinate ascent algorithms for penalized-likelihood transmission image reconstruction.," *IEEE Trans Med Imaging*, vol. 16, pp. 166-175, 1997.
- [34] O. Schillaci, F. Calabria, M. Tavolozza, C. Ciccio, M. Cariani, C. R. Caracciolo, *et al.*, "18F-choline PET/CT physiological distribution and pitfalls in image interpretation: experience in 80 patients with prostate cancer.," *Nucl Med Commun*, vol. 31, pp. 39-45, 2010.
- [35] IAEA, "Quality assurance for PET and PET/CT systems," *IAEA Human Health Series 1*, 2009.
- [36] T. Pan and H. Zaidi, "Attenuation correction strategies for positron emission tomography/computed tomography and 4-Dimensional positron emission tomography/computed tomography," *PET Clin*, vol. 8, pp. 37-50, 2013.
- [37] I. Bezrukov, H. Schmidt, F. Mantlik, N. Schwenzer, C. Brendle, B. Scholkopf, *et al.*, "MR-based attenuation correction methods for improved PET quantification in lesions within bone and susceptibility artifact regions.," *J Nucl Med*, vol. 54, pp. 1768-1774, 2013.
- [38] J. Ouyang, S. Y. Chun, Y. Petibon, A. A. Bonab, N. Alpert, and G. El Fakhri, "Bias atlases for segmentation-based PET attenuation correction using PET-CT and MR.," *IEEE Trans Nuc Sci*, vol. 60, pp. 3373-3382, 2013.
- [39] D. Izquierdo-Garcia, S. J. Sawiak, K. Knesaurek, J. Narula, V. Fuster, J. Machac, *et al.*, "Comparison of MR-based attenuation correction and CT-based attenuation correction of whole-body PET/MR imaging.," *Eur J Nucl Med Mol Imaging*, vol. 41, pp. 1574-1584, 2014.
- [40] H. Arabi, O. Rager, A. Alem, A. Varoquaux, M. Becker, and H. Zaidi, "Clinical assessment of MR-guided 3-class and 4-class attenuation correction in PET/MR.," *Mol Imaging Biol*, vol. 7, no. 2, pp. 264-276, 2015.

- [41] V. Keereman, Y. Fierens, T. Broux, Y. De Deene, M. Lonneux, and S. Vandenberghe, "MRI-based attenuation correction for PET/MRI using ultrashort echo time sequences.," *J Nucl Med*, vol. 51, pp. 812-818, 2010.
- [42] Y. Berker, J. Franke, A. Salomon, M. Palmowski, H. C. Donker, Y. Temur, *et al.*, "MRI-based attenuation correction for hybrid PET/MRI systems: A 4-class tissue segmentation technique using a combined Ultrashort-Echo-Time/Dixon MRI sequence.," *J Nucl Med*, vol. 53, pp. 796-804, 2012.
- [43] A. P. Aitken, D. Giese, C. Tsoumpas, P. Schleyer, S. Kozerke, C. Prieto, *et al.*, "Improved UTE-based attenuation correction for cranial PET-MR using dynamic magnetic field monitoring.," *Med Phys*, vol. 41, p. 012302, 2014.
- [44] A. Rezaei and J. Nuyts, "Simultaneous reconstruction of the activity image and registration of the CT image in TOF-PET," *IEEE Nuclear Science Symposium and Medical Imaging Conference (NSS/MIC)*, 2013, pp. 1-3.
- [45] R. Boellaard, M. B. Hofman, O. S. Hoekstra, and A. A. Lammertsma, "Accurate PET/MR quantification using time of flight MLAA image reconstruction.," *Mol Imaging Biol*, vol. 16, pp. 469-477, 2014.
- [46] V. Y. Panin, M. Aykac, and M. E. Casey, "Simultaneous reconstruction of emission activity and attenuation coefficient distribution from TOF data, acquired with external transmission source.," *Phys Med Biol*, vol. 58, pp. 3649-3669, 2013.
- [47] C. C. Watson, "Supplemental transmission method for improved PET attenuation correction on an integrated MR/PET.," *Nucl Instr Meth A*, vol. 734, Part B, pp. 191-195, 2014.
- [48] Y. Berker, F. Kiessling, and V. Schulz, "Use of scattered coincidences for emission-based estimation of attenuation map in PET," *IEEE Nuclear Science Symposium and Medical Imaging Conference (NSS/MIC)*, 2012, pp. 2285-2287.
- [49] C. M. Laymon and T. G. Turkington, "Calculation of attenuation factors from combined singles and coincidence emission projections.," *IEEE Trans Med Imaging*, vol. 18, pp. 1194-1200, 1999.
- [50] H. Rothfuss, V. Panin, A. Moor, J. Young, I. Hong, C. Michel, *et al.*, "LSO background radiation as a transmission source using time of flight.," *Phys Med Biol*, vol. 59, pp. 5483-5500, 2014.

Chapter 10

Emission-based estimation of lung attenuation coefficients for attenuation correction in time-of-flight PET/MR

Abolfazl Mehranian and Habib Zaidi

Phys Med Biol (2015) in press

Abstract

Purpose: In standard segmentation-based MRI-guided attenuation correction (MRAC) of PET data on hybrid PET/MRI systems, the inter/intra-patient variability of linear attenuation coefficients (LACs) is ignored owing to the assignment of a constant LAC to each tissue class. This can lead to PET quantification errors, especially in the lung regions. In this work, we aim to derive continuous and patient-specific lung LACs from time-of-flight (TOF) PET emission data using the maximum likelihood reconstruction of activity and attenuation (MLAA) algorithm.

Methods: The MLAA algorithm was constrained for estimation of lung LACs only in the standard 4-class MR attenuation map using Gaussian lung tissue preference and Markov random field smoothness priors. MRAC maps were derived from segmentation of CT images of 19 TOF-PET/CT clinical studies into background air, lung, soft tissue and fat tissue classes, followed by assignment of predefined LACs of 0, 0.0224, 0.0864 and 0.0975 cm^{-1} , respectively. The lung LACs of the resulting attenuation maps were then estimated from emission data using the proposed MLAA algorithm. PET quantification accuracy of MRAC and MLAA methods was evaluated against the reference CT-based AC method in the lungs, lesions located in/near the lungs and neighbouring tissues.

Results: The results show that the proposed MLAA algorithm is capable of retrieving lung density gradients and compensate fairly for respiratory-phase mismatch between PET and corresponding attenuation maps. It was found that the mean of the estimated lung LACs generally follow the trend of the reference CT-based attenuation correction (CTAC) method. Quantitative analysis revealed that the MRAC method resulted in average relative errors of $-5.2 \pm 7.1\%$ and $-6.1 \pm 6.7\%$ in the lungs and lesions, respectively. These were reduced by the MLAA algorithm to $-0.8 \pm 6.3\%$ and $-3.3 \pm 4.7\%$, respectively.

Conclusion: In conclusion, we demonstrated the potential and capability of emission-based methods in deriving patient-specific lung LACs to improve the accuracy of attenuation correction in TOF PET/MR imaging, thus paving the way for their adaptation in the clinic.

I. INTRODUCTION

Hybrid positron emission tomography/magnetic resonance imaging (PET/MRI) technology combines the physiological and metabolic information provided by PET with the structural and functional information provided by MRI. Over the last decade, this hybrid imaging modality attracted a great deal of attention and many efforts have been directed towards addressing the challenges encountered in system design and quantitative imaging, thus paving the way to explore its potential and clinical applications [1, 2]. In this context, attenuation correction (AC) is one of the major challenges facing quantitative PET/MR imaging [3, 4].

In contrast to x-ray computed tomography (CT), the MRI signal is correlated with hydrogen proton density, relaxation time properties of tissues and the selected pulse timing parameters, rather than electron density. As such, there is no straightforward approach to directly map MR image intensities to PET 511-keV attenuation coefficients as in PET/CT. Several approaches have been proposed for attenuation correction in PET/MR including (i) MRI-based attenuation map generation (MRAC), (ii) transmission measurements and (iii) emission based estimation of PET linear attenuation coefficients (LACs). In the first category of methods, MR images are either segmented into several tissue classes followed by assignment of predefined attenuation coefficients to each class [5, 6] or used to generate pseudo-CT images through atlas registration and machine learning techniques [7-11]. In fast gradient-echo MR pulse sequences, usually used to acquire whole-body MRAC maps, cortical and spongy bones cannot be well discriminated from air and surrounding soft tissues owing to their low water content and short transverse relaxation time. Therefore, bones are either replaced by soft tissue or predicted by pseudo-CT generation techniques. MRI field-of-view truncation and metal-induced magnetic susceptibility artefacts are other limitations that need to be addressed when using this category of methods.

The second category of methods measures directly the LACs using external positron-emitting sources [12] or background radiation of LSO crystals [13] for simultaneous emission/transmission acquisition in time-of-flight (TOF) PET/MRI. In these revisited transmission-based attenuation correction methods, the time-of-flight information is used to separate the emission data from transmission. The major issue is the low count statistics of the transmission scan limited by the emission scan time per bed position. In consequence, the measured attenuation maps might suffer from noise and introduce additional noise and bias in the emission maps.

The last approach consists in estimating attenuation information directly from the emission data. In this category of techniques, the attenuation coefficients or attenuation sinograms are estimated either without reconstruction of the activity map, based on the Helgason-Ludwig consistency conditions of the attenuated Radon transform [14-17], or with simultaneous maximum likelihood reconstruction of activity and attenuation (MLAA) or attenuation correction factors (MLACF) [18-21]. According to consistency conditions, a given noise-free emission data only arises under certain attenuation conditions and vice versa. These conditions do not model the statistical variability of the emission data and generally cannot uniquely estimate attenuation information. However, based on the range consistency conditions of TOF attenuated Radon transform, Defrise *et al* [17] recently showed that attenuation correction factors can be uniquely determined from PET TOF data up to a constant scaling factor. In the maximum likelihood framework, the statistical nature of the data is properly modelled; however, the estimated activity and attenuation maps or attenuation correction factors are not unique and often suffer from cross talk artefacts, where the features of the activity map propagates into the attenuation map and vice versa. With the advent of TOF PET/MRI scanners, Salomon *et al* imposed MR anatomical information on the TOF-MLAA estimation of attenuation coefficients [22]. Thereby, the noise and cross-talk artefacts were considerably reduced. Later, Rezaei *et al* demonstrated that the inherent spatial constraint of TOF-PET data suppresses the cross-talks in the simultaneous reconstruction of activity and attenuation [23]. However, the activity maps are globally scaled and the attenuation maps present with a position-dependent scaling. Aside from the scale problem, the performance of MLAA algorithms depends on TOF timing resolution, emission count statistics and the spatial distribution of the radiotracer, which supports the estimation of attenuation coefficients. More recently, the combination of transmission- and emission-based approaches has been explored in the joint estimation of activity and attenuation using rotating rod [24] or sparse point transmission sources [25]. This combination could circumvent the shortcomings of standalone transmission- and emission-based methods.

Current commercial PET/MRI systems employ segmentation-based MRAC for attenuation correction of PET data. In these methods, MR images are segmented into 3 or 4 tissue classes, namely background air, lung, fat and non-fat soft tissues, followed by assignment of constant LACs to each tissue class. Overall, these techniques

were reported to result in PET quantification bias in terms of standardized uptake value (SUV) of <5% in most soft tissue lesions [5, 26]. However, the substitution of bones by soft tissue can lead to SUV errors ranging from 8% to 27% in bony structures [5, 27]. Moreover, inter/intra-patient heterogeneity of attenuation coefficients in different tissue classes is ignored, which can lead to a high variance of SUV errors, especially in the lungs. The determination of patient-specific lung LACs is a challenging task, since the pulmonary parenchyma and vasculature and thus lung LACs vary considerably among patients by as much as 30%, depending on gender, body height, pathological conditions [28], breathing patterns [29] and body positioning [30]. As such, different attenuation coefficients have been assigned to lung tissue class, ranging from 0.018 to 0.035 cm⁻¹ [5, 31]. In addition, the mis-segmentation of soft tissue lesions, specifically in the mediastinal sides of the lungs, can lead to substantial lesion quantification errors.

A limited number of studies focused on the derivation of patient-specific lung attenuation coefficients in segmentation-based MRAC methods. Marshall *et al* established a linear mapping function between MRI and CT image intensities of the lungs in order to predict the mean of lung LACs for each patient [32]. Lonn *et al* [33] derived a linear relationship between lung volume and mean LACs for the prediction of mean lung attenuation coefficients. Overall, the MRI-to-CT mapping function requires a standardized MRI protocol and is influenced by the presence of diamagnetic susceptibility and flow-related artefacts. Moreover, the volume-to-LAC prediction model does not take into account the impact of factors, such as gender, age, pathological conditions and body positioning. Emission-based derivation of lung LACs has also been explored. Madsen and Lee used the consistency conditions to refine an initial lung contour obtained from a lung atlas and the MLAA framework to estimate the attenuation coefficients [34]. Recently, Berker *et al* explored a constrained TOF-MLAA algorithm for the estimation of mean lung LACs in 5-class MRAC maps (including bones as 5th class) [35]. The results obtained using Monte Carlo simulated PET/CT studies showed a high bias in PET quantification, possibly because of out-of-field accidental coincidences, error propagation into the lungs and the unsolved scaling problem of the MLAA algorithm.

More recently, we proposed an approach to improve the performance of the MLAA algorithm by incorporating MRI spatial and CT statistical information in the joint estimation of activity and attenuation using a mixture of Gaussian model [36]. In this approach, a continuous attenuation map is estimated from the emission data under the constraint of a multi-class Gaussian prior with suppression of cross-talk and scale problems. In the current work, we simplified this algorithm to only estimate lung attenuation coefficients in the 4-class MRI-guided attenuation correction of clinical studies with the aim of demonstrating the potential of emission-based AC methods in deriving patient-specific lung LACs, thus paving the way for a smooth translation of these methods into clinical TOF PET/MR imaging.

II. MATERIAL AND METHODS

II. A Constrained MLAA

In TOF-PET, the statistical variability of measured data, g_{it} , in a line-of-response (LOR) i and TOF bin t is best modelled by a Poisson distribution with expected value:

$$\bar{g}_{it} = n_i a_i \sum_{j=1}^J c_{ijt} \lambda_j + n_i \bar{s}_{it} + \bar{r}_{it} \quad (1)$$

where λ_j denote activity values at voxel j , c_{ijt} is the geometric probability detection of annihilation events emitted from voxel j along LOR i in TOF bin t , n_i are detector normalization factors, a_i is attenuation survival probability of annihilation photons along LOR i , \bar{s}_{it} is the model-based expected estimate of scatter coincidences and \bar{r}_{it} is the expected value of random coincidences, obtained by smoothing the measurements of a delayed coincidence window. In this work, only the lung attenuation coefficients of 4-class MR attenuation maps are assumed to be unknown, therefore, a_i can be decomposed into the product of known and unknown attenuation factors [37]:

$$a_i = \exp\left(-\sum_{k \notin \mathbb{L}} l_{ik} \mu_k\right) \exp\left(-\sum_{k \in \mathbb{L}} l_{ik} \mu_k\right) \quad (2)$$

where μ_k and l_{ik} are attenuation values of voxel k and the intersection length of LOR i with voxel k . \mathbb{L} is the set of all voxels belonging to the lungs, obtained from segmentation of MR images. The lung attenuation

coefficients can therefore be estimated using the following joint maximum a posteriori estimation of activity and attenuation:

$$(\hat{\lambda}, \hat{\mu}) = \operatorname{argmax}_{\lambda \geq 0, \mu \geq 0} \left\{ \sum_{it} \{g_{it} \log(\bar{g}_{it}) - \bar{g}_{it}\} - \frac{\beta}{2} \sum_{j \in \mathbb{L}} \sum_{k \in N_j} \omega_{jk} (\mu_k - \mu_j)^2 - \frac{\gamma}{2} \sum_{j \in \mathbb{L}} \left(\frac{\mu_j - \bar{\mu}}{\sigma} \right)^2 \right\} \quad (3)$$

where the objective function consists of the following terms: the Poisson log-likelihood of the measurements, a Markov random field (MRF) smoothing prior and a Gaussian tissue preference. Since the joint tomographic image reconstruction problem is highly ill-posed, it is necessary to constrain the solution space by favouring smooth solutions and penalizing the estimates inconsistent with our expectations. The quadratic MRF prior in Eq. (3) favours the attenuation maps that are smooth based on the local interactions of each voxel j with its neighbouring voxels in the neighbourhood N_j . In this study, a second-order neighbourhood was used around the j^{th} voxel with 26 nearest neighbours. ω_{jk} is inversely proportional to the distance between voxels j and k . The hyper-parameters β and γ are defined for weighting the impact of the priors. In this study, the Gaussian prior is a uni-modal function centred at the expected value, $\bar{\mu}$, of lung attenuation coefficients obtained from a patient population. Based on the modelled standard deviation, σ , of the LACs and the strength of the γ parameter, this Gaussian lung preference prior penalizes the large variation of the estimated lung LACs from their expected value.

II. B Optimization

The joint estimation problem defined in Eq. (2) is not necessarily strictly concave [38], therefore finding a global maximizer is not guaranteed. Since the activity and attenuation are coupled in this problem, an alternating iterative optimization approach is used to reach at least a (strict) local minimizer. As in the joint alternate-maximize (JAM) [38] and MLAA [18, 23] algorithms, at each iteration, maximization is performed with respect to activity (λ -step) while keeping the attenuation constant and then with respect to attenuation (μ -step) with the most recent estimate of activity. In the λ -step, the problem is reduced to an emission maximum likelihood optimization problem that can be solved using a conventional TOF ordinary Poisson ordered subset expectation maximization (OP-OSEM) algorithm. In the μ -step, the problem is reduced to a transmission maximum a posteriori optimization problem that can be solved using an ordered subset separable paraboloidal surrogates (OS-SPS) or maximum likelihood for transmission tomography (OS-MLTR) algorithms. MLTR uses De Pierro's additive convexity and Jensen inequality to define an easy-to-optimize surrogate for the transmission log-likelihood function [39, 40]. The MRF and Gaussian priors are strictly concave functions; therefore the resulting problem can be easily optimized.

The resulting alternating optimization algorithm at the n^{th} global iteration consists of four main steps defined by Eqs (4–7). First, the attenuation survival factors are calculated from the current attenuation map. At the first iteration, they are derived from the initial 4-class MRAC map. The activity is then estimated using a TOF-OPOSEM with several sub-iterations. In the next step, the total activity ψ_i along LOR i is calculated from the estimated activity to serve as the blank scan in the following transmission reconstruction by the non-TOF forward projection of the activity and normalizing and attenuating the resulting sinograms. Finally, the attenuation map is updated using a non-TOF OS-MLTR algorithm with several sub-iterations only over the lungs using the function δ .

$$a_i^n = e^{-\sum_j l_{ij} \mu_j^n} \quad (4)$$

$$\lambda_j^{n+1} = \frac{\lambda_j^n}{\sum_i c_{ij} n_i a_i^n} \sum_{it} c_{ijt} n_i a_i^n \frac{g_{it}}{n_i a_i^n \sum_{kt} c_{ikt} \lambda_k^n + n_i \bar{s}_{it} + \bar{r}_{it}} \quad (5)$$

$$\psi_i^n = n_i a_i^n \sum_{jt} c_{ijt} \lambda_j^{n+1} \quad (6)$$

$$\mu_j^{n+1} = \mu_j^n + \alpha \delta_j \left(\frac{\sum_i l_{ij} \frac{\psi_i^n}{\psi_i^n + b_i} (\psi_i^n + b_i - g_i) - \gamma \frac{\mu_j^n - \bar{\mu}}{\sigma^2} - \beta \frac{\partial R_{MRF}(\mu^n)}{\partial \mu_j}}{\sum_j l_{ij} \frac{(\psi_i^n)^2}{\psi_i^n + b_i} \sum_k l_{ik} - \frac{\gamma}{\sigma^2} + \beta \frac{\partial^2 R_{MRF}(\mu^n)}{\partial^2 \mu_j}} \right) \quad (7)$$

where $b_i = n_i \bar{s}_i + \bar{r}_i$ are background counts in LOR i , $c_{ij} = \sum_t c_{ijt}$, $g_i = \sum_t g_{it}$ and $\bar{s}_i = \sum_t \bar{s}_{it}$ are time-integrated quantities, $\alpha > 0$ is a step size parameter. R_{MRF} is the MRF quadratic smoothing prior defined in Eq. (3). For the lung set \mathbb{L} , δ_j is defined as:

$$\delta_j = \begin{cases} 1, & j \in \mathbb{L} \\ 0, & j \notin \mathbb{L} \end{cases} \quad (8)$$

Figure 1(a) illustrates schematically the flowchart of the MLAA algorithm, which alternates between λ -step (OSEM) and μ -step (OS-MLTR) with n global iterations. In this study, we used 15 global iterations, 1 iteration and 2 subsets for the λ -step and 1 iteration and 3 subsets for μ -step. The activity was uniformly initialized inside the reconstruction field-of-view (FOV), while the attenuation was initialized by an initial 4-class MR-based attenuation map and only updated for voxels belonging to the lungs. As discussed in section II.E, in this work, MR attenuation maps were derived from CT images. For both OSEM and OS-MLTR reconstructions, the scatter component is estimated using the initial MRAC map and TOF single scatter simulation algorithm implemented in Siemens VG50 e7 tool. Following the update of the lung attenuation coefficients after n global iterations of the constrained MLAA algorithm, the final PET activity map is reconstructed using the standard clinical image reconstruction protocol using the updated attenuation and a new scatter estimate. Figure 1(b) summarizes the reconstruction procedure followed in this study. As discussed in the *Results* section, we experimentally set the involved hyper-parameters to $\alpha = 1.5$, $\beta = 80$, $\gamma = 0.75$ for all clinical datasets.

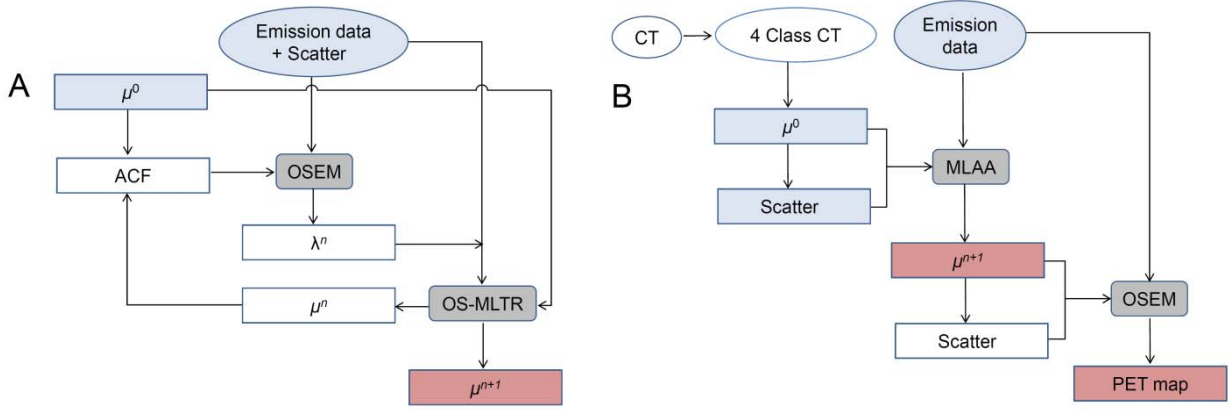


Figure 1. (A) Flowchart of the MLAA algorithm, which alternates between an OSEM activity reconstruction and an OS-MLTR attenuation reconstruction. (B) Flowchart of the whole procedure followed in this study. First, the CT images are segmented into 4-class attenuation maps, representing standard 4-class MRAC maps. Then the MLAA algorithm is initialized by the MRAC attenuation and corresponding scatter sinograms. In the next step, the estimated attenuation maps are used for an ordinary OSEM reconstruction with the parameters used in clinical setting.

II. C Data Acquisition and Image Reconstruction

Clinical PET/CT studies were acquired on the Biograph mCT Flow Edge 128 scanner (Siemens Healthcare, Erlangen). The PET component of the scanner consists of 4 rings of 48 detector blocks, each containing 13×13 LSO crystals with dimensions of $4 \times 4 \times 20 \text{ mm}^3$ (total number of 32448 physical crystals). Considering the gaps between block rings, this configuration results in 55 crystal rings covering an axial FOV of 218 mm and a transaxial FOV of 700 mm. PET data were acquired with maximum ring difference of 49 planes in continuous bed motion (CBM) mode. The coincidence window width is 4.06 ns with an effective TOF timing resolution of 580 ps. PET images were reconstructed using Siemens VG50 e7 tool with an OP-OSEM algorithm, incorporating all corrections (scatter, random, dead time, decay, attenuation, and normalization) into the reconstruction procedure, with point spread function (PSF) modelling and TOF information. The default manufacturer-provided reconstruction parameters for OSEM+PSF+TOF were used (2 iterations and 21 subsets). The single-bed image matrix size is $200 \times 200 \times 109$ with $4 \times 4 \times 2 \text{ mm}^3$ voxels. For the joint reconstruction of activity and lung attenuation values, an in-house TOF PET image reconstruction software was developed for the native geometry of the mCT scanner. The list-mode data of the scanner are histogrammed in 4D sinograms with

400 radial bins, 168 azimuthal angles, 621 planes (in 9 segments with span 11) and 13 time bins of 312.5 ps width. The MLAA images were reconstructed using a matrix size of $200 \times 200 \times 109$ per bed. For large axial FOVs, the data acquired in CBM mode are chunked into conventional bed positions, which are then reconstructed separately. In this work, we selected the bed positions that axially covered the whole lungs (usually 1 or 2 beds). After the MLAA estimation of attenuation maps, the corresponding attenuation maps were assembled and the final activity images were reconstructed using the e7 tools.

II. D Clinical Studies

In this retrospective study, a total number of 19 patients (8 women, 11 men; average age 56.5 ± 19.7 years), who underwent ^{18}F -FDG ($n = 17$) and ^{18}F -Choline ($n = 2$) PET/CT examinations, were included and analyzed. The clinical indications of the examinations included the staging and evaluation of head and neck cancer, thyroid carcinoma, lung cancer, bronchial carcinoma, breast cancer, lymphoma, liver cancer, colorectal carcinoma, cervical cancer, and prostate cancer. The patients had an average body mass index (BMI) of $24.3 \pm 6.1 \text{ kg/m}^2$ and were injected with an activity of $257.8 \pm 43.6 \text{ MBq}$ for ^{18}F -FDG and $329.1 \pm 1.2 \text{ MBq}$ for ^{18}F -Choline. After an uptake period of 60 and 0 minutes for FDG and FCH administrations, respectively, whole-body PET/CT scanning was performed in continuous bed motion mode from the mid thigh to the vertex of the head with bed speed of 0.7 mm/sec, corresponding to 3 minutes per bed position in the conventional step and go acquisition mode. The average acquisition time was 23.2 ± 5.6 minutes. A whole-body CT scan protocol was performed using CAREdose for PET attenuation correction using the following parameters: 100-120 kVp, 150 mAs, 0.3 sec. tube rotation, 30.7 mm bed speed per rotation and 5 mm slice thickness.

II.E MR attenuation map generation

The standard 4-class MRI-based attenuation maps were derived by segmenting CT images of patients into 4 tissue classes including background air, lung, fat, and non-fat soft tissues. The lungs were semi-automatically segmented using a supervised seeded region growing technique implemented in the ITK-SNAP software [41]. Background air was automatically segmented using simple thresholding after removing the CT bed. The fat tissue class was segmented by thresholding CT intensity values between -470 and -53 Hounsfield units (corresponding to PET attenuation coefficients between 0.05 and 0.095 cm^{-1}). The complement of the segmented classes was then defined as soft-tissue class. In this procedure, bones and air pockets are assigned to soft tissue class. Mean attenuation coefficients of 0, 0.0224, 0.0864 and 0.0975 cm^{-1} were assigned to background, lungs, fat and non-fat soft tissue classes, respectively. In this work, we used the same mean value of lungs implemented in the MRAC procedure on the Siemens mMR scanner (Siemens Healthcare, Erlangen) [42]. For the lung tissue prior in Eq. (3), the mean and intra-patient standard deviation of 0.0224 cm^{-1} and 0.0107 cm^{-1} were used, respectively. The standard deviation was obtained by fitting a Gaussian to the histogram of lung LACs of 10 CT datasets. The lung set in Eq. (8) was derived by down-sampling the lung tissue class to the MLAA image reconstruction matrix size. The attenuation map on the mCT is obtained by down-sampling 512×512 CT or 4-class CT images to the resolution of 400×400 , followed by a 4-mm isotropic Gaussian filtering. The estimated MLAA attenuation maps were therefore up-sampled to this resolution and then the lung LACs in the 4-class CT images were replaced by the estimated ones.

II. F Data Analysis

A volume-of-interest (VOI)-based analysis was performed to calculate the relative PET quantification error (bias) with respect to the reference CT-based attenuation correction (CTAC)-PET as follows:

$$\text{Bias} = 100 \times \frac{SUV_x - SUV_{CTAC}}{SUV_{CTAC}} \quad (9)$$

where x is the PET image reconstructed using the standard MRAC and constrained MLAA attenuation correction methods. For each patient, circular VOIs were defined on the lungs (upper, middle and lower portions of the left and right lungs) as well as normal tissue regions surrounding the lungs including the liver, descending aorta, myocardium, and 3rd thoracic vertebrae (T3). Moreover, an 80% iso-contour VOIs were defined on lesions located in/near the lungs. A total number of 70 lesions were identified. For each VOI, the mean (μ), standard deviation (σ) and root-mean-squared error of the bias ($\sqrt{\mu^2 + \sigma^2}$) was calculated over the 19 patients. The concordance between the SUVs was evaluated using Bland-Altman plots. The statistical significance of

differences in SUV bias was also evaluated using the Wilcoxon signed-rank test. The differences were considered statistically significant for p -values less than 0.05. Moreover, the mean and standard deviation of the estimated lung LACs were calculated for each patient over all lung voxels and compared with CTAC and MRAC attenuation maps.

III. RESULTS

Figure 2 compares the CT-based attenuation map (CTAC) of a representative patient with the standard 4-class MRAC map and the improved MRAC map over the lungs using the proposed constrained MLAA algorithm in two different display windows. The figure also displays the lung tissue class overlaid on the CTAC image. As shown in the CTAC maps, the lungs in this patient have a congested structure and high density gradients in antero-posterior and cranio-caudal directions. These patient-specific details are not reflected in the MRAC map, whereas the MLAA algorithm not only can accurately retrieve the lung density gradient in a continuous fashion but also compensates for the segmentation errors in the lung tissue class by increasing the LACs around the partially segmented soft tissue structures (see the sagittal slices). The mean lung LACs of the CTAC, MRAC and MLAA attenuation maps of this dataset (filtered by a 4-mm FWHM Gaussian filter) were 0.0286 , 0.0230 and 0.0276 cm^{-1} , respectively.

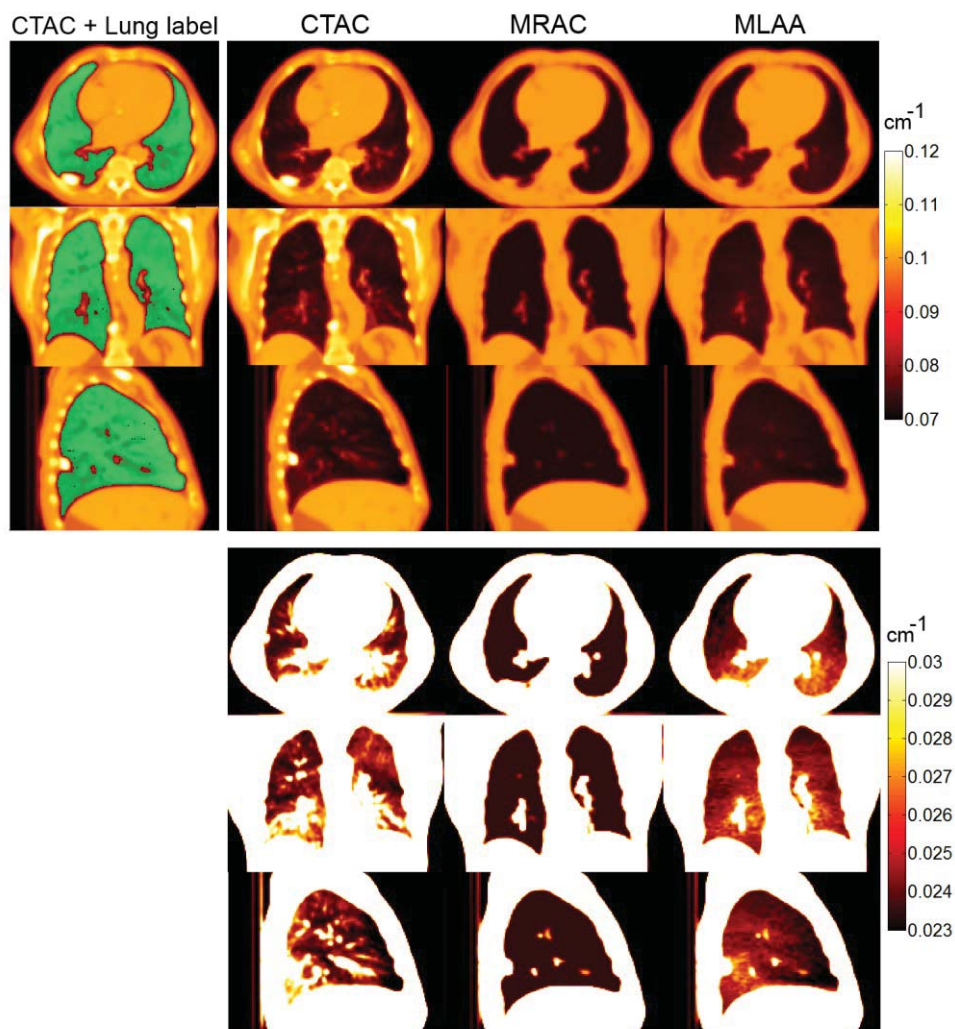


Figure 2. Comparison of the attenuation map derived by the standard 4-class MR-based map (MRAC) with the map obtained by the improved MLAA algorithm and the reference CTAC map in two different display windows. The lung tissue class overlaid on the CTAC map is shown on the left column.

Figure 3 compares the profiles of MRAC and MLAA attenuation maps with the ground truth CTAC profiles. As can be seen, the MLAA algorithm effectively estimates the attenuation gradients in the same way as the CTAC. However, because of respiratory motion of the lungs during PET acquisition, the MLAA profiles are blurred and do not preserve local details. Moreover, in our improved MLAA algorithm, an MRF smoothing prior is invoked to suppress noisy estimations due to the limited count statistics of the whole-body PET acquisition protocols (equivalent to 3 minutes per bed).

Table 1 summarizes the mean and standard deviation of lung attenuation coefficients calculated by the three techniques in all 19 patients. The LACs were calculated from the derived attenuation maps, filtered by a 4-mm FWHM Gaussian filter, for all voxels belonging to the lungs. Therefore, the MRAC attenuation maps present with a standard deviation around the predefined LAC of 0.0224 cm^{-1} . In the MLAA attenuation maps of some patients, we observed elevated lung LACs close to the diaphragm and heart due to respiratory-phase mismatch between PET and CT acquisitions and cardiac motion, respectively. This observation was made by the authors through visual inspection of the MLAA attenuation maps. Note that we employed TOF-OSEM algorithm for activity reconstruction. It has been demonstrated that TOF capability can reduce respiratory-phase mismatch artefacts in PET activity maps [43]. Therefore in some patients, respiratory artefacts were only observable in the MLAA attenuation maps. Figure 4 graphically compares the mean lung LACs of the MRAC and MLAA maps with the reference CTAC map. The results show that overall the emission-based derivation of LACs using the MLAA algorithm follow the trend of the CTAC LACs, except in a few patients, where the estimated LACs are substantially higher than the reference values, while MRAC LACs are almost constant with small deviations from the assigned value of 0.0224 cm^{-1} . The overestimated MLAA LACs in patients No. 2 and 14 should be ascribed to the substantially increased lung LACs induced by respiratory-phase mismatch.

Figure 5 shows PET and CT images of a patient having a liver lesion and respiratory PET/CT mismatch, together with the MRAC and MLAA attenuation maps using the lung display window. The MLAA attenuation map shows the increase of lung LACs in the vicinity of the right diaphragm, implying the presence of respiratory mismatch, which is confirmed on the sagittal view of the CTAC PET image where the top rim of the liver shows an abrupt decrease of activity. As can be seen in the sagittal slices, the MLAA attenuation map can also effectively predict the antero-posterior density gradient of the lungs in this patient dataset. Figure 6 further illustrates the performance of the proposed MLAA algorithm by comparing the activity and attenuation profiles of the dataset shown in figure 5. The activity profiles show an underestimation of the lesion's SUV by the standard MRAC method, while MLAA was able to considerably increase the lesion's SUV values toward those obtained by CTAC PET images. Over the liver, there is a considerable increase of tracer uptake in the MLAA PET image, which is brought about by the corresponding increased LACs, as shown in figure 6(b). Note that the SUV values of the MLAA are lower than those of the CTAC over the lesion. This should be ascribed to the fact that this soft-tissue lesion was mis-segmented as can be seen on the sagittal images of figure 5. This result highlights the ability of the MLAA algorithm to compensate for lung segmentation errors.

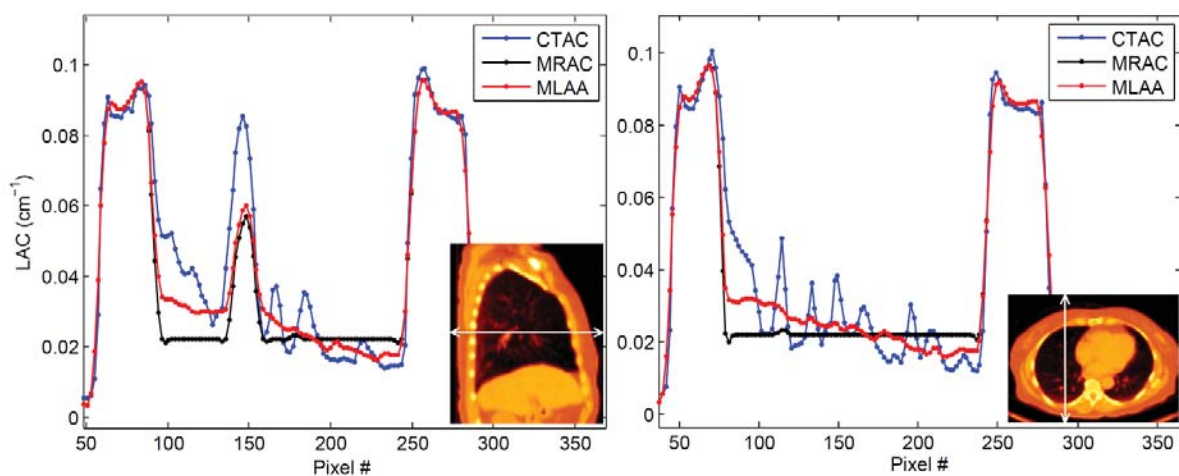


Figure 3. Comparison of attenuation profiles corresponding to the attenuation maps shown in figure 2.

Table 1. Mean and standard deviation of lung attenuation coefficients of 19 clinical datasets calculated using the evaluated AC methods. In the MLAA attenuation maps of some patients, respiratory phase mismatch (RM) and cardiac motion (CM) were observed and reported.

Patient No.	CTAC	MLAA	MRAC	Comment
1	0.0303 ± 0.0100	0.0351 ± 0.0055	0.0221 ± 0.0018	
2	0.0209 ± 0.0064	0.0279 ± 0.0049	0.0224 ± 0.0018	RM
3	0.0286 ± 0.0134	0.0276 ± 0.0068	0.0230 ± 0.0045	
4	0.0253 ± 0.0089	0.0284 ± 0.0053	0.0227 ± 0.0037	RM & CM
5	0.0329 ± 0.0105	0.0287 ± 0.0057	0.0230 ± 0.0043	RM
6	0.0301 ± 0.0085	0.0274 ± 0.0046	0.0225 ± 0.0022	CM
7	0.0261 ± 0.0127	0.0250 ± 0.0035	0.0225 ± 0.0023	
8	0.0220 ± 0.0107	0.0242 ± 0.0053	0.0225 ± 0.0014	
9	0.0264 ± 0.0068	0.0272 ± 0.0043	0.0226 ± 0.0014	RM
10	0.0252 ± 0.0045	0.0245 ± 0.0016	0.0225 ± 0.0012	
11	0.0250 ± 0.0145	0.0254 ± 0.0053	0.0231 ± 0.0010	RM
12	0.0293 ± 0.0114	0.0287 ± 0.0061	0.0232 ± 0.0024	RM & CM
13	0.0256 ± 0.0074	0.0249 ± 0.0028	0.0224 ± 0.0010	
14	0.0229 ± 0.0097	0.0282 ± 0.0055	0.0222 ± 0.0016	RM
15	0.0207 ± 0.0071	0.0232 ± 0.0032	0.0225 ± 0.0014	
16	0.0198 ± 0.0063	0.0243 ± 0.0031	0.0221 ± 0.0001	RM
17	0.0275 ± 0.0086	0.0280 ± 0.0065	0.0233 ± 0.0056	
18	0.0203 ± 0.0048	0.0241 ± 0.0025	0.0225 ± 0.0011	
19	0.0246 ± 0.0056	0.0240 ± 0.0024	0.0226 ± 0.0017	

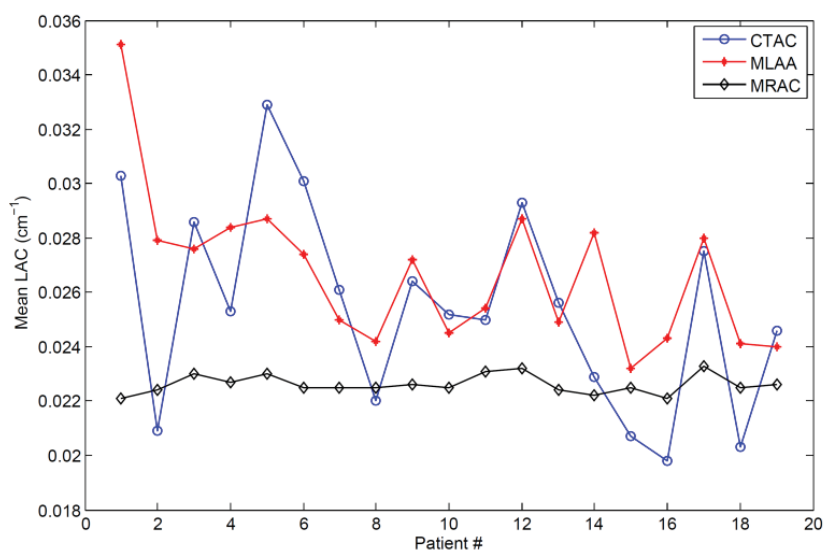


Figure 4. Comparison of the mean lung LACs of MRAC and MLAA attenuation maps with the reference CTAC map in all 19 patients.

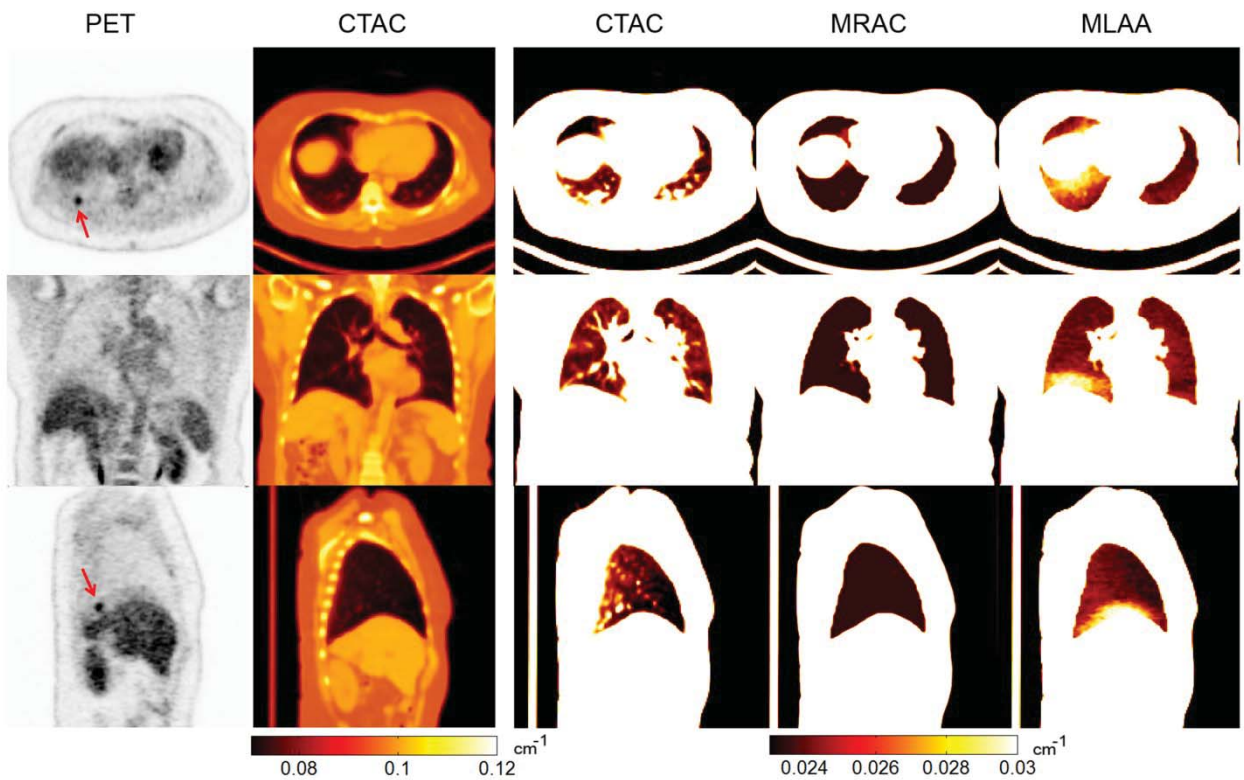


Figure 5. PET and CT images of a patient having a liver lesion and respiratory phase mismatch between CT and PET acquisitions, together with the MRAC and MLAA attenuation maps in different display windows.

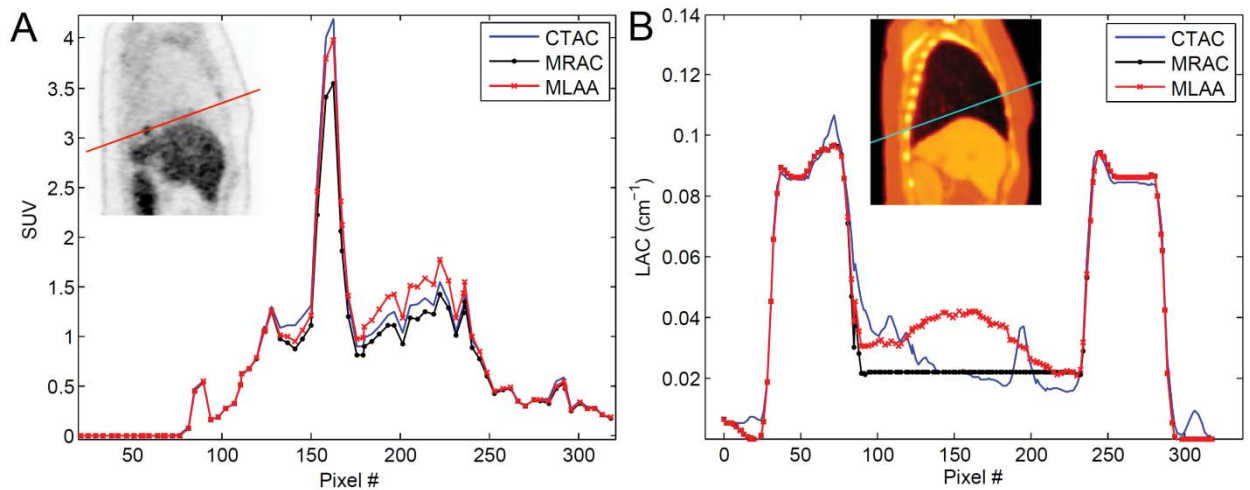


Figure 6. Comparison of activity (A) and attenuation (B) profiles of the dataset shown in figure 5 over the liver lesion.

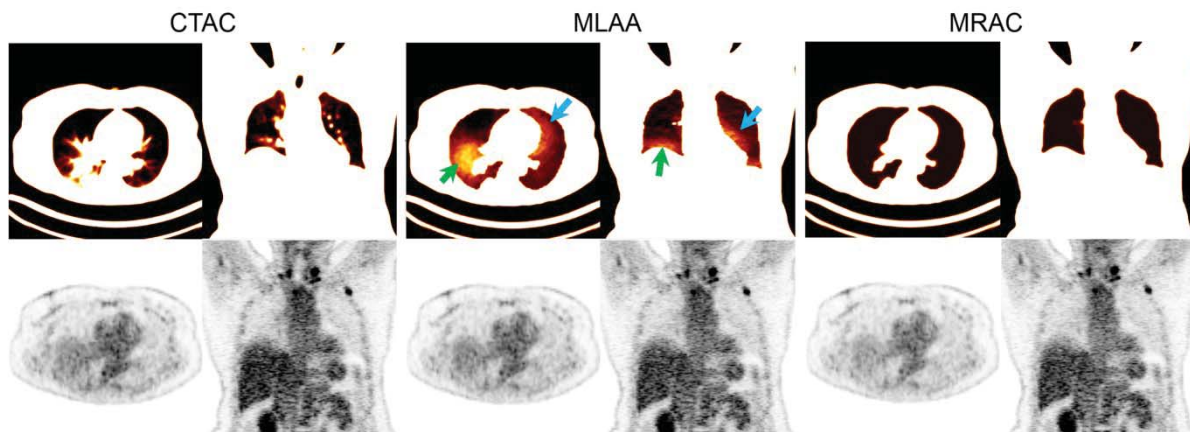


Figure 7. Top: The attenuation maps of a patient with respiratory and cardiac motion in lung display window. Bottom: qualitative comparison of the corresponding attenuation corrected PET images.

Figure 7 shows the attenuation maps of another patient presenting with respiratory and cardiac motion together with their corresponding PET images. The visual inspection of the MLAA attenuation map shows the presence of cardiac and respiratory motion and the potential of the emission-based algorithm to produce improved attenuation maps. However, the qualitative comparison of the PET images shows that the various AC methods result in similar lesion detectability and conspicuity in this dataset.

The quantitative PET accuracy of the proposed MLAA algorithm was further evaluated in all patient datasets using VOI-based analysis in comparison with the standard MRAC and CTAC methods. Table 2 summarizes the mean, standard deviation (SD) and root-mean-squared error (RMSE) of SUV_{mean} bias in VOIs defined on the upper (U), middle (M) and lower (L) regions of the left (L) and right (R) lungs, as well as the adjacent normal tissue regions and lesions. Figure 8(A) compares the bias results in the lungs. In this figure, the markers show the mean of the bias in each VOI, whereas the horizontal bars and vertical boxes indicate the mean and standard deviations of the bias between VOIs in each region. The results demonstrate that the MLAA algorithm generally gives rise to a reduced mean bias over all regions of the lungs, especially in the lower parts, since normally there is a cranio-caudal density gradient in the lungs, with increased LACs towards the base of the lungs. For all VOIs defined in the lungs ($n = 114$), the MRAC method resulted in an underestimation of tracer uptake of $-5.2 \pm 7.1\%$ with a RMSE of 8.8%, while the MLAA method yielded an error of $-0.8 \pm 6.3\%$ with a RMSE of 6.4% (Table 2). Although this algorithm decreases the mean of the bias toward zero, the standard deviation of the bias is not remarkably reduced, which should be ascribed to the sub-optimal regularization parameters and number of iterations used. However, the statistical analysis, revealed a significant difference between the performances of the different attenuation correction methods.

Table 2. Relative PET quantification errors [mean \pm SD, (RMSE)] of MRAC and MLAA methods in different regions of interest with CTAC serving as reference.

ROI	MRAC	MLAA	P-value
Upper Left Lung	-4.1 ± 6.7 (7.9)	-1.0 ± 7.0 (7.0)	<0.0001
Middle Left Lung	-2.9 ± 6.2 (6.9)	0.4 ± 5.5 (5.6)	<0.0001
Lower Left Lung	-8.8 ± 5.5 (10.4)	-3.2 ± 5.3 (6.2)	<0.0001
Upper Right Lung	-2.6 ± 7.2 (7.7)	0.3 ± 7.4 (7.4)	<0.0001
Middle Right Lung	-4.5 ± 7.6 (8.9)	0.4 ± 6.3 (6.3)	<0.0001
Lower Right Lung	-8.2 ± 7.1 (10.9)	-1.8 ± 6.0 (6.3)	<0.0001
Total Lungs	-5.2 ± 7.1 (8.8)	-0.8 ± 6.3 (6.4)	<0.0001
Liver	-6.1 ± 2.4 (6.6)	-5.4 ± 2.1 (5.7)	<0.0005
Aorta	-7.1 ± 4.8 (8.6)	-4.2 ± 3.5 (5.5)	<0.0001
Myocardium	-9.5 ± 4.3 (10.4)	-5.7 ± 3.2 (6.5)	<0.0001
T3 vertebra	-14.1 ± 2.5 (14.3)	-12.0 ± 2.1 (12.2)	<0.0001
Lesions	-6.1 ± 6.7 (9.1)	-3.3 ± 4.7 (5.7)	<0.0001

Figure 8(b) illustrates the impact of the emission-based estimation of lung attenuation coefficients on quantification errors in adjacent normal organs to the lungs including the liver, aorta, myocardium, 3rd thoracic vertebra; as well as the identified lesions in all patients. As presented in Table 2, the results show a statistically significant reduction of the bias in neighbouring organs, especially in the myocardium and aorta. The results also show that the attenuation coefficients of the lung can impact the PET bias over the vertebra, where the LACs of bones have been substituted by those of soft tissue in both MRAC and MLAA attenuation maps. Nonetheless, the MLAA reduced the mean of bone bias from -14.1% to -12.0% over all patients. For the VOIs defined in the lesions ($n = 70$), the MRAC method resulted in an underestimation of $-6.1 \pm 6.7\%$ with a RMES of 9.1% , which was reduced by the MLAA method to $-3.3 \pm 4.7\%$ with a RMSE of 5.7% . Most of the lesions were mediastinal lymph node involvements, for which the mis-segmentation of soft tissue structures, such as pulmonary vessels and bronchioles, into the lung tissue class is unavoidable for current standard MR pulse sequences.

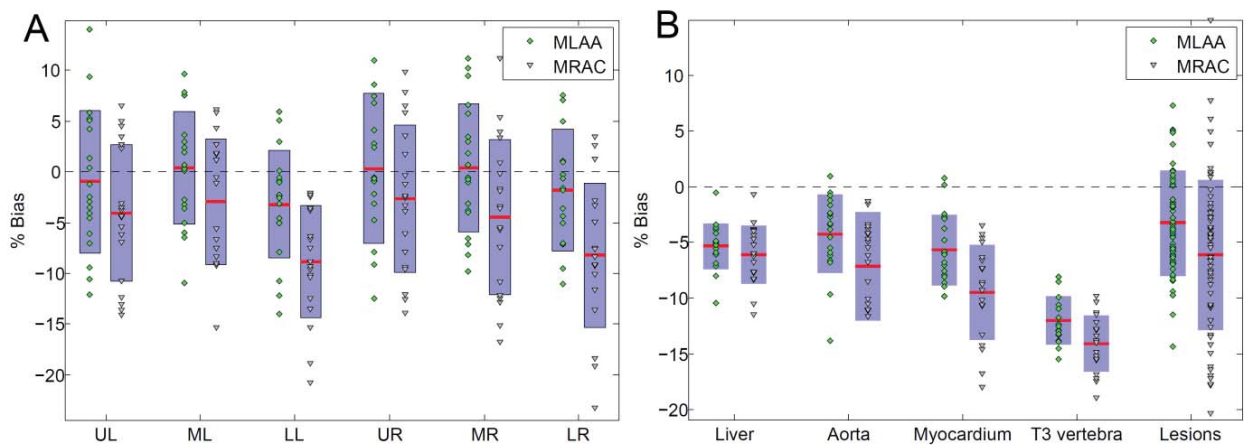


Figure 8. Relative SUV errors of MRAC and MLAA attenuation correction methods in (A) six lung regions and (B) normal tissues close to the lungs with reference CTAC PET images. Means and one-standard deviations are indicated by the horizontal bars and vertical boxes, respectively.

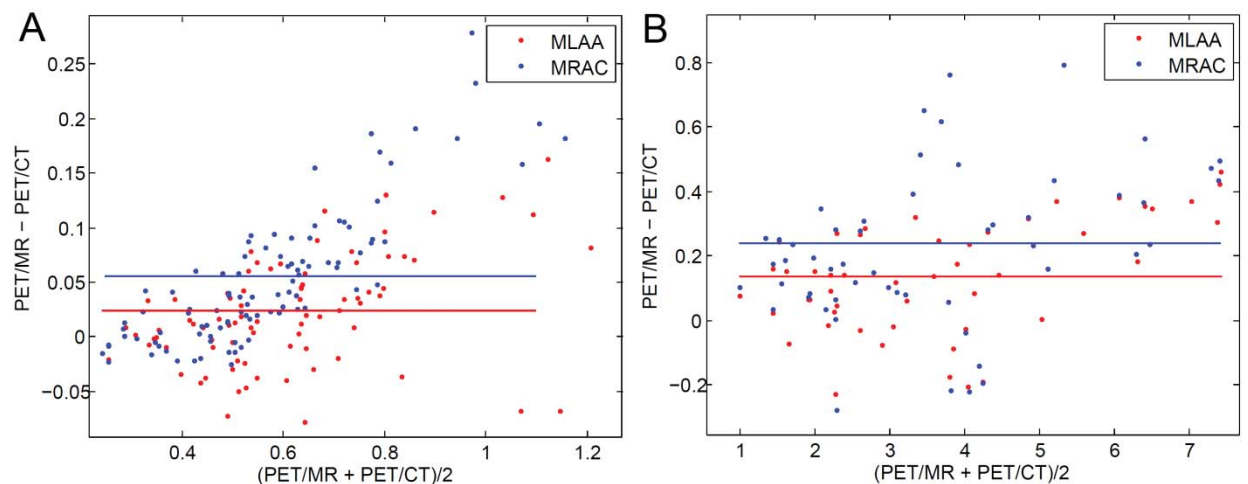


Figure 9. Bland-Altman plots of SUVmean estimated using MRAC and MLAA PET images with respect to CTAC PET images for (A) all lung VOIs and (B) all lesions.

The AC methods were further analyzed in terms of SUV concordance with the reference CTAC technique. Figure 9 shows the Bland-Altman plots for the lung VOIs and malignant lesions. As can be seen, both MRAC and MLAA methods show a systematic bias in the SUV estimates of lung tissues and lesions. However, consistent with the results presented in Table 2, the mean of the bias (horizontal lines) is reduced by the MLAA attenuation correction method.

The performance of the proposed MLAA algorithm depends on the involved parameters, such as the number of iterations and subsets, the magnitude of regularization parameters, β and γ , and the step size α of the MLTR algorithm. In this work, we heuristically optimized these parameters for a few patient datasets and employed them for all 19 patients. The Gaussian tissue preference prior is the essential element of the proposed algorithm. In fact, this algorithm derives the lung LACs in an interval between the standard 4-class MRAC method and the original MLAA algorithm, depending on the γ weighting factor. Figure 10 compares the mean \pm half-standard deviation of the estimated lung LACs using the MLAA algorithm with the MRAC and reference CTAC techniques for patient No. 11 (see Table 1) with the weighting factor increasing from zero (corresponding to the original MLAA) to 1. The lung tissue prior, parameterized over a patient population, in fact penalizes the large deviation of the attenuation coefficients from the expected values, depending on the γ parameter. As shown in figure 10, very low values of γ reduce the algorithm to the original MLAA, which results in a high error in estimating the mean LACs. This should be attributed to out-of-field accidental coincidences, error propagation into the lungs from adjacent regions (because bones are replaced by soft tissue in the 4-class MRAC maps) and the still unsolved scaling problem of the MLAA algorithm. On the other hand, for very large values of γ , the proposed MLAA algorithm is reduced to the standard MRAC method, which guarantees a safe-failure method. We nearly optimized this parameter for a few clinical studies and employed it for the rest of patient datasets. As mentioned earlier, we chose $\gamma = 0.75$, $\beta = 80$, $\alpha = 1.5$ for all patient datasets. Our preliminary results showed that there is greater flexibility in selecting the last two parameters than the first one. Finally, as shown in figure 11, we obtained the 15 global iterations as a near-to-optimal number of iterations for a few datasets and utilized it for all other datasets.

IV. DISCUSSION

Recently, TOF-PET technology has been implemented on clinical PET scanners with the aim of improving lesion detectability and image quality, as well as reducing acquisition time and/or patient's administrated activity [44]. With the advent of TOF-PET scanners, the simultaneous maximum likelihood estimation of activity and attenuation has regained popularity [23]. Emission-based attenuation correction strategies are particularly promising in PET/MR imaging for overcoming the quantification errors induced by conventional segmentation-based AC methods [45]. Based on our previous work [36], we report on the use of a constrained MLAA algorithm for patient-specific emission-based estimation of lung attenuation coefficients with the aim of improving existing 4-class MRAC methods.

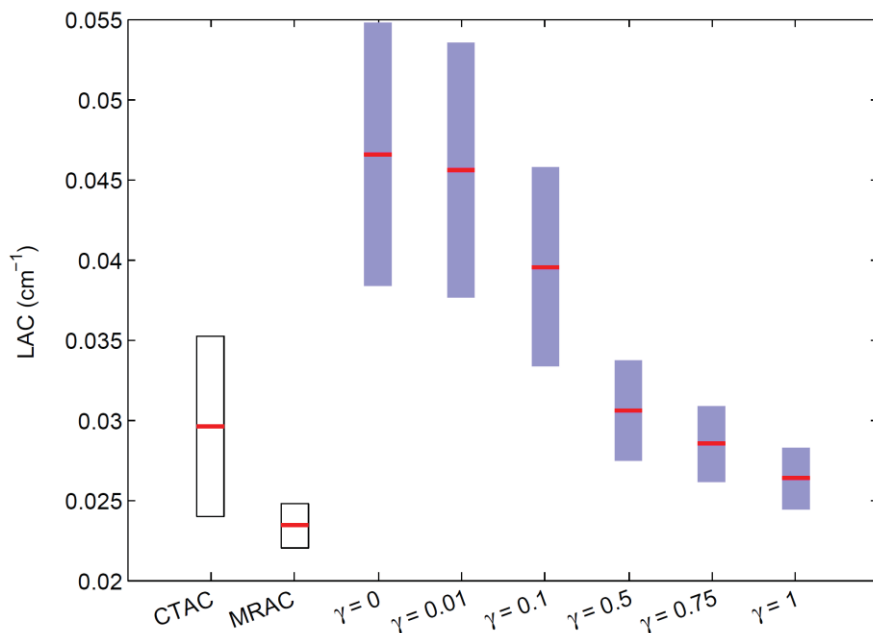


Figure 10. Impact of the γ weighting parameter of the lung tissue preference prior on the performance of the proposed constrained MLAA algorithm. The horizontal bars and vertical boxes indicate the mean and standard deviation of lung attenuation coefficients for patient No. 11 (see Table 2).

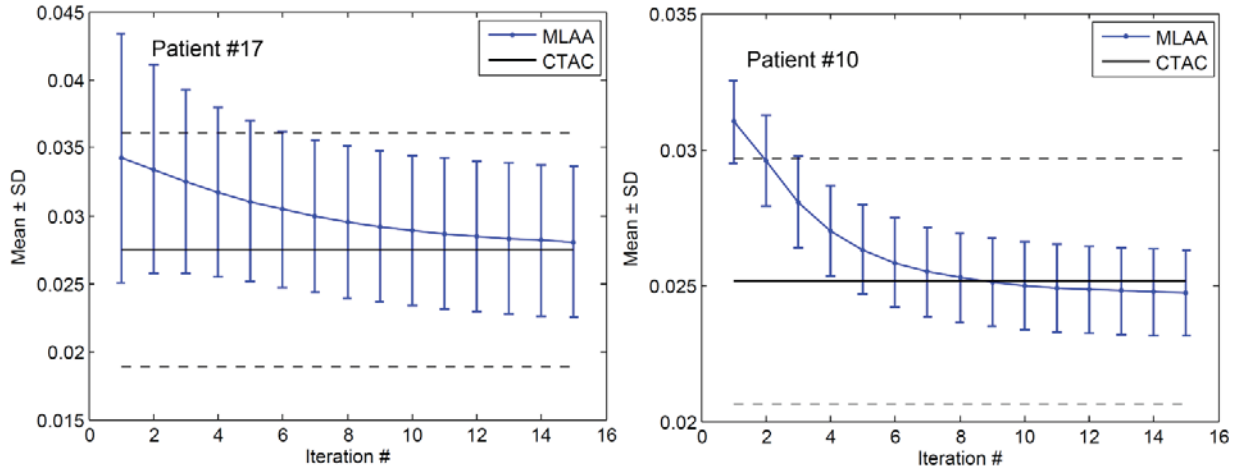


Figure 11. Mean and standard deviation (error bars) of lung LACs in two patients as a function of iteration number. The horizontal solid and dashed lines represent the mean \pm standard deviation of CTAC lung LACs, respectively.

Among the different tissue classes defined in segmentation-based AC methods, the lungs have the largest inter-patient LAC variability with a standard deviation of 0.004 cm^{-1} [26, 46], which is similar to the standard deviation of mean CTAC attenuation coefficients (Table 1). This standard deviation is about 20 times higher than that of soft tissue [26]. Therefore, if patient-specific lung LACs are not considered in MRAC maps, PET quantification errors up to 26% might result [46]. In [5] and [27], a LAC of 0.018 cm^{-1} was assigned to the lungs, resulting in PET quantification bias of $1.9 \pm 2.3\%$ and $-0.5 \pm 13.3\%$ in lung lesions and lung normal tissues, respectively. In earlier studies, a linear attenuation coefficient of 0.024 cm^{-1} was assigned to the lungs, resulting in relative errors of $13.5 \pm 10.7\%$ [47] and $7.7 \pm 3.0\%$ [11]. Ouyang *et al* [48] reported a relative error of $4.4 \pm 14.4\%$ for SUV estimates of the lungs when using lung LACs of 0.0276 cm^{-1} . Our results exhibited an average SUV bias of $-5.2 \pm 7.1\%$ when using lung LACs of 0.0224 cm^{-1} in the standard MRAC method. The discrepancy between the reported errors should be attributed to the assignment of different lung LACs and the usage of different lung segmentation algorithms. The results presented in Table 1 and figure 4 demonstrate that the MLAA algorithm is generally in agreement with patient-specific lung attenuation coefficients determined using the CTAC method, except in a few patients, where severe respiratory motion and elevated LACs in the posterior regions of the lungs were observed. Overall, the proposed AC method reduced the bias in the lung tissue to $-0.8 \pm 6.3\%$. The results presented in Table 2 indicate that the MLAA technique noticeably outperformed the MRAC method in the lower lobes of the lungs, where the lung attenuation coefficients are commonly higher than in the upper lobes. In these regions, the MRAC and MLAA methods resulted in an average bias of $-8.5 \pm 6.3\%$ and $-2.5 \pm 5.6\%$, respectively. These results along with those shown in figures 2, 3 and 5 demonstrate that the proposed AC method can fairly capture the voxel-wise intra-patient variability of lung LACs.

In the case of respiratory mismatch between the reference CTAC and PET images, only MLAA-AC method shows increased attenuation values in the vicinity of the diaphragm. Therefore, in these cases, the MLAA approach overestimates the activity with respect to the reference CTAC method. However, the LACs derived from CTAC do not reflect the actual ones. Regarding the evaluation of the AC methods, we performed a class-wise analysis to provide a global metric for the estimated attenuation coefficients over the whole lung (Table 1). In this case, the differences due to respiratory mismatch between the proposed approach and the CTAC method are not distinguishable. However, according to our experience the outperformance of MLAA over MRAC in the lower part of the lungs is mainly due to the fact that the MLAA algorithm retrieves well the lung density gradients. In the SUV evaluations, we used a VOI-based analysis. The placement of a single VOI in the lower portions of the lungs partly excludes the SUV differences due to respiratory mismatch between the proposed approach and the CTAC method.

Among MRI-guided AC methods, atlas-based registration and pattern recognition (AT&PR) methods predict continuous LACs, thus considering intra-patient variability. The technique proposed by Hofmann *et al* [47] incorporates the local structures of MR images and co-registered CT atlases into Gaussian process regression (GPR) kernels to predict patient-specific attenuation maps. In spite of considerable SUV bias reduction in soft-tissue and bony structures, this method exhibited large bias in the lungs as much as the standard 4-class MRAC method. In fact, lung tissues have low proton densities and short transverse relaxation times. As such, lung MR intensities in standard MR sequences are low and do not provide sufficient information to easily distinguish lung density variations. Recently, Arabi and Zaidi embedded the correlation between lung volume and lung mean LACs into the GPR kernels and showed that their improved AT&PR method reduces the lung SUV bias from 8.9% to 4.1% [49]. Ultra-short echo time (UTE) MR pulse sequences have also been investigated for the detection and visualization of lung parenchyma density to improve lung segmentation and bone depiction [50]. However, UTE pulse sequences are timing-consuming and sensitive to magnetic field inhomogeneities and are therefore, not yet clinically feasible in whole-body MRAC.

Although the mean lung LACs are low compared to other tissue classes, the lung's volume is large and therefore non patient-specific and inaccurate assignment of attenuation values to the lungs can affect the quantification accuracy of the neighbouring organs and lesions. The MLAA algorithm can reduce SUV quantification errors in different neighbouring tissues by deriving patient-specific lung LACs (Table 2, figure 8). In particular, it was found that for lesions in/close to the lungs, this algorithm can reduce the bias from -6.1% to -3.3% . As shown in figure 6, the algorithm is promising especially in terms of reducing the adverse effect of respiratory phase mismatch between PET and MR on the quantification of liver lesions uptake [51].

Over 114 VOIs defined in the lungs, the MRAC and MLAA methods resulted in maximum SUV underestimation of -23.3 and -14.0% , and maximum SUV overestimation of 11.1 and 15.0% , respectively. As can be seen in figure 8(a), the MLAA algorithm did not noticeably reduce the standard deviation of the errors compared to the MRAC method. This should be attributed to the potentially sub-optimal weighting factor of the Gaussian tissue prior used in our MLAA algorithm, the intrinsic limitations and count-dependency of the emission-based AC methods and the contribution of out-of-field accidental coincidences. The latter is more prominent in the work of [35], where high SUV errors were observed on Monte Carlo simulated PET/CT datasets. In contrast, our proposed MLAA method showed a promising performance and demonstrated the potential and benefits of emission-based AC methods. The primary advantage of our method compared to Berker *et al* is the derivation of continuous lung attenuation values that can not only capture the lung density gradients but also fairly compensate for respiratory mismatch, cardiac motion and segmentation errors. The shortcoming of our voxel-wise estimation of LACs compared to their class-wise approach is the higher noise and possibly the lower convergence rate of the algorithm. To tackle these problems, we incorporated a MRF smoothing prior in the algorithm and initialized it with the standard 4-class MRAC map. Our simplified MLAA algorithm is in essence similar to the one proposed by [37] for the compensation of arm truncation of MRAC maps, except that they used a bi-modal Gaussian intensity prior to favour the separation of soft tissue attenuation values from air. However, this prior is not twice continuously differentiable and might result in instability of the solution.

To this end, it is worth to recognize the limitations of this study and highlight future directions for improving the performance of the proposed algorithm. Emission-based estimation of attenuation coefficients depends on the biodistribution of the tracer in the body. In fact, the attenuation map cannot be completely estimated for LORs that are out of the support of the activity distribution, especially for specific tracers that have a localized uptake. In our patient population, the clinical studies encompassed ^{18}F -FDG ($n = 17$) and ^{18}F -Choline ($n = 2$) scans. For the bed positions of interest to us, the biodistribution of ^{18}F -Choline is almost similar to that of ^{18}F -FDG, except in the brain [52]. Therefore, our assertion that both tracers support well the estimation of attenuation is justified. However, whether the local differences in uptake pattern influences the estimated attenuation values remains to be demonstrated. As shown in figure 10, the performance of our method depends highly on the selected γ parameter. The choice of the hyper-parameters for MAP image reconstruction is usually not straightforward. In this work, we nearly optimized this parameter for a few patient datasets (3-5) by trial and error and used it for all other patient datasets. Although this parameter selection approach allowed for the evaluation of the method over a reasonable patient population, the selected parameter might not be optimal for all datasets, especially in cases where it is not high enough to penalize the high LAC deviations induced by error propagation from neighbouring tissue classes and out-of-field accidental coincidences. An adaptive selection of this parameter can be achieved using discrete data consistency conditions [53] or hierarchical Bayesian approach for its iterative estimation [54],

which will be investigated in future work. Similarly, we heuristically selected the update schedule of the MLAA algorithm with a fixed number of global iterations for all patients. Future work will focus on defining a stopping criterion based on decreasing consistency error or Kullback-Leibler distance.

V. CONCLUSION

The proposed constrained MLAA algorithm provides a promising and feasible method for deriving patient-specific lung attenuation maps in TOF PET/MR imaging. It was demonstrated that this algorithm retrieves the lung density gradients and can compensate for respiratory motion artefacts. Our results showed that the conventional 4-class MRAC method resulted in average SUV errors of -5.2% and -6.1% in normal lung tissues and lesions, respectively, in/near the lungs. Emission-based estimation of lung LACs using the MLAA algorithm reduced the errors to -0.8% and -3.3% , respectively. In conclusion, the results achieved using the proposed algorithm suggest that emission-based estimation of lung attenuation coefficients in the MLAA framework using lung tissue preference priors show promise for attenuation correction of PET/MR imaging.

ACKNOWLEDGEMENT

This work was supported in part by the Swiss National Science Foundation under Grant SNSF 31003A-149957 and the Indo-Swiss Joint Research Programme ISJRP 138866.

REFERENCES

- [1] J. A. Disselhorst, I. Bezrukov, A. Kolb, C. Parl, and B. J. Pichler, "Principles of PET/MR Imaging.," *J Nucl Med*, vol. 55, no. Supplement 2, pp. 2S-10S, May 12, 2014.
- [2] D. A. Torigian, H. Zaidi, T. C. Kwee, B. Saboury, J. K. Udupa, Z.-H. Cho, and A. Alavi, "PET/MR Imaging: Technical aspects and potential clinical applications.," *Radiology*, vol. 267, no. 1, pp. 26-44, 2013.
- [3] I. Bezrukov, F. Mantlik, H. Schmidt, B. Scholkopf, and B. J. Pichler, "MR-based PET attenuation correction for PET/MR imaging.," *Semin Nucl Med*, vol. 43, no. 1, pp. 45-59, Jan, 2013.
- [4] H. Zaidi, "Is MRI-guided attenuation correction a viable option for dual-modality PET/MR imaging?," *Radiology*, vol. 244, no. 3, pp. 639-642, September 1, 2007, 2007.
- [5] A. Martinez-Moller, M. Souvatzoglou, G. Delso, R. A. Bundschuh, C. Chefd'hotel, S. I. Ziegler, N. Navab, M. Schwaiger, and S. G. Nekolla, "Tissue classification as a potential approach for attenuation correction in whole-body PET/MRI: Evaluation with PET/CT data.," *J Nucl Med*, vol. 50, no. 4, pp. 520-526, Apr, 2009.
- [6] Z. Hu, S. Renisch, B. Schweizer, T. Blaffert, N. Ojha, T. Guo, J. Tang, C.-H. Tung, J. Kaste, V. Schulz, I. Torres, and L. Shao, "MR-based attenuation correction for a whole-body PET/MR system." pp. 2119-2122.
- [7] M. Hofmann, F. Steinke, V. Scheel, G. Charpiat, J. Farquhar, P. Aschoff, M. Brady, B. Scholkopf, and B. J. Pichler, "MRI-based attenuation correction for PET/MRI: A novel approach combining pattern recognition and Atlas registration.," *J Nucl Med*, vol. 49, no. 11, pp. 1875-1883, Oct 16, 2008.
- [8] E. Schreibmann, J. A. Nye, D. M. Schuster, D. R. Martin, J. Votaw, and T. Fox, "MR-based attenuation correction for hybrid PET-MR brain imaging systems using deformable image registration.," *Med Phys*, vol. 37, no. 5, pp. 2101-2109, 2010.
- [9] A. Johansson, M. Karlsson, and T. Nyholm, "CT substitute derived from MRI sequences with ultrashort echo time.," *Med Phys*, vol. 38, no. 5, pp. 2708-2714, May, 2011.
- [10] B. K. Navalpakkam, H. Braun, T. Kuwert, and H. H. Quick, "Magnetic resonance-based attenuation correction for PET/MR hybrid imaging using continuous valued attenuation maps.," *Invest Radiol*, vol. 48, no. 5, pp. 323-332, May, 2013.
- [11] H. R. Marshall, J. Patrick, D. Laidley, F. S. Prato, J. Butler, J. Theberge, R. T. Thompson, and R. Z. Stodilka, "Description and assessment of a registration-based approach to include bones for attenuation correction of whole-body PET/MRI.," *Med Phys*, vol. 40, no. 8, pp. 082509, Aug, 2013.
- [12] P. Mollet, V. Keereman, J. Bini, D. Izquierdo-Garcia, Z. A. Fayad, and S. Vandenberghe, "Improvement of attenuation correction in time-of-flight PET/MR imaging with a positron-emitting source.," *J Nucl Med*, vol. 55, no. 2, pp. 329-336, Feb, 2014.
- [13] H. Rothfuss, V. Panin, A. Moor, J. Young, I. Hong, C. Michel, J. Hamill, and M. Casey, "LSO background radiation as a transmission source using time of flight.," *Phys Med Biol*, vol. 59, no. 18, pp. 5483-5500, Sep 21, 2014.
- [14] A. Welch, C. Campbell, R. Clackdoyle, F. Natterer, M. Hudson, A. Bromiley, P. Mikecz, F. Chillcot, M. Dodd, P. Hopwood, S. Craib, G. T. Gullberg, and P. Sharp, "Attenuation correction in PET using consistency information.," *IEEE Trans Nucl Sci*, vol. 45, no. 6, pp. 3134-3141, 1998.
- [15] A. V. Bronnikov, "Reconstruction of attenuation map using discrete consistency conditions.," *IEEE Trans Med Imaging*, vol. 19, no. 5, pp. 451-462, May, 2000.
- [16] K. Kacperski, "Attenuation correction in SPECT without attenuation map." pp. 3820-3822.
- [17] M. Defrise, A. Rezaei, and J. Nuyts, "Time-of-flight PET data determine the attenuation sinogram up to a constant.," *Phys Med Biol*, vol. 57, no. 4, pp. 885-899, Feb 21, 2012.
- [18] J. Nuyts, P. Dupont, S. Stroobants, R. Benninck, L. Mortelmans, and P. Suetens, "Simultaneous maximum a posteriori reconstruction of attenuation and activity distributions from emission sinograms.," *IEEE Trans Med Imaging*, vol. 18, no. 5, pp. 393-403, May, 1999.
- [19] A. Krol, J. E. Bowsher, S. H. Manglos, D. H. Feiglin, M. P. Tornai, and F. D. Thomas, "An EM algorithm for estimating SPECT emission and transmission parameters from emissions data only.," *IEEE Trans Med Imaging*, vol. 20, no. 3, pp. 218-232, Mar, 2001.
- [20] M. Landmann, S. N. Reske, and G. Glattig, "Simultaneous iterative reconstruction of emission and attenuation images in positron emission tomography from emission data only.," *Med Phys*, vol. 29, no. 9, pp. 1962-1967, Sep, 2002.

- [21] A. Rezaei, M. Defrise, and J. Nuyts, "ML-reconstruction for TOF-PET with simultaneous estimation of the attenuation factors.," *IEEE Trans Med Imaging*, vol. 33, no. 7, pp. 1563-1572, Jul, 2014.
- [22] A. Salomon, A. Goedicke, and T. Aach, "Simultaneous reconstruction of activity and attenuation in multi-modal ToF-PET.." pp. 339-342.
- [23] A. Rezaei, M. Defrise, G. Bal, C. Michel, M. Conti, C. Watson, and J. Nuyts, "Simultaneous reconstruction of activity and attenuation in time-of-flight PET.," *IEEE Trans Med Imaging*, vol. 31, no. 12, pp. 2224-2233, 2012.
- [24] V. Y. Panin, M. Aykac, and M. E. Casey, "Simultaneous reconstruction of emission activity and attenuation coefficient distribution from TOF data, acquired with external transmission source.," *Phys Med Biol*, vol. 58, no. 11, pp. 3649-3669, Jun 7, 2013.
- [25] C. C. Watson, "Supplemental transmission method for improved PET attenuation correction on an integrated MR/PET.," *Nucl Instr Meth A*, vol. 734, Part B, pp. 191-195, 1/11/, 2014.
- [26] V. Schulz, I. Torres-Espallardo, S. Renisch, Z. Hu, N. Ojha, P. Börnert, M. Perkuhn, T. Niendorf, W. Schäfer, H. Brockmann, T. Krohn, A. Buhl, R. Günther, F. Mottaghy, and G. Krombach, "Automatic, three-segment, MR-based attenuation correction for whole-body PET/MR data.," *Eur J Nucl Med Mol Imaging*, vol. 38, no. 1, pp. 138-152, 2011.
- [27] H. Arabi, O. Rager, A. Alem, A. Varoquaux, M. Becker, and H. Zaidi, "Clinical assessment of MR-guided 3-class and 4-class attenuation correction in PET/MR.," *Mol Imaging Biol*, vol. 7, no. 2, pp 264-276, 2015.
- [28] R. Karimi, G. Tornling, H. Forslund, M. Mikko, A. Wheelock, S. Nyren, and C. M. Skold, "Lung density on high resolution computer tomography (HRCT) reflects degree of inflammation in smokers.," *Respir Res*, vol. 15, pp. 23, 2014.
- [29] P. J. Robinson, and L. Kreel, "Pulmonary tissue attenuation with computed tomography: comparison of inspiration and expiration scans.," *J Comput Assist Tomogr*, vol. 3, no. 6, pp. 740-748, Dec, 1979.
- [30] L. Gattinoni, P. Pelosi, G. Vitale, A. Pesenti, L. D'Andrea, and D. Mascheroni, "Body position changes redistribute lung computed-tomographic density in patients with acute respiratory failure.," *Anesthesiology*, vol. 74, no. 1, pp. 15-23, Jan, 1991.
- [31] J. H. Kim, J. S. Lee, I. C. Song, and D. S. Lee, "Comparison of segmentation-based attenuation correction methods for PET/MRI: Evaluation of bone and liver standardized uptake value with oncologic PET/CT data.," *J Nucl Med*, vol. 53, no. 12, pp. 1878-1882, Dec, 2012.
- [32] H. R. Marshall, F. S. Prato, L. Deans, J. Theberge, R. T. Thompson, and R. Z. Stodilka, "Variable lung density consideration in attenuation correction of whole-body PET/MRI.," *J Nucl Med*, vol. 53, no. 6, pp. 977-984, Jun, 2012.
- [33] A. R. Lonn, and S. D. Wollenweber, "Estimation of mean lung attenuation for use in generating PET attenuation maps." pp. 3017-3018.
- [34] M. T. Madsen, and J. R. Lee, "Emission based attenuation correction of PET images of the thorax." pp. 967-971.
- [35] Y. Berker, A. Salomon, F. Kiessling, and V. Schulz, "Lung attenuation coefficient estimation using Maximum Likelihood reconstruction of attenuation and activity for PET/MR attenuation correction." pp. 2282-2284.
- [36] A. Mehranian, and H. Zaidi, "Joint estimation of activity and attenuation in whole-body TOF PET/MRI using constrained Gaussian mixture models," *IEEE Trans Med Imaging*, vol. in press, 2015.
- [37] J. Nuyts, G. Bal, F. Kehren, M. Fenchel, C. Michel, and C. Watson, "Completion of a truncated attenuation image from the attenuated PET emission data.," *IEEE Trans Med Imaging*, vol. 32, no. 2, pp. 237-246, Sep 21, 2013.
- [38] N. H. Clinthorne, J. A. Fessler, G. D. Hutchins, and W. L. Rogers, "Joint maximum likelihood estimation of emission and attenuation densities in PET." pp. 1927-1932.
- [39] J. Nuyts, B. De Man, P. Dupont, M. Defrise, P. Suetens, and L. Mortelmans, "Iterative reconstruction for helical CT: a simulation study.," *Phys Med Biol*, vol. 43, no. 4, pp. 729-737, Apr, 1998.
- [40] J. A. Fessler, E. P. Ficaro, N. H. Clinthorne, and K. Lange, "Grouped-coordinate ascent algorithms for penalized-likelihood transmission image reconstruction.," *IEEE Trans Med Imaging*, vol. 16, no. 2, pp. 166-175, Apr, 1997.

- [41] P. A. Yushkevich, J. Piven, H. C. Hazlett, R. G. Smith, S. Ho, J. C. Gee, and G. Gerig, "User-guided 3D active contour segmentation of anatomical structures: significantly improved efficiency and reliability.," *Neuroimage*, vol. 31, no. 3, pp. 1116-1128, Jul 1, 2006.
- [42] I. Bezrukov, H. Schmidt, F. Mantlik, N. Schwenzer, C. Brendle, B. Scholkopf, and B. J. Pichler, "MR-based attenuation correction methods for improved PET quantification in lesions within bone and susceptibility artifact regions.," *J Nucl Med*, vol. 54, no. 10, pp. 1768-1774, Oct, 2013.
- [43] A. Mehranian, and H. Zaidi, "Impact of time-of-flight PET on quantification errors in MRI-based attenuation correction," *J Nucl Med*, vol. 56, no. 4, pp 635-641, 2015.
- [44] M. Conti, "Focus on time-of-flight PET: the benefits of improved time resolution.," *Eur J Nucl Med Mol Imaging*, vol. 38, no. 6, pp. 1147-1157, 2011.
- [45] A. Salomon, A. Goedicke, B. Schweizer, T. Aach, and V. Schulz, "Simultaneous reconstruction of activity and attenuation for PET/MR.," *IEEE Trans Med Imaging*, vol. 30, no. 3, pp. 804-813, 2011.
- [46] V. Keereeman, R. V. Holen, P. Mollet, and S. Vandenberghe, "The effect of errors in segmented attenuation maps on PET quantification.," *Med Phys*, vol. 38, no. 11, pp. 6010-6019, 2011.
- [47] M. Hofmann, I. Bezrukov, F. Mantlik, P. Aschoff, F. Steinke, T. Beyer, B. J. Pichler, and B. Scholkopf, "MRI-based attenuation correction for whole-body PET/MRI: Quantitative evaluation of segmentation- and Atlas-based methods.," *J Nucl Med*, vol. 52, no. 9, pp. 1392-1399, Sep, 2011.
- [48] J. Ouyang, S. Y. Chun, Y. Petibon, A. A. Bonab, N. Alpert, and G. El Fakhri, "Bias atlases for segmentation-based PET attenuation correction using PET-CT and MR.," *IEEE Trans Nucl Sci*, vol. 60, no. 5, pp. 3373-3382, 2013.
- [49] H. Arabi, and H. Zaidi, "MRI-based pseudo-CT generation using sorted atlas images in whole-body PET/MRI." p. *in press*.
- [50] K. Zeimpekis, G. Delso, F. Wiesinger, P. Veit-Haibach, G. von Schulthess, and R. Grimm, "Investigation of 3D UTE MRI for lung PET attenuation correction [abstract].," *J Nucl Med*, vol. 55, no. 1_MeetingAbstracts, pp. 2103, May 1, 2014, 2014.
- [51] A. Mehranian, and H. Zaidi, "Clinical assessment of emission- and segmentation-based MR-guided attenuation correction in whole-body time-of-flight PET/MRI," *J Nucl Med*, vol. 56, no. 6, pp 877-883, 2015.
- [52] O. Schillaci, F. Calabria, M. Tavolozza, C. Ciccio, M. Carlanì, C. R. Caracciolo, R. Danieli, A. Orlacchio, and G. Simonetti, "18F-choline PET/CT physiological distribution and pitfalls in image interpretation: experience in 80 patients with prostate cancer," *Nucl Med Commun*, vol. 31, no. 1, pp. 39-45, 2010.
- [53] V. Y. Panin, F. Kehren, J. Hamill, and C. Michel, "Application of discrete data consistency conditions for selecting regularization parameters in PET attenuation map reconstruction.," *Phys Med Biol*, vol. 49, no. 11, pp. 2425-2436, 2004.
- [54] K. Moon Gi, and A. K. Katsaggelos, "General choice of the regularization functional in regularized image restoration," *IEEE Trans Image Process*, vol. 4, no. 5, pp. 594-602, 1995.

Chapter 11

Clinical assessment of emission- and segmentation- based MR- guided attenuation correction in whole-body time-of-flight PET/MRI

Abolfazl Mehranian and Habib Zaidi

J Nuc Med 56(6), 877-883 (2015)

Abstract

Purpose: The joint maximum likelihood reconstruction of activity and attenuation (MLAA) for emission-based attenuation correction has regained attention since the advent of time-of-flight PET/MRI. Recently, we improved the performance of the MLAA algorithm using an MRI-constrained Gaussian mixture model (GMM). In this study, we compare the performance of our proposed algorithm with standard 4-class MR-based attenuation correction (MRAC) implemented on commercial systems.

Methods: Five head and neck ^{18}F -FDG patients were scanned on the Philips TF PET/MRI and Siemens mCT PET/CT scanners. Dixon fat and water MR images were registered to CT images. MRAC maps were derived by segmenting the MRI into 4 tissue classes and assigning predefined attenuation coefficients. For MLAA-GMM, MR images were segmented into known tissue classes, including fat, soft tissue, lung, background air and an unknown MR low-intensity class encompassing cortical bones, air cavities and metal artifacts. A co-registered bone probability map was also included in the unknown tissue class. Finally, the GMM prior was constrained over known tissue classes of attenuation maps using uni-modal Gaussians parameterized over a patient population.

Results: The results showed that the MLAA-GMM algorithm outperforms the MRAC method by differentiating bones from air gaps and providing more accurate patient-specific attenuation coefficients of soft tissue and lungs. It was found that the MRAC and MLAA-GMM methods resulted in average SUV errors of -5.4% and -3.5% in the lungs, -7.4% and -5.0% in soft tissues/lesions, -18.4% and -10.2% in bones, respectively.

Conclusion: The proposed MLAA algorithm is promising for accurate derivation of attenuation maps on TOF PET/MR systems.

I. Introduction

Hybrid positron emission tomography/magnetic resonance imaging (PET/MRI) systems have provided new opportunities for enhancing the diagnostic confidence of PET and MRI findings through fusion of complementary structural and molecular information [1]. The potential of PET/MRI in establishing a new multi-parametric imaging paradigm has been a driving force for developing innovative solutions to tackle the challenges of these dual-modality systems.

Accurate attenuation correction (AC) of PET data is one of the major challenges of quantitative PET/MRI imaging [2]. In these systems, attenuation maps at 511 keV should ideally be derived from the acquired MR images. However, in contrary to x-ray computed tomography (CT), MRI signals are not correlated with electron density and photon attenuating properties of tissues, but rather to proton density and magnetic relaxation properties. Therefore, there is no unique global mapping technique to convert MRI intensities to attenuation coefficients. In addition, lung tissues and cortical bones, which are two important tissue types in attenuation maps, exhibit low signals on images acquired using conventional MR pulse sequences owing to their low water content and short transverse relaxation time. Therefore, the lungs, bones and air pockets, which also produce a low signal, cannot be well differentiated from each other for the generation of MRI segmentation-based attenuation maps. Ultra-short echo time (UTE) and zero echo time (ZTE) MR pulse sequences have been investigated for the detection and visualization of bones as well as lung parenchyma [3-5]. However, UTE/ZTE MRI is timing-consuming and sensitive to magnetic field inhomogeneities and, as such, it is not yet clinically feasible for whole-body MRI-guided attenuation correction (MRAC) of PET data. Current commercial PET/MRI systems employ MRI segmentation-based approaches as the standard AC method. In these methods, MR images are segmented into 3 or 4 tissue classes, that is, background air, lung, fat and non-fat soft tissues, and predefined constant attenuation coefficients are assigned to each tissue class [6, 7]. However, inter/intra-patient heterogeneity of attenuation coefficients in the different tissue classes is ignored by these approaches. Moreover, since bones and air cavities cannot be well discriminated in conventional MR sequences, these tissue classes are often replaced by soft tissue, which can lead to significant bias in PET tracer uptake quantification in different organs [8, 9]. Hence, other AC techniques based on atlas registration, external transmission sources and PET emission data have been explored and revisited in PET/MRI imaging.

In atlas registration-based approaches, co-registered MR-CT atlas datasets are used to derive a pseudo CT image from the patient's MR image or to learn a mapping function that predicts a pseudo CT image [10, 11]. These methods can solve the MRAC problem, particularly in brain imaging, provided that a perfect registration between the atlas and different patients can be achieved. However, such a registration is rarely possible in whole-body PET/MRI, owing to substantial anatomical differences between patients as well as the limitations of registration algorithms. With advances in PET detector technology, time-of-flight (TOF) PET capability has been recently introduced in clinical PET/CT and PET/MRI scanners with the aim of improving lesion detectability and image quality, as well as reducing acquisition time and the administrated activity of radiopharmaceuticals [12]. Following the recent rebirth of TOF-PET, transmission- and emission-based methods have been revisited for deriving patient-specific attenuation maps in PET/MRI, thus potentially circumventing the uncertainties and obstacles of both standard and UTE/ZTE MRAC methods. In transmission-based approaches, attenuation coefficients are directly measured using external positron-emitting sources [13] or background radiation of LSO crystals [14] in a simultaneous transmission and emission acquisition mode. TOF information is then used to separate transmission from emission data. The limited timing resolution of current TOF PET scanners; however, does not allow for perfect separation of transmission data from emission data. Therefore, the calculated attenuation coefficients might be non-uniformly scaled and different from their expected values [13]. In contrast, emission-based approaches only rely on emission data for joint maximum likelihood estimation of activity and attenuation maps (MLAA) [15, 16]. In fact, recent studies have demonstrated that both activity and attenuation distributions can be determined from TOF emission data, up to an unknown scaling factor [16, 17].

Emission-based AC methods are promising in TOF PET/MRI, where MRI anatomical information can be exploited to guide the estimation of the attenuation map. With the advent of sequential TOF PET/MRI systems, Salomon *et al.* [18] employed both TOF and MRI anatomical information to constrain the MLAA algorithm. In their approach, MR images are segmented into many regions over which the attenuation coefficients are iteratively estimated from the emission data. Despite the fact that this approach substantially reduces noise and

cross-talk artifacts between activity and attenuation maps, the reconstructed attenuation maps suffer from mis-segmentation errors and the quantitative performance of the algorithm depends on the accurate correction of the scaling problem. We recently proposed an approach to employ MRI spatial and CT statistical information in the joint estimation of activity and attenuation using a constrained Gaussian mixture model (GMM) [19]. In contrast to Salomon’s method, MR images are segmented into a few tissue classes and incorporated into the GMM model. This approach allows the derivation of continuous attenuation maps with noise suppression, cross-talk and the scale problem. In this work, we evaluated the performance of the proposed MLAA-GMM algorithm with standard 4-class MRAC over a patient population and demonstrated the potential advantage of MRI-guided emission-based AC methods over conventional MRI-guided segmentation based approaches.

II. Material and methods

II.A. PET/MRI and PET/CT clinical data acquisition

In this retrospective clinical study, five patients with head and neck carcinoma were scanned on the Philips Ingenuity TF PET/MRI and the Siemens Biograph mCT flow PET/CT scanners as part of clinical workup. The average age and body mass index of patients were 57 ± 5 years and 24.6 ± 5.1 kg/m², respectively. The patients were injected with an average of 271 ± 9.3 MBq of ¹⁸F-FDG and following a standard uptake time of 60 minutes during which various MR sequences are acquired, underwent a whole-body PET/MRI scan with arms-down position. After an interval of 10-20 minutes, the patients underwent a complementary PET/CT imaging of 10-12 minutes also with arms-down position. MRI acquisition was performed on the Achieva 3T MRI subsystem of the PET/MRI scanner. A whole-body scan was acquired in shallow breathing mode using a 3D multi-echo FFE Dixon technique using the following parameters: TR = 5.7 ms, TE1/TE2 = 1.45/2.6, flip angle = 10° and slice thickness of 3 mm, matrix size of 680 × 680. PET/CT scanning was performed in continuous bed motion mode with bed speed of 1.1 mm/sec, equivalent to 3 minutes per bed position in step and shoot mode. For CT-based attenuation correction (CTAC) of PET data, a multi-slice CT scan protocol was performed using the following parameters: 100-120 kVp, 150 mAs and 5 mm slice thickness. Supplemental Figure 1 shows a flowchart of acquisition protocol used in this study. The TOF PET data of the mCT scanner was used for joint reconstruction of activity and attenuation maps and the anatomical MR images acquired on the Ingenuity PET/MRI scanner were used for MRI-guided MLAA and 4-class MRAC methods. In-phase (IP) MR images were deformably registered to CT images using the Elastix software [20], with 5-level multi resolution registration and Mattes mutual information criterion. The resulting transformation fields were then used for registration of fat and water images.

II.B. Attenuation map generation

II.B.1 MRI-guided emission-based attenuation map

In the framework of the maximum likelihood estimation, the MLAA algorithm jointly estimates activity (λ) and attenuation (μ) maps by maximization of the Poisson log-likelihood of time-of-flight PET emission data, i.e.

$$(\hat{\lambda}, \hat{\mu}) = \operatorname{argmax}_{\lambda \geq 0, \mu \geq 0} \left\{ \sum_{it} g_{it} \log \left(n_i a_i \sum_j c_{ijt} \lambda_j + \bar{b}_{it} \right) - n_i a_i \sum_j c_{ijt} \lambda_j + \bar{b}_{it} \right\} \quad \text{Eq. 1}$$

where g_{it} is the number of prompt coincidences measured by the PET scanner along line-of-response (LOR) i in TOF bin t ; \bar{b}_{it} is the expected number of random and scattered coincidences; n_i is detector normalization factors; $a_i = \exp(-\sum_j l_{ij} \mu_j)$ is attenuation factors; c_{ijt} is the geometric probability detection of annihilation events emitted from voxel j along LOR i in TOF bin t and l_{ij} is the intersection length of LOR i with voxel j in millimeters. Since the activity and attenuation variables are coupled in Eq. (1), the MLAA algorithm follows an iterative alternating maximization approach [16]. In this approach, the algorithm alternates between an emission and a transmission maximum likelihood image reconstruction problem, which are respectively solved by a TOF ordinary Poisson ordered subset expectation maximization (OSEM) algorithm and a non-TOF ordered subset maximum likelihood for transmission tomography (OS-MLTR) algorithm. In the proposed MLAA-GMM algorithm, we employed a transmission maximum-a-posteriori (MAP) image reconstruction for estimation of attenuation by exploiting a Markov random field smoothness function (R_{MRF}) and a mixture of Gaussians model (R_{GMM}), defined as follows:

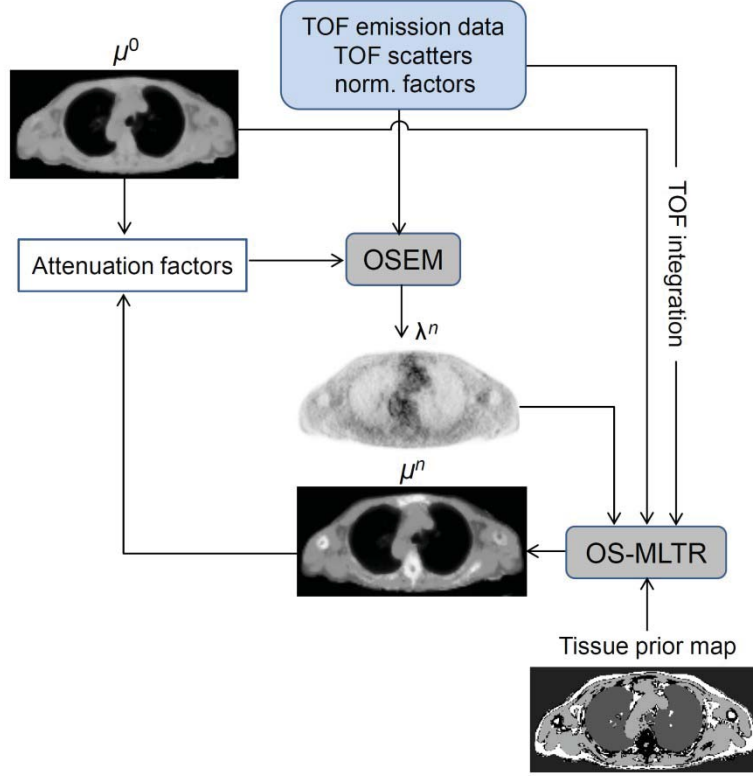


Figure 1. Flowchart of the MLAA-GMM algorithm, which alternates between an OSEM activity reconstruction and an OS-MLTR attenuation reconstruction. The algorithm is initialized by a 4-class MRAC attenuation map and MRI-based scatter sinograms. The GMM model is spatially constrained by the tissue prior map.

$$R_{MRF}(\mu) = -\beta \sum_j \sum_{k \in N_j} \frac{\omega_{jk}}{2} (\mu_k - \mu_j)^2 \quad \text{Eq. 2}$$

$$R_{GMM}(\mu) = \gamma \sum_j \log \left\{ \sum_{h=1}^H \frac{\rho_h}{\sqrt{2\pi}\sigma_h} \exp \left(-\frac{1}{2} \left(\frac{\mu_j - \bar{\mu}_h}{\sigma_h} \right)^2 \right) \right\} \quad \text{Eq. 3}$$

R_{MRF} favors attenuation maps that are smooth based on the weighted (ω) differences between voxel j and its neighboring voxels in the neighborhood N_j . R_{GMM} models the statistical distribution (histogram) of linear attenuation coefficients (LACs) in attenuation maps at 511-keV as a mixture of H known Gaussian functions with mean $\bar{\mu}_h$, standard deviation σ_h and mixture proportion ρ_h [21]. The parameters β and γ weight the impact of the penalty functions. In the proposed MLAA-GMM algorithm, the R_{GMM} is iteratively approximated using a convex surrogate and spatially constrained by MRI anatomical information using a tissue prior map. This prior map contains known and unknown tissue classes, over which uni-modal Gaussians and a mixture of Gaussians are respectively imposed on the estimation of LACs during OS-MLTR algorithm. Figure 1 presents the flowchart of the proposed MLAA-GMM algorithm. In this work, the algorithm was initialized by a uniform activity map and a 4-class MRAC map.

For generation of the tissue prior map (Figure 2), Dixon water and fat MR images are segmented into 4 known tissue classes including fat, soft tissue, lungs and background air, and an additional unknown tissue class corresponding to the regions with low MR intensity (i.e. cortical bones, air pockets and metal induced susceptibility artifacts). Due to partial volume averaging and incomplete Dixon water and fat separation, spongy bones might possess moderate MR intensities in water images and therefore be classified as known soft and fat tissue classes instead of the unknown class. To eliminate this misclassification, we subtracted the fat from water images and used a bone probability map, obtained from a co-registered average CT, to insure the inclusion of bones into the unknown class. The soft-tissue class was segmented by thresholding the fat-suppressed water images. The fat class was defined based on the voxels of the fat image whose intensities are 50% larger than the water image. The lungs and background air were segmented from IP MR images using a supervised seeded region-growing method implemented in the ITK-SNAP software [22]. In the proposed MLAA method, a mixture

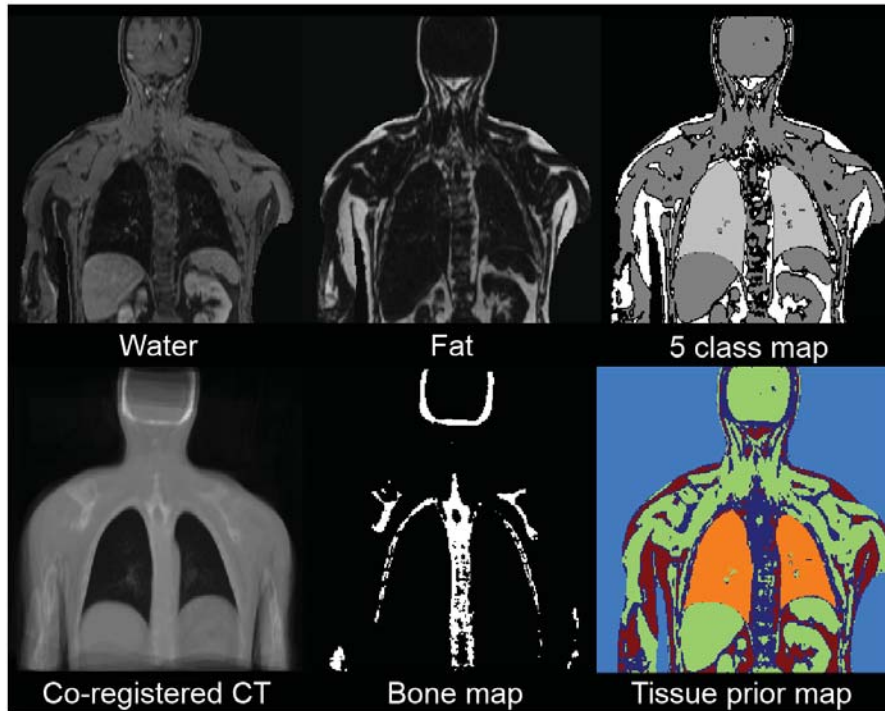


Figure 2. Derivation of the tissue prior map. Fat and water Dixon images are segmented into background air, fat, soft tissue, lungs and a low-intensity class (5-class). The possible position of bones is determined from a co-registered average CT image.

of 4 Gaussians representing inside air, fat/soft mixture and bone was used to guide the attenuation estimation over the unknown tissue class. The parameters of the mixture model and uni-modal Gaussians were estimated from 10 whole-body CTAC maps [19]. Supplemental Figure 2 presents the estimated parameters.

II.B. 2 MRI-guided segmentation-based attenuation map

Standard 4-class MRAC maps were derived by segmenting the Dixon water and fat images into 4 tissue classes: background air, lung, fat, and non-fat soft tissues. The background air, lungs and fat tissue classes were obtained with the same procedure used for deriving the tissue prior map. The non-fat soft tissue class was then defined as the complement of the segmented classes. In this procedure, all bones, air pockets and susceptibility artifacts are assigned to the non-fat soft tissue class. Mean attenuation coefficients of 0, 0.0224, 0.0864 and 0.0975 cm^{-1} were assigned to background air, lungs, fat and non-fat soft tissue classes, respectively. The CT bed attenuation map was also added to the resulting MRAC maps.

II.B. 3 CT-based attenuation map

For comparison of the MLAA and MRAC methods against a reference attenuation correction method, CT-based attenuation maps were generated for each patient using Siemens e7 tools. High-resolution CT images were down-sampled to a resolution of 400×400. CT Hounsfield units were then converted to 511 keV attenuation values using a kVp-dependent bilinear mapping approach. The resulting maps were finally smoothed to the resolution of PET images using 4-mm FWHM isotropic Gaussian filtering.

II.C. PET image reconstruction

TOF PET data acquired on the mCT PET/CT scanner were reconstructed using a 3D time-of-flight OSEM algorithm with 3 different AC methods: MRI-guided emission-based, MR-guided segmentation-based and CT-based. PET images were reconstructed with 3 iterations and 21 subsets and a matrix size of 200×200 with 4×4×2 mm^3 voxels. For the MLAA-GMM algorithm, an in-house software was developed for the native geometry of the mCT scanner with the following specifications: 400 radial bins, 168 azimuthal angles, 621 planes and 13 TOF bins.

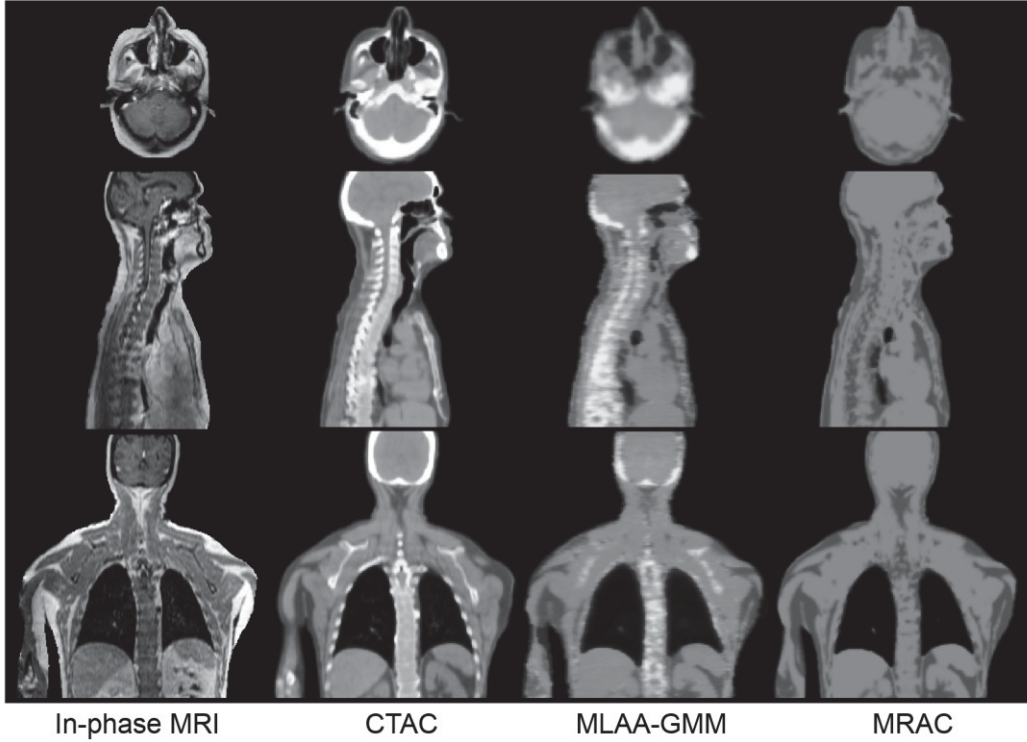


Figure 3. Comparison of 4-class MRAC and MLAA-GMM attenuation maps with their reference CTAC map from a representative ^{18}F -FDG PET/CT/MRI study. The display window is $0.08 \pm 0.055 \text{ cm}^{-1}$.

The coincidence window width and effective TOF resolution of the scanner are 4.1 and 0.58 ns, respectively. The activity and attenuation maps were reconstructed with 1 iteration and 2 subsets of the OSEM algorithm and 1 iteration and 3 subsets of the OS-MLTR algorithm with 20 global iterations. As mentioned above, the algorithm was initialized with a 4-class MRAC map with a TOF scatter simulated using the same MRAC map. Based on our previous work [19], the β and γ parameters (in Eqs. 2 and 3) were experimentally set to 80 and 0.015, respectively. The estimated attenuation maps were then used for a standard OSEM PET image reconstruction.

II.D. Quantitative evaluation

The relative quantification error (bias) in the standardized tracer uptake (SUV) was calculated on a volume of interest (VOI) basis for each patient with respect to the reference CTAC-PET as follows:

$$Bias = 100 \times \frac{SUV_m - SUV_{CTAC}}{SUV_{CTAC}} \quad \text{Eq. 4}$$

where m is the attenuation correction method used (MLAA or MRAC). For each patient, 14 VOIs were defined on normal tissue regions including the lungs (upper, middle and lower portions of left and right lungs), aorta, liver, myocardium, thyroid, cerebrum, 4th cervical (C4), 3rd thoracic (T3) and 4th lumbar (L4) vertebra. VOIs were also defined on lesions localized on CTAC-PET images. For the defined VOIs, the mean (μ), standard deviation (σ) and root-mean-squared error (RMSE) of bias ($\sqrt{\mu^2 + \sigma^2}$) was calculated. The correlation between SUV_{MRAC} and SUV_{MLAA} and reference SUV_{CTAC} was determined using Pearson correlation analysis. The concordance between the SUVs was evaluated using Bland-Altman plots. The statistical differences in SUV bias was also calculated using the paired-sample t -test. The differences were considered statistically significant for $P < 0.05$.

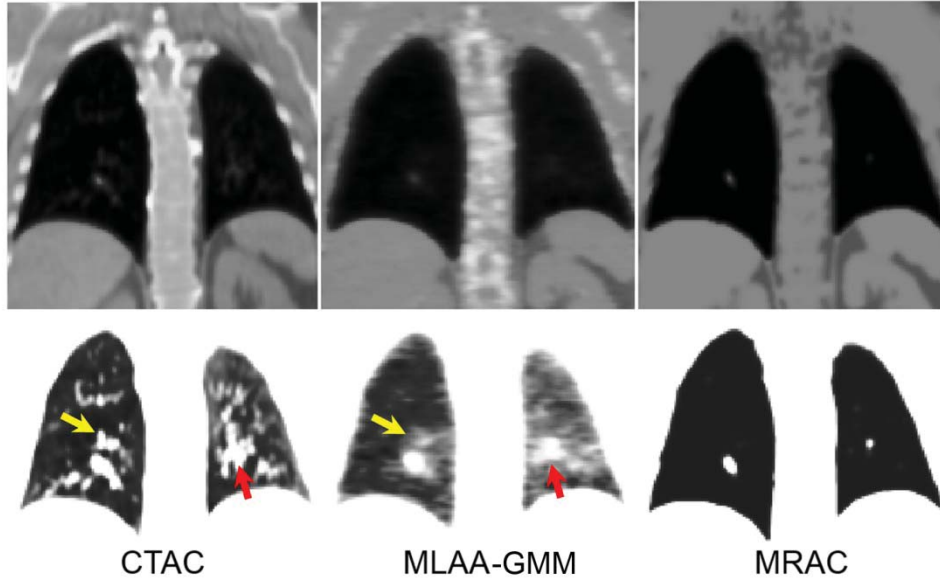


Figure 4. Close-up views of the lungs in different displaying windows. Top: $0.08 \pm 0.055 \text{ cm}^{-1}$, bottom: $0.03 \pm 0.03 \text{ cm}^{-1}$.

III. Results

Figure 3 compares the CTAC map of a representative patient with the attenuation maps obtained using the proposed MLAA-GMM algorithm and the 4-class MRAC method. As shown, the MLAA-GMM algorithm can reasonably well estimate the attenuation coefficients of bones and discriminate air cavities, particularly paranasal sinuses. In contrast, the bones and air gaps in the MRAC maps are simply replaced by soft tissue, which can lead to quantification errors in the reconstructed PET images. Figure 4 shows the close-up views of the attenuation maps over the lungs in different displaying windows. The CTAC map shows that the lungs of this patient have a congested structure especially in the left lung. As indicated by the arrows, some of the condensed soft tissue structures in the MRAC map have been erroneously segmented into lung tissue class, whereas the MLAA-GMM algorithm compensates for the mis-segmentation of these structures and also retrieves lung density gradients. Note that because of respiratory motion of the lungs during PET acquisition and count-dependent performance of the MLAA algorithm, the estimated attenuation coefficients cannot preserve all local details. For this dataset, the lung attenuation coefficients of the CTAC, MLAA and MRAC attenuation maps, filtered by a 4-mm FWHM Gaussian filter, were 0.0293 ± 0.0077 , 0.0301 ± 0.0075 , $0.0225 \pm 0.0003 \text{ cm}^{-1}$, respectively. Supplemental Figure 3 compares the attenuation maps of another patient study, where the MLAA-GMM algorithm also compensates for a mis-segmented pathology and accurately retrieves the lung density gradient in a continuous fashion. Figure 5 shows activity and attenuation maps of another study in which the MLAA algorithm also compensated for respiratory phase-mismatch between activity and attenuation maps. As pointed by the arrow, the uptake at the upper lobe of the liver has been underestimated by CTAC and MRAC methods due to under-correction of attenuation. As shown on the attenuation maps and profiles, the MLAA algorithm estimates correctly the underlying attenuation experienced by the emission data and therefore increases liver uptake, thus improving the detection and quantification of possible upper-lobe lesions.

Table 1 compares the mean \pm standard deviation of linear attenuation coefficients of different tissue classes of the CTAC, MLAA and MRAC attenuation maps calculated over all patient datasets. For these class-wise calculations, the lung, fat and soft tissue classes were obtained from the tissue prior map built for each patient (see Figure 2). The bone class was derived by thresholding CTAC images at 0.109 cm^{-1} . As can be seen, the main difference between MLAA and MRAC methods sits over the lungs and bones, for which the maximum PET quantification errors occurs when using standard MRAC methods. The results show that the MLAA-GMM algorithm outperforms the MRAC method over these tissue classes by estimating mean and standard deviation of LACs which are closer to those of the reference CTAC method. The proposed method, however, slightly over- and under-estimates the mean of the LACs of lungs and bones. In fat and soft tissue classes, both MLAA and

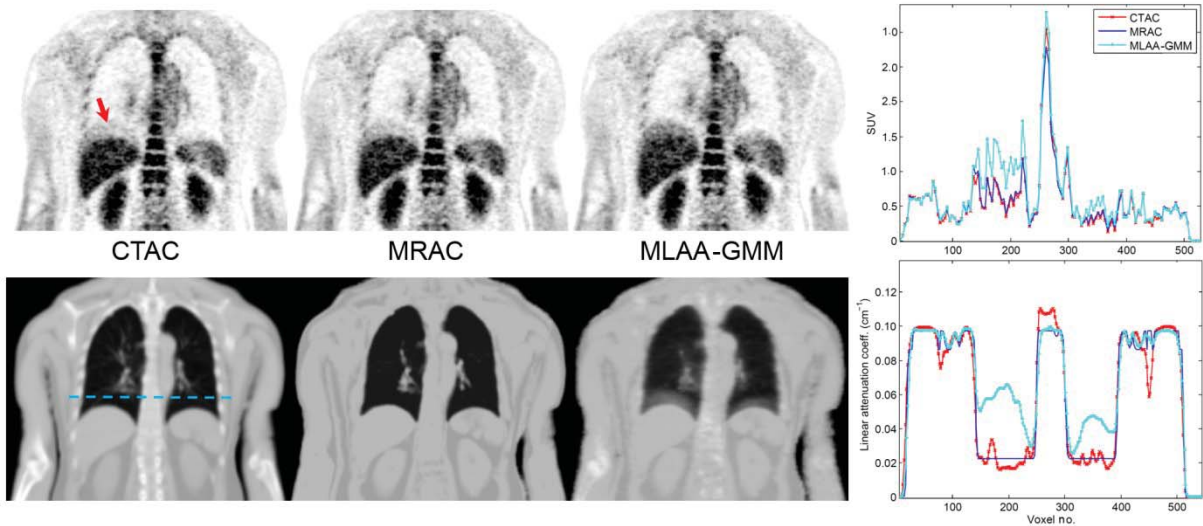


Figure 5. PET images and attenuation maps of a patient presenting with respiratory-phase mismatch between PET and CT/MRI acquisitions. The activity and attenuation profiles along the dashed line shown on the CTAC attenuation map are also shown.

Table 1. Mean \pm standard deviation of LACs of different tissue classes of CTAC, MLAA and MRAC attenuation maps calculated over all clinical studies.

	Lung	Fat	Soft tissue	Bone
CTAC	0.025 ± 0.009	0.087 ± 0.009	0.098 ± 0.008	0.118 ± 0.012
MLAA	0.027 ± 0.008	0.086 ± 0.010	0.097 ± 0.006	0.104 ± 0.012
MRAC	0.022 ± 0.001	0.086 ± 0.004	0.097 ± 0.001	0.095 ± 0.005

MRAC attenuation maps have a similar mean as the CTAC maps, while the standard deviations of only MLAA's LACs are close to those of CTAC maps.

The quantitative PET performance of MRI-guided attenuation correction methods was further evaluated in comparison with the CTAC method using VOI-based analysis. Table 2 summarizes the mean, standard deviation and root-mean-squared error of SUV_{mean} bias in VOIs defined in normal tissue and lesions. Figure 6(A) shows the errors in each VOI, grouped for the lung and soft tissue organs, while Figure 6(B) shows the results for VOIs defined on bones or soft tissues located close to bones. In this figure, the markers show the mean of bias in each VOI, while the horizontal bars and vertical boxes indicate the mean and two-standard deviations of the bias between VOIs in each region. The results show that the MLAA-GMM algorithm generally gives rise to a reduced RMSE bias over all regions. For VOIs defined in the lungs ($n = 30$), the MRAC method underestimates SUV_{mean} by $-5.4 \pm 12.0\%$ with a RMSE of 13.1%, while MLAA-GMM reduces the errors to $-3.5 \pm 6.6\%$ with a RMSE of 7.5%. For the total VOIs defined on the aorta, myocardium, liver and thyroid ($n = 20$), MRAC and MLAA-GMM methods resulted in average SUV errors of $-7.0 \pm 6.6\%$ (9.6% RMSE) and $-4.9 \pm 5.5\%$ (7.4% RMSE), respectively. Over the lesions ($n = 11$), which were mainly mediastinal lymphoma, the MLAA-GMM reduced the errors from $-9.0 \pm 5.4\%$ with RMSE of 10.5% to $-4.5 \pm 5.3\%$ with RMSE of 7.0%. Finally, for all regions in or near bones ($n = 20$), the MRAC and MLAA algorithms resulted in an average SUV error of $-18.4 \pm 7.9\%$ (20.0% RMSE) and $-10.2 \pm 6.5\%$ (12.1% RMSE), respectively. The statistical analysis revealed that there is an overall significant difference ($P < 0.05$) between the proposed MLAA-GMM and MRAC methods in bones, malignant lesions and most soft tissue regions. The results also showed that the bias differences in the lungs are insignificant.

The SUV correlation and concordance of the MLAA and MRAC methods with reference CTAC was further evaluated. Figure 7 (top panel) shows the scatter plots of the SUV_{mean} in all studied VOIs between PET-CTAC, PET-MRAC and PET-MLAA with correlation and regression coefficients. The results show that PET-MLAA and PET-MRAC are highly correlated with PET-CTAC with R^2 values of 0.982 and 0.992, respectively. Figure 7 (bottom panel) shows the results of Bland-Altman concordance analysis. The limits of agreement (LA) were calculated from logarithmically transformed values. Differences and LA are expressed as a function of average

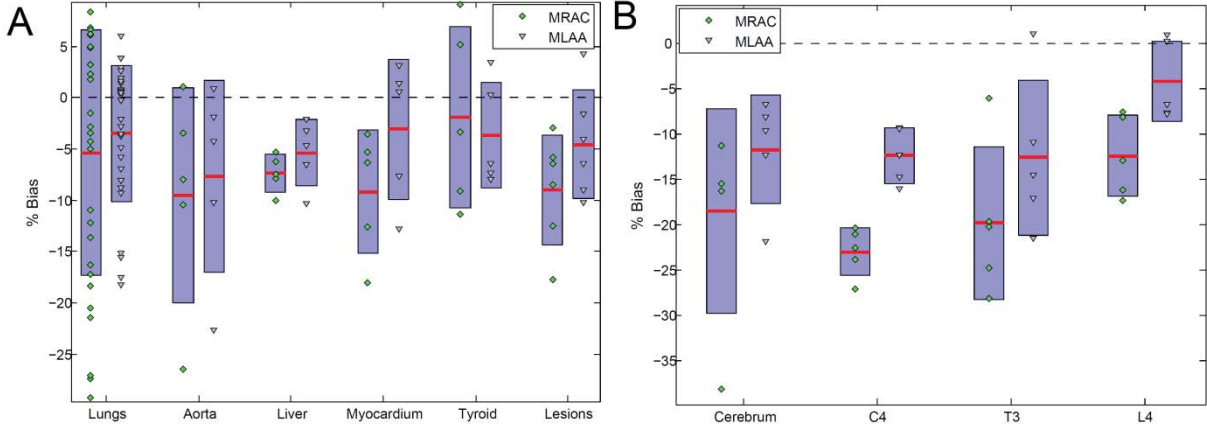


Figure 6. Mean SUV errors between PET-MRAC and PET-MLAA with respect to reference PET-CTAC images in VOIs defined on (A) normal tissues and lesions, and (B) in/near bones. Means and 2 standard deviations are indicated by horizontal bars and vertical boxes, respectively.

Table 2. Quantification bias [Mean \pm SD, (RMSE)%] of PET-MRAC and PET-MLAA in different tissues with respect to PET-CTAC used as reference.

VOI	MRAC	MLAA	P-value
Lung	-5.4 ± 12.0 (13.1)	-3.5 ± 6.6 (7.5)	0.1605
Aorta	-9.5 ± 10.5 (14.1)	-7.6 ± 9.3 (12.1)	0.0942
Liver	-7.4 ± 1.8 (7.6)	-5.4 ± 3.2 (6.3)	0.0376
Myocardium	-9.2 ± 6.0 (11.0)	-3.1 ± 6.8 (7.5)	0.0027
Thyroid	-1.9 ± 8.8 (9.0)	-3.6 ± 5.1 (6.3)	0.6574
Lesions	-9.0 ± 5.4 (10.5)	-4.5 ± 5.3 (7.0)	0.0237
Cerebrum	-18.5 ± 11.3 (21.6)	-11.6 ± 6.0 (13.1)	0.0503
C4	-22.9 ± 2.7 (23.1)	-12.3 ± 3.1 (12.7)	0.0011
T3	-19.8 ± 8.4 (21.5)	-12.6 ± 8.6 (15.2)	<0.001
L4	-12.4 ± 4.5 (13.2)	-4.2 ± 4.4 (6.1)	<0.001

SUVs. As shown by the regression lines of the difference, MRAC and MLAA attenuation correction methods result in a systematic underestimation of SUV by up to 9.85% and 6.75%, respectively. However, MLAA clearly outperforms MRAC by reducing the errors and their dispersion.

IV. Discussion

Interest in the estimation of PET attenuation maps from emission data has recently been revived in the context of TOF PET/MRI attenuation correction to overcome the limitations and quantification errors of standard segmentation-based MRAC methods [18, 19]. In this work, we compared the performance of our previously reported MLAA algorithm with the standard MRAC method to demonstrate the potential of emission-based AC methods in TOF PET/MRI imaging.

In segmentation-based MRAC methods, the mis-segmentation of the lungs and the assignment of non patient-specific lung attenuation coefficients can result in PET quantification errors. Our results demonstrated that, consistent with previously reported results [23], the MRAC method results in errors in the lungs of up to 26% (Figure 6). Due to their low proton density and short T_2^* relaxation time, the lungs show low signal intensity in the fast gradient-recalled echo (GRE) pulse sequences conventionally used in whole-body MRI acquisitions. Therefore, in conjunction with the limitations of segmentation-based MRAC algorithms, the soft tissue structures of the lungs, for example, pulmonary vessels and bronchioles, might be miss-segmented into lung class. Our results showed that the MLAA-GMM algorithm not only fairly compensates for the mis-segmentations but also derives more patient-specific lung LACs (Figure 4 and Supplemental Figure 3). Hence, as reported in Table 2, the RMSE in the lungs was reduced from 13.1% to 7.5%. In contrary to Salomon *et al* [18],

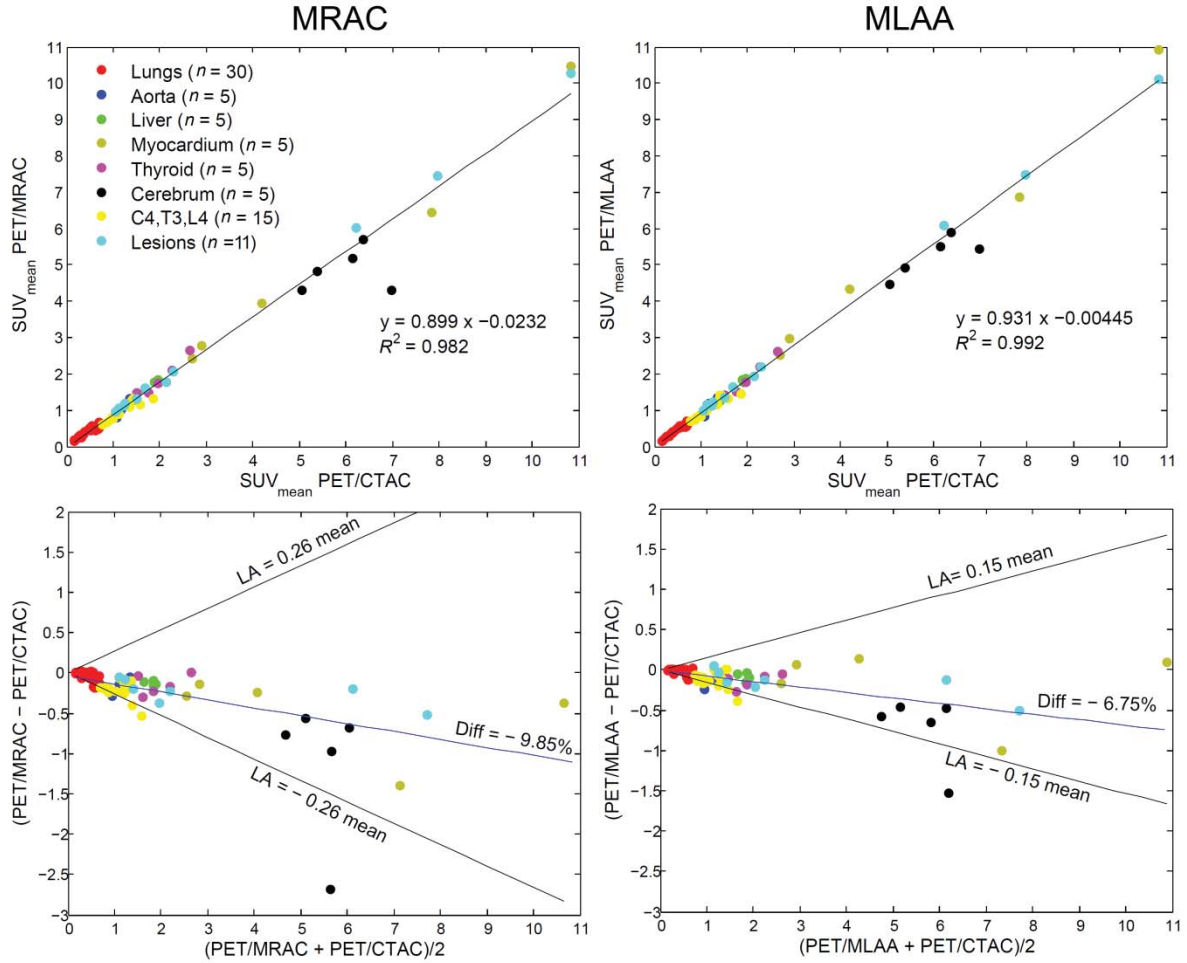


Figure 7. (Top) Scatter plots between the SUV_{mean} of PET images reconstructed using CTAC, MLAA-GMM and MRAC attenuation correction methods. (Bottom) SUV_{mean} Bland-Altman concordance plots.

our proposed MLAA estimates continuous attenuation coefficients and thus retrieves the lung density gradients and intra-patient variability of lung attenuation coefficients. Continuous lung LACs can also be derived from atlas-registration-based AC methods. However, these approaches had a limited success owing to the low signal of the lungs [10].

Another limitation of segmentation-based MRAC is that the identification of bones, which produce low signal intensity in GRE MRI pulse sequences, is very challenging. In 4-class MRAC maps, the bones are replaced by soft tissue, which based on our results can lead to a mean bias of -18.4% , which is consistent with the $>15\%$ errors reported previously [9, 23]. As demonstrated in this work, the proposed MLAA-GMM algorithm is capable of estimating bone attenuation coefficients, thus outperforming the MRAC method by reducing the mean error to -10.2% . Bezrukov *et al.* reported that a combination of segmentation and atlas-registration based AC methods can effectively reduce bone SUV errors of the 4-class MRAC from -16.1% to -4.7% [8]. However, the performance of these techniques depends on accurate atlas registration and robust prediction of attenuation coefficients. In contrast, several CT images are registered to patient's IP MR image in our MRI-constrained MLAA algorithm to only roughly indicate the position of the bones. Therefore, this technique is in principle not subjected to mis-registration errors.

As indicated in Supplemental Figure 2, we set the means of Gaussian models defined in known tissue classes to the mean LACs used in the 4-class MRAC maps. Therefore, for very high values of the γ parameter in Eq. 3, the MLAA-GMM is essentially reduced to a 4-class MRAC method. The results show that the MLAA and MRAC methods present similar mean LACs in fat and soft tissue classes (Table 1); however, only for MLAA the standard deviation (inter/intra-variability) of LACs are similar to the reference CTAC method. Combined

with more accurate derivation of lung and bone LACs, our MLAA-GMM approach resulted in improved quantitative performance over soft tissue organs compared with the MRAC method (Table 2).

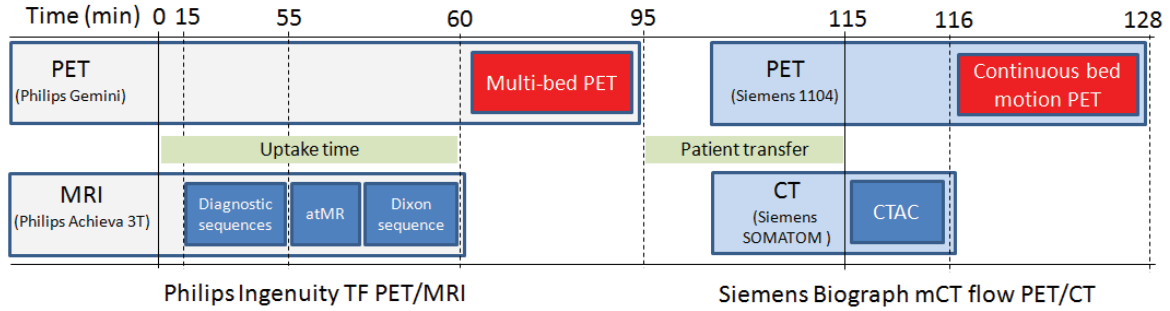
The results of this feasibility study demonstrate the potential of the emission-based AC methods for accurate attenuation correction in TOF PET/MRI. However, it is worth highlighting the limitations of the proposed algorithm and the study conducted herein. Similar to other MAP reconstruction techniques, the performance of the MLAA-GMM depends on the selection of the regularization parameters, especially the γ parameter of the GMM model. In this work, we set the γ and the β parameter in Eq. 2 to experimentally optimized values for a few simulation and clinical studies [19]. In general, the MLAA algorithm is time consuming since it alternates between an emission and transmission tomographic reconstruction. The preparation of a tissue prior map can further increase the computational burden of the proposed MLAA-GMM method. In this first clinical study, a relatively small number of PET/MR/CT datasets could be included. Therefore, the statistical significance of our results might be subject to a degree of uncertainty. Future work will focus on further evaluation of the studied AC methods using a large clinical patient database acquired with different tracers to pave the way for translation of emission-based AC methods into the clinic.

V. Conclusion

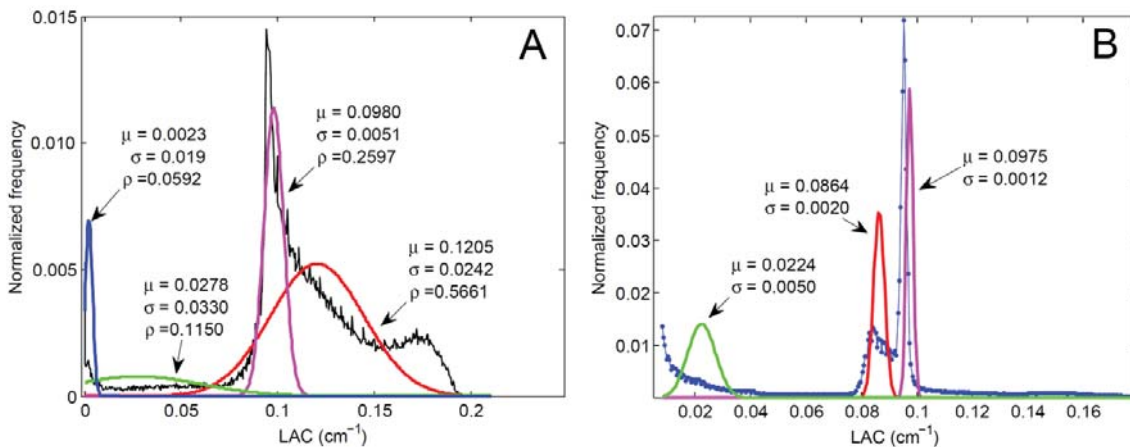
In this work, the performance of an MRI-guided emission-based AC method was compared with the standard segmentation-based MRAC method using clinical studies. It was demonstrated that the proposed constrained MLAA algorithm is promising for deriving patient-specific attenuation maps, especially in the lungs and bones. Our results showed that the MRAC method resulted in average SUV errors of -5% and -18% in the lungs and bones, while the proposed algorithm reduced the errors to -3% and -10% , respectively. It can be concluded that emission-based attenuation correction is promising in clinical TOF PET/MRI imaging and presents the potential to replace conventional segmentation-based methods implemented on commercial systems.

Acknowledgments

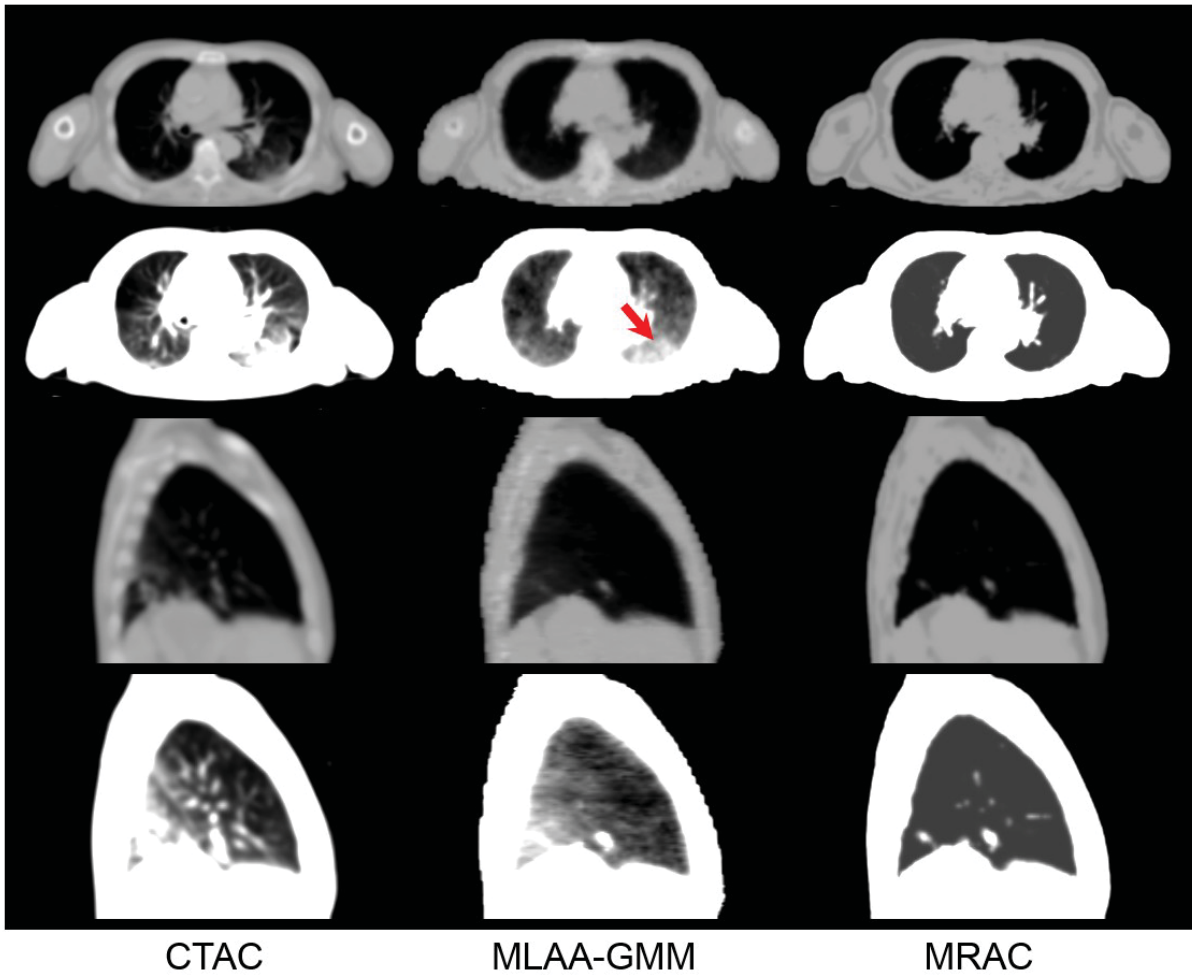
This work was supported in part by the Swiss National Science Foundation under Grant SNSF 31003A-149957 and the Indo-Swiss Joint Research Programme ISJRP-138866



SUPPLEMENTAL FIGURE 1. Diagram of the data acquisition protocol for PET/MRI and complementary PET/CT scans. During the uptake period, the patients undergo various diagnostic MRI scans (40-min) followed by a Dixon and Philips atMR sequences (about 2.5 min each), the latter being used for attenuation correction of the PET data. A 30 min whole-body PET scan is then followed. After the patient transfer time of 10-20 min, a head and neck complementary PET/CT scan is acquired for about 13 min.



SUPPLEMENTAL FIGURE 2. (A) The estimated mean (μ), standard deviation (σ), and mixture proportion (ρ) parameters of the Gaussian mixture model used in this work. The parameters were obtained from 10 whole-body CTAC maps (5 males and 5 females) using an expectation maximization algorithm. (B) The uni-modal Gaussians used for the known fat, non-fat soft and lung tissue classes are overlaid on the histogram of attenuation coefficients of a single patient dataset. Note that in this study, we set the means of uni-modal Gaussians to those of tissue attenuation coefficients used in the standard 4-class MRI-guided attenuation correction.



SUPPLEMENTAL FIGURE 3. Comparison of attenuation maps produced by the standard 4-class MRI-based method (MRAC) and the MLAA algorithm with the reference CTAC maps in two different displaying windows. Note the improvement brought by the MLAA approach.

References

- [1] D. A. Torigian, H. Zaidi, T. C. Kwee, B. Saboury, J. K. Udupa, Z.-H. Cho, and A. Alavi, "PET/MR Imaging: Technical aspects and potential clinical applications," *Radiology*, vol. 267, no. 1, pp. 26-44, 2013.
- [2] I. Bezrukov, F. Mantlik, H. Schmidt, B. Scholkopf, and B. J. Pichler, "MR-Based PET attenuation correction for PET/MR imaging," *Semin Nucl Med*, vol. 43, no. 1, pp. 45-59, Jan, 2013.
- [3] V. Keereman, Y. Fierens, T. Broux, Y. De Deene, M. Lonneux, and S. Vandenberghe, "MRI-based attenuation correction for PET/MRI using ultrashort echo time sequences," *J Nucl Med*, vol. 51, no. 5, pp. 812-8, 2010.
- [4] K. Zeimpekis, G. Delso, F. Wiesinger, P. Veit-Haibach, G. von Schulthess, and R. Grimm, "Investigation of 3D UTE MRI for lung PET attenuation correction," *J Nucl Med*, vol. 55, no. Supplement 1, pp. 2103, 2014.
- [5] A. Martinez-Möller, M. Souvatzoglou, G. Delso, R. A. Bundschuh, C. Chefd'hotel, S. I. Ziegler, N. Navab, M. Schwaiger, and S. G. Nekolla, "Tissue classification as a potential approach for attenuation correction in whole-body PET/MRI: evaluation with PET/CT data," *J Nucl Med*, vol. 50, no. 4, pp. 520-526, 2009.
- [6] H. Zaidi, N. Ojha, M. Morich, J. Griesmer, Z. Hu, P. Maniawski, O. Ratib, D. Izquierdo-Garcia, Z. A. Fayad, and L. Shao, "Design and performance evaluation of a whole-body Ingenuity TF PET-MRI system," *Phys Med Biol*, vol. 56, no. 10, pp. 3091-3106, Apr 20, 2011.
- [7] I. Bezrukov, H. Schmidt, F. Mantlik, N. Schwenzer, C. Brendle, B. Schölkopf, and B. J. Pichler, "MR-based attenuation correction methods for improved PET quantification in lesions within bone and susceptibility artifact regions," *J Nucl Med*, vol. 54, no. 10, pp. 1768-1774, 2013.
- [8] H. Arabi, O. Rager, A. Alem, A. Varoquaux, M. Becker, and H. Zaidi, "Clinical assessment of MR-guided 3-class and 4-class attenuation correction in PET/MR," *Mol Imaging Biol*, Aug 6, 2014.
- [9] M. Hofmann, F. Steinke, V. Scheel, G. Charpiat, J. Farquhar, P. Aschoff, M. Brady, B. Schölkopf, and B. J. Pichler, "MRI-based attenuation correction for PET/MRI: a novel approach combining pattern recognition and atlas registration," *J Nucl Med*, vol. 49, no. 11, pp. 1875-1883, 2008.
- [10] B. K. Navalpakkam, H. Braun, T. Kuwert, and H. H. Quick, "Magnetic resonance-based attenuation correction for PET/MR hybrid imaging using continuous valued attenuation maps," *Invest Radiol*, vol. 48, no. 5, pp. 323-32, May, 2013.
- [11] S. Surti, "Update on Time-of-Flight PET Imaging," *J Nucl Med*, vol. 56, no. 1, pp. 98-105, Jan, 2015.
- [12] P. Mollet, V. Keereman, J. Bini, D. Izquierdo-Garcia, Z. A. Fayad, and S. Vandenberghe, "Improvement of attenuation correction in time-of-flight PET/MR imaging with a positron-emitting source," *J Nucl Med*, vol. 55, no. 2, pp. 329-36, Feb, 2014.
- [13] H. Rothfuss, V. Panin, A. Moor, J. Young, I. Hong, C. Michel, J. Hamill, and M. Casey, "LSO background radiation as a transmission source using time of flight," *Phys Med Biol*, vol. 59, no. 18, pp. 5483-500, 2014.
- [14] J. Nuyts, P. Dupont, S. Stroobants, R. Benninck, L. Mortelmans, and P. Suetens, "Simultaneous maximum a posteriori reconstruction of attenuation and activity distributions from emission sinograms," *IEEE Trans Med Imaging*, vol. 18, no. 5, pp. 393-403, 1999.
- [15] A. Rezaei, M. Defrise, G. Bal, C. Michel, M. Conti, C. Watson, and J. Nuyts, "Simultaneous reconstruction of activity and attenuation in Time-of-Flight PET," *IEEE Trans Med Imaging* vol. 31, no. 12, pp. 2224-33, 2012.
- [16] M. Defrise, A. Rezaei, and J. Nuyts, "Time-of-flight PET data determine the attenuation sinogram up to a constant," *Phys Med Biol*, vol. 57, no. 4, pp. 885-899, Feb, 2012.
- [17] A. Salomon, A. Goedicke, B. Schweizer, T. Aach, and V. Schulz, "Simultaneous reconstruction of activity and attenuation for PET/MR," *IEEE Trans Med Imaging*, vol. 30, no. 3, pp. 804-813, 2011.
- [18] A. Mehranian, and H. Zaidi, "Joint estimation of activity and attenuation in PET/MR using MR-constrained Gaussian priors."
- [19] S. Klein, M. Staring, K. Murphy, M. A. Viergever, and J. P. Pluim, "Elastix: a toolbox for intensity-based medical image registration," *IEEE Trans Med Imaging*, vol. 29, pp. 196-205, 2010.

- [20] J. M. M. Anderson, K. Yoon-Chul, and J. T. Votaw, "Concurrent segmentation and estimation of transmission images for attenuation correction in positron emission tomography.," *IEEE Trans Nuc Sci*, vol. 56, no. 1, pp. 136-146, 2009.
- [21] P. A. Yushkevich, J. Piven, H. C. Hazlett, R. G. Smith, S. Ho, J. C. Gee, and G. Gerig, "User-guided 3D active contour segmentation of anatomical structures: significantly improved efficiency and reliability," *Neuroimage*, vol. 31, no. 3, pp. 1116-28, 2006.
- [22] V. Keereman, R. V. Holen, P. Mollet, and S. Vandenberghe, "The effect of errors in segmented attenuation maps on PET quantification," *Med Phys*, vol. 38, no. 11, pp. 6010-9, Nov, 2011.

Chapter 12

Conclusions and future perspectives

I. Conclusions

Hybrid dual-modality PET/CT and PET/MRI imaging systems have provided new opportunities for enhancing the diagnostic confidence of PET findings as well as facilitating patient management and treatment. The combination of different imaging modalities, however, necessitates innovative and cutting-edge technologies to tackle the challenges encountered in instrumentation, data acquisition and quantitative performance, thus enabling to realize the potential of hybrid imaging. This dissertation presents original contributions focusing on the development and validation of new algorithms that provide practical and robust solutions for the most prevalent challenges and limitations of image reconstruction and quantitative procedures in hybrid PET/CT and PET/MRI. To this end, the main contributions accomplished during this dissertation are summarized in the following:

- 1) Development of robust metal artifact reduction algorithms for improving image quality of diagnostic CT images and CT-derived attenuation maps in 3D cone-beam CT and PET/CT imaging. The recovery of the CT projections corrupted by metallic implants was formulated as a regularized inverse problem. The sparsity regularization techniques and the prior information obtained from a tissue-classified CT images and prior image were utilized in the estimation of the missing projection data. A poly-chromatic CT simulator was developed to objectively evaluate the performance of the proposed MAR algorithms with respect to an artifact-free ground truth CT image. The objective and subjective evaluation of the proposed algorithms against current standard and state-of-the-art algorithms in simulation and clinical studies showed that the proposed algorithms are promising and can effectively reduce artifacts independent of the size and position of metallic implants. It was also demonstrated that the proposed algorithms can robustly utilize the information obtained from prior CT images without introducing new artifacts. In addition, the performance of five different MAR algorithms was evaluated in patients with primary hip replacement. This comparative study showed that the proposed 3D MAR and the state-of-the-art NMAR algorithm outperforms the other MAR algorithms for the reduction of artifacts arising from hip prostheses.
- 2) Development and evaluation of an accelerated proximal preconditioned gradient optimization algorithm for anatomically-guided PET image reconstruction based on the penalized weighted least-squares objective function. The algorithm was derived using a proximal splitting technique to reduce the original problem into easy-to-optimize sub-problems. In this algorithm, the dual formulation of edge-preserving total variation (TV) prior was generalized to weighted TV and Huber priors. The proposed algorithm was accelerated with ordered subsets and step size optimization and evaluated for three different preconditioners. It was demonstrated that the proposed algorithm outperforms current state-of-the-art separable paraboloidal surrogates accelerated with ordered subsets.
- 3) Development and derivation of an iteratively reweighted L_1 norm regularization for compressed sensing MR image reconstruction by iterative linearization of the non-convex smoothly clipped absolute deviation (SCAD) regularization. A single-coil CS-MRI acquisition model was considered with three different k -space sampling patterns. The resulting regularized least-squares optimization problem was solved using the alternating direction method of multipliers, and the closed-form solutions were derived for the resulting subproblems for two different sparsifying transforms. It was demonstrated that the linearized SCAD regularization invokes a weighted soft-thresholding rule, associated with L_1 norm regularization that asymptotically approaches a hard thresholding rule associated with L_0 norm regularization. It was found that the linearized SCAD norm possesses promising asymptotic behavior and can outperform the L_1 norm regularization which has been extensively utilized in the context of compressed sensing and sparsity regularization.
- 4) Clinical evaluation of the impact of time-of-flight PET technology on the reduction of PET quantification errors induced by standard MRI segmentation-based attenuation correction (MRAC) used on emerging TOF PET/MR imaging systems. The results of this first clinical study showed that TOF

can substantially reduce quantification errors due to erroneous attenuation maps where bones and heterogeneity of attenuation maps are ignored and the metallic and respiratory-artifacts are present in the maps. To explore the limiting impact of TOF on MRAC PET quantification errors, an in-house TOF-PET simulator was developed for the native geometry of the Siemens mCT PET system. The simulation results further supported the clinical findings, as the timing resolution is improved, the quantification errors are reduced especially over the bones, where the maximum errors occur. It was concluded that MRI-based attenuation correction should be less of a concern on future TOF PET/MR scanners with improved timing resolution.

- 5) Development of a constrained mixture of Gaussian model (GMM) for improving the performance of the maximum likelihood reconstruction of activity and attenuation (MLAA) for TOF PET/MR imaging. Patient-specific multi-class spatial information of MRI as well as statistical information of CT attenuation maps parameterized over a patient population was incorporated into the GMM prior and used to constrain the estimation of the attenuation map in the MLAA framework. The performance of the proposed MLAA algorithm was compared with two current state-of-the-art MLAA algorithms for two different tracer distributions. The results showed that our proposed algorithm outperforms its counterparts in suppressing the cross-talk and scaling problems of activity and attenuation and thus produces PET images of improved quantitative accuracy. It was concluded that the proposed algorithm effectively exploits the MRI information and can pave the way toward accurate emission-based attenuation correction in TOF PET/MRI.
- 6) Development and clinical evaluation of a constrained MLAA algorithm for deriving patient-specific lung attenuation maps in TOF PET/MR imaging using a Gaussian lung tissue preference prior. In this work, only lung attenuation values in the standard 4-class MRAC maps were derived from emission data. It was demonstrated that the proposed MLAA algorithm can retrieve lung density gradients and compensate for respiratory motion artifacts and lung miss-segmentation errors, thus providing a promising and feasible method for deriving patient-specific lung attenuation coefficients from TOF emission data. This study provided a reliable approach for the smooth translation of emission-based attenuation correction methods into clinical TOF PET/MR imaging.
- 7) Clinical comparison of emission- and segmentation-based attenuation correction methods in whole-body TOF PET/MR imaging. In this first clinical study, we demonstrated the potential of the proposed MLAA algorithm as a promising emission-based attenuation correction method in PET/MRI.
- 8) We reviewed the tremendous efforts made during the last decade for developing solutions and algorithms to the challenges encountered in deriving attenuation maps. We categorized the MRAC algorithms in to three generic groups of segmentation-, atlas registration- and emission-based methods. The characteristics, quality and recent advances of each method were then elaborated. In an outlook, we anticipated that (i) the most promising attenuation correction methods will likely be achieved by hybrid techniques combining the three categories of MRAC methods to take advantage of the positive aspects of each class of methods. (ii) Technological advances in time-of-flight PET as well as U/ZTE MRI sequences will progressively continue to respectively provide opportunities in mitigating the adverse effects of inaccurate attenuation correction and deriving more accurate attenuation maps to finally put an end to the research in this field.

II. Future perspectives

The studies presented in this dissertation are linked to the field of multimodal molecular imaging. The continuous technical advances in data acquisition and signal processing has been a driving force in this field, which has opened new opportunities for co-localization of complementary structural and molecular information. Future directions of research should focus on further development and evaluation of the proposed algorithms and methods exploiting advanced technologies in modern dual-modality PET/CT and PET/MR imaging systems.

The metal artifact reduction algorithms proposed in this work were evaluated on a generic projection space obtained from the forward projection of the original uncorrected CT images. Moreover, the corrupted projection data were identified from the forward projection of metallic objects, segmented from the uncorrected images. It has been shown that the identification of the missing projections and their recovery on original scanner-specific CT sinograms is more effective than on generic artificial sinograms. Further evaluation of the proposed algorithms in the native geometry of the scanner is one of the future directions that can better realize the efficiency of the algorithms in clinical datasets. The evaluation of the proposed 3D MAR algorithm for metal artifact reduction in image-guided radiation therapy using 3D cone-beam CT scans is another interesting path. For this task, an on-the-fly forward projector and a statistical iterative algorithm have been developed for the native geometry of the Varian on-board imager (OBI) and will be used in future work. Metal artifact reduction in the case of multiple or large metallic implants where a large amount of data are corrupted is a challenging task. However, the introduction of tissue-classified CT prior images into MAR algorithms has considerably improved their performance. Recently, several manufacturers have released commercial MAR software exploiting the prior images for the suppression of metallic artifacts. Future work might also include the implementation of these multi-step or iterative MAR methods and comparison of their performance with the algorithms proposed in this thesis. The performance of this new generation of MAR algorithms depends on the accuracy of the prior images and their ability to best exploit the prior information for all types of metallic implants without introducing new artifacts. Another possible direction is the development of robust methods for deriving accurate prior images as well as including the modified wavelet coefficients of uncorrected CT images for improving the performance of algorithms and better preserving the anatomical information about metallic implants.

The proposed proximal preconditioned gradient algorithm was targeted for anatomically-guided PET image reconstruction for random-corrected PET data or the data acquired with high count statistics where the statistical variability of measured data can be modeled by a Gaussian distribution. Future work will focus on evaluating the proposed algorithm using a large PET/MRI clinical dataset and compare its performance with other maximum a posteriori algorithms. Nowadays, in modern PET scanners, the Poisson distribution is mainly used to model noisy projection data. More sophisticated proximal splitting techniques such as Douglas-Rachford splitting algorithm or variable splitting in an augmented Lagrangian framework can be explored for extending the algorithm for likelihood models based on Poisson noise. Moreover, the combination of time-of-flight and point spread function (PSF) technologies with MRI-guided PET image reconstruction is another interesting direction of research, which can maximize the potential of simultaneous PET/MRI. The combination of these techniques allows the reduction of inherent noise of PET data and also the errors induced by PSF reconstruction. Another potential future direction of work presented in this work is the extension of the proposed anatomically weighted total variation prior to a non-local TV prior and the evaluation of its performance with non-local means filtering, which has recently attained a great deal of attention in PET and medical imaging in general.

The field of compressed sensing (CS) has grown quickly and gained tremendous interest, since it provides a theoretically sound and computationally tractable method to accurately recover signal from the data acquired at sampling rates far below the Shannon-Nyquist limit. One of the major applications of CS technique is in sub-Nyquist MRI data acquisition and image reconstruction, which leads to reduced data acquisition time. CS-MRI is especially attractive for simultaneous PET/MRI with several time-consuming anatomical, functional and motion-tacking supplementary scans. In combination with parallel MRI (pMRI), CS is a particularly promising approach for ultra-short echo time (UTE) data acquisition for the visualization of structures with very short transverse magnetization such as bones and lungs. In this study, a single-coil CS MRI model was considered for the evaluation of the proposed linearized SCAD regularization. Future work might evaluate the algorithm for sensitivity encoded (SENSE) parallel MRI, which is amenable to combination with compressive sensing. Moreover, the proposed method was evaluated for Cartesian approximation of radial and spiral k -space trajectories. Future work also includes the application of the SCAD-ADMM algorithm for non-Cartesian MR data and therefore derivation of closed-form or iterative solutions to the sub-problems of the ADMM algorithm. The theoretical and experimental evaluation showed that the linearization of the SCAD norm invokes an adaptively reweighted L_1 norm which asymptotically behaves as L_1 and L_0 norms based on the selected scale parameters. Performance assessment of this norm with a family of reweighted L_1 norms and L_0 homotopic norms within the presented augmented Lagrangian framework is another possible direction for future investigations. In this study, the two scale parameters of the SCAD norm were heuristically set to obtain the best performance. An

alternative way to choose the involving pair parameters could be two-dimensional grids search using some criteria such as cross validation and L-curve methods, which is deferred to future work.

In a first clinical study, we demonstrated the great potential of time-of-flight PET technology for the reduction of PET quantification errors induced by standard MRI-based attenuation correction methods in PET/MRI. It was shown that TOF PET can both qualitatively and quantitatively reduce the artifacts and errors. Future work will focus on the further evaluation of the influence of TOF on increasing the diagnostic confidence of PET findings in the presence of metal-induced susceptibility and respiratory-phase mismatch artifacts on a large clinical database. Our results using a small number of patients showed that these artifacts not only result in quantification errors but also impair and complicate the qualitative interpretation of PET data in non-TOF image reconstruction. Conversely, TOF PET image reconstruction can substantially reduce the artifacts and quantification errors. Another interesting path for continuation of this work is the evaluation of TOF PET image reconstruction on reduction of the errors induced by metallic artifacts in TOF PET/CT scanners. This is promising for situations where MAR algorithms fail to completely reduce severe metal artifacts, usually occurring with multiple closely-seated metallic implants such as dental fillings, vertebra fixing screws, ... etc.

Following the recent rebirth of TOF PET, simultaneous estimation of activity and attenuation has regained popularity for attenuation correction on hybrid PET/MRI systems with spin-off applications in respiratory-phase misalignment correction between CT-based attenuation and PET activity maps in PET/CT systems. The joint estimation is especially attractive for PET/MRI to circumvent the uncertainties and obstacles of both standard and UTE MRAC methods. In this work, a constrained Gaussian mixture model was employed to regulate the estimation of attenuation based on MRI and CT prior information. A direct result of this model is the penalization of large deviations of attenuation coefficients from their expected values. Therefore, the scaling of attenuation and activity as well as noise and cross-talk artifacts in the attenuation map were remarkably suppressed. However, the performance of the proposed MLAA-GMM and lung constrained MLAA algorithms depends highly on the strength of weighting factors of the GMM prior. The choice of the hyper-parameters for regularized image reconstruction is usually not straightforward. In this work, we nearly optimized this parameter for a few patient datasets by trial and error and used it for all patient datasets. Future work includes the development of algorithms for the adaptive selection of this factor using discrete data consistency conditions or hierarchical Bayesian approach for its iterative estimation. Similarly, we heuristically selected the update schedule of the MLAA algorithm with a fixed number of global iterations for all patients. Another future path is to systematically evaluate the performance of the proposed MLAA algorithm for different update schedules and therefore to define a stopping criterion to reduce the number of parameters to be chosen. In the proposed algorithm, the GMM prior was spatially constrained using a tissue prior map obtained from Dixon fat and water MRI data and a co-registered bone probability map. The bone map was introduced to eliminate the mis-segmentations of the low-intensity spongy bones with surrounding tissues in water images. The derivation of bone maps includes the registration of multiple CT to MR images, which increases the number of preprocessing steps and the overall processing time. In brain studies, the bone map registration step can be skipped since the skull can be properly included in the tissue prior map. Moreover, the combination of T1 and proton-density weighted imaging and MR sequences that provide bone-cartilage contrast (i.e. T2-weighted water-excitation dual-echo steady-state and T2-weighted multi-echo data image combination) might provide a solution to better distinguish fat and soft-tissue from spongy bones, thus enabling to eliminate the bone probability map. Future work will therefore focus on the evaluation of the algorithm in brain studies without bone map generation step. In this study, the scatter sinograms were simulated using a 4-class MRAC attenuation map, which ignores bones. Future work also includes the evaluation of the impact of MRAC on single scatter simulation compared with the standard CTAC method and its implications on joint estimation of activity and attenuation in PET/MRI. Using simulation and clinical studies, it was demonstrated that the proposed GMM prior can reduce the dependency of the MLAA algorithm on count statistics and activity distribution. The performance of the algorithm was evaluated for two different tracers. However, in-depth investigation using different tracers and a large clinical database is highly commended to better evaluate the improvements achieved by the proposed algorithm.

In the last study conducted in this dissertation, a relatively small number of PET/MR/CT datasets could be included due to the limited prevalence of complementary PET/MRI and PET/CT studies in the clinical workup. Therefore, the statistical significance of our results might be subjected to a degree of uncertainty. Future work will focus on further evaluation of the studied attenuation correction methods using a large clinical database acquired with different tracers to further analyze the performance of the proposed MLAA algorithm.

Acknowledgements

I always dreamed pursuing a PhD program in which I can substantially learn about and investigate in model-based image reconstruction techniques in medical imaging. Although it took a lot of coffee and CPU time, today this dream became a reality. In these three years, I had the opportunity to investigate, develop and implement iterative image reconstruction and data correction techniques in PET/CT and PET/MRI imaging. However, it could not have been realized without the support and contributions of many people. Hence, I would like to take this opportunity to acknowledge all of them.

In particular, I express my gratitude to my advisor, Prof. Habib Zaidi, for his supports, encouragements and constructive guidance. Over these years, he encouraged me to have initiative in conducting the projects and to develop the necessary skills for becoming an independent early-stage researcher. I am really indebted of his support and vision.

I extend my gratitude to Prof. Sviatoslav Voloshynovskiy, my thesis co-advisor, for continuous encouragements and taking the administrative measures of my thesis and examinations. I am really impressed and inspired by his analytical skills in the formulation and parameterization of any professional and daily problem.

I would like to thank Prof. Mohammad Reza Ay, my mastership's advisor, who believed in my research abilities and encouraged me to follow a PhD program at PinLab.

I am grateful to the members of jury, Profs. Johan Nuyts, Freek Beckman, Jean-Philippe Thiran, Osman Ratib, Minerva Becker for examining my thesis. I am highly honored by the presence of Johan Nuyts, one of the celebrated experts in the field of model-based image reconstruction, as the member of jury. I also would like especially thank to Prof. Osman Ratib, the head of the department of nuclear medicine at HUGE for being warm, cordial and supportive to all researchers in the department.

I also would like to thank my colleague Fotis Kotasidis, with whom I had a lot of fruitful discussions and consultations about PET image reconstruction, particularly for the development of image reconstruction tools for clinical datasets, as well as PET pharmacokinetic modeling. I am really grateful to Fotis for his insightful advices and being open to discussions at anytime.

I also thank Nikolaos Karakatsanis and Hossein Arabi, with whom I also had very interesting discussions for whole-body dynamic PET imaging, time-of-flight PET image reconstruction and MR-based attenuation correction techniques. I extend my gratitude to Tianwu Xie, Giulia Di Domenicantonio, Jan Perhac, Sara Trombella, David Garcia and my former colleagues Daniel Gutierrez and Rameshwar Prasad.

My appreciation also goes to the reviewers of my journal articles for their constructive criticisms and suggestions that undoubtedly improved the overall quality of my work. I learnt a lot from their sometime harsh comments, especially, the fact that the maturity of a scientific work is as much important as its novelty.

I also thank the personal and staff of the department of nuclear medicine for their direct and indirect supports. I thank for the financial support from Swiss National Science Foundation and University of Geneva.

Last but not least, I would like to express my deepest gratitude to my parents for their support, encouragement and attempts to facilitate the academic education of their talented children.

Abolfazl Mehranian

14 May 2015
Geneva

List of publications

Peer-reviewed journals:

1. Mehranian A, Arabi H, Zaidi H, "Magnetic resonance imaging-guided attenuation correction in PET/MRI: challenges, solutions and opportunities" **Med Phys**, *submitted*
2. Mehranian A, and Zaidi H "Clinical assessment of emission- and segmentation-based MRI guided attenuation correction in whole-body TOF PET/MRI", **J Nucl Med**, 56, No. 6, pp 877-883 (2015).
3. Mehranian A, and Zaidi H "Emission-based estimation of lung attenuation coefficients for PET/MR attenuation correction", **Phys Med Biol**, (2015), *in press*
4. Mehranian A, and Zaidi H "Impact of time-of-flight PET on quantification errors in MRI-based attenuation correction", **J Nuc Med**, 56, No. 4, , pp 635-641 (2015).
5. Mehranian A, and Zaidi H "Joint estimation of activity and attenuation in whole-body TOF PET/MRI using constrained Gaussian mixture models" **IEEE Trans Med Imaging**, (2015), *in press*
6. Abdoli M, Mehranian A, Ailianou A, Becker M, and Zaidi H, "Comparative methods for hip prosthesis metal artifact reduction in pelvic CT ", **Phys Med Biol**, *under revision*
7. Mehranian A, Ay MR, Rahmim A and Zaidi H "3D prior image constrained projection completion for X-ray CT metal artifact reduction " **IEEE Trans Nucl Sci**, Vol. 60, No. 5, pp 1-15 (2013).
8. Mehranian A, Salighe Rad H, Ay MR, Rahmim A and Zaidi H "Smoothly clipped absolute deviation (SCAD) regularization for compressed sensing MRI using an augmented Lagrangian scheme", **Magn Reson Imaging**, 31(8), 1399-1411 (2013).
9. Mehranian A, Ay MR, Rahmim A and Zaidi H "X-ray CT metal artifact reduction using wavelet domain L_0 sparse regularization" **IEEE Trans Med Imaging**, Vol. 32, No. 9, pp 1707-1722 (2013).
10. Mehranian A, Rahmim A, Ay MR, Kotasidis F and Zaidi H "An ordered-subsets proximal preconditioned gradient algorithm for edge-preserving PET image reconstruction" **Med Phys**, Vol. 40, No. 5, pp 052503-14 (2013).

Conferences proceedings and abstracts:

1. Mehranian A, and Zaidi H "Clinical evaluation of emission- and segmentation-based MR guided attenuation correction in whole-body PET/MRI", **61st SNMMI Annual Meeting**, 2015, *in press*
2. Mehranian A, and Zaidi H "Accelerated time-of-flight (TOF) PET image reconstruction using TOF bin subsetization", **61st SNMMI Annual Meeting**, 2015, *in press*
3. Mehranian A, and Zaidi H "Emission-based estimation of lung attenuation coefficients for PET/MR attenuation correction", **61st SNMMI Annual Meeting**, 2015, *in press*
4. Mehranian A, and Zaidi H "Impact of time-of-flight PET on quantification errors in MRI-based attenuation correction", **61st SNMMI Annual Meeting**, 2015, *in press*
5. Mehranian A and Zaidi H " Joint estimation of activity and attenuation in PET/MR using MR-constrained Gaussian priors", **IEEE NSS MIC Conference**, 2014, *in press*
6. Abdoli M, Mehranian A, Ailianou A, Becker M, Zaidi H, "Comparative methods for metal artifact reduction in CT" **IEEE NSS MIC Conference**, 2014, *in press*
7. Mehranian A and Zaidi H "Joint estimation of activity and attenuation in TOF-PET/MR using constrained Gaussian mixture models" **60th SNMMI Annual Meeting**, Saint-Louis, USA, 7–11 June 2014, *J Nucl Med*, Vol. 55, Suppl. 1, pp 645.
8. Mehranian A and Zaidi H "MR constrained simultaneous reconstruction of activity and attenuation maps in brain TOF-PET/MR imaging" **PSMR 2014 MR-PET Workshop**, Kos, Greece, 19-21 Mai 2014, *EJNMMI Physics* 1, Suppl. 1, pp A55.
9. Mehranian A, Rahmim A, Ay MR and Zaidi H "An ordered-subsets proximal preconditioned gradient algorithm for total variation regularized PET image reconstruction" **IEEE NSS MIC Conference**, Anaheim, CA USA, 29 October – 3 November 2012, pp 3375-3382.

10. Mehranian A, Salighe Rad H, Rahmim A, Ay MR and Zaidi H "Smoothly clipped absolute deviation (SCAD) regularization for compressed sensing MRI using an augmented Lagrangian scheme" **IEEE NSS MIC Conference**, Anaheim, CA USA, 29 October – 3 November 2012, pp 3646-3653.
11. Mehranian A, MR Ay, A Rahmim, H Zaidi "Sparsity Constrained Sinogram Inpainting for Metal Artifact Reduction in X-ray Computed Tomography" **IEEE NSS MIC Conference**, Barcelona, Spain, 23-29 October 2011, pp3694–3699.
12. Mehranian A, MR Ay, A Rahmim, H Zaidi "Metal Artifact Reduction in CT-Based Attenuation Correction of PET using Sobolev Sinogram Restoration" **IEEE NSS MIC Conference**, Barcelona, Spain, 23-29 October 2011, pp2936-2942.